

**DESIGN AND SYNTHESIS OF CONFORMATIONALLY
FLEXIBLE AROMATIC AMIDES AND ESTERS: STUDY OF
BIOLOGICAL, SOLID STATE AND CHEMICAL SENSING
PROPERTIES**

THESIS

SUBMITTED TO THE

SAVITRIBAI PHULE PUNE UNIVERSITY

FOR THE DEGREE OF

DOCTOR OF PHILOSOPHY

IN

CHEMISTRY

BY

RUPESH LILADHAR GAWADE

RESERCH SUPERVISOR

Dr. (Mrs.) V. G. PURANIK

RESERCH CO-SUPERVISOR

Dr. R. G. GONNADE

PHYSICAL AND MATERIAL CHEMISTRY DIVISION

CSIR-NATIONAL CHEMICAL LABORATORY

PUNE 411 008, INDIA

SEPTEMBER 2016

Dedicated to my Beloved Family.....



For you!

*“The journey never ends; it begins with new perspective
and new challenge”*

CERTIFICATE

This is to certify that the work incorporated in the thesis entitled "**Design and Synthesis of Conformationally Flexible Aromatic Amides and Esters: Study of Biological, Solid State and Chemical Sensing Properties**" submitted by **Rupesh Liladhar Gawade** was carried out by him under my supervision at the CSIR-National Chemical Laboratory, Pune, India. Such materials, obtained from other sources have been duly acknowledged in the thesis.

Date:

(Dr. Vedavati G. Puranik)

Division of Physical and
Material Chemistry

Research Guide

CSIR-National Chemical Laboratory
Pune-411008, India.

(Dr. Rajesh G. Gonnade)

Research Co-Guide



CSIR-National Chemical Laboratory (India)

DECLARATION

I hereby declare that the thesis entitled "**Design and Synthesis of Conformationally Flexible Aromatic Amides and Esters: Study of Biological, Solid State and Chemical Sensing Properties**" submitted for Ph.D. degree to the Savitribai Phule Pune University has been carried out at CSIR-National Chemical Laboratory, under the guidance of **Dr. (Mrs.) V. G. Puranik** and co-guidance of **Dr. Rajesh G. Gonnade**. This work is original and has not been submitted in part or full by me for any degree or diploma to any university.

Date:

Physical and Material Chemistry Division

(Rupesh Liladhar Gawade)

CSIR-National Chemical Laboratory

Pune-411008.

Acknowledgement

I thank my guide Dr. Mrs. Vedavati G. Puranik for giving me the opportunity to work under her guidance and pursue my PhD at CSIR-NCL. Her in-depth understanding of science helped me to enhance my scientific aptitude and thinking. I am immensely grateful to my co-guide Dr. Rajesh G. Gonnade for teaching me crystallography at great detail. His passion towards science and strategic approach towards problem solving helped me to develop my scientific vision and writing. My guide and co-guide provided the excellent scientific niche which mitigated the obstacle for exploring new sciences and learning new things. I wish to express my deep sense of gratitude and profound thanks to my research supervisors Dr. (Mrs.) Vedavati G. Puranik and Dr. Rajesh G. Gonnade for introducing me to the fascinating field of crystallography.

I thank our former director Dr. Sourav Pal and current director Dr. Ashwini Nangia for providing financial support and world-class facilities. I thank Dr. R. R. Joshi and Dr. Mrs. R. R. Joshi for allowing me to learn and perform organic reactions under their guidance. I thank Dr. Nithynandan for guiding me for designing the chemical sensing experiments. I thank Dr. Ayesha Khan, UOP for teaching me cell culture and molecular biology studies. I thank Dr. Deepti Deobagkar, UOP for allowing me to work under her guidance and setting up molecular biology experiments. I am grateful to Dr. Avinash Kumbhar, Dr. Mrs. Anupa Kumbhar and Dr. Mrs. Sunitha Salunke, UOP for their positive inputs during discussions of my PhD problems. I thank Dr. P. R. Rajmohan, Dr. Kumar Vanka, Dr. Rahul Banerjee for their encouragement and valuable suggestions. I thank Dr. Uddhvesh Sonavane and Dr. Rajendra Joshi, CDAC for teaching me molecular docking and allowing me to use their high end facilities. I am grateful to Dr. Sanjayan for collaborating and giving an opportunity to work on exciting structures.

I thank SAC Chairman, Dr. M. Shashidhar, for helping and guiding me for scientific and administration related issues during my PhD journey. I thank Mrs. Kolhe and Mrs. Puranik for helping for the PhD related documentation.

I thank my family for supporting me during this journey, without their help this was an impossible goal. Their support and inspiration help me to nurture my passion and devote myself with full strength. I am grateful to my mother and father who did lot of scarifices and worked hard for my education and intellectual development. I thank my wife Debamitra for constantly motivating and inspiring me during this journey. Her intellectual and fruitful inputs helped me to work on my weaknesses and to design strategies for completion of doctoral work. I am thankful to my brothers Aashish, Dipak and sister Amruta and Debanjana for their constant encouragement and support.

I thank my friends Dr. Tukaram, Dr. Shivaji, Sachin, Dr. Anil, Dipesh, Amol, Dr. Siddhangouda, Dr. Sangram and Dr Majid for teaching chemistry to non-chemist person (me). I specially thank Amol for his help for conduction NMR studies. Their guidance helped me to design my own experiments. I am grateful to Deepak, Ravi and Dr. Sanjay Negi for providing me the opportunity to work on my managerial and leadership skills. I am thankful to Dr. Manas and Dr. Priyabarta Panigrahi for guiding me on Bioinformatics assignments during my PhD. I thank Dr. Himadri for his intellectual discussions. I am grateful to Dr. Joyashish Debgupta who guided and taught me electrochemistry.

I thank my colleagues Pranaya, Mrs. Pooja, Shridhar, Ekta, Samir, Veer, Nivedita, Sanjay, Awais, Neethu, Tiwary, Abhilash, Suvarna and Harish for providing cheerful environment and helping me for setting up my experiments. My entrepreneurial skills enhanced while working with the excellent team.

*I began this journey as amateur student who had curiosity to learn and explore. At the end of the journey I find myself as highly motivated scientific personnel who loves, accepts and enjoys scientific challenges. I thank all those who accompanied me during this journey. **“The journey never ends; it begins with new perspective and new challenge”**. I dedicate my PhD to my mother and wife.*

Rupesh Liladhar Gawade

CONTENTS

Title	Page No.
Abbreviations	i
Abstract of the thesis.	iii
List of publications	xxvi
Chapter 1: The Structure-property relationship (SPR) between conformationally flexible procainamide analogues and their DNA hypomethylating effect	
Introduction	2
Result and discussion	5
Conclusion	24
Experimental methods	26
References	46
Chapter 2A: Design and synthesis of conformationally flexible 1D architecture of Cu⁺² coordination complex: study of vapochromic and anion sensing properties	
Introduction	52
Result and discussion	59
Conclusion	89
Experimental methods	90
References	97
Chapter 2B: The Structure-property relationship between conformationally flexible Benzophenone-quinoline conjugates and their turn-on acid sensing properties	
Introduction	100

Result and discussion	103
Conclusion	140
Experimental methods	141
References	162

Chapter 3: Study of conformational polymorphism of flexible sulfonamides and sulphoester having alternating electron rich and electron deficient aromatics

Introduction	166
Result and discussion	168
Conclusion	227
Experimental methods	228
References	246

Chapter 4. Design and synthesis of conformationally flexible *p*-substituted sulphoester trimers: investigating substituent effect on π -stacking interaction in solution and solid state

Introduction	252
Result and discussion	263
Conclusion	286
Experimental methods	291
References	308

Summary	310
Future Scope	312
List of papers and patents published (related to thesis)	313
List of conferences attended	313
List of papers not related to thesis	314

Abbreviations

Anhd.	Anhydrous
Aq.	Aqueous
Conc.	Concentrated
Sat.	Saturated
Calcd.	Calulated
D ₂ O	Deuterium Oxide
DCM	Dichloromethane
dil.	Dilute
DMF	<i>N, N</i> -Dimethylformamide
DMSO	Dimethyl sulfoxide
eq.	Equivalent
Et ₃ N	Triethylamine
G	Gram
h	Hour
Hz	Hertz
IR	Infrared
LC-MS	Liquid chromatography-Mass Spectrometry
HR-MS	High Resolution - Mass Spectrometry
Mp	Melting point
mg	Milli gram
min.	Minutes
mL	Milliliter
mmol	Milli moles
NMR	Nuclear Magnetic Resonance

Nu	Nucleophile
ORTEP	Oak Ridge Thermal Ellipsoid Plot Program
Ph	Phenyl
Py	Pyridine
<i>rac-</i>	Racemic
rt	Room Temperature (23-30 °C)
Rf	Retention factor
TLC	Thin layer chromatography
s	singlet
d	doublet
t	triplet
q	quartet
m	multiplet
br.	broad
PNC	Prenuclei clustering
DPV	Differential Pulse Voltametry

Abstract of the thesis

Conformational flexibility is attributed to the ability of the molecules to adopt different orientations due to free rotation along the single bond. The knowledge of conformational flexibility is essential to study protein structure-function; protein folding, dynamic nature of DNA, protein-drug and DNA-drug binding.¹⁻⁵ Moreover, polymer and material science also seek the understanding of conformational flexibility of monomeric units in order to construct structurally dynamic polymers.⁶⁻⁷

Generally, molecules possess translational, rotational and vibrational motions. Translational motion is defined as the shift of position of molecules from one point to another point in three dimensions. Translational motion does not contribute for the conformational flexibility. However, it significantly affects the entropy and collision frequency of the molecules. Vibrational motion is defined as the motion that causes the changes in the shape of the molecule. The stretching vibration changes the bond length between the two atoms whereas; bending vibration changes the bond angle between the three atoms in the molecule. Rotational motion is of two types namely, 1) principle rotational motion which occurs when whole molecule rotates around the principle axis and 2) intramolecular rotation when the atoms connected by bond rotates with respect to each other. The intramolecular rotation is the major contributing factor for the conformational variation within the molecule. The rotation across the bond changes the torsional angle that causes significant conformational change. Intramolecular rotation occurs freely if the two atoms are linked by single bond. However, the internal rotation is hindered when the atoms are joined by higher order bonds i.e. double or triple. Moreover, the internal rotation is also constrained by the presence of rigid moieties such as aromatic, cyclic moieties (adamantane) and lone pair bearing atoms(e.g. nitrogen, oxygen etc.) at certain positions within molecule. Overall effect of intra-molecular motion governs the entropic association amongst the molecules. Conformational flexibility within the molecule can be regarded as global flexibility and represented as the cumulative value of local flexibility terms,

$$G_f = L_1 + L_1 \dots \dots \dots L_n$$

G_f: Global flexibility within the molecule

$L_{1\dots n}$: Local flexibility terms within the molecule

The decrease of conformational flexibility corresponding to the structural variation is shown in figure 1. The alkyl chain without any substitution is highly flexible, however, incorporation of sulfoester, sulfonamide, carboester and carboxamide moieties decrease the global flexibility in the descending order. The analysis is presented based on the CSD database search.⁸

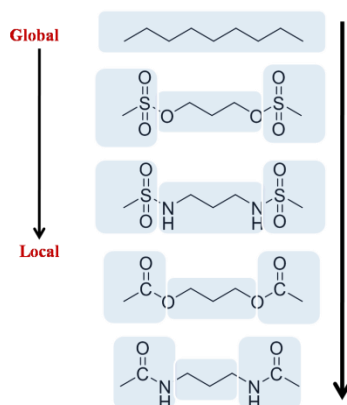


Figure 1. Un-substituted and substituted alkyl chain and the order of decrease in the global conformational flexibility.

Rotational motion in conjunction with the vibrational motion determines the conformational space within which the molecules are free to rotate. Conformational space of the molecules is marked by vander Waals radii of the atoms present within the molecule. The homogenous or heterogeneous mixture of molecules in gaseous state possesses highest entropy because of the least association between the molecules. The change in the state of the matter from gaseous to solution state results in the decrease of entropy and increase in the frequency of effective collision. The effective collision can be defined as the collision between the two molecules which has resulted in the form of dimeric or multimeric association. For the chemical reactions, the effective collision forms strong bonds such as ionic, covalent or coordinate to form reactive intermediate or transition state. However, in case of regulatory reaction, e.g. enzyme-substrate reactions, the effective collision form strong non-covalent (acid-base, salt bridges, hydrogen bonding, hydrophobic) interactions. Furthermore, for multimeric reactions such as crystallization, the transition state may represent the formation of prenuclei clustering (PNC) during nucleation. As per the free energy equation,

$$\Delta G = \Delta H - T\Delta S$$

ΔG : change in the free energy of the system.

T: absolute temperature

ΔH : Change in the enthalpy of the system.

ΔS : Change in the entropy of the system.

The spontaneity of favorable processes are associated with the increase in the entropy, however, in the dimeric or multimeric molecular association, entropy of the system decreases. This is compensated by the decrease in the enthalpy of system. The released heat content is driven by the effective collision that occurs when the two molecules establish strong intermolecular association with each other. Their intermolecular interaction can be characterized by conformational flexibility which allows them to organize and achieve the best fit (complementary interactions). The best fit between any two molecules is possible only when the attractive intermolecular forces between them dominate the entropic penalty of the system. This also forms the basis of important processes such as cell-cell signaling, enzymatic reactions and immune response (antigen-antibody binding), drug-DNA/protein binding, crystallization. Enzyme-substrate binding involves conformational sampling of the substrate molecules and the best pose is chosen for the activation or inhibition of the enzyme. Similarly structure-based drug designing involves identification of multi-pocket(receptor) binding ligands with intrinsic conformational flexibility. **Figure 2** illustrates the cartoon representation of dimeric and multimeric association of conformationally flexible and rigid compounds.

In depth understanding of the structural insight to construct the compounds with predictable association during the transition state, is the basis of many fields such as organic and inorganic crystal engineering,⁹⁻¹¹ drug design⁵ and custom made sensors.¹²⁻¹³ Recently launched Anti-AIDS drug design programme mainly focused on finding conformationally flexible inhibitors of reverse transcriptase enzymes owing to its high antigenic variation within the drug binding pocket. Similar strategy is adopted by the solid-state and material scientists for modulating the topological and physicochemical properties of the pharmaceutical compounds, sensory molecules and porous materials (MOF, COF, Zeolites etc.).¹⁴⁻¹⁷

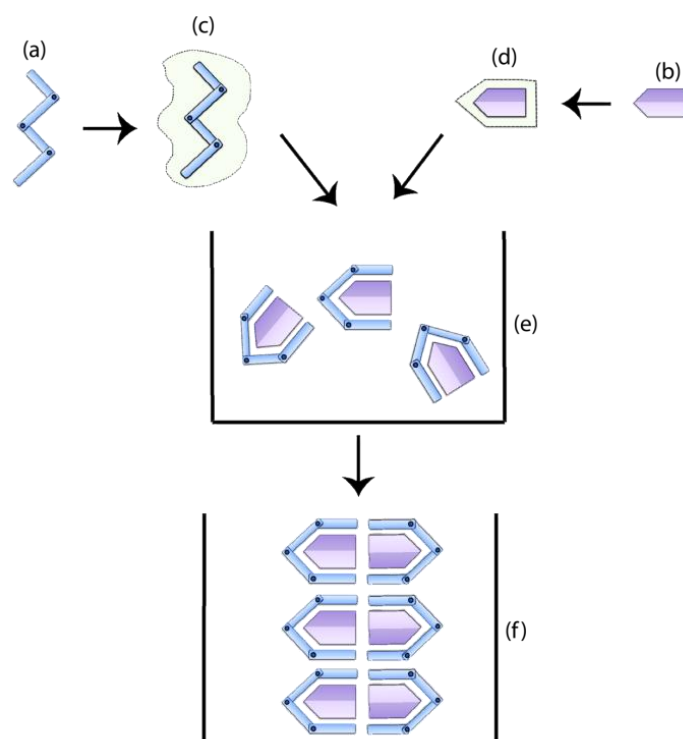


Figure 2. (a) Conformationally flexible Molecule A, (b) Conformationally rigid Molecules B, having different size and shape, (c) and (d) represents conformational space of A and B that is marked by their vander Waals radii, (e) Conformational adaptability and best possible fitting (association) between flexible A and rigid B molecules at the effective collision e.g. enzyme-substrate binding, drug-protein binding, (f) extension of dimeric association in 2D/3D to form self-assembly e.g. nucleation, polymerization.

As a part of my doctoral work, we have designed conformationally flexible organic/inorganic aromatic compounds in order to study its structure property correlation. The conformational flexibility was used as tool for achieving the effective collision between the guest and host or desired conformation. The flexibility is incorporated by using flexible alkyl chain in conjunction with amide/ester moieties. In each chapter, the lead compound is chosen to study its excited yet unexplored properties associated with its molecular architecture in solution or solid state. The derivatives of the compounds under study were designed to relate the structure-property relation (SPR) in order to investigate the mechanistic basis of their properties. Based on the investigation we also hypothesized the putative mechanism and scope of

improving the activity parameters for compounds under study. The graphical overview of the work undertaken in the thesis is depicted in the figure 3. In chapter 1, the lead compound was chosen as procainamide drug whose conformationally flexible side chain derivatives were used for structure property relation. The binding affinity of these derivatives towards guest i.e. CpG rich DNA was used to evaluate their differential DNA hypomethylating effect. In chapter 2A, conformationally flexible Cu(II) coordination complex displaying metamorphic property in three dimensional packing architecture was constructed as host. The guest (anions and solvent) exchange ability of the complex was investigated in solid state to elucidate the mechanism and exploring its sensing applications. In chapter 2B, the shift in the absorption and emission properties of designed benzophenones-quinoline conjugates (host) were used

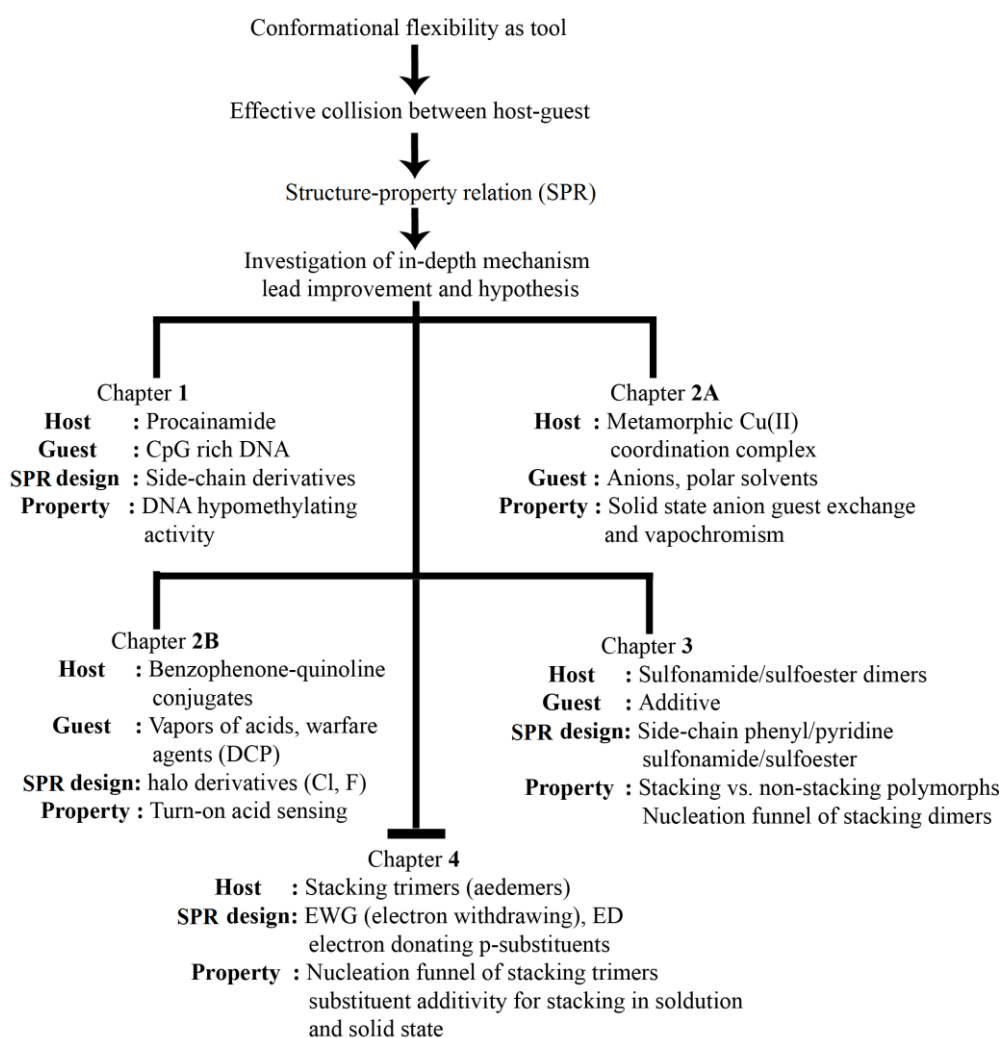


Figure 3. Depiction of overview of work undertaken in thesis in different chapters.

for studying their application for solid state detection of acids vapors and chemical warfare agent (guest). Differential reactivity and turn-on response of the derivatives were used to investigate the putative mechanism of their action and lead improvement. In chapter 3, alternating electron rich (phenyl/pyridine) and electron poor (*p*-nitro benzene) aromatic units joined together with sulfonamide/sulfoester containing flexible hinge (host) were designed for studying their conformational polymorphism (stacking vs. non-stacking) in solid state in the presence of additive. The study unravels the nucleation funnel of sulfonamide/sulfoester containing compounds possessing varying H-bonding propensities and the role of additive effect at prenucleation clustering. The study is further extended in chapter 4; however, here trimers containing varying substituent at the para position of electron poor ring were used for investigating the nucleation funnel of stacking trimmers and elucidating the role of additivity of substituent in solution and solid state.

Chapter 1: The Structure-property relationship (SPR) between conformationally flexible procainamide analogues and their DNA hypomethylating effect

In chapter 1, the structure-property relation (SPR) between the side-chain topology of conformationally flexible procainamide analogues and their DNA hypomethylating activity was investigated. The conformational flexibility of side-chain is attributed to the presence of -CH₂-CH₂- spacer that allowed variation in the dihedral angle between plane containing 4-amino benzamide and side-chain moieties. Synthesized derivatives comprise of flexible (dimethyl), constrained (pyrrolidine, piperidine, morpholine) and planar aromatic (pyridine, phenyl) side chain motifs as shown in the Figure 4. Due to the conformational flexibility, the molecules have easily adapted their bioactive conformation and achieved maximum structural association within binding site pocket of the CpG rich DNA. We simulated their effective collision i.e. DNA binding affinity using docking study. In this study we considered the structural constraints terms of planar carboxamide group and flexibility terms of side-chain to generate the bioactive conformation. Further, these conformations were used for docking and best pose was chosen for the comparative analysis. The comparison between the docked conformations and bioactive properties (differential pulse voltametry, *in vitro* cytotoxicity, global methylation index, DNMT-1 inhibition) revealed significant correlation. The structure-property study has

unrevealed the putative mechanism of DNA hypomethylating effect of procainamide and also gave lead (compound **1**) with enhanced activity.

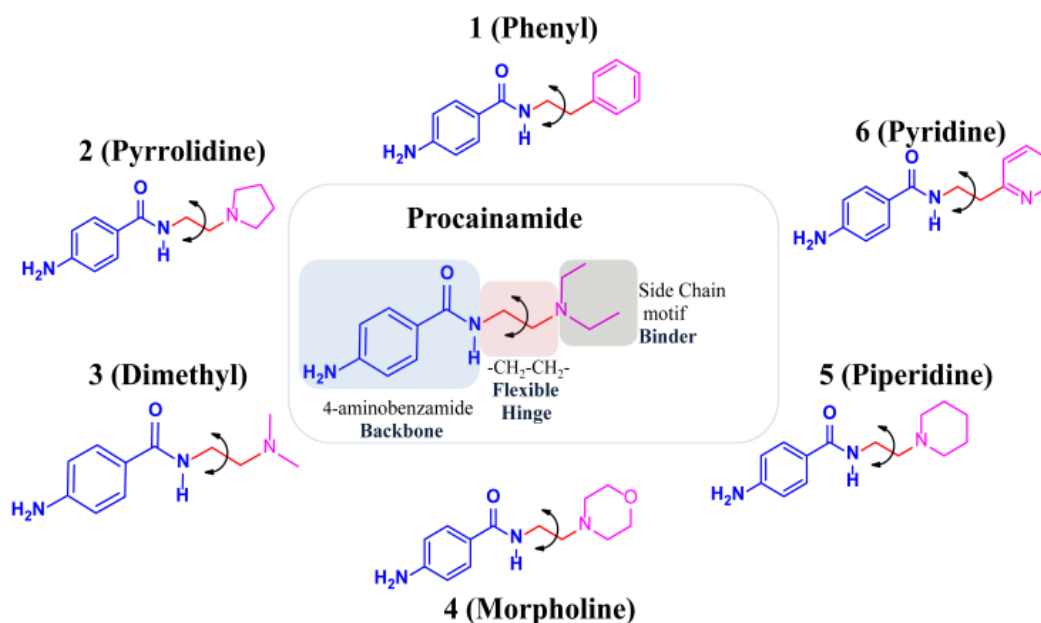


Figure 4. Description of pharmacophore features of procainamide and molecular structures of its side chain motif derivatives **1-6**.

Chapter 2A: Design and synthesis of conformationally flexible 1D architecture of Cu⁺² coordination complex: study of vapochromic and anion sensing properties

In chapter **2A**, we explored the three dimensional conformational flexibility of solid state metamorphic architecture consisting of conformationally flexible ligand and reporter metal centre (Cu⁺²) for entrapment of guest analytes. For designing of the ligand, clues were sought from chapter **1**. The compound **1**(phenyl) upon intercalation forms $\pi\cdots\pi$ stacking interactions with dG nucleobase and become integral part of DNA ladder (**figure 5**). Further, the carboxamide functionality of **1** has supplemented the association by forming N-H \cdots O H-bonding with dG nucleobase. We envisioned that the compound **1** can be used as ligand which may form the ladder like packing arrangement similar to DNA by establishing intermolecular stacking interaction that may also provide spatial rigidity. The joining of these ladders with strong H-bonded glue (amide...amide synthons) and flexible metal coordination sphere may provide conformationally flexible 3D coordination framework (**Figure 6**). We used isonicotinamide instead of 4-aminobenzamide backbone for providing metal

coordination site. The Cu(II) metal is used as reporter group due to its strong colorimetric property.

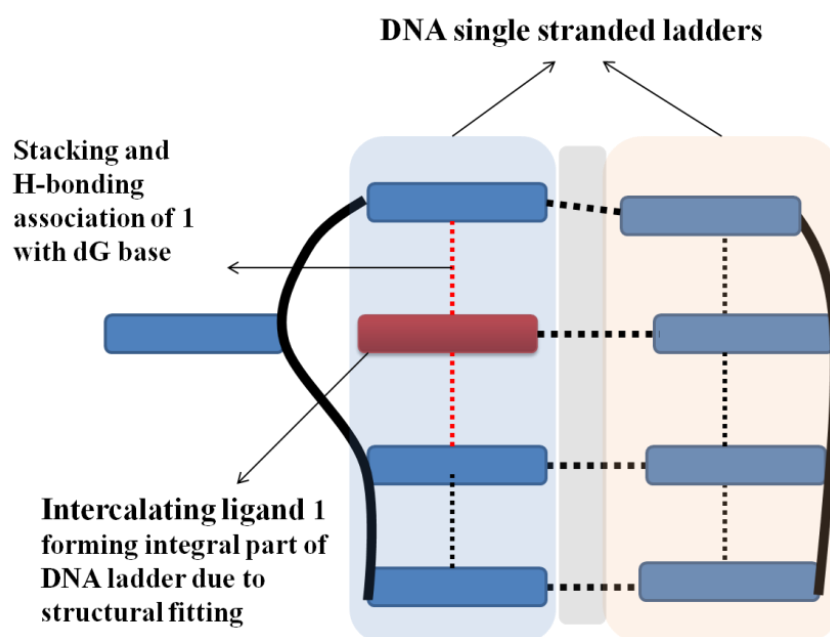
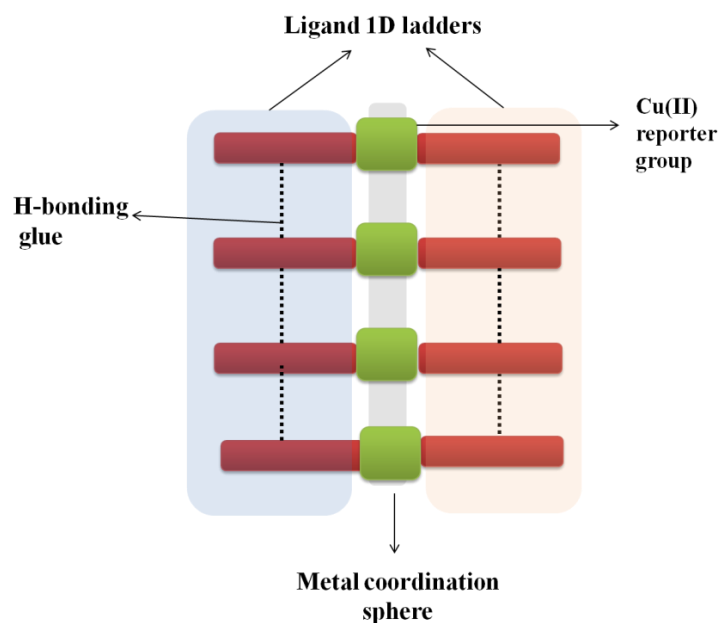
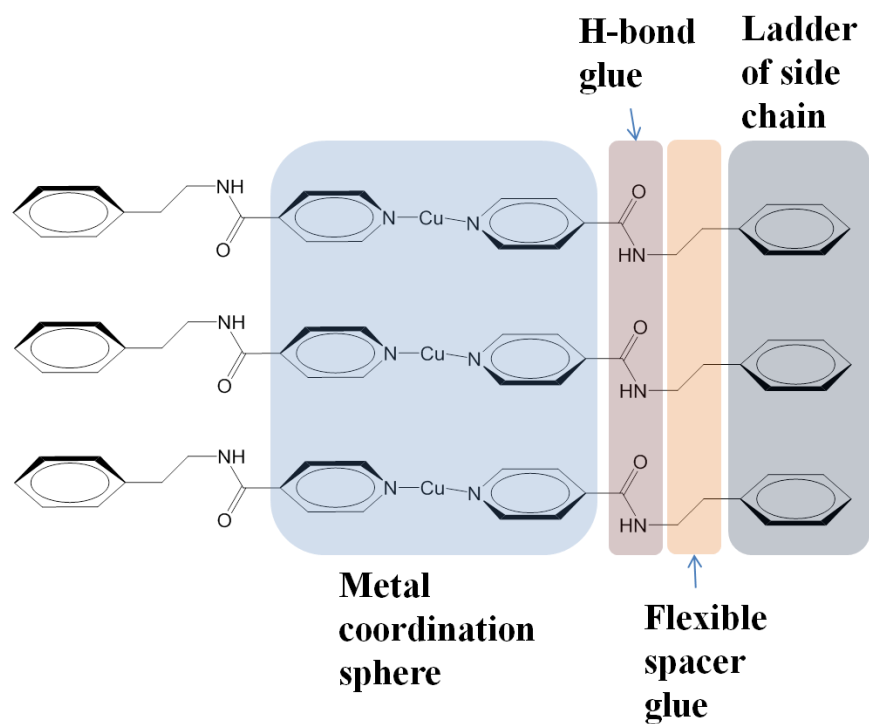


Figure 5. The depiction of interaction between compound 1 in chapter 1, inside DNA intercalation pocket.



(a)



(b)

Figure 6. The predicted ladder like packing arrangement of Cu(II)-ligand coordination complex in solid state (a) cartoon depiction (b) structural depiction

We designed metal-coordinated one-dimensional extended architecture comprising isonicotinamide conjugated with phenethylene group as supramolecular reagent and Cu^{+2} as reactive metal centre. Both the groups are joined together by - $\text{CH}_2\text{-CH}_2\text{-}$ spacer. Interplay of strong hydrogen bonding and weak intermolecular forces provided conformationally metamorphic 3D supramolecular assembly for entrapping the guest moieties having different shapes and sizes. We studied its vapochromic response towards polar/nonpolar solvent vapours which prompted us to investigate its applicability for detecting Cl^- , Br^- , SCN^- , CH_3COO^- and HCOO^- anionic guests in completely aqueous media. Crystallographic evidences, solid state UV absorbance and *in-situ* E-SEM study provided mechanistic insight and structural basis of its metamorphic nature. The 1D hydrophilic channel submerged in the hydrophobic cavity allowed the guest exchange and structural rearrangement at the metal coordination site resulting in the change in the colorimetric properties. The chromic change is attributed to the shift in the excited state properties i.e. metal ligand transfer transfer (MLCT). The presence of 1D channel acts as template and prevented the crumbling of crystal lattice during guest exchange. Thereby, solid-solid guest exchange/transfer could occur similar to that of Oswald ripening.

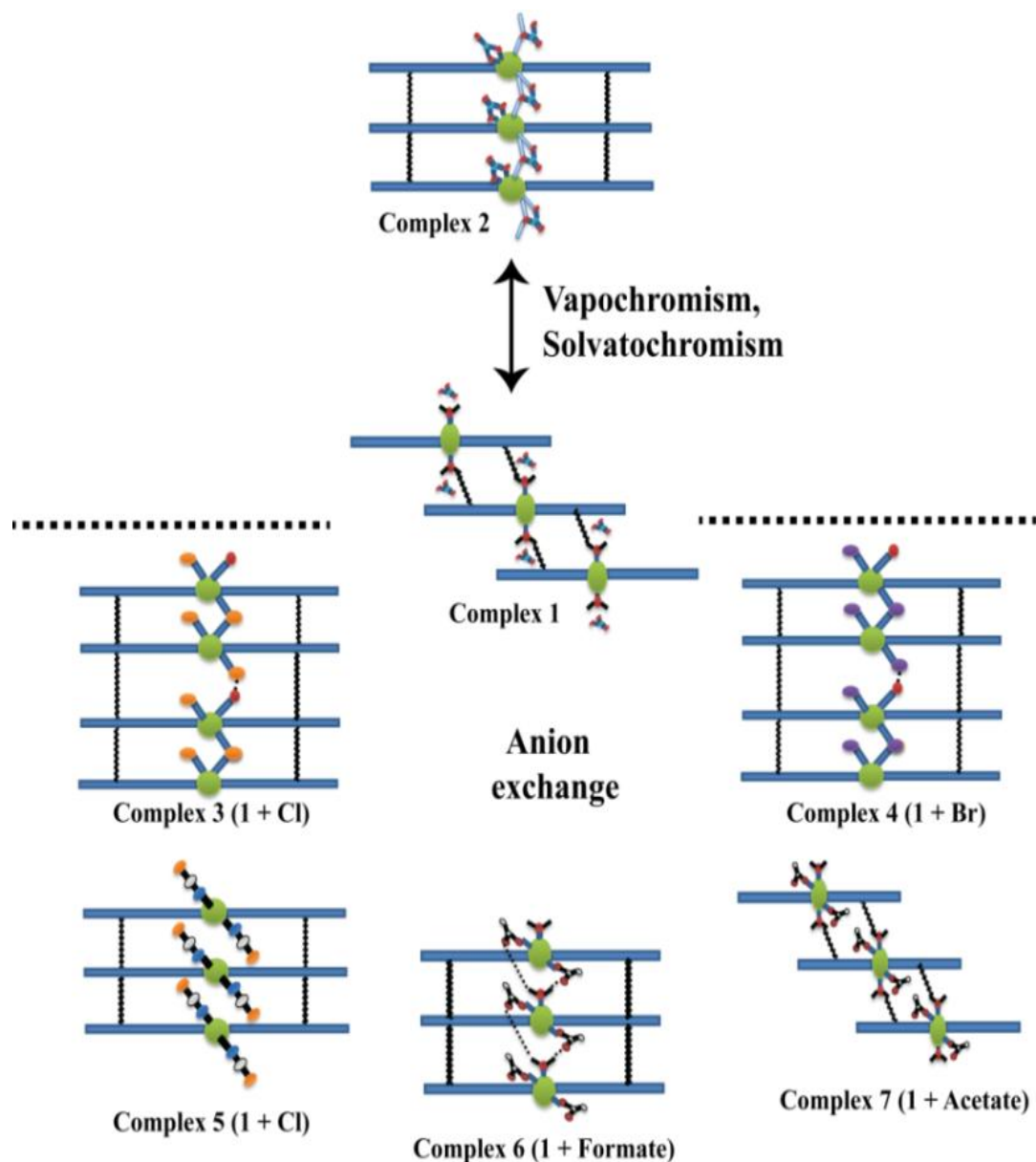


Figure 7. Illustration of the structural transformation metamorphic architecture of complex **1** after entrapment of guest molecules. Coordination framework of complex **1** act as transformable template which show vapochromic, solvatochromic response to vapors of polar solvent and guest-induced chromism for solution/solid state anion exchange (anions like Cl^- , Br^- , SCN^- , HCOO^- , CH_3COO^-).

Finally we demonstrated the enigmatic potential of the compounds to discriminate between the chloride and bromide salts by simple grinding method. **Figure 7** illustrates the pictorial depiction of structural transformation of metamorphic architecture of complex **1** after entrapment of guest molecules.

Chapter 2B: The Structure-property relationship between conformationally flexible Benzophenone-quinoline conjugates and their turn-on acid sensing properties

In chapter 1 and chapter 2A, we observed that when two rigid moieties or functional fragments are interconnected with flexible spacers, bioactivity (DNA intercalating nature) or sensing properties (solid state guest exchange) are significantly enhanced due to the allowed conformational adaptability of ligands. Taking that into account, we designed our chapter 2B in which two rigid moieties benzophenone and quinoline which can share charge transfer donor and acceptor relation with each other are joined together by flexible Ar-NH-Ar spacer (**figure 8**). These benzophenone-quinoline conjugates showed remarkable shift in their absorption and emission properties when exposed to vapors of volatile acids or chemical warfare agent mimic DCP (Diethyl chloro phosphate). The shift in their excited state properties is attributed to the formation of azaquinazolinium ions when exposed to acidic condition. For our study different derivatives were prepared by substituting chlorine (Cl) and fluorine (F) at X1 and X2 positions to study structure-property correlation pertaining to their reactivity and turn-on fluorescent activity (**Figure 9**). Excess of H⁺ ions mediate *O*-protonation of benzophenones to generate carbocations. The conformational flexibility of Ar-NH-Ar fragment allowed the tandem intramolecular C(sp²)⁺-N cyclization that occurs between electrophilic carbocation and nucleophilic Nitrogen (N1) of quinoline and involves almost 180° rotation of dihedral angle between the quinoline and protonated benzophenone groups. Further transfer of positive charge generates a chiral centre and cationic nitrogen (azonia) (**Figure 10**). Acid (H⁺) promoted intramolecular cyclization and ratio-metric response of the probes were studied by X-ray crystallography, NMR and spectroscopic methods. Further, fluorescence enhancement and the role of halogen bonding interaction were investigated by structure-property relation and DFT/TDDFT calculation. Reversible nature of highly active probe was demonstrated by simple experimental protocol. The reactivity of the probe depends on the acidity of the solution which is attributed to the differential affinity towards proton. The compounds with substituted -Cl atom (C9) showed highest enhancement (12 times) in the fluorescence which is attributed to solution state three centre N-Cl-N⁺ halogen bonding (**figure 11**). The reversible nature and solid state turn-on response showed

potential application of these compounds for the onsite detection of acid leaks and chemical warfare agents (DCP). The applicability of highest active compound **3d** for onsite-detection is demonstrated by constructing an alarming device.

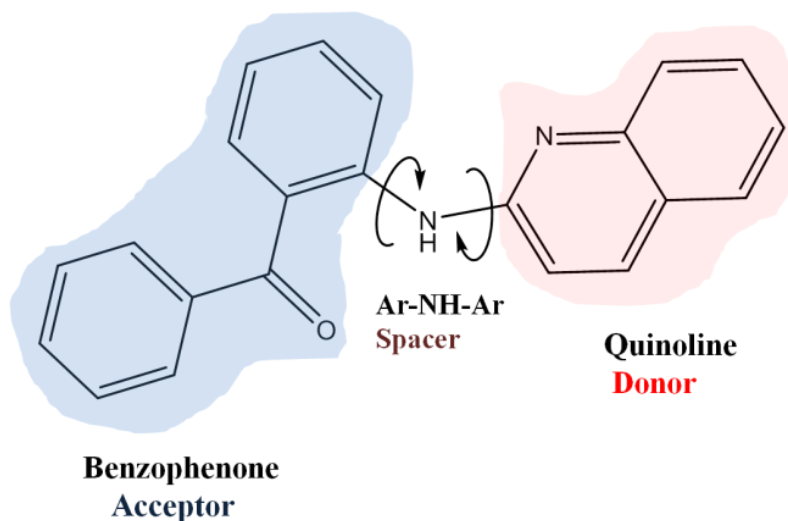


Figure 8. Depiction of benzophenone-quinoline conjugate separated by Ar-NH-Ar spacer.

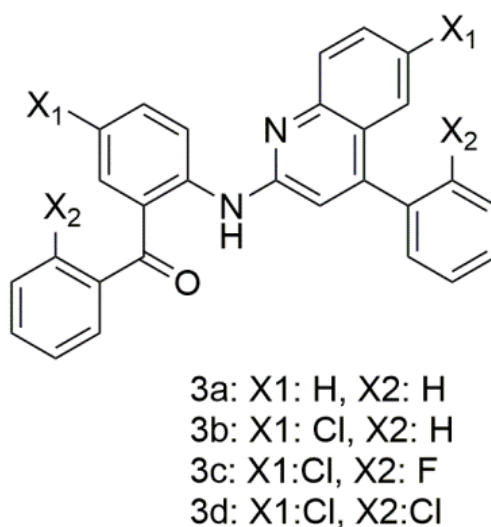


Figure 9. The halo derivatives of benzophenone-quinoline turn-on probe conjugates designed for studying structure-property(acid sensing).

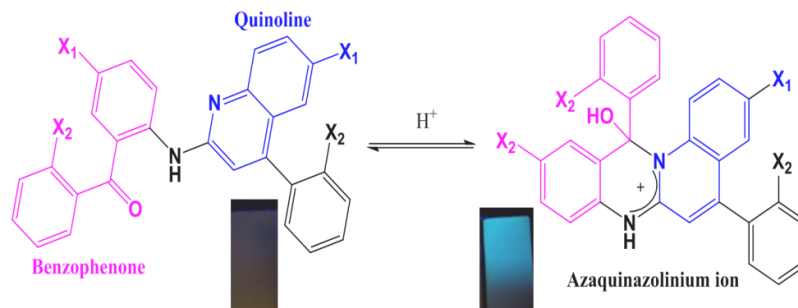
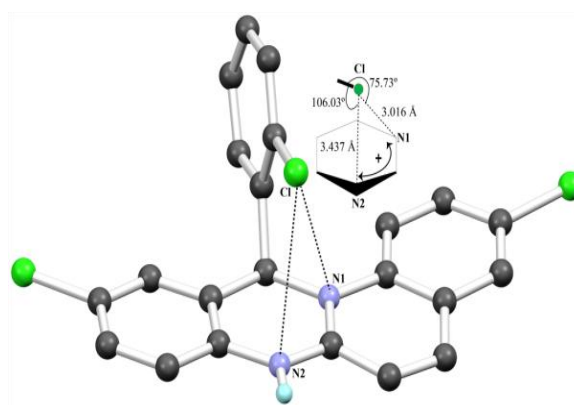
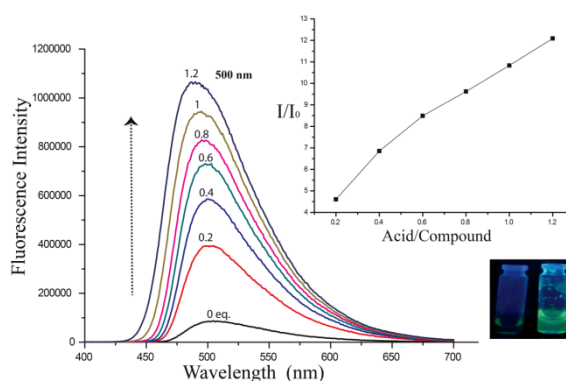


Figure 10. The mechanism and solid state response of quinoline-benzophenone conjugates as acid sensor. Non-fluorescent benzophenone-quinoline conjugates form fluorescent azaquinazolinium ions under the acidic condition and show remarkable changes in the absorption and emission bands.



(a)



(b)

Figure 11. (a) Geometrical parameters of intramolecular interactions of Cl and N atoms of **4d**, (b) Fluorescence spectra of the **3d** (1.67 mM) in chloroform on addition of 0.2, 0.4, 0.6, 0.8 and 1 eq. of HCl in MeOH.

Chapter 3: Study of Conformational polymorphism of flexible sulfonamides and sulfoesters having alternating electron rich and electron deficient aromatics

In chapter 3, we used dimers possessing alternating electron rich and electron deficient aromatics for exploring solid state stacking vs. non-stacking polymorphs. The aromatic units are joined together by flexible hinge comprising of sulphonamide/sulfoester group and $-\text{CH}_2-\text{CH}_2-$ spacer. Generally the sulphonamide/sulfoester groups are flexible as compared to its counterpart carboxamide groups which are constrained and rigid. Furthermore, sulphonamide groups provide more hydrogen rich environment owing to its higher H-bonding propensity compare to sulfoester moiety (**Figure 12**). The reason behind using sulphonamide/sulfoester group is to allow more conformational flexibility to attain the desired conformations in solid state. The comparative analysis of stacking vs. non-stacking polymorphs offers the understanding of role of H-bonding and stacking interactions during the nucleation process especially at the pre-nucleation clustering. The study may unravel the nucleation funnel of compounds which possess the propensity of forming stacked structures in the solid state.

In chapter 3, for investigating the role of stacking interaction during nucleation event of crystallization, we used candidate compounds which are inspired from the compound 1 and 2 of chapter 1 with some modification. The *p*-amino group was replaced with *p*-nitro group and carboxamide functionality is replaced with sulfonamide/sulfoester groups. The molecular structures of compounds 1-4 are provided in the **figure 13**. *p*-nitro substituted arene unit serve as electron deficient aromatic surface due to electron withdrawing effect of nitro group whereas the unsubstituted phenyl or pyridine rings serve as electron rich aromatic face. Both the groups are joined together with conformationally flexible sulfoester /sulfonamide hinge in conjunction with $-\text{CH}_2-\text{CH}_2-$ spacer. Stacking polymorphs were obtained in all the crystallization trials in spite of many crystallization trials. To obtain non-stacking polymorphs non-isostructural pyrazinamide additive was used. The generated conformational and packing polymorphs share interesting thermodynamic relationship with each other and also revealed phase transition behaviour. The detailed investigation and comparative study highlighted the pivotal role played by extended $\pi\cdots\pi$ stacking supramolecular assembly along with $\text{N-H}\cdots\text{O}/\text{N-H}\cdots\text{N}/\text{C-H}\cdots\text{O}$

hydrogen bonding in dictating the self-assembly thereby provide stability to *syn* PNC during nucleation process.¹⁸ The intervention of stable stacking assembly by introducing additives generates new metastable polymorphs (**Figure 14**). The pyrazinamide additive played a pivotal role for providing an alternate nucleation path (crystallographic gene!) which aid in capturing the elusive polymorphs by epitaxial method. We speculated that it is possible to predict and generate selective polymorphic form using tailor made auxiliaries, although, it is critical for designing such additives in more general way to control its inhibition or promotion. The studies undertaken in chapter 3 revealed the need of detailed investigation of behavior of stacking interaction in solution and solid state. In depth understanding of their exact role in different states of the matter may unravel the mystery of topological variation and structural dynamic nature of large biomolecules such as DNA and RNA which are self-assembled via extended stacking interactions.

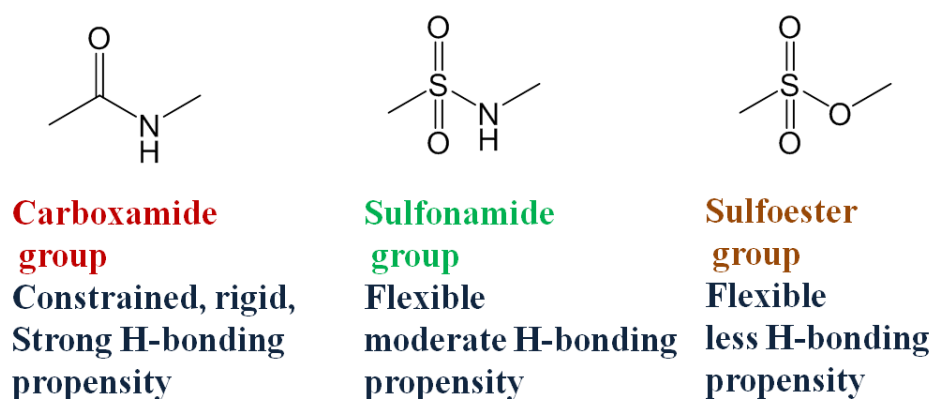


Figure 12. The comparative analysis of carboxamide, sulfonamide and sulfoester functionalities.

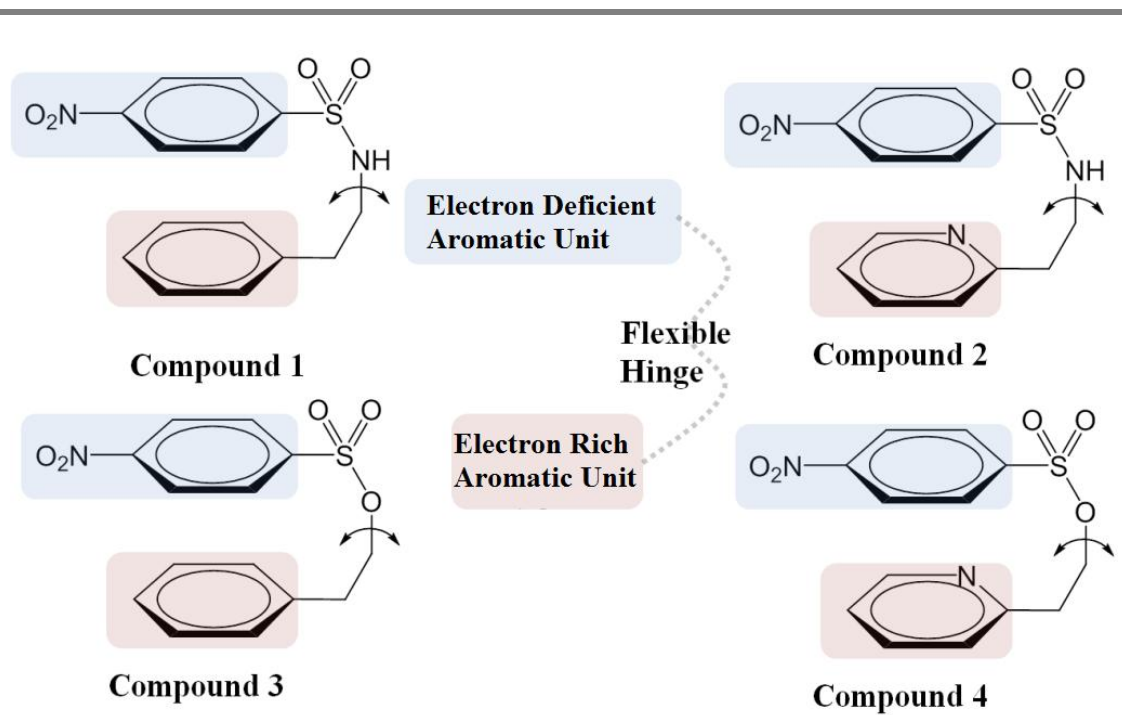


Figure 13. The molecular structures of compounds 1-4.

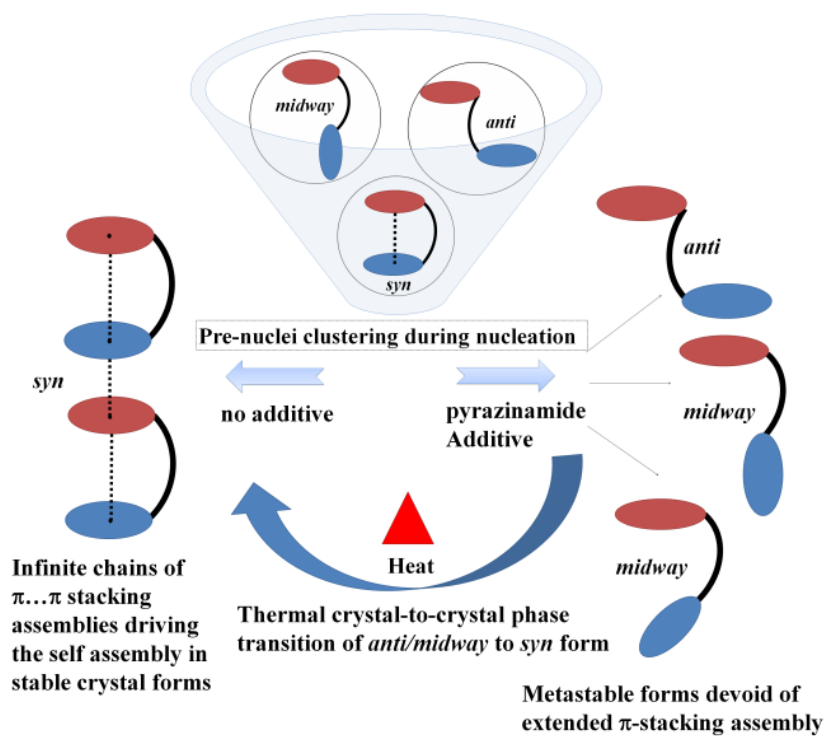


Figure 14. Cartoon illustration of nucleation process of candidate sulfonamide / sulfoester compounds with and without additive.

Conformationally flexible sulfonamide/sulfoester derivatives constituting electron-rich and electron-deficient aromatic rings were synthesized to study the

interplay between π -stacking and hydrogen bonding synthons. The structure directing role played by the extended chain of π -stacking assemblies even in the presence of strong hydrogen bonding in tuning the *syn-anti* conformational switching during nucleation has been investigated by capturing their thermodynamically stable and additive mediated elusive metastable polymorphs.

Chapter 4. Design and Synthesis of conformationally flexible *p*-substituted Sulphoester Trimers: Investigating Substituent Effect on π -stacking Interaction in Solution and Solid State.

In chapter 4, In order to evaluate the role of substituent for stabilizing the stacking interactions in solution and solid state, we used aromatic trimeric system with sulfoester hinge and -CH₂-CH₂- spacer. The trimers were chosen over the dimers mainly due to, 1) amplifying solution state stacking signal during 2D NMR studies and 2) trimers will have more constrain for achieving the stacking geometry with lowest entropy that would give better comparison. Sulfoester were chosen over sulfonamide for minimizing the contributing factors of strong electrostatic interaction for influencing the intramolecular geometry of the trimer. The trimer contains two *p*-substituted aromatic units present at the extreme end of the molecules and one aromatic unit as base. The *p*-substituted aromatic units and aromatic base are joined together *via* sulfoester hinge and -CH₂-CH₂- spacer with centre of symmetry lies at the centroid of base (**Figure 15**). To study the role of substituent, strong electron withdrawing (-NO₂, -CN), weakly electron withdrawing (-Cl, -Br), neutral (-H) and electron donating (-OCH₃) groups were used for substitution at the para position of the aromatic unit 1 (**Figure 16**).

For investigating stacked conformation in solution state 2D NOESY studies were undertaken. Solid state geometries were investigated by single crystal structure analysis. After analyzing the stacking parameters obtained from crystal structures and NMR studies, we speculated the transition mechanism from solution state stacking to solid state stacking through the nucleation funnel. The compounds CN, Cl, Br and H trimers exist in *syn* conformation in under-saturated solution state. OCH₃ trimer reveal *anti* conformation at the similar condition. During the nucleation stage, the PNC of these trimers may achieve either of *syn*, *midway* or *anti* conformation that depends on

the balance between the entropic cost of stacking and non-stacking conformation in multimeric association. Constrained intra-molecular stacking geometry may possess lowest entropy than the *midway* or *anti* conformation, however, intra and intermolecular extended stacking interactions may compensate overall entropic barrier. Here, the crucial role is played by the intramolecular stacking pull which is corroborated by intramolecular non-covalent interactions other than stacking interactions. Out of four *syn* trimers in solution state, -Cl and -Br achieve the *syn* conformation in the solid state, whereas, -CN and -H trimer exist in the non-stacked conformation i.e. *midway* and *anti* conformation respectively (**Figure 17**). Moreover, we envisioned that if the molecule has achieved *syn* geometry in more constrained solid state, it is more likely that it may exist in *syn* conformation in solution state as well. Therefore, we predicted that -NO₂ trimer may also exist in *syn* conformation in the solution state. As expected the -OCH₃ trimer form unstacked *midway* structure in the solid state.

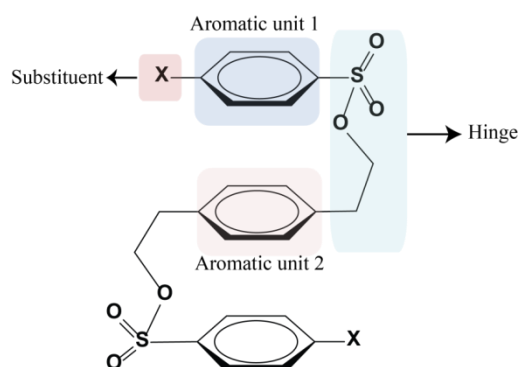


Figure 15. The design of trimeric system used for the investigating the nucleation funnel of stacked structures.

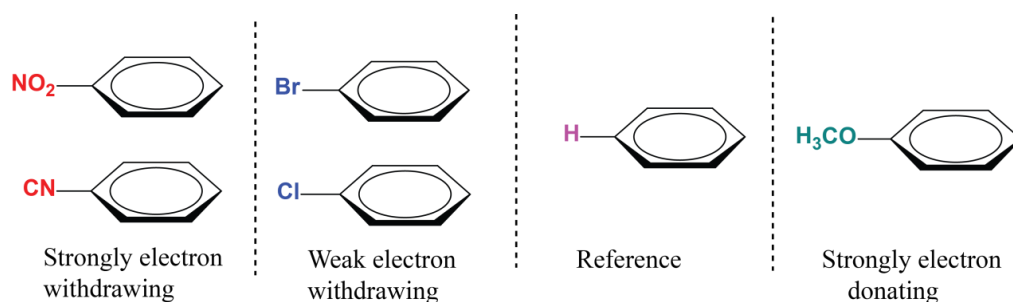


Figure 16. The substituent at the *para* position of aromatic unit 1 used for the investigation.

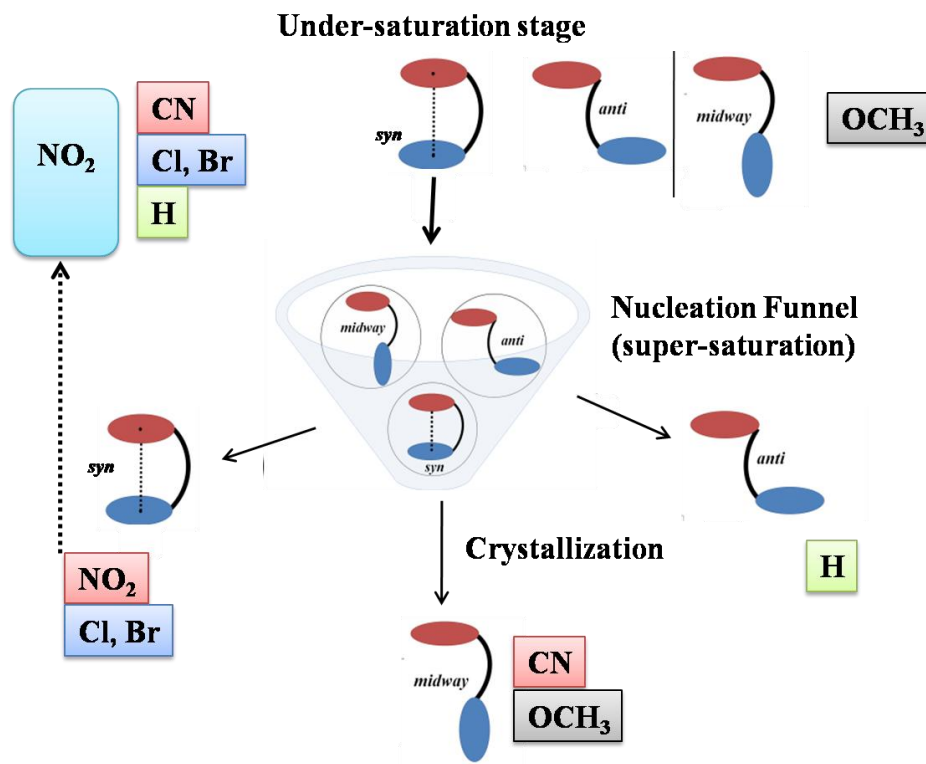


Figure 17. Cartoon illustration of existence *syn/midway* and *anti* conformations of different trimers which is elucidated on the basis of 2D NOESY and crystal structure data.

In compilation we put forth different model for explaining the role of substituent interaction in the solution and the solid state. For elucidating the solution state stacking interaction, we gave combined model which takes into account, contribution from electrostatic and dispersive terms. The clues were sought from the knowledge of polar/pi model and direct through space interaction model.¹⁹ According to our model, Stacking interaction in solution state is determined by E_{stacking} which is sum of $E_{\text{x-cg}}$ (energy of dispersive interaction between the substituent and opposite aromatic base), E_{prep} (energy of polarized repulsion between the aromatic rings) and E_{att} (energy of polarized attraction).

$$E_{\text{stacking}} = E_{\text{X-Cg}} + E_{\text{Prep}} + E_{\text{Patt}}$$

X: Substituent

C_g: Opposite aromatic ring

P_{rep}: Polarized repulsion between aromatic rings

P_{att}: Polarized attraction between aromatic rings

For solid state stacking interactions, we put forth substituent-substituent interaction model. Polarization of electron density is by far most striking feature of the any supra-molecular interactions. Anisotropic distribution of electron density causes partitioning of electrostatic potential forming δ^+ and δ^- regions. Last few decades this was mystery for supramolecular chemist, but evolution of solid state and NMR instrumentation has made possible to probe non-covalent interactions between two atoms. Charge density and high end theoretical calculations have proved that non-covalent interaction are the result of attractive interaction between positive region of one atom with negative region of other atom (σ hole bonding). Polarization of electron density is observed in many atoms such as oxygen and halogens. It increases with the lighter to heavier atom also validated by experimental methods. According to our model, interaction between substituents of opposite aromatic rings majorly contributes as one of the driving force for stabilizing $\pi \cdots \pi$ stacking interactions in crystalline state (**Figure 18**).

Figure 18. Structural depiction of polar/ pi model, direct through space interaction model and substituent-substituent interaction model.

In summary, we constructed conformationally flexible molecular architecture comprising rigid moieties interconnected by 1) amides (carboxamide/sulfonamide) or esters (carboester/sulfoester) and 2) flexible short chain spacers (-CH₂-CH₂-or C-NH-C-) and studied their bioactive (DNA hypomethylation), Chapter 1, sensing (anion sensing, acid sensing, Chapters 2A and 2B respectively) and polymorphic properties (stacking vs. unstacked polymorphs, Chapters 3 and 4 respectively). The derivatives of lead compound were systematically designed in order to investigate the mechanistic basis of their properties. We further extended our research by synthesizing

the aromatic stacking trimers to unravel the mystery behind the 1) effect of substituent on stacking geometry in different medium (solution and solid state) and 2) the behavioral pattern and role of substituent during the prenuclei clustering at nucleation process. Finally we put forth new theories for explaining the role of substituent for stabilizing the $\pi\cdots\pi$ stacking interaction in the solution and the solid state. The stacking interactions in solution are explained by combining the electrostatic polarization and dispersion terms whereas the stacking interaction in solid state is described by substituent-substituent interaction model.

References:

1. R. Huber and W. S. Bennett, *Biopolymers*, **1983**, 22, 261-279.
2. H. J. Dyson and P. E. Wright, *Curr. Opin. Struct. Biol.*, **2002**, 12, 54-60.
3. A. Marko, V. Denysenkov, D. Margraf, P. Cekan, O. Schiemann, S. T. Sigurdsson and T. F. Prisner, *J. Am. Chem. Soc.*, **2011**, 133, 13375-13379.
4. R. Rohs, I. Bloch, H. Sklenar and Z. Shakked, *Nucleic Acids Res.*, **2005**, 33, 7048-7057.
5. H. A. Carlson and J. A. McCammon, *Mol. Pharmacol.*, **2000**, 57, 213-218.
6. V. Percec, D. Schlueter, J. C. Ronda, G. Johansson, G. Ungar and J. P. Zhou, *Macromolecules*, **1996**, 29, 1464-1472.
7. J. Srivastava, D. L. Barber and M. P. Jacobson, *Physiology*, **2007**, 22, 30-39.
8. F. H. Allen, *Acta Crystallogr., Sect. B: Struct. Sci.*, **2002**, 58, 380-388.
9. G. R. Desiraju, *Angew. Chem., Int. Ed. Engl.*, **1995**, 34, 2311-2327.
10. B. Moulton and M. J. Zaworotko, *Chem. Rev.*, **2001**, 101, 1629-1658.
11. A. J. Blake, N. R. Champness, P. Hubberstey, W.-S. Li, M. A. Withersby and M. Schröder, *Coordin. Chem. Rev.*, **1999**, 183, 117-138.
12. S. R. Forrest and M. E. Thompson, *Chem. Rev.*, **2007**, 107, 923-925.
13. L. E. Kreno, K. Leong, O. K. Farha, M. Allendorf, R. P. Van Duyne and J. T. Hupp, *Chem. Rev.*, **2011**, 112, 1105-1125.
14. O. Hugon, M. Sauvan, P. Benech, C. Pijolat and F. d. r. Lefebvre, *Sens. Actuators, B*, **2000**, 67, 235-243.
15. M. L. Teodoro and L. E. Kaviraki, *Curr. Pharm. Des.*, **2003**, 9, 1635-1648.
16. M. Totrov and R. Abagyan, *Curr. Opin. Struct. Biol.*, **2008**, 18, 178-184.

17. D. Gebauer, M. Kellermeier, J. D. Gale, L. Bergstram and H. Calfen,
Chem.Soc. Rev., **43**, 2348-2371.

18. C. R. Martinez and B. L. Iverson, *Chem. Sci.*, **2012**, 3, 2191-2201.

List of Publications:

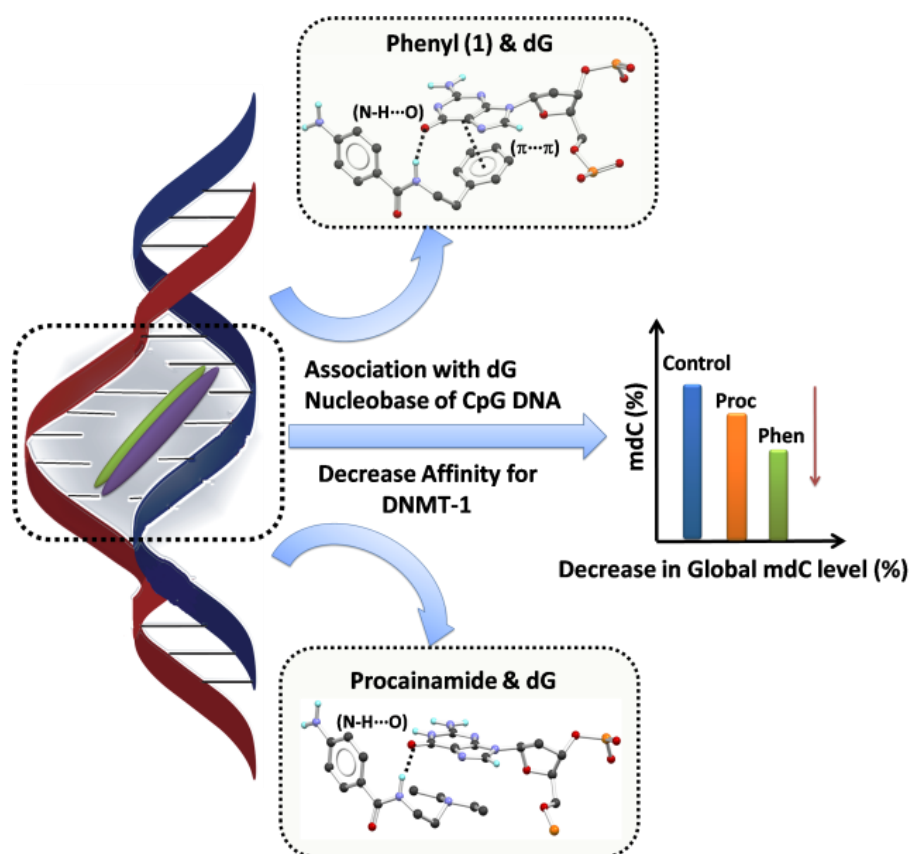
1. **R. L. Gawade**, D. K. Chakravarty, A. Kotmale, E. Sangtani, P. V. Joshi, A. Ahmed, M. V. Mane, S. Das, K. Vanka, P. R. Rajamohanan, V. G. Puranik, and R. G. Gonnade, "Additive Mediated *Syn-Anti* Conformational Tuning at Nucleation to Capture Elusive Polymorphs: Remarkable Role of Extended π -Stacking Interactions in Driving the Self-Assembly," *Cryst. Growth Des.*, **2016**, *16*, 2416–2428.
2. **R. L. Gawade**, D. K. Chakravarty, J. Debgupta, E. Sangtani, S. Narwade, R. G. Gonnade, V. G. Puranik, and D. D. Deobagkar, "Comparative study of dG affinity vs. DNA methylation modulating properties of side chain derivatives of procainamide: insight into its DNA hypomethylating effect," *RSC Adv.*, **2016**, *6*, 5350–5358.
3. **R. L. Gawade**, R. G. Gonnade and V. G. Puranik, "Metal coordination complex for detection of vapors and anions and process for the preparation thereof " **2016**, WO2016056027 A1
4. **R. L. Gawade**, R. G. Gonnade and V. G. Puranik, "Anion Sensing Disc: Cu(II) Based Novel Coordination complex with Structurally Dynamic 1D Hydrogen-bonded Network ", *to be communicated*
5. **R. L. Gawade**, R. G. Gonnade and V. G. Puranik, "Acid Responsive Intramolecular Turn-on Fluorescence of Benzophenone-Quinoline conjugates in Solution and Solid State ", *to be communicated*
6. **R. L. Gawade**, R. G. Gonnade and V. G. Puranik, "Nucleation funnel of stacking sulfoestertrimers: unravelling the mystery of substituent effect", *to be communicated*

Chapter 1

The Structure-property Relationship (SPR) between Conformationally Flexible Procainamide Analogues and their DNA Hypomethylating Effect

Most of the results presented in this chapter are published in the following paper:

R. L. Gawade, D. K. Chakravarty, J. Debgupta, E. Sangtani, S. Narwade, R. G. Gonnade, V. G. Puranik and D. D. Deobagkar; "Comparative study of dG affinity vs. DNA methylation modulating properties of side chain derivatives of procainamide: insight into its DNA hypomethylating effect." *RSC Advances*, 6, 2016, 5350-5358.



"DNA hypomethylating property of procainamide and its derivatives is attributed to their association with the dG nucleobase of partially denatured CpG rich DNA which further reduces their affinity for regulatory proteins such as DNMT-1. Phenyl side chain derivative of procainamide caused the highest drop in global % mdC level owing to its strongest binding affinity with the dG base".

Introduction:

The epigenetic regulation for e.g DNA methylation and histone modifications play remarkable role in embryonic development, cellular differentiation, suppression of transposons, X-chromosome inactivation, and long-term memory.¹ It reversibly regulates gene expression without altering the nucleotide sequence of the genome. DNA methylation is one of the key epigenetic regulations that occur in CpG rich DNA clusters called “CpG islands” located at the promoter region of genes.²The process involves covalent addition of the methyl group at 5-carbon position of the cytidine. DNA methylation profiles are significantly altered in cancer cells compare to normal cells which can be used as diagnostic and prognostic markers for many cancer types.³ Global hypomethylation in cancer cells induces genomic instability due to undermethylation of endogenous retroviral elements, oncogenes, and heterochromatic DNA repeats. However, aberrant hypermethylation of CpG islands associated with the promoter regions of tumor suppressor genes is accountable for uncontrolled growth.³ The DNA hypomethylating agents are used for (DHAs) reducing aberrant methylation level of regulatory genes for treating cancer and neurological disorders.⁴ Nucleoside analogs for e.g. 5-azacytidine, 5-aza-2'-deoxycytidine, zebularine, and 5-fluoro-2'-deoxycytidine inhibit DNA methyltransferase(DNMT) enzymes and thus reduces the aberrant methylation level in cancer cells.⁵ However, their clinical side effects and mutagenicity remained a great concern. Non-nucleoside methylation modulators provide promising alternative due to their non-genotoxicity and non-mutagenicity. They can be broadly categorized into three major classes based on their site of action and binding modes. The catalytic/allosteric site (protein) binding compounds are categorised in class I which interfere with the catalytic activity of the DNMTs⁶ whereas the class II compounds are CpG rich DNA binders which form complex with DNA and reduces their affinity for DNMT proteins.⁷ The class III includes the compounds which compete with DNA substrate and block the DNA-binding pocket of DNMT proteins.⁸ FDA approved drugs procaine and procainamide have been explored as DNA hypomethylating agents (DHA) against numerous malignancies as well as type-II diabetes both in *vitro* and in *vivo*.⁹ An interesting feature of their action is their ability to modulate DNA methylation level at sub-lethal concentration which make them suitable candidates for the combinatorial chemotherapeutic approach.^{10,11} Co-administration of procaine and procainamide with known anticancer drugs has

shown higher potency against many cancer types¹² and yet the exact mechanism of their DNA methylation modulating activity is not clearly understood. Their interaction with genomic DNA was first reported when patients undergoing prolonged therapy of procainamide and procaine showed the presence of antinuclear antibodies in the serum. Moreover, 30% of them developed systemic lupus erythematosus syndrome.¹³ Pathogenesis of procainamide was attributed to the stabilization of immunogenic CpG rich Z-DNA and affinity towards CpG rich DNA sequences.¹⁴ The relation between CpG rich DNA binding affinity and DNA methylation modulating property of procainamide was first recognized by Lee *et al.*¹⁵ They have shown that the procainamide could be inhibiting the binding of DNMT-1 to hemimethylated DNA which leads to the suppression of its catalytic activity. Based on that, procainamide was categorized as class II demethylating agent. However, recent reports including the docking studies¹⁶ of procainamide with constructed homology models suggested that it may form strong association with amino acids (Arg174) of DNA binding pocket of DNMT-1 protein which may reduce its affinity for 2'-deoxycytidine of target hemimethylated DNA. These reports highlighted the role of procainamide as class III methylation modulator.

Structure-activity relation (SAR) of bioactive compounds can be used to study their mechanism of action.¹⁷ This strategy also offers the lead for improving the therapeutic value of the drugs. Identifying pharmacophore moiety within the drug molecule is important for SAR study whose presence is essential to trigger the desired biological response. We used similar approach for our investigation. Reported evidences of structurally analogous compound procaine¹⁸ have been used as clues to choose selective derivatives of procainamide. Procaine showed the strong association with the guanine base compared to other nucleobases which is attributed to the strong hydrogen bonding between 4-amino benzoic acid backbone and guanine base. Constrained side chain derivatives of procaine exhibits improved demethylating effect¹⁸ compared to their flexible counterparts. Similarly, side chain derivatives of procainamide may also possess differential DNA hypomethylating activity if its pharmacophore moiety i.e. 4-aminobenzamide (anchoring site) remains unmodified. In this chapter we planned to replace the side chain moiety of procaine with aromatic and acyclic motifs attached to flexible hinge $-\text{CH}_2-\text{CH}_2-$ to study its binding affinity and the role of to study its binding affinity.

We here report the synthesis of procainamide derivatives which comprise of flexible (dimethyl), constrained (pyrrolidine, piperidine, morpholine) and planar aromatic side chain motifs (pyridine, phenyl) without modifying 4-amino benzamide backbone. Diethyl side-chain of procainamide is flexible due to free rotation of both the ethyl moieties covalently linked to tertiary nitrogen. The affinity of procainamide and its derivatives for dG nucleobase in the neutral and bound state have been investigated using DPV (differential pulse voltametry) and molecular docking study respectively. Further, we studied growth inhibitory properties of these compounds towards MCF-7 cancer cell lines. Global DNA methylation level was quantified at a sub-lethal concentration to evaluate *in vitro* cyto-toxicity and suitability as DHA. The differences in the affinity towards dG nucleobase and CpG rich DNA, cytotoxic effect, global hypomethylation at sub-lethal level (MCF-7 cancer cell line) are correlated with the structural features of side chain motifs. The SPR study has helped in deriving the relation between dG affinity and DNA methylation modulating activity of procainamide and its derivatives. Based on the results obtained we have also hypothesized the plausible mechanism by which procainamide may act as DHA in cancer cells.

Result and discussion:

Chemistry

Procainamide derivatives were prepared as per the reported procedure.¹⁹ The addition reaction of 4-nitro benzoyl chloride with the primary amines in the presence of triethylamine base form corresponding 4-nitro carboxamides. Further, nitro group is reduced in the presence of catalytic amount of Pd/C and H₂ to afford **1-6** (Figure 1.1). These compounds were named based on the nature of their side chains. The details of their characterization data and synthetic procedure are provided in experimental methods. Good quality crystals were obtained and used for single crystal X-ray diffraction studies. The purity profiles of all the compounds are provided in experimental methods. Purified compounds were further used for biological studies.

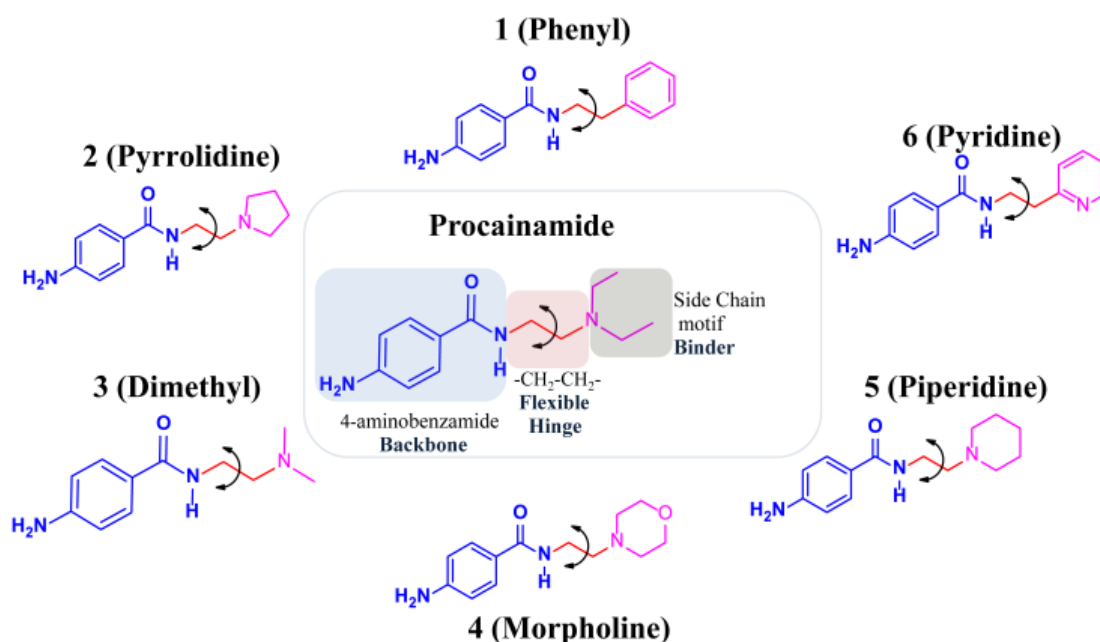
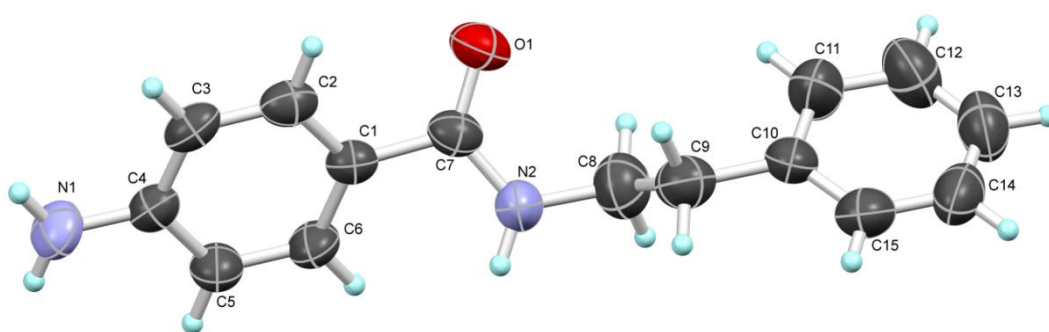


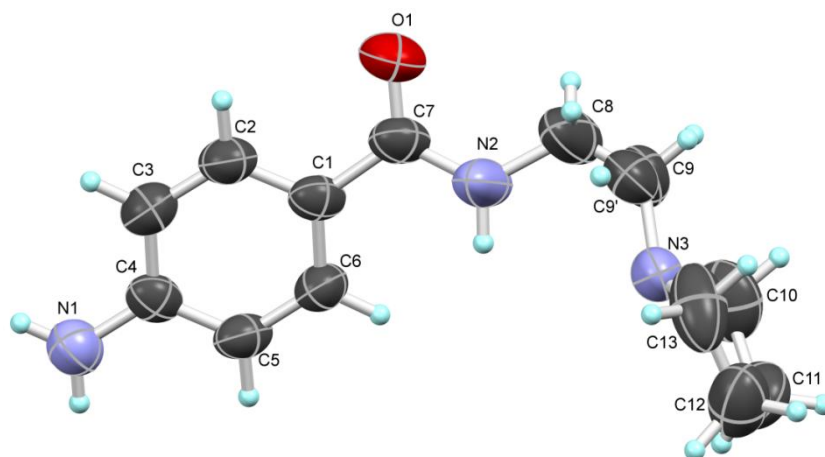
Figure 1.1. Description of pharmacophore features of procainamide and molecular structures of its side chain motif derivatives **1-6**.

Crystallography

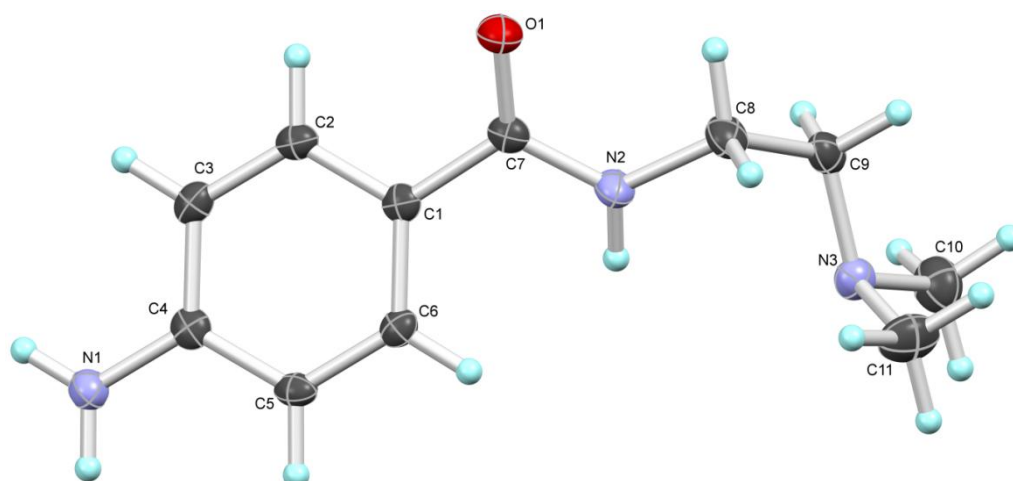
Molecular conformations in crystal and solution state share significant analogy. Crystal structures of iso-structural compounds provide insight into the preferred molecular association, and allowed torsional constraints of the pharmacophore.²⁰ All the compounds were crystallized from dichloromethane-petroleum ether solvent mixture by a slow evaporation method. Single crystal X-ray diffraction studies were performed on a Bruker Smart Apex II X-ray diffractometer. ORTEPs were drawn with 30-50% ellipsoids probability level containing H-atoms with arbitrary radii (**figure 1.2**). Atomic coordinates of procainamide were obtained from Cambridge Structural Database (CSD, CCDC number 694545).²¹ Based on reported studies,¹⁸ the 4-aminobenzamide of procainamide may play a pivotal role as backbone moiety of pharmacophore. Alkyl chain (-CH₂-CH₂- hinge) may play a significant role in providing conformational flexibility to side chains (binder) (**Figure 1.1**) and eventually responsible for the structural variation. Structure overlay (**Figure 1.3a**) and variations in the torsion angles τ_1 (C1-C7-N-C8), τ_2 (C7-N-C8-C8), and τ_3 (N-C8-C9-R) are tabulated in (**Figure 1.3b, Table 1.1**). As envisioned, the dihedral angles across 4-aminobenzamide backbone showed less deviation whereas torsional variation across side-chains displayed the significant differences.



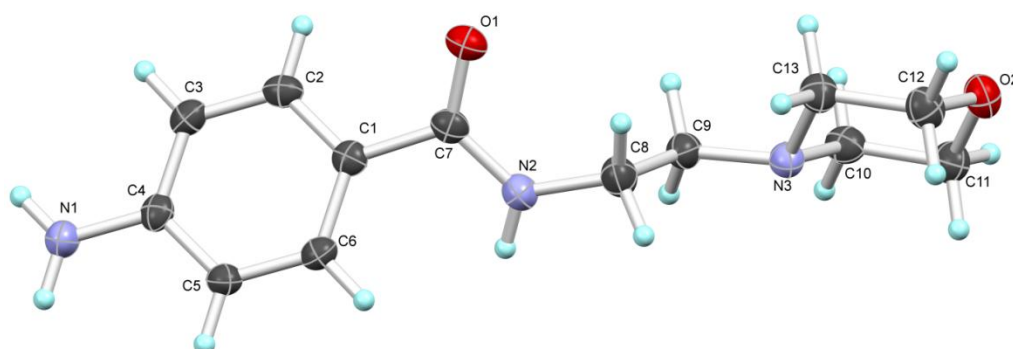
(a)



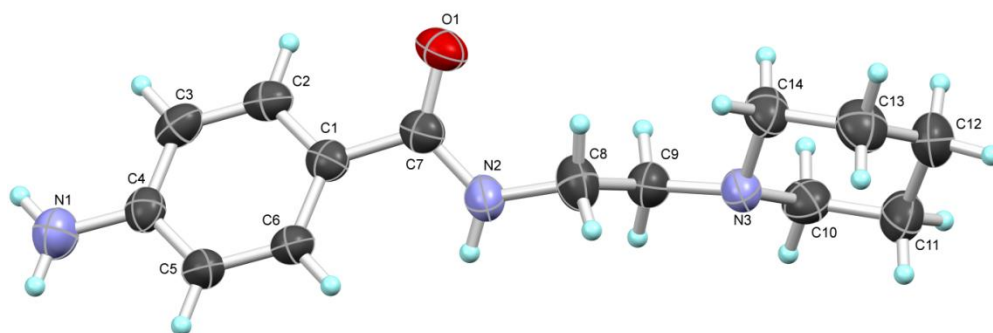
(b)



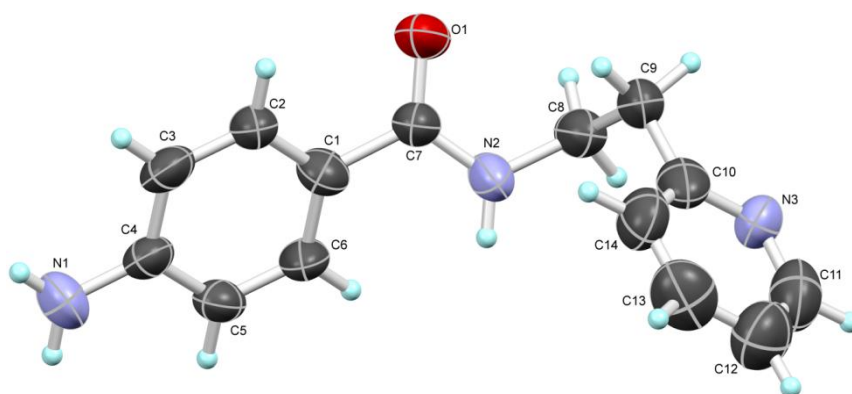
(c)



(d)



(e)



(f)

Figure 1.2. ORTEPs of compounds (a)1 (b) 2 (c)3 (d)4 (e)5 and (f)6

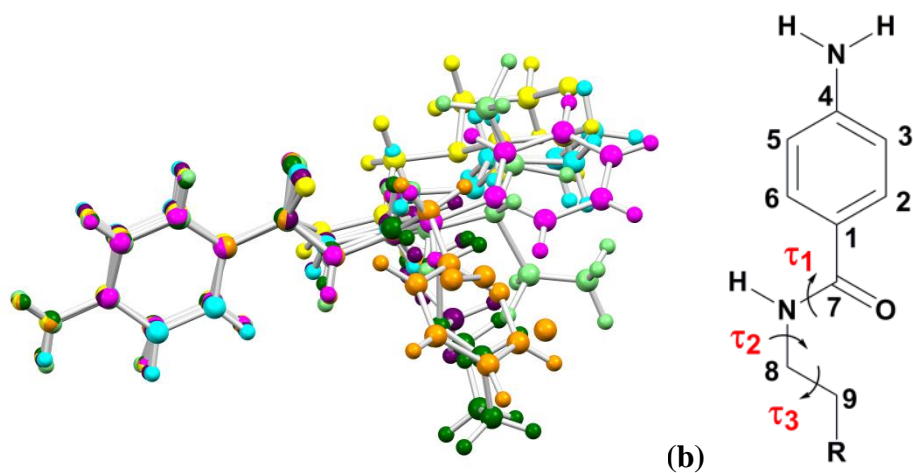


Figure 1.3.(a) Structure overlay of procainamide and its derivatives 1(magenta), 2(green), 3(purple), 4(yellow), 5(cyan), 6(orange), proc (light green) and (b) scheme displaying different torsion angles; τ_1 (C1-C7-N-C8), τ_2 (C7-N-C8-C9), and τ_3 (N-C8-C9-R).

Compounds	$\tau_1(^{\circ})$	$\tau_2(^{\circ})$	$\tau_3(^{\circ})$
Phenyl(1)	171.71	94.6	179.08
Pyrrolidine(2)	172.68	-168.93	-51.77
Dimethyl(3)	-175.34	-139.39	-61.58
Morpholine(4)	-172.43	-101.03	-164.72
Piperidine(5)	-170.0	-105.96	-167.33
Pyridine(6)	173.80	84.44	71.66
Procainamide	166.14	88.18	173.24

Table 1.1. Torsion angles (τ_1 – τ_3) of compounds **1-6** and procainamide extracted from their crystal structures.

Electrochemical studies

Electroactivity of nucleobases has been studied for their quantification in biological samples as well as to study their interaction with other chemical species.²² DPV study and DFT investigations reported¹⁸ for procaine and DNA bases reveals that binding affinity of procaine towards DNA bases is in the order $G > A > T > C$. The strongest binding affinity for guanine base in neutral form is attributed to coplaner C-H \cdots N and N-H \cdots O hydrogen bonding between of procaine and guanine. Similarly, procainamide may also show strong association with guanine base owing to the presence of 4-aminobenzamide moiety. CpG rich DNA consists of alternate arrangement of guanine and cytosine bases linked *via* phosphate-deoxyribose backbone. In view of this, binding affinity towards guanine was utilized as a parameter for SAR study. We envisaged that the binding affinity investigation with dG instead of guanine base may give broader view and significant variation for deriving SAR based on the fact that guanine conjugated to deoxyribose sugar residue

provides multiple interaction sites. Redox electrochemical behavior of guanine is shown in the **figure 1.4**. To study the differential affinity of procainamide and its derivatives (**1-6**) to dG nucleobase base in a neutral form, DPV was performed using CHI 900b potentiostat with a pulse amplitude of 50 mV, pulse width of 0.2s and a pulse period of 0.5s (for detailed procedure see experimental methods). **Figure 1.5a** displays the differential pulse voltammograms of pure dG as well as dG in the presence of procainamide and compounds **1-6**. When the GC electrode potential, kept in a solution of dG, is made more positive with respect to the open circuit potential (OCP), a clear peak is observed at 0.79 V (vs. SCE, 0.1 M KCl) (there is no peak observed for the buffer solution (blank) alone, **Figure 1.6**) due to the oxidation of dG as shown in the reaction mechanism in **figure 1.4**. Moreover, when the concentration ratio of dG to compound is kept constant in all the experiments (dG to compound ratio: 4), the peak current density of dG oxidation drops in the presence of carboxamide ligands (**1-6** and procainamide) (**Figure 1.5**). The results indicate that the ligands bind to dG in the solution and hence number of free dG molecules depletes. As a result, peak current density showed sharp decrease in the presence of ligands. It invariably suggests that the drop in peak current of dG is attributed to the interactions of the procainamide and compounds **1-6** with dG. However, the extent of the drop in the peak current is different and related to the structural features of side-chain motifs of ligands. Phenyl substituent caused the maximum drop in peak current of dG (**Figure 1.5b**) and thus displays more affinity for dG. The binding affinity of procainamide derivatives (according to **Figure 1.5b**) follow the order, phenyl(**1**) > pyridine (**6**) \approx piperidine (**5**) > morpholine(**4**) > procainamide > dimethyl (**3**) \approx pyrrolidine (**2**). The slight broad peak observed prior to the dG peak is due to the oxidation of compound **1-6** and procainamide that is demonstrated by control experiment for Phenyl (**1**, **Figure 1.6**). A peak observed at 0.6 V (vs. SCE, 0.1 M KCl) prior to dG oxidation peak is attributed to the oxidation of phenyl(**1**) to form radical cation whereas the peak that appears after dG peak, corresponds to the oxidative decomposition/cleavage of the compound-dG complex on the application of a more positive potential. It is supported by the fact that dG, as well as phenyl derivative alone, do not show such peak after the oxidation potential of dG which is observed only in case of mixed solutions of dG and compounds. Careful observation of these peaks reveals that the phenyl-dG complex requires much higher potential

than any other compound-dG complex and therefore it is most stable complex. This result indirectly suggests the possibility of strong binding of phenyl with dG.

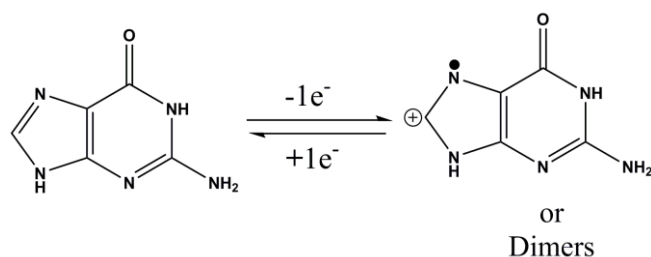


Figure 1.4. Scheme displaying redox behaviour of guanine base

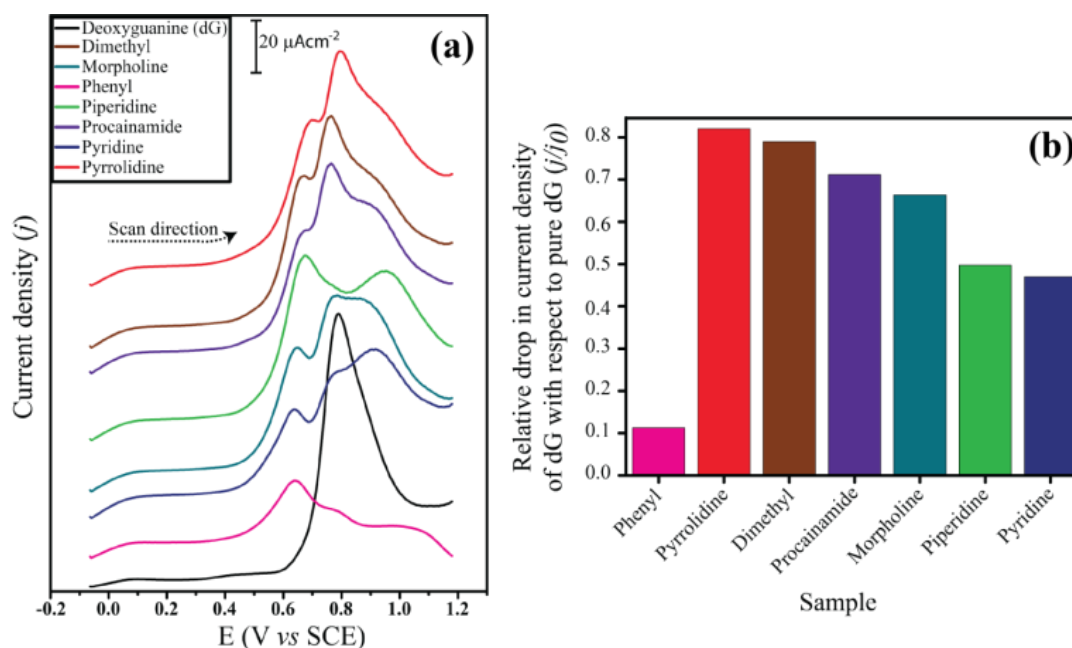


Figure 1.5. (a) Differential pulse voltammograms of dG in the presence of compounds **1-6** and procainamide; glassy carbon, Pt-foil and standard calomel electrode (SCE, 0.1 M KCl) are used as working, counter and reference electrodes respectively (pulse amplitude of 50 mV, pulse width of 0.2s and a pulse period of 0.5s); systematic drop in peak current density (j) in presence of different compounds suggest their differential binding affinity to dG; (b) relative drop in peak current density (j) of dG with respect to peak current of pure dG (j_0) (j is normalized with respect to j_0).

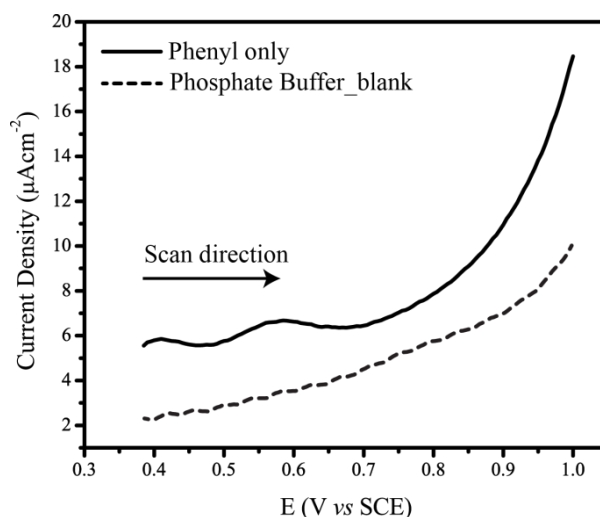


Figure 1.6. Differential pulse voltammogram of phenyl derivative **1** alone under identical condition used for the study of compound-dG interactions, DPV for only buffer (blank) is also shown for comparison; appearance of peak in case of phenyl drug suggests its oxidation.

Molecular docking study

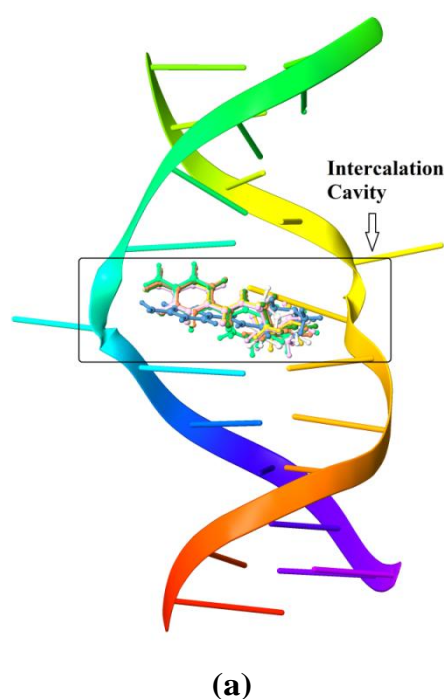
Many experimental evidences were reported for predicting the association of procainamide with CpG rich DNA. However, two reports provided important clues about their preferential affinity: 1) shift in the midpoint of transition is observed during salt-induced B-Z transition of poly CpG DNA in the presence of procainamide¹⁴ and 2) it shows specific affinity for hemimethylated-DNMT-1 bound complex over unmethylated-DNMT-1 bound counterpart.¹⁵ Cellular processes that involve dynamic variation in the topology of DNA such as maintenance methylation, B-Z transition, replication, DNA modification and repair share common structural features. Partial denaturation of DNA and flipping out of bases at the target site is observed during these events due to special constraints.²³ We envisioned that procainamide may show more affinity for partially denatured CpG rich DNA and driving force is provided by its affinity for the dG base. To validate our hypothesis we used (DNA-ligand) molecular docking.

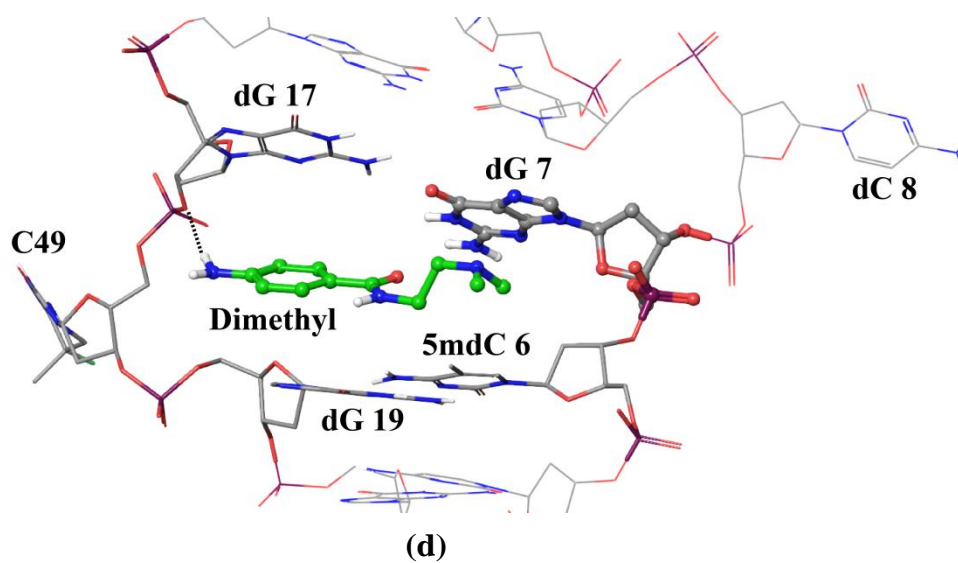
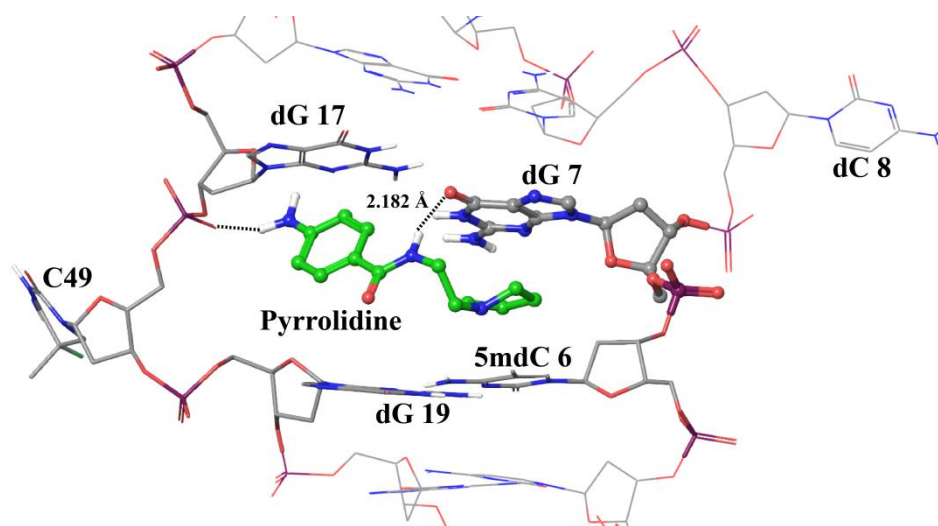
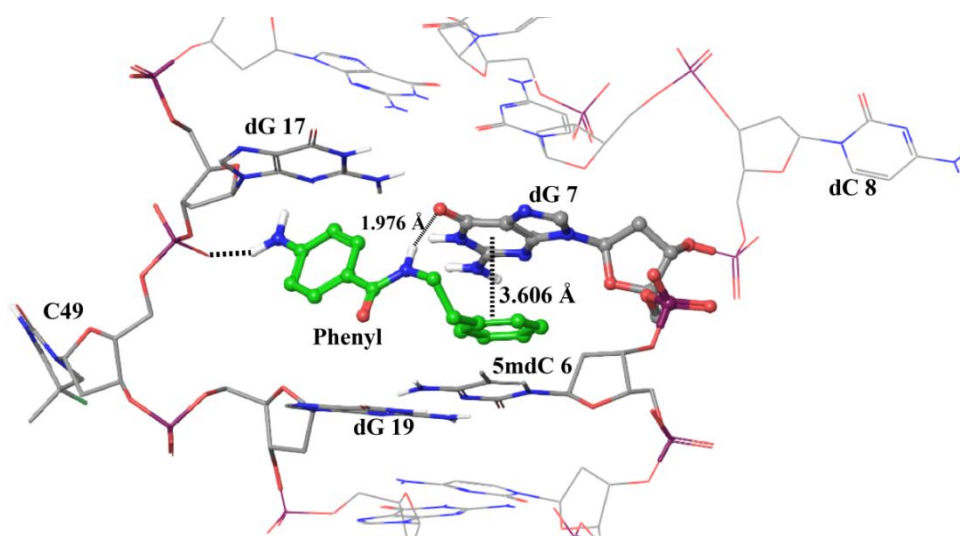
Docking study provides a good assessment of sequence specificity and intercalation mechanism of DNA-binding drugs.²⁴ The significant variation is observed for the topology of minor groove size within the crystal structures of AT-rich and GC-rich DNA sequences²⁵ due to which, it is advisable to use crystal coordinates instead of modeled DNA for carrying out docking study with minor

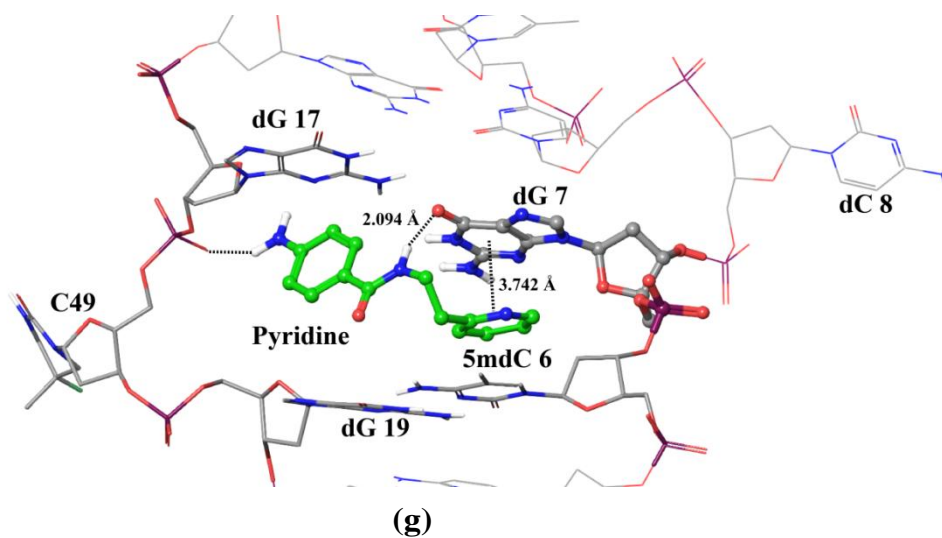
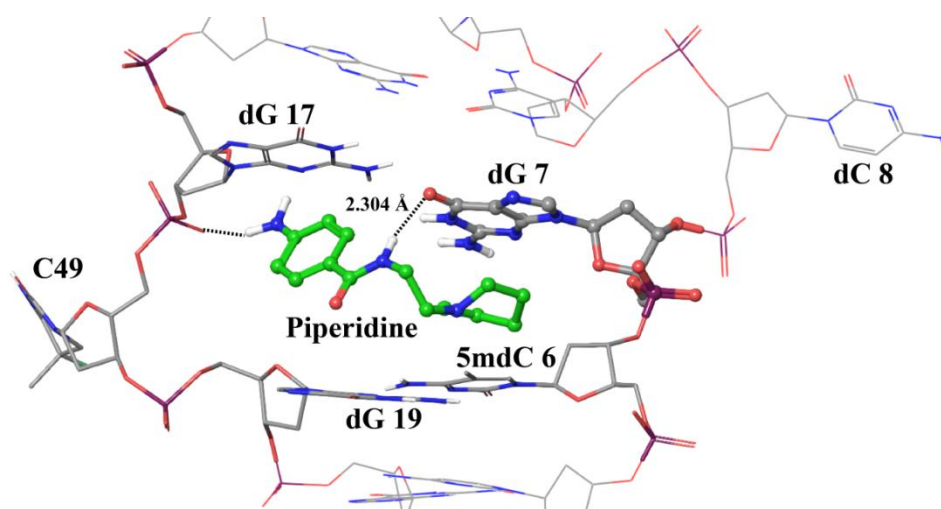
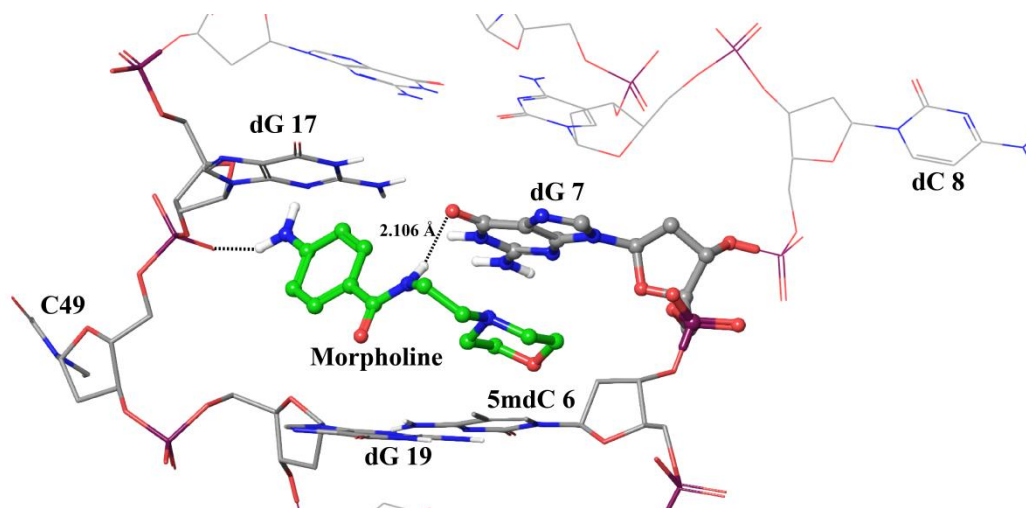
groove binding agents. The atomic coordinates of CpG rich hemimethylated DNA (hmDNA) were obtained from RCSB Protein Data Bank (PDB ID:4DA4) and used for docking study.²⁶ Structural analysis reveals that the H-bonding groups of dG bases are exposed by partial denaturation of DNA. Non-conventional pyrimidine:pyrimidine base pairing between dG bases and flipping out of nucleobases forms small intercalation cavity at the target site.

Docking was performed with Schrodinger Maestro Suite.²⁷ Detailed procedure and docking protocol are provided in experimental methods. Post-docking minimization and residue-wise interaction parameters were calculated from docked poses. The selection of reliable and bioactive conformers is crucial for docking analysis. Atomic coordinates of compounds **1-6** and CSD database survey²⁸ (**Figure 1.36, Table 1.3**) was used to find out permissible variation for torsion angle τ_1 that lies within the range of 160°-180°. The filtering of the docked poses has been carried out where ligand confirmation matched with our cut-off value. Furthermore, conformers with lowest glide scores were used for comparative studies. Structural overlay and torsional parameters of ligand conformations were extracted from docked poses and are provided in experimental methods (**Figure 1.37, Table 1.4**). Docking analysis with hemimethylated DNA reveals that all the compounds are docked inside the intercalation cavity of the DNA minor groove (**Figure 1.7a**) and have formed a strong association with a dG base of target site except the dimethyl derivative. Carboxamide N-H of 4-aminobenzamide backbone formed strong N-H...O hydrogen bonding interaction with the C=O of the dG base whereas N-H of *p*-amino group formed a N-H...O hydrogen bonding with O acceptor of phosphodiester linkage of DNA (**Figure 1.7b-h**). Although all the derivatives except the dimethyl (**3**) showed similar binding features, variation in their H-bonding geometries with the dG base was observed (**Figure 1.8a**). Glide score (docking score) was used to evaluate binding affinity for hmDNA whereas, H-bonding distance, H-bonding energy and van der Waals energy were taken into account for assessing the binding affinity for dG at the target site. Based on the glide score and other parameters affinity trend for hmDNA was found to be in the order, phenyl (**1**) > pyridine (**6**) > pyrrolidine (**2**) > piperidine (**5**) > morpholine (**4**) > procainamide > dimethyl (**3**). H-bonding energy score (**E1**) between ligands and dG residue revealed phenyl (**1**), procainamide, and pyridine (**6**) derivatives form strong hydrogen bonding interaction with dG nucleobase

(Figure 1.8a). The van der Waals interaction energy scores (E2) suggests that all the derivatives except dimethyl (5) are strongly associated *via* van der Waals forces with dG nucleobase in addition to their H-bonding interactions. Docked poses of phenyl and pyridine showed the formation of parallel displaced π -stacking interaction between benzene/pyridine moieties with pyrimidine ring of the dG base. The geometrical parameters for stacking interactions (Cg...Cg distance for phenyl 3.588 Å and pyridine 3.613 Å, the dihedral angle between aromatic rings α for phenyl 15.85° and for pyridine 18.67°) suggests benzene ring of phenyl(1) form comparatively stronger π ... π interaction than pyridine ring of compound 6 (Figure 1.8b and figure 1.38). The molecular docking study reveals that the side-chain topology of compounds plays a remarkable role for binding to CpG rich hmDNA. The Strength of the binding affinity enhances as the rigidity and bulkiness of side chain motif increases. The comparative analysis revealed that hydrogen bonding between 4-aminobenzamide backbone and dG nucleobase in the intercalation cavity allowed all the derivatives to dock inside the minor groove but the strength of their association within target site is further increased by other non-covalent interactions between side chain and target base. The aromatic side chain in phenyl (1) showed the highest affinity which is attributed to the formation of π ... π stacking interaction with the dG base.







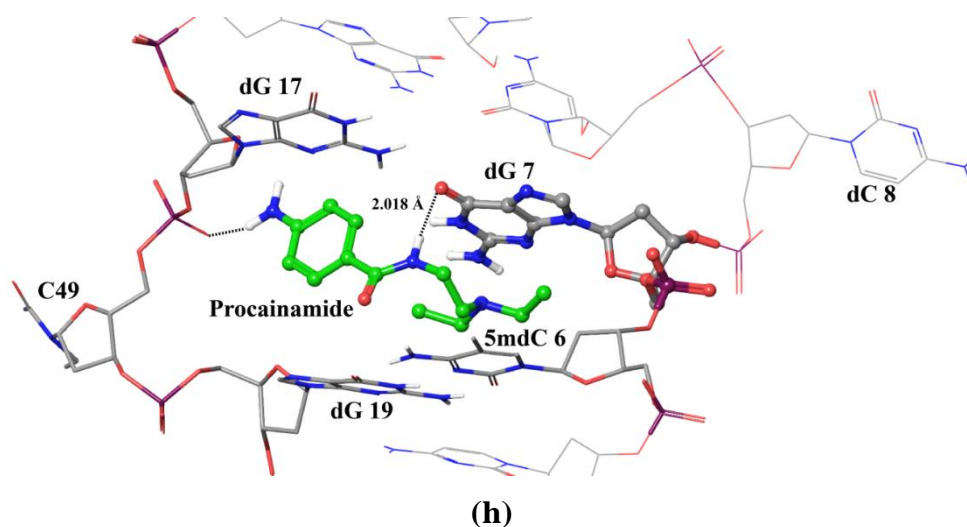


Figure 1.7. (a) Compilation of docked poses showed most favourable binding site lies within intercalation cavity. Detailed view of individual docked poses of (b) phenyl (c) pyrrolidine (d) dimethyl (e) morpholine (f) piperidine (g) pyridine (h) procainamide with hmDNA, showing strong H-bonding association with dG nucleobase(except dimethyl) and O-acceptor of phosphodiester linkage at the target site.

Compounds	Glide Score	Affinity towards dG		
		H-bond Distance(Å)	E1	E2
Phenyl (1)	-8.33	1.976	-1	-7.618
Pyrrolidine (2)	-7.839	2.182	-0.795	-8.242
Dimethyl (3)	-4.254	-----	-----	-----
Morpholine (4)	-7.72	2.106	-0.987	-8.787
Piperidine (5)	-7.796	2.304	-0.434	-8.245
Pyridine (6)	-8.182	2.094	-1	-8.388
Procainamide	-6.769	2.018	-1	-7.506

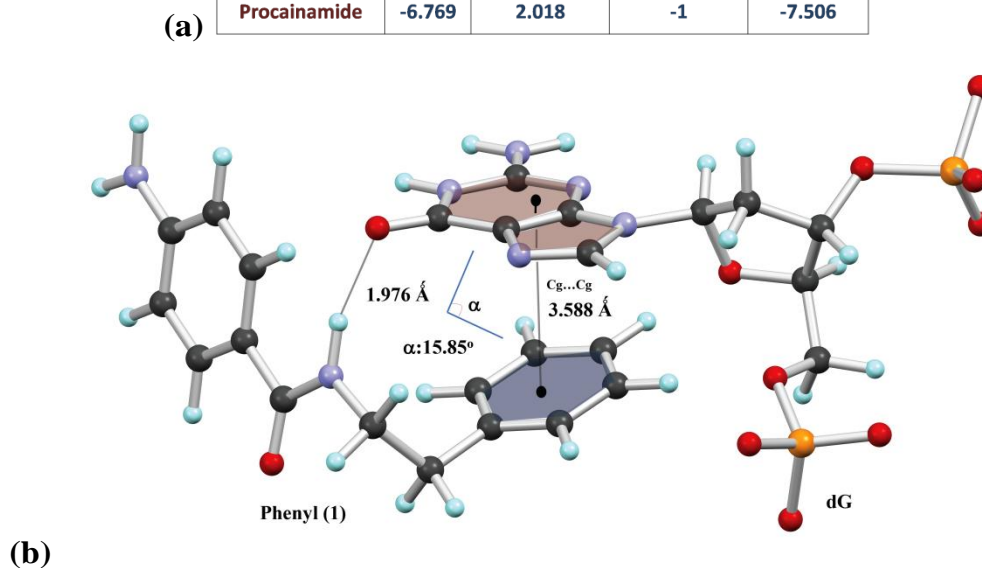


Figure 1.8. (a) Tabulated glide score, affinity parameters to dG residue (H-bond distance, hydrogen bond score E1, van der Waals association energy score E2) of docked poses of procainamide and derivatives (1-6) with hmDNA and (b) structural depiction of association between phenyl (1) and dG base at the target site *via* H-bonding and aromatic $\pi \cdots \pi$ stacking interaction

Cytotoxicity study

Cytotoxicity efficacy of all the compounds towards MCF-7 breast cancer cell lines was investigated using MTT assay. Five concentrations of compounds from 100 μ M to 500 μ M at 24h, 48h, and 72h time points were used to treat the cell line. Detailed procedure and protocol are provided in experimental methods. The results depicted in **figures 1.9-1.11** showed that all the derivatives (1-6) and procainamide were non-cytotoxic at 24h and 48h time points. Interestingly, even after 72h and 100 μ M concentration of compounds did not exhibit obvious cytotoxicity and viability

ranges from 80% to 100%. However, at 500 μM concentration and 72h time point, cytotoxicity profiles showed significant variation (**Figure 1.12**). Phenyl (**1**) showed 50% cell death with the highest cytotoxic effect whereas pyridine (**6**) and dimethyl (**3**) derivatives possess moderate cytotoxicity. Procainamide, pyrrolidine (**2**), piperidine (**5**), and morpholine (**4**) derivatives display the absence of significant cell death even at the highest concentration. The observed trend for the growth inhibiting properties towards breast cancer cell line is in the order, phenyl (**1**) > dimethyl (**3**) > pyridine (**6**) > pyrrolidine (**2**) > piperidine (**5**) > morpholine (**4**) > procainamide.

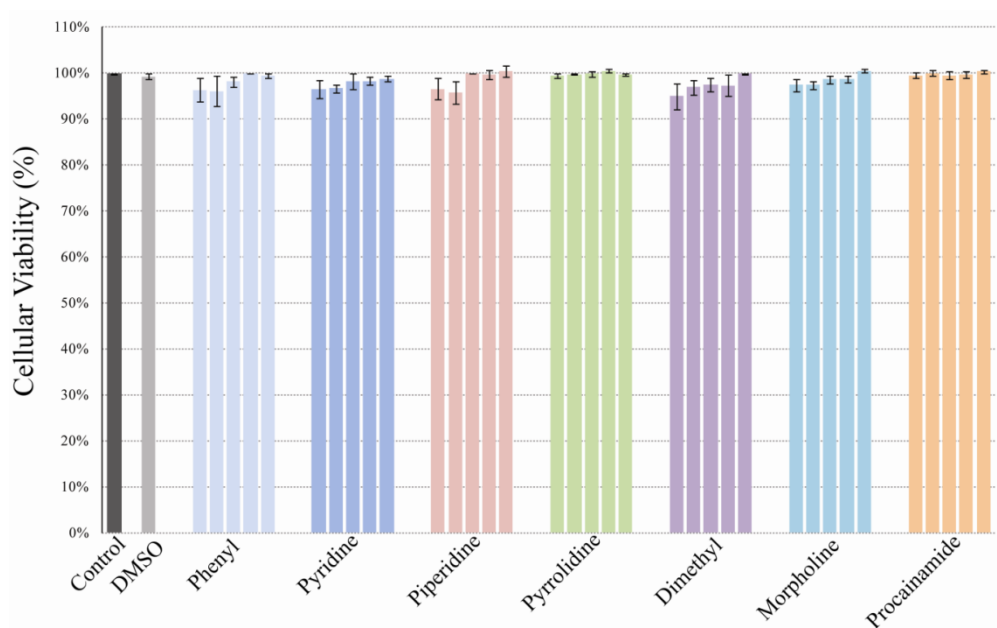


Figure 1.9 Cell viability study after 24h time point for compounds **1-6** and procainamide and concentration ranging from 100-500 μM . (X: conc. of compounds and Y: Cell viability in %).

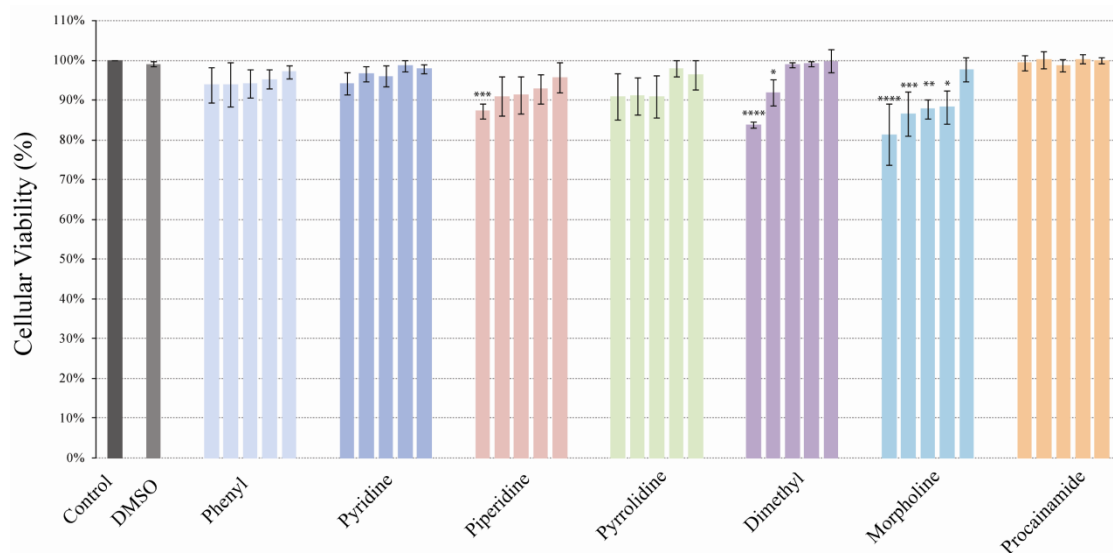


Figure 1.10 .Cell viability study after 48h time point for compounds **1-6** and procainamide and concentration ranging from 100-500µM. (X: conc. of compounds and Y: cell viability in %)

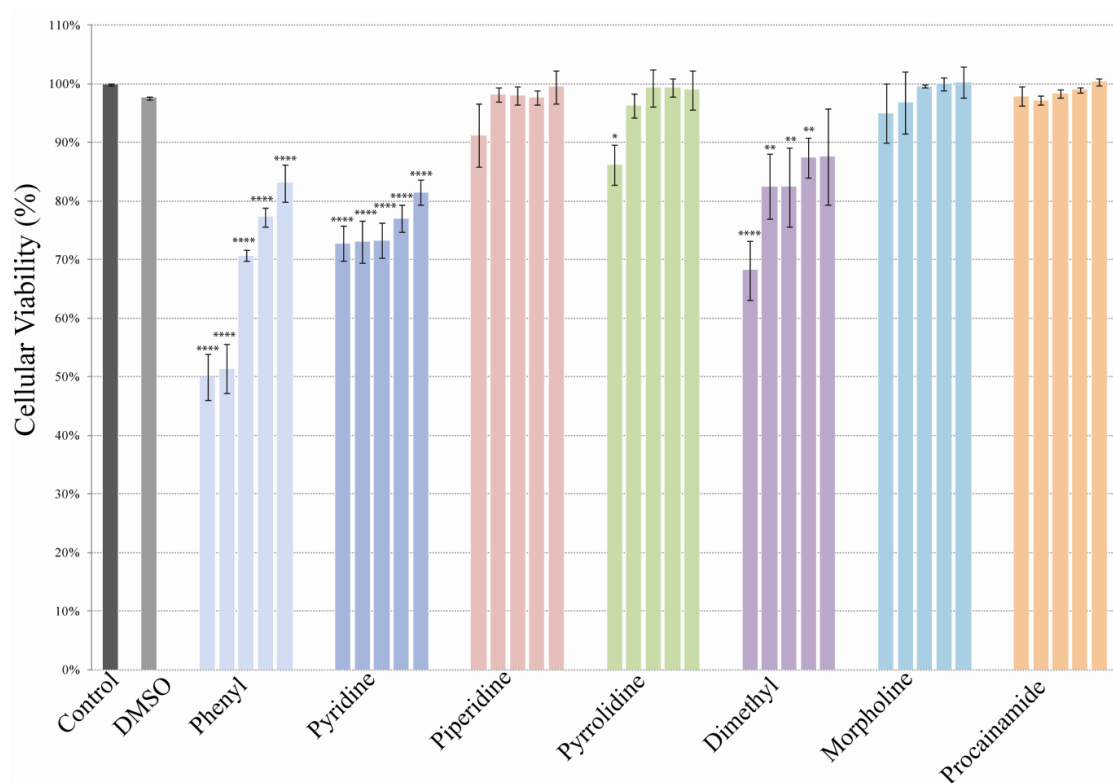


Figure 1.11 Cell viability study after 72h time point for compounds **1-6** and procainamide and concentration ranging from 100-500 µM. (X: conc. of compounds and Y: cell viability in %)

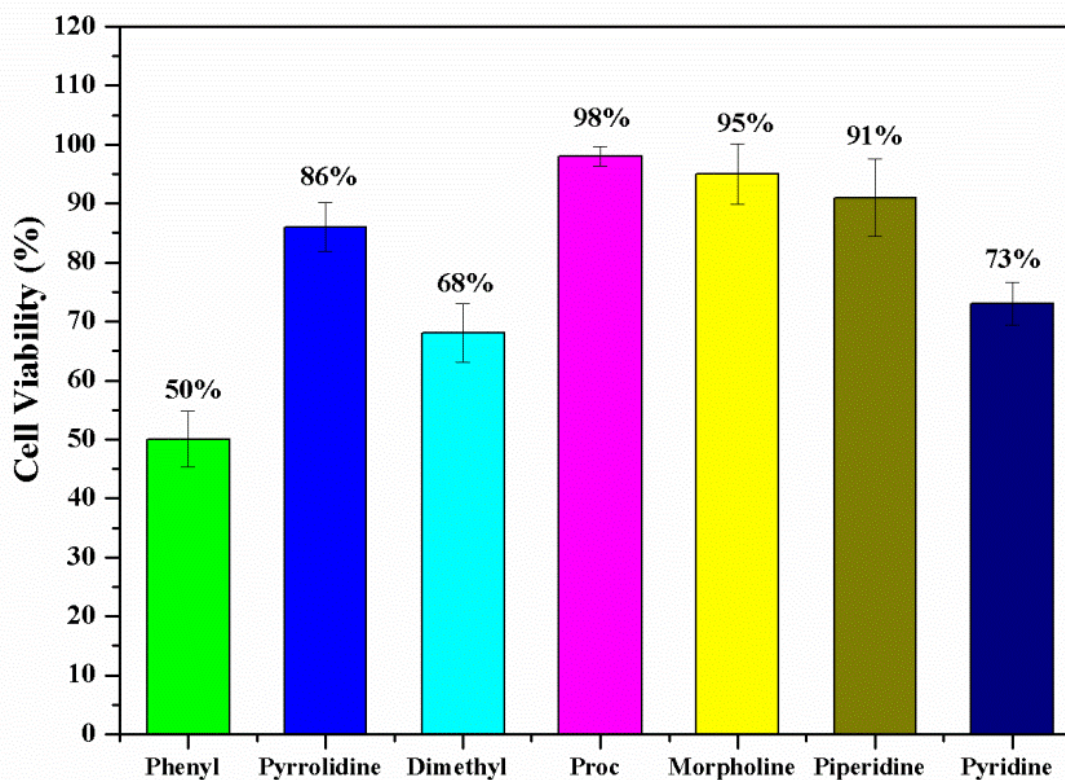


Figure 1.12. A comparison of % cell viability assay after 72 h of treatment with 500 μM conc. of procainamide and its derivatives (**1-6**) towards MCF-7 cancer cell line.

Global methylation quantification

Procainamide and its derivatives (**1-6**) showed differential affinity towards the dG base in neutral form, partially denatured CpG rich DNA and cytotoxicity towards breast cancer cell line. However, their cytotoxic effect alone may not infer their candidature as DHA. Secondly, procainamide can be used for combinatorial drug therapy mainly because, 1) it reduces aberrant methylation (at sub-lethal level) and 2) increases vulnerability of cancer cells for strong anticancer drugs.^{11,12} Shift in the global methylation level in MCF-7 cancer cells at sub-lethal concentration of compounds is used as a crucial parameter for SAR. So far, many techniques and methods have been reported for quantifying global methylation levels. Some of them are luminometric, electrophoretic, pyro-sequencing, HPLC and colorimetric-based assays.²⁹ For our purpose, ELISA based methylated DNA quantification kit (colorimetric) assay from Abcam was used for determination of % 5-methyl-2'-deoxycytidine content (% mdC) in treated and untreated MCF-7 cancer cells. The

detailed are provided in the experimental methods. The two negative controls (C1 and C2) were used for this study. Control C2 (0.5% DMSO) was used to remove the error of demethylating effect of DMSO solvent.³⁰ 5-azacytidine (5 μ M) was used as a positive control for comparison. Methylation level in negative control DNA samples, C1(no DMSO) and C2(0.5% DMSO) ranges from 5.37% to 5.68% which is similar to the reported values in published literature.³¹ Positive control revealed highest decrease in global methylation level whereas trend in the decrease in methylation level for procainamide and its derivatives(1-6) is in the order, phenyl (1)>piperidine (5)>procainamide > dimethyl (3)>morpholine (4) \approx pyridine (6)>pyrrolidine (2)(Figure 1.13). The highest decrease in the methylation level was observed for phenyl (1). The reports have shown that slight modulation in global methylation level is attributed to significant change at the gene regulation level,³² which suggested phenyl derivative can be used as DHA at sub-lethal concentration.

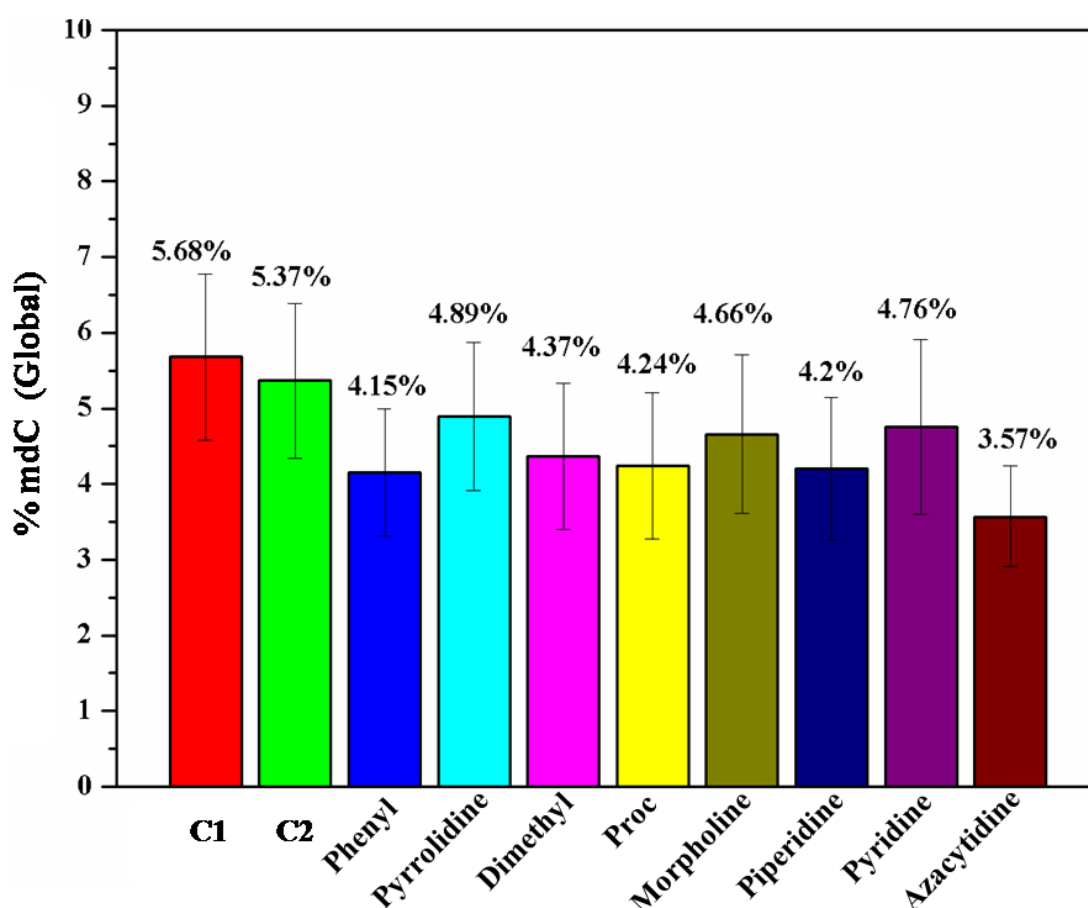


Figure 1.13. A comparison of global methylation quantification (%) after 72h of treatment with 100 μ M conc. of procainamide, its derivatives (1-6) and controls (C1= blank, C2= 0.5% DMSO) towards MCF-7 cancer cell. lines.

DNA Methyltransferase-1 activity assay

DNMT-1 inhibition assay was carried out to understand the mechanistic basis of procainamide and its analogues. The comparative analysis of DNMT-1 inhibitory activity of highest demethylating compound **1**(phenyl) and procainamide was carried out using the EpiQuik DNA Methyltransferase 1 activity/inhibitor screening assay core kit (P-3006A). At 100 μM concentration, compound **1**(phenyl) and procainamide have shown comparable reduction in the activity of DNMT-1 which may be due to the similar mechanism of their action (**Figure 1.14**).

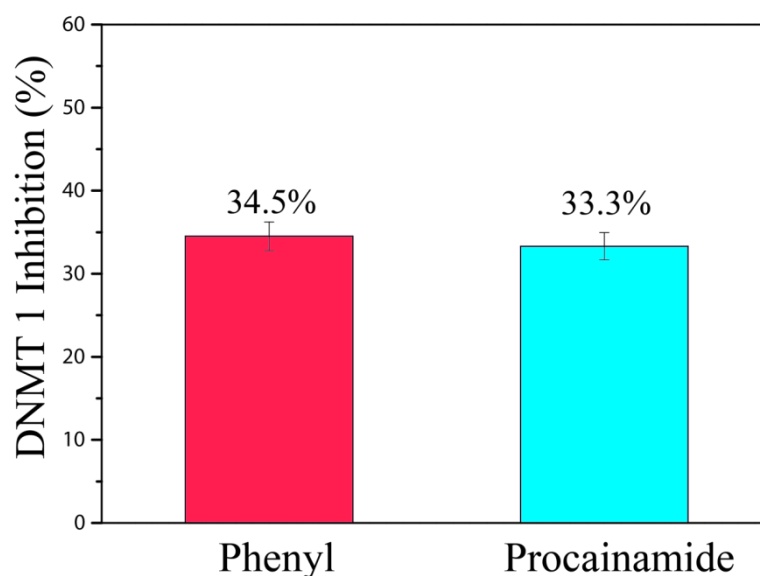


Figure 1.14. A comparison of *in vitro* DNMT-1 inhibitory activity (%) of compound **1**(phenyl) and procainamide at 100 μM conc. (DMSO 0.01%).

Conclusion

Four parameters, 1) dG affinity (neutral state), 2) CpG rich binding affinity, 3) cytotoxicity to MCF-7 cancer cell lines and 4) % mdC level (global) showed significant variation with respect to the topology of side-chain motifs of procainamide and its derivatives. DPV study revealed that aromatic side chains containing, phenyl (**1**) and pyridine (**6**) derivatives display strong association with the dG base in a neutral form whereas flexible side chain containing, dimethyl (**3**) and procainamide derivatives show the least association. Constrained heterocyclic side chain derivatives morpholine (**4**) and piperidine (**5**) showed intermediate association with dG base except pyrrolidine (**2**). DPV results demonstrated significant correlation with docking study with partially denatured hmDNA. Phenyl (**1**) and pyridine (**6**) derivatives showed $\pi\cdots\pi$ stacking interaction with the dG base that manifested their strong association with CpG rich hmDNA. Conversely, flexible dimethyl (**3**) and procainamide displayed the least affinity. Based on glide score, constrained heterocyclic side chain containing derivatives possess intermediate (between aromatic and flexible side chain derivatives) binding affinity. Combined results signify that the aromatic side chains have a higher affinity towards CpG rich DNA due to their strong intermolecular association with dG nucleobase.

Cytotoxicity data revealed good agreement with DPV/docking study. It is used to evaluate the sub-lethal concentration of procainamide and its derivatives **1-6**. Interestingly all the compounds have shown the decrease in %mdC level in comparison with control in MCF is attributed to their affinity towards CpG rich DNA especially to dG base. Moreover, phenyl (**1**) showed a higher demethylating effect compared to other derivatives (**2-6**) including its parent analogue procainamide. The slightly higher demethylating effect of **1** is attributed to its strong association with dG nucleobase *via* hydrogen bonding and aromatic $\pi\cdots\pi$ stacking interaction within the CpG rich minor groove of DNA. Procainamide has been shown to induce structural changes in the tertiary topology of DNA.¹⁴ On the similar context, strong association of phenyl (**1**) with CpG rich DNA may alter its active conformation required by regulatory proteins such as DNMT-1 and consequently inhibit protein-DNA binding. Thus, our study provides mechanistic insight into the plausible mode of

methylation modulating activity of procainamide and its active side-chain derivatives. Our systematic investigation also provides a rapid method of screening for finding the novel non-nucleoside DNA binding (CpG rich) demethylating agents as shown in the **figure 1.15**. The screening involves four primary steps before going for *in vivo* trial. Step 1) will involve the rapid evaluation of binding affinity of compounds for a dG base in a neutral form. The extent of affinity will be determined by the drop in the peak current density. Step 2) comprise of docking simulation study with hmDNA to evaluate the affinity to partially denatured CpG rich DNA. The step 3) will evaluate cytotoxicity and sub-lethal concentration at *in vitro*. Finally increase or decrease in the global methylation level in cancer cells would decide the candidature of the compounds as DHA.

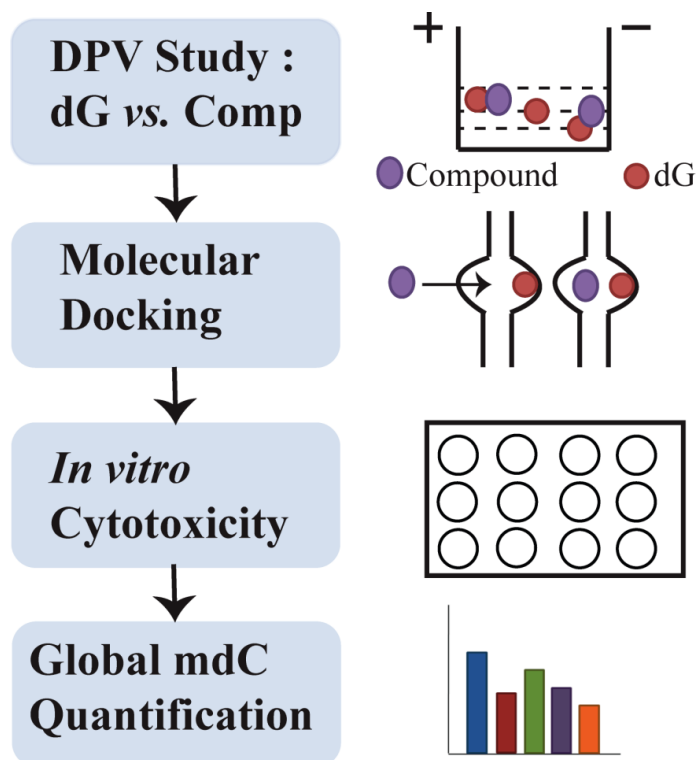


Figure 1.15.Cartoon illustration of protocol for the rapid method of screening for non-nucleosidal CpG DNA binding methylation modulators.

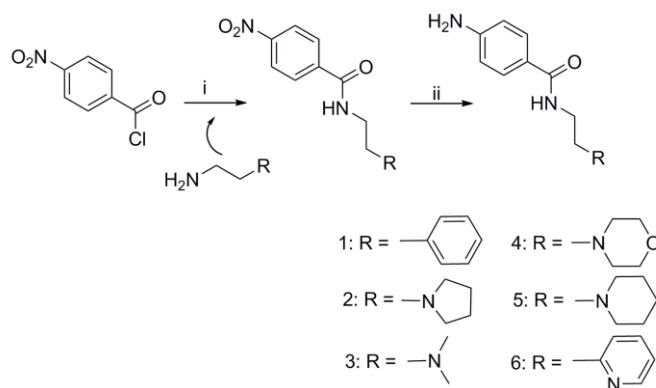
Experimental methods:

General scheme of synthesis of compounds 1-6

Compounds **1-6** were synthesized as per the reported procedure. To the stirring solution of primary amines (21.56 mmol, 2 equi.) in dry DCM, dry Et₃N (3.76 mL, 26.95 mmol, 2.5 eq) was added drop wise followed by slow addition of 4-nitrobenzoyl chloride (2g, 10.78 mmol) in dry DCM (20 mL) at 0°C. The reaction mixture was allowed to reach room temperature and was further stirred for 8 h. The solvent was evaporated under vacuum and ethyl acetate solvent was added to the crude solid reaction product. The mixture was then sequentially washed twice with saturated solution of NaHCO₃ and once with brine. The organic layer was dried over anhydrous Na₂SO₄ and evaporated under vacuum to obtain crude nitro intermediate product. 4-nitro carboxamide intermediate was used without purification for reduction step (ii).

Nitro to amine reduction was carried out in the presence of catalytic amount (10%) of Pd/C, H₂ (60 psi) in ethanol solvent at room temperature. After 8-9 h of reaction time, completion of reaction was monitored by thin layer chromatography (Ethyl acetate:methanol: 95:5) solvent system and ninhydrin reagent (pink colouration for amine spot was observant). The crude reaction mixture was filtered through celite bed to remove Pd catalyst and solvent was evaporated under vacuum to yield crude solid compound. Purification was carried out using column chromatography (20% Ethyl acetate:light petroleum to 3% methanol: Ethyl acetate solvent system) to yield compound **1-6**. Purified products were further crystallized from DCM/petroleum ether solvent system to obtain single crystals for crystal structure analysis and biological studies.

NMR spectra were recorded on AC 200MHz Bruker NMR spectrometer and HR-MS spectra were obtained from Thermoscientific Q Exactive instrument.



Reagents and condition: (i) DCM, Et₃N, 2-Phenethylamine for 1, 1-(2-Aminoethyl)pyrrolidine for 2, N,N-Dimethylethylenediamine for 3, 4-(2-Aminoethyl)morpholine for 4, 1-(2-Aminoethyl)piperidine for 5, 2-(2-Pyridyl)ethylamine for 6, RT, 8h, (ii) EtOH, Pd/C, H₂, 60 mbar, RT, 8h.

Figure 1.16. General scheme of synthesis

Experimental Synthesis:

4-amino-N-phenethylbenzamide (1) was prepared as above (general scheme of synthesis) using phenethyl amine (2.72 mL, 21.56 mmol, 2eq) to yield compound **1**. ¹H NMR (200MHz, CDCl₃) δ = 7.61 - 7.47 (m, 2 H), 7.39 - 7.27 (m, 2 H), 7.27 - 7.18 (m, 3 H), 6.75 - 6.55 (m, 2 H), 5.99 (br. s., 1 H), 3.95 (br. s., 2 H), 3.70 (q, *J* = 6.8 Hz, 3 H), 2.92 (t, *J* = 6.8 Hz, 2 H); HR-MS: (C₁₅H₁₆N₂O) 241.1335 (M+H)⁺, 263.1154 (M+Na)⁺.

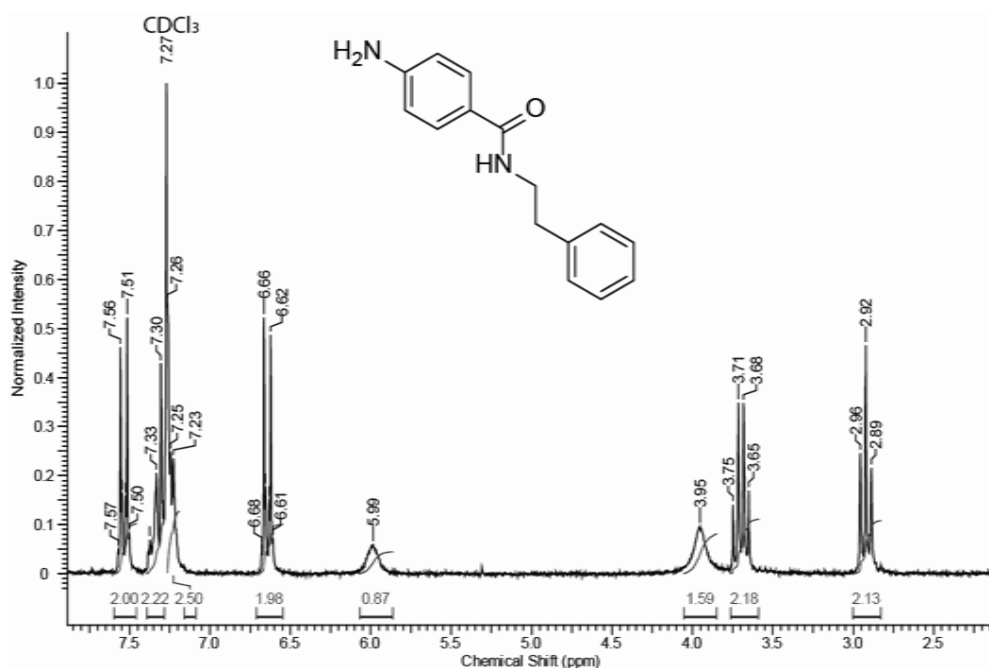


Figure 1.17. ¹H NMR of 4-amino-N-phenethylbenzamide.

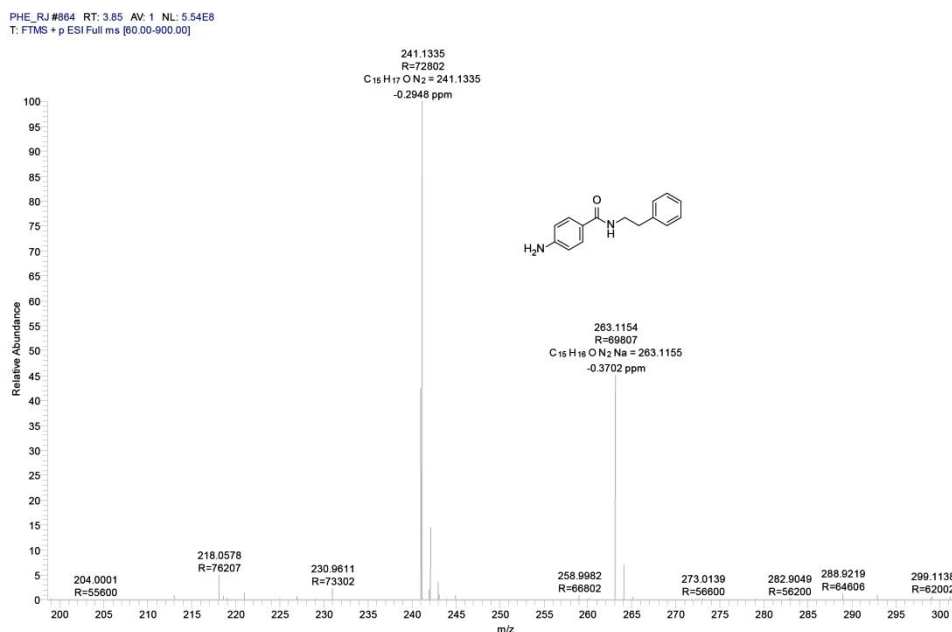


Figure 1.18.HR-MS of 4-amino-N-phenethylbenzamide.

4-amino-N-(2-(pyrrolidin-1-yl)ethyl)benzamide (2) was prepared as above using 2-pyrrolidinoethylamine, (2.73 mL, 21.56 mmol, 2 eq) to yield compound **2**. ¹H NMR (200 MHz, CDCl₃) δ = 7.63 (d, *J* = 8.6 Hz, 2 H), 6.67 (m, 3 H), 3.95 (br. s., 2 H), 3.53 (q, *J* = 5.3 Hz, 2 H), 2.69 (m, 2 H), 2.56 (m, 4 H), 1.79 (m, 4 H); HR-MS: (C₁₃H₁₉N₃O) 234.1601 (M+H)⁺.

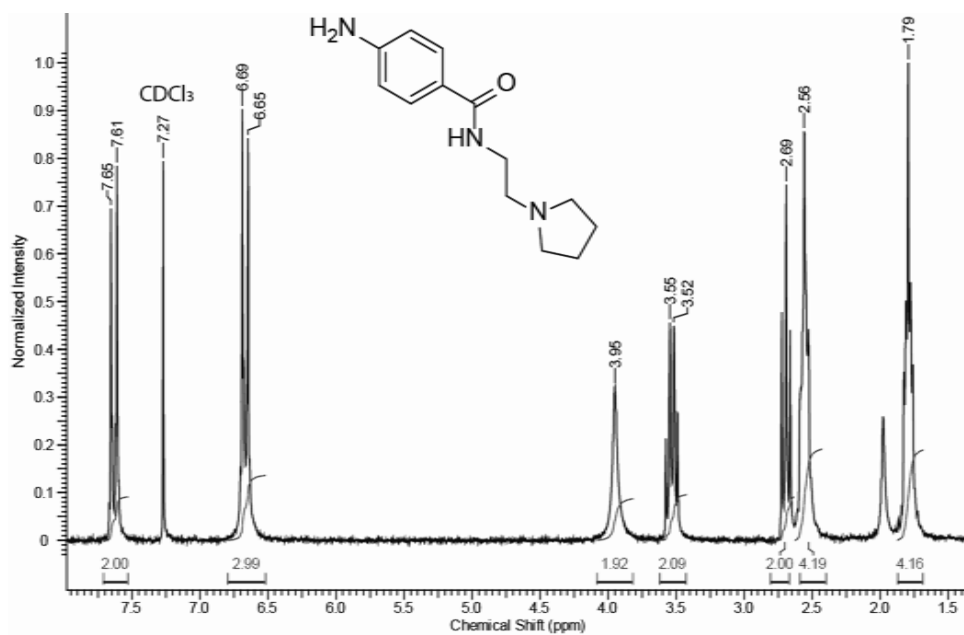


Figure 1.19.¹H NMR of 4-amino-N-(2-(pyrrolidin-1-yl)ethyl)benzamide

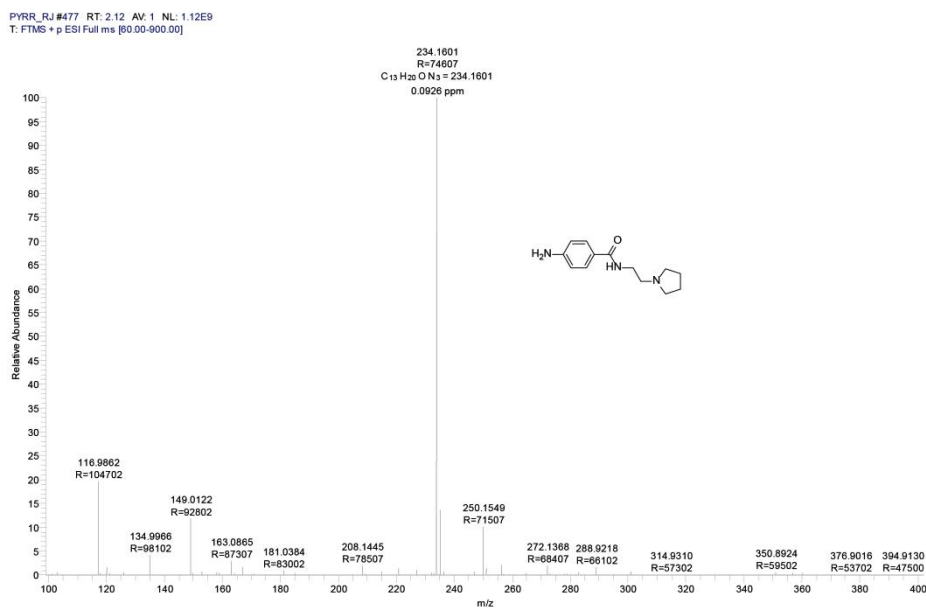


Figure 1.20. HR-MS study 4-amino-N-(2-(pyrrolidin-1-yl)ethyl)benzamide.

4-amino-N-(2-(dimethylamino)ethyl)benzamide (3) was prepared as above using 2-(Dimethylamino)ethylamine, (2.36 mL, 21.56 mmol, 2 eq) to yield compound **3**. ¹H NMR (200MHz,CDCl₃) δ = 7.70 - 7.56 (m, 2 H), 6.76 - 6.57 (m, 3 H), 3.96 (br. s., 2 H), 3.58 - 3.42 (m, 2 H), 2.51 (t, *J* = 5.9 Hz, 2 H), 2.31 - 2.20 (m, 6 H). HR-MS: (C₁₁H₁₇N₃O) 208.1444 (M+H)⁺, 230.1262 (M+Na)⁺

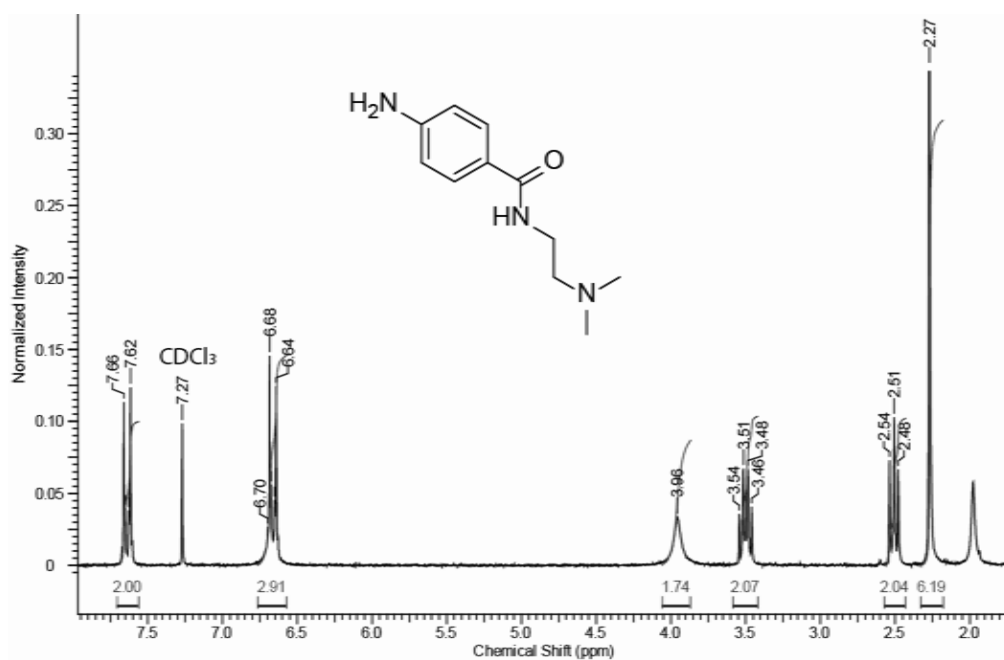


Figure 1.21. ¹H NMR of 4-amino-N-(2-(dimethylamino)ethyl)benzamide.

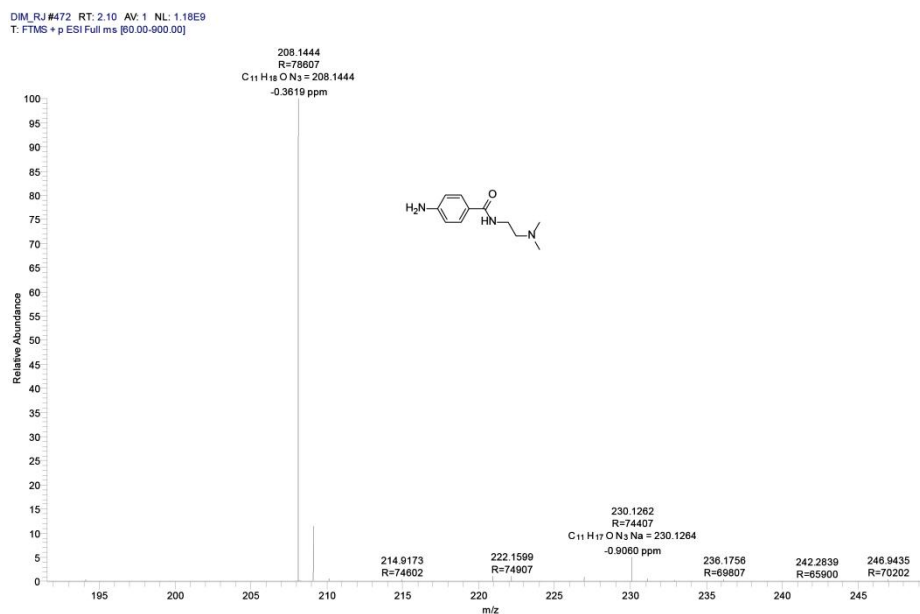


Figure 1.22. HR-MS study of 4-amino-N-(2-(dimethylamino)ethyl)benzamide.

4-amino-N-(2-morpholinoethyl)benzamide (4) was prepared as above using 2-morpholinoethylamine, (2.83 mL, 21.56 mmol, 2 eq) to yield compound **4**. ¹H NMR (200MHz, CDCl₃) δ = 7.69 - 7.52 (m, 2 H), 6.73 - 6.64 (m, 2 H), 6.61 (br. s., 1 H), 3.97 (br. s., 2 H), 3.83 - 3.63 (m, 4 H), 3.60 - 3.41 (m, 2 H), 2.59 (t, *J* = 6.1 Hz, 2 H), 2.55 - 2.42 (m, 4 H); HR-MS: (C₁₃H₁₉N₃O₂) 250.1550 (M+H)⁺.

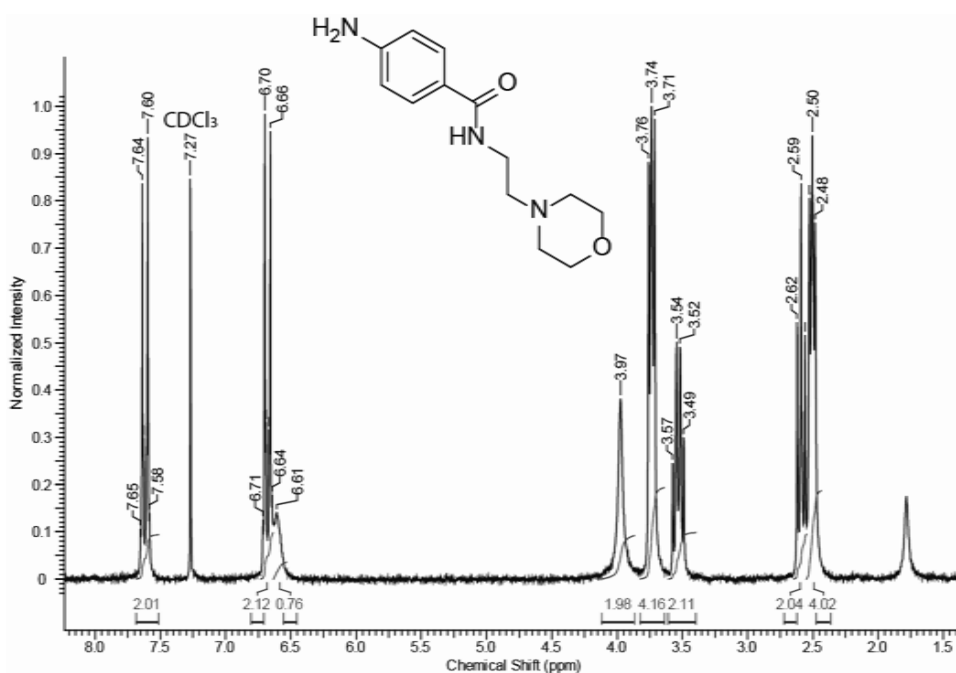


Figure 1.23. ¹H NMR of 4-amino-N-(2-morpholinoethyl)benzamide

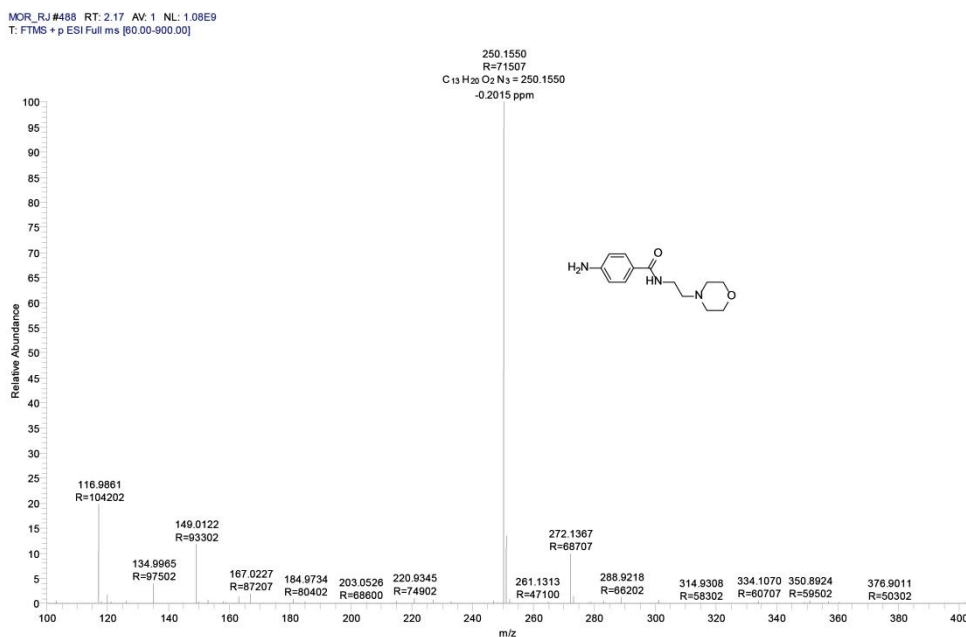


Figure 1.24. HR-MS of 4-amino-N-(2-morpholinoethyl)benzamide.

4-amino-N-(2-(piperidin-1-yl)ethyl)benzamide (5) was prepared as above using 2-piperidinoethylamine, (3.07 mL, 21.56 mmol, 2 eq) to yield compound **5**. ¹H NMR (200MHz, CDCl₃) δ = 7.70 - 7.53 (m, 2 H), 6.81 (br. s., 1 H), 6.72 - 6.55 (m, 2 H), 3.96 (br. s., 2 H), 3.59 - 3.42 (m, 2 H), 2.55 (t, J = 6.1 Hz, 2 H), 2.43 (d, J = 5.2 Hz, 4 H), 1.69 - 1.53 (m, 4 H), 1.53 - 1.34 (m, 2 H); HR-MS: (C₁₄H₂₁N₃O) 248.1756 (M+H)⁺.

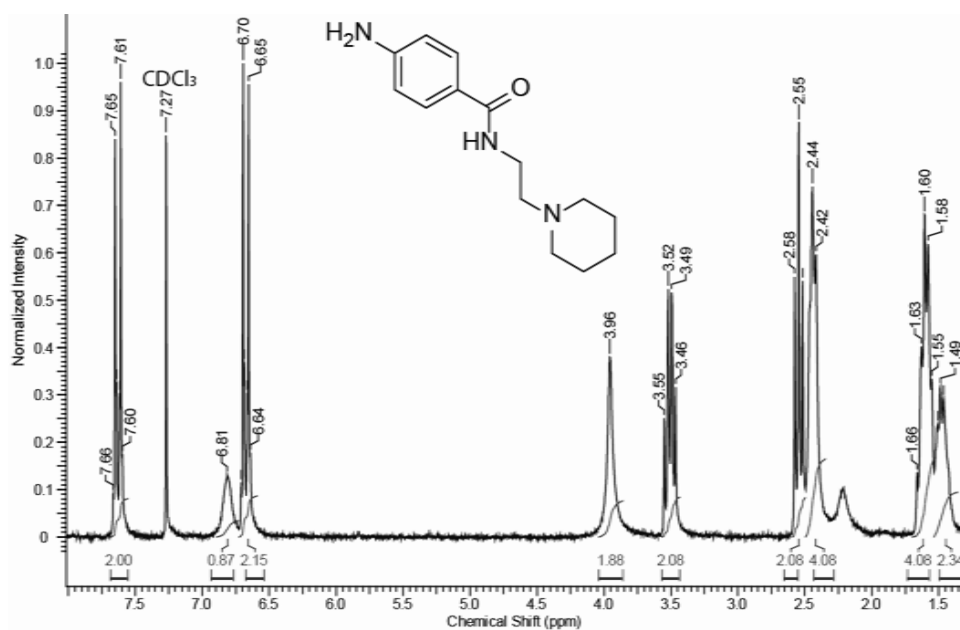


Figure 1.25. ¹H NMR of 4-amino-N-(2-(piperidin-1-yl)ethyl)benzamide

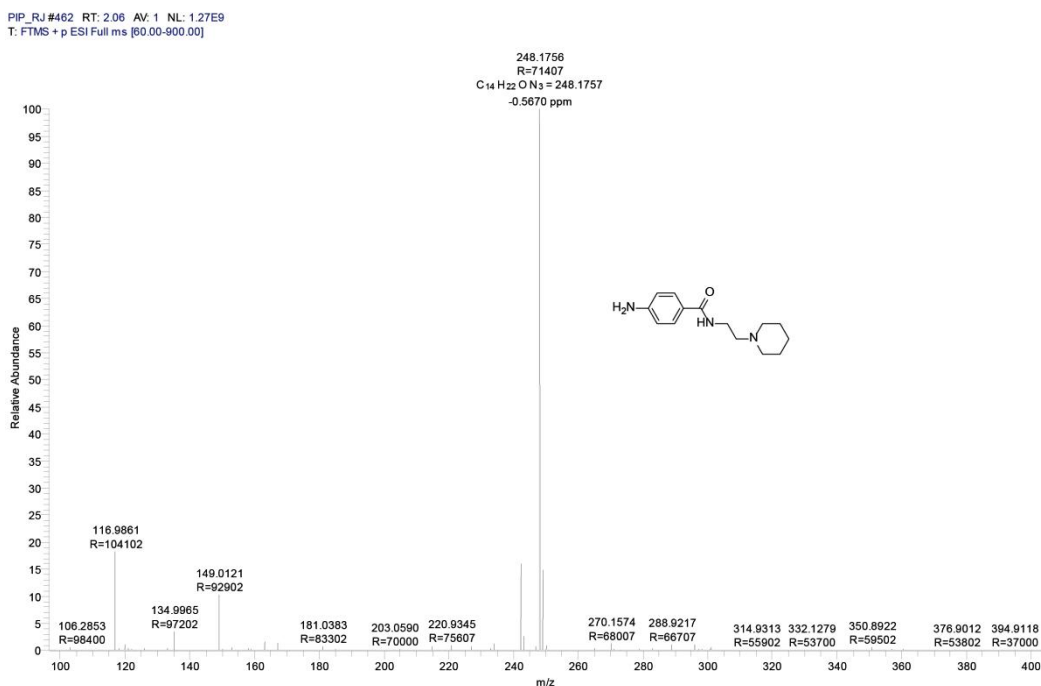


Figure 1.26. HR-MS of 4-amino-N-(2-(piperidin-1-yl)ethyl)benzamide.

4-amino-N-(2-(pyridin-2-yl)ethyl)benzamide (6) was prepared as above using 2-(2-pyridyl)ethylamine, (2.58 mL, 21.56 mmol, 2 eq) to yield compound **6**. ¹H NMR (200MHz, Acetonitrile-d₃) δ = 8.31 - 8.30 (m, 1 H), 7.51 - 7.37 (m, 1 H), 7.29 (d, *J* = 8.3 Hz, 2 H), 7.07 - 6.78 (m, 3 H), 6.40 (d, *J* = 8.5 Hz, 2 H), 4.31 (br. s., 2 H), 3.44 (q, *J* = 6.6 Hz, 2 H), 2.78 (t, *J* = 6.9 Hz, 2 H); HR-MS: (C₁₄H₁₅N₃O) 242.1288 (M+H)⁺.

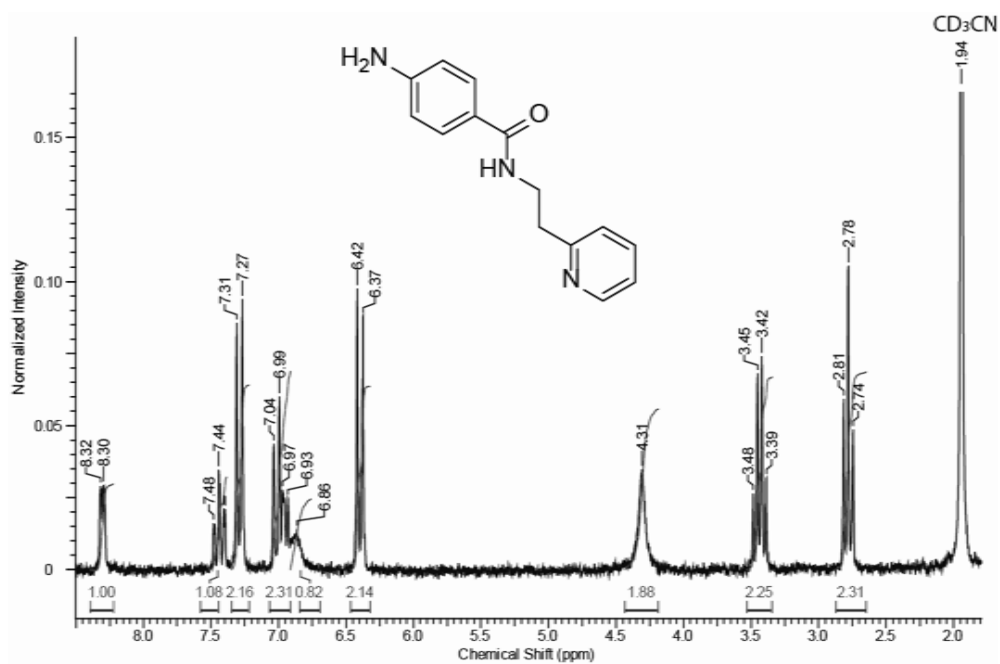


Figure 1.27. ¹H NMR of 4-amino-N-(2-(pyridin-2-yl)ethyl)benzamide.

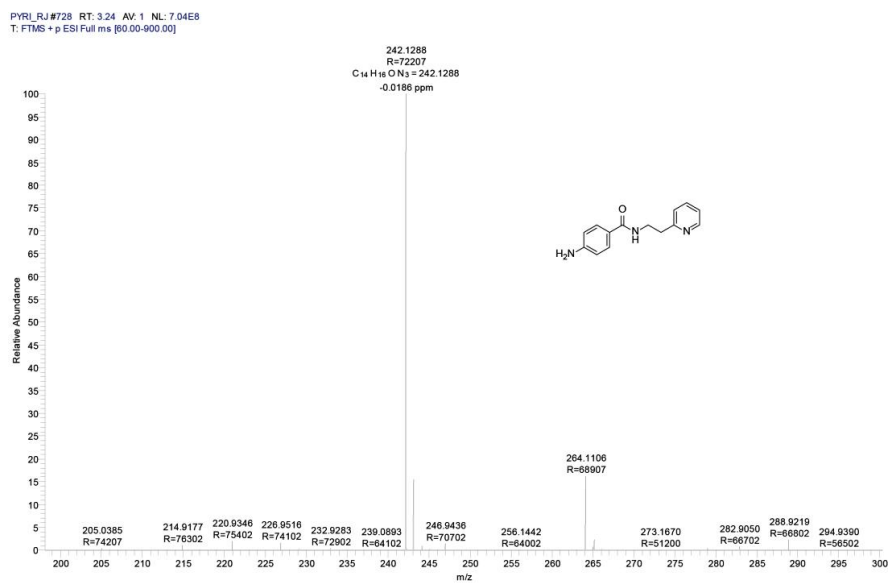
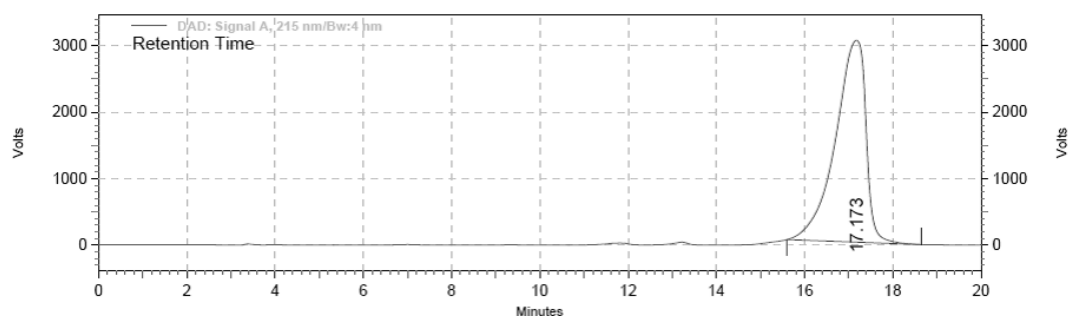


Figure 1.28. HR-MS/MS of 4-amino-N-(2-(pyridin-2-yl)ethyl)benzamide.

HPLC purity profiles of compounds

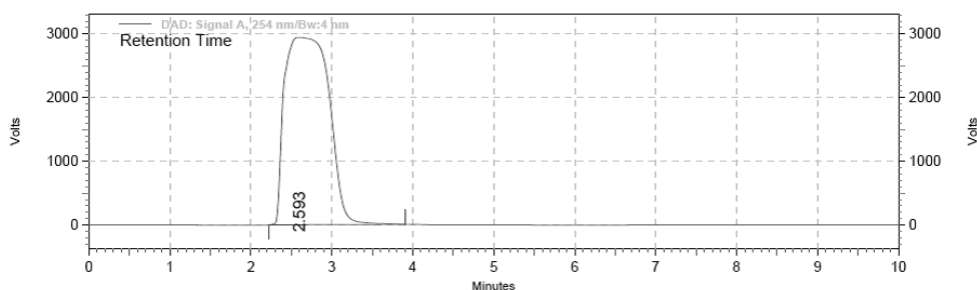


DAD: Signal A,
215 nm/Bw:4 nm
Results

Retention Time	Area	Area %	Height	Height %
17.173	306667676	100.00	6366379	100.00
Totals	306667676	100.00	6366379	100.00

Column: C18
Flow rate: 1ml/min
Solvent system: 50% MEOH 50% H₂O

Figure 1.29.HPLC % purity profile of compound1(phenyl).

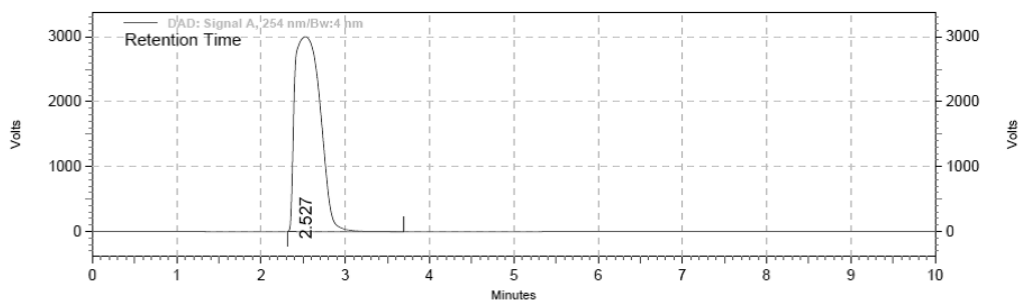


DAD: Signal A,
254 nm/Bw:4 nm
Results

Retention Time	Area	Area %	Height	Height %
2.593	235132622	100.00	6171088	100.00
Totals	235132622	100.00	6171088	100.00

Column: C18
Flow rate: 1ml/min
Solvent system: 40% MEOH 60% H₂O

Figure 1.30.HPLC % purity profile of compound 2 (pyrrolidine)

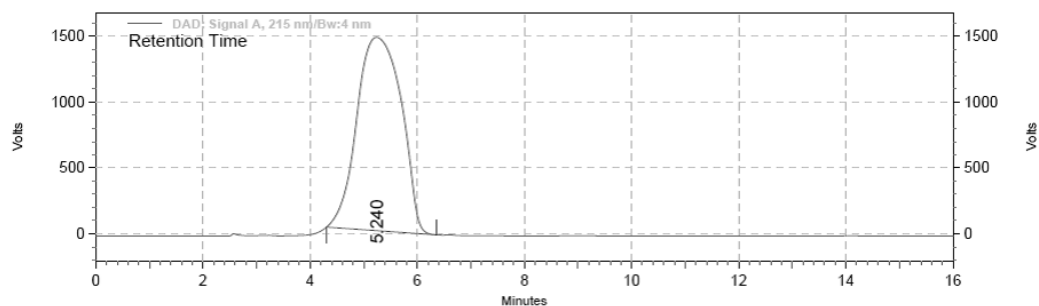


DAD: Signal A,
254 nm/Bw:4 nm
Results

Retention Time	Area	Area %	Height	Height %
2.527	132152744	100.00	6293410	100.00
Totals				
	132152744	100.00	6293410	100.00

Column: C18
Flow rate: 1ml/min
Solvent system: 40% MEOH 60% H2O

Figure 1.31.HPLC % purity profile of compound3 (dimethyl)

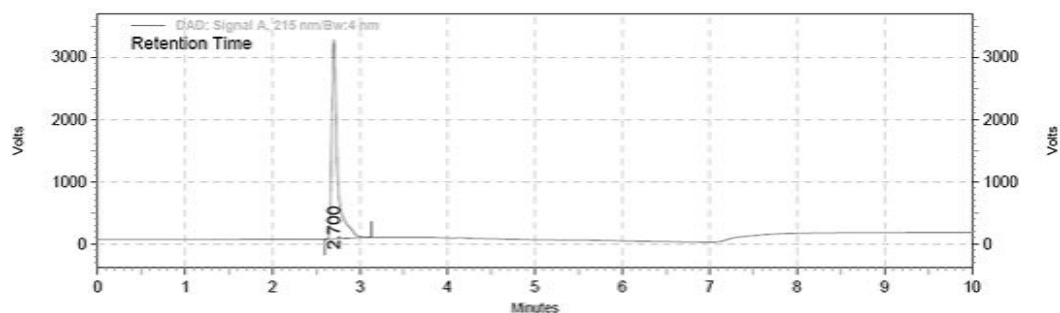


DAD: Signal A,
215 nm/Bw:4 nm
Results

Retention Time	Area	Area %	Height	Height %
5.240	178026317	100.00	3078417	100.00
Totals				
	178026317	100.00	3078417	100.00

Column : C18
Flow Rate- 1.0 ml/min
Eluent: 30%MEOH 70%H2O

Figure 1.32.HPLC % purity profile of compound4 (morpholine)

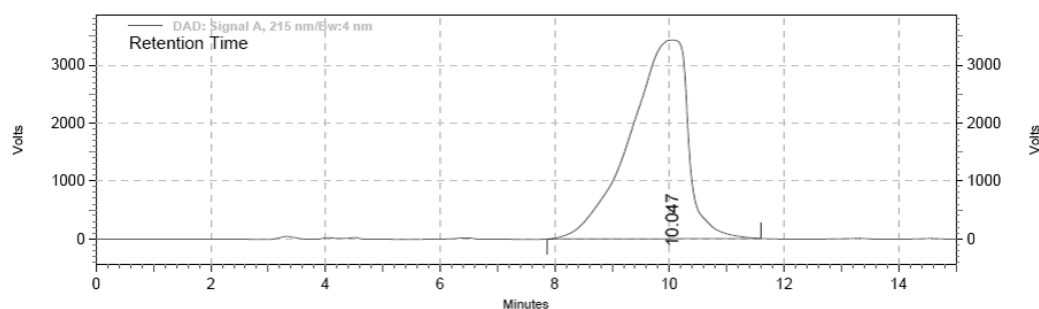


DAD: Signal A,
215 nm/Bw:4 nm
Results

Retention Time	Area	Area %	Height	Height %
2.700	30231970	100.00	6719091	100.00
Totals		30231970	6719091	100.00

Column: C18
Flow rate: 1ml/min
Solvent system: 40% MEOH 60% H2O

Figure 1.33.HPLC % purity profile of compound5 (piperidine)



DAD: Signal A,
215 nm/Bw:4 nm
Results

Retention Time	Area	Area %	Height	Height %
10.047	505561942	100.00	7196492	100.00
Totals		505561942	7196492	100.00

Column: C18
Flow rate: 1ml/min
Solvent system: 40% MEOH 60% H2O

Figure 1.34.HPLC % purity profile of compound6 (pyridine)

X-ray Crystallography:

Single crystal structure of all compounds **1-6** were determined by measuring X-ray intensity data on a Bruker SMART APEX II single crystal X-ray CCD diffractometer having graphite-monochromatised Mo-K α ($\lambda = 0.71073$ Å) radiation. The X-ray generator was operated at 50 kV and 30 mA. A preliminary set of cell constants and an orientation matrix were calculated from total 36 frames. The optimized strategy used for data collection consisted different sets of φ and ω scans with 0.5° steps in φ/ω . Data were collected keeping the sample-to-detector distance fixed at 5.00 cm. The X-ray data acquisition was monitored by APEX II program suit. All the data were corrected for Lorentz-polarization and absorption effects (Multi scan) using SAINT and SADABS programs integrated in APEX II package.³³ The structures were solved by direct methods and refined by full matrix least squares, based on F^2 , using SHELX-97.³⁴ Molecular diagrams were generated using ORTEP-3³⁵ and Mercury programs.³⁶ Geometrical calculations were performed using SHELXTL³⁴ and PLATON.³⁷ The H atoms in **1** (phenyl), **2** (pyrrolidine) and **5** (piperidine) crystals were placed in idealized positions (C-H = 0.93 Å for the phenyl H atoms, C-H = 0.97 Å for the methyl H-atoms and N-H = 0.86 Å for the amide H atom) and constrained to ride on their parent atoms [$U_{\text{iso}}(\text{H}) = 1.2 U_{\text{eq}}(\text{C})$]. The H-atoms for the **3**(dimethyl), **4**(morpholine) and **6**(pyridine) crystals were also placed in idealized positions however with different C-H distances (C-H = 0.95 Å for the phenyl H atoms, C-H = 0.99 Å for the methyl H-atoms and N-H = 0.88 Å for the amide H atom) and constrained to ride on their parent atoms [$U_{\text{iso}}(\text{H}) = 1.2 U_{\text{eq}}(\text{C})$]. The crystals of **6**(pyridine) showed the presence of disordered solvent molecule.

Table 1.2: Crystallographic data table for compounds 1-6

Crystal Data	1(Phenyl)	2(Pyrrolidine)	3(Dimethyl)
Formula	C ₁₅ H ₁₆ N ₂ O	C ₁₃ H ₁₉ N ₃ O	C ₁₁ H ₁₇ N ₃ O
M _r	240.30	233.31	207.28
Crystal Size, mm	0.25 x 0.09 x 0.06	0.09 x 0.08 x 0.03	0.28 x 0.12 x 0.08
Temp. (K)	296(2)	296(2)	100(2)
Crystal Syst.	Orthorhombic	Orthorhombic	Orthorhombic
Space Group	<i>P</i> 2 ₁ 2 ₁ 2 ₁	<i>P</i> 2 ₁ 2 ₁ 2 ₁	<i>P</i> 2 ₁ 2 ₁ 2 ₁
<i>a</i> /Å	9.5732(13)	6.391(3)	5.9755(3)
<i>b</i> /Å	9.6932(13)	13.847(7)	13.1272(8)
<i>c</i> /Å	14.0706(18)	14.418(7)	14.4992(8)
α°	90	90	90
β°	90	90	90
γ°	90	90	90
<i>V</i> /Å ³	1305.7(3)	1276.0(11)	1137.34(11)
<i>Z</i>	4	4	4
<i>D</i> _{calc} /g cm ⁻³	1.222	1.214	1.211
<i>m</i> /mm ⁻¹	0.078	0.079	0.080
<i>F</i> (000)	512	504	448
<i>Ab. Correct.</i>	multi-scan	multi-scan	multi-scan
<i>T</i> _{min} / <i>T</i> _{max}	0.9953/0.9808	0.9980/0.9929	0.9936/0.9779
2 θ _{max}	50	50	50
Total reflns.	13719	6182	5135
uniquereflns.	2289	2235	1995
<i>h, k, l</i> (min, max)	(-11, 10), (-11, 11), (-15, 16)	(-7, 7), (-16, 14), (-17, 16)	(-7, 6), (-15, 11), (-17, 14)
<i>R</i> _{int}	0.0645	0.0566	0.0275
No. of para	163	163	139
<i>R</i> <i>I</i> [<i>I</i> > 2 σ (<i>I</i>)]	0.0671	0.0567	0.0306
<i>wR</i> 2 [<i>I</i> > 2 σ (<i>I</i>)]	0.1611	0.1347	0.0812
<i>R</i> <i>I</i> [all data]	0.0885	0.1058	0.0319
<i>wR</i> 2 [all data]	0.1711	0.1635	0.0824
goodness-of-fit	1.236	0.998	1.045
$\Delta\rho_{\max}, \Delta\rho_{\min}$ (eÅ ⁻³)	+0.331, -0.249	+0.177, -0.147	+0.249, -0.211
CCDC no.	1425934	1425935	1425936

Crystal Data	4(Morpholine)	5(Piperidine)	6(Pyridine)
Formula	C ₁₃ H ₁₉ N ₃ O ₂	C ₁₄ H ₂₁ N ₃ O	C ₁₄ H ₁₅ N ₃ O
M _r	249.31	247.34	241.29
Crystal Size, mm	0.32 x 0.12 x 0.09	0.25 x 0.09 x 0.07	0.15 x 0.08 x 0.05
Temp. (K)	100(2)	296(2)	296 (2)
Crystal Syst.	Orthorhombic	Orthorhombic	Orthorhombic
Space Group	<i>P</i> 2 ₁ 2 ₁ 2 ₁	<i>P</i> 2 ₁ 2 ₁ 2 ₁	<i>P</i> -4 2 ₁ c
<i>a</i> /Å	9.3267(14)	9.624(2)	19.720(5)
<i>b</i> /Å	9.8628(15)	10.246(3)	19.720(5)
<i>c</i> /Å	14.061(2)	13.768(3)	8.161(2)
α°	90	90	90
β°	90	90	90
γ°	90	90	90
<i>V</i> /Å ³	1293.4(3)	1357.5(6)	3173.6(14)
<i>Z</i>	4	4	8
<i>D</i> _{calc} /g cm ⁻³	1.280	1.210	1.010
<i>m</i> /mm ⁻¹	0.088	0.078	0.066
<i>F</i> (000)	536	536	1024
<i>Ab. Correct.</i>	multi-scan	multi-scan	multi-scan
<i>T</i> _{min} / <i>T</i> _{max}	0.9921/0.9723	0.9945/0.9807	0.9967 /0.9902
2 θ _{max}	50	50	50
Total reflns.	6521	5609	12797
uniquereflns.	2263	2383	2746
<i>h, k, l</i> (min, max)	(-11, 11), (-11, 11), (-16, 13)	(-11, 11), (-5, 12), (-16, 16)	(-23, 21), (-17, 23), (-9, 9)
<i>R</i> _{int}	0.0229	0.0766	0.2880
No. of para	163	164	165
<i>R</i> 1 [<i>I</i> > 2 σ (<i>I</i>)]	0.0305	0.0643	0.1515
<i>wR</i> 2 [<i>I</i> > 2 σ (<i>I</i>)]	0.0757	0.1486	0.3264
<i>R</i> 1 [all data]	0.0322	0.0790	0.2503
<i>wR</i> 2 [all data]	0.0766	0.1626	0.4111
goodness-of-fit	1.089	1.004	1.004
$\Delta\rho_{\max}, \Delta\rho_{\min}$ (eÅ ⁻³)	+0.235, -0.173	+0.359, -0.333	+0.613, -0.360
CCDC no.	1425937	1425938	1425939

Differential Pulse Voltammetry

(DPV) was performed using CHI 900b potentiostat with pulse amplitude of 50 mV, pulse width of 0.2 s and a pulse period of 0.5 s. A three electrode system containing glassy carbon (GC, 3 mm diameter) as working electrode, Pt-foil as counter electrode and a standard calomel electrode (SCE, 0.1 M KCl) as reference electrode, was employed for this purpose. 0.1 M phosphate buffer (pH 7.4) was used as electrolyte. 0.1 M stocks were prepared for procainamide, compounds **1-6** and 2-deoxyguanosine (dG) in cell culture grade DMSO. The solutions of dG and compound were mixed thoroughly and the dG to compound ratio was kept constant at 4.0 for all the experiments. All the solutions were incubated at 37°C for 1 h before doing DPV experiments. Final concentrations of dG and compounds were 790.5 μM and 197.6 μM respectively. Potential was scanned from anodically from -0.25 to 1 V vs SCE with an increment in potential of 4 mV at 30°C. Each measurement was repeated thrice and the average was taken as the final result. The surface of GC electrode was renewed every time by mechanical polishing with 0.1 μm alumina powder followed by sonication in deionized (DI) water for 5 min. Similarly, the electrochemical cell was also washed thoroughly after each experiment.

Docking Study:

To perform the molecular docking, starting conformations of compound **1-6** were extracted from their crystal coordinates. Bioactive conformations were generated using MacroModel module and further minimized with OPLS2005 force field in Maestro 9.1 (Schrödinger LLC, New York, NY, 2010). Generated possible conformations of compounds were further used for docking study. Crystal structures of CpG rich partially denatured hemimethylated (hmDNA) were obtained from

Glide Score	H-bond Score (E1)	Van der Waals Energy score (E2)
It is an empirical scoring function that estimates the ligand bonding free energy. It is inclusive of (electrostatic, van der Waals) contributions as well as rewarding or penalizing interactions which influence ligand binding. It is used to score docked poses and compare their relative binding affinities. ³⁸	The H-bond per-residue interaction term is calculated for estimating the strength of H-bonding interaction between the ligand and a given residue. The more negative score suggests stronger hydrogen bonding. The score takes into account the types of atoms involved and geometry of hydrogen bonding. ³⁹	Van der Waals energy term (E2) gives the estimates van der Waals association and steric attraction between ligand and given residue. ⁴⁰

PDB ID: 4DA4. Protein preparation wizard was utilized to remove protein component and perform optimization. DNA biomolecule was subjected to restrained minimization using OPLS 2005 force-field. Further grids were generated so that entire DNA molecules fit within grid box and the centre lies at the centroid of DNA strands. The larger gridbox size was used to allow docking with entire DNA molecule. Flexible docking method was performed with extra-precision (XP) implemented in Glide without applying constraints during docking. The post docking minimization was performed and binding energy with interacting residues was calculated. Docking poses were filtered based cut-off assigned for τ_1 which is 160° - 180° . Torsion angle parameters and structure overlay of ligand conformations from chosen docked poses are depicted in figure 1.36 and table 1.4.

CSD survey

CSD survey was carried out using CCDC conquest version 1.17⁴¹The molecular structure of the query is depicted in figure below. Torsion angle τ_1 (C1-C7-N2-C8) was used as parameter for statistical analysis. Almost for 92% hits torsion angle τ_1 lies within the range of **160.112° -179.980°**.

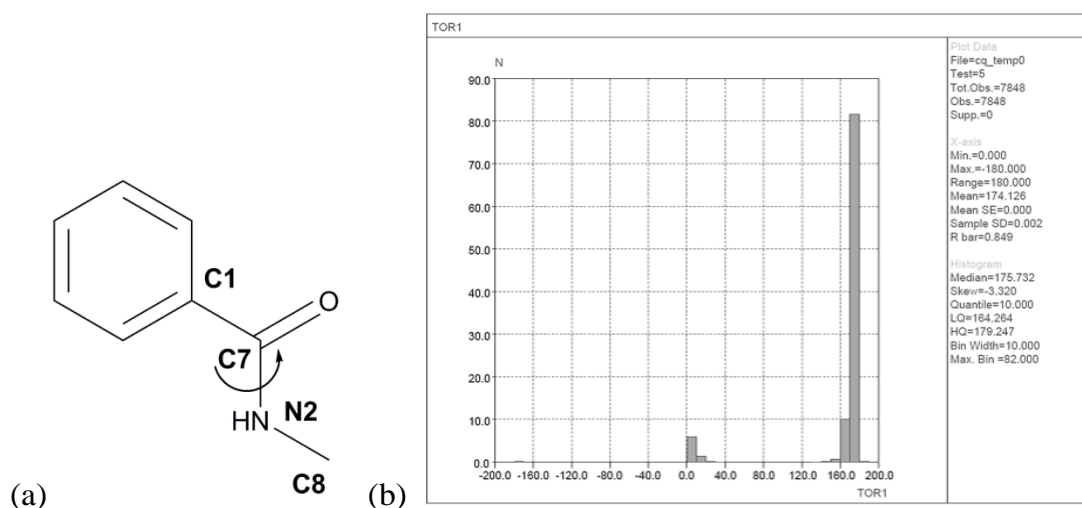


Figure 1.36.(a)Molecular structure of query (b) XY plot of X-torsion range and Y- number of hits %

Table1.3.Number of hits,torsion anglerrange and %hits

No of hits	Range (°)	%
6398	170.002-179.980	81.92
785	160.112-169.994	10.05
54	150.098-159.950	0.691
463	0-9.926	5.92
110	10.012-19.667	1.40

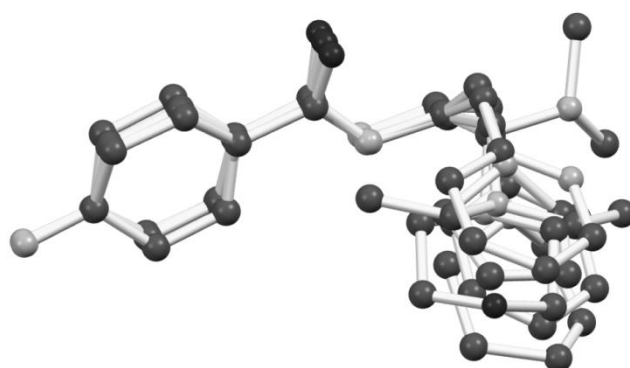


Figure 1.37 .Overlay of ligand conformations of compounds **1-6** and procainamide extracted from docked poses.

Table 1.4 .Torsion angle table τ_1 of ligand conformations from selected docked poses.

Comp.	Phenyl	Pyrrolidine	piperidine	Morpholine	dimethyl	Pyridine	Procainamide
τ_1	179.22	-178.84	-178.81	-175.69	178.58	177.75	179.45

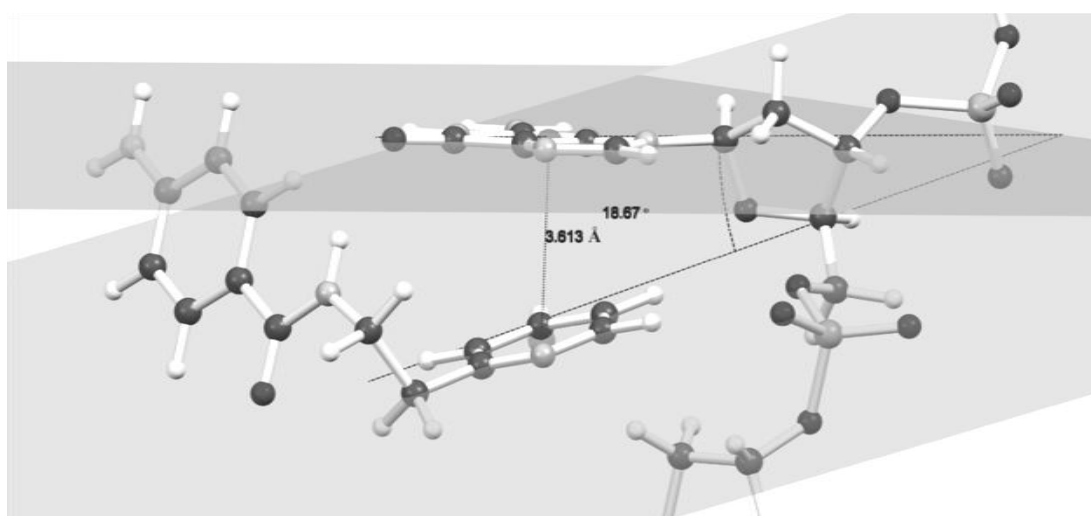


Figure 1.38 . $\pi \cdots \pi$ stacking geometry of compound **6** (pyridine) with dG base at the target site (extracted from docked pose) displaying Cg...Cg distance (centroid to centroid distance between aromatic rings) and dihedral angle α between the aromatic rings.

Cytotoxicity Assay:

The cell lines MCF-7 were procured from National Center for Cell sciences Repository, Pune. Cell viability after compound treatment was analyzed by MTT assay. MCF-7 cells were seeded in 96-well plate (day 0) with seeding density of ~7500 cells/well. After 24h, the media was changed and 5 μ L of compound dissolved in DMSO at concentration ranging from 100 μ M to 500 μ M was added to 95 μ L media (final DMSO conc. 0.5%). Control wells contained cells in MEM media or cell treated with 0.5% DMSO (DMSO control). The plates were incubated at 37°C in 5% CO₂ incubator overnight. After 24 h., 10 μ L of 3-(4,5-dimethylthiazol-2-yl)-2,5-diphenyltetrazoliumbromide (MTT, Himedia, 0.5mg/mL) was added in culture medium in each well. After 3.5 h incubation at 37°C in 5% CO₂, the culture media was removed and 150 μ L of DMSO (HiMedia, India) was added in each well to dissolve the formazan salts. The absorbance of the color developed was recorded at 550nm and 620nm using automatic plate reader. The independent experiments were set up in biological triplicates for 24, 48, and 72 hrs and each experiment was performed in technical and biological triplicates. The graph for cell viability was plotted using Microsoft Excel 2007 version and performed One-way ANOVA to test the statistical significance for the outcomes at $P < 0.05$.

Global methylation quantification assay

The experiment was performed using EpiSeeker methylated DNA Quantification Kit (ab117128) as per the Manufacturer's protocol. MCF-7 cells with a density of $\sim 1 \times 10^6$ cells in T-25 flasks were treated with 25 μ L of compounds (100 μ M, 0.5% DMSO) for 72 h at 37°C in 5% CO₂ incubator. After 72 h, DNA was isolated from cells using phenol: chloroform method. The purity of the DNA was determined by 260/280 ratio. 100 mg of the isolated pure DNA were bound with binder solution to the wells provided by the kit. As such the plate was incubated at 37°C for 90min. The DNA was washed with buffer to remove excess of binding solution. It was then incubated with primary antibody for 1 h at 37°C, followed by secondary antibody for 30min at RT. The relative percentage of 5-methyl cytosine was colorimetrically quantified by reading absorbance at 450nm. The experiments

were performed in technical duplicate and biological triplicates. The graphs were plotted using OriginLab software.

Calculation

$$5\text{mC } \% = \left(\frac{(\text{Sample OD} - \text{Negative Control OD}) / \text{Sample DNA (ng)}}{((\text{Positive Control OD} - \text{Negative Control OD}) \times 2) / \text{Positive Control DNA (ng)}} \right) \times 100$$

DNMT-1 Inhibition Assay.

For DNMT1 assay EpiQuik DNAMethyltransferase 1 Activity/Inhibitor Screening Assay Core Kit (P-3006A) has been used and the protocol for the assay is followed as per the manufacturer's instruction. The compounds (**1** and PCA) at 100 μ M conc. (DMSO at 0.01%) are incubated with substrate and pure DNMT1 protein for 1.5 h in assay buffer. As control experiment DMSO at 0.01% also have been tested but not included in the graph due to obvious minute amount of inhibition. The inhibition is then colorimetrically quantified using antibody specific for 5-methyl cytosine and reading absorbance at 450nm. The result is expressed in percent inhibition using the given formula

$$\text{Inhibition } \% = 1 - \frac{\text{OD (no inhibitor control - blank)}}{\text{OD (inhibitor sample - blank)}} \times 100\%$$

References:

1. (a) J. C. Rice and C. D. Allis, *Curr. Opin. Cell Biol.*, 2001, **13**, 263-273;(b) R. Jaenisch and A. Bird, *Nat. Genet.*, 2003, **33**, 245-254;(c) W. Reik, *Nature*, 2007, **447**, 425-432;(d) P. A. Jones and D. Takai, *Science*, 2001, **293**, 1068-1070;(e) F. Mohn and D. Schübeler, *Trends Genet.*, 2009, **25**, 129-136;(f) R. K. Slotkin and R. Martienssen, *Nat. Rev. Genet.*, 2007, **8**, 272-285;(g) W. Reik and A. Lewis, *Nat. Rev. Genet.*, 2005, **6**, 403-410;(h) S. N. Rajpathak, D. D. Deobagkar, *Curr. Pharm. Des.*, 2014, **20**, 1778-1785;(i) S. N. Rajpathak, S. K. Vellarikkal, A. Patowary, V. Scaria, S. Sivasubbu and D. D. Deobagkar, *PLoS One*, 2014, **9**, e100076;(j) A. Kelkar and D. Deobagkar, *Epigenetics*, 2010, **5**, 612-618;(k) N. Tsankova, W. Renthal, A. Kumar and E. J. Nestler, *Nat. Rev. Neurosci.*, 2007, **8**, 355-367.
2. A. M. Deaton and A. Bird, *Genes Dev.*, 2011, **25**, 1010-1022.
3. (a) M. Ehrlich, *Oncogene*, 2002, **21**, 5400-5413;(b) M. Ehrlich, *Eoigenomics*, 2009, **1**, 239-259;(c) R. J. W. O'Neill, M. J. O'Neill and J. A. M. Graves, *Nature*, 1998, **393**, 68-72;(d) S. P. Kabekkodu, S. Bhat, R. Radhakrishnan, A. Aithal, R. Mascarenhas, D. Pandey, L. Rai, P. Kushtagi, G. P. Mundyat and K. Satyamoorthy, *J. Biol. Chem.*, 2014, **289**, 10637-10649;(e) P. M. Das and R. Singal, *J. Clin. Oncol.*, 2004, **22**, 4632-4642;(f) Q. W. Chen, X. Y. Zhu, Y. Y. Li and Z. Q. Meng, *Oncol. Rep.*, 2014, **31**, 523-532;(g) M. Esteller, *Oncogene*, 2002, **21**, 5427-5440.
4. (a) J. P. Issa, *Clin. Cancer Res.*, 2007, **13**, 1634-1637;(b) F. Lyko and R. Brown, *J. Natl. Cancer Inst.*, 2005, **97**, 1498-1506;(c) C. B. Yoo and P. A. Jones, *Nat. Rev. Drug Discov.*, 2006, **5**, 37-50;(d) X. Yang, F. Lay, H. Han and P. A. Jones, *Trends Pharmacol. Sci.*, 2010, **31**, 536-546;(e) S. Heerboth, K. Lapinska, N. Snyder, M. Leary, S. Rollinson and S. Sarkar, *Genet. Epigenet.*, 2014, **6**, 9-19.
5. (a) J. K. Christman, *Oncogene*, 2002, **21**, 5483-5495;(b) C. Stresemann and F. Lyko, *Int. J. Cancer*, 2008, **123**, 8-13;(c) J. C. Cheng, C. B. Matsen, F. A. Gonzales, W. Ye, S. Greer, V. E. Marquez, P. A. Jones and E. U. Selker, *J. Natl. Cancer Inst.*, 2003, **95**, 399-409;(d) Q. Zhao, J. Fan, W. Hong, L. Li and M. Wu, *SpringerPlus*, 2012, **1**, 65.

6. (a) S. Castellano, D. Kuck, M. Viviano, J. Yoo, F. LÓpez-Vallejo, P. Conti, L. Tamborini, A. Pinto, J. L. Medina-Franco and G. Sbardella, *J. Med. Chem.*, 2011, **54**, 7663-7677;(b) M. Z. Fang, Y. Wang, N. Ai, Z. Hou, Y. Sun, H. Lu, W. Welsh and C. S. Yang, *Cancer Res.*, 2003, **63**, 7563-7570;(c) D. K. Dipl.-Chem, L. Schermelleh, S. Manetto, H. Leonhardt and T. Carell, *Angew. Chem., Int. Ed.*, 2008, **47**, 1515-1518;(d) Z. Liu, S. Liu, Z. Xie, R. E. Pavlovicz, J. Wu, P. Chen, J. Aimiwu, J. Pang, D. Bhasin, P. Neviani, J. R. Fuchs, C. Plass, P. K. Li, C. Li, T. H. M. Huang, L. C. Wu, L. Rush, H. Wang, D. Perrotti, G. Marcucci and K. K. Chan, *J. Pharmacol. Exp. Ther.*, 2009, **329**, 505-514;(e) T. Suzuki, R. Tanaka, S. Hamada, H. Nakagawa and N. Miyata, *Bioorg. Med. Chem. Lett.*, 2010, **20**, 1124-1127.
7. C. Gros, L. Fleury, V. Nahoum, C. Faux, S. Valente, D. Labella, F. Cantagrel, E. Rilova, M. A. Bouhleb, M. H. David-Cordonnier, I. Dufau, F. Ausseil, A. Mai, L. Mourey, L. Lacroix, and P. B. Arimondo, *J. Biol. Chem.*, 2015, **290**, 6293-6302.
8. R. L. Fagan, D. E. Cryderman, L. Kopelovich, L. L. Wallrath and C. Brenner, *J. Biol. Chem.*, 2013, **288**, 23858-23867.
9. (a) Z. Gao, Z. Xu, M. S. Hung, Y. C. Lin, T. Wang, M. Gong, X. Zhi, D. M. Jablons and L. You, *Oncol. Rep.*, 2009, **22**, 1479-1484;(b) X. Lin, K. Asgari, M. J. Putzi, W. R. Gage, X. Yu, B. S. Cornblatt, A. Kumar, S. Piantadosi, T. L. DeWeese, A. M. De Marzo and W. G. Nelson, *Cancer Res.*, 2001, **61**, 8611-8616;(c) B. Segura-Pacheco, C. Trejo-Becerril, E. Perez-Cardenas, L. Taja-Chayeb, I. Mariscal, A. Chavez, C. Acuña, A. M. Salazar, M. Lizano and A. Dueñas-Gonzalez, *Clin. Cancer Res.*, 2003, **9**, 1596-1603;(d) M. Tada, F. Imazeki, K. Fukai, A. Sakamoto, M. Arai, R. Mikata, T. Tokuhisa and O. Yokosuka, *Hepatol. int.*, 2007, **1**, 355-364;(e) A. Villar-Garea, M. F. Fraga, J. Espada and M. Esteller, *Cancer Res.*, 2003, **63**, 4984-4989;(f) W. F. El-Hadidy, A. R. Mohamed and H. F. Manna, *Alexandria Journal of Medicine*, 2015, **51**, 65-71.
10. Y. S. Lin, A. Y. Shaw, S. G. Wang, C. C. Hsu, I. W. Teng, M. J. Tseng, T. H. Huang, C. S. Chen, Y. W. Leu and S. H. Hsiao, *J. Biomed. Sci.*, 2011, **18**, 3.

11. (a) C. Fenoglio, E. Boncompagni, B. Chiavarina, S. Cafaggi, M. Cilli and M. Viale, *Anticancer Res.*, 2005, **25**, 4123-4128;(b) M. Viale, I. Pastrone, C. Pellecchia, M. O. Vannozzi, S. Cafaggi and M. Esposito, *Anti-Cancer Drugs*, 1998, **9**, 457-463;(c) M. Viale, M. O. Vannozzi, I. Pastrone, M. A. Mariggió, A. Zicca, A. Cadoni, S. Cafaggi, G. Tolino, G. Lunardi, D. Civalleri, W. E. Lindup and M. Esposito, *J. Pharmacol. Exp. Ther.*, 2000, **293**, 829-836;(d) J. G. Zhang, L. F. Zhong, M. Zhang, and Y. X. Xia, *Arch. Toxicol.*, 1992, **66**, 354-358;(e) A. Zicca, S. Cafaggi, M. A. Mariggió, M. O. Vannozzi, M. Ottone, V. Bocchini, G. Caviglioli and M. Viale, *Eur. J. Pharmacol.*, 2002, **442**, 265-272.
12. (a) O. Altundag, K. Altundag and M. Gunduz, *Med. Hypotheses*, 2004, **63**, 684-687;(b) L. Halby, C. Champion, C. Sénamaud-Beaufort, S. Ajjan, T. Drujon, A. Rajavelu, A. Ceccaldi, R. Jurkowska, O. Lequin and W. G. Nelson, A. Guy, A. Jeltsch, D. Guianvarc'h, C. Ferroud and P. B. Arimondo, *ChemBioChem*, 2012, **13**, 157-165.
13. M. M. Reidenberg and D. E. Drayer, *Angiology*, 1986, **37**, 968-971.
14. (a) T. J. Thomas and R. P. Messner, *Arthritis Rheum.*, 1986, **29**, 638-645;(b) W. Zacharias and W. J. Koopman, *Arthritis Rheum.*, 1990, **33**, 366-374.
15. B. H. Lee, S. Yegnasubramanian, X. Lin and W. G. Nelson, *J. Biol. Chem.*, 2005, **280**, 40749-40756.
16. N. Singh, A. Dueñas-González, F. Lyko and J. L. Medina-Franco, *ChemMedChem*, 2009, **4**, 792 – 799.
17. J. D. McKinney, A. Richard, C. Waller, M. C. Newman and F. Gerberick, *Toxicol. Sci.*, 2000, **56**, 8-17.
18. (a) S. Castellano, D. Kuck, M. Sala, E. Novellino, F. Lyko and G. Sbardella, *J. Med. Chem.*, 2008, **51**, 2321-2325;(b) G. Ping, G. Lv, S. Gutmann, C. Chen, R. Zhang and X. Wang, *J. Nanosci. Nanotechnol.*, 2006, **6**, 91-94;(c) G. Lv, Z. Chen, J. Zheng, F. Wei, H. Jiang, R. Zhang and X. Wang, *J. Mol. Struct.: THEOCHEM*, 2010, **939**, 44-52.
19. H. R. Lawrence, M. P. Martin, Y. Luo, R. Pireddu, H. Yang, H. Gevariya, S. Ozcan, J. Y. Zhu, R. Kendig, M. Rodriguez, R. Elias, J. Q. Cheng, S. M. Sebt, E. Schonbrunn and N. J. Lawrence, *J. Med. Chem.*, 2012, **55**, 7392-7416.

20. (a) K. A. Brameld, B. Kuhn, D. C. Reuter and M. Stahl, *J. Chem. Inf. Model.*, 2008, **48**, 1-24;(b) H. F. G. Velec, H. Gohlke and G. Klebe, *J. Med. Chem.*, 2005, **48**, 6296-6303.
21. O. M. Peeters, N. M. Blaton, C. J. De Ranter, O. Denisoff and L. Molle *Cryst. Struct. Commun.*, 1980, **9**, 851-856.
22. (a) H. E. S. Kara, *Bioelectrochemistry*, 2014, **99**, 17-23; (b) R. M. Shubietah, A. Z. A. Zuhri and A. G. Fogg, *Fresenius' J. Anal. Chem.*, 1994, **348**, 754-757;(c) E. Palecek and M. Bartosik, *Chem. Rev.*, 2012, **112**, 3427-3481;(d) N. Li, L. Guo, J. Jiang and X. Yang, *Biophys. Chem.*, 2004, **111**, 259-265.
23. S. KlimaŠauskas, Z. Liutkeviciute and D. Daujotyte, *Biophysics and the Challenges of Emerging Threats*, Springer Netherlands, 2009, Ch. Biophysical Approaches To Study DNA Base Flipping, pp. 51-64.
24. (a) C. G. Ricci and P. A. Netz, *J. Chem. Inf. Model.*, 2009, **49**, 1925-1935;(b) H. K. Srivastava, M. Chourasia, D. Kumar and G. N. Sastry, *J. Chem. Inf. Model.*, 2011, **51**, 558-571.
25. (a) E. P. Bishop, R. Rohs, S. C. J. Parker, S. M. West, P. Liu, R. S. Mann, B. Honig and T. D. Tullius, *ACS Chem. Biol.*, 2011, **6**, 1314-1320;(b) S. C. J. Parker and T. D. Tullius, *Curr. Opin. Struct. Biol.*, 2011, **21**, 342-347.
26. J. Song, M. Teplova, S. Ishibe-Murakami and D. J. Patel, *Science*, 2012, **335**, 709-712.
27. (a) R. A. Friesner, J. L. Banks, R. B. Murphy, T. A. Halgren, J. J. Klicic, D. T. Mainz, M. P. Repasky, E. H. Knoll, M. Shelley, J. K. Perry, D. E. Shaw, P. Francis and P. S. Shenkin, *J. Med. Chem.*, 2004, **47**, 1739-1749;(b) Schrödinger Suite 2011 Protein Preparation Wizard; Epic version 2.3, Schrödinger, LLC, New York, NY, 2012; Impact version 5.8, Schrödinger, LLC, New York, NY, 2012; Prime version 3.1, Schrödinger, LLC, New York, NY, 2012. Suite 2012: LigPrep, version 2.5, Schrödinger, LLC, New York, NY, 2012.
28. F. H. Allen, *Acta Cryst.*, 2002, **B58**, 380-388.
29. (a) S. Lisanti, W. A. W. Omar, B. Tomaszewski, S. De Prins, G. Jacobs, G. Koppen, J. C. Mathers and S. A. S. Langie, *PLoS ONE*, 2013, **8**, e79044;(b) A. Kelkar and D. Deobagkar, *Epigenetics*, 2009, **4**, 415-420.

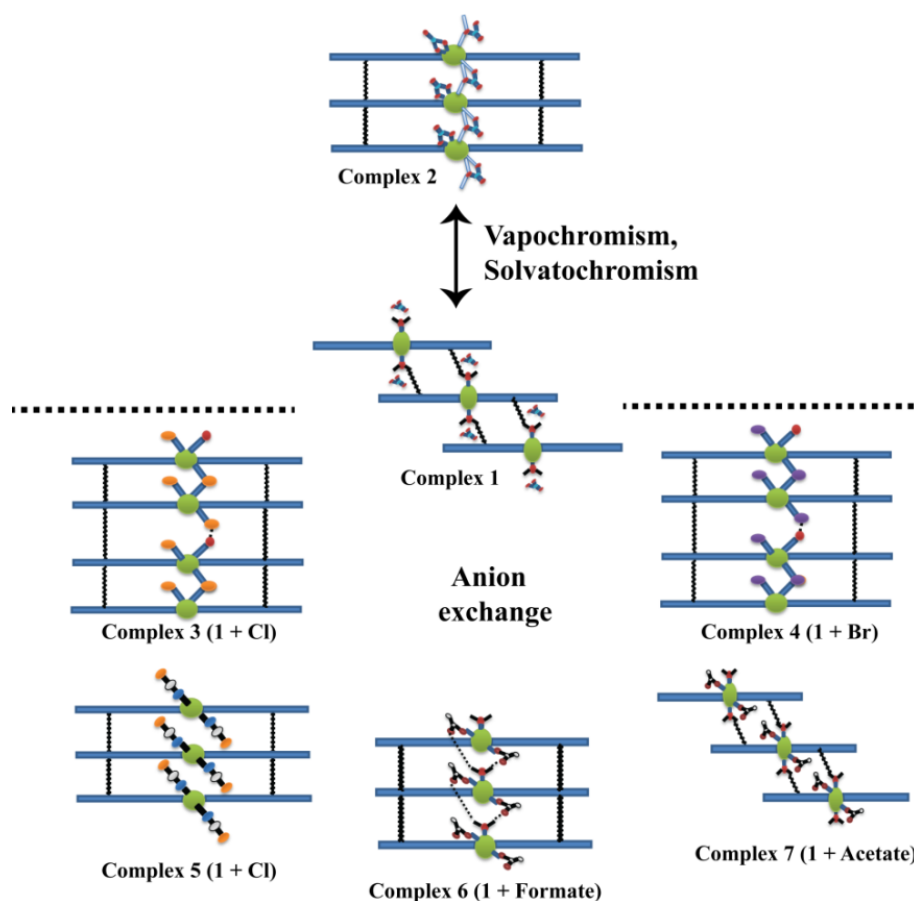
-
30. M. Iwatani, K. Ikegami, Y. Kremenska, N. Hattori, S. Tanaka, S. Yagi and K. Shiota, *Stem Cells*, 2006, **24**, 2549-2556.
 31. M. Batchman, S. Uribe-Lewis, X. Yang, M. Williams, A. Murrell and S. Balasubramanian, *Nat. Chem.*, 2014, **6**, 1049-1055.
 32. S. Shpyleva, S. Ivanovsky, A. de Conti, S. Melnyk, V. Tryndyak, F. A. Beland, S. J. James and I. P. Pogribny, *PLoS ONE*, 2014, **9**, e113712.
 33. Bruker, 2007; APEX2, SAINT, and SADABS: Bruker AXS Inc., Madison, Wisconsin, USA.
 34. Sheldrick, G. M. *Acta Cryst.* 2008, *A64*, 112 – 122.
 35. Farrugia, L. J. *J. Appl. Cryst.* 2012, *45*, 849-854.
 36. Macrae, C. F.; Bruno, I. J.; Chisholm, J. A.; Edgington, P. R.; McCabe P.; Pidcock, E.; RodriguezMonge, L.; Taylor, R.; van de Streek J.; Wood, P. A. *J. Appl. Crystallogr.* 2008, *41*, 466-470.
 37. Spek, A. L. *Acta Cryst.* 2009, *D65*, 148-155.
 38. <http://www.schrodinger.com/kb/1027>
 39. <http://www.schrodinger.com/kb/635>
 40. <http://www.schrodinger.com/kb/731>
 41. I. J. Bruno, J. C. Cole, P. R. Edgington, M. Kessler, C. F. Macrae, P. McCabe, J. Pearson and R. Taylor, *Acta Cryst.*, 2002, *B58*, 389-397.

Chapter 2A

Design and Synthesis of Conformationally Flexible 1D Architecture of Cu^{+2} Coordination Complex: Study of Vapochromic and Anion Sensing Properties

Most of the results presented in this chapter are published in the following patent:

R. L. Gawade, R. G. Gonnade and V. G. Puranik " Metal coordination complex for detection of vapors and anions and the process for the preparation thereof ", WO 2016/056027.



(Coordination framework of complex 1 act as transformable template which show vapochromic, solvatochromic response to vapors of polar solvent and guest-induced chromism for solution/solid state anion exchange(anions like Cl^- , Br^- , SCN^- , HCOO^- , CH_3COO^-)

Introduction:

The field of optical chemo-sensors has attracted many researchers due to their numerous applications in biological, chemical, environmental and material sciences.¹⁻⁵ In-depth understanding of the structural features of the host and guest is essential for designing the suitable chemo-sensors. The host-guest interactions of sensor materials obey the principles of enzymology. On the basis of their mode of action, sensor material can be divided into two categories type I and II. Type I materials are one-guest-one-host type sensors which generally comply with the principle of lock and key model, and bind to specific guest (**Figure 2.1a**) whereas type II sensor materials follow the mode of action based on the induced fit model of enzyme-substrate reaction and bind to heterogeneous guest molecules. Essentially the binding pocket of type II sensors act as transformable template which accommodate wide range of guests having different size, shape, topology and nature (**Figure 2.1b**). Moreover, induced fit binding is also preferred over lock-key model for synthesizing cost-effective wide spectrum sensors. The guest analytes may exist in the vapour, solution or solid form. Furthermore, physical conditions like humidity, temperature and mechanical stress (pressure) can also represent as a guest environment.

Depending upon the nature of guest molecules and mode of detection, optical sensors may be categorised in following types:

- 1) **Vapochromic**: The compounds which can bind to vapours/gaseous form of guest analytes and show colorimetric change.
- 2) **Solvatochromic**: The compounds which can bind to solvent molecules (polar/nonpolar) and show colorimetric change.
- 3) **Mechanochromic**: The compounds which changes the colorimetric properties when subjected to the mechanical stress such as grinding.
- 4) **Thermochromic**: The compounds which changes the colorimetric properties when subjected to different temperatures.

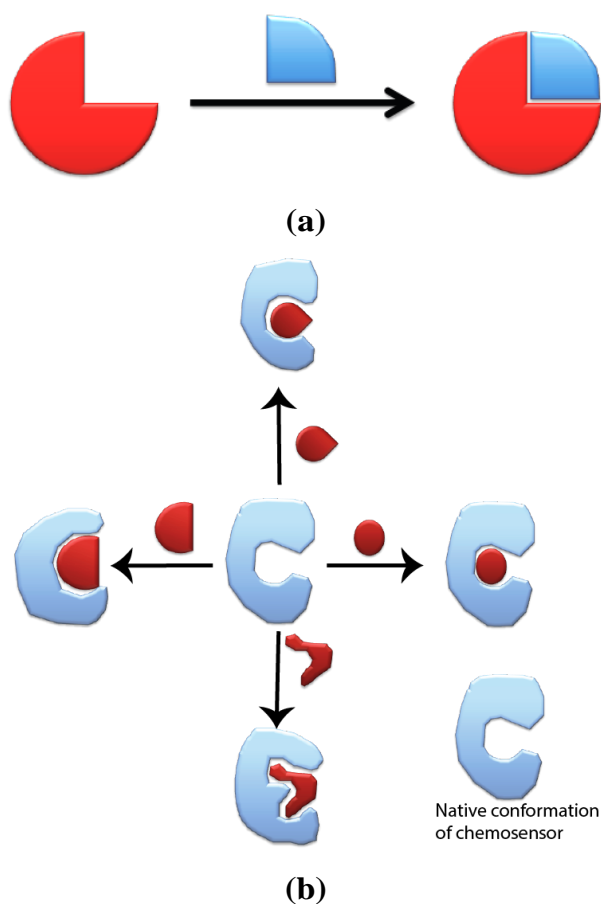


Figure 2.1. Depiction of design and mechanism of chemo-sensors which are based on (a) Lock and key model and binds to specific guest, (b) induced-fit model and binds to multiple substrates of complex nature.

There are countless man-made compounds that are highly toxic and carcinogenic in nature. Their release in the environment can drastically impact human wellbeing. If inhaled or consumed *via* contaminated food or water, can lead to vomiting, dizziness, sleepiness, rapid heartbeat and at high level can even cause death.⁶⁻⁸ Bhopal gas tragedy is one of the largest man-made disasters happened in India due to leakage of methyl isocyanate gas, killing over ~4000 people.⁹ Industrial advancement of 21st century has witnessed many such incidents at small or large scale. Excessive use of toxic reactants or release of hazardous products at industrial level has increased the risk of many such disasters. Therefore, there is a huge upsurge in last 2-3 decades for attempting to design and synthesize suitable sensors for toxic compounds.

Transition metal complexes are mainly used for designing wide spectrum chemo-sensors due to their strong charge transfer properties. MLCT

(metal to ligand charge transfer) and LMCT (Ligand to metal charge transfer) of transition metal complexes are susceptible to their coordination sphere.¹⁰⁻¹² Small change in the metal coordination causes large shift in the excited state properties which can be measured by UV-vis or fluorescent spectroscopic tools. Few transition metal complexes which change their optical properties in the presence of guest molecules are listed below in **table 2.1**,

Table 2.1: The list of few organometallic compounds reported as chemosensors

Sr. No.	Name of the compound	Nature	Optical property	Mechanism	Applications	Ref.
1.	Zr ⁴⁺ coordinated 9-fluorenone-2,7-dicarboxylic acid	MOF	Shift in luminescent property	Shift in the excited state properties	Vapochromic effect for distinguishing polar and non-polar solvents	13
2.	Fluorescent organic octahedron encapsulated by metal organic polyhedron (MOP)	MOP	Shift in luminescent property	Shift in the excited state properties and specific molecular capture	Vapochromic effect for detection of acetone vapors	14
3.	Metal-chelate complexes [Cu(acac){Me ₂ NCH ₂ CH ₂ NMe(CH ₂) _n OMe}][Tf ₂ N] {[1][Tf ₂ N]	Ionic liquids	Shift in absorption properties	Shift in the <i>d-d</i> transition energy : solvent donor	Solvatochromism	15
4.	Alkynyl-Phosphine Copper Clusters: [Cu ₆ (C ₂ R) ₄ {(PPh ₂) ₃ CH} ₂][PF ₆] ₂ (R = 4-X-C ₆ H ₄ (1-5) and C ₅ H ₄ N (6); X = NMe ₂ (1), OMe (2), H (3), Ph (4), CF ₃ (5))	Hexanuclear Cu(I) clusters	Shift in emission properties	Solvent coordination shifts MLCT(metal to ligand charge transfer)	Solvatochromism	16
5.	[Au(i.m.(CH ₂ py) ₂) ₂ (Cu(MeCN) ₂) ₂] ³⁺	Bimetallic coordination complex	Shift in emission properties	Shift in Au-Cu bond distance: coordination to solvent	Vapochromism	17
6.	CdSO ₄ coordination network {[Cu ₂ (4-pmpmd) ₂ (CH ₃ OH) ₄ (opd) ₂ ·2H ₂ O] _n [4-pmpmd = N,N'-bis(4-pyridylmethyl)phenyldiimide; opd = o-phthalic acid]	MOF	Shift in absorption properties	Coordination to solvent molecule and shift in MLCT	Vapochromism (MeOH, EtOH, benzene, and cyclohexane) and detection of gases(CO ₂ , N ₂ , H ₂ , and CH ₄)	18

So far, the accumulation of hazardous analytes was prevented by introducing stringent acts and laws for their limited usage. However, the pollutants like anions can't be prevented by these laws mainly because they are

essential component of the production process and their strong hydrophilic nature. The mining, metal refining and many chemical factories which utilize metal salts for the production process release tons of anionic pollutants in the environment. These pollutants can leached into the ground water and contaminate the irrigation sites; thereby they can enter into the food-chain. The excess levels of anions have shown to be highly toxic for the human health and can cause multiple organ failure. The detection and removal of anions from highly competitive media like water is the uphill battle.

Many crystalline solids such as coordination polymers, MOFs (metal-organic frameworks)¹⁹⁻²¹ and COFs (covalent organic frameworks)²²⁻²⁴ have been explored as soft porous materials for the detection and removal of toxic compounds. However 1D or 2D extended architecture comprising tailor-made ligands and structure directing metal centres provides suitable alternative to their rigid architecture.²⁵⁻²⁹ Construction of such structurally dynamic 1D/2D assembly entails supra-molecular reagents and reactive metal centres. Generally cumulative effect of hydrogen bonding,³⁰ halogen bonding³¹ and π -stacking synthons³² provides strong structural integrity. 1D/2D frameworks that are glued by these non-covalent forces, serve as metamorphic template for capturing wide range of guest molecules and the subsequent change in the coordination environment forms the basis for their suitability as molecular sensors. Designing such metamorphic architecture for simultaneous detection and removal of toxic anions in competitive media (water, polar solvents) is a one of the major objectives of inorganic crystal engineering.³³⁻³⁵

Using the inorganic crystal engineering approach, the suitable compound from the ligand library can be chosen to form coordination framework with the metal reporter group such as Cu(II) (colorimetric), Pt(II) (luminescent). So far, many such frameworks are reported which show structural transformation after binding to the analyte. Changes in the optical properties are attributed to the alteration in the metal coordination, chemical structure of ligand or metal-metal distance (for dimetallic compounds). Furthermore, many of these literature reports employed labile anionic source for detection e.g. TBA (tetrabutyl ammonium) salts instead of alkali salts. Secondly, media was not completely aqueous (100% water) and solid state detection systems displayed narrow spectrum sensing ability. While undertaking literature survey, we came across

interesting case of Cu(II) based coordination complex (PCP3) reported for trapping carbon monoxide gas. This Cu(II) coordination complex served as excellent example of induced fit model. The mechanism of detection is very well elucidated and states that guest analytes (CO) show cooperative binding at the receptor sites (**Figure 2.2**).³⁶ The binding of each guest analyte further opens up reaction channel allowing more molecules to get trapped by coordination. The accelerated binding mode is possible when the receptor/host molecules possess 1D/2D or 3D reaction channels.

Based on the literature reports we designed ideal system of metal-based sensory probes that comprise of metal centers which can acts as colorimetric reporter group and bind to anionic guest due to its Lewis acidic nature. Tailor made 1D metal-ligand coordination framework provides conformational flexibility for trapping guest molecules in solid state. The ligand comprises of flexible spacer and neutral organic scaffolds that strengthens the framework *via* strong hydrogen bonding whereas weak forces such as stacking interaction provides spatial rigidity. The schematic representation of the same is shown in the **figure 2.3**.

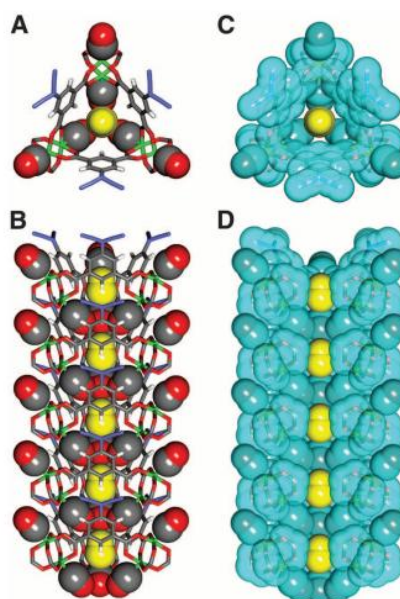


Figure 2.2. X-ray crystal structures of CO-adsorbed PCP 3. (A and B) Top and side views of CO adsorbed channel. (C and D) Top and side views of CO-adsorbed channel with van der Waals surfaces depicted in light blue. Colour code: Cu (green), C (gray), N (blue), O (red) and H (white). Coordinated (gray and red) and noncoordinated (yellow) CO molecules are shown in a CPK model. In (D), parts of the aryl moieties have been omitted for clarity.³⁶

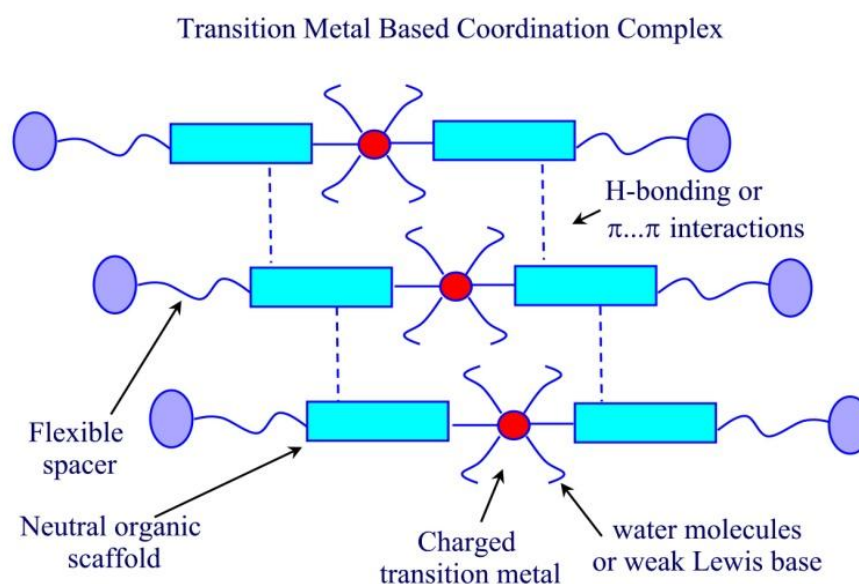


Figure 2.3. The schematic representation of design strategy of transition based coordination complex for anion sensing.

In this chapter, we have designed 1D extended architecture comprising pyridine carboxamide conjugated with phenethylene group as supramolecular reagent and Cu^{2+} as reactive metal centre. Interplay of strong and weak intermolecular forces and conformational flexibility of rotatable groups provide structurally dynamic 1D supramolecular assembly. We studied its vapochromic response towards polar/nonpolar solvent vapours which has prompted us to investigate its applicability for detecting Cl^- , Br^- , SCN^- , CH_3COO^- and HCOO^- anionic guests in completely aqueous media. Crystallographic evidences, solid state UV reflectance and *in-situ* E-SEM study provided the mechanistic insight and structural basis of its metamorphic nature of this novel metal-based sensors. Additionally we have also demonstrated the enigmatic potential of the compounds to discriminate between the chloride and bromide salts by simple grinding method.

Result and discussion:

Structure of Ligand

In this study pyridine carboxamides are used as supramolecular reagent mainly due to the presence of, 1) metal coordination site of pyridyl nitrogen and 2) conventional carboxamide synthons that strengthens the 3D structural assembly. For our study we incorporated alkyl chain (-CH₂-CH₂-) spacer between pyridine carboxamide and aromatic side chain for providing conformational flexibility to the ligand so that it will allow easy guest exchange at the metal center. The phenyl side chain is used for providing the spatial rigidity due to its bulkyness. (**Figure 2.4**).

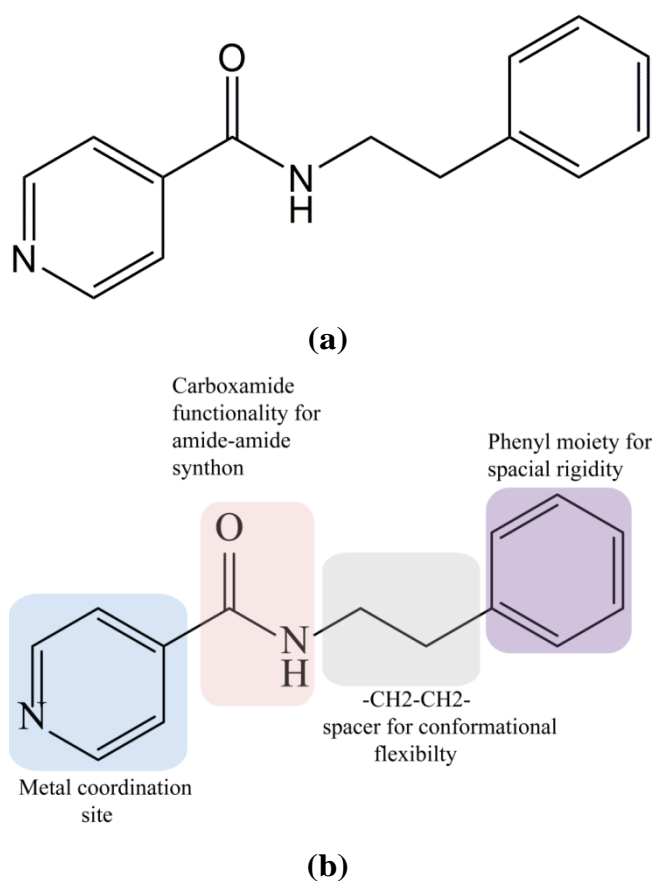


Figure 2.4. (a) Molecular structure of ligand (**L**) (b) Design and significance of its components.

Accordingly, ligand (**L**) was synthesized as per the reported procedure (details are provided in the experiental methods and **figure 2.36**). Needle shaped crystals were grown from methanol/DCM solvent mixture which crystallizes in monoclinic $P2_1/n$ spacegroup. The molecular structure and

ORTEP of ligand drawn with 50% ellipsoid probability level are depicted in the **figures 2.4** and **2.5**. Dihedral angle between pyridine ring and phenyl side-chain is 71.62° (**Figure 2.5**), which revealed tilted arrangement of phenyl moiety with respect to pyridine ring. As expected the molecules are assembled along *b*-axis through amide...amide N-H...O=C hydrogen bonding interaction to form 1D linear chains. The neighbouring crystallographic 2_1 -screw axis related chains along the *c*-axis are linked through rather a weak C-H...N interactions (**Figure 2.6**) to generate the 2D sheet structure. Molecular packing viewed down the *b*-axis revealed joining of the adjacent 2D sheets orthogonally along the *i*-axis through C-H...N, C-H...O and edge-to-face C-H... π contacts(**figure 2.7**).

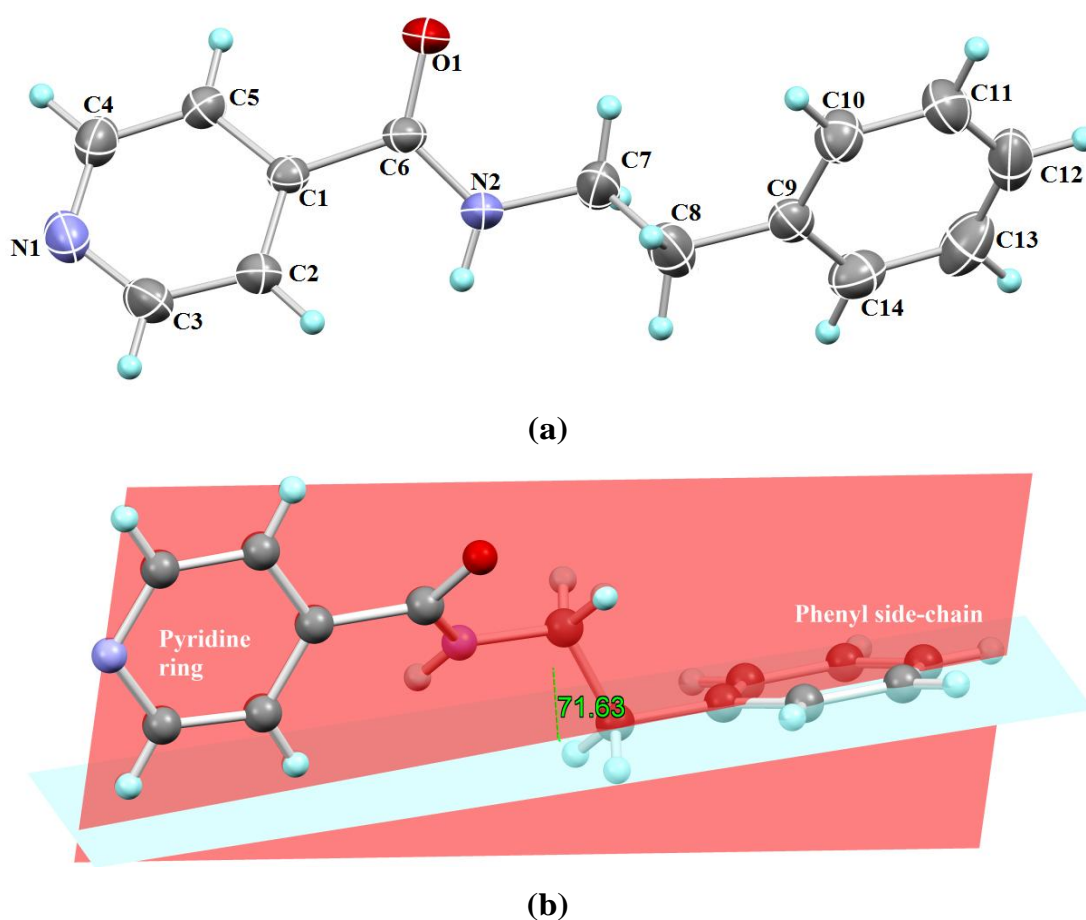


Figure 2.5. (a) ORTEP of ligand (b) The dihedral angle ($\tau_1:71.63^\circ$) between the plane containing pyridine ring (red) and plane containing phenyl side-chain (blue).

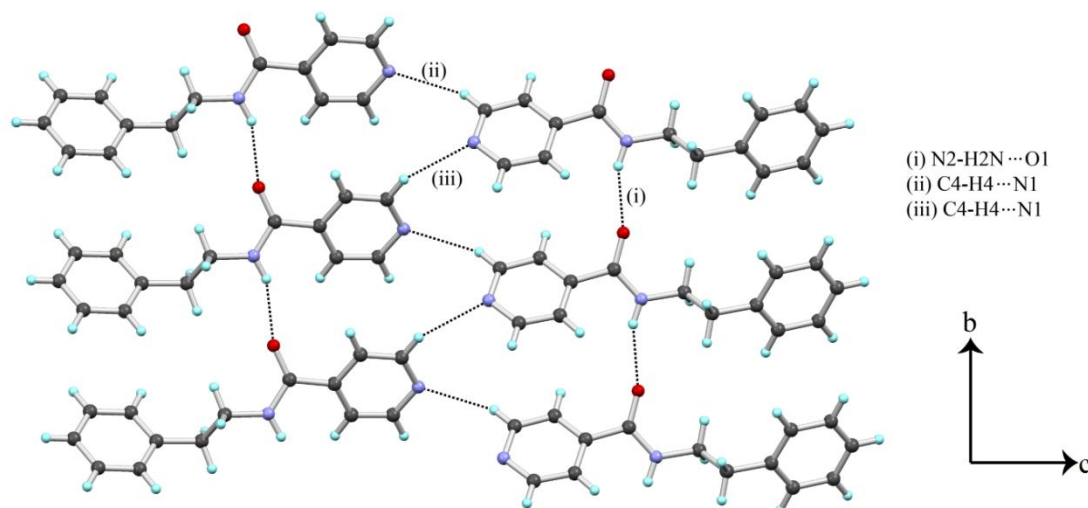


Figure 2.6. The flat helical arrangement of 1D chain on the *bc* plane.

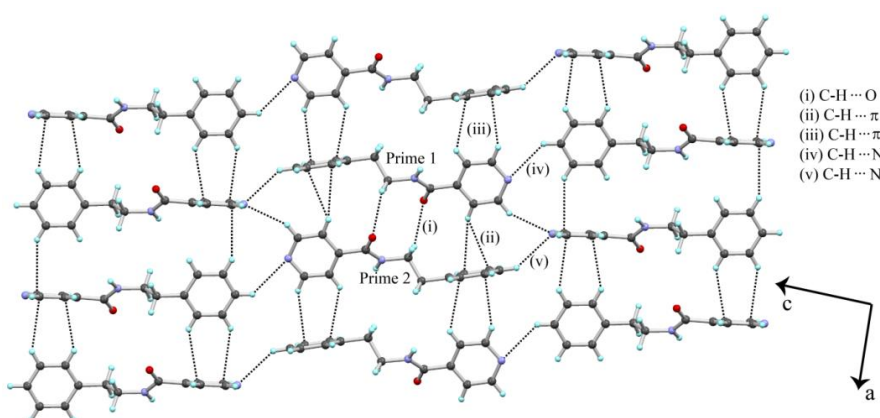


Figure 2.7. Molecular packing of 2D sheets orthogonally through C-H... π , C-H...N and C-H...O contacts.

Structure of Cu²⁺ Coordination Complex

Cu(II) complex **1**, tetra-aquabis(N-phenethylisonicotinamide) copper(II) nitrate was prepared by reacting two equivalents of (**L**) with Cu(NO₃)₂·2H₂O in dry methanol and refluxed for overnight. Crude reaction mixture was crystallized in methanol/water solvent mixture to yield green coloured block crystals. The molecular structure and ORTEP of complex **1** are depicted in **figure 2.8**. The complex is crystallized in monoclinic *P*2₁/*n* space group with half molecule in the asymmetric unit while the other half is generated by inversion operation. The metal atom is situated at the inversion centre and carboxamide groups of the ligands are arranged in the trans configuration. Cu(II) resides at the centre of slightly distorted octahedral geometry. Four water molecules are coordinated at the equatorial position and two monodentate

ligands are coordinated at the axial position. Cu(II)-O3(water) distance is elongated 2.318 Å, on the other hand Cu(II)-N1(pyridine, 2.022 Å) and Cu(II)-O2(water, 2.001 Å) distances are slightly shortened (**Figure 2.8**). Two nitrate counterions are present outside the coordination sphere of the metal.

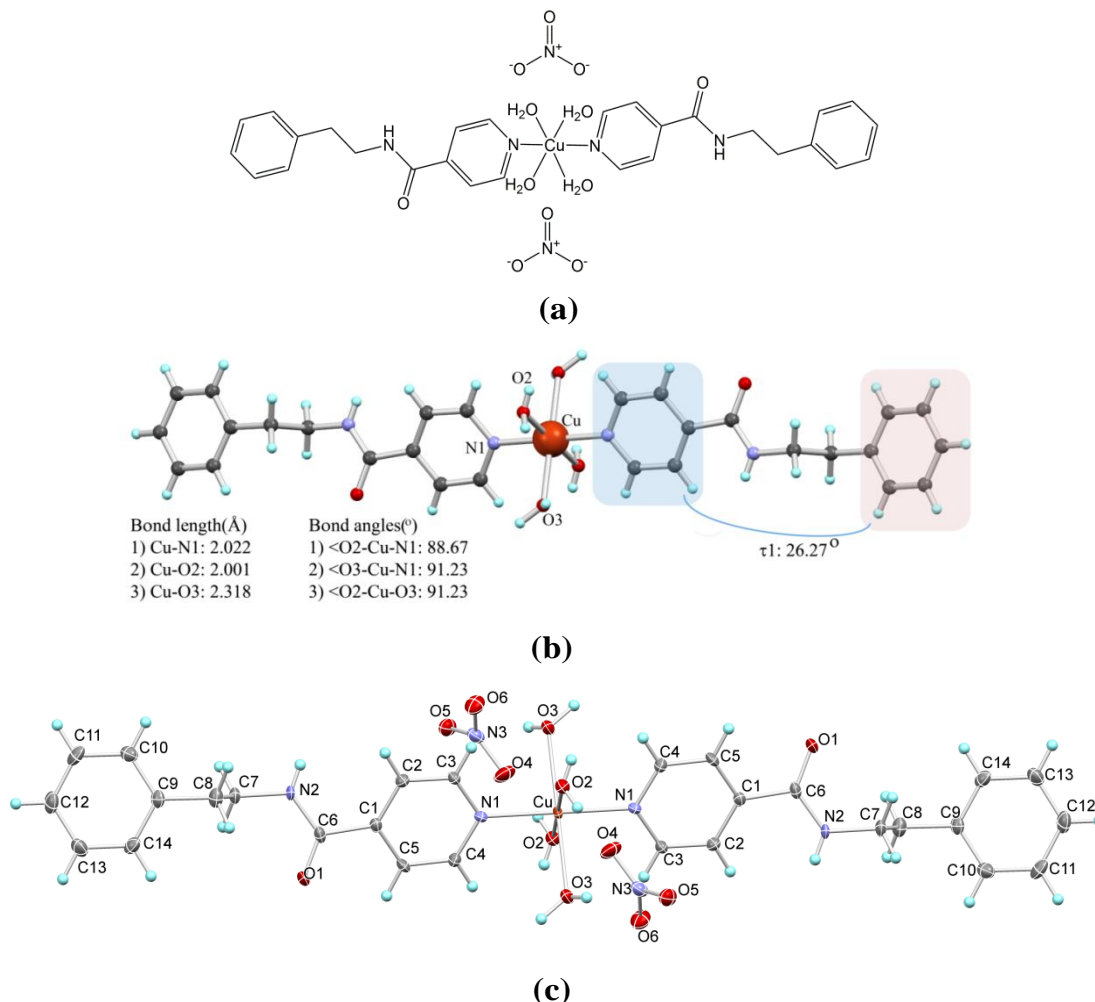


Figure 2.8. (a) Molecular structure of complex **1**, (b) ball and stick model of complex **1** with selected atom labelling. The geometrical parameters of bond lengths, bond angles and torsion angle (τ_1) between pyridine ring and phenyl moiety of the ligand is also displayed and (c) ORTEP of complex **1**.

Centrosymmetrically related molecules of complex **1** form 1D layered structure along *bc* plane via O-H...O=C hydrogen bonding interactions involving coordinated water (O3-H31) and carbonyl oxygen (O1) of the carboxamide group (**Figure 2.9a**). The peculiar feature observed in the crystal structure of complex **1** is the formation of hydrophilic network along *a* axis connecting nitrate ion and metal coordinated water molecules via O-H...O H-

bonding to generate the hydrophilic mesh (**Figure 2.9b**). Further, these layers are embedded in the hydrophobic pocket created by phenyl side-chains of interpenetrating molecules linked through N-H \cdots O hydrogen bonding between ligand and nitrate anion along the *b*-axis and metal coordinated pyridyl rings (**Figure 2.10**). Cartoon representation of 2D assembly of complex **1** is shown in the **figure 2.10c** which describe that hydrophobic bricks of pyridine and phenyl rings, have entrapped the hydrophilic channel that comprises of repeating unit of Cu(II)-water-nitrate-water-Cu(II) contacts.

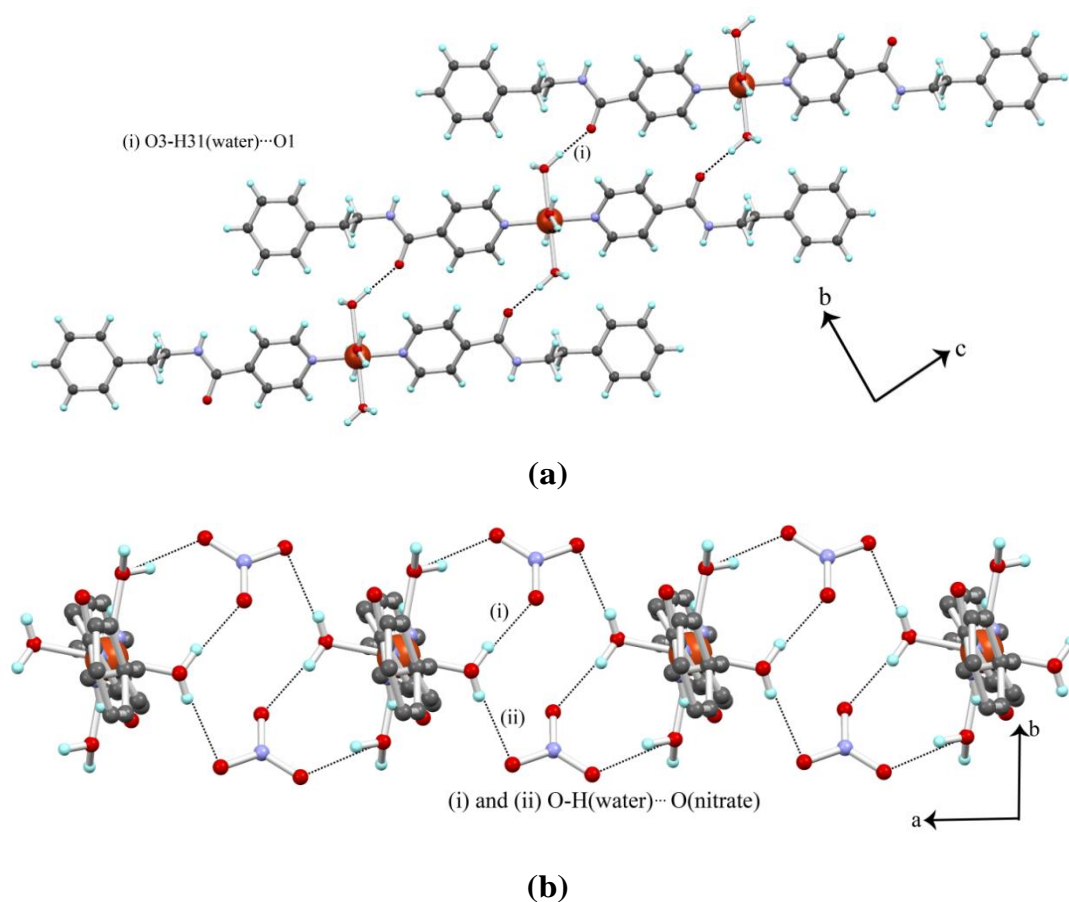
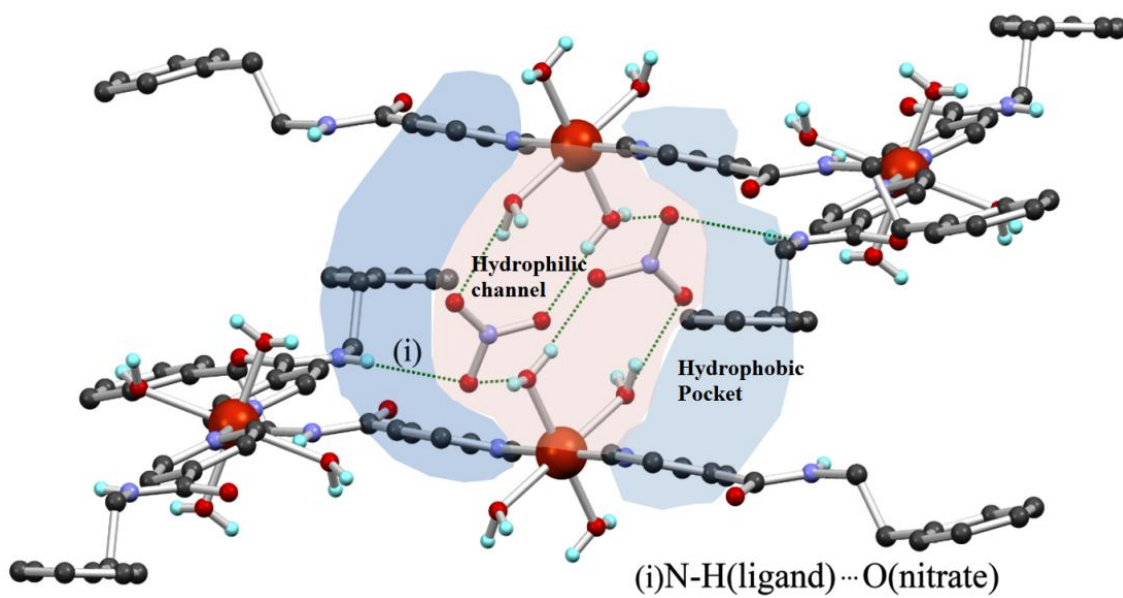
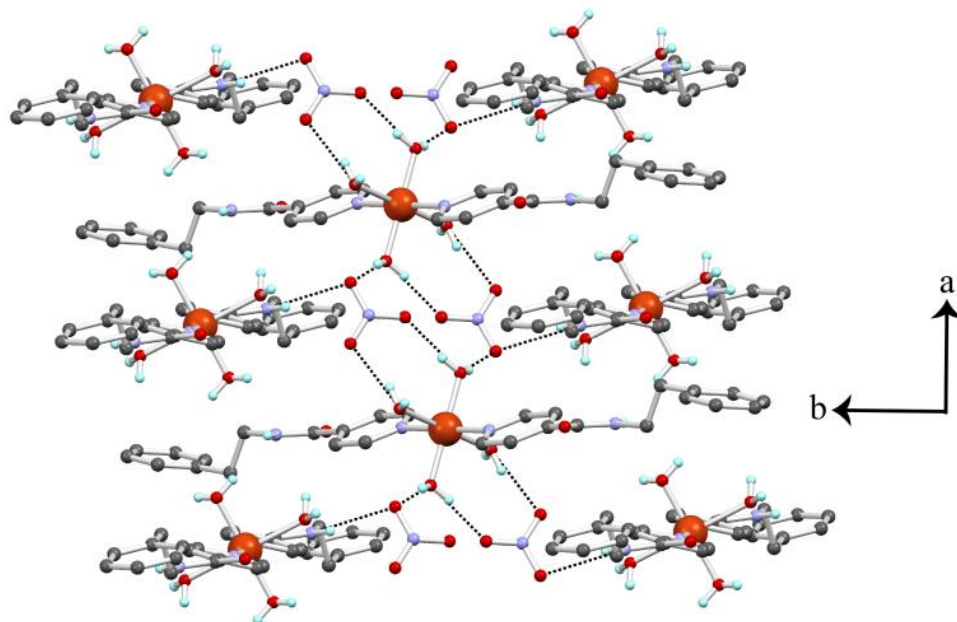


Figure 2.9. (a) hydrogen bonded 1D layer along *bc* plane in complex **1** (b) Nitrate-water network weaving the molecular layers along *a* axis.



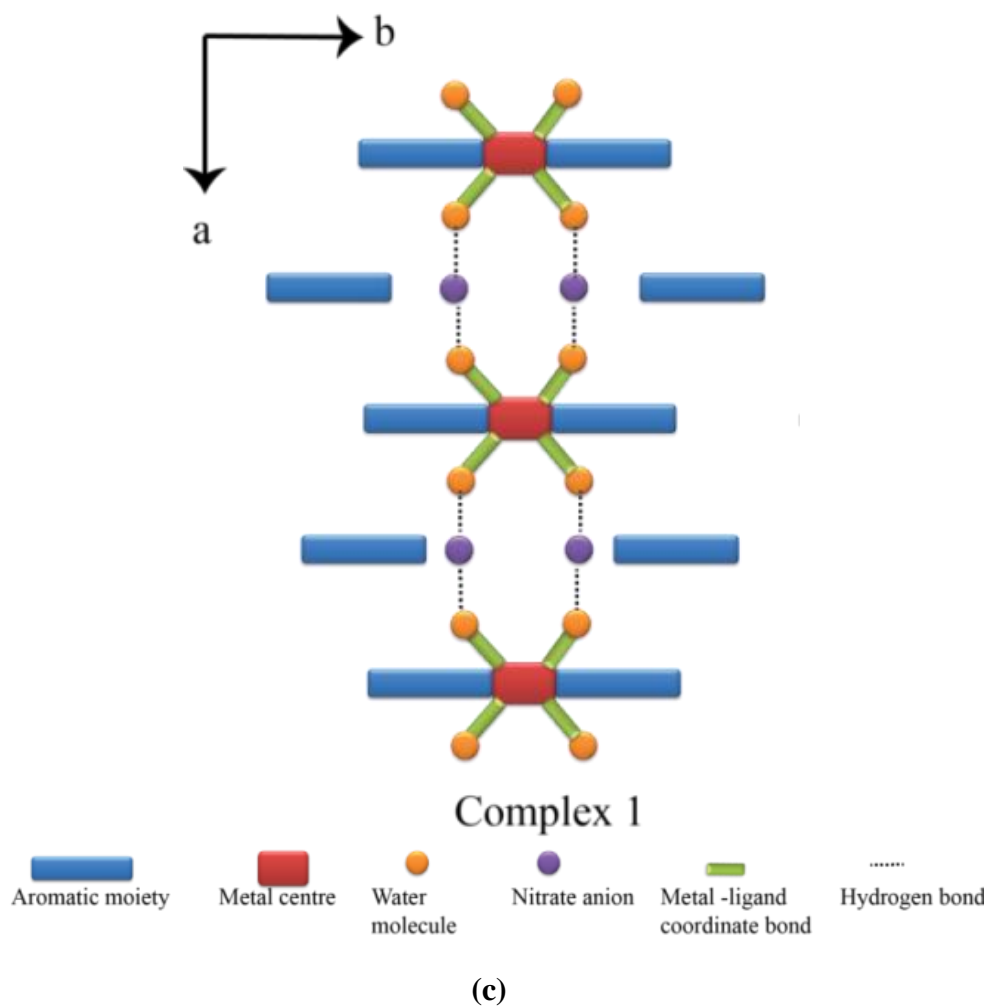


Figure 2.10. (a) Molecular packing along *a* axis, (b) hydrophilic channel formed by metal coordinated water and nitrate mesh that is embedded in the hydrophobic pocket, (c) cartoon presentation of 1D association of hydrophilic channel and hydrophobic architecture.

Significant change in the colour of complex **1** crystals (green to blue) was observed upon heating beyond 100°C (thermochromism). Weight loss occurred during thermogravimetric (TGA) study is attributed to the release of all the four coordinated water molecules (~10%, **Figure 2.11**). Similar observation was noticed when complex **1** crystals were exposed to methanol vapours (vapochromism) or soaked (suspended) in methanol solvent (solvatochromism). To understand thermo and vapochromic behaviour of the complex **1**, their crystals were grinded to form disc and then exposed to methanol vapors. The solid state UV reflectance spectra of complex **1** before and after the exposure of methanol vapors (complex **2**) showed significant

variation. The reflectance λ_{\max} of complex **1** is centered at 375 nm which is attributed to its green colour. However, The reflectance λ_{\max} of complex **1** after methanol exposure (upon transformation to complex **2**) showed red shift and centered at 445 nm (**Figure 2.12**).

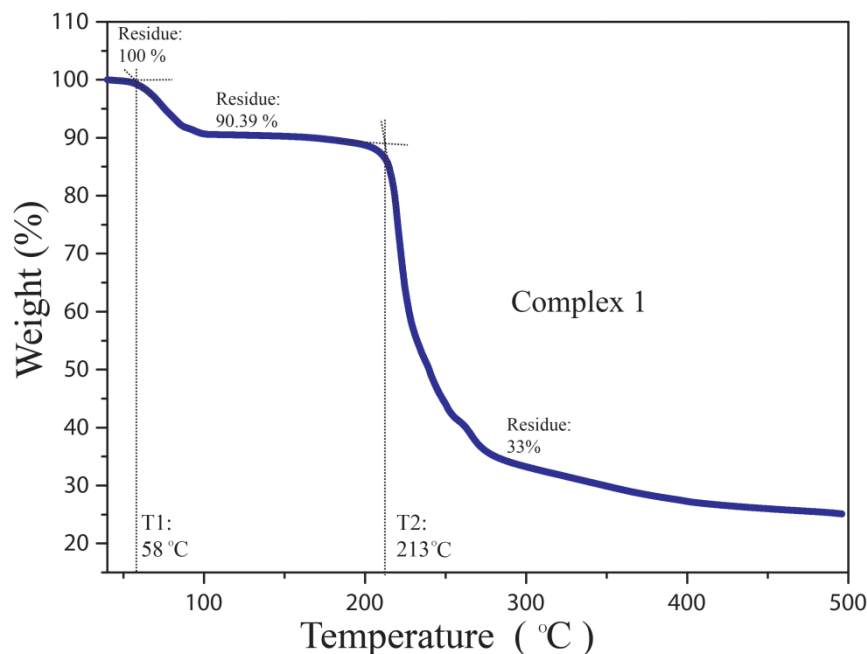


Figure 2.11. TGA of crystal of complex **1**

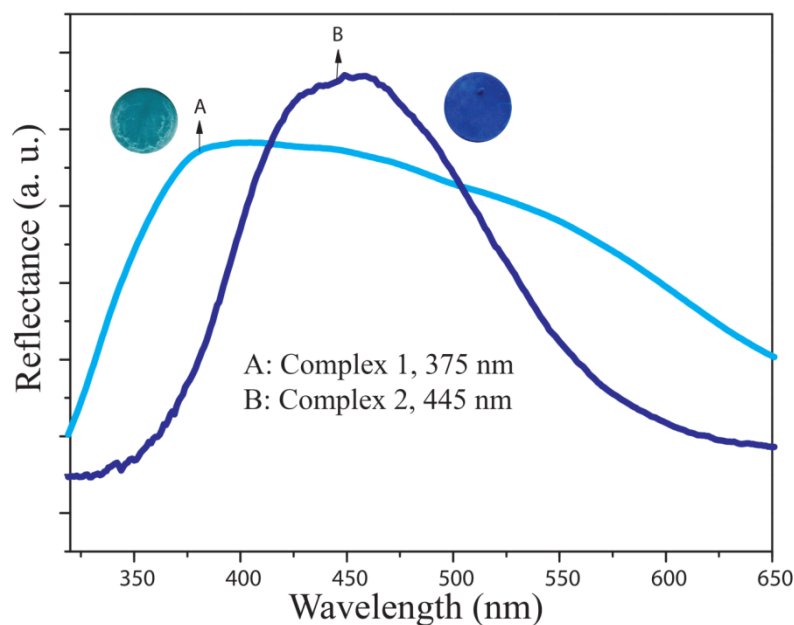


Figure 2.12. Solid state UV reflectance spectra of complex **1** and complex **2**.

Crystals of **1** were dispersed in dry methanol and then heated till compound gets sparingly soluble. The colour of the solid changed to dark blue. The mixture is then filtered and the filtrate was allowed to evaporate at room

temperature to afford needle shaped crystals of Complex **2**, dinitrate bis(N-phenethylisonicotinamide)copper(II). Molecular structure and ORTEP of complex **2** are provided in the **figure 2.13**. Single crystal structure analysis showed interesting structural transformation. Molecular structure of repeating unit of complex **2** and geometrical parameters are depicted in **figure 2.13**. It crystallized in monoclinic $P2_1$ chiral space group with one molecule in the asymmetric unit. The Cu(II) cation do not acquire the special position (inversion centre) unlike complex **1** due to different structure. Octahedral geometry at Cu(II) in complex **2** is distorted because of the release of coordinated water molecules. Escape of four water molecules from the coordination sphere of Cu(II) cation paves the way for nitrate anions to coordinate to the Cu(II) cation. Four oxygen atoms of two bidentate nitrate anions and two pyridyl nitrogen atoms of the monodentate ligand (L) coordinate with the Cu(II) cation to make the distorted octahedral geometry at the metal centre. Dihedral angle between pyridyl ring and phenyl moiety is 2.94° which suggests that they are co-planar. However, the dihedral angle between pyridyl rings (79.64°) attached to the metal centre is much deviated with respect of complex **1**. The carboxamide group of ligand has retained the trans geometry with respect to each other while coordinating with Cu(II) metal. Interestingly, one of the oxygen atom of coordinated nitrate ion acts as bridging ligand to form 1D polymeric chain structure along the *a* axis. The one-dimensional chain is supplemented by conventional N-H \cdots O=C hydrogen bonding interactions engaging the amide NH and carbonyl C=O groups, similar to the crystal structure of ligand (**Figure 2.14**). These chains are further intermingled *via* rather a weak interactions such as C-H \cdots O and C-H \cdots π along two fold screw (along *b* axis) to generate herringbone type packing along *c* axis (**Figure 2.15**). Aromatic units of complex **2** i.e. pyridyl and phenyl moieties are arranged like ladder and provided the spatial rigidity to the packing.

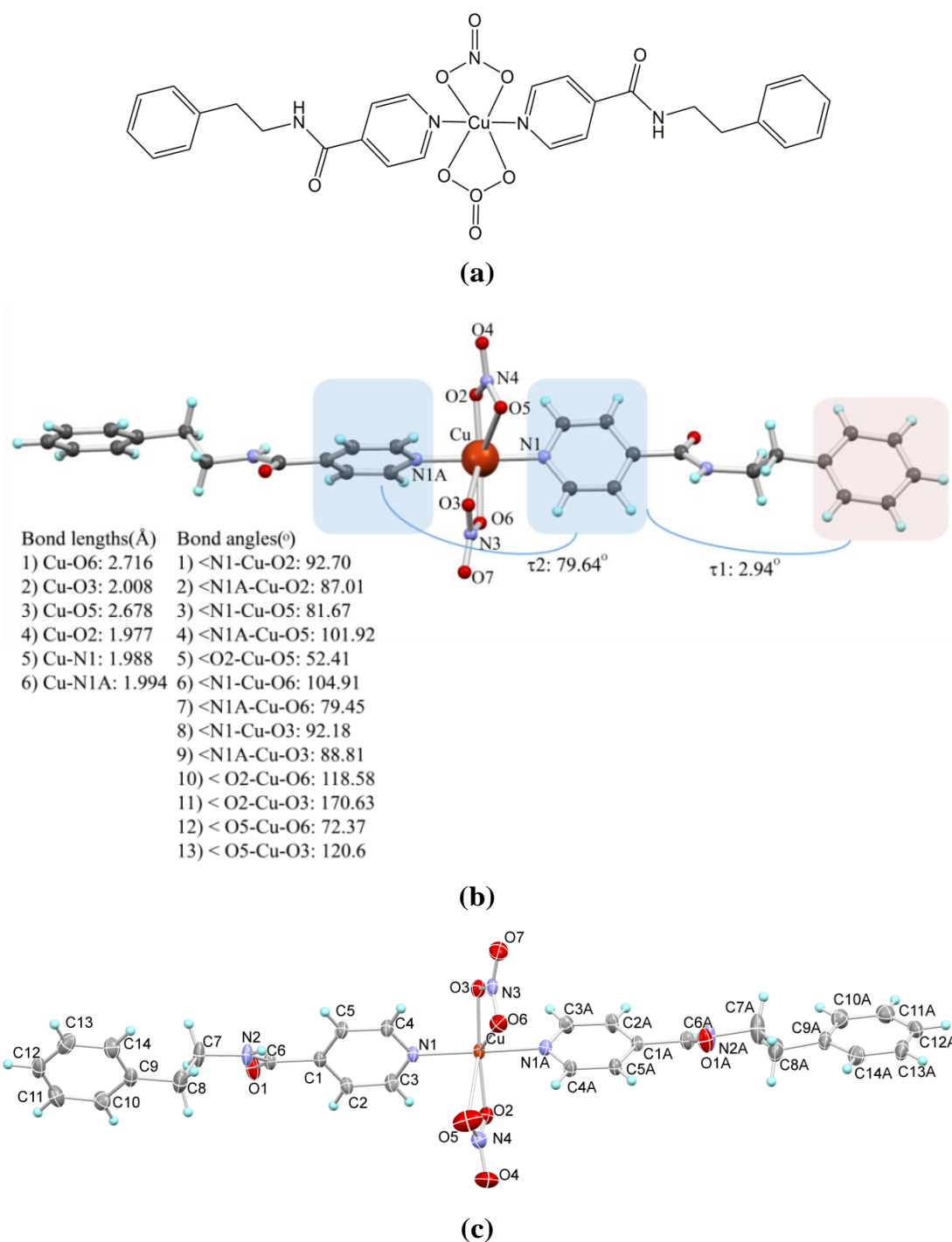


Figure 2.13. (a) Molecular structure of complex **2**, (b) geometrical parameters obtained from crystal structures of complex **2** such as bond length, bond angles and torsional angles τ_1 (dihedral angle between pyridine ring and phenyl moiety) and τ_2 (dihedral angle between pyridyl rings attached to metal centre), (c) ORTEP of complex **2**.

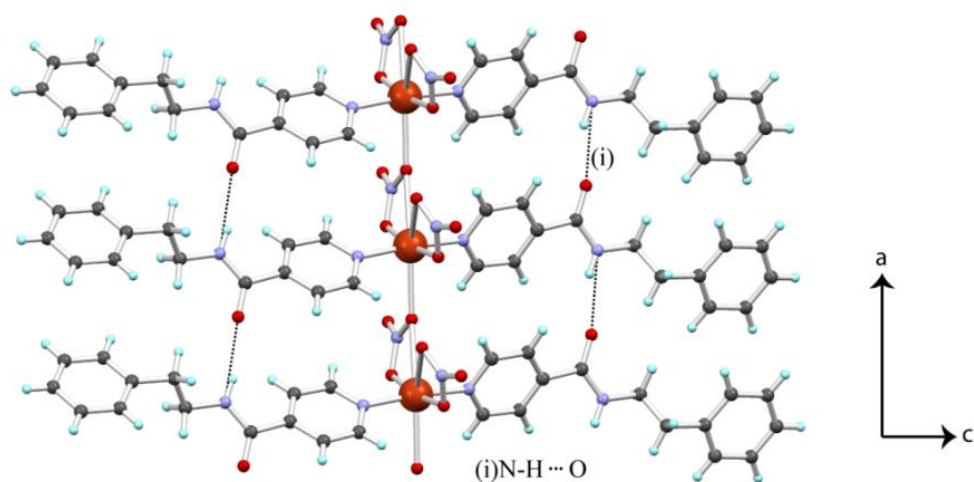


Figure 2.14. The polymeric chain formed through bridging of nitrate anion further supplemented by strong N-H...O hydrogen bonding.

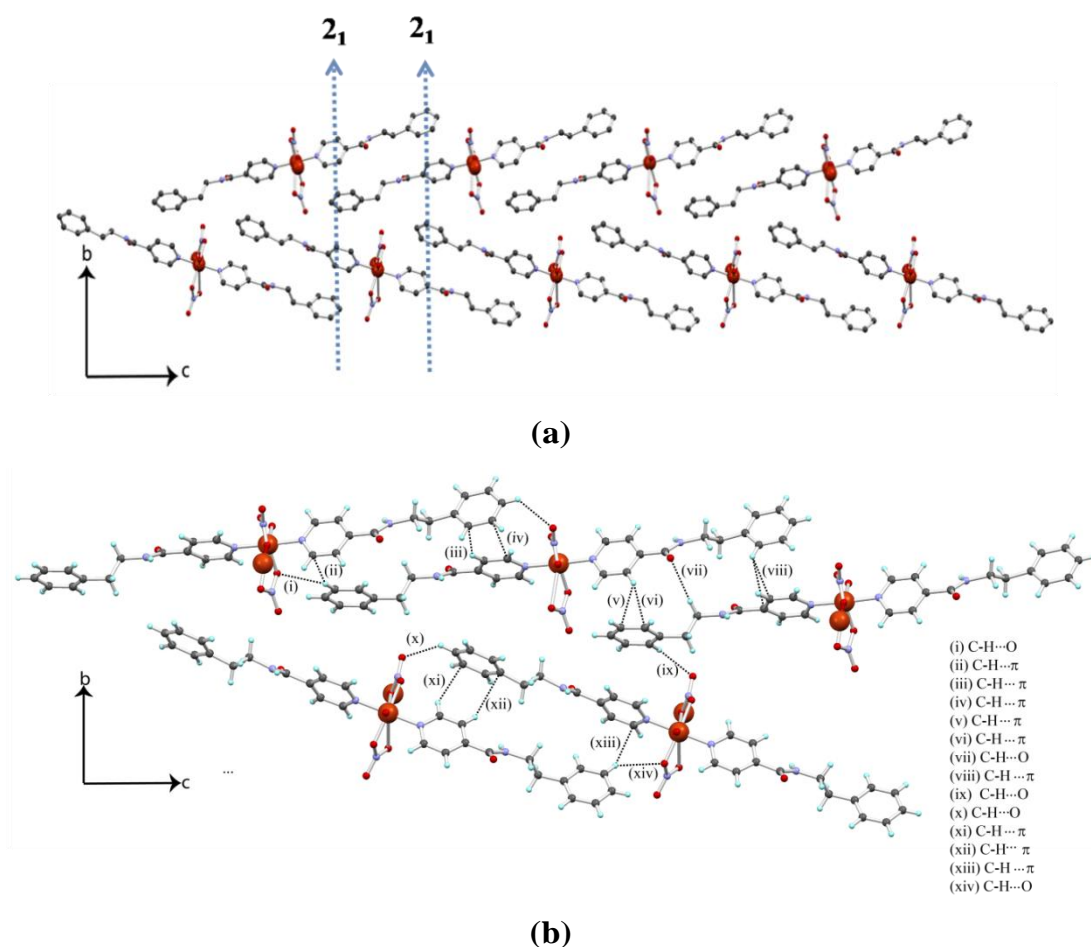


Figure 2.15. (a) Intermingling of 1D layers along 2_1 screw to generate herringbone packing along c axis, (b) depiction of weak intermolecular C-H...O and C-H... π interactions which are involved in weak association of the close layers.

Overlay of experimental PXRD patterns of complex **1** and complex **2** revealed significant conformational differences (**Figure 2.16**). To generalize the vapochromic behaviour of complex **1**, it was grinded to generate the fine polycrystalline powder and spread on the glass plate. The plate was placed in crystallization chambers containing solvent. The position of the glass plate in the chamber was kept at a suitable height from the solvent so that the vapors of the solvent can pass over the glass plate. This crystallization assembly was covered with glass plate (**Figure 2.17**). After the exposure to the solvent vapors, the green-colored fine powder turned blue in methanol, ethanol, acetone, DMSO (dimethyl sulfoxide) and THF (tetra hydro furan) vapors. The rate of the change of colour of the crystals was different for different solvents. For example, in methanol solvent, the colour change occurred in seconds, while in less volatile solvents such as DMSO, the time taken for naked eye colorimetric change was up to 2-3 hours.

Reversibility of the process was also monitored by keeping blue powder of complex **2** in closed chamber containing water. The colorimetric changes from blue to green (Complex **1**) revealed the reversible nature of vapochromic phenomenon. No colorimetric change was observed in solvent such as chloroform, dichloromethane, ethylacetate and benzene. Overlay of experimental PXRD patterns methanol, ethanol, THF and DMSO vapors exposed powder of complex **1** is provided in the **figure 2.18**.

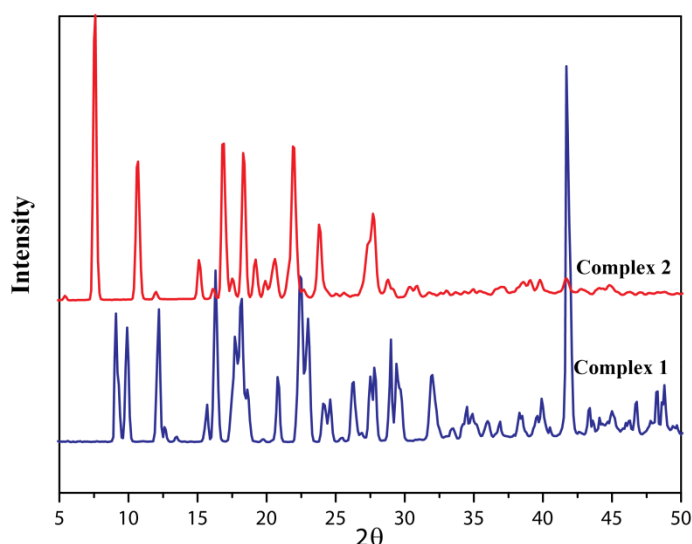


Figure 2.16. Overlay of experimental PXRD patterns of complex **1** and complex **2**.

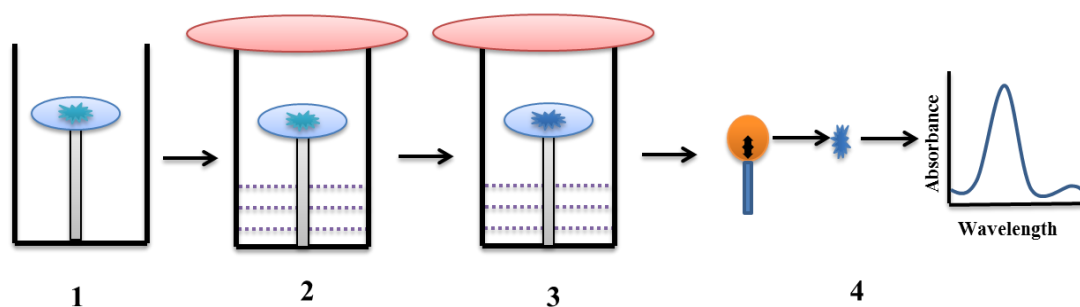


Figure 2.17. Vapochromism experiment, (1) crystallization chamber with powder of green crystals of complex **1**, (2) closed assembly containing solvent and powder, (3) which turned blue (complex **2**) on exposure to solvent vapours and (4) recording of UV absorption/reflectance/PXRD spectra.

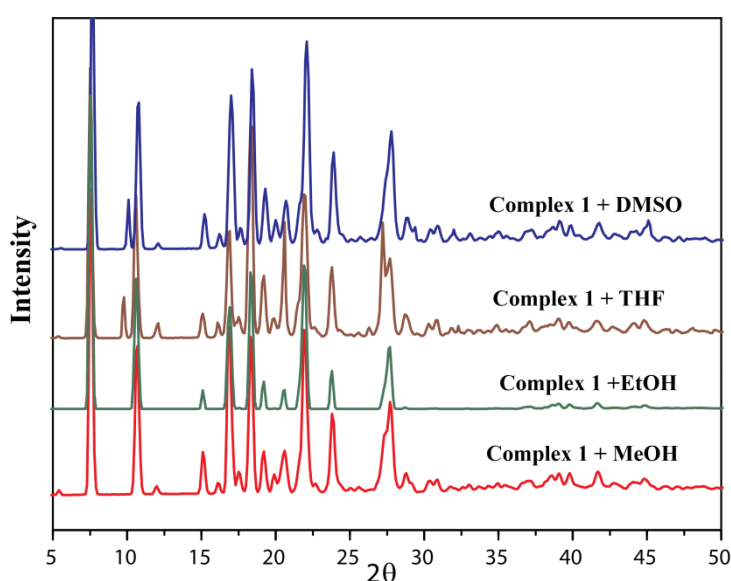


Figure 2.18. Overlay of experimental patterns of complex **1** after exposure with methanol, ethanol, THF and DMSO solvent vapors.

Based on the experimental observation, it is evident that the complex **1** has structurally transformed to complex **2** in the presence of vapors of polar solvents. Hydrogen bonding interactions with polar solvents might have played a significant role in this transformation. To rationalize the reason behind the solid-to-solid structural transformation of coordination framework in complex **1** to 1D polymeric chain in complex **2**, we have carefully studied their crystal structures. Generally crystal-to-crystal phase transition requires 1D/2D channels along which the reaction takes place without causing major damage or alteration to the crystal lattice.³⁷⁻³⁸

In complex **1**, the channel is observed along the *a*-axis where hydrogen bonded 1D layers are tethered together by nitrate-water mesh. The interaction of polar solvent vapors may have occurred at the (100) crystal interface which is more hydrophilic than other faces of the crystals and also provide extended 1D channels for reaction to occur. This interface provide multiple interaction sites formed by protruded layers of hydrophilic and hydrophobic regions (**figure 2.19**). The reaction channel observed along *a*-axis consists of hydrophilic core formed by the presence of metal coordinated water molecules, and uncoordinated nitrate anions in the close vicinity (**Figure 2.20**). The H-bonding interaction between the coordinated water and polar solvent molecules may have weakened the Cu-O(water) coordinate bond resulting in the generation of vacant coordination site. Further, nitrate anions which are flanking near the metal centre opportunistically acquire the vacated positions by forming the new Cu-O(nitrate) dative bonds. At this stage, the structural change would have crumbled the crystal lattice which is prevented by hydrophobic network. The newly formed Cu-nitrate coordination pulls the molecules along *a* axis in close proximity and propel the intermingling layers of hydrophobic region away from each other. Nitrate anion serve as bridging ligand to form 1D coordination polymer. During this structural transition, the flexible nature of metal-pyridine coordination bonds and ethylene spacer might have played significant role by allowing structural rearrangement of rigid pyridyl and phenyl side-chain to accommodate the molecular transformation respectively. Eventually, loss of coordinated water molecules establish conventional carboxamide to carboxamide H-bonding which further strengthens the crystal lattice. Due to the presence of 1D channel, structural rearrangement occurs readily at the coordination site. The cartoon representation of the structural transformation of complex **1** to complex **2** is given in the **figure 2.20-2.21**. As observed, the reversible transformation of blue-green crystals upon exposure of water vapour follows reverse reaction where Cu(II)-nitrate coordination bond breaks and replaces it with Cu(II)- water coordination.

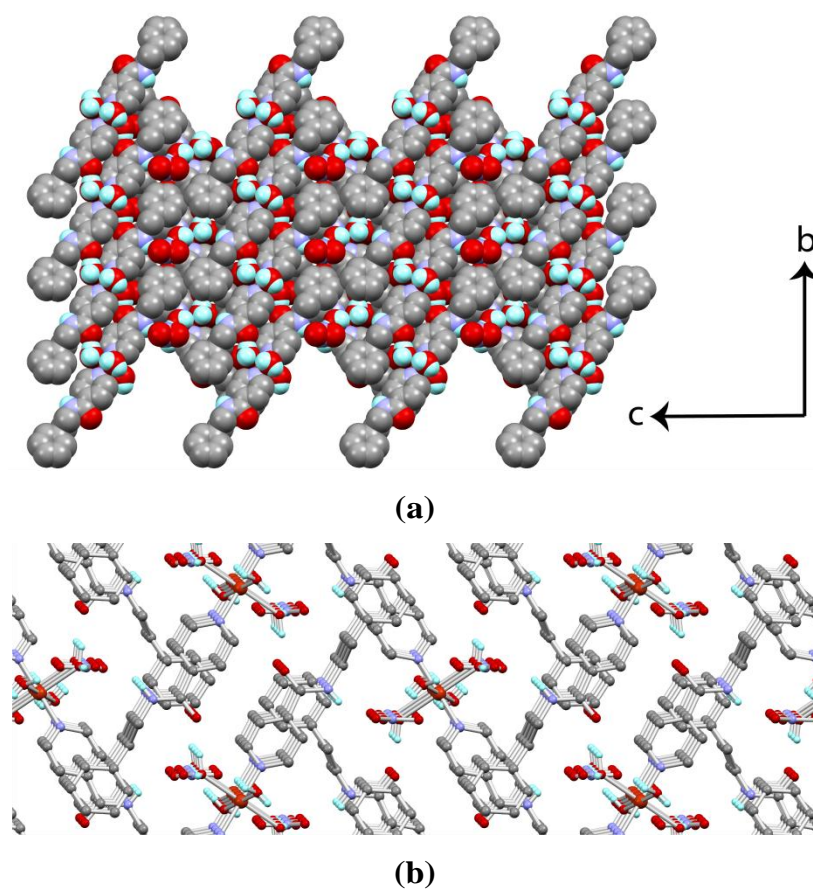


Figure 2.19. (a) Spacefill molecular packing along *a* axis and (011) crystal interface showing hydrophilic chains embedded in the hydrophobic pocket, (b) section of molecular packing in (a) shown in ball and stick style.

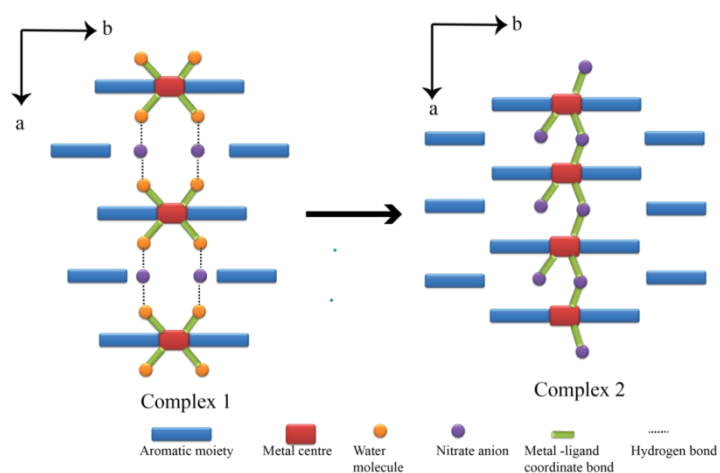


Figure 2.20. Cartoon representation of transformation of complex 1 to complex 2 when exposed to polar solvent vapors.

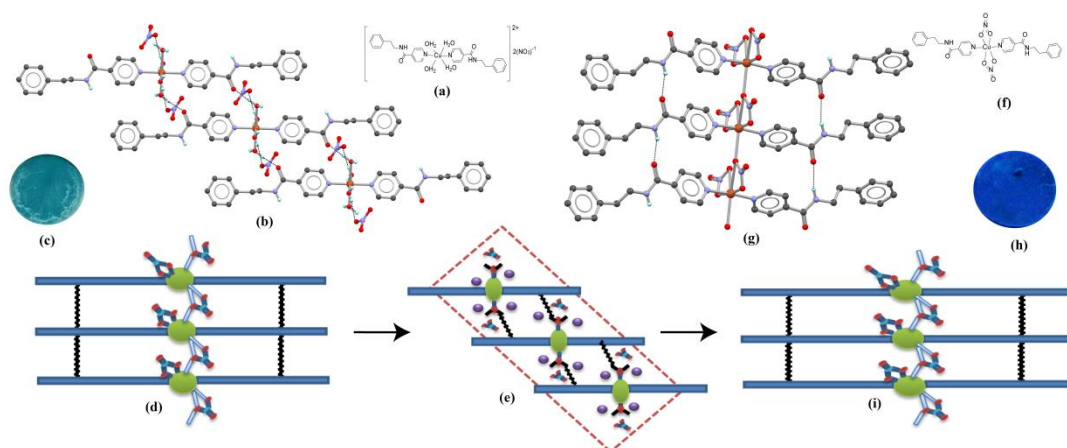


Figure 2.21. (a) Molecular structure of complex **1**, (b) 1D molecular packing arrangement of complex **1**, (c) disc of complex **1** made by pressing the its powder, (d) cartoon representation molecular packing of complex **1**, (e) Speculated interaction of polar solvent vapors with crystal of complex **1**, (f) molecular structure of complex **2**, (g) 1D molecular packing of complex **2**, (h) disc of complex **1** made by pressing the its powder, (i) cartoon representation of structural tranformation in complex **2**.

Inspired from the vapochromic response of complex **1**, we also investigated the anion exchange ability of complex **1** and **2** in complete water media. We designed screening strategy on the similar basis of vapochromism experiment. Complex **1** (H_2O to X where X : Cl^- , Br^- , SCN^- , HCOO^- , CH_3COO^-) revealed anion exchange ability by exhibiting colorimetric change which can even be detected by naked eye.

To study the spectral response of complex **1** during anion exchange, its crystals were grinded to generate fine polycrystalline powder. Circular disc were made out of this dry powder, which is then suspended in aqueous solution of tetrabutylammonium (TBA)/ammonium salts or alkali metal salts of various anions. Colour of the disc changed rapidly after coming in the contact with corresponding anionic solution. We obtained solid state UV-vis reflectance spectra of the solid material. Observed reflectance spectra showed significant differences in their λ_{max} values for the corresponding anions tabulated in **figure 2.22**. The values for Cl^- (485 nm), Br^- (532 nm), SCN^- (522nm), CH_3COO^- (425 nm) and HCOO^- (442nm) were observed. The naked eye colorimetric change in

the discs were observed corresponding to particular anion and is depicted in the figure 2.22.

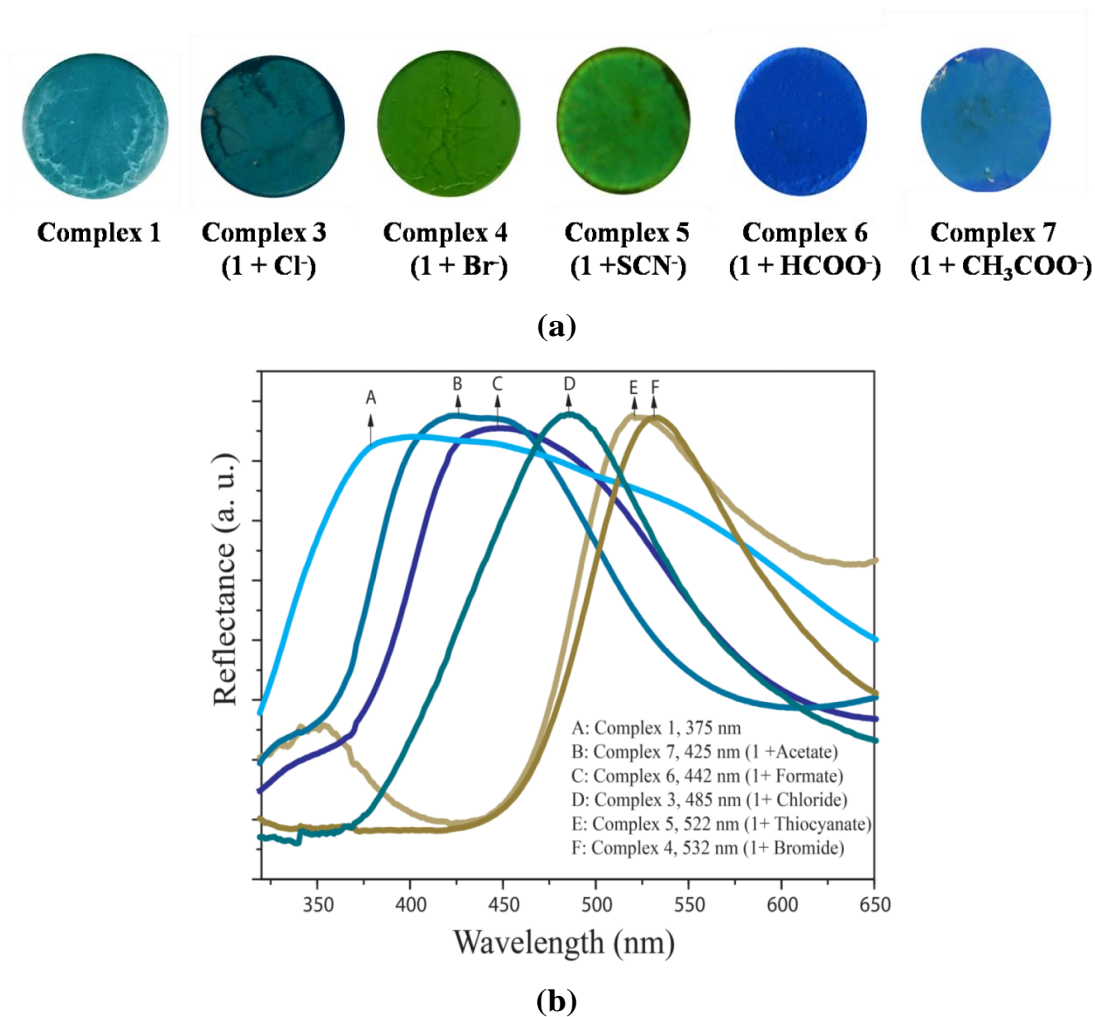


Figure 2.22. (a) Colorimetric change observed in disc after anion exchange experiments, (b) solid state UV reflectance of complex 1 in the presence of chloride, bromide, thiocyanate, formate and acetate solution.

We observed the rapid colorimetric change of disc materials in aqueous anionic solution. To probe the mechanism we have undertaken *in situ* E-SEM study. The E-SEM of crystals surface topology of complex 1 with and without water media revealed interesting observations. Without water, surface topology of the crystals was smooth whereas on dipping it in the water the surface turned porous. One drop of aqueous anionic solution of chloride anion was poured onto the crystals and E-SEM image was grabbed immediately. Porous surface of the crystals was then filled with small crystallite particles, making it rough (Figure 2.23). Based on the E-SEM study we speculated that, the interaction of

water at the crystal surface creates heterogenous pores (different sizes). Further, the aqueous anionic solution travels along the reaction channel similar to the vapochromic effect. Here, water acts as a vehical which delivers the corresponding anion at the copper centre. The structural transition of complex **1** forms their respective (anion) exchanged products. The rate of reaction (i.e breaking and formation of bonds) is so fast that structurally transformed domains of reaction products form heterogenous sizes of crystallites (anion exchanged complex) that remains entangled on the parent crystal of complex **1**. As the rection proceeds towards the core of the parent crystal, crystallites form solid mass intertwined by cumulative force of weak non-covalent interactions and does not get crumbled. The phenomenon is similar to the Oswald ripening effect.

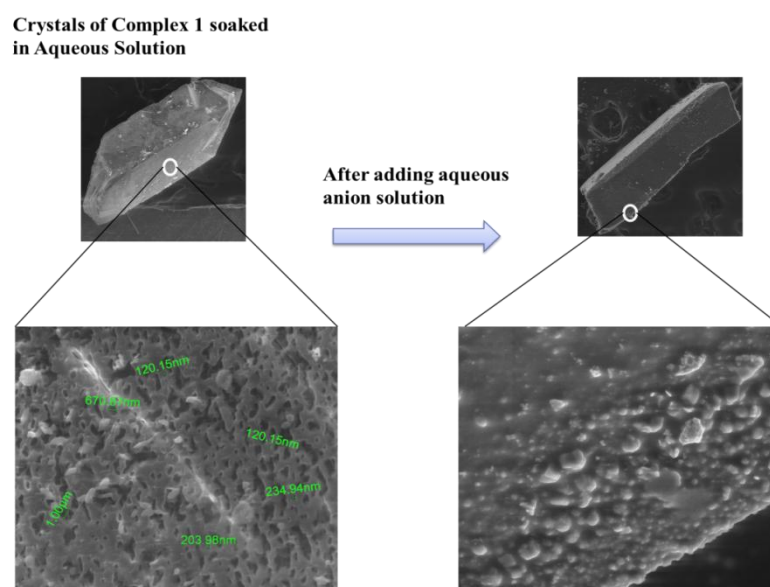


Figure 2.23. E-SEM images of complex **1** when soaked in the aqueous media with and without anionic solution.

To validate the solid-to-solid state transfer of anionic guests, we have investigated anion exchange studies using solvent free grinding. In this experiment we took white KCl and KBr powder and grinded with the crystal of complex **1** in 1:20 (Complex **1**: KCl/KBr) ratio. The color of the powder changed upon grinding which coincided with their solution state anion exchange products. UV-vis reflectance λ_{\max} of the grounded material matched with corresponding anion conjugated compounds obtained after the solution state anion exchange studies (**Figure 2.24**). These experiment proved that the solid-to-solid structural tranformation may have occured by Oswald Ripening

similar to that of the solution state anion exchange studies in aqueous media. We have listed the λ_{\max} values obtained for complex **1**+ X (X:Cl, Br) mixture from the solution and solvent free anion exchange studies (**Table 2.2**).

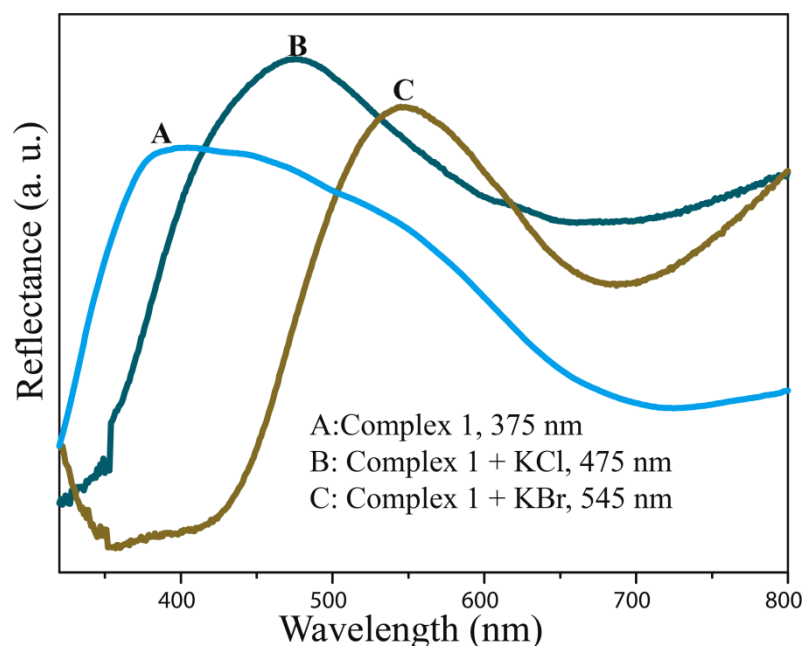


Figure 2.24. Solid state UV-vis reflectance of compounds obtained after solvent free grinding of complex **1** with KCl and KBr powder.

	λ_{\max} Solution-state (nm)	λ_{\max} Solid-state (nm)
Complex 1	375	-----
Complex 1 +KCl	485	475
Complex 1 +KBr	532	545

Table 2.2. Solution and solid state UV-vis reflectance λ_{\max} values

The molecular basis of guest exchange ability of complex **1** was investigated by crystal structure analysis. The aqueous solution of reaction products from anion exchange experiment was warmed till compound gets sparingly soluble in water. Clear liquid was kept for the crystallization by slow-cooling method. Overlay of PXRD patterns of simulated crystal structures (retrieved from the single crystal XRD data) with their experimental patterns (solution state anion exchanged products) were found to be completely in

agreement, which suggested the uniformity of the reaction products (see experimental methods for plots). TGA data of the reaction products also substantiated the crystal structures. Although guest anions possess different shape, size and coordinating tendency, highly flexible nature of 1D framework in complex **1** easily adapted to accommodate guest anions. The changes in the coordination environment of Cu(II) centre in the presence of different anions imparted variation in their colorimetric change. The difference in the color of the crystalline powder (for different anions) is attributed to shift in the MLCT (Metal to ligand charge transfer) properties.

Crystal structures of complex **3** (complex **1**+Cl), monoaqua-trichloro-(μ 2-chloro)-tetrakis (N-phenethylisonicotinamide)- dicopper(II) and complex **4**(complex**1**+Br),monoaqua-tribromo-(μ 2-bromo)-tetrakis(N-phenethyl isonicotinamide) – dicopper (II) showed isostructurality due to the similar topology and coordinating tendency of anions. Molecular structure and ORTEP of complex **3** are provided in the **figure 2.25**. Structural investigation of complex **3** (Complex **1**+Cl) revealed that the molecular transformation might have been occurred similar to the vapochromic phase transition. However, the strongest 1D chain is formed by tethering the molecules along the *c*-axis that is perpendicular to the reaction channel (along *a*-axis). In complex **1**, molecules are held by water-carboxamide H-bonding interaction along *c* axis. During anion exchange process, when the removal of coordinated water molecules create vacant coordination sites, the chloride anions compete with the nitrate anion for coordinating to the metal centre. However, spherical chloride anions predominate the event and acquire the coordination site. Although the reaction has occurred through hydrophilic channel along *a* axis, the molecules along *c* axis are pulled by bridging nature of chloride anion. The repeating unit of complex **3** comprises of two Cu(II) centres, prime **1** and prime **2**. Both the metal centres are coordinated to two monodentate ligands *via* Cu-N (pyridyl) dative bond and show distorted octahedral geometries. Interestingly, the carboxamide groups of the axially coordinated ligands are arranged in the *syn* configuration that forms the strong carboxamide-to-carboxamide N-H...O=C H-bonding between the two layers. Cu(II) centre of prime **1** molecule is coordinated to two chloride anions and one water molecule. One of the

coordinated chloride anion acts as bridging ligand to link the Cu(II) centres of prime **1** and prime **2** molecules. The Cu(II) centre of prime **2** molecule is coordinated to two (free) chloride and one bridging chloride anion. The bilayer repeating units are associated along *c* axis *via* weak O-H...Cl halogen bonding contacts at the coordination sphere and strong N-H...O=C H-bonding between the ligands to form 1D chain (**Figure 2.25c**). The TGA analysis of complex **3** revealed slight weight loss centred at 75 °C which corresponds to the removal of one water molecule present outside the coordination sphere (**Figure 2.26**). The water molecule serve as interlinking agent to connect 1D chains along *a* axis *via* the strong O-H...O hydrogen bonding interactions and weak O-H...Cl interactions to stabilize the 3D assembly (**Figure 2.27**).

Even after repeated trials, we could not obtain good quality crystals of complex **4** (1+ Br). The electron density extracted from the weak structure data and similarity of unit cell parameters (**table 2.3**) with complex **3** revealed close resemblance with structure of **3** i.e formation of strong 1D chains along *c*-axis. The molecular structure of complex **4** is shown in **figure 2.28**. Moreover, the major difference is observed in their TGA data. The slight weight loss (equivalent to one water molecule) which was observed in complex **3** was not seen in the TGA data of complex **4** which suggests the absence of water molecule outside the coordination sphere (**figure 2.29**).

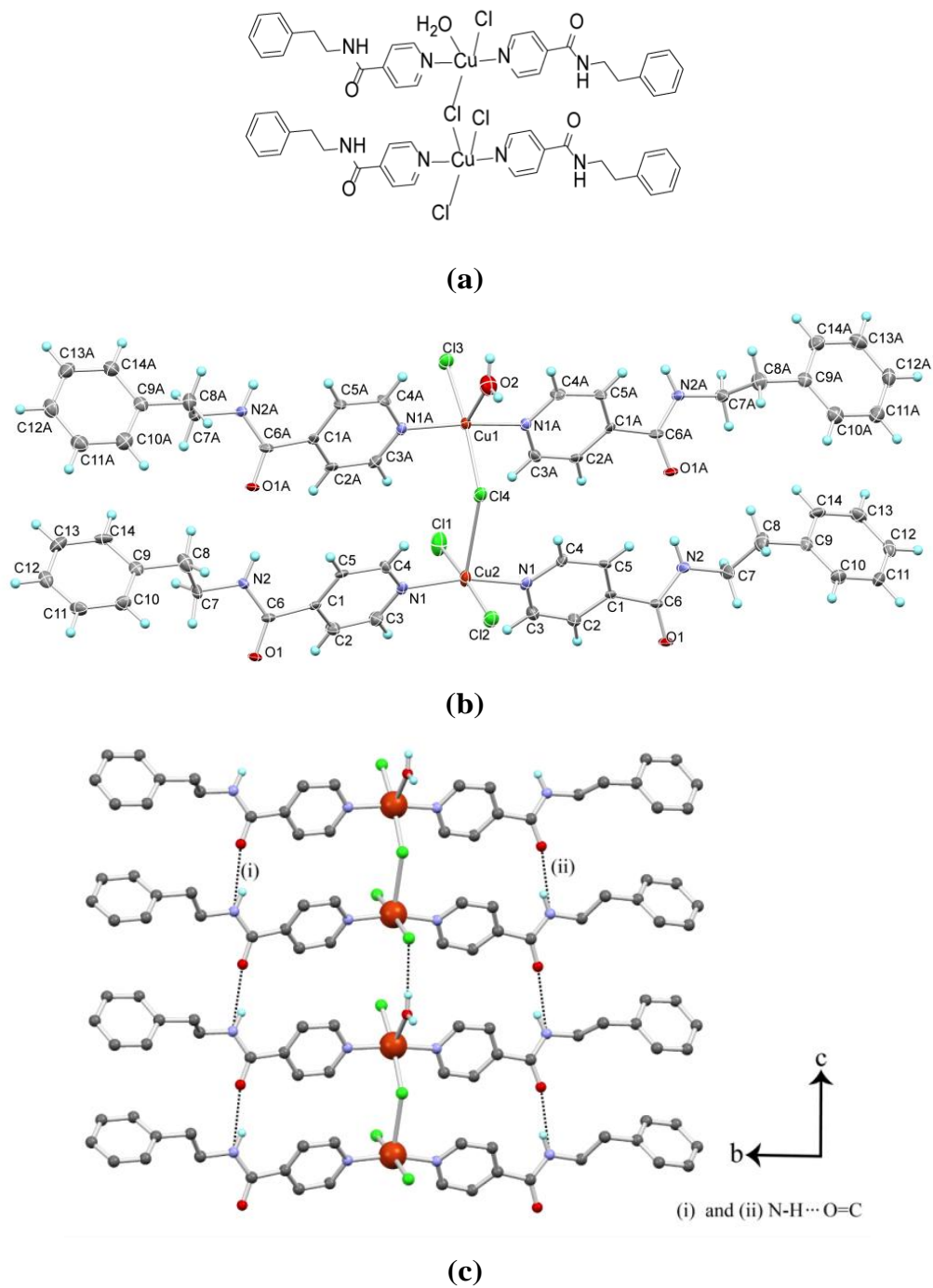


Figure 2.25. (a) Molecular structure, (b) ORTEP of complex **3**, (c) 1D association of repeating unit in complex **3** along *c*-axis via N-H...O=C H-bonding and O-H...Cl halogen bonding.

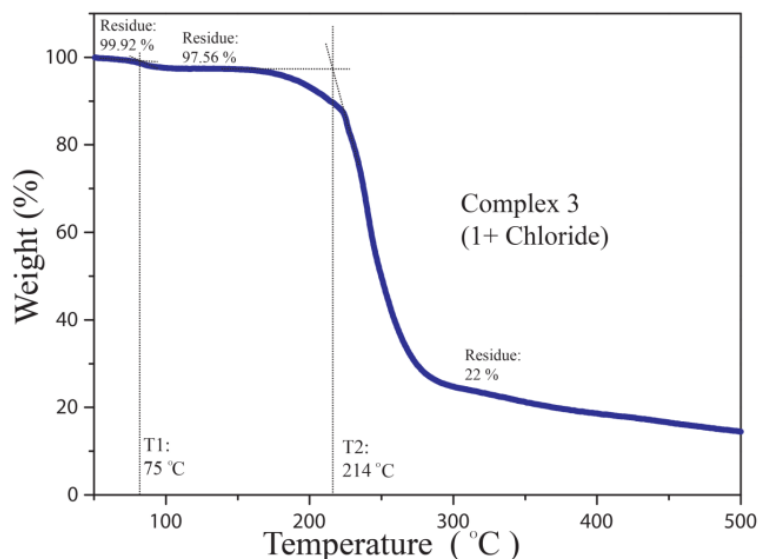


Figure 2.26. TGA data of complex **3**, revealing loss of water molecules at 75 °C (present outside the coordination sphere) and major degradation peak centred at 214 °C.

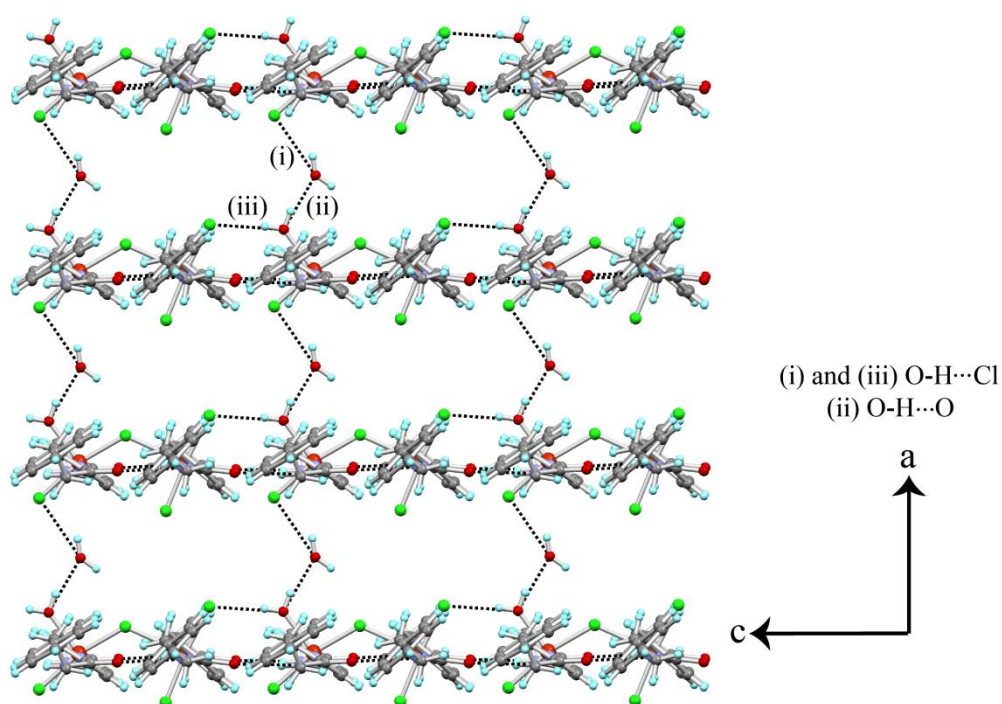


Figure 2.27. Molecular packing in complex **3** along ac plane formed via H-bonding involving interlinking water molecule present outside the coordination sphere.

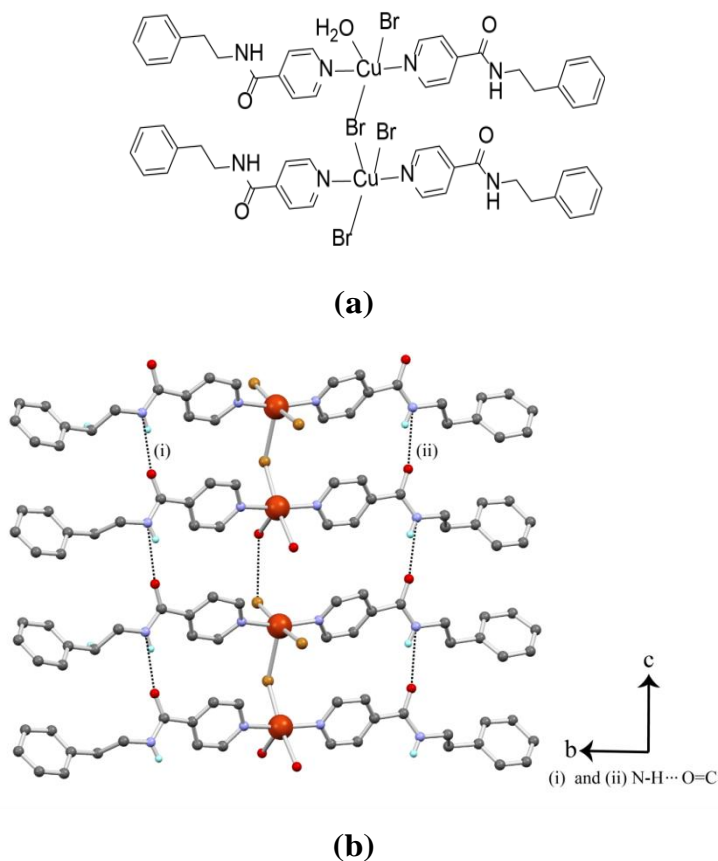


Figure 2.28. (a) Molecular structure, (b) 1D association of repeating unit in complex **4** along *c*-axis via N-H...O=C H-bonding and C-H...Br halogen bonding interactions similar to observed for analogous crystal structure of complex **3**.

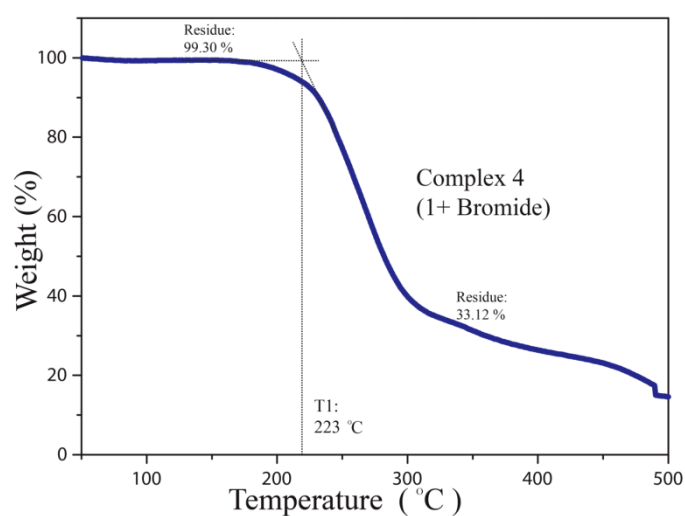


Figure 2.29. TGA data of complex **4**, revealing major degradation peak centred at 223 °C.

Crystal structure of complex **5** (complex **1** + SCN), di-(N-thiocyanato)-bis(N-phenethylisonicotinamide) Cu(II) revealed close match with the complex **2**. The molecular structure and ORTEP of **5** are provided in the **figure 2.30**. The structure shows that the axially coordinated thiocyanate anions do not serve as bridging ligands. The 1D chain along *a*-axis is strengthened by N-H...O=C H-bonding between ligands similar to observed for complex **2** (**figure 2.30c**). The TGA data substantiates the crystal data of complex **5** which showed major weight loss at 238 °C corresponding to the decomposition of the crystal lattice (**Figure 2.31**).

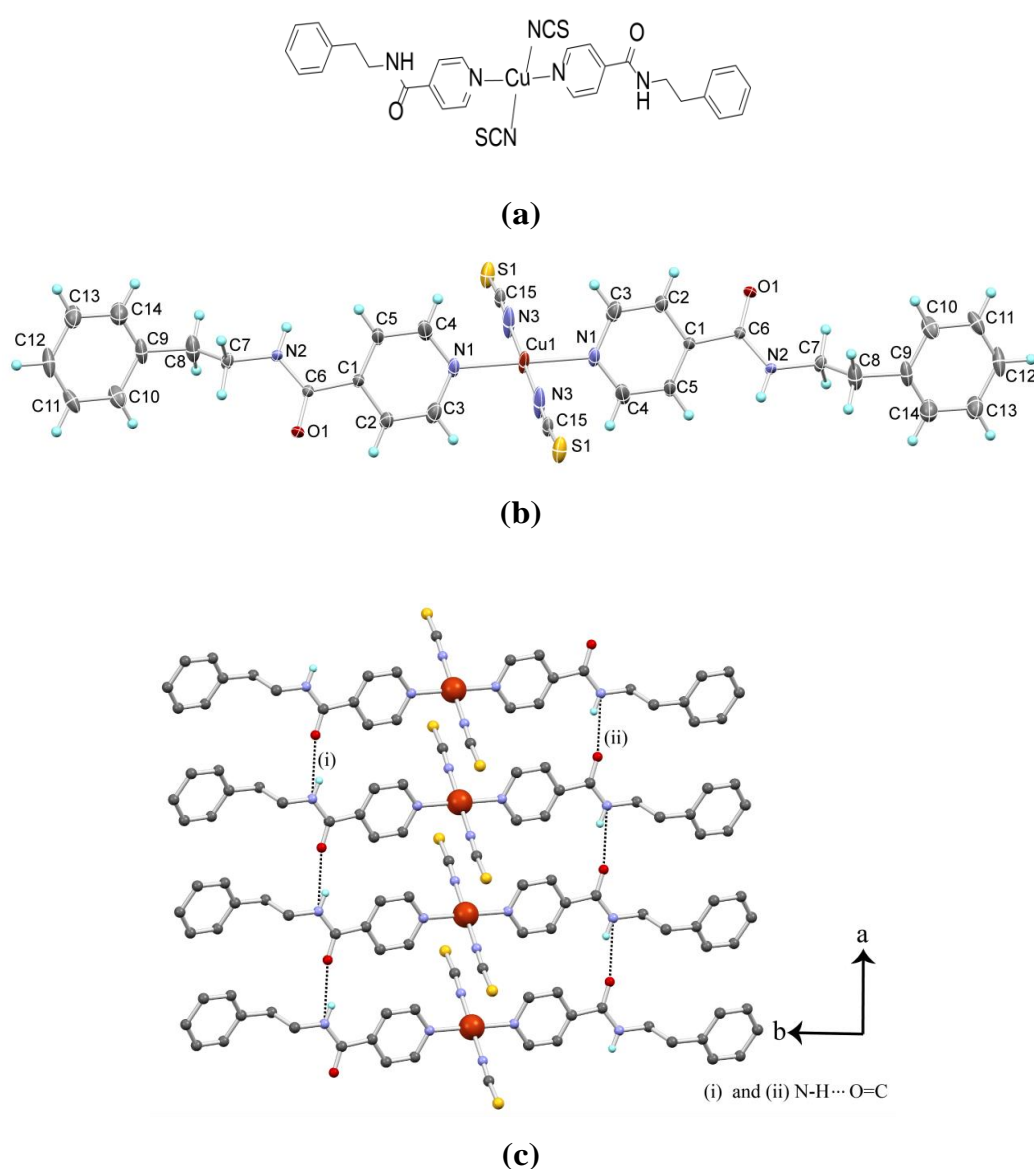


Figure 2.30. (a) Molecular structure, (b) ORTEP of complex **5** and (c) 1D association of repeating unit in complex **5** along *a* axis via N-H...O=C H-bonding.

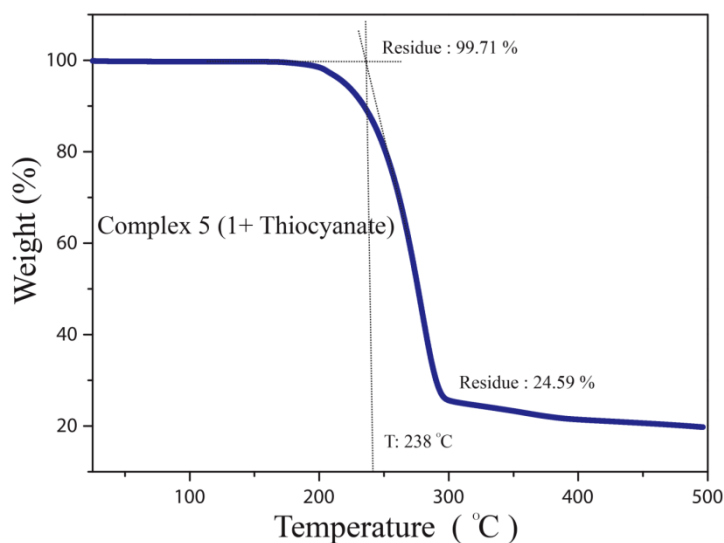


Figure 2.31. TGA data of complex **5**, revealing major degradation peak centred at 238 °C.

Anion exchanged crystal structures of complex anions such as formate (complex **6**), aqua-bis(formato)-bis(N-phenethylisonicotinamide)-copper(II) and acetate (complex **7**) diaqua-bis(acetato-)-bis(N-phenethylisonicotinamide)-copper(II), showed interesting structural features. The molecular structures and ORTEPs of complex **6** and **7** are depicted in **figure 2.32**. Crystal structure of complex **6** revealed close match with complex **2**, however, crystal structure of complex **7** showed isostructurality with complex **1**. In complex **6**, metal centre is coordinated with two formate anions and one water molecules whereas in complex **7**, metal centre is coordinated to two acetate anions and two water molecules. The major difference is observed in their packing arrangement.

The coordinated nitrate anions in complex **2** have been replaced by formate anions in complex **6**. One of the formate anions acts as bridging ligand to form 1D coordination polymer similar to what is observed for complex **2**. Moreover, the 1D chain is strengthened by carboxamide-carboxamide H-bonding between the ligands along *a* axis (**Figure 2.33a**). In case of complex **7**, the strongest 1D association is observed along *c* axis similar to the observed for complex **1**. In this case, each Cu(II) centre is coordinated to two monodentate ligands in the axial position as in the case of complex **1**. However, one pair of equatorially coordinated water molecules is replaced by acetate anions in complex **7**. The coordinated water molecule establish the 1D association with

water-ligand (carboxamide) H-bonding whereas acetate anions forms intramolecular O-H...O H-bonding interactions with coordinating water molecules (**Figure 2.33b**). The TGA analysis of complex **6** and **7** substantiated their crystal structure data (**Figure 2.34**). We speculated that, 1) In case of complex **6**, reaction pathway and structural rearrangement to form 1D polymeric chain occurred in parallel fashion. However, 2) in case of complex **7**, the structural rearrangement (along *c* axis) and reaction pathway (along *a* axis) travelled perpendicular to each other.

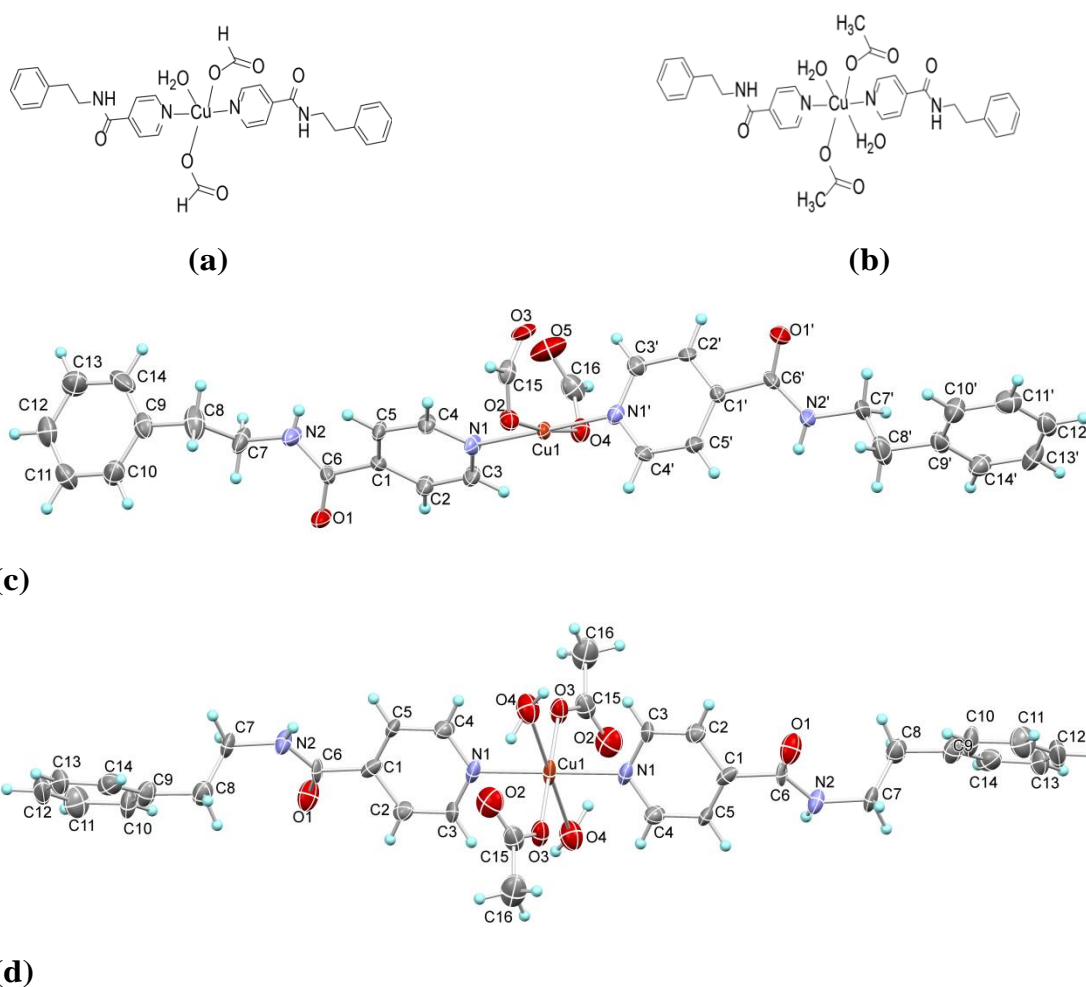


Figure 2.32. Molecular structures of (a) complex **6** and (b) complex **7**. ORTEPs of (c) complex **6** and (d) complex **7**.

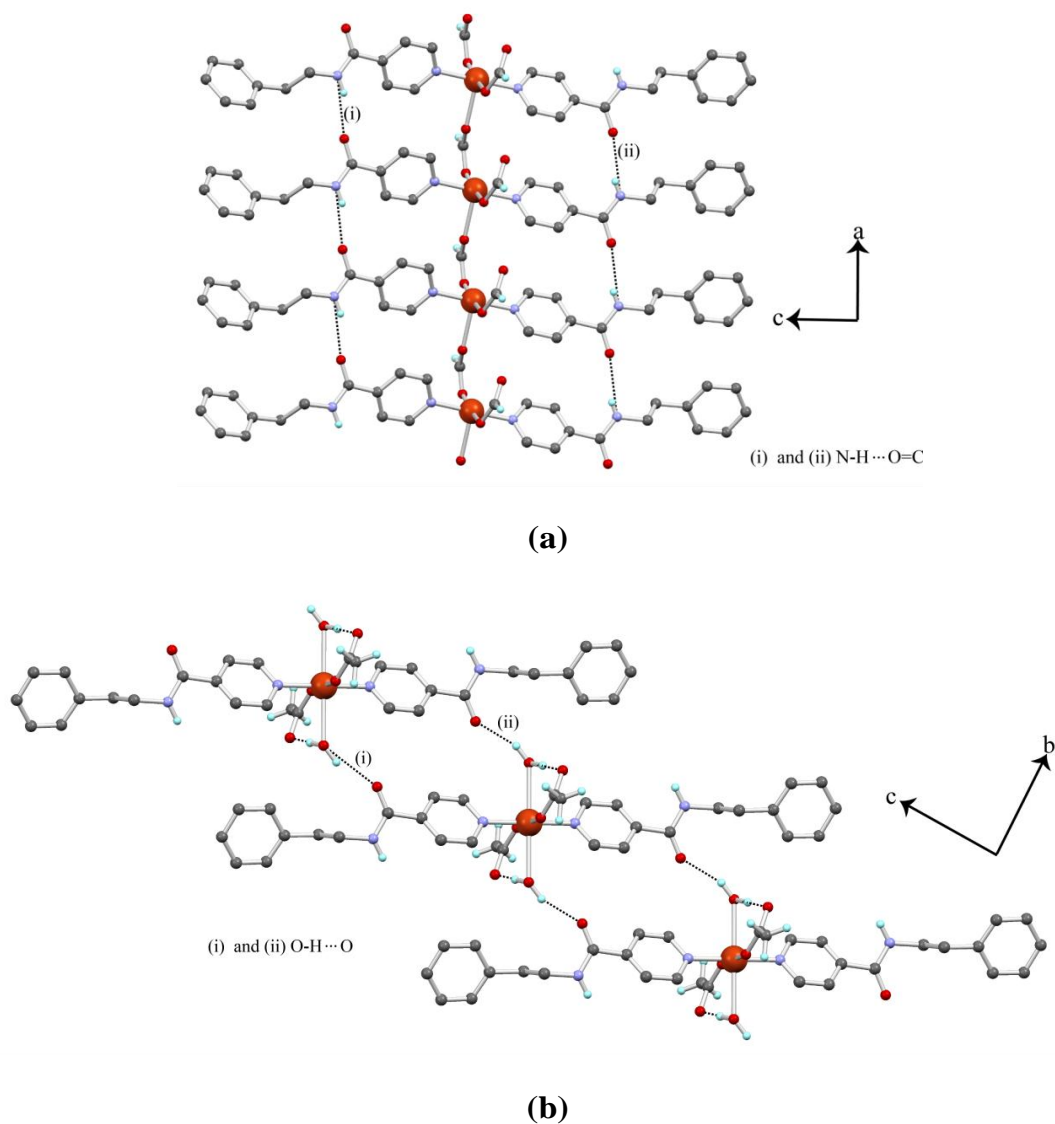
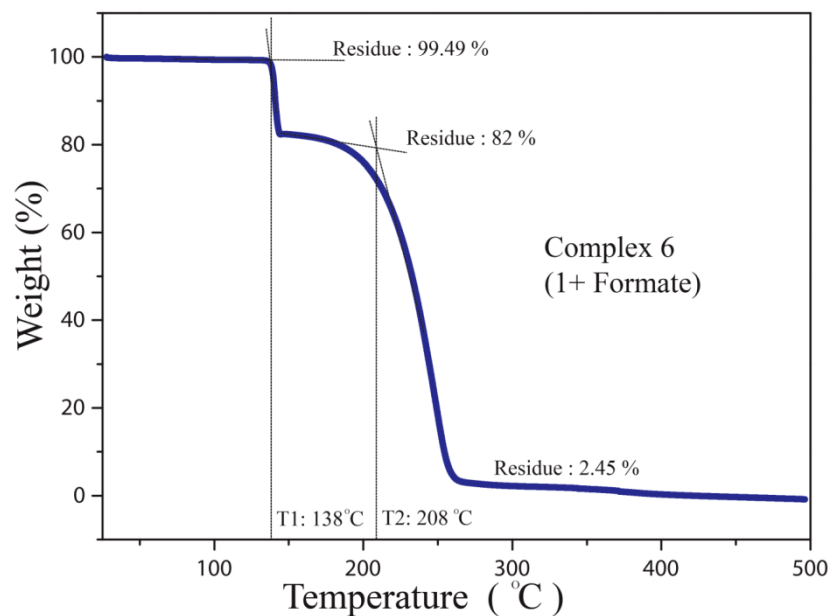
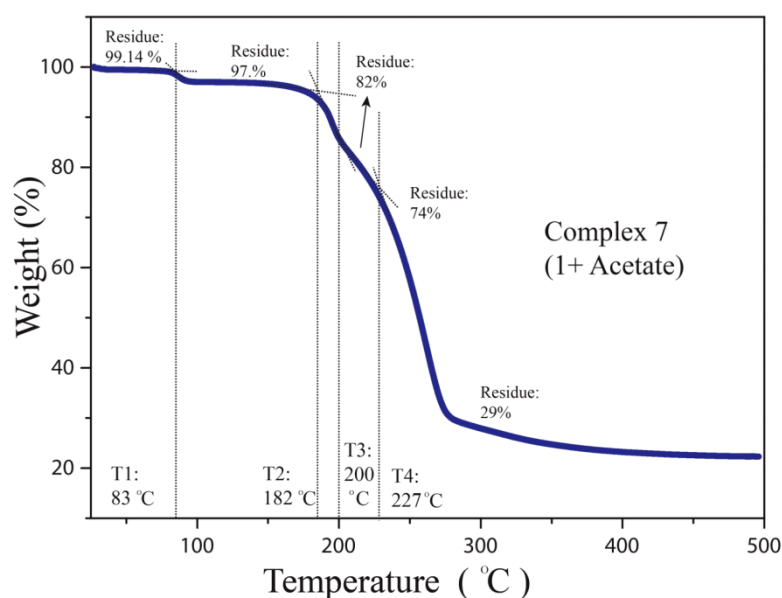


Figure 2.33. Molecular structures of (a) complex 6 and (b) complex 7. ORTEPs of (c) complex 6 and (d) complex 7.



(a)



(b)

Figure 2.34.(a) TGA data of complex **6**, revealing moderate weight loss of 18% centred at 138 °C and major degradation peak centred at 208 °C, **(b)** TGA data of complex **7**, revealing slight weight loss centred at 83 °C and major accumulative weight loss when heated beyond 227 °C.

Based on the structure data, we speculated that the transformation of complex **1** to anion exchanged products may have followed similar mechanism as that of vapochromic response and reaction has occurred along the channel (*a*-axis) in

complex **1**. Molecules may have conjoined along the same path as in the case complexes **5**, **6** or perpendicular to the direction of reaction channel i.e along *c*-axis as in the case of complexes **3**, **4** and **7**. The ligand framework has played remarkable role by providing rigid and strong 1D framework which was structurally transformable. The 1D transformation of coordination framework in complex **1** to the 1D coordination framework of anion exchanged products is depicted in the **figure 2.35**.

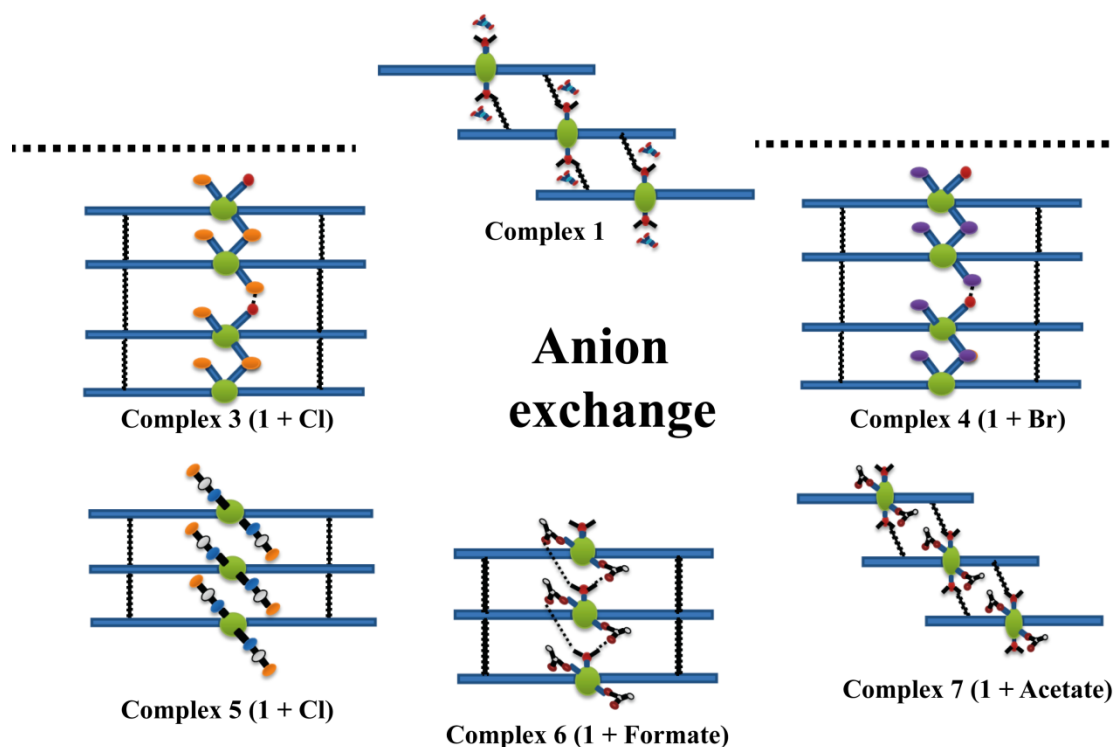


Figure 2.35. Cartoon representation of transformation of 1D coordination framework of complex **1** to its respective anion exchange products complexes **3-7**. Here, blue coloured bricks represent ligand (**L**), containing two major aromatic moieties (pyridyl and phenyl rings), black wavy lines joining the blue bricks represent H-bonding interaction (either carboxamide-to-carboxamide or carboxamide-to-water), green sphere at the centre of blue bricks represent Cu(II) metal centre, coloured atoms possessing, spherical or complex topology and are connected by dative bonds (blue) near to the metal centre represent coordination sphere.

Conclusion:

We have constructed novel, rapid responsive, structurally dynamic Cu(II) coordination complex (complex **1**) for reversible vapochromic detection of polar solvent vapors, and detection and separation of anions from complete aqueous media. The vapo- and guest induced chromic effect of complex **1** is attributed to its flexible and three dimensionally metamorphic framework constituted by conformationally flexible ligand and guest responsive metal centre. The 1D hydrophilic channel submerged in the hydrophobic cavity allowed the guest exchange and structural rearrangement at the metal coordination site resulting in the change in the colorimetric properties. The chromic change is attributed to the shift in the excited state properties i.e. MLCT. However, strong carboxamide-to-carboxamide and water-to-carboxamide H-bonding synthons have accommodated the structural change by forming the 1D rigid network which are further strengthened by weak contacts such as halogen bonding and aromatic interactions in other dimensions. The aromatic moieties of ligands provided the spatial rigidity due to their bulkiness and ladder like arrangement. The cumulative effect of the presence of 1D channel which acts as template and inter molecular non-covalent association prevented the crumbling of crystal lattice during guest exchange. Thereby, solid-solid guest exchange/transfer could occur following a similar mechanism as that of Oswald Ripening effect.

Experimental methods:

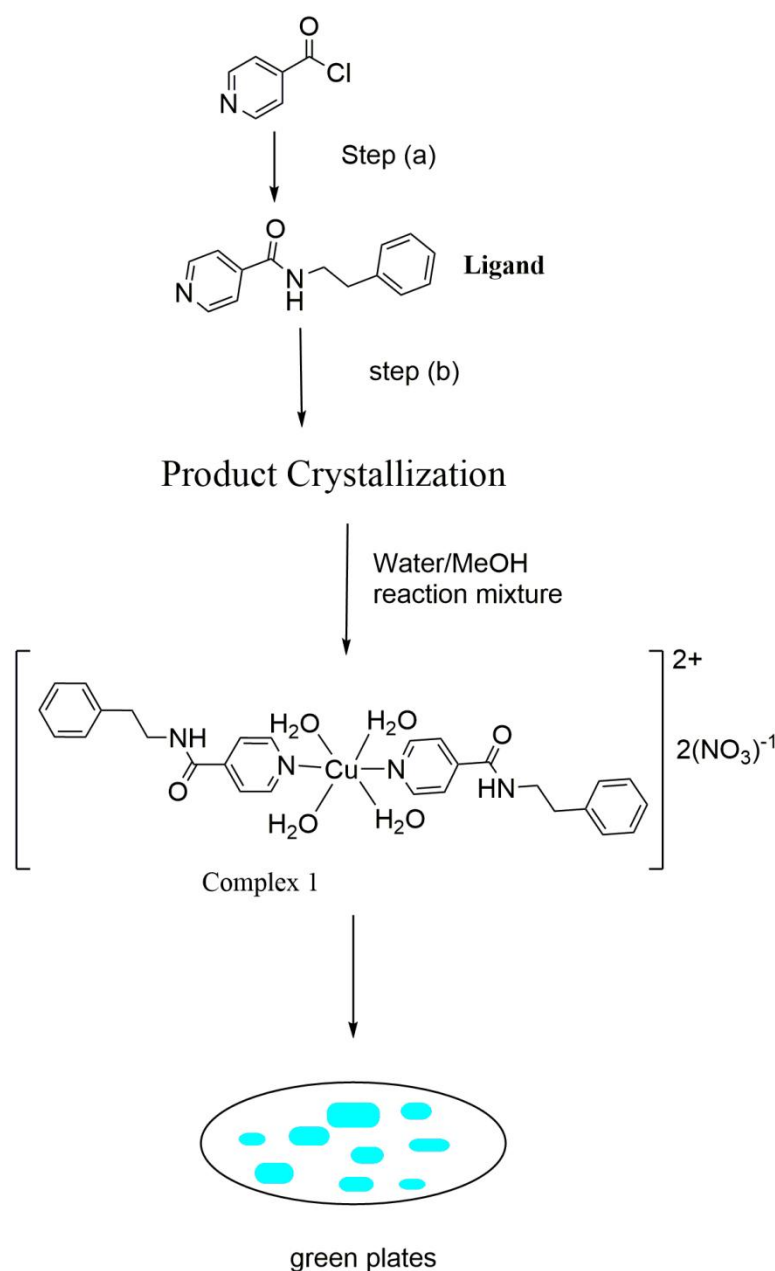


Figure 2.36. General scheme of synthesis of complex 1.

Step (a) Synthesis of N-phenethylisonicotinamide ligand:

To the stirred solution of isonicotinoylchloride in dry DCM, dry triethylamine (Et_3N , 1.1 eq.) was added drop wise at 0°C . To this reaction mixture, 2-phenethylamine (1:1 equivalents) was added slowly. The reaction mixture was kept stirring for ~8 h at room temperature. DCM was evaporated under reduced pressure to get crude residue to which ethyl acetate was added and sequentially washed with saturated solution of NaHCO_3 and brine. The organic layer was dried over solid Na_2SO_4 and evaporated in vacuum to get crude product which after column

chromatography purification yielded compound (L). : ^1H NMR (200 MHz, CD_3OD) δ = 8.67 (t, J = 5.3 Hz, 1 H), 8.64 (m, 2 H), 7.72 - 7.69 (m, 2 H), 7.26 (m, 5 H), 3.64 - 3.57 (m, 2 H), 2.85 (t, J = 7.4 Hz, 2 H).

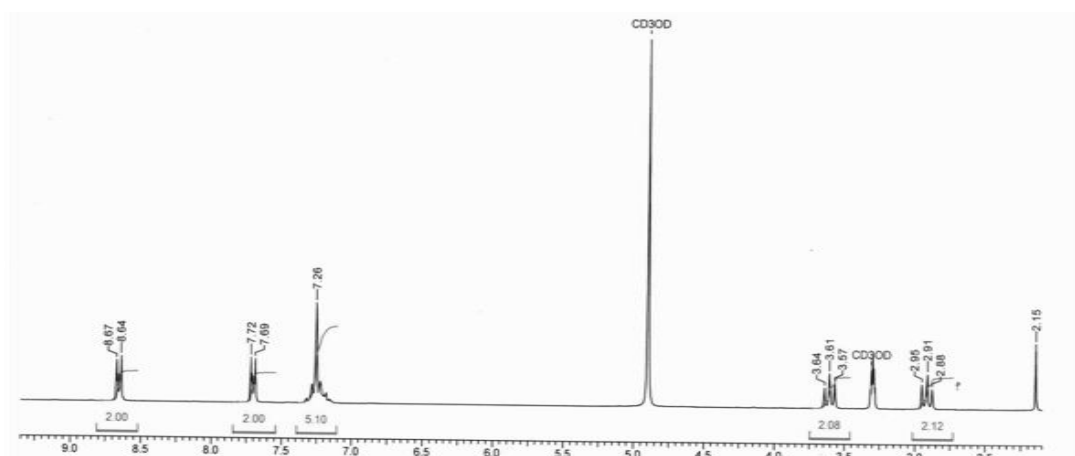


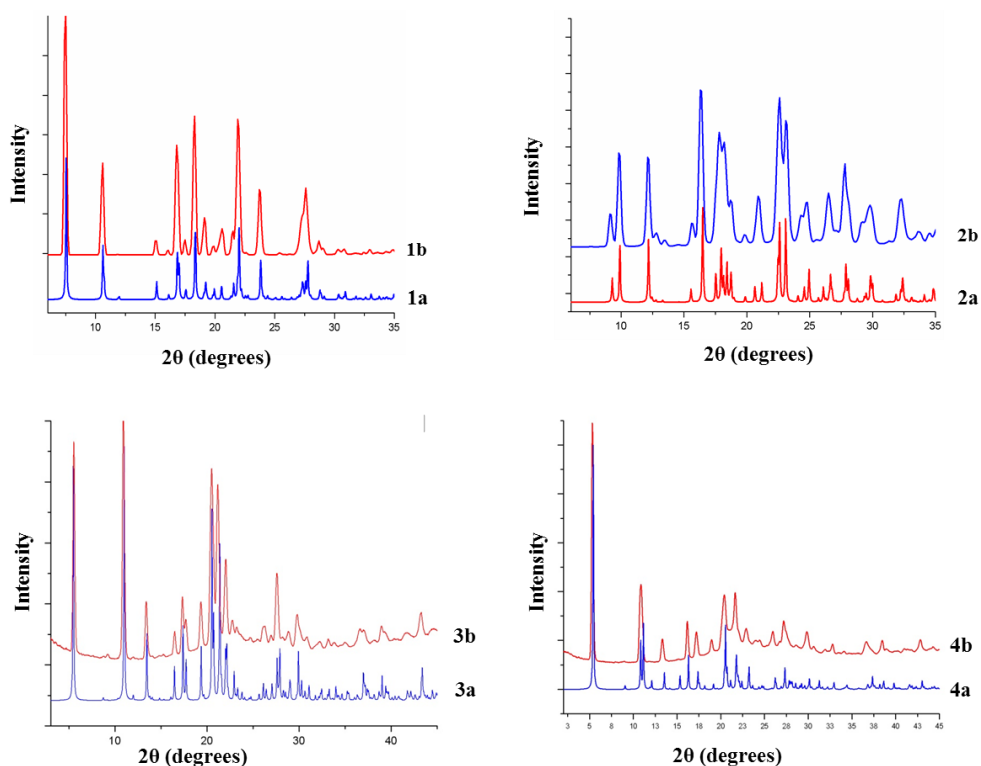
Figure 2.37. ^1H NMR of N-phenethylisonicotinamide (L)

Step (b) Synthesis of complex 1tetraaquabis(N-phenethylisonicotinamide)copper(II)nitrate

Complex (1) was synthesized by adding dry methanolic solution of compound I (2.1 equivalent) to $\text{Cu}(\text{NO}_3)_2 \cdot 3\text{H}_2\text{O}$ and stirred for 15 minutes. The reaction mixture was then refluxed for ~8 h. The reaction mixture was filtered to remove unwanted residue kept for crystallization in the vessel to allow slow evaporation of methanol/water solvent mixture at room. NMR data was not obtained due paramagnetic nature of metal centre.

Comparative analysis of experimental and simulated PXRD pattern obtained from single crystal:

To understand the mechanism of sensing and associated chromogenic change, to the aqueous anionic solution of TBAX salts (X: Cl^- , Br^- , SCN^- , HCOO^- , CH_3COO^-) one equivalent of insoluble blue powder of complex **1** was suspended. After chromogenic change was observed the obtained powder was repeatedly washed with water, air dried and powder X-ray diffraction patterns were recorded on Rigaku instrument at continuous scanning rate of 2° 2θ /min using Cu $K\alpha$ radiation (40 kV, 30 mA) with the intensity of the diffracted X-ray being collected at intervals of 0.1° 2θ . A nickel filter was used to remove Cu $K\beta$ radiation. Simulated powder pattern of single crystal structure analysis matched with collected experimental powder pattern after sensing experiment at room temperature and thus validated illustrated mechanism of anion detection.



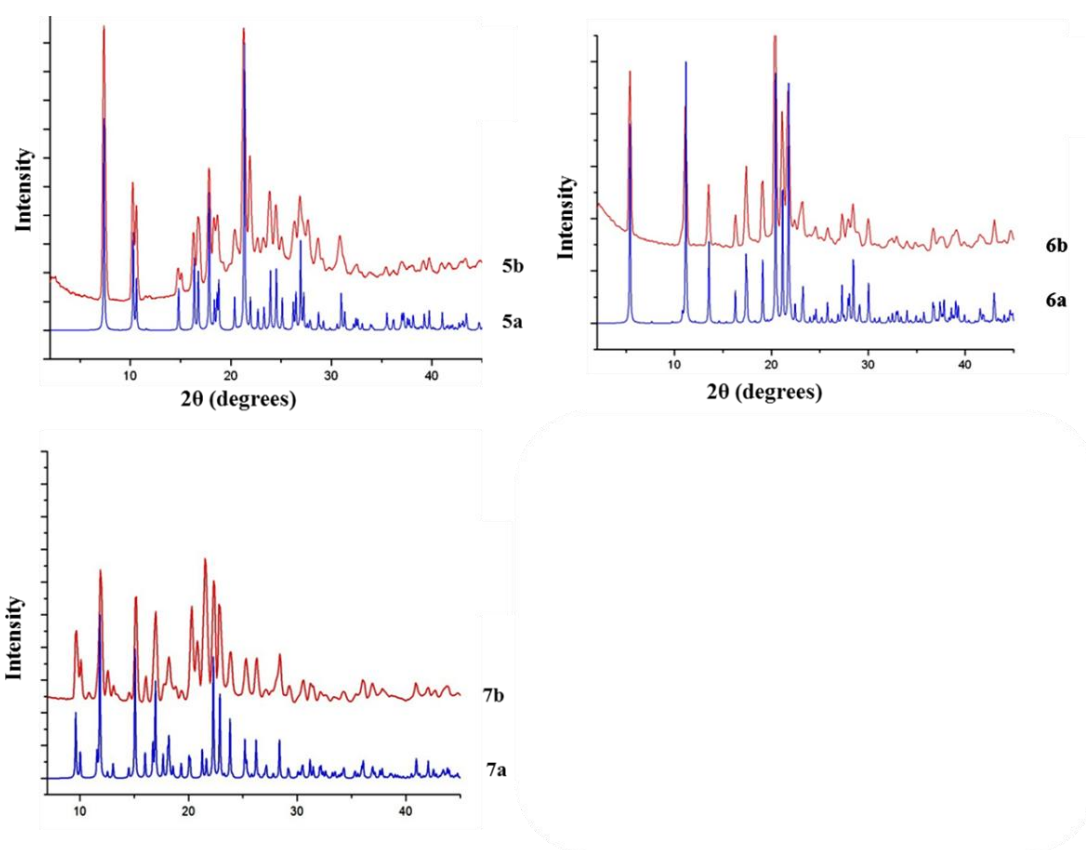


Figure 2.38. (1a) and (1b) represents simulated and experimental PXRD pattern of complex **2**, (2a) and (2b) represents simulated and experimental PXRD pattern of complex **1**, (3a) and (3b) represents simulated and experimental PXRD pattern of Complex **3** (chloride anion) , (4a) and (4b) represents simulated and experimental PXRD pattern of complex **4** (bromide anion). (5a) and (5b) represents simulated and experimental PXRD pattern of complex **5** (thiocyanate anion), (6a) and (6b) represents simulated and experimental PXRD pattern of complex **6** (formate anion), (7a) and (7b) represents simulated and experimental PXRD pattern of complex **7** (acetate anion).

X-ray Crystallography: Single crystal structure of all compounds were determined by measuring X-ray intensity data on a Bruker SMART APEX II single crystal X-ray CCD diffractometer having graphite-monochromatised Mo-K α ($\lambda = 0.71073 \text{ \AA}$) radiation. The X-ray generator was operated at 50 kV and 30 mA. A preliminary set of cell constants and an orientation matrix were calculated from total 36 frames. The optimized strategy used for data collection consisted different sets of φ and ω scans with 0.5° steps in φ/ω . Data were collected keeping the sample-to-detector distance fixed at 5.00 cm. The X-ray data acquisition was monitored by APEX2 program suit. All the data were corrected for Lorentz-polarization and absorption effects (multi-scan) using SAINT and SADABS programs integrated in APEX2 package. The structures were solved by direct methods and refined by full matrix least squares, based on F, using SHELX-97. Molecular diagrams were generated using ORTEP-3 and Mercury programs. Geometrical calculations were performed using SHELXTL and PLATON.

Table 2.3. Crystallography data table

Crystal Data	Ligand (L)	Complex 1	Complex 2	Complex 3 (1 + Cl)	Complex 4 (1 + Br)
Formula	C ₁₄ H ₁₄ N ₂ O	C ₂₈ H ₃₆ CuN ₂ O _{6.2} (NO ₃)	C ₂₈ H ₂₈ CuN ₆ O ₈	C ₅₆ H ₆₀ Cl ₄ Cu ₂ N ₈ O ₆	C ₆₀ HBr ₄ Cu ₂ N ₈ O ₄
M _r	226.27	712.17	640.10	1210.00	1344.41
Crystal Size, mm	0.47x 0.16 x 0.01	0.41x 0.25 x 0.13	0.37 x 0.25 x 0.11	0.15 x 0.07 x 0.05	0.12 x 0.06 x 0.03
Temp. (K)	296(2)	296(2)	296(2)	296 (2)	296 (2)
Crystal Syst.	Monoclinic	Monoclinic	Monoclinic	Monoclinic	Monoclinic
Space Group	<i>P</i> ₂ ₁ / <i>n</i>	<i>P</i> ₂ ₁ / <i>n</i>	<i>P</i> ₂ ₁	<i>P</i> ₂ ₁ / <i>m</i>	<i>P</i> ₂ ₁ / <i>m</i>
<i>a</i> /Å	8.3116(2)	8.1061(2)	5.10940(9)	8.2526(6)	8.1749(6)
<i>b</i> /Å	5.1887(1)	19.0316(3)	16.6434(3)	32.265(2)	32.598(2)
<i>c</i> /Å	28.4560(6)	10.4257(6)	16.6448(3)	10.1273(7)	10.2294(8)
α ⁰	90	90	90	90	90
β ⁰	96.440(1)	104.109(1)	98.3010(10)	90.281(4)	90.434(4)
γ ⁰	90	90	90	90	90
<i>V</i> /Å ³	1219.46(4)	1559.87(10)	1400.61(4)	2696.6(3)	2725.9(1)
Z	4	2	2	2	2
<i>D</i> _{calc} /g cm ⁻³	1.232	1.516	1.518	1.490	1.638
<i>m</i> /mm ⁻¹	0.079	0.773	0.842	1.046	3.767
<i>F</i> (000)	480	742	662	1252	1294
<i>Ab. Correct.</i>	Multi-scan	Multi-scan	Multi-scan	Multi-scan	Multi-scan
<i>T</i> _{min} / <i>T</i> _{max}	0.9635 /0.9992	0.7447/0.9068	0.9146/0.7475	0.9496/0.8589	0.6607/ 0.8954
2 θ _{max}	50	50	50	50	50
Total reflns.	9162	11978	13869	63651	29132
Uniquereflns.	1519	2166	4861	4832	4380
<i>h, k, l</i> (min, max)	-9, 9 -5, 6 -33,33	-9, 9 -20, 22 -10,12	-6, 6 -19, 19 -19,19	-9, 9 -38, 38 -12,12	-9, 9 -38, 38 -12,11
<i>R</i> _{int}	0.0506	0.0713	0.0384	0.0473	0.1091
No. of para	154	228	388	367	302
<i>R</i> [<i>I</i> > 2 σ (<i>I</i>)]	0.0554	0.0450	0.0394	0.0895	0.2110
<i>wR</i> ₂ [<i>I</i> > 2 σ (<i>I</i>)]	0.1441	0.1071	0.0676	0.1871	0.4813
<i>R</i> [all data]	0.0805	0.0642	0.0541	0.0916	0.2148
<i>wR</i> ₂ [all data]	0.1606	0.1164	0.0724	0.1880	0.4911
goodness-of-fit	1.057	1.030	1.009	1.318	2.223
$\Delta\rho$ _{max} , $\Delta\rho$ _{min} (e Å ⁻³)	+0.187, - 0.213	+1.004, - 1.002	+0.212, - 0.271	+1.413, - 1.609	+8.532, - 1.885

Crystal Data	Complex 5 (1 + SCN)	Complex 6 (1 + HCOO⁻)	Complex 7 (1 + CH₃COO⁻)
Formula	C ₃₀ H ₂₈ Cu N ₆ O ₂ S ₂	C ₃₀ H ₃₀ Cu N ₄ O ₆	C ₃₂ H ₃₈ Cu N ₄ O ₈
M _r	632.24	606.12	670.20
Crystal Size, mm	0.12 x 0.09 x 0.05	0.22x 0.09 x 0.08	0.09 x 0.07 x 0.03
Temp. (K)	150(2)	100(2)	296(2)
Crystal Syst.	Monoclinic	Monoclinic	Monoclinic
Space Group	<i>P</i> 2 ₁ / <i>n</i>	<i>P</i> 2 ₁ / <i>c</i>	<i>P</i> 2 ₁ / <i>n</i>
<i>a</i> /Å	5.0908(4)	5.1417(8)	8.616(4)
<i>b</i> /Å	16.6106(13)	16.324(3)	18.363(9)
<i>c</i> /Å	16.9652(14)	33.007(4)	10.587(5)
α°	90	90	90
β°	92.475(4)	98.930(8)	108.526(7)
γ°	90	90	90
<i>V</i> /Å ³	1433.3(2)	2736.8(7)	1588.2(13)
<i>Z</i>	2	4	2
<i>D</i> _{calc} /g cm ⁻³	1.465	1.471	1.401
<i>m</i> /mm ⁻¹	0.947	0.850	0.744
<i>F</i> (000)	654	1260	702
<i>Ab. Correct.</i>	Multi-scan	Multi-scan	Multi-scan
<i>T</i> _{min} / <i>T</i> _{max}	0.8948/ 0.9542	0.883/0.959	0.9780/0.9360
2 θ _{max}	50	50	50
Total reflns.	25479	36357	10057
Uniquereflns.	1803	4485	2781
<i>h, k, l</i> (min, max)	-6, 6 -19, 19 -18,20	-6, 6 -19, 19 -39,39	-10, 10 -21, 21 -11,12
<i>R</i> _{int}	0.0506	0.1121	0.2091
No. of para	268	370	234
<i>R</i> 1 [<i>I</i> > 2 σ (<i>I</i>)]	0.0809	0.1053	0.1011
<i>wR</i> 2 [<i>I</i> > 2 σ (<i>I</i>)]	0.1318	0.1652	0.2275
<i>R</i> 1 [all data]	0.1407	0.1120	0.1972
<i>wR</i> 2 [all data]	0.1592	0.1665	0.2911
goodness-of- fit	1.067	1.321	1.143
$\Delta\rho_{\max}, \Delta\rho_{\min}$ (e Å ⁻³)	+0.987, -0.762	+0.614, -1.372	+1.009, -1.349

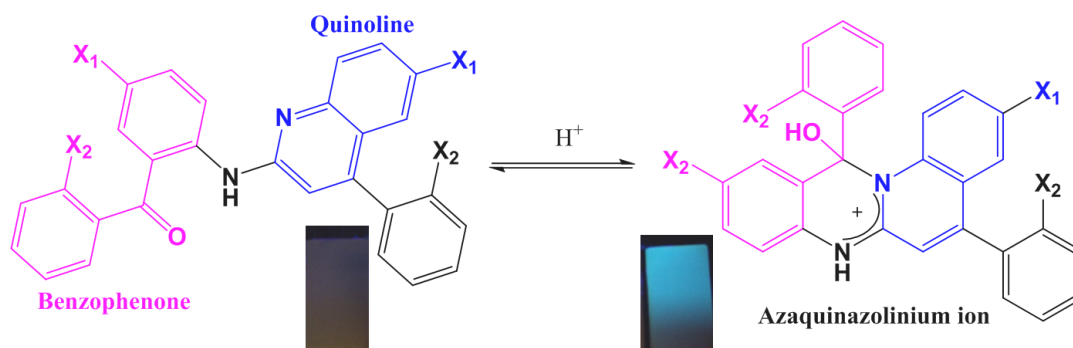
References:

1. Y. Salinas, Y., R. Martínez-Mañez, M. D. Marcos, F. I. Sancenón, A. M. Costero, M. Parra and S. Gil, *Chem. Soc. Rev.*, 2012, **41**, 1261-1296.
2. R. Elghanian, J. J. Storhoff, R. C. Mucic, R. L. Letsinger and C. A. Mirkin, *Science*, 1997, **277**, 1078-1081.
3. M. E. Germain and M. J. Knapp, *Chem. Soc. Rev.*, 2009, **38**, 2543-2555.
4. N. A. Rakow and K. S. Suslick, *Nature*, 2000, **406**, 710-713.
5. B. Valeur and M. r. N. Berberan-Santos, *Molecular fluorescence: principles and applications*, John Wiley & Sons.
6. J. C. Caldwell, T. J. Woodruff, R. Morello-Frosch and D. A. Axelrad, *Toxicol. and Ind. Health*, 1998, **14**, 429-454.
7. M. Kampa and E. Castanas, *Environ. Pollut.*, 2008, **151**, 362-367.
8. B. N. Ames, R. Magaw and L. S. Gold, *Science(Washington)*, 1987, **236**, 271-279.
9. E. Broughton, *Environ. Health*, 2005, **4**, 1.
10. J. W. Steed, *Chem. Soc. Rev.*, 2009, **38**, 506-519.
11. T. Gunnlaugsson, M. Glynn, G. M. Tocci, P. E. Kruger and F. M. Pfeffer, *Coordin. Chem. Rev.*, 2006, **250**, 3094-3117.
12. O. S. Wenger, *Chem. Rev.*, 2013, **113**, 3686-3733.
13. F. Drache, V. Bon, I. Senkovska, M. Adam, A. Eychmuller and S. Kaskel, *Eur. J. Inorg. Chem*, 2016.
14. L. Bai, A. Jana, H. P. Tham, K. T. Nguyen, P. Borah and Y. Zhao, *Small*, 2016, **12**, 3302-3308.
15. Y. Funasako, T. Mochida, K. Takahashi, T. Sakurai and H. Ohta, *Chem. Eur. J.*, 2012, **18**, 11929-11936.
16. I. S. Krytchankou, I. O. Koshevoy, V. V. Gurzhiy, V. A. Pomogaev and S. P. Tunik, *Inorg. Chem.*, 2015, **54**, 8288-8297.
17. C. E. Strasser and V. J. Catalano, *JACS*, 2010, **132**, 10009-10011.
18. G.B. Li, L. Li, J.-M. Liu, T. Yang and C.-Y. Su, *Cryst. Growth Des.*, 2013, **13**, 1518-1525.
19. L. E. Kreno, K. Leong, O. K. Farha, M. Allendorf, R. P. Van Duyne and J. T. Hupp, *Chem. Rev.*, 2011, **112**, 1105-1125.

20. B. Chen, L. Wang, F. Zapata, G. Qian and E. B. Lobkovsky, *JACS*, 2008, **130**, 6718-6719.
21. B. Chen, Y. Yang, F. Zapata, G. Lin, G. Qian and E. B. Lobkovsky, *Adv. Mater.*, 2007, **19**, 1693-1696.
22. H. Furukawa and O. M. Yaghi, *JACS*, 2009, **131**, 8875-8883.
23. W. Morris, C. J. Doonan, H. Furukawa, R. Banerjee and O. M. Yaghi, *JACS*, 2008, **130**, 12626-12627.
24. S. Kandambeth, A. Mallick, B. Lukose, M. V. Mane, T. Heine and R. Banerjee, *JACS*, 2012, **134**, 19524-19527.
25. M. Albrecht and G. van Koten, *Angew. Chemie*, 2001, **40**, 3750-3781.
26. E. J. O'Neil and B. D. Smith, *Coordin. Chem. Rev.*, 2006, **250**, 3068-3080.
27. C. W. Rogers and M. O. Wolf, *Coordin. Chem. Rev.*, 2002, **233**, 341-350.
28. M. H. Keefe, K. D. Benkstein and J. T. Hupp, *Coordin. Chem. Rev.*, 2000, **205**, 201-228.
29. D. Braga, *J. Chem. Soc., Dalton Trans.*, 2000, **21**, 3705-3713.
30. W. Hamilton and J. A. Ibers, *Hydrogen bonding in solids*, 1968.
31. P. Metrangolo, G. Resnati, T. Pilati and S. Biella, *Halogen Bonding in crystal engineering*, Springer Berlin Heidelberg, 2007, 105-136.
32. E. R. T. Tiekink and J. Zukerman-Schpector, *The importance of Pi-interactions in crystal engineering: frontiers in crystal engineering*, John Wiley & Sons.
33. A. J. Blake, N. R. Champness, P. Hubberstey, W.-S. Li, M. A. Withersby and M. Schroder, *Coordin. Chem. Rev.*, 1999, **183**, 117-138.
34. L. Brammer, *Chem. Soc. Rev.*, 2004, **33**, 476-489.
35. L. Brammer, J. C. M. Rivas, R. Atencio, S. Fang and F. C. Pigge, *J. Chem. Soc., Dalton Trans.*, 2000, **21**, 3855-3867.
36. H. Sato, W. Kosaka, R. Matsuda, A. Hori, Y. Hijikata, R. V. Belosludov, S. Sakaki, M. Takata and S. Kitagawa, *Science*, 2014, **343**, 167-170.
37. K. M. Sureshan and M. S. Shashidhar, *Tetrahedron. Lett.*, 2000, **41**, 4185-4188.
38. M. I. Tamboli, S. Krishnaswamy, R. G. Gonnade and M. S. Shashidhar, *Chem. Eur. J*, 2013, **19**, 12867-12874.

Chapter 2B

The Structure-property Relationship Between Conformationally Flexible Benzophenone-quinoline Conjugates and their Turn-on Acid Sensing Properties



Non-fluorescent Benzophenone-quinoline conjugates form fluorescent azaquinazolinium ions under the acidic condition and show remarkable changes in the absorption and emission bands.

Introduction:

Acids are important chemicals with large scale applications in many industrial processes such as manufacturing of fertilizers, refining of metals and pharmaceutical production etc. In recent years, many industrial disasters have been reported which are caused by acid leaks.¹ The inhalation of acidic fumes shows adverse effects on human health. Moreover, their release in the environment causes widespread damages to the surrounding ecosystem. Acidic toxins are also used as chemical warfare agents due to their lethal effect. Many incidences were reported where acid leakage caused life threatening injuries to people and industrial workers. Due to volatile nature of acid fumes they possess ability to form large acid clouds which can spread to over larger distance and cause mass-destruction. Recently reported acid spillage accidents are tabulated below.

Sr. No.	Disasters	Place	Date	Deaths/Affected
1.	Eight tonnes of HF acid leak	South-eastern city of Gumi, South Korea	September 27, 2012	5 deaths and more than 3000 people affected
2.	Hydrochloric Acid Leakage	Tokyo Electric Power Company, Japan	October 24, 2012	28 people affected

Turn-on fluorescent probes are mostly preferred over colorimetric probe because their released photon energy can be used in the electric signalling devices. Reactivity and structural transformation of probe are the key factors for their designing. The development of reliable means for the early detection of acid leakage is one of the major challenges of today's industrial world. To date many techniques have been reported, but optical methods provide promising platform due to their rapid response and visual detection.²The

designing of acid responsive and reversible turn-on probes is one of the active fields of research. Recent advances have implemented many chemical reactions, however, the structural rearrangements which include ring opening/closure reactions have gained much attention.³ The analyte induced conformational change causes significant shift in their absorption and emission spectra that forms the basis of their detection. So far rhodamine and fluorescein based compounds are extensively investigated for their acid and pH responsive properties.⁴ Zhi-Qiang Hu *et al*⁵ reported a highly sensitive rhodamine B-2-aminobutenedioate conjugate which can detect the pH range of 4.0–6.5. When the H⁺ concentration reaches the detection range, the spirolactam unit of rhodamine B-2-aminobutenedioate was opened, which resulted in the dramatic change in the absorbance and emission profiles of the compounds. Shincheol Kang *et al.* reported Rhodaminehydrazide-based chemosensors which showed solid state turn-on response to the volatile acid gases.⁶ Kotaro Tateno *et al.* published a report on nitro-group-substituted L-shaped pentacycles, pyrrolo[1,2-a][1,8]naphthylidines based compounds.⁷ These compounds emit green to orange fluorescence upon addition of trifluoroacetic acid (TFA).

There is immense upsurge for finding novel acid sensing probes which possess properties like, reusability, reactivity in solid state, strong emission (light-up probe) and applicability in the alarming device for the on-site detection. The general design of cyclization based sensory system is shown in the **Figure 2.39**. Organic probe contains two sites namely, receptor group and the signalling group. Receptor group binds to anionic/ cationic part of the pollutant which induces structural transformation. Cyclization brings receptor group and signalling group together to form conjugated system and emit fluorescence when excited at certain wavelength. The cyclization converts non-emissive conjugates of receptor-signalling moieties into emissive species. Highly reactive ARC (acid responsive component) and fast responsive FC (fluorescent component) chemical moieties may be conjugated by combinatorial approach to design wide range of probes.³

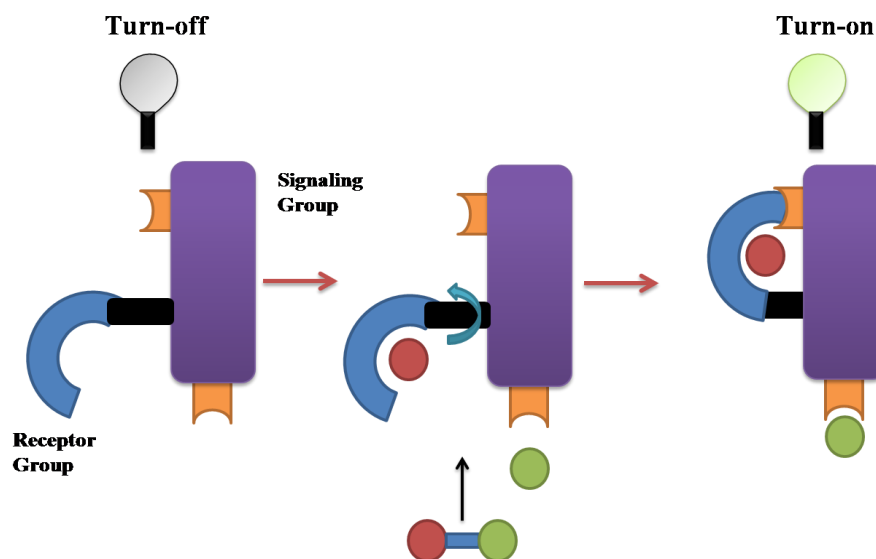


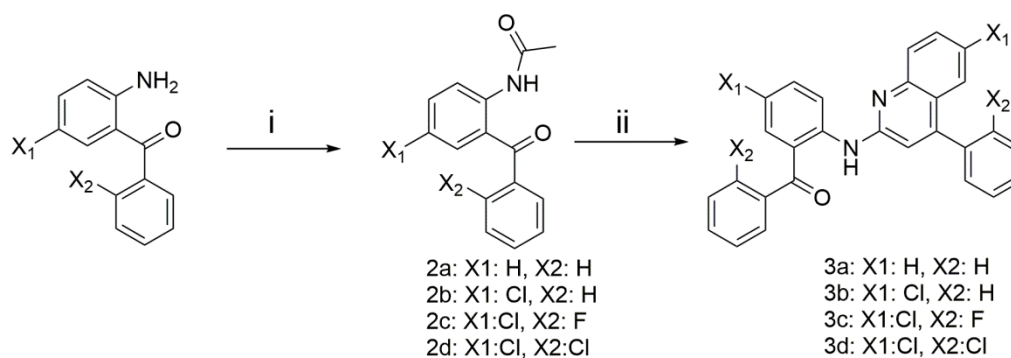
Figure 2.39. General design cyclization based organic chemosensors.

The azonia aromatic chromophores are used as dyes and fluorescent probes due to their charge transfer properties.⁸ Their incorporation as core chemical moiety have been employed as suitable strategy for designing of sensory probes. Literature survey reveals that the azaquinazolinium heterocycles can be prepared by acid catalyzed condensation reaction between quinolines and benzophenones.⁹ In the present context of designing the suitable sensory probe, we envisaged that if quinolines and benzophenones are fused together as a conjugated system, they can be effectively used for the *in situ* generation of acid responsive aromatic azaquinazolinium ions.

This chapter deals with study on quinoline-benzophenone conjugates. The compounds were synthesized and their differential turn-on fluorescent activities were studied, in solution and in solid state, upon exposure with acids and diethyl chlorophosphate (DCP) which mimics chemical warfare agent. Acid (H^+) promoted intramolecular cyclization and ratio-metric response of the probes was studied by X-ray crystallography, NMR and spectroscopic methods and DFT/TDDFT calculations. Further, the role of halogen bonding interactions in fluorescence enhancement has been investigated using crystallography and theoretical calculations. Reversible nature of highly active probe was demonstrated by simple experimental protocol.

Result and Discussion:

Compounds **3a** - **3d** were prepared according to the reported procedure¹⁰ from their substituted 2-amino benzophenones as shown in the **scheme 2.1**. Initially the reactants were acetylated in acetic acid to give acetanilides **2a-2d** which were further heated in the subsequent step at 90°C in the presence 10 eq. to afford **3a-3d**. Different derivatives were prepared by substituting chlorine (Cl) and fluorine (F) at X₁ and X₂ positions (scheme 2.1) to study structure-property correlation pertaining to their turn-on fluorescent activity. Detailed synthetic procedure and characterization data is provided in experimental methods. All the compounds were yellowish and non-fluorescent.



Reagents and Condition:(i) Sodium acetate , acetic anhydride, reflux, rt, 1h (ii) PPA, 90 °C, 18h
Scheme 2.1: General synthetic procedure of compounds **3a-3d**

The Acid (H⁺) mediated formation of azaquinazolinium ions **4a-4d** is studied by X-ray crystallography and ¹H NMR techniques. Crystallization of **3a**, **3b** and **3d** in chloroform yielded yellow crystals. However, we failed to grow the X-ray quality single crystals of **3c** under similar crystallization conditions. ORTEPs of compound **3a**, **3b** and **3d** are provided in the **Figure 2.40**. Structure overlay of all the three compounds revealed grossly similar conformation with slight change in the orientation of terminal rings (**Figure 2.41**). The similar conformation of the central motifs paves the way for the formation of six membered intramolecular N-H···O hydrogen bonding interactions with graph set notation S(6)¹¹, wherein S(6) denotes a ring motif (**Figure 2.42, Table 2.4**).

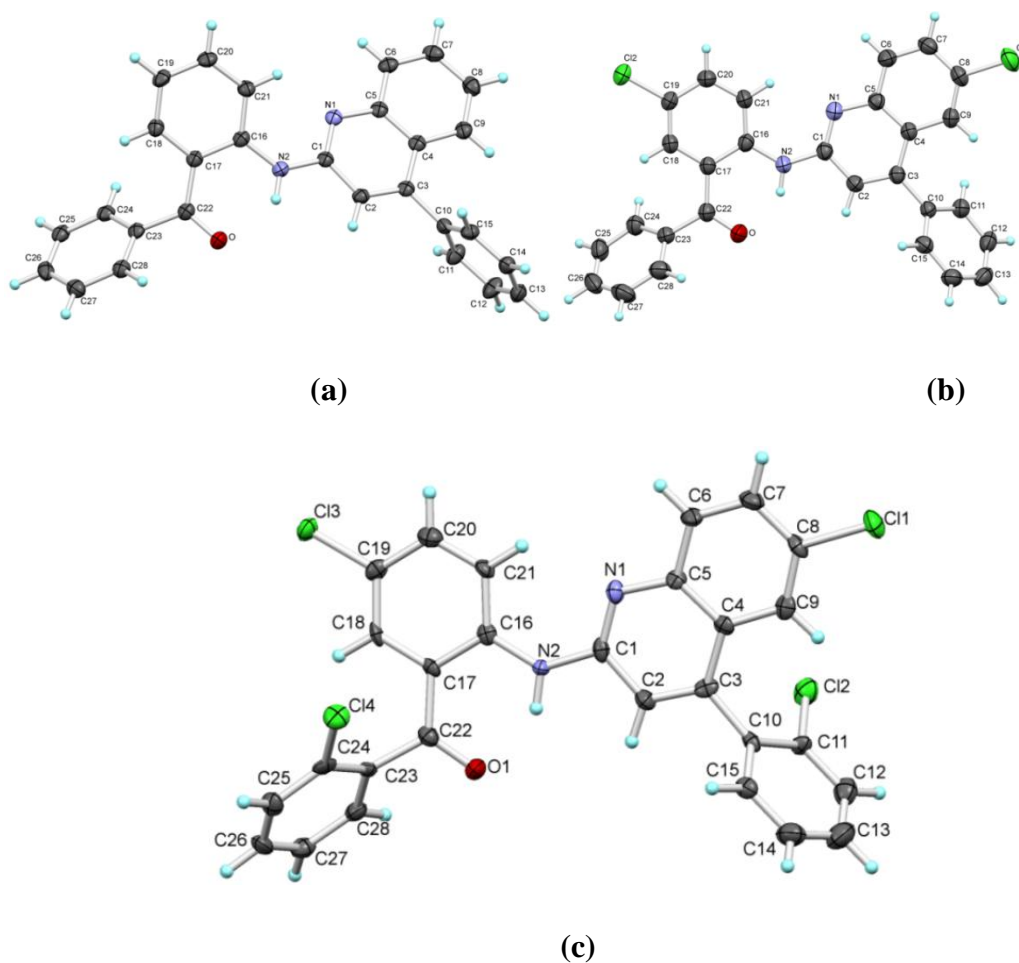


Figure 2.40. ORTEP diagrams of (a) **3a**, (b) **3b** and (c) **3d**. Ellipsoids are drawn at 30 % probability.

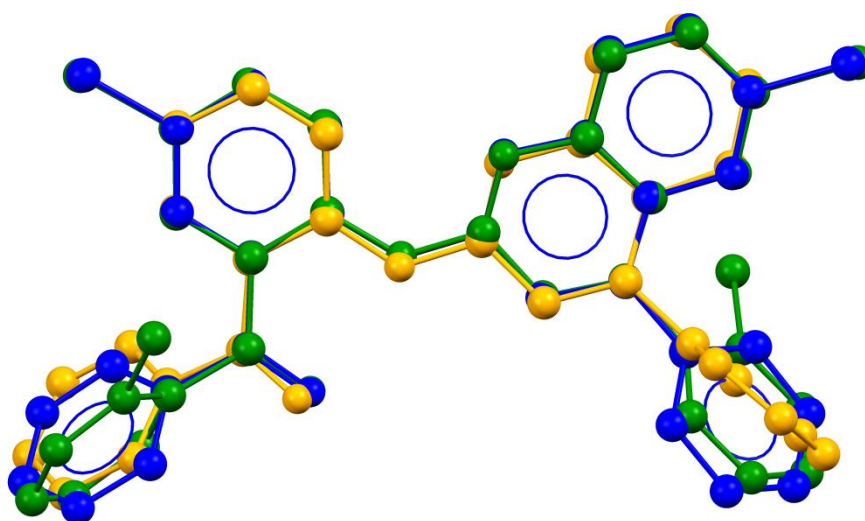


Figure 2.41. Structure overlay of compounds **3a** (orange), **3b** (blue) and **3d**(green).

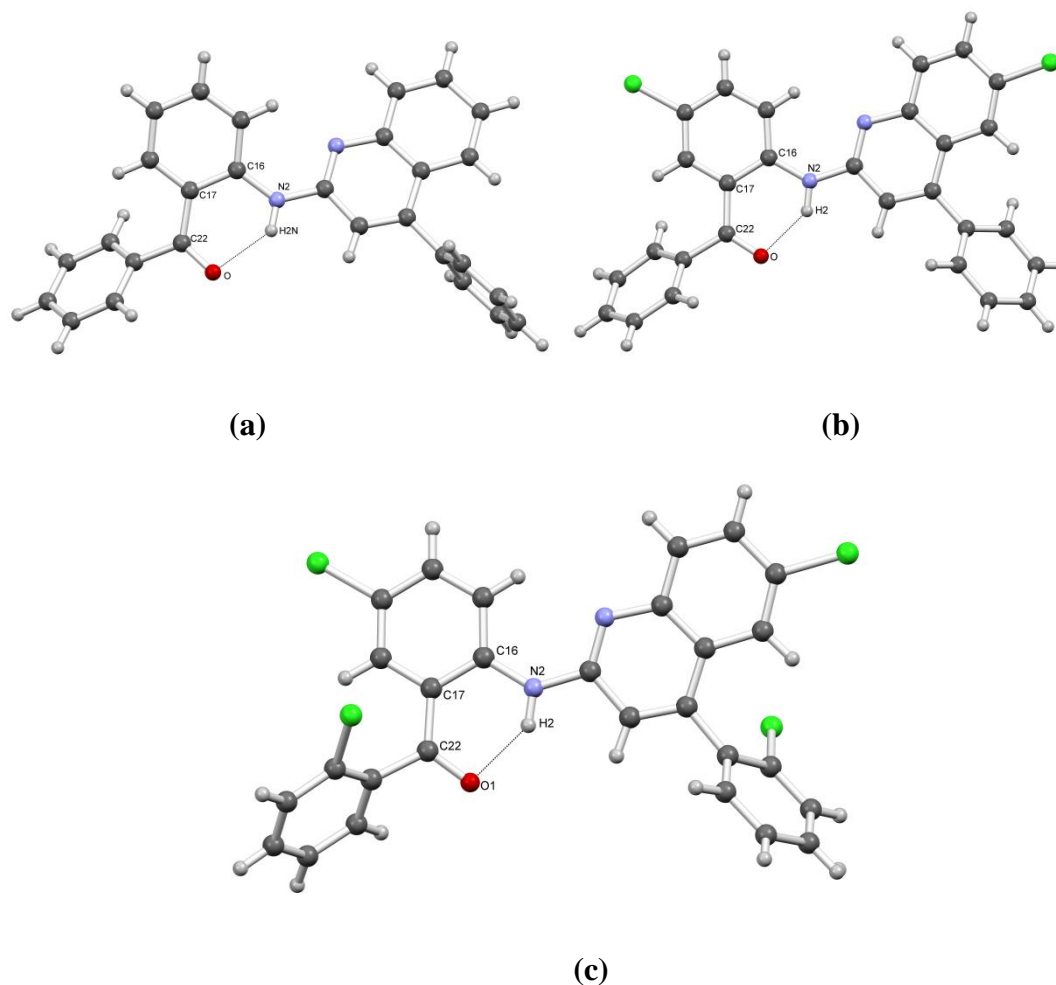


Figure 2.42. Six member intramolecular N-H...O hydrogen bonding in **3a**, **3c** and **3d**.

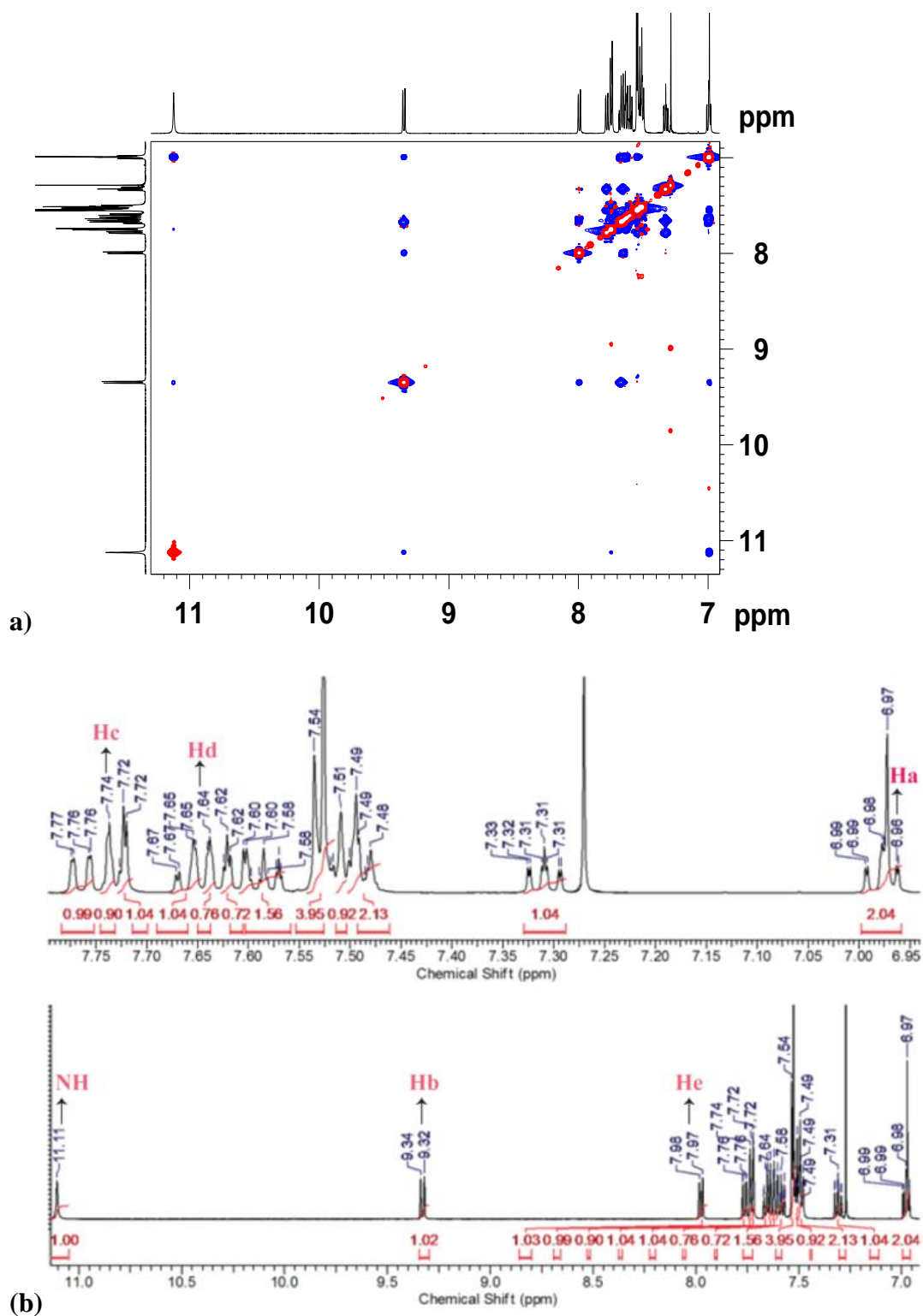
Table 2.4. Geometrical parameters of intramolecular N-H...O hydrogen bonding in **3a**, **3b** and **3d**

Compounds	D-H...A (Å)	D-H (Å)	H...A (Å)	D...A (Å)	D-H...A/ α (°)
3a	N2-H2N...O1	0.88	1.99	2.689	135
3b	N2-H2...O1	0.88	1.89	2.619	140
3d	N2-H2...O1	0.88	1.91	2.656	141

2D NMR experiments were carried out to study the solution state conformation in which the signals were assigned based on 2D NOESY. We used compound **3a** as the reference compound. The study revealed the presence of long-range inter-residual nOe between N-H vs Ha, N-H vs Hb, N-H vs Hc along with Hb vs Hd and Hb vs He (**Figure 2.43-2.44**). The combine study of ¹H NMR and X-ray

crystallography revealed that molecule possess similar conformation in solid and solution state.

The crystallization of **3b**, **3c** and **3d** in acidic methanol (1 eq. HCL) yielded fluorescent crystals of **4b**, **4c** and **4d** (**Figure 2.45**) respectively. However, crystallization of **3a** under similar conditions produced fluorescent sticky solid mass. Crystal structure analysis of **4b-4d** revealed the formation of 7, 12-dihydroquinolino[2,1-b]quinazolin-13-ium based hydrochloride salts by electrophilic addition-protonation under acidic condition. Structural analysis revealed that, the excess of H⁺ ions mediate *O*-protonation of benzophenones to generate carbocations. The tandem intramolecular C(sp²)⁺-N cyclization occurs between electrophilic carbocation and nucleophilic Nitrogen(N1) of quinoline. Further transfer of positive charge generates a chiral centre and cationic nitrogen (azonia) (**Figure 2.46**). All the compounds belong to centrosymmetric triclinic space group *P*-1 with one molecule in the asymmetric unit, except in **4d** which also contained three molecules of chloroform as solvent of crystallization. Crystal structure analysis revealed the generation of chiral center in the newly formed cyclized products and the centrosymmetric space group confirm that the product is racemic. The central fused ring is almost co-planar with the quinoline and adjoining aromatic moiety. The difference in the dihedral angles is less than 7° which suggested the planar geometry and extended conjugation of multi-aromatic core formed after cyclization (**Figure 2.47-2.49**). Based on the structure data, the bond length C1-N1 and C1-N2 showed partial double bond character which suggests the resonant charge transfer N1 and N2 (N to N⁺).



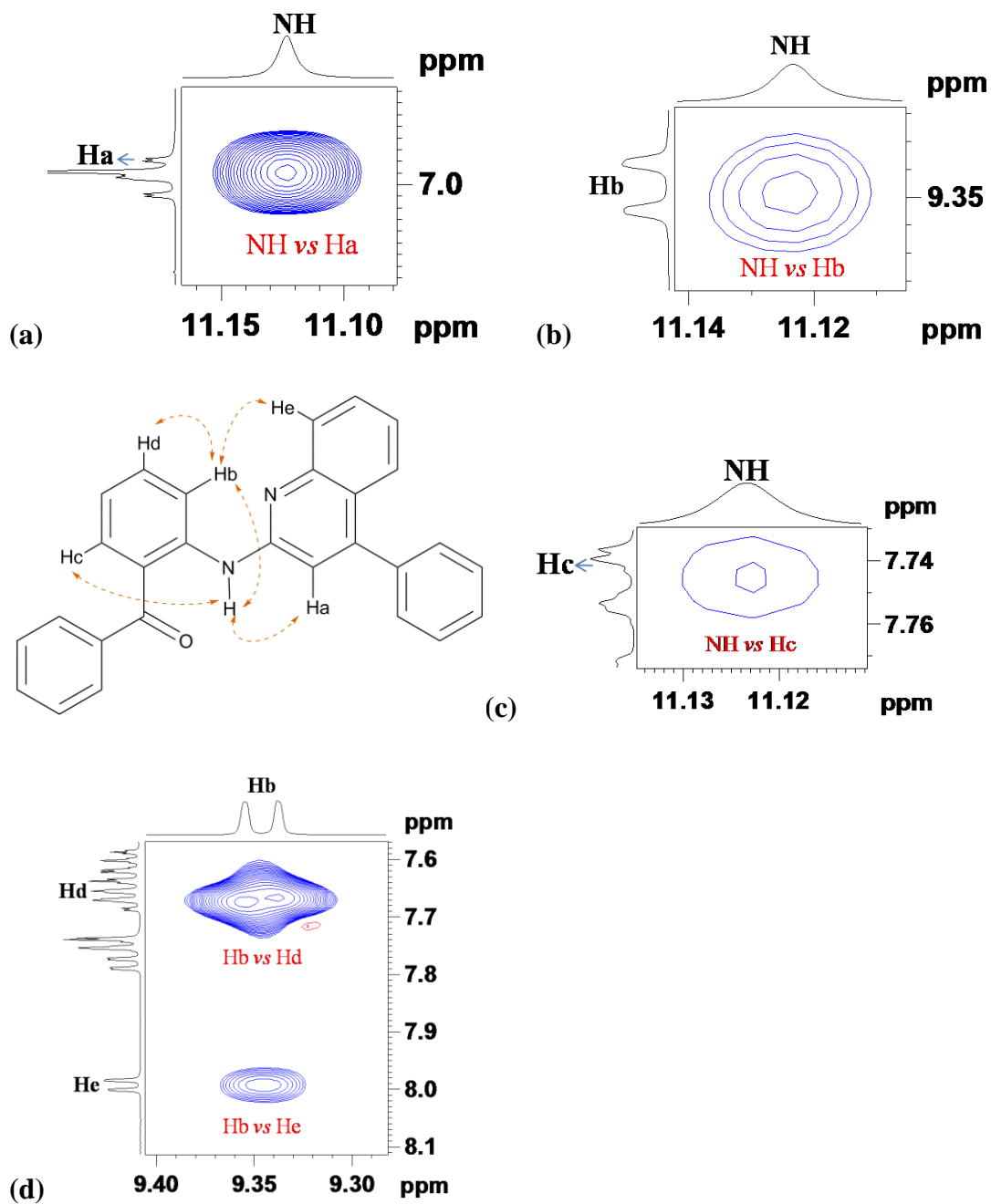


Figure 2.44. Long-range inter-residual nOe between (a) NH vs. Ha (b) N-H vs. Hb (c) N-H vs. Hc (d) Hb vs. Hd and Hb vs. He.

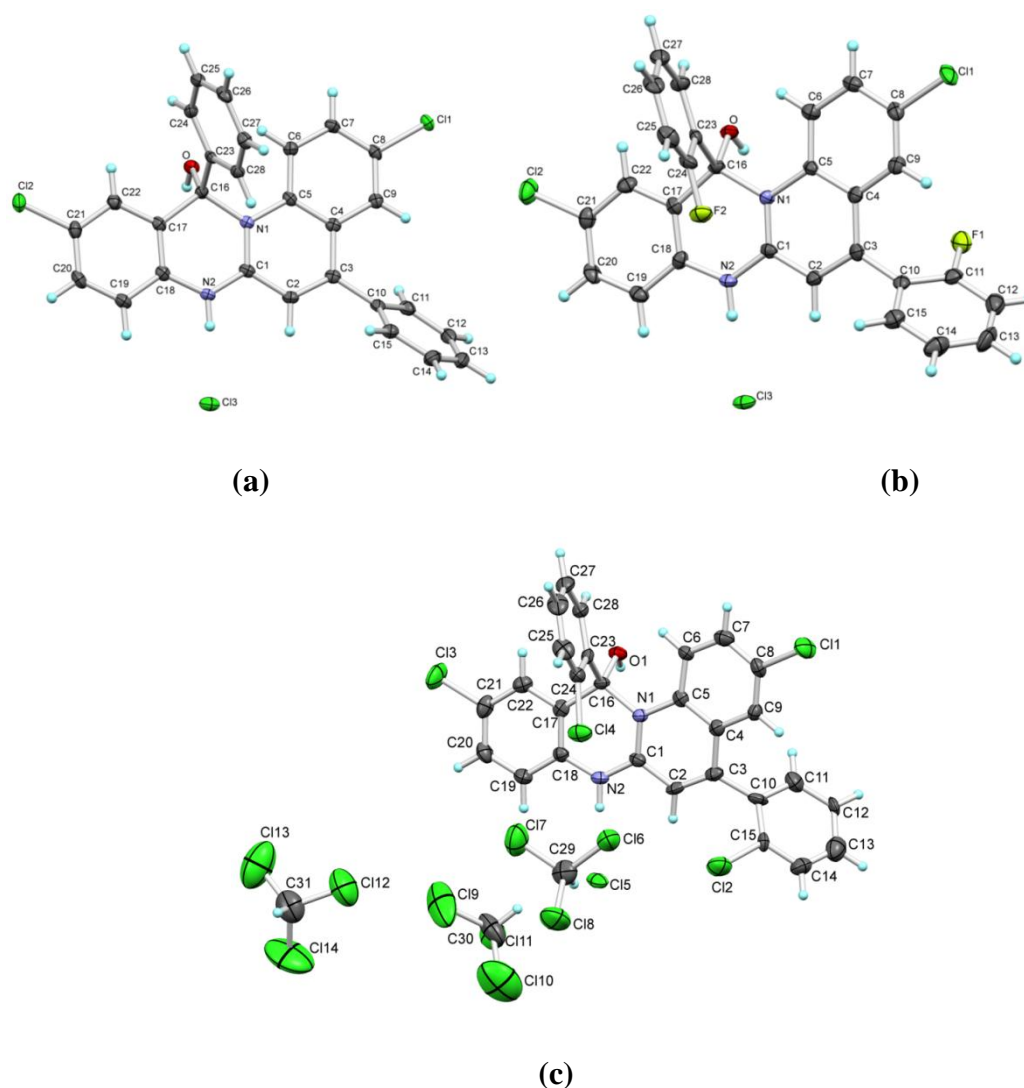


Figure 2.45. ORTEP diagrams of (a) 4b, (b) 4c and (c) 4d. Ellipsoids are drawn at 30% probability.

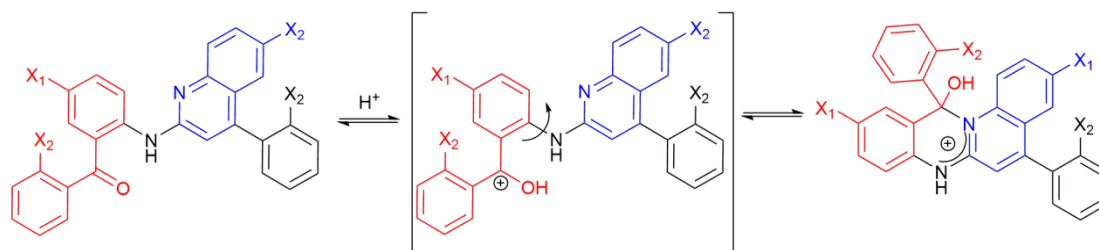


Figure 2.46. Reaction Mechanism of acid mediated intramolecular cyclization and formation of aza-quinazolinium ions from quinoline-benzophenone conjugates.

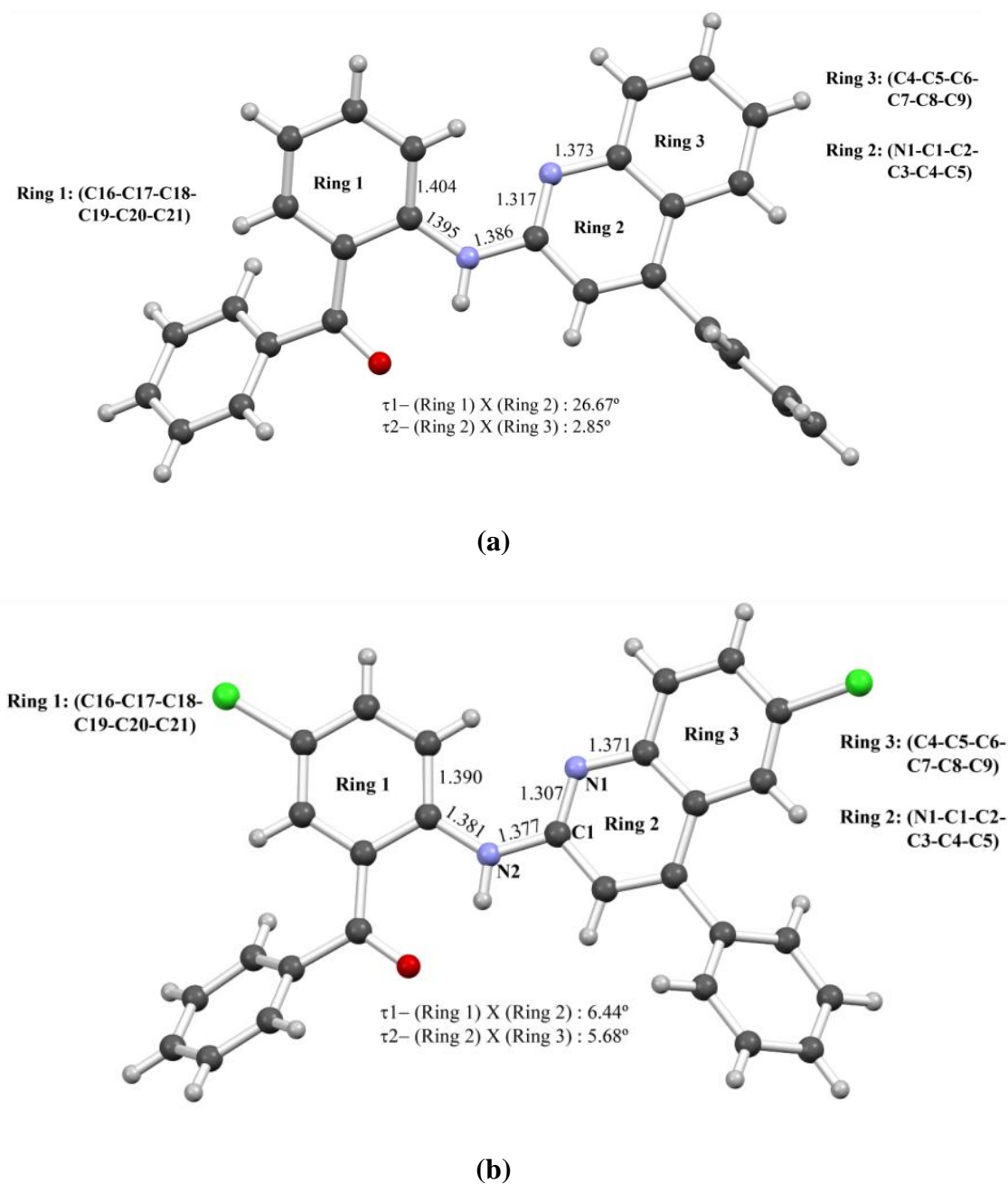


Figure 2.47. Depiction of geometrical parameters in the crystal structure of (a) 3a and (b) 3b.

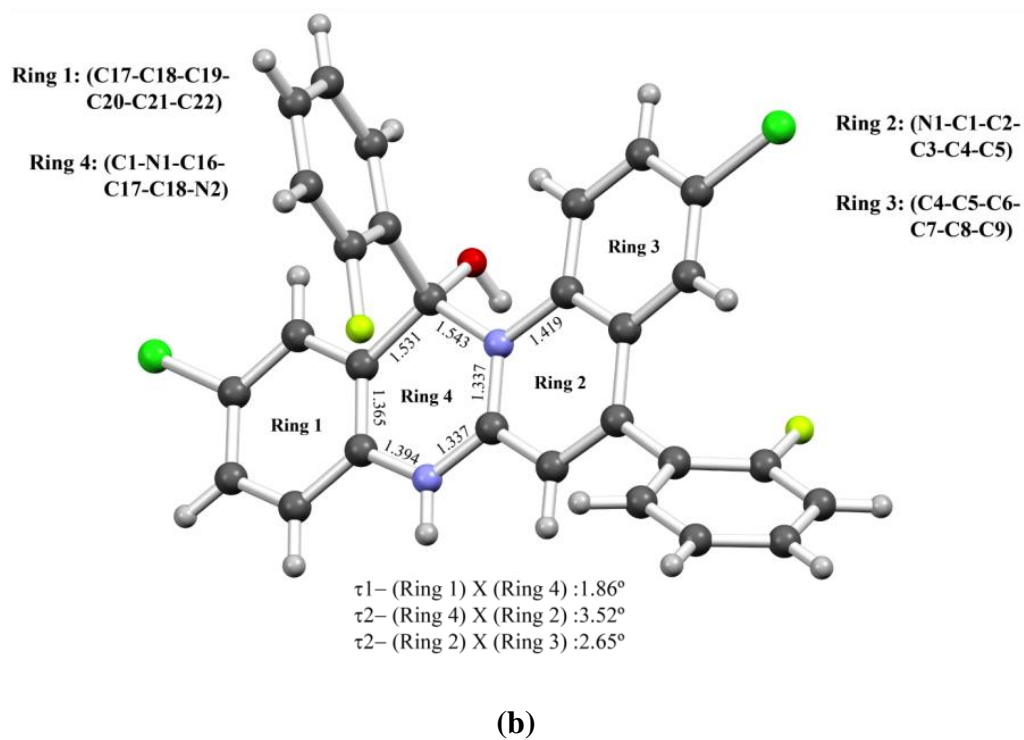
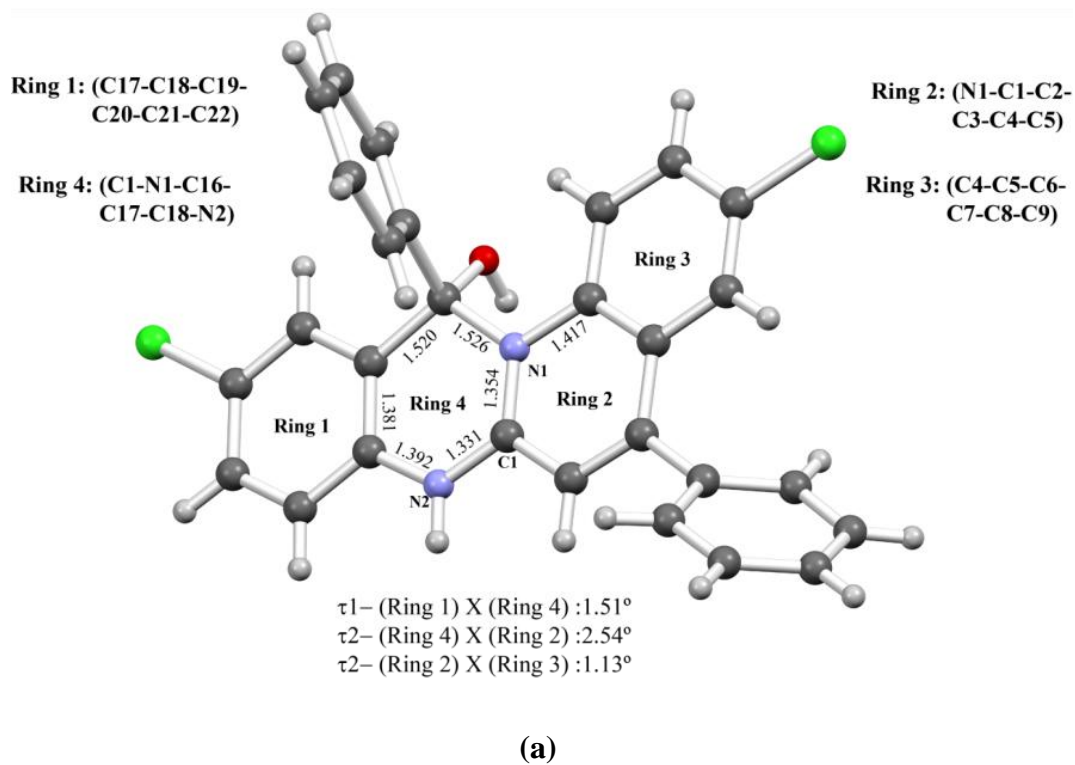
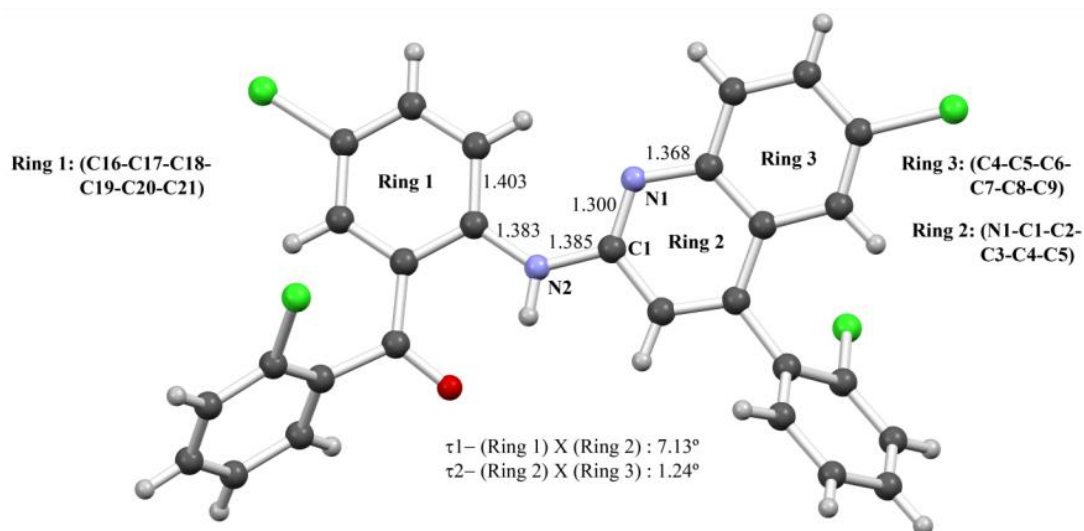
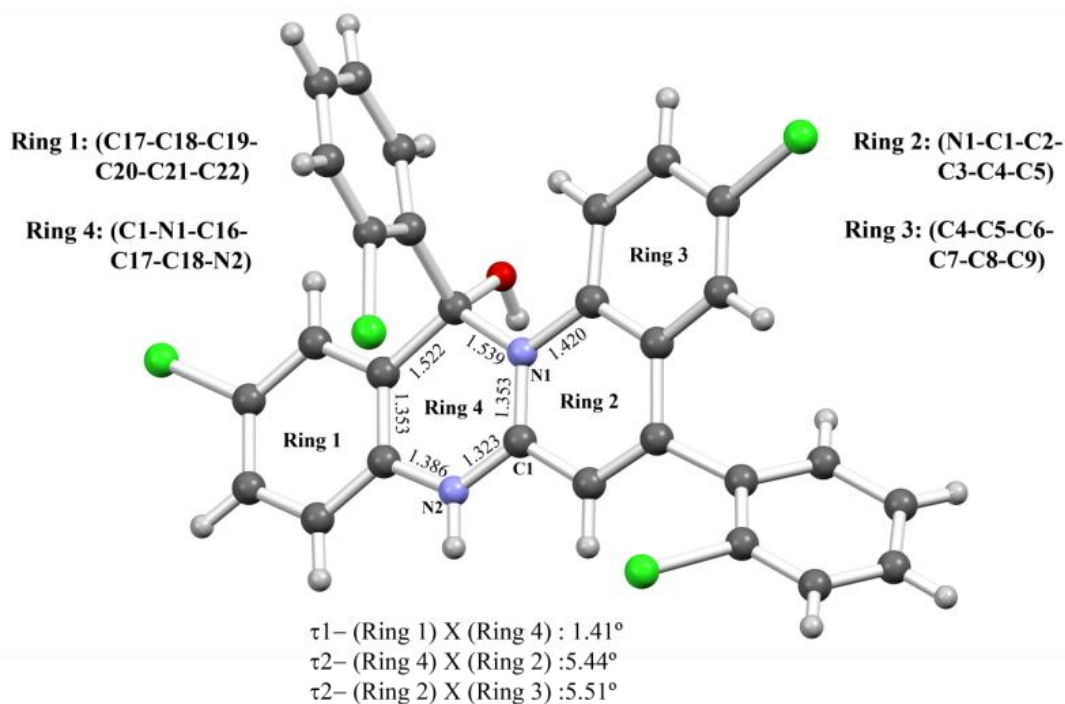


Figure 2.48. Depiction of geometrical parameters in the crystal structure of (a) **4b** and (b) **4c**.



(a)



(b)

Figure 2.49. Depiction of geometrical parameters in the crystal structure of (a) **3d** and (b) **4d**.

^1H NMR spectroscopic investigation substantiates the reaction mechanism. The Hb protons of **3a** - **3d** showed deshielding effect compared to other aromatic protons due to coupling with quinolinic nitrogen N1. The disappearance of Hb proton upon addition of HCl is attributed to the acid catalyzed cyclization reaction resulting

in the breaking of coupling between N1 and Hb proton (**Figure 2.50-2.53**). NH and Ha protons showed slight up-field shift due to structural transformation.

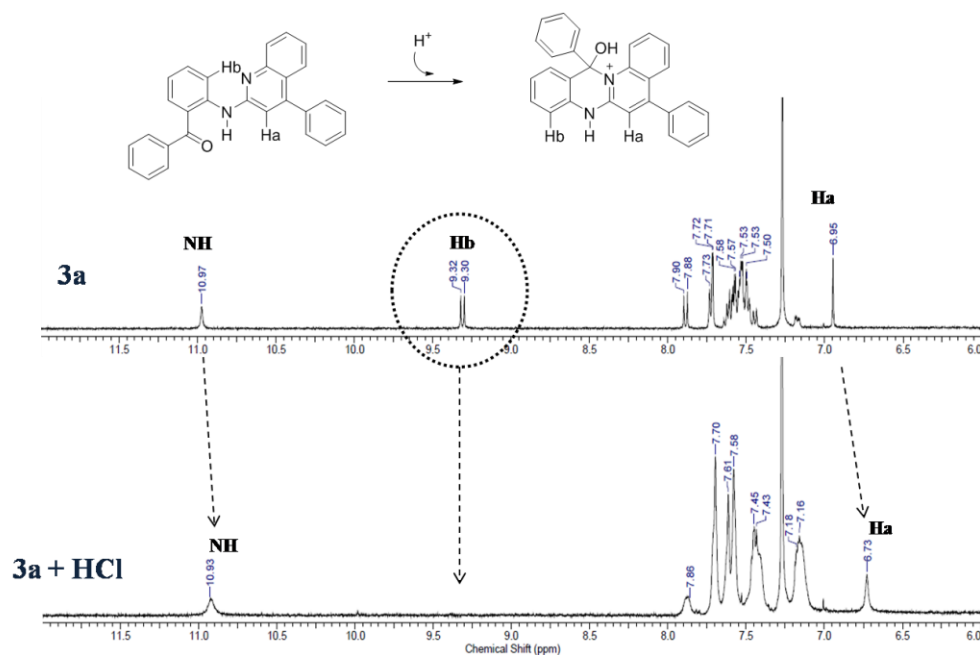


Figure 2.50. ^1H NMR spectra of (**3a**) and (**3a + HCl, 1:1**) and associated changes of chemical shift of NH, Hb, Ha protons.

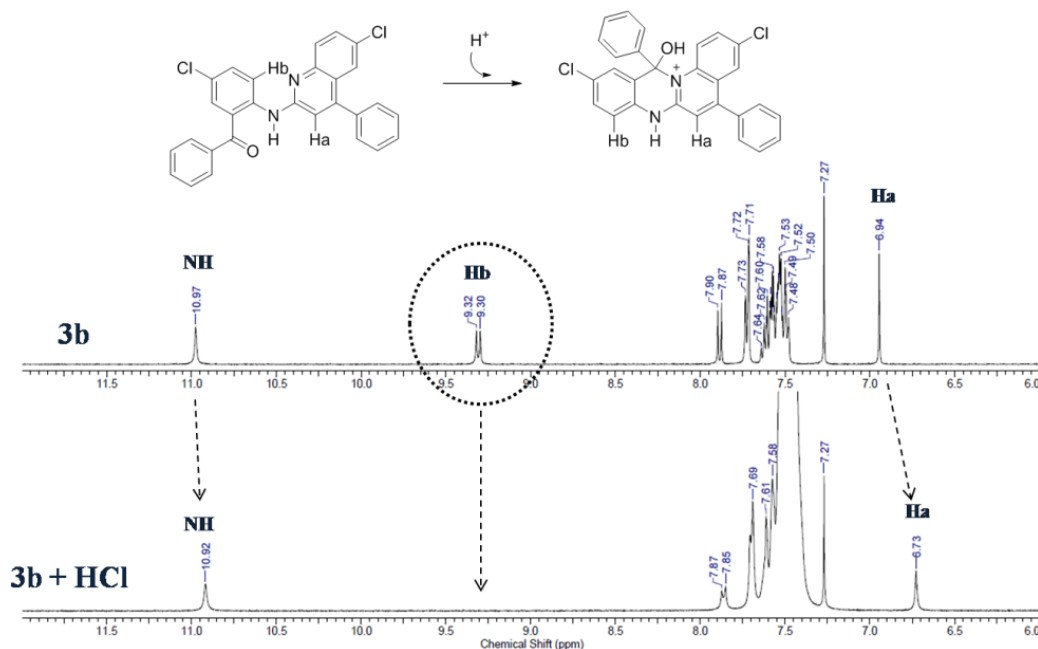


Figure 2.51. ^1H NMR spectra of (**3b**) and (**3b + HCl, 1:1**) and associated changes of chemical shift of NH, Hb, Ha protons.

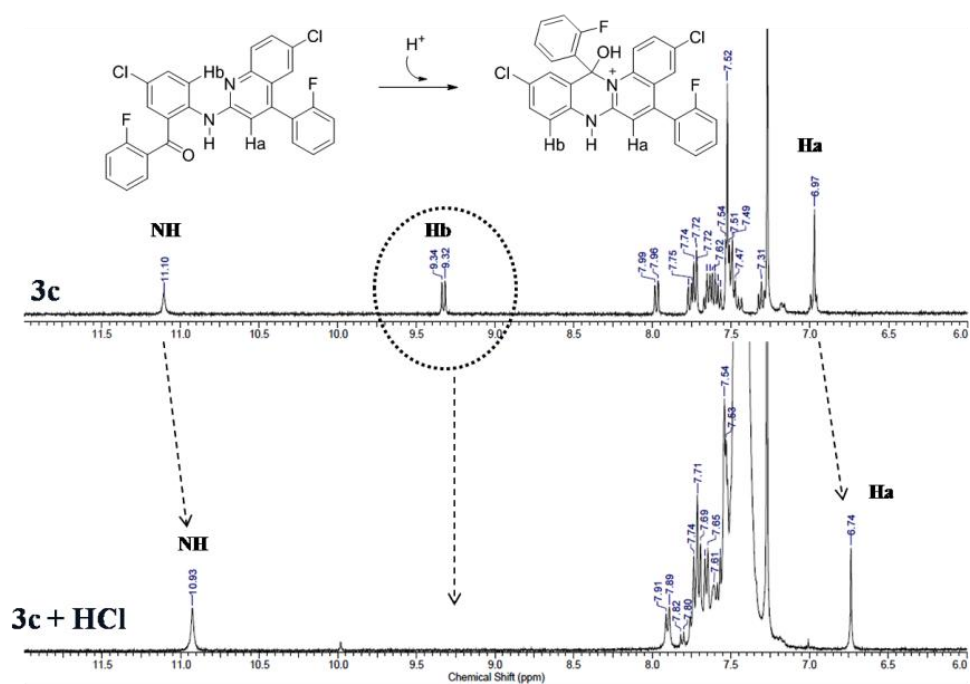


Figure 2.52. ^1H NMR spectra of (**3c**) and (**3c** + **HCl**, **1:1**) and associated changes of chemical shift of NH, Hb, Ha protons.

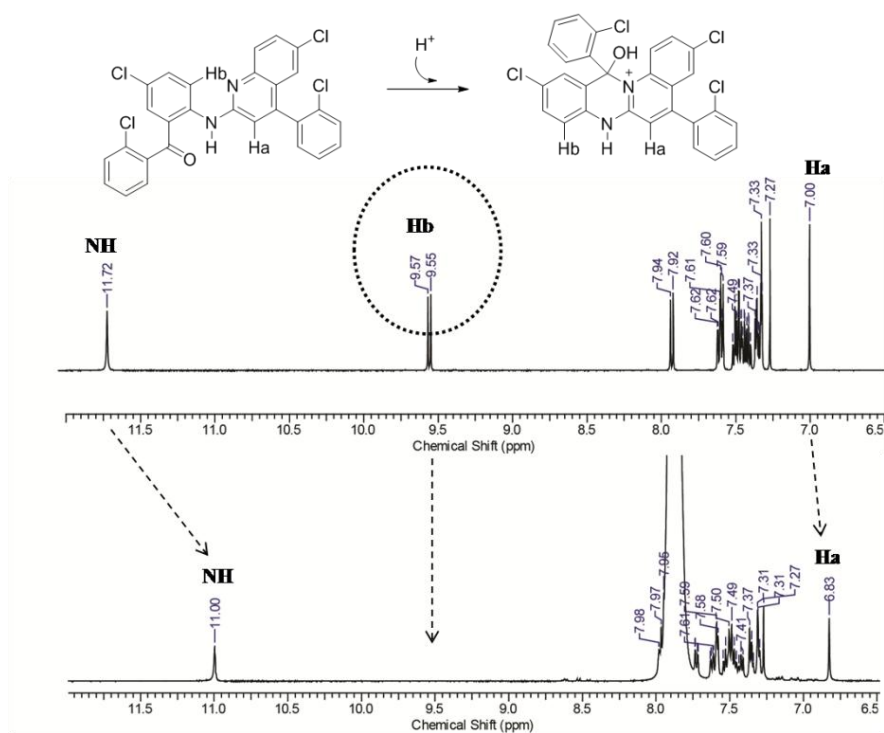
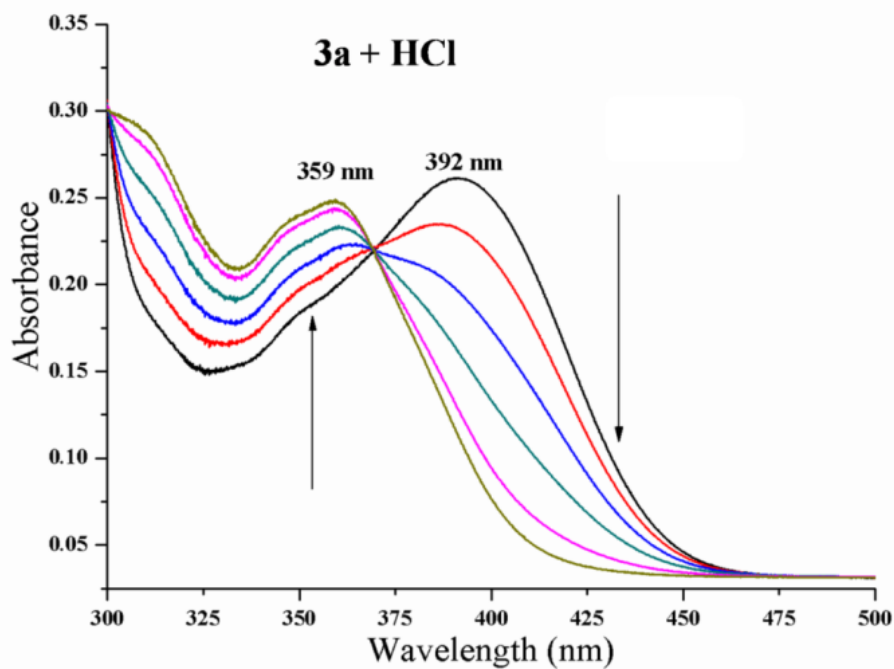


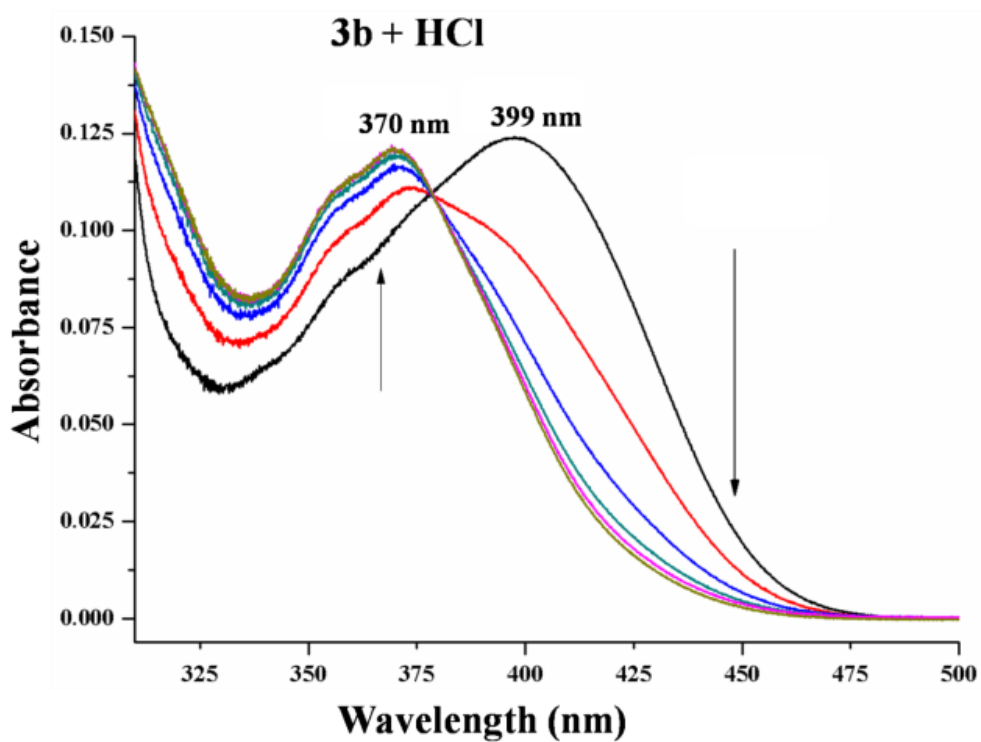
Figure 2.53. ^1H NMR spectra of (**3d**) and (**3d** + **HCl**, **1:1**) and associated changes of chemical shift of NH, Hb, Ha protons.

UV-vis and fluorescence spectroscopic studies of compounds **3a-3d** revealed significant changes in the spectra upon addition of acidic analytes. The UV-vis

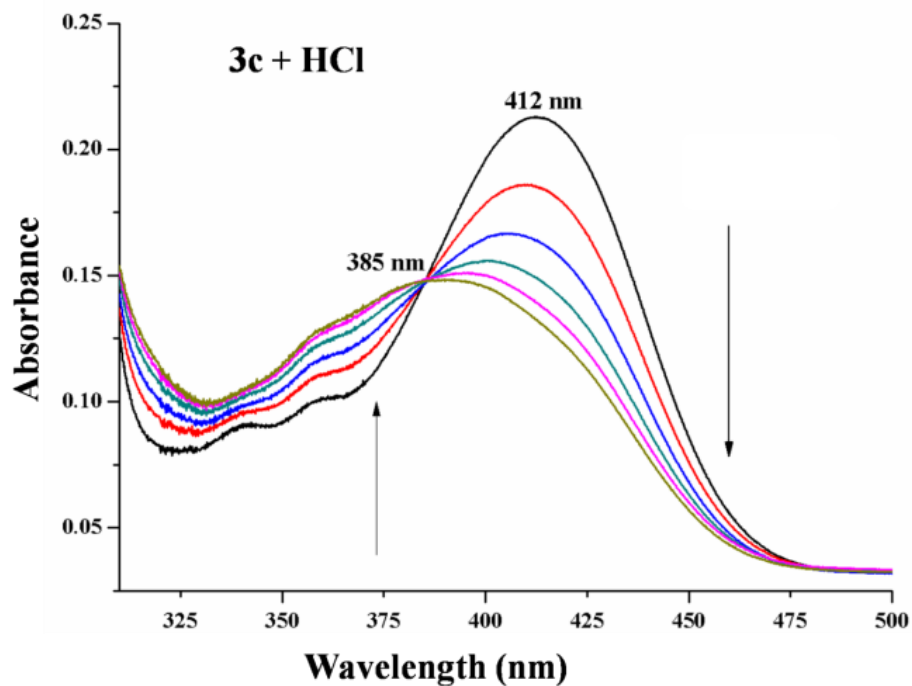
spectra of **3a** - **3d** showed characteristic peaks in the visible region with their λ_{\max} value centered at 392 nm, 399 nm, 412 nm and 412 nm respectively. The absorbance maximum was blue-shifted upon sequential addition of methanolic solution of HCl (**Figure 2.54**). Blue-shift in their λ_{\max} caused decolouration of the solution which could even be observed by naked eye. The single isosbestic points suggested the generation of a single major products. All the compounds (**3a** - **3d**) showed differential reactivity towards strong acid, i.e. H_2SO_4 , moderately strong acid, HNO_3 and weak acid, CH_3COOH (**Figure 2.55-2.58**). They displayed stoichiometric blue shifting of λ_{\max} in the presence of H_2SO_4 similar to that of HCl. Compound **3a** showed stoichiometric blue shift for HNO_3 , however, **3b** and **3d** did not showed similar effect even after addition of 1 eq. of HNO_3 . Further, none of these compounds showed spectral shift under weak acidic condition i.e. in the presence of CH_3COOH (1 eq.). These results suggest that the substitution of hydrogens in **3a** by halogen atoms in **3b-3d** (at X_1 and X_2 positions, scheme 2.1) have significantly modulated their reactivity towards acids. To better rationalize the reason behind their differential reactivity, the estimation of proton affinity values of carbonyl group of **3a-3d** were calculated using DFT calculation (functional:B3LYP and functional 6-31g*).¹² Requirement of strong acidic environment by **3b**, **3c** and **3d** was attributed to their low proton affinity values i.e. -247.655 Kcal, -245.73 Kcal and -241.204 Kcal respectively whereas reactivity of **3a** in slightly less acidic condition is attributed to its highest affinity value -251.197 Kcal.



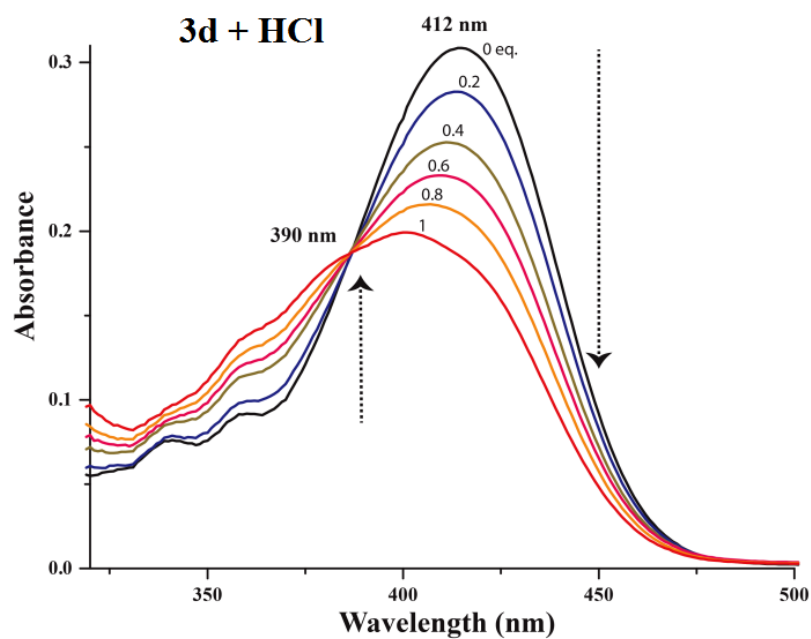
(a)



(b)

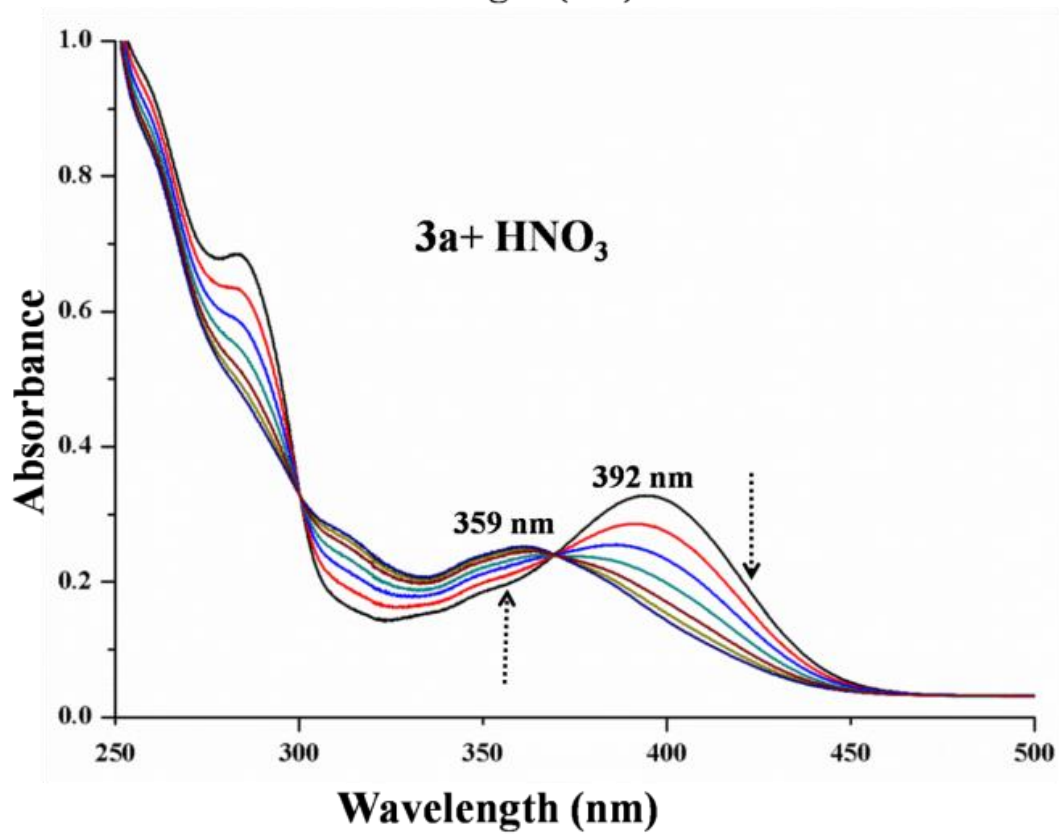
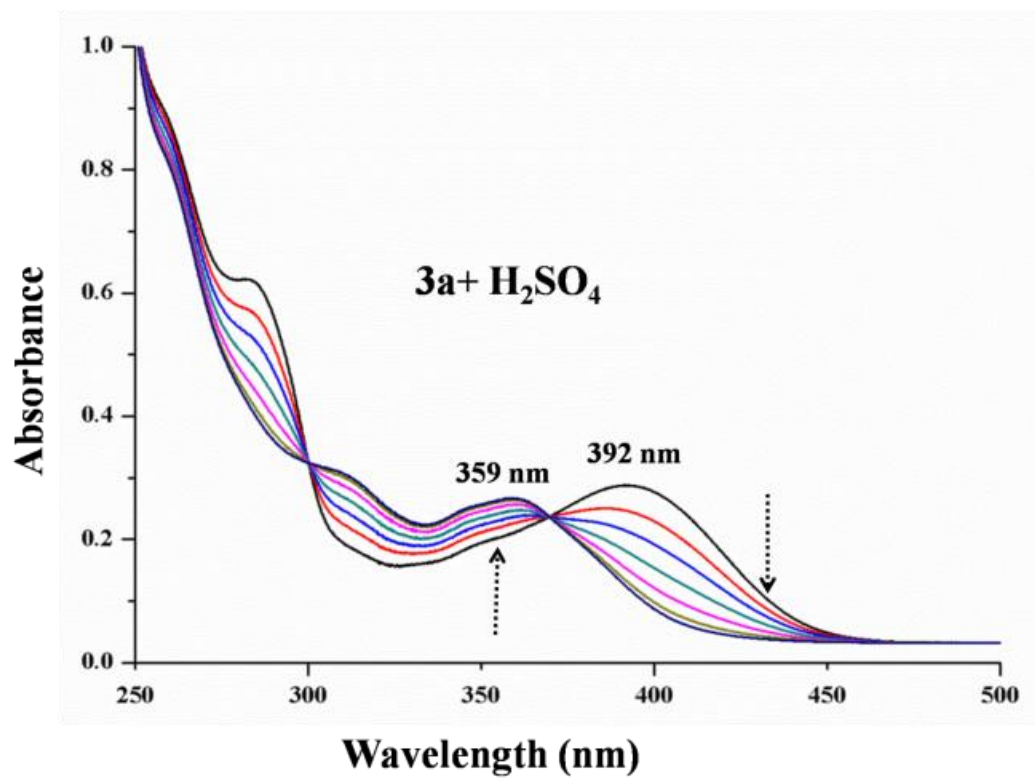


(c)



(d)

Figure 2.54. UV-vis absorbance titration profile of (a) **3a** (10 μM), (b) **3b** (20 μM), (c) **3c** (10 μM), and (d) **3d** (20 μM) in CHCl_3 solution upon addition of HCl (in MeOH) (0.2, 0.4, 0.6, 0.8 and 1.0 eq.).



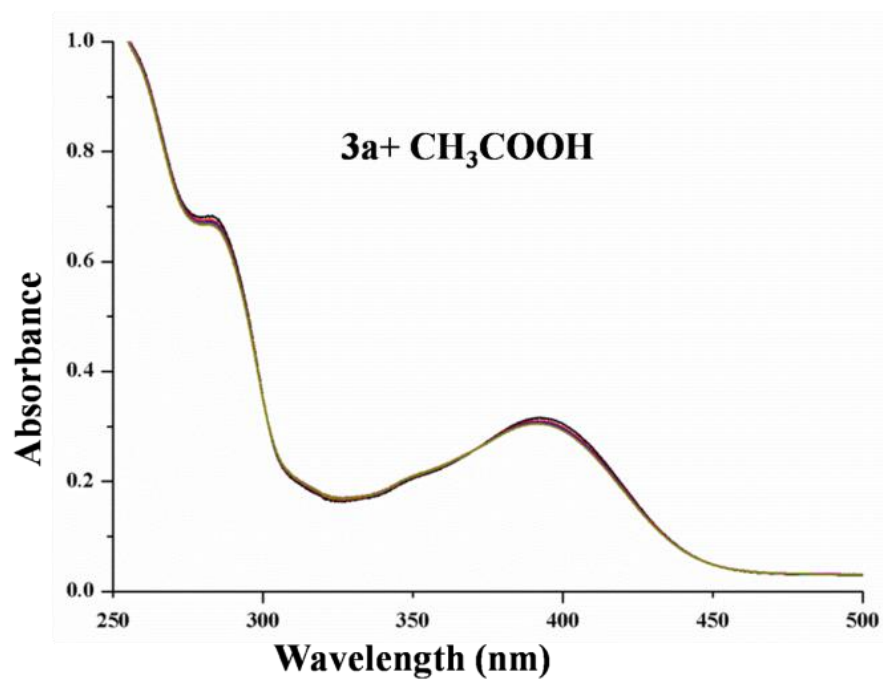
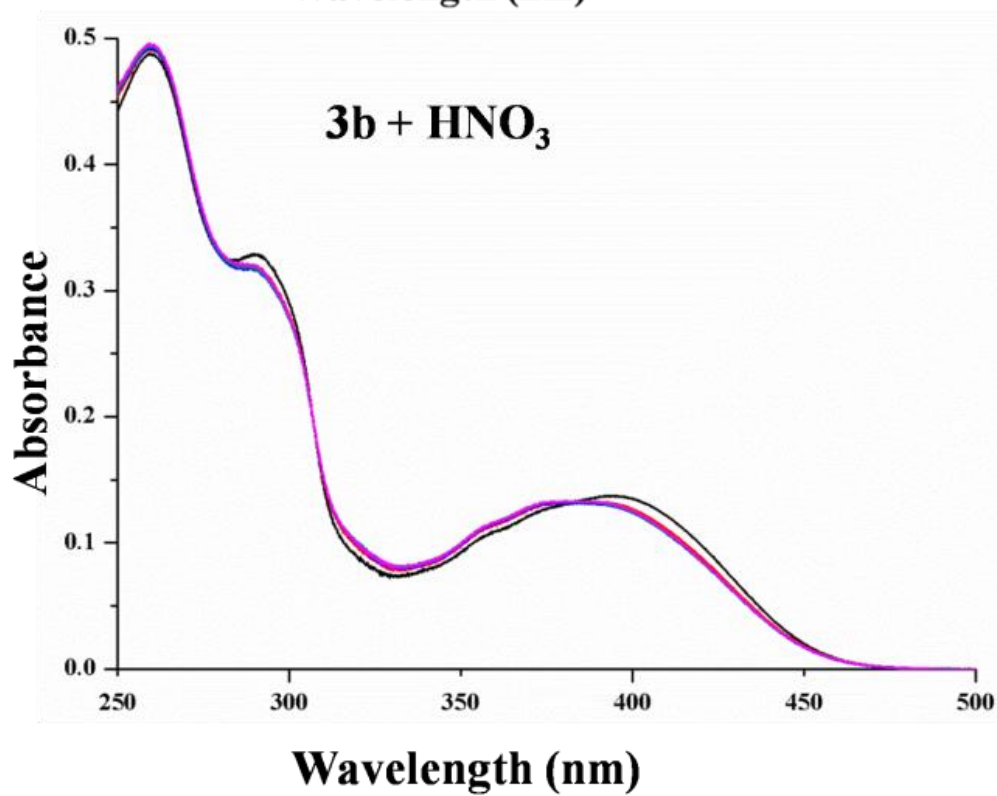
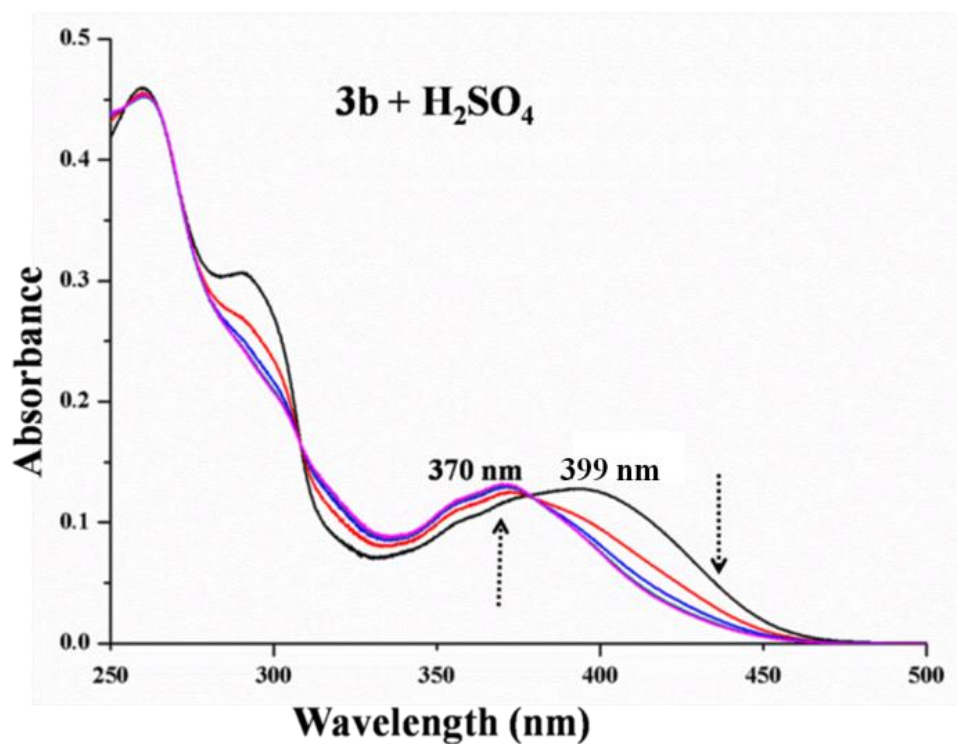


Figure 2.55. UV-vis absorbance titration profile of **3a** (10 μ M) in CHCl_3 solution upon addition of H_2SO_4 , HNO_3 and CH_3COOH (in MeOH) (0.2, 0.4, 0.6, 0.8 and 1.0 eq).



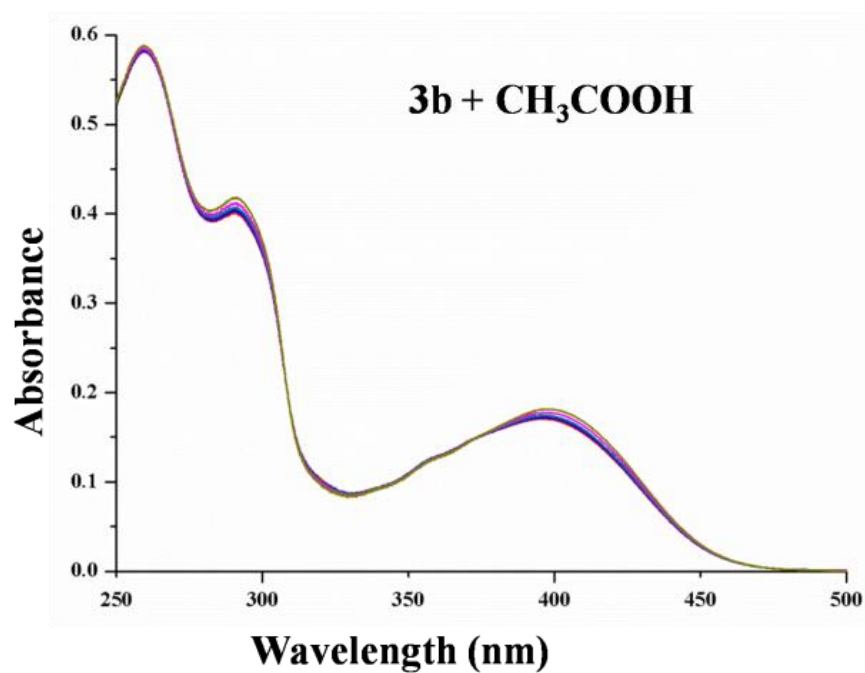
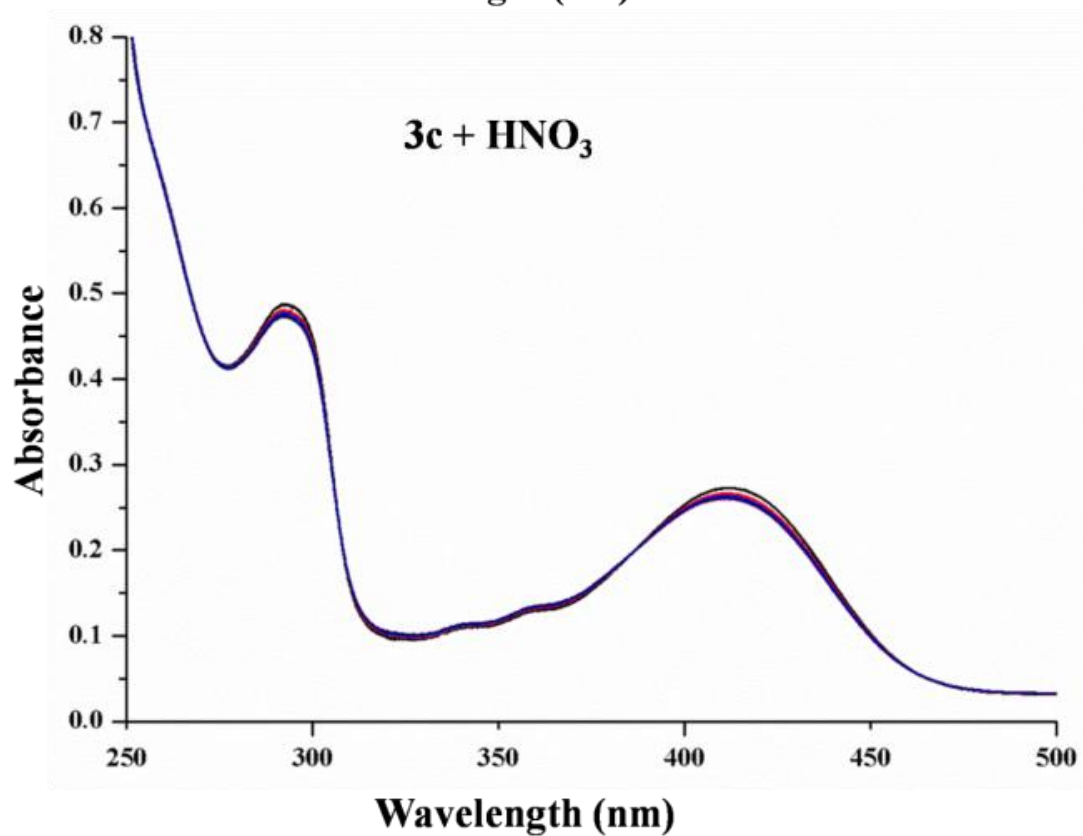
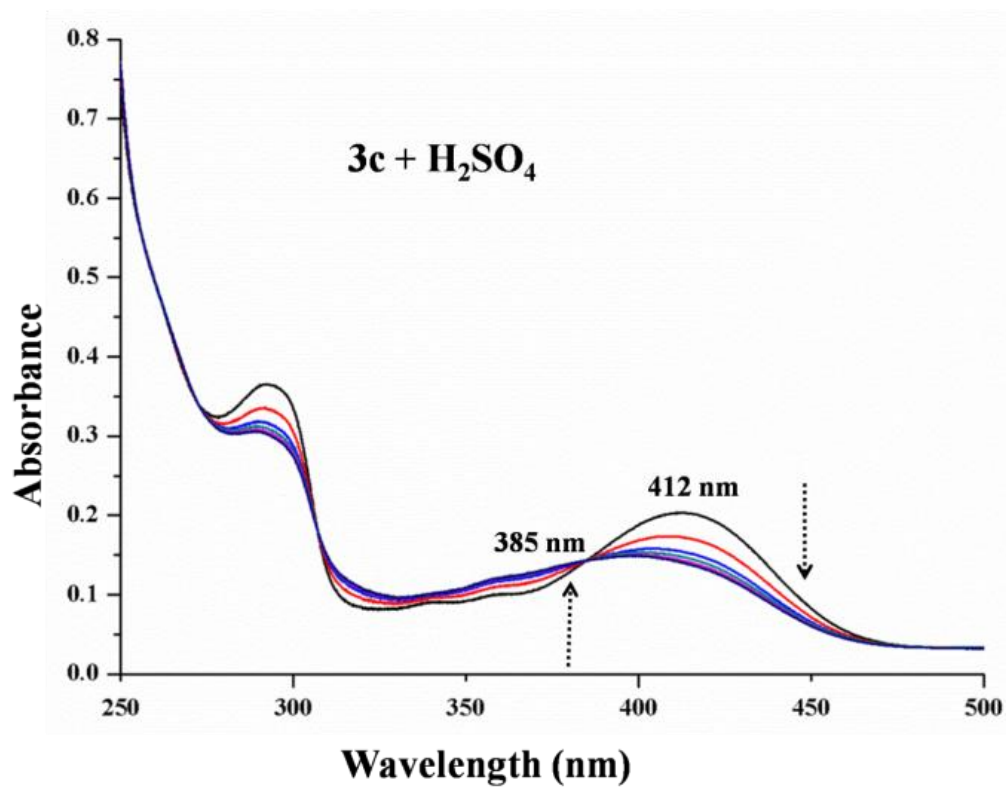


Figure 2.56. UV-vis absorbance titration profile of **3b** (20 μM) in CHCl_3 solution upon addition of H_2SO_4 , HNO_3 and CH_3COOH (in methanol) (0.2, 0.4, 0.6, 0.8 and 1.0 eq.).



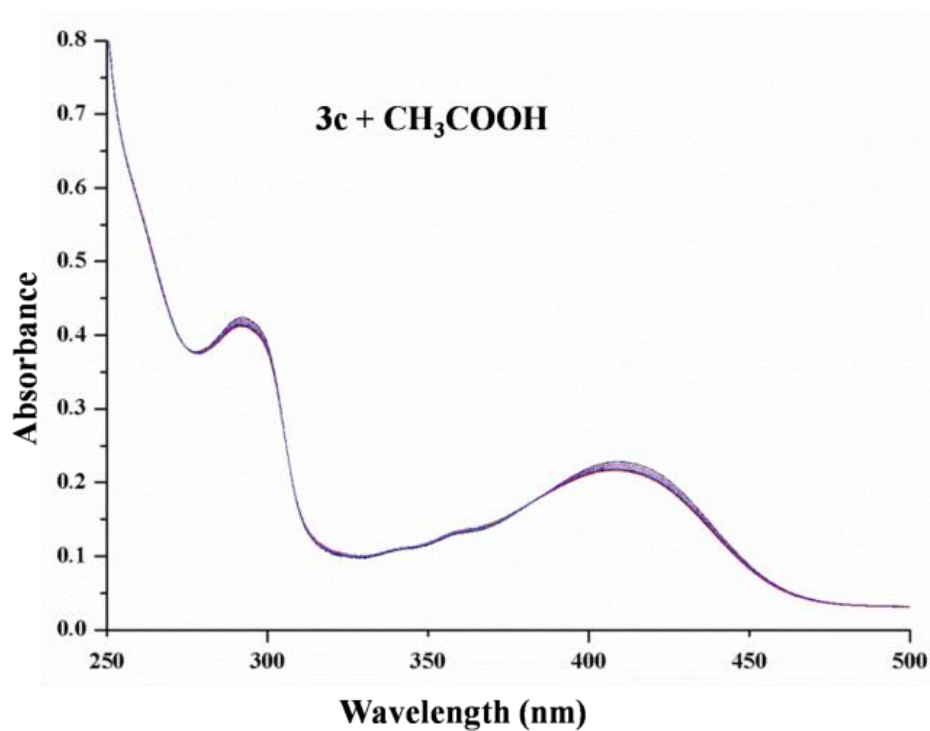
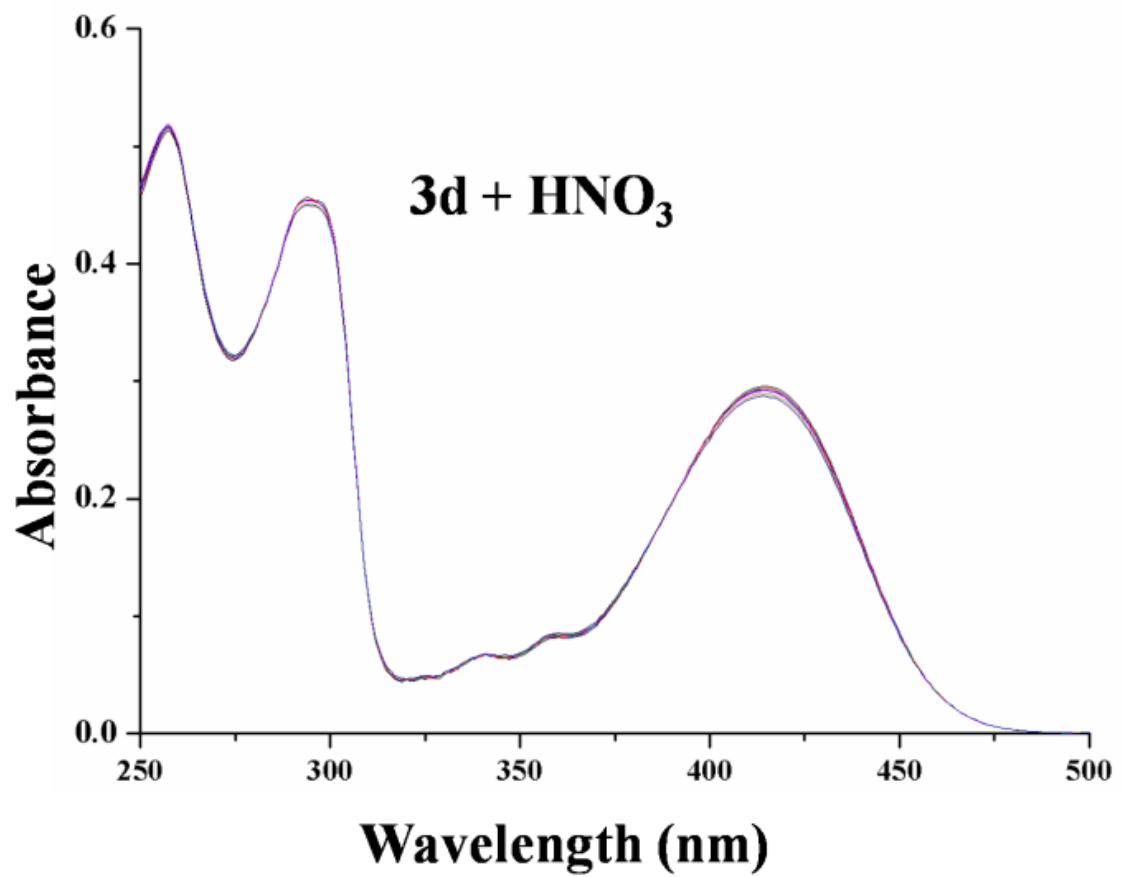
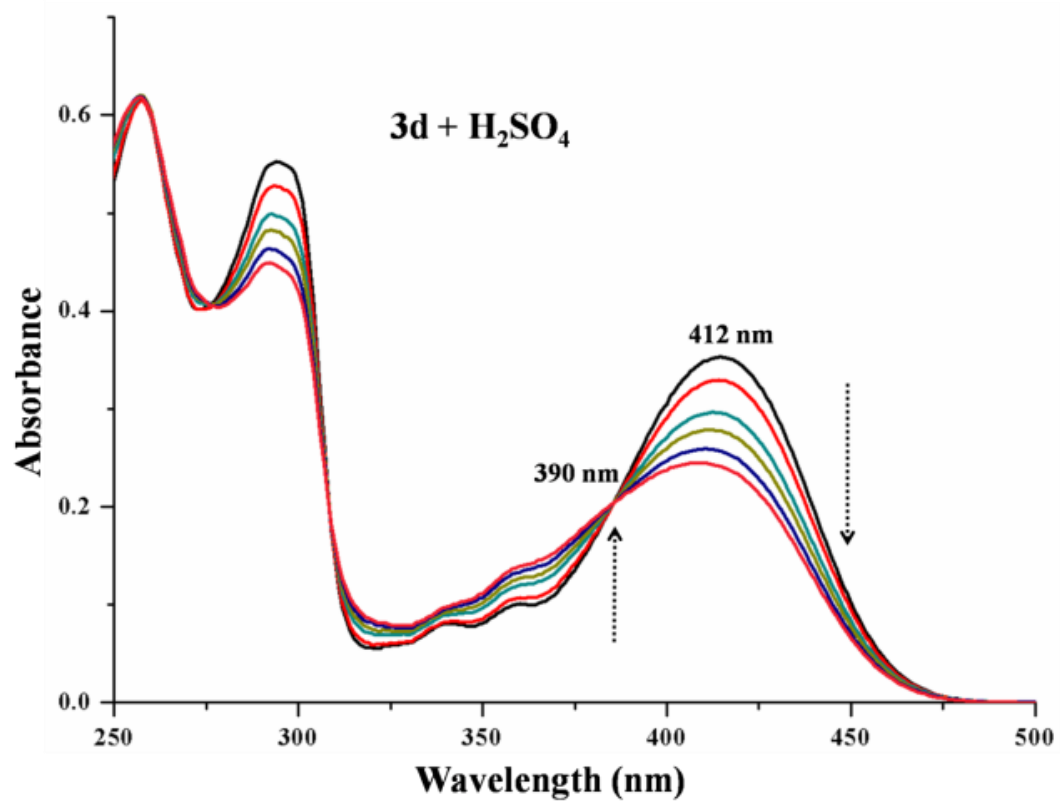


Figure 2.57. UV-vis absorbance titration profile of **3c** (10 μ M) in CHCl_3 solution upon addition of H_2SO_4 , HNO_3 and CH_3COOH (in methanol) (0.2, 0.4, 0.6, 0.8 and 1.0 eq.).



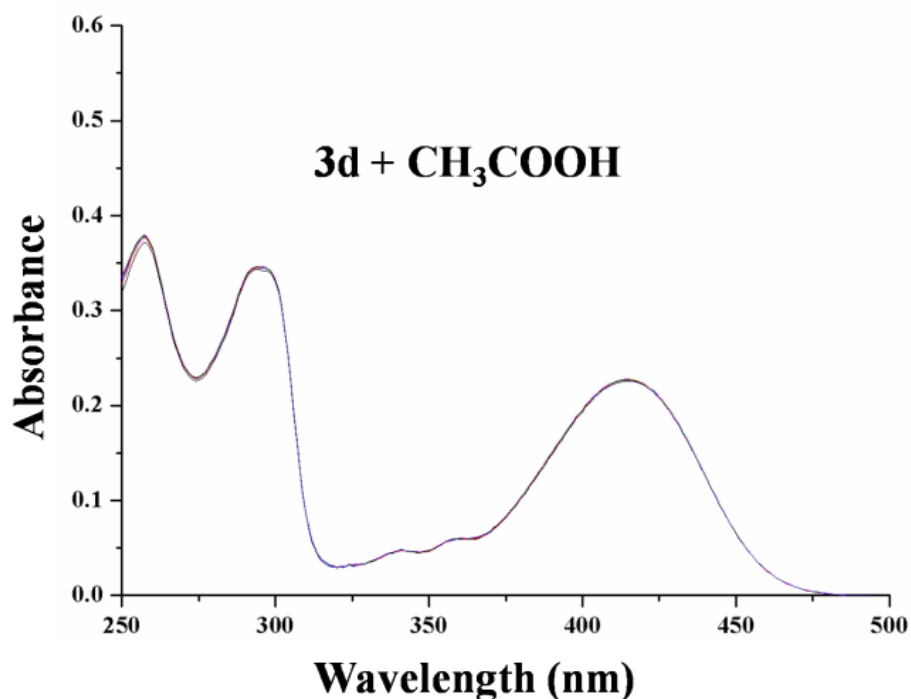


Figure 2.58. UV-vis absorbance titration profile of **3d** (20 μ M) in CHCl_3 solution upon addition of H_2SO_4 , HNO_3 and CH_3COOH (in methanol) (0.2, 0.4, 0.6, 0.8 and 1.0 eq.).

Remarkable increase in the fluorescence intensity of **3a-3d** was observed upon serial addition of methanolic HCl. However, I/I_0 vs. acid/compound ratio showed differential enhancement in the fluorescence intensity. When excited at 360 nm, emission profile of **3d** showed maximum enhancement of intensity (12.5 times) (**Figure 2.59**) compared to the emission profiles of **3a-3c**. Compounds **3a-3c** showed moderate enhancement (3.6, 2.6, 2.5 times respectively, **Figure 2.60-2.62**).

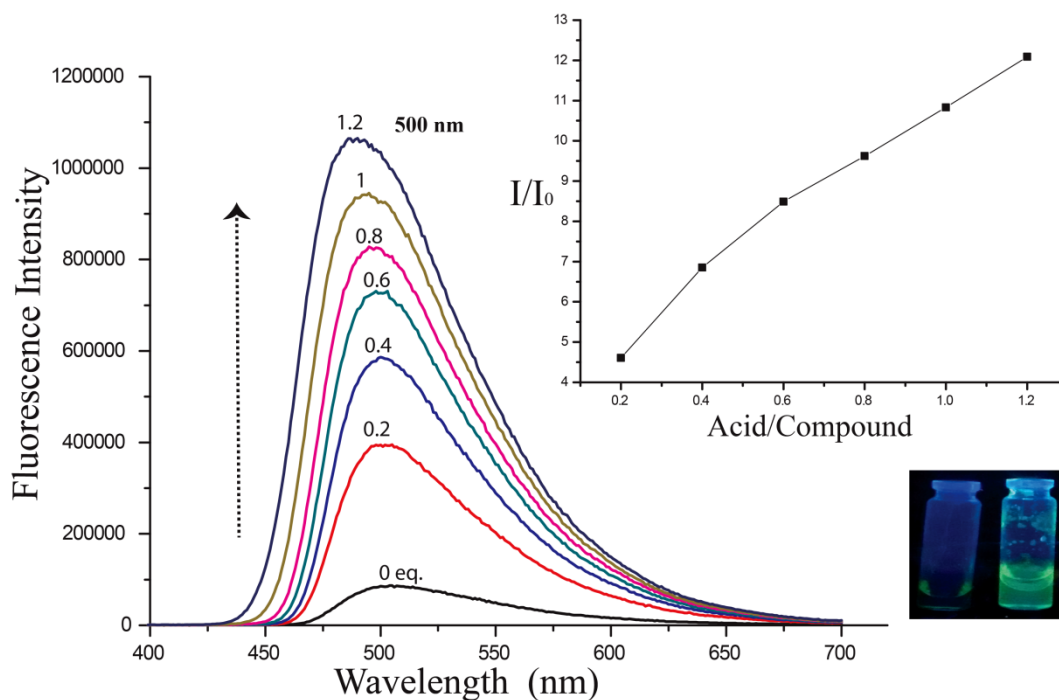


Figure 2.59. Fluorescence spectra of the **3d** (1.67 mM) in chloroform on addition of 0.2, 0.4, 0.6, 0.8 and 1 eq. of HCl in methanol.

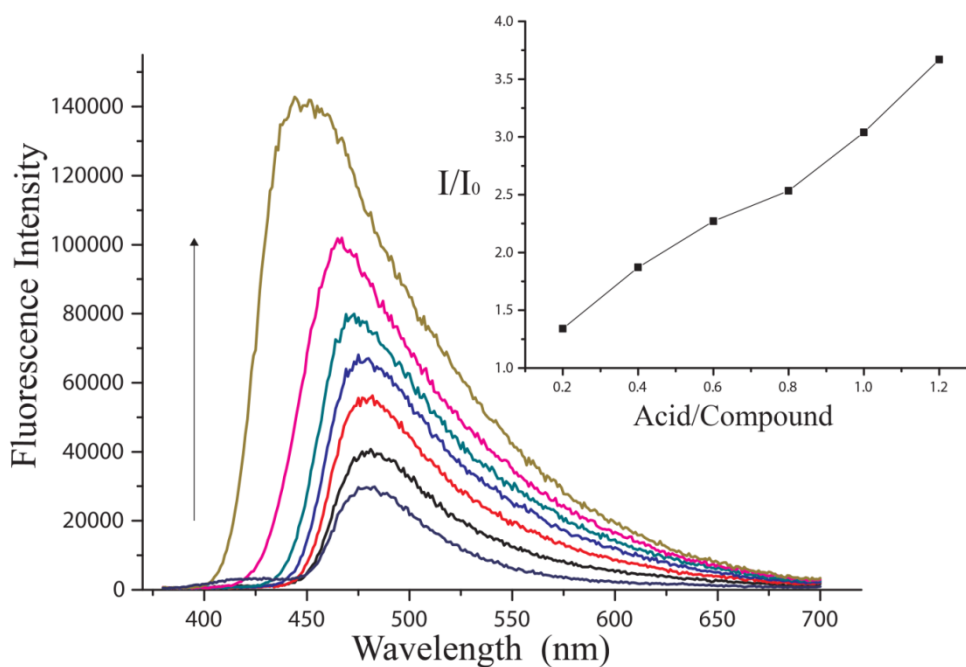


Figure 2.60. Fluorescence titration profile of **3a** (1.67 mM) in CHCl_3 solution upon addition of HCl (in methanol) (0.2, 0.4, 0.6, 0.8 and 1.0, 1.2 eq.). 3.6 times increase in the fluorescence intensity is observed at 480 nm.

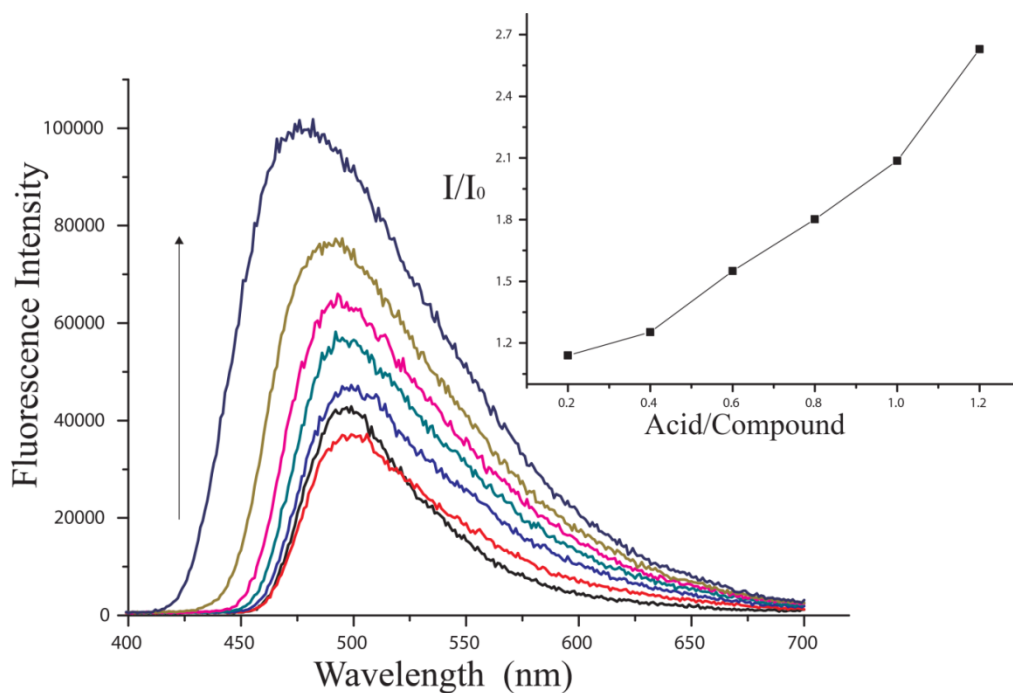


Figure 2.61. Fluorescence titration profile of **3b** (1.67 mM) in CHCl_3 solution upon addition of HCl (in methanol) (0.2, 0.4, 0.6, 0.8 and 1.0, 1.2 eq.). 2.6 times increase in the fluorescence intensity is observed at 500 nm.

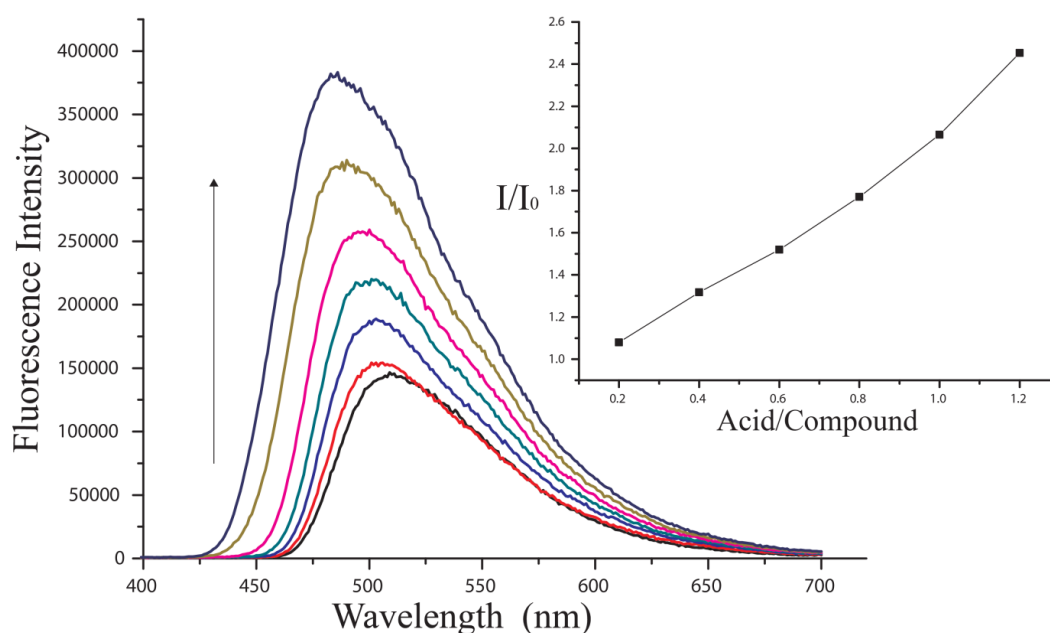


Figure 2.62. Fluorescence titration profile of **3c** (1.67 mM) in CHCl_3 solution upon addition of HCl (in methanol) (0.2, 0.4, 0.6, 0.8 and 1.0, 1.2 eq.). 2.5 times increase in the fluorescence intensity is observed at 510 nm.

The quantum-chemical investigation of chromogenic and fluorogenic spectral response was performed using Gaussian 09 suite of programs.¹³ The geometries of ground state structures of compounds **3a** - **3d** and **4a** - **4d** were optimized using density functional theory (DFT). For geometry optimization B3LYP functional and the 6-31g* basis sets were used. Optimized structures of **3a** - **3d** and **4a** - **4d** showed close match with the conformation of molecules observed in their crystal structures. The HOMO electron density in **3a** - **3d** is distributed mainly over quinoline moiety whereas LUMO electron density resides over benzophenone moiety (**Figure 2.63-2.66**). The yellow color of the compounds **3a** - **3d** is attributed to the intramolecular charge transfer (ICT)¹⁴ between quinoline (donor) and benzophenone (acceptor) groups. Moreover, the formation of azaquinazolinium heterocycle upon N-alkylation converts the lone pair over N1 into a σ bond. Consequently HOMO shifts into low lying orbital resulting in the increase in HOMO-LUMO energy gap (**table 2.5**). The decolouration and blue shift in the λ_{\max} of compounds **3a** - **3d** on addition of acid could be due to the weakening of ICT within the molecule.

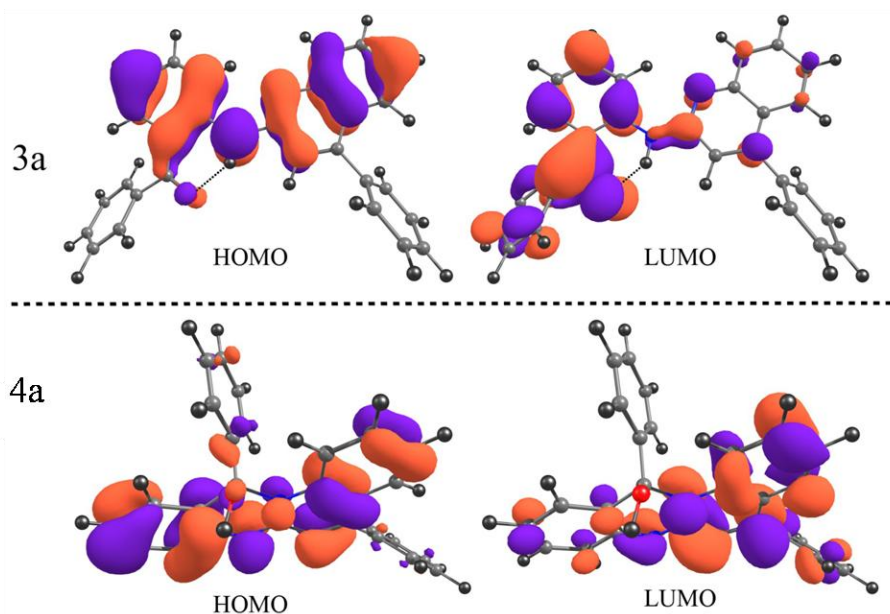


Figure 2.63. HOMOs and LUMOs of **3a** and **4a**.

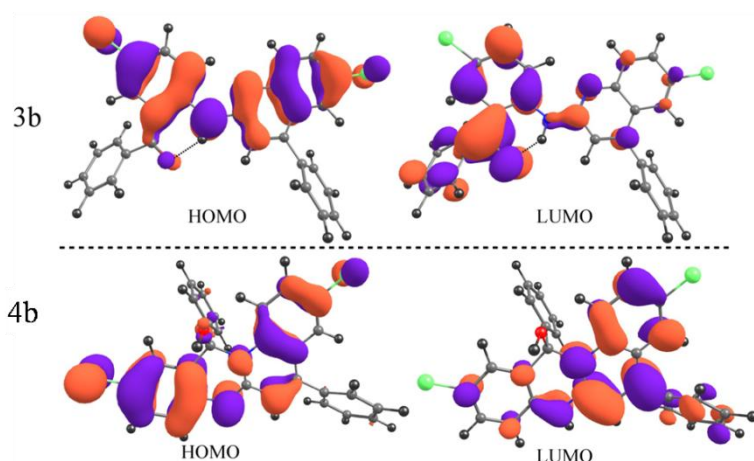


Figure 2.64. HOMOs and LUMOs of 3a and 4a.

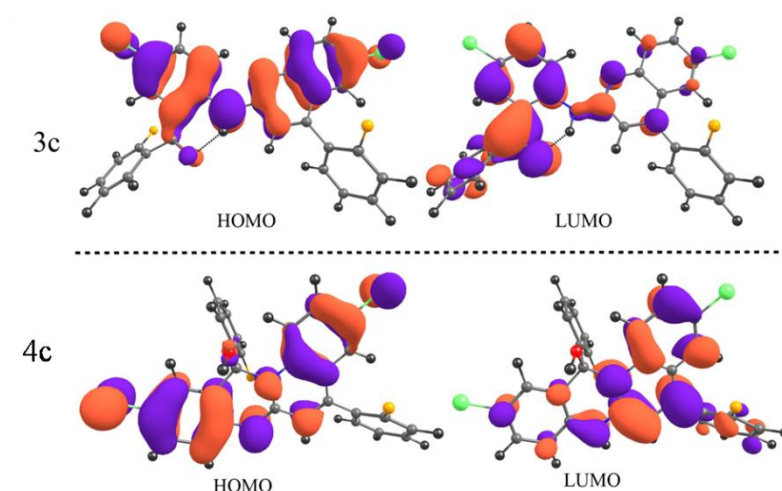


Figure 2.65. HOMOs and LUMOs of 3c and 4c.

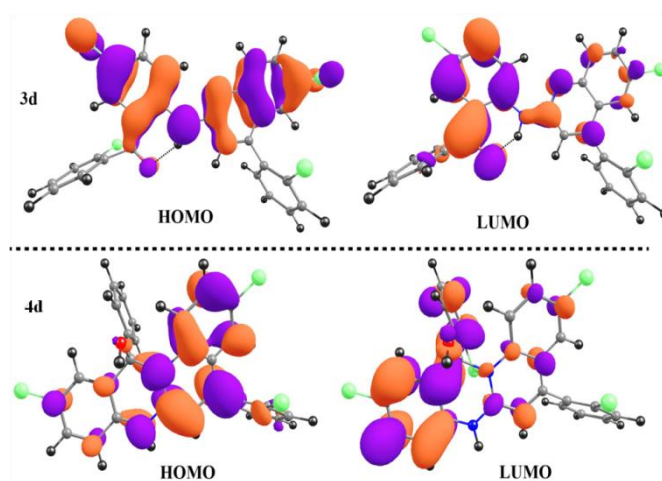


Figure 2.66. HOMOs and LUMOs of 3d and 4d.

Table 2.5. Calculated and experimental λ_{max} values and calculated HOMO-LUMO energy gap.

Compounds	Calculated HOMO-LUMO Egap		Experimental λ_{max}	
	eV nm		eV nm	
3a	2.9763	416.57	3.1628	392
4a	3.2856	377.35	3.4439	360
3b	2.9071	426.48	3.1073	399
4b	3.1432	394.45	3.3508	370
3c	2.9323	422.82	3.0092	412
4c	3.1399	394.87	3.2203	385
3d	3.0002	413.26	3.0092	412
4d	3.2129	385.89	3.1790	390

TD-DFT calculation on compounds **4a-4d** revealed the location of frontier HOMO-LUMO orbitals on the tetracyclic aromatic core (**Figure 2.63-2.66**). Thus, fluorescent nature of **4a-4d** is attributed to the extended conjugation of cyclized products.¹⁵ In compounds **4a-4c**, the fragment N1-C1-N2 participates in the excitation state transition. However, the same fragment in **4d** is devoid of LUMO electron densities. This could be because of the disruption of N to N⁺ charge transfer by some intramolecular interactions that further enhances its turn-on efficiency.¹⁶ Finally we hypothesized that, N-alkylation have switched -off the through space intramolecular charge transfer between N-donor of quinoline and benzophenone acceptor group,

which in turn activates the fluorescence from the donor chromophore containing extensively conjugated azaquinazolinium ring.

The fluorine and chlorine atoms (position X2 on benzophenone moiety) in **4c** and **4d** respectively formed three centered short intra-molecular contacts termed as ‘halogen bonding’ interaction with both nitrogen atoms of the azaquinazolinium ring. The geometrical parameters of these interactions are provided in the **figures 2.67-2.68**. The structure data reveals that F...N1 (2.689 Å) contact is shorter than F...N2 (3.054 Å) contact in **4c**. Similarly, Cl...N1(3.016Å) contact is shorter than Cl...N2 (3.437 Å) contact in **4d**. Generally, structure data provides dynamic equilibrium of conformations in the solution state. Moreover, we observed resonant charge transfer between N1 and N2 atoms in **4c** and **4d**. Therefore three centre halogen bonding N-X-N⁺ (X: Cl, F) may be existing in dynamic state which involves continuous hopping of positive charge between N1 and N2. Therefore geometrical parameters of N-X-N⁺ is varying in the solution state. The single point energy calculation¹⁶ was carried out using optimized conformations of **4c** and **4d** to validate the structure data observation. The B3LYP basis sets with 6-31g* functional and PBF (chloroform) solvation model was used for the DFT calculation. The electrostatic potential maps of both the compounds revealed the presence of intra-molecular and non-covalent electrostatic interaction between the halogen atom X (X:Cl, F) and nitrogen atom of the quinazolinium ring which is shown with the dotted lines(**Figure 2.69-2.70**). Halogen bonding has been vigorously studied in solid state for the design of functional material.¹⁷ However, its study in solution is very limited.¹⁸ Nevertheless, many solution state charge transfer reactions have been reported wherein halogen bonding interactions has played significant role.¹⁸ Recently Zou *et al.* reported the formation of intermolecular strong I...N (Iodine...nitrogen) halogen bonding interactions that disrupted intramolecular PET (photo induced electron transfer) charge separation of ciprofloxacin resulting in the enhancement of fluorescence. Obviously, the questions, why compound **4d** showed the maximum enhancement of fluorescence intensity compare to **4c**. Halogen bonding interactions is the attractive interaction between electrophilic region (acceptor) of halogen and nucleophilic region(donor) in another molecular entity or atom (**Figure 2.71a**).¹⁸ As the polarization of electron density increases, the strength of halogen bonding increases which is in the order I > Br >Cl> F. Based on the literature survey, the electron density over fluorine atom is

isotropic and therefore fluorine contacts are termed as fluorine bond instead of halogen bonding interaction (**figure 2.71b**). Many a times they are formed by packing constraints in the solid state. However, the strength of $F\cdots X$ (X is electron pair donor atom) interaction when compared with interactions involving other halogen atoms $Y\cdots X$ (Y: Cl, Br, I and X : donor atom) is much weaker. In the present scenario, the charge transfer between N to N^+ is weakened by halogen bonding $Cl\cdots N$ interaction which has resulted in the enhancement of the emission efficiency of **4d**. However, the same is not observed for **4c** owing to weaker strength of $F\cdots N$ association.¹⁹

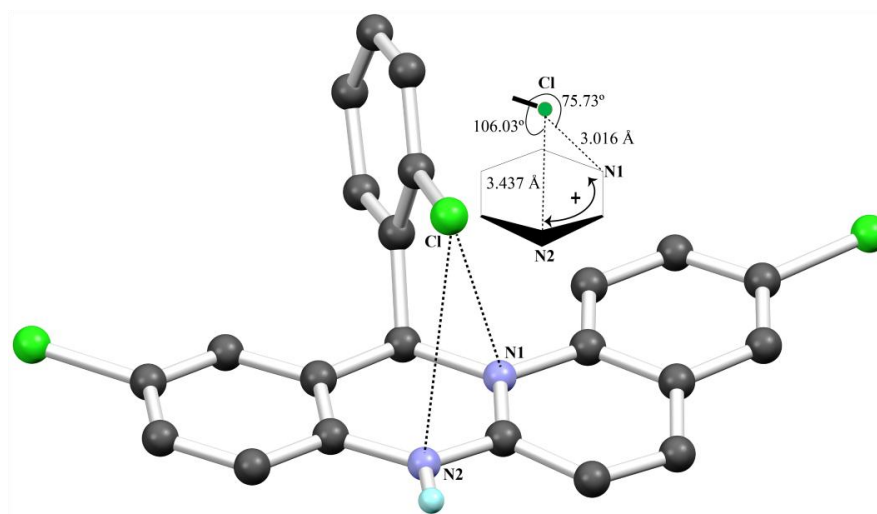


Figure 2.67. Geometrical parameters of intramolecular interactions of Cl and N atoms of **4d**.

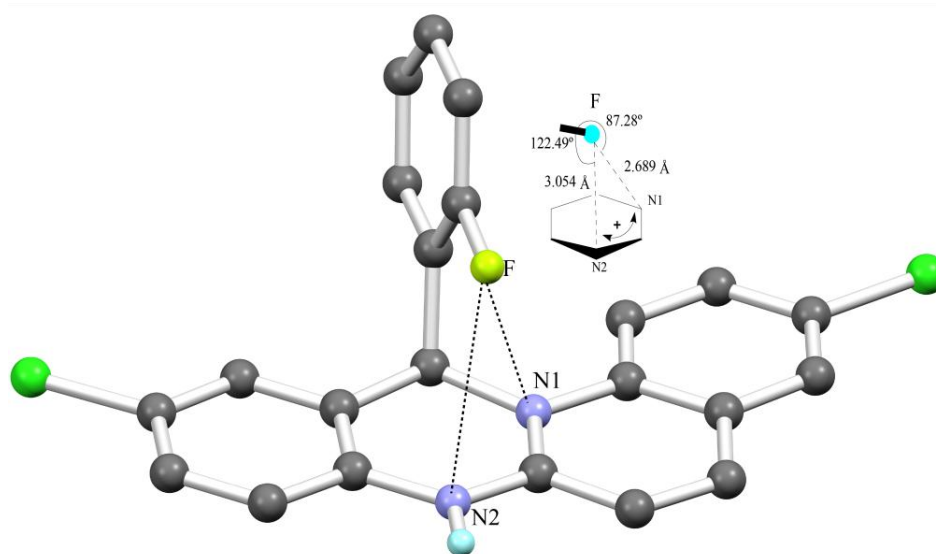


Figure 2.68. Geometrical parameters of intramolecular interactions of F and N atoms of **4d**.

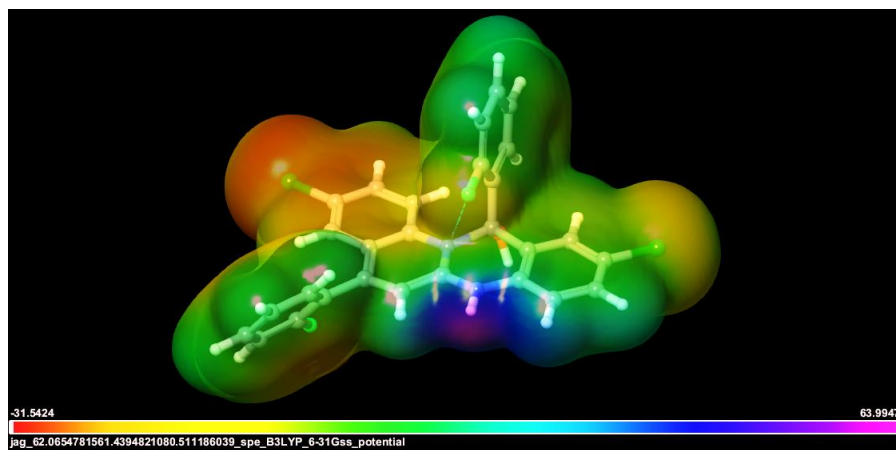


Figure 2.69. Electrostatic potential map of **4c** obtained from single point energy calculation (B3LYP/6-31g*) revealed intramolecular electrostatic interaction F \cdots N.

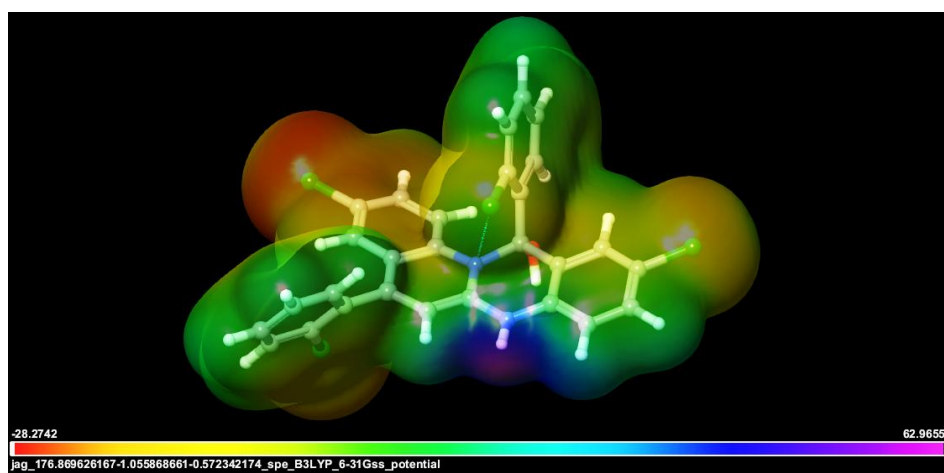


Figure 2.70. Electrostatic potential map of **4c** obtained from single point energy calculation (B3LYP/6-31g*) revealed intramolecular electrostatic interaction Cl \cdots N.

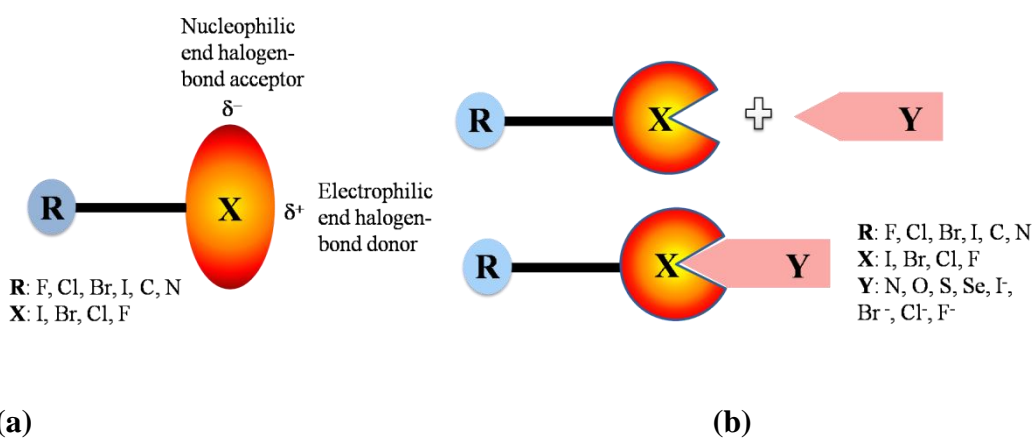


Figure 2.71. (a) 2D depiction of polarization of electron density of halogen atom and (b) schematic representation of halogen bonding.

The turn-on fluorescent behavior of compound **3d** towards acidic analyte was investigated in solid state by exposing the dry coated silica plate with acid vapors for different time intervals. Decolouration of acid exposed area on the silica plate revealed the formation of azaquinazolinium ion, **4d** even in the solid state. The fluorescent probe was prepared by dissolving 1.0 mg of compound **3d** in chloroform. The silica coated aluminium paper (TLC plate) of size 3cm was dipped in yellow coloured chloroform solution of **3d** and air dried. The fluorescent detection of acid vapours was carried out by exposing the dried coated paper to the vapours of volatile acid HCl for 0, 5, 10, 15 and 20 seconds and observed under UV (365 nm) (**Figure 2.72**). The distinct trend is observed for the time dependent response on the fluorescence intensity which is driven by acidity in the environment.

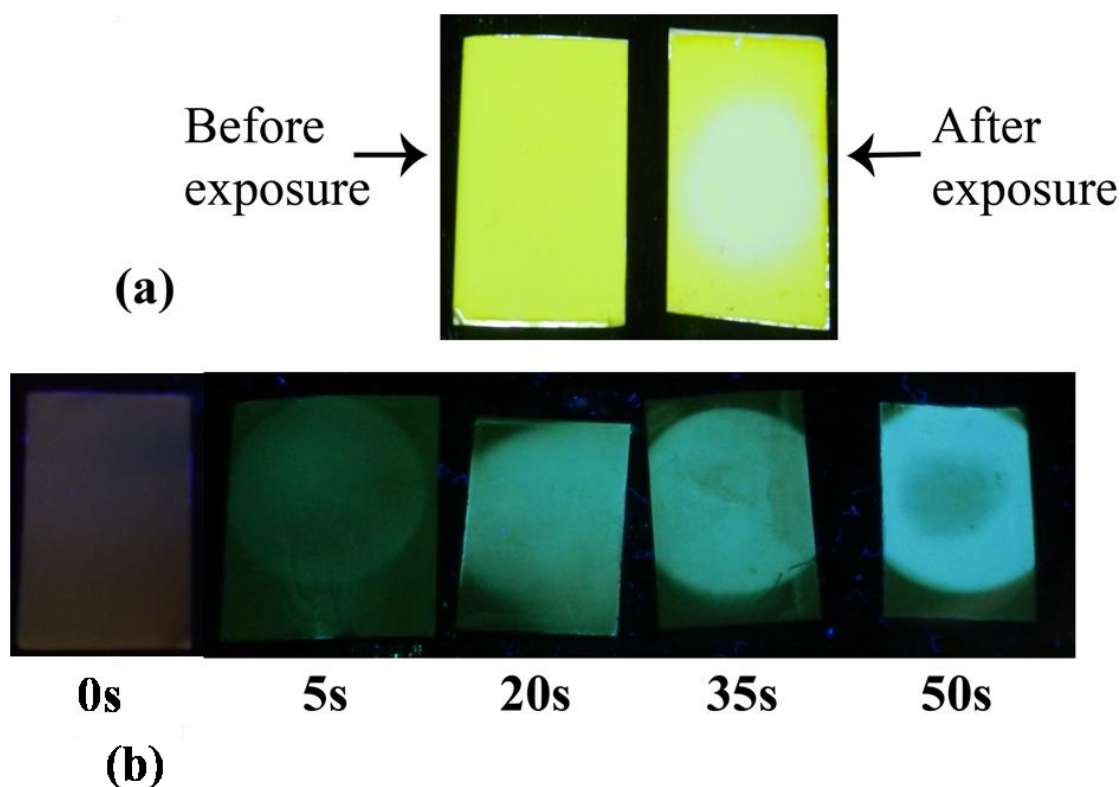


Figure 2.72. Solid-state turn-on response of **3d** (coated on silica plate) upon exposure to HCl vapors at 0, 5, 20, 35, 50 seconds.

All these compounds showed reversible reactivity to the acid analytes i.e. reappearance of yellow color and fluorescence quenching of **4a-4d** was observed upon exposure to water (proton donor) in solution as well as solid states. The reversible nature of the compounds provide promising platform for constructing cost-

effective and reusable acid sensing probe. Furthermore, the reversibility is validated by TLC-MS experiment. (Figure 2.73). The experimental protocol demonstrating reusability of the compound **3d** is given in the figure 2.74. In the first step, acid exposed silica paper was treated with few drops of water to quench the fluorescence; the yellow colour reappeared on the coated paper. The re-appearance of yellow colour is the characteristic of conversion of π to π^* in **4d** to n to π^* in **3d** which has resulted in the red shift of λ_{\max} . The paper was then dried in the oven and again exposed to the volatile acid vapours. Optical and fluorescent images were photographed during each step. The experiment was repeated many times.

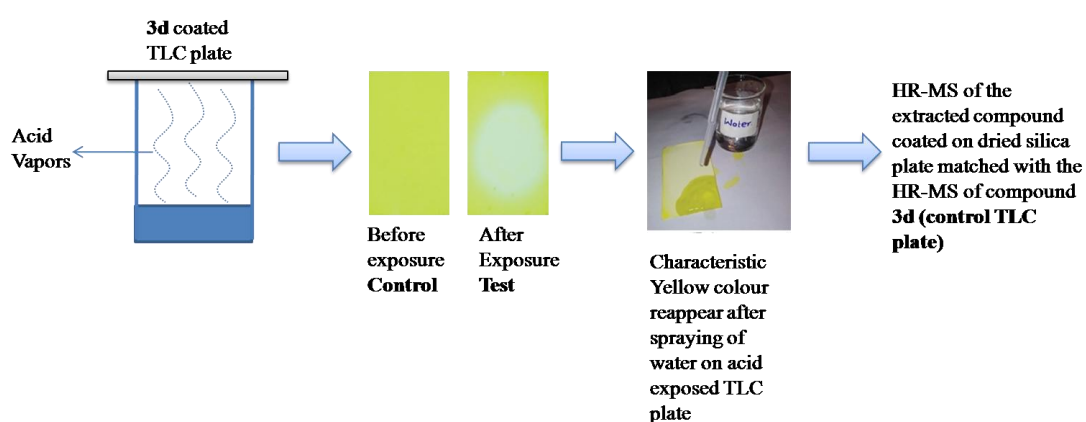


Figure 2.73. TLC-MS experiment

Description of each step:

Step a: Compound **3d** was dissolved in the chloroform.; **Step b:** silica plates were used and soaked in chloroform solution of **3d**; **Step c:** silica plates were dried ; **Step d:** compound coated yellow coloured silica plates when observed under UV, no fluorescence was observed.; **Step e:** out of two plates, one plate was exposed to HCl acid vapour whereas other plate was used as control; **Step f:** decolouration of acid exposed area was observed; **Step g:** when observed under UV(360 nm), the acid exposed silica plate showed strong fluorescence. ; **Step h:** water was sprayed onto the acid exposed silica plate which regained its yellow colour; **Step i & j:** wet silica plate was air dried; **Step k:** dried silica plate was once again exposed to HCL acid vapours.; **Step l:** decolouration and fluorescence was observed form the acid exposed silica plate.

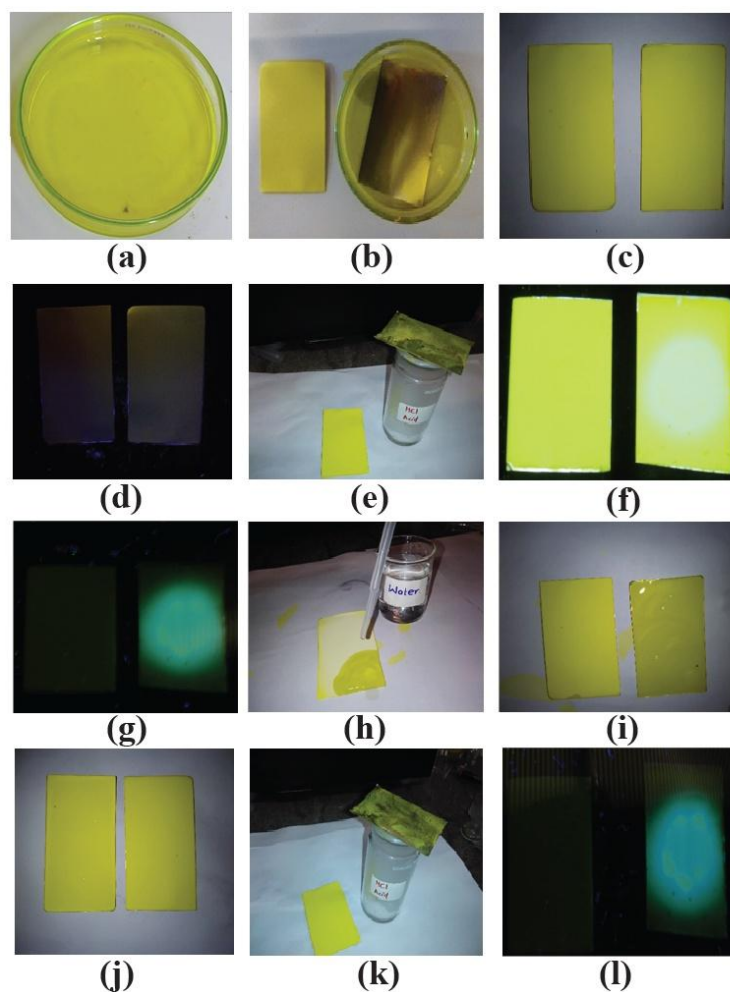


Figure 2.74. Demonstration of reusability and reversible nature of compound **3d** for the detection of HCl acid vapours.

The applicability of highest active probe **3d** for the solid state detection of chemical warfare agent mimic was also investigated. The mechanistic study was performed using UV-vis and ^1H NMR titration (**Figure 2.75-2.76a**). The UV-vis spectroscopic study revealed blue shifting of the peak to 390 nm as observed for the methanolic HCl, however, the blue-shifting was not ratiometric. The weak response is attributed to the less acidic nature of DCP. Moreover, ^1H titration study resembles with that of acid titrations suggesting similar mechanism of turn-on fluorescence. The solid state naked eye response towards DCP analyte was demonstrated by keeping **3d** coated silica plate in the closed chamber for about 5 min containing 10 μL of DCP analyte (**figure 2.76b**). The distinct difference between control (unexposed) and test (exposed) plate was observed.

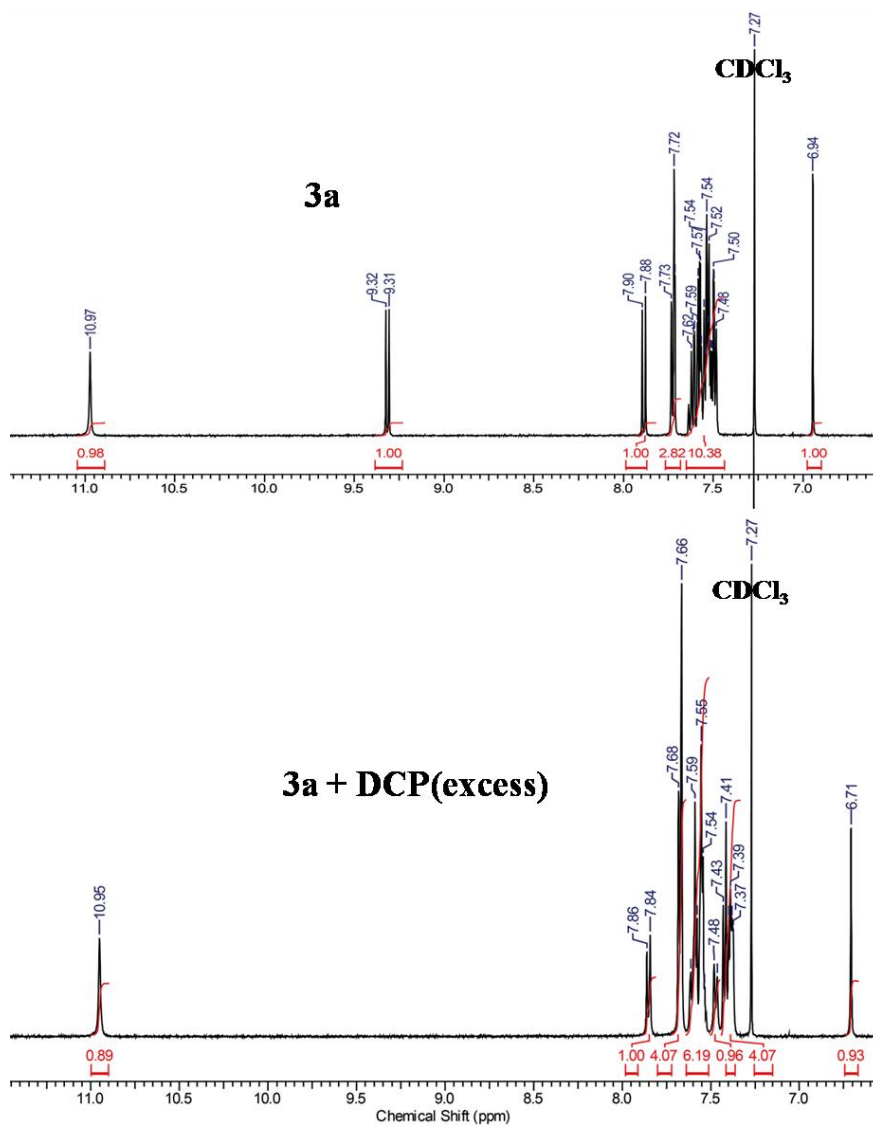


Figure 2.75. ^1H NMR spectra of (**3d**) and (**3d** + DCP).

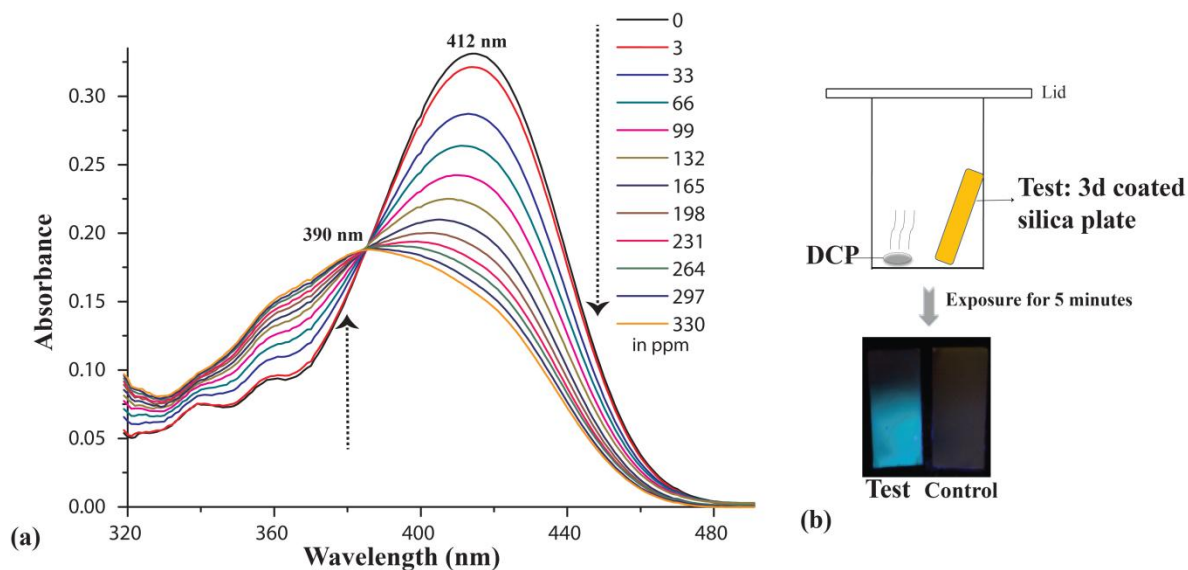


Figure 2.76. (a) UV-vis spectra of **3d** (20 μ M) in chloroform on addition of different amounts of DCP in chloroform, and (b) solid state detection of DCP and comparison of test and control plates.

Construction of sensor devices:

To check the real time applicability of compound **3d**, the electronic device was constructed. The circuit is shown in the **figure 2.77** which is used in conjunctions with our probe **3d**. The circuit is based on CdS Light Dependent Resistor (LDR) or Photo-resistor. Significance of CdS LDR is that it absorbs visible light energy, due to which there occur a change in resistance of LDR. This basic light sensor circuit is of a relay output activated switch. When no light is present i.e. in darkness, the resistance of the LDR is very high in the mega ohms ($M\Omega$'s) range so zero base bias is applied to the transistor and the relay is de-energised or "OFF". As the light level increases the resistance of the LDR starts to decrease causing the base bias voltage to rise. At some point determined by the potential divider network formed with resistor, the base bias voltage is high enough to turn the transistor "ON" and thus activate the relay which in turn is used to control some external circuitry. As the light level falls back to darkness again the resistance of the LDR increases causing the base voltage of the transistor to decrease, turning the transistor and relay "OFF" at a fixed light level determined again by the potential divider network. We have attached alarm to the relay, which gets "ON" whenever relay gets activated. The same thing happens when relay get deactivated, alarm gets "OFF" (**Figure 2.78**).

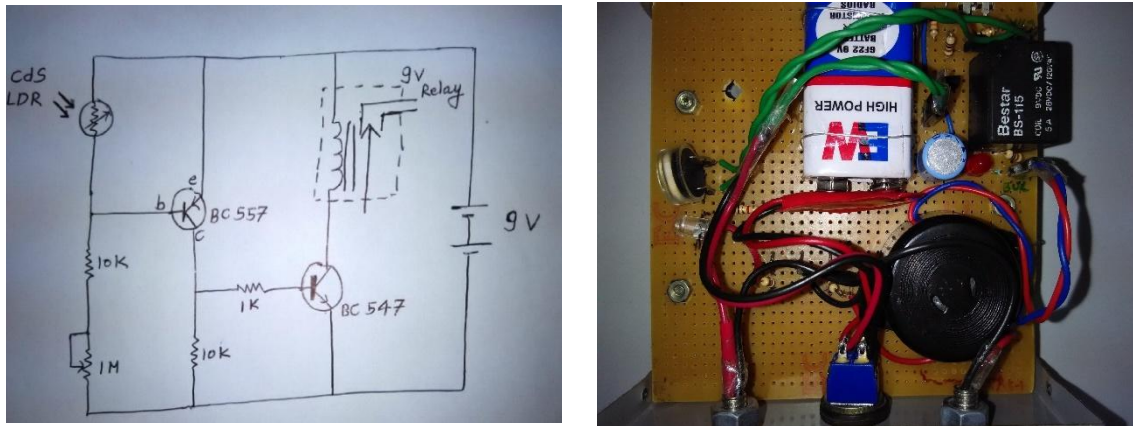
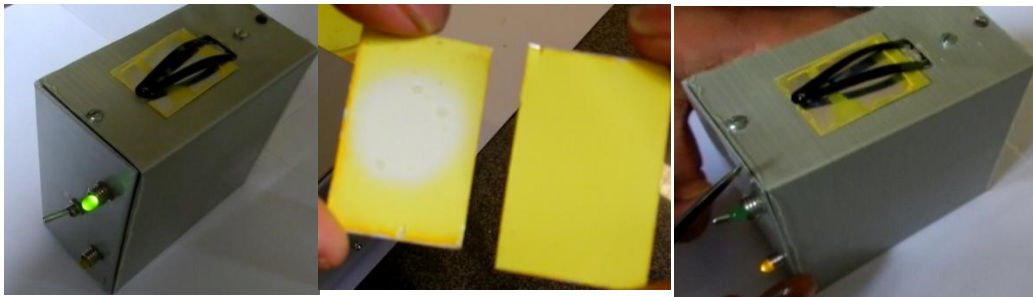


Figure 2.77. Electronic circuit and different parts of the sensor device.



(a)

(b)

(c)

Figure 2.78. (a) Alarm off (green) for unexposed plate (b) Decoloration of the acid exposed area (c) Alarm on (orange) when acid exposed plate is put on the detection socket.

Conclusion:

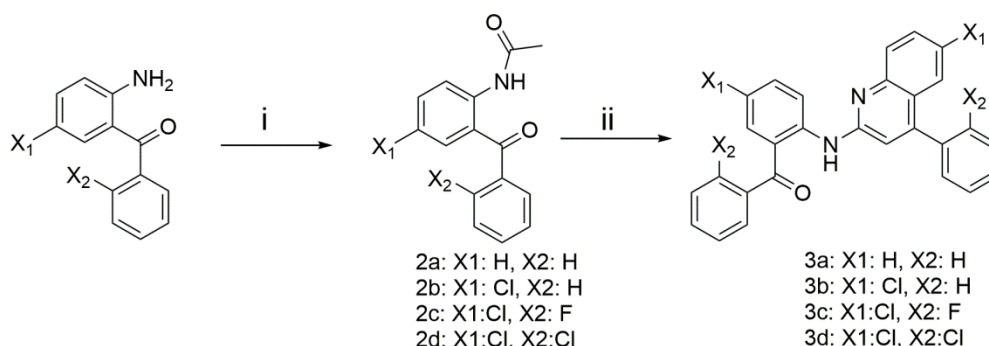
The designed benzophenone-quinoline conjugates can be used for the solid and solution state detection of acids. The acid mediated intra-molecular cyclization converts non-emissive conjugates into the emissive azaquinazolinium ions. The subsequent transformation shows remarkable changes in the absorption and emission bands. Turn-on mechanism and emission efficiency is attributed to the extended conjugation of cyclized products. The reactivity of the probe depends on the acidity of the solution which is attributed to the differential affinity towards proton. The compounds with substituted -Cl atom (C9) showed highest enhancement in the fluorescence which is attributed to solution state three centre N-Cl-N⁺ halogen bonding. The reversible nature and solid state turn-on response showed potential application of these compounds for the onsite detection of acid leaks and chemical warfare agents (DCP). The applicability of highest active compound **3d** for onsite-detection is demonstrated by constructing alarming device.

Experimental Methods:

General Scheme of synthesis:

(i) To the mixture of substituted and un-substituted 2-aminobenzophenones (0.01M) in acetic anhydride (3 mL), 0.01 M anhydrous sodium acetate was added. The reaction mixture was then heated at reflux for 1h. After the completion of reaction the mixture was cooled to room temperature and further quenched by addition of 20 mL of cold water. The resultant white precipitate was purified by crystallization using ethanol solvent.

(ii) The product from step (i) was used as starting material for step (ii) to which 10 eq. (by weight) of PPA (polyphosphoric acid) was added. The semi-solid material was heated at 90 °C for 48 hours. The reaction mixture was then cooled to room temperature. Saturated sodium carbonate solution was slowly added to neutralize the crude acidic reaction mixture. The yellow precipitate was collected and washed with water. It was purified by flash column chromatography using (5% ethyl acetate: light petroleum) solvent system.



Reagents and Condition: (i) Sodium acetate, acetic anhydride, reflux, rt, 1h (ii) PPA, 90 °C, 18h

Synthesis of N-(2-benzoylphenyl)acetamide (2a): To the mixture of 2-amino benzophenone (1.972 g) in acetic anhydride, anhydrous sodium acetate (0.82 g) was added and reflux for 1 h. After completion of reaction, the reaction mixture was cooled to room temperature and further quenched by addition of cold water (20 mL). White coloured solid was obtained which was further crystallized in ethanol solvent to yield pure product of **2a** with (80-82 %) yield. ¹H NMR (400 MHz, Chloroform-d) δ = 10.83 (br. s., 1 H), 8.64 (d, J = 8.2 Hz, 1 H), 7.73 - 7.67 (m, 2 H), 7.64 - 7.53 (m, 3 H), 7.53 - 7.46 (m, 2 H), 7.12 - 7.06 (m, 1 H), 2.25 - 2.22 (m, 3 H) chemical shift in

ppm. The compound is reported previously by F. Luo, J. Yang, Z. Li, H. Xiang and X. Zhou, *Eur. J. Org. Chem.*, **2015**, 2463-2469.

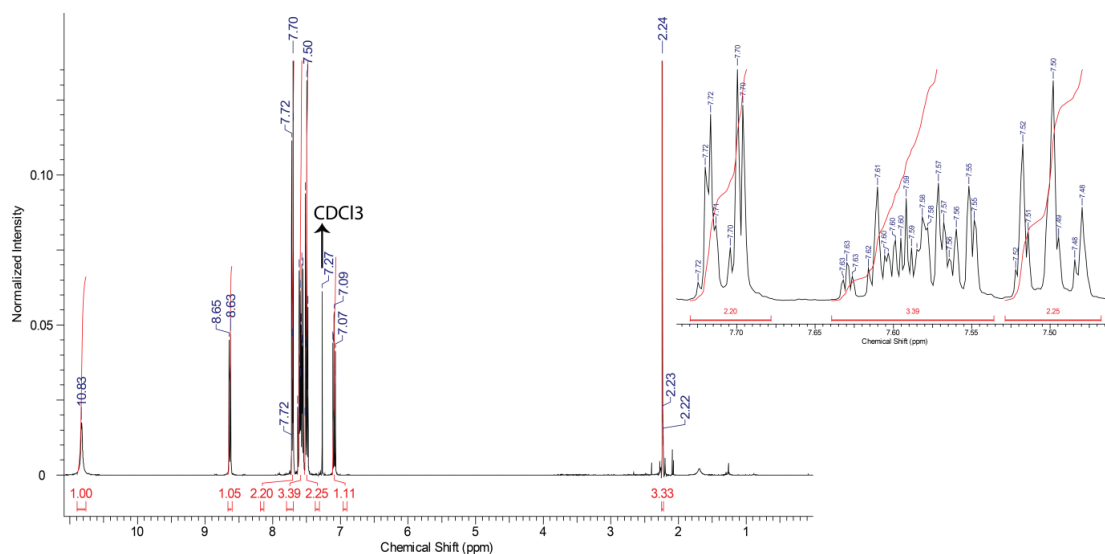


Figure 2.79. ^1H NMR of N-(2-benzoylphenyl)acetamide (**2a**).

Synthesis of phenyl(2-((4-phenylquinolin-2-yl)amino)phenyl)methanone (3a**):** 1g of **2a** was added to the 10 g of PPA . The reaction mixture was heated at 90 °C for 48 h and further cooled to room temperature. Slow addition of saturated sodium carbonate solution formed yellow coloured precipitate. The precipitate was washed with water and purified by flash column chromatography (solvent system, ethyl acetate: petroleum ether) to afford **3a** (60-62% yield). ^1H NMR (500 MHz , Chloroform-d) δ = 11.10 (br. s., 1 H), 9.33 (d, J = 8.5 Hz, 1 H), 7.98 (d, J = 8.5 Hz, 1 H), 7.79 - 7.71 (m, 3 H), 7.69 - 7.56 (m, 4 H), 7.55 - 7.52 (m, 4 H), 7.52 - 7.46 (m, 3 H), 7.34 - 7.29 (m, 1 H), 7.01 - 6.95 (m, 2 H); ^{13}C NMR(125 MHz): 199.9, 152.9, 150, 147.8, 144, 139.4, 137.9, 134.4, 134.3, 131.9, 129.7, 129.5, 129.4, 128.5, 128.4, 128.2, 127.7, 125.6, 123.7, 123.4, 121.6, 119.8, 119.3, 114.9 (chemical shift in ppm); HR-MS: ($\text{C}_{28}\text{H}_{21}\text{N}_2\text{O}$) 401.1648 ($\text{M}+\text{H}$) $^+$

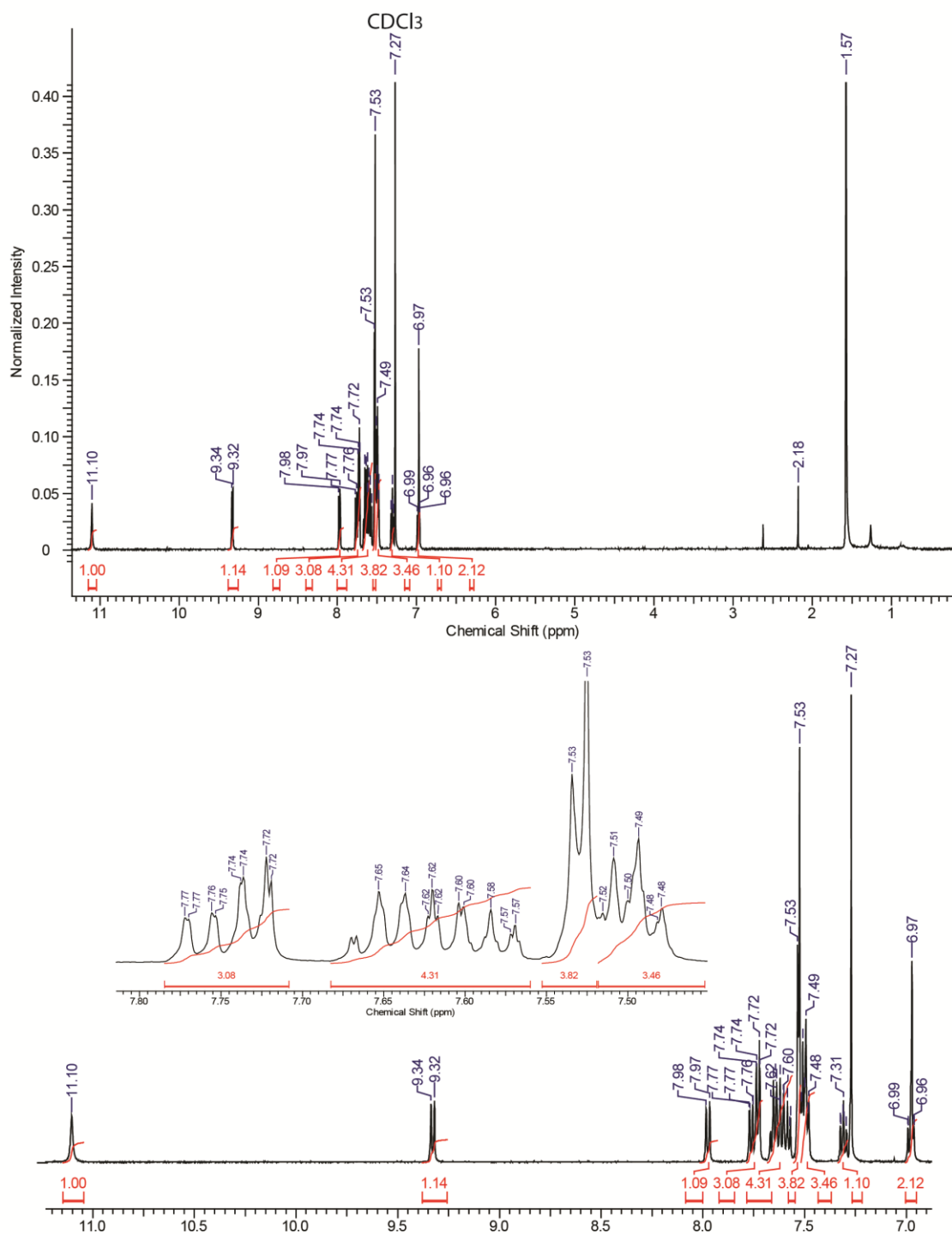


Figure 2.80. ^1H NMR of phenyl(2-((4-phenylquinolin-2-yl)amino)phenyl)methanone (3a).

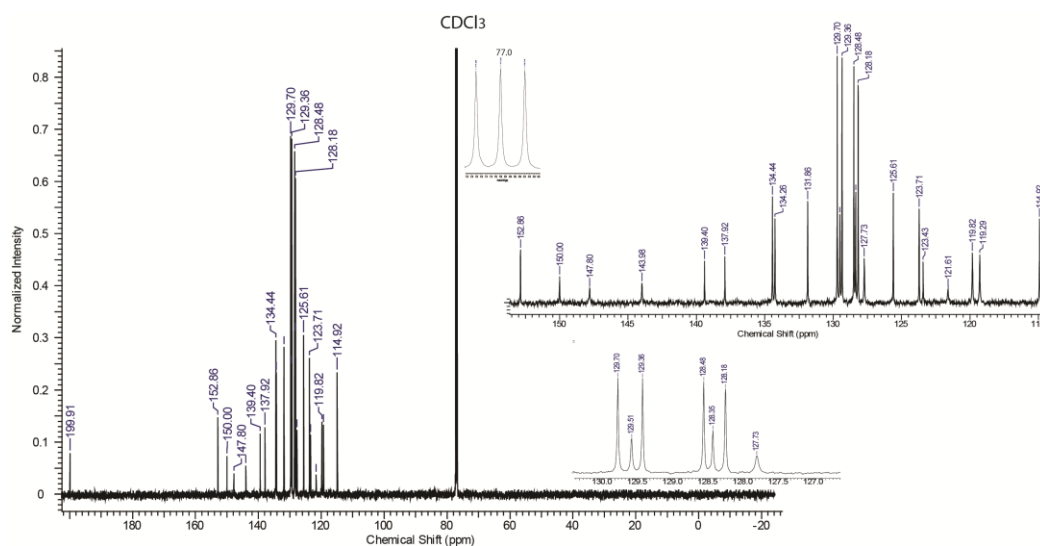


Figure 2.81. ^{13}C NMR of phenyl(2-((4-phenylquinolin-2-yl)amino)phenyl)methanone (3a).

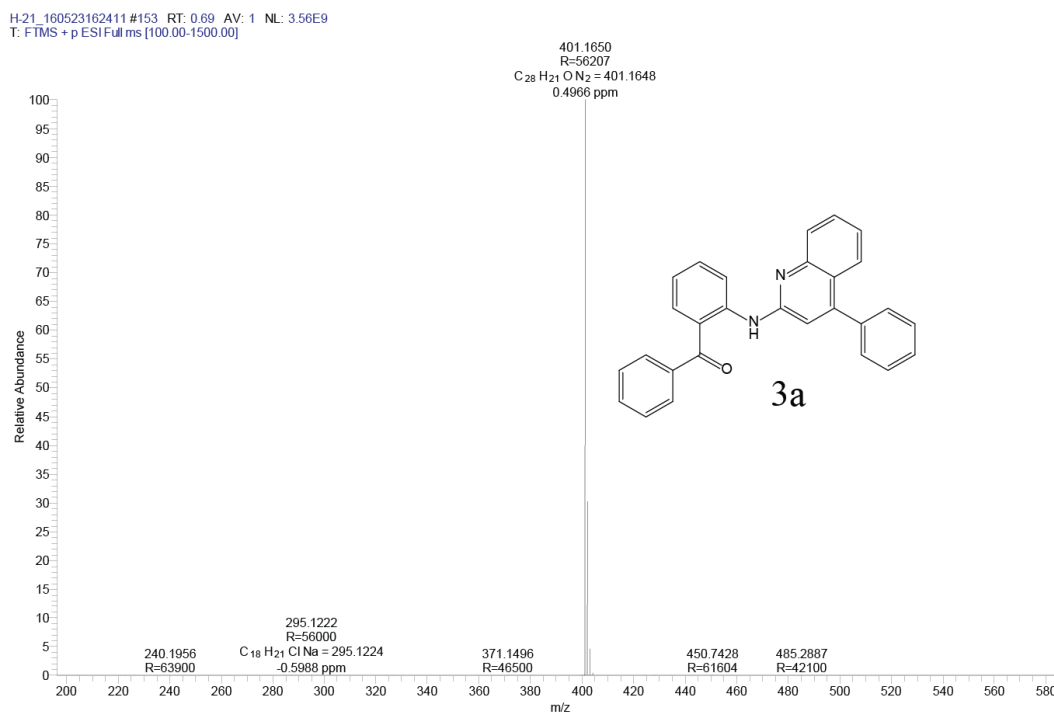


Figure 2.82. HR-MS of phenyl(2-((4-phenylquinolin-2-yl)amino)phenyl)methanone (3a).

Synthesis of N-(2-benzoyl-4-chlorophenyl)acetamide (2b): compound **2b** was synthesized similar to the procedure described for **2a**, using 2-amino-5-chlorobenzophenone (2.317 g). White precipitate was purified by crystallization to obtain large crystals of **2b** with yield of (80-82%) ^1H NMR (200 MHz, Chloroform-d) $\delta = 10.63$ (br. s., 1 H), 8.69 - 8.53 (m, 1 H), 7.77 - 7.59 (m, 3 H), 7.59 - 7.46 (m, 4 H), 2.26 - 2.19 (m, 3 H). The compound was reported previously by N. P. Peet, S. Sunder, R. J. Barbuch, M. R. Whalon, E. W. Huber and J. C. Huffman, *J. Heterocycl. Chem.*, 1989, **26**, 1611-1617.

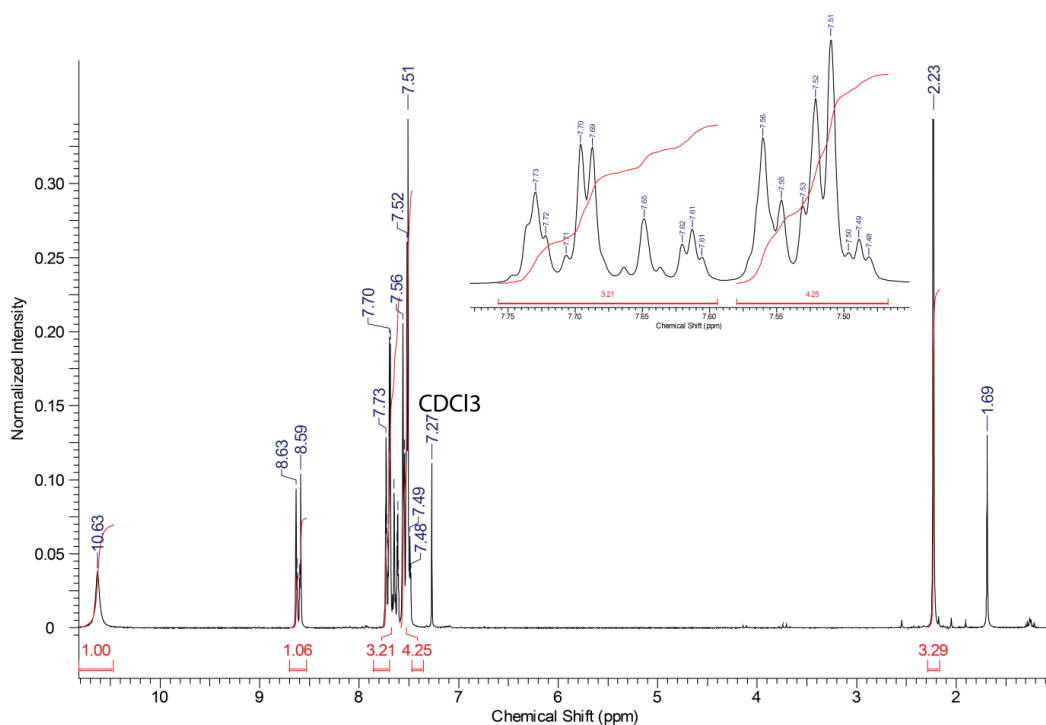


Figure 2.83. ^1H NMR of N-(2-benzoyl-4-chlorophenyl)acetamide(**2b**).

Synthesis of N-(2-benzoyl-4-chlorophenyl)acetamide (3b): Semi-solid reaction mixture of compound **2b** (1g) and PPA (10 g) was heated at 90 °C for 48 h as explained previously. Yellow coloured precipitate was obtained after slow addition of saturated sodium carbonate solution. The precipitate was washed with water and purified by flash column chromatography to afford **3b** (65% yield). ^1H NMR (500 MHz, Chloroform-d) $\delta = 10.98$ (s, 1 H), 9.42 - 9.22 (m, 1 H), 7.93 - 7.86 (m, 1 H), 7.76 - 7.68 (m, 3 H), 7.67 - 7.43 (m, 12 H), 6.97 - 6.92 (m, 1 H); HR-MS:($\text{C}_{28}\text{H}_{19}\text{Cl}_2\text{N}_2\text{O}$) 469.0873 (M+H) $^+$. The compound was reported previously by N. P. Peet, S. Sunder, R. J. Barbuch, M. R. Whalon, E. W. Huber and J. C. Huffman, *J. Heterocycl. Chem.*, 1989, **26**, 1611-1617.

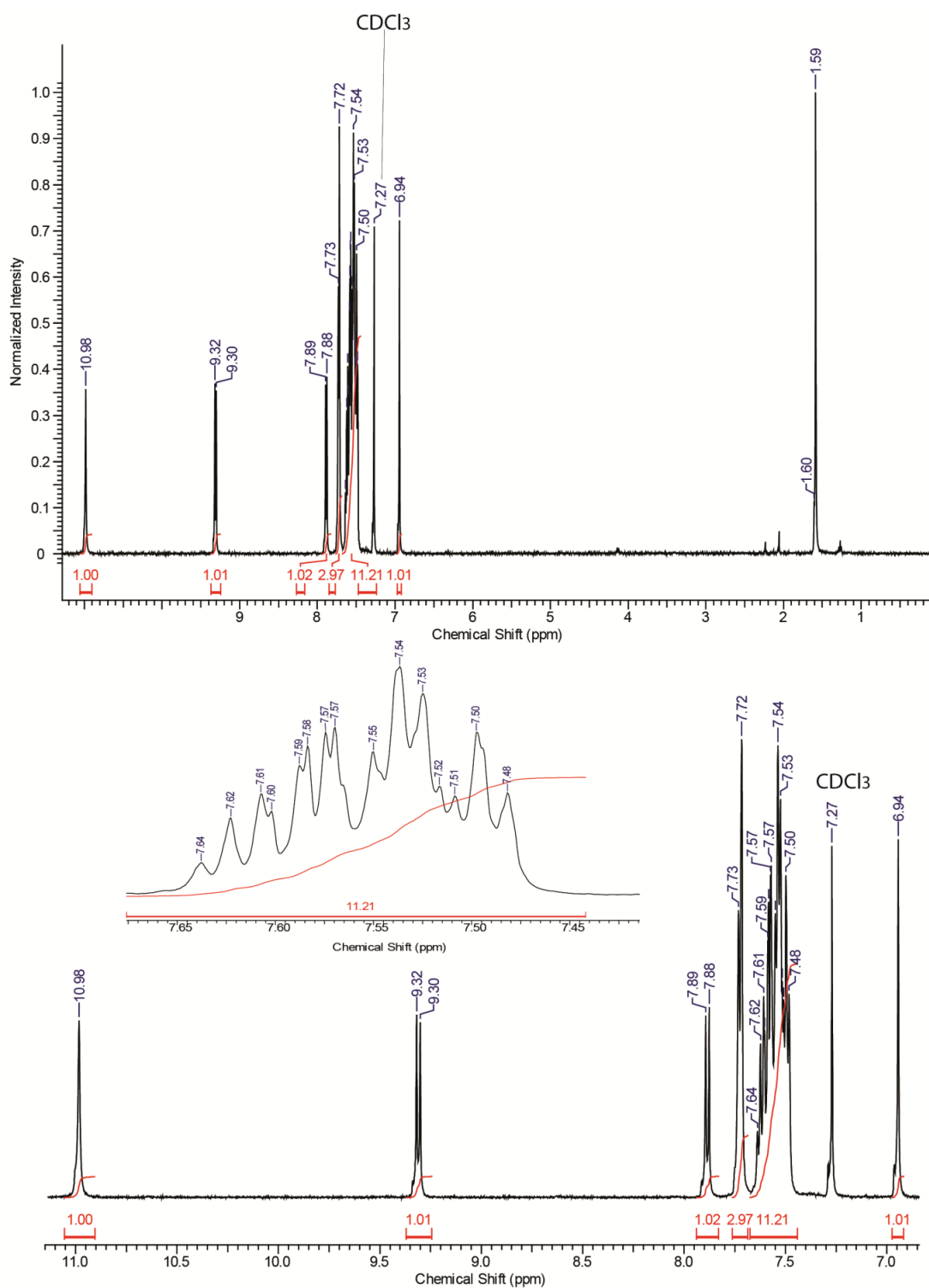


Figure 2.84. ^1H NMR of N-(2-benzoyl-4-chlorophenyl)acetamide (**3b**).

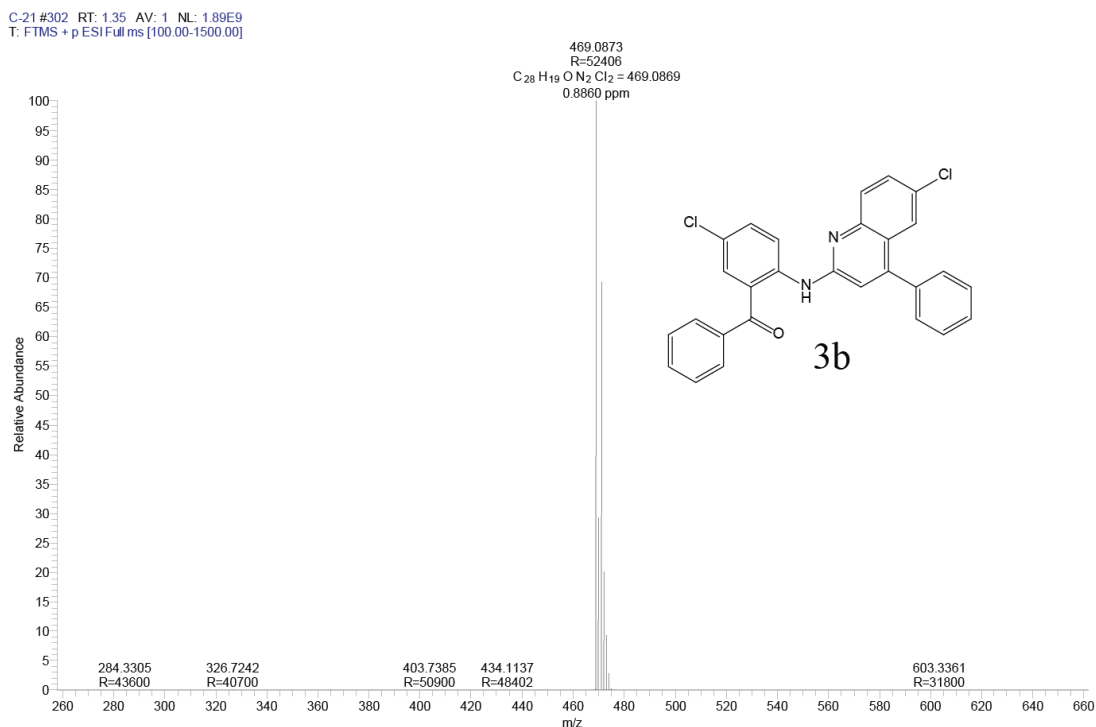


Figure 2.85. HR-MS of N-(2-benzoyl-4-chlorophenyl)acetamide (**3b**).

Synthesis of N-(4-chloro-2-(2-fluorobenzoyl)phenyl)acetamide (2c): Compound **2c** was synthesized as shown above using 2-Amino-5-chloro-2'-fluorobenzophenone (2.497 g). White precipitate was purified by crystallization to afford **2c** with the yield (78-80%). ¹H NMR (200 MHz, Chloroform-d) δ = 11.18 (br. s., 1 H), 8.74 (d, J = 9.0 Hz, 1 H), 7.66 - 7.49 (m, 2 H), 7.45 (m, 2 H), 7.33 (dd, J = 1.0, 7.5 Hz, 1 H), 7.25 - 7.14 (m, 1 H), 2.31 - 2.24 (m, 3 H). ¹³C NMR (101 MHz, CDCl₃) 196.0, 169.4, 160.8, 158.3, 139.7, 135.2, 133.6, 133.1, 130.2, 127.3, 126.8, 124.5, 123.5, 122.4, 116.6, 25.5 chemical shift in ppm.

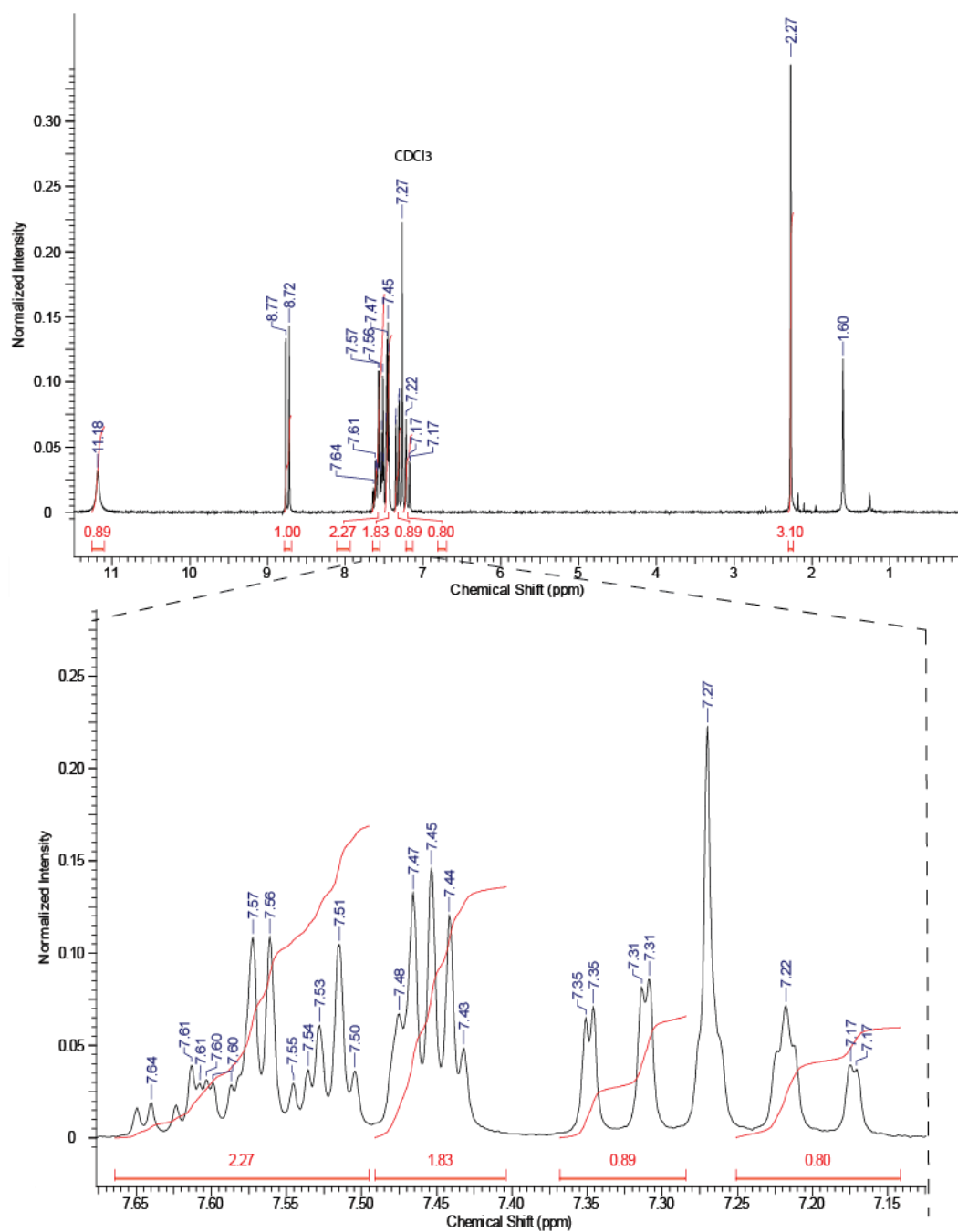


Figure 2.86. ^1H NMR of N-(4-chloro-2-(2-fluorobenzoyl)phenyl)acetamide (**2c**).

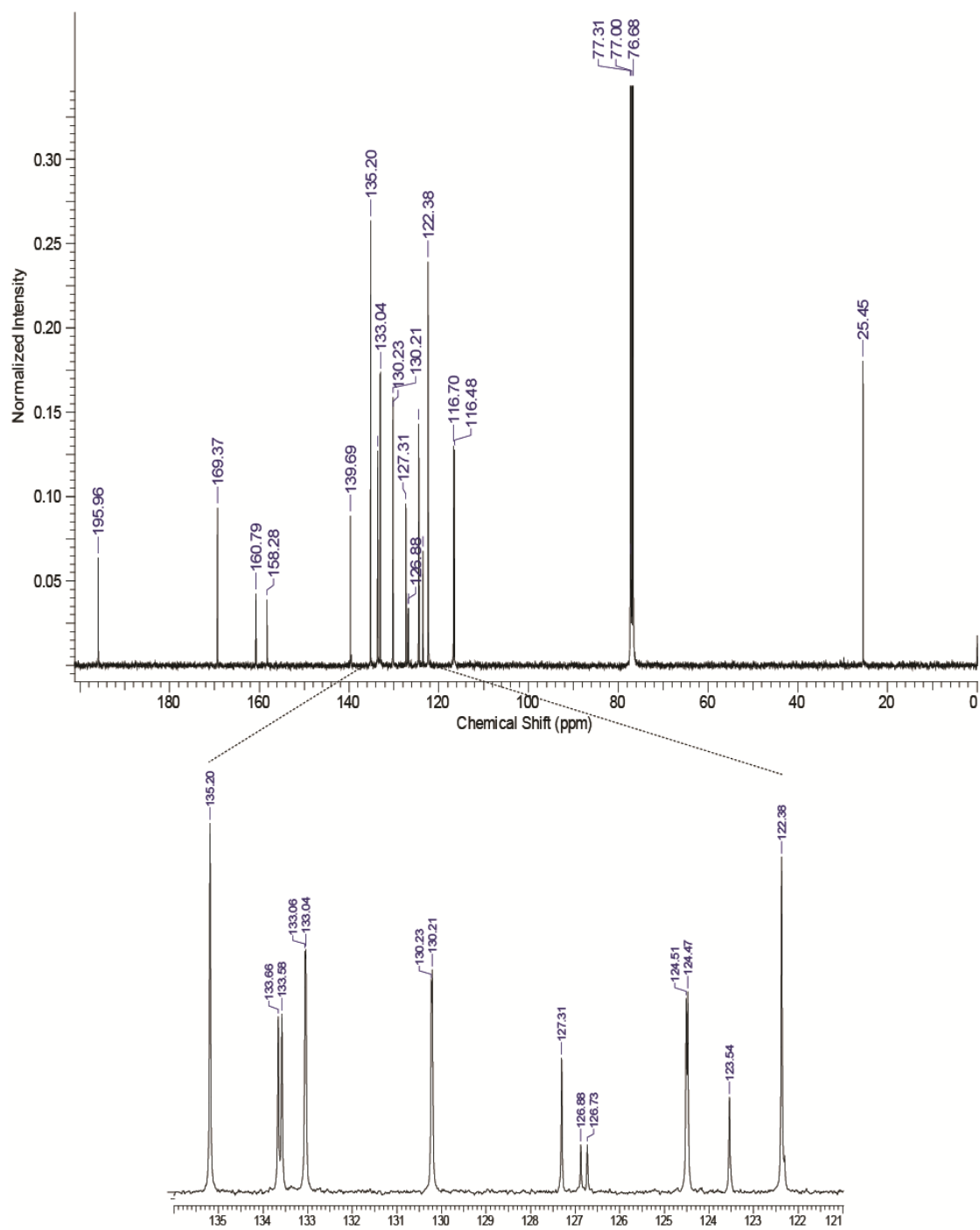


Figure 2.87. ^{13}C NMR of N-(4-chloro-2-(2-fluorobenzoyl)phenyl)acetamide (2c).

Synthesis of (5-chloro-2-((6-chloro-4-(2-fluorophenyl)quinolin-2-yl)amino)phenyl)(2-fluorophenyl)methanone (3c): Semi-solid reaction mixture of compound **2c** (1g) with **PPA** (10g) was heated at 90 °C for 48 h. After the completion of reaction saturated solution of sodium carbonate was slowly added to afford yellow precipitate. The precipitate was then washed with water and purified by column chromatography to afford **3c** with the yield of 62-65%. ¹H NMR (500 MHz, Chloroform-d) δ = 11.54 (s, 1 H), 9.47 (d, J = 9.2 Hz, 1 H), 7.92 (d, J = 8.9 Hz, 1 H), 7.64 - 7.58 (m, 2 H), 7.58 - 7.51 (m, 2 H), 7.51 - 7.45 (m, 3 H), 7.43 - 7.37 (m, 1 H), 7.36 - 7.28 (m, 3 H), 7.22 (t, J = 9.0 Hz, 1 H), 7.02 (s, 1 H); ¹³C NMR (125 MHz, Chloroform-d) δ = 195.9, 160.5, 160.3, 158.5, 158.3, 152.5, 145.8, 143.5, 142.9, 135.4, 133.5, 133.0, 131.4, 130.9, 130.5, 130.1, 129.8, 129.3, 127.4, 127.3, 124.5, 124.4, 124.3, 122.0, 121.1, 116.9, 116.6, 116.4, 116.1 (chemical shift in ppm); HR-MS: C₂₈H₁₇Cl₂F₂N₂O₅ 505.0681 (M+H)⁺

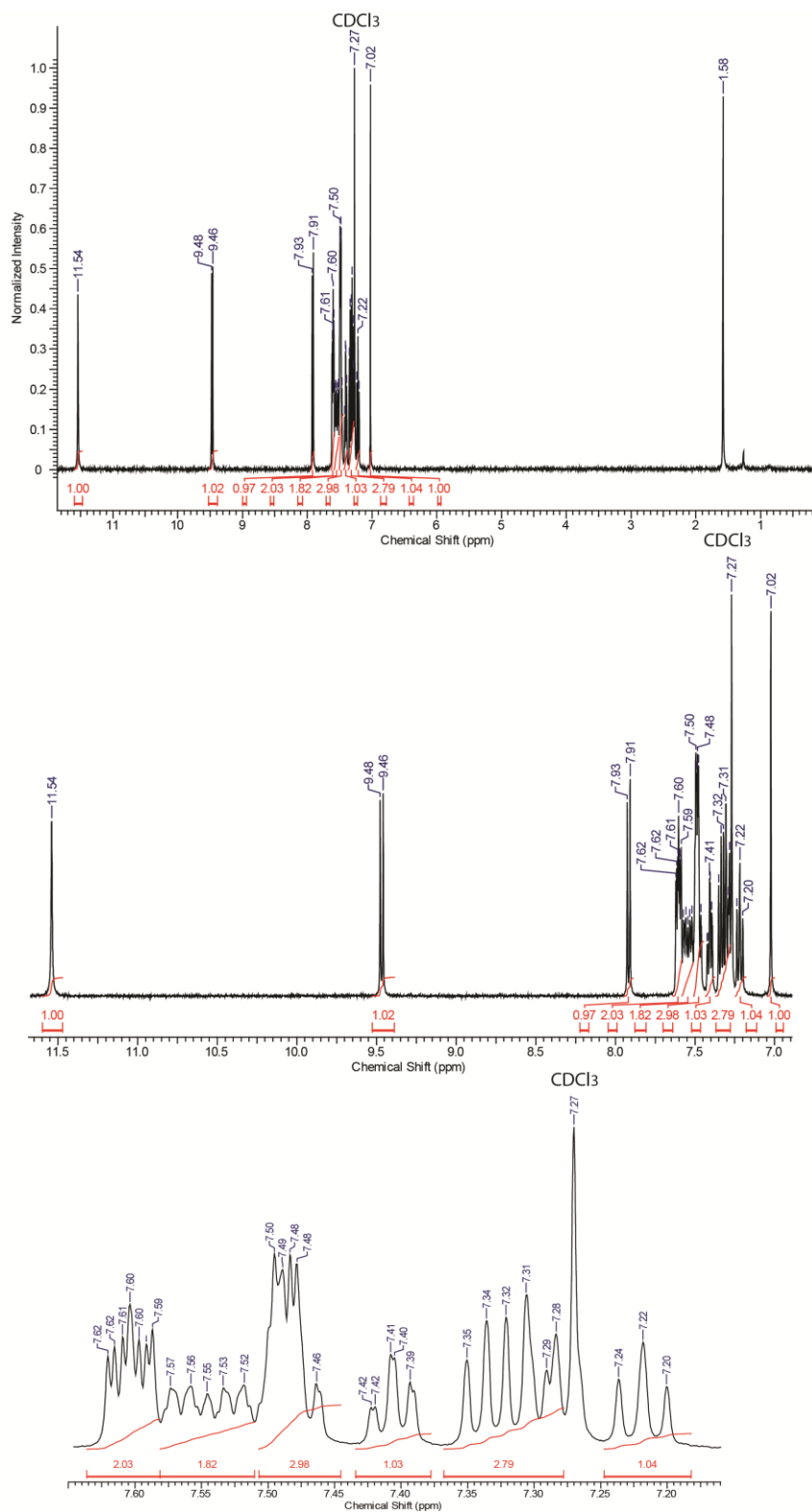


Figure 2.88. ^1H NMR of (5-chloro-2-((6-chloro-4-(2-fluorophenyl)quinolin-2-yl)amino)phenyl)(2-fluorophenyl)methanone (**3c**).

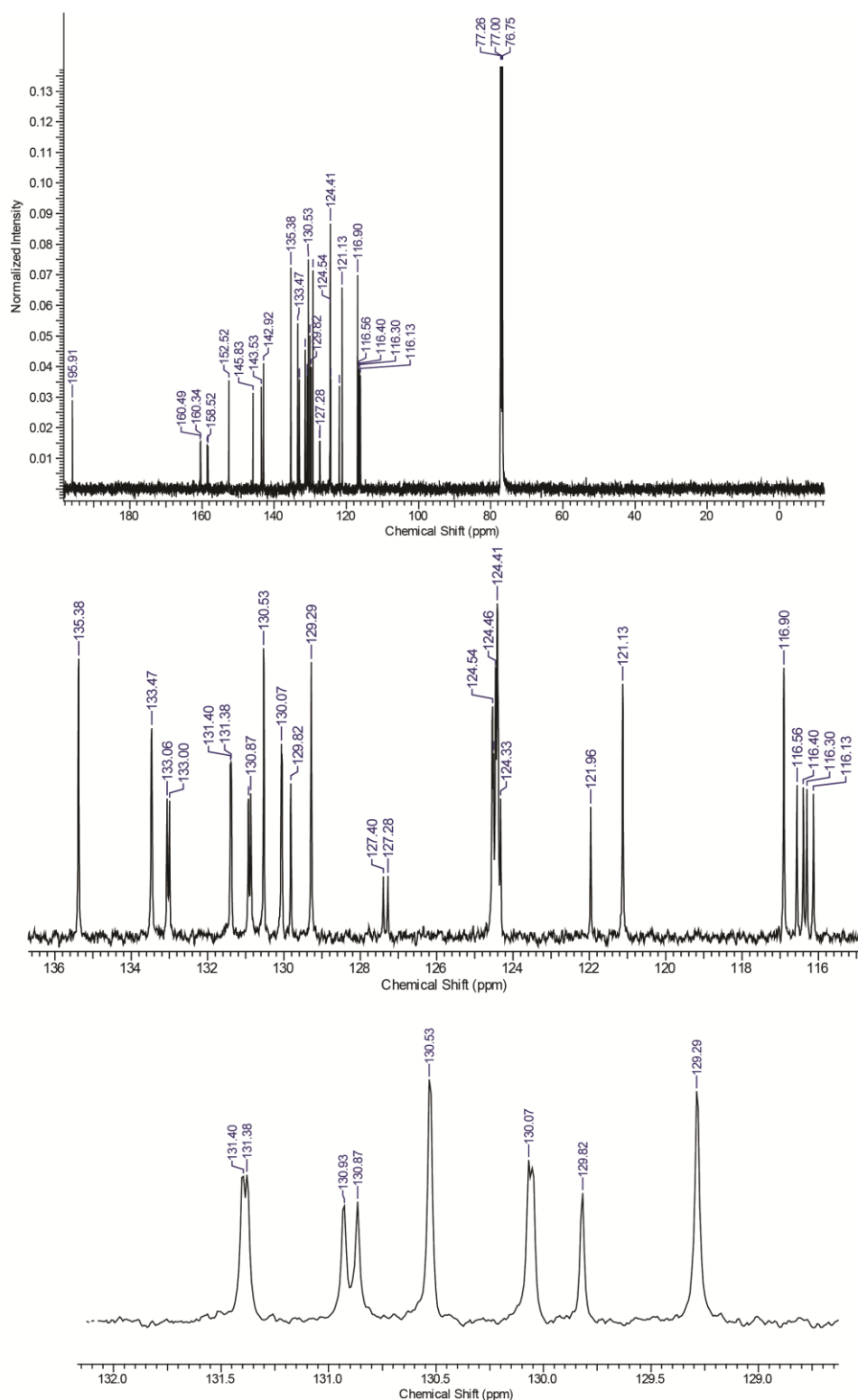


Figure 2.89. ^{13}C NMR of (5-chloro-2-((6-chloro-4-(2-fluorophenyl)quinolin-2-yl)amino)phenyl)(2-fluorophenyl)methanone (**3c**).

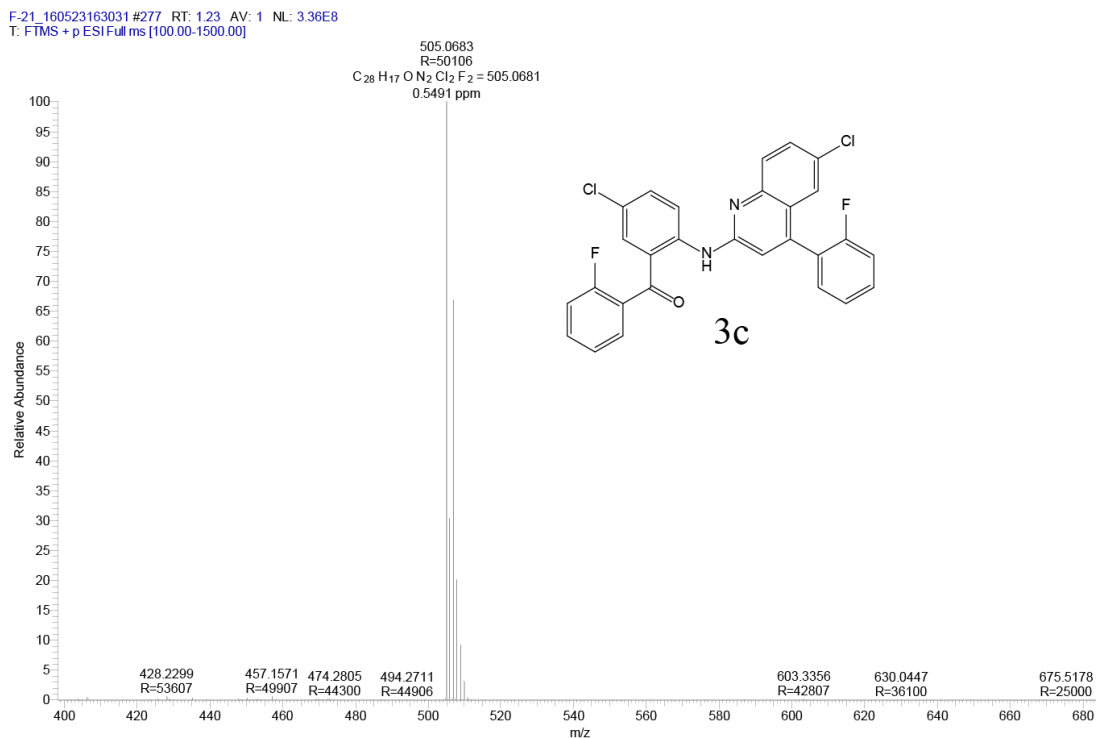


Figure 2.90. HR-MS of (5-chloro-2-((6-chloro-4-(2-fluorophenyl)quinolin-2-yl)amino)phenyl)(2-fluorophenyl)methanone (**3c**).

Synthesis of N-(4-chloro-2-(2-chlorobenzoyl)phenyl)acetamide (2d): Compound **2d** was prepared by similar procedure which was used for **2a** using 2-Amino-2',5-dichlorobenzophenone (2.661 g). The white precipitate is crystallized from ethanol solvent to obtain white needle shaped crystals of **2d** with the yield of (75-78%). ¹H NMR (400 MHz, Chloroform-d) δ = 11.41 (br. s., 1 H), 8.80 (d, J = 9.2 Hz, 1 H), 7.58 - 7.46 (m, 3 H), 7.46 - 7.37 (m, 1 H), 7.36 - 7.28 (m, 2H), 2.28 (br.s., 3H); ¹³CNMR (100MHz, chloroformd) δ = 198.3, 169.5, 140.4, 138, 135.6, 133.4, 131.7, 130.4, 128.7, 127.3, 126.9, 122.5, 122.3, 25.6 (chemical shift in ppm).

Synthesis of (5-chloro-2-((6-chloro-4-(2-chlorophenyl)quinolin-2-yl)amino)phenyl)(2-chlorophenyl)methanone (**3d**). Semisolid reaction mixture of compound **2d** (1 g) and PPA (10 g) was heated at 90 °C for 48 h. Further, the reaction mixture was cooled to room temperature to which saturated solution of sodium carbonate was added. The resulted yellow coloured precipitate was washed with water and purified by repeated crystallization to afford **3d** with the yield of 58-60%. ¹H NMR (500 MHz, chloroform-d) δ = 11.72 (s, 1 H), 9.56 (d, J = 9.2 Hz, 1 H), 7.93 (d, J = 8.9 Hz, 1 H), 7.64 - 7.57 (m, 3 H), 7.53 - 7.39 (m, 5 H), 7.38 - 7.34 (m, 2 H), 7.33 (t, J = 2.4 Hz, 2 H), 7.00 (s, 1 H); ¹³C NMR (126 MHz, chloroform-d) δ = 198.0, 152.6, 146.8, 145.7, 143.5, 138.5, 135.7, 133.7, 133.1, 131.3, 131.1, 130.9, 130.6, 130.2, 130.0, 129.9, 129.3, 128.6, 127.0, 126.9, 124.5, 124.3, 121.0, 116.6 (chemical shift in ppm); HR-MS: C₂₈H₁₇Cl₃ ³⁷ClN₂O 539.0060 (M+H)⁺

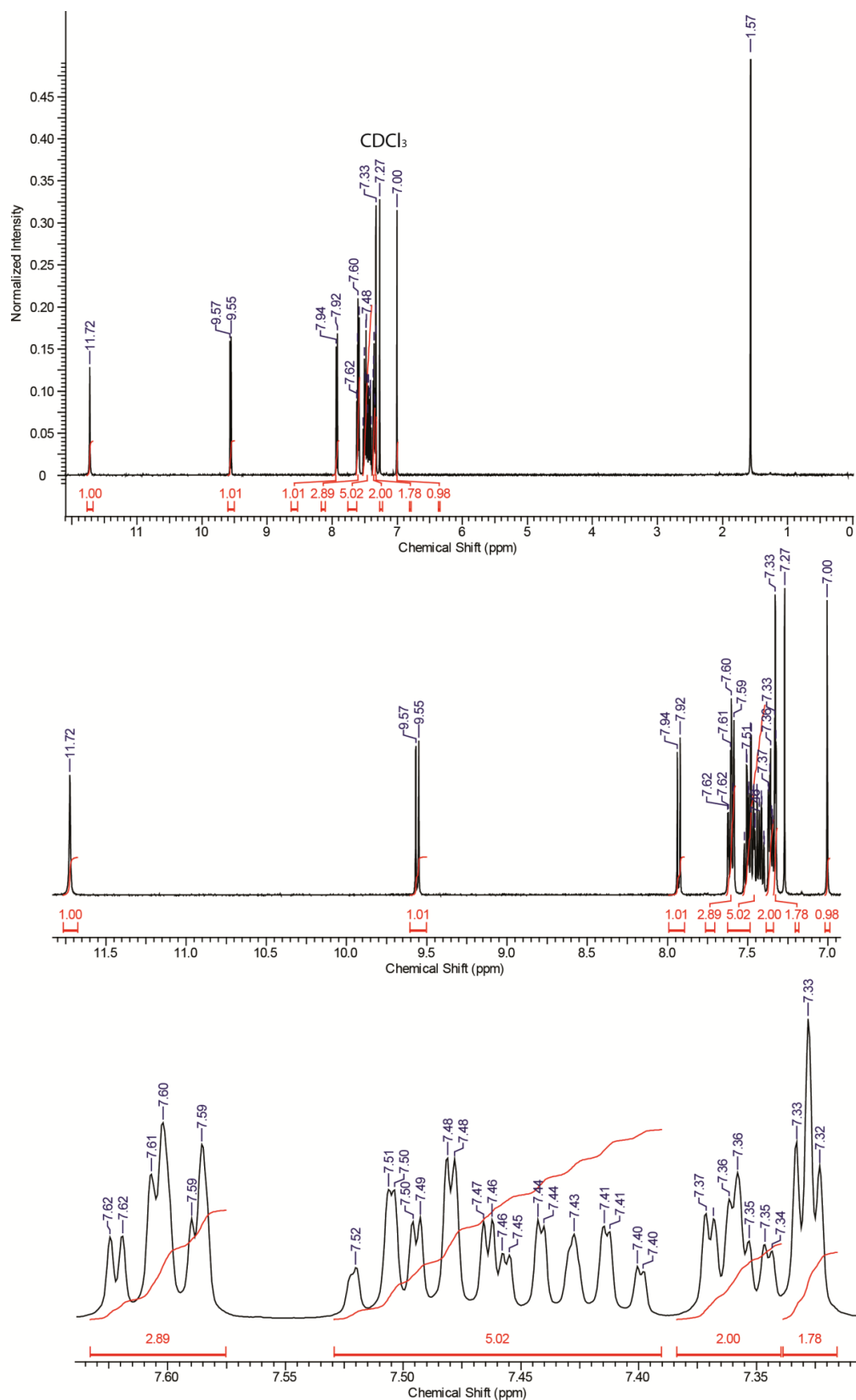


Figure 2.93. ^1H NMR of (5-chloro-2-((6-chloro-4-(2-chlorophenyl)quinolin-2-yl)amino)phenyl)(2-chlorophenyl)methanone(**3d**).

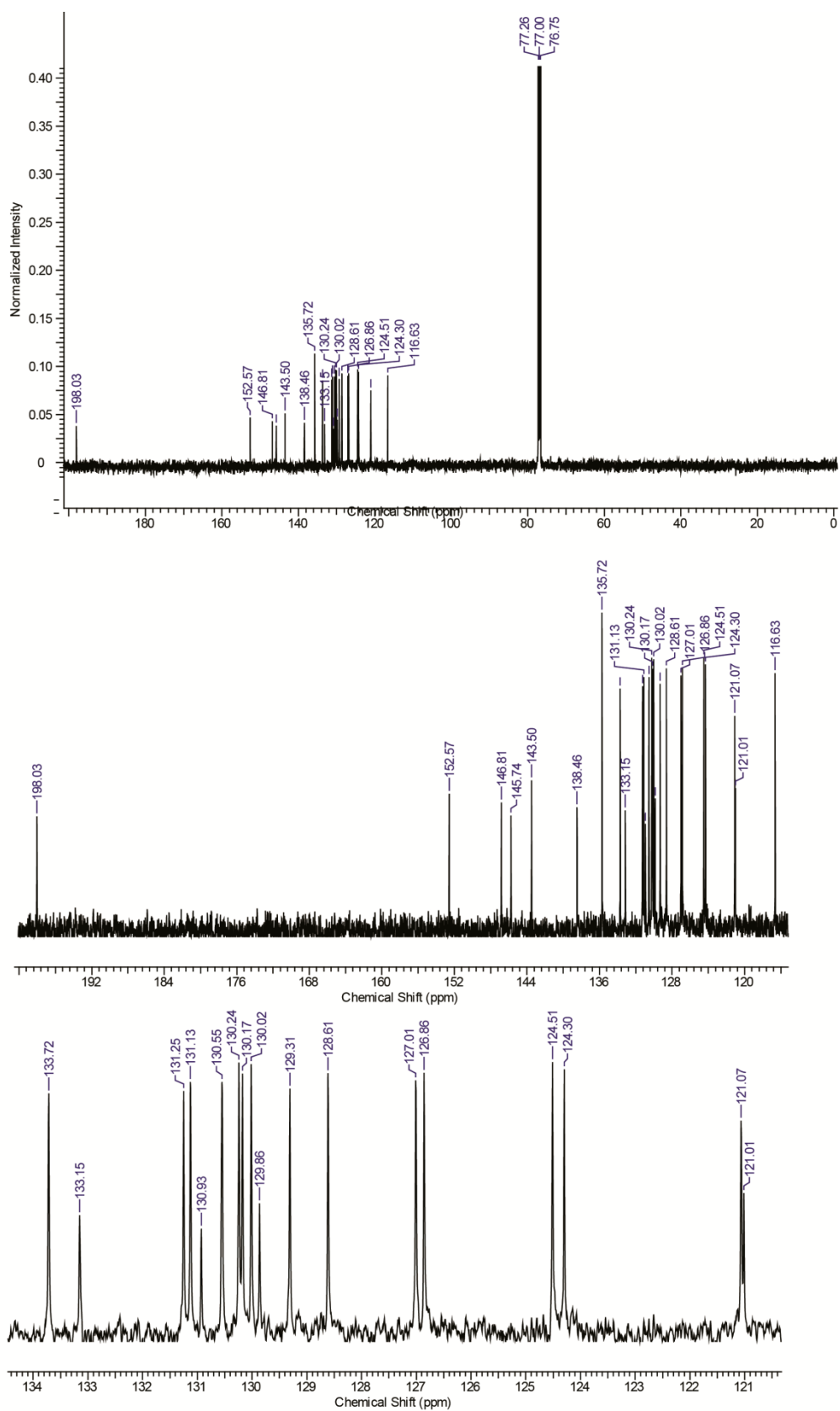


Figure 2.94. ^{13}C NMR of (5-chloro-2-((6-chloro-4-(2-chlorophenyl)quinolin-2-yl)amino)phenyl)(2-chlorophenyl)methanone(**3d**).

CL-21_160523162100 #405 RT: 1.82 AV: 1 NL: 3.02E8
T: FTMS + p ESI Full ms [100.00-1500.00]

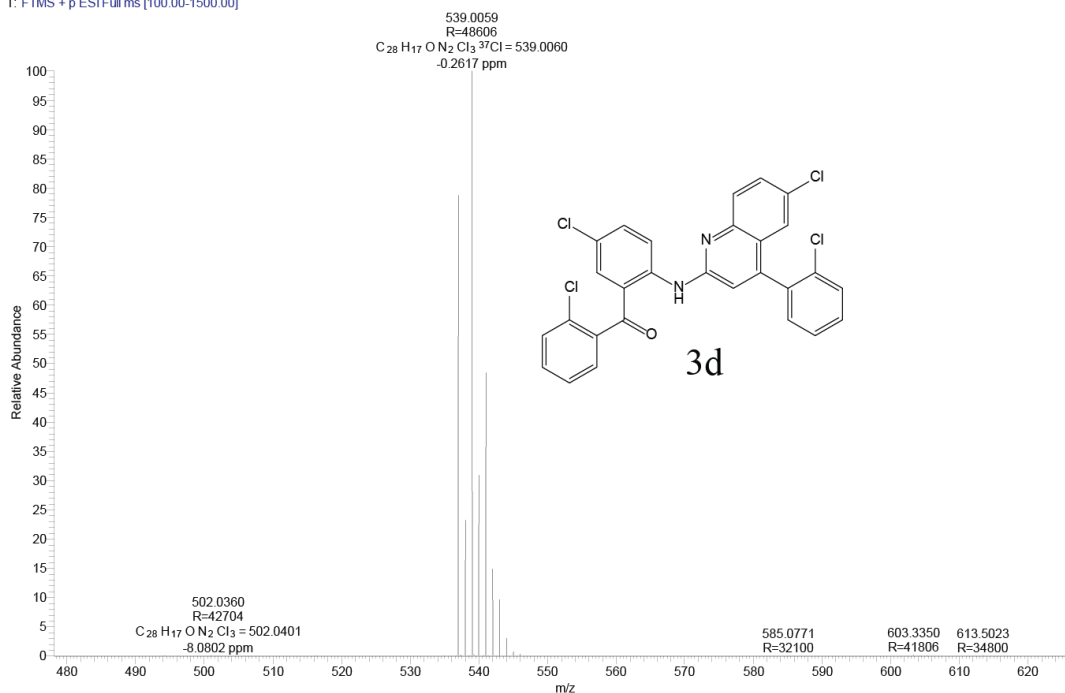


Figure 2.95. HR-MS of (5-chloro-2-((6-chloro-4-(2-chlorophenyl)quinolin-2-yl)amino)phenyl)(2-chlorophenyl)methanone(**3d**).

X-ray Crystallography: Single crystal structure of all compounds were determined by measuring X-ray intensity data on a Bruker SMART APEX II single crystal X-ray CCD diffractometer having graphite-monochromatised Mo-K α ($\lambda = 0.71073 \text{ \AA}$) radiation. The X-ray generator was operated at 50 kV and 30 mA. A preliminary set of cell constants and an orientation matrix were calculated from total 36 frames. The optimized strategy used for data collection consisted different sets of φ and ω scans with 0.5° steps in φ/ω . Data were collected keeping the sample-to-detector distance fixed at 5.00 cm. The X-ray data acquisition was monitored by APEX2 program suit. All the data were corrected for Lorentz-polarization and absorption effects (Multi scan) using SAINT and SADABS programs integrated in APEX2 package. The structures were solved by direct methods and refined by full matrix least squares, based on F, using SHELX-97. Molecular diagrams were generated using ORTEP-3 and Mercury programs. Geometrical calculations were performed using SHELXTL and PLATON. The H-atoms for the **3a**, **3b**, **3d**, **4b**, **4c**, **4d** crystals were placed in idealized positions however with different C-H distances (C-H = 0.95 \AA for the phenyl H atoms, C-H = 0.99 \AA for the methyl H-atoms and N-H = 0.88 \AA for the amide H atom) and constrained to ride on their parent atoms [$U_{\text{iso}}(\text{H}) = 1.2 U_{\text{eq}}(\text{C})$].

Table 2.6. Crystallography data table

Crystal Data	3a	3b	3d
Formula	C ₂₈ H ₂₀ N ₂ O	C ₂₈ H ₁₈ Cl ₂ N ₂ O	C ₂₈ H ₁₆ Cl ₄ N ₂ O
M _r	400.46	469.34	538.23
Crystal Size, mm	0.36 x 0.15 x 0.12	0.42 x 0.31 x 0.25	0.31 x 0.07 x 0.04
Temp. (K)	100(2)	100(2)	200(2)
Crystal Syst.	Triclinic	Monoclinic	Triclinic
Space Group	<i>P</i> -1	<i>P</i> 2 ₁ / <i>n</i>	<i>P</i> -1
<i>a</i> /Å	10.0148(5)	15.081(5)	4.8608(19)
<i>b</i> /Å	10.5944(5)	7.314(3)	10.244(4)
<i>c</i> /Å	10.6188(5)	21.017(8)	23.425(9)
α ⁰	94.323(2)	90	88.876(8)
β ⁰	110.357(2)	106.321(6)	88.069(9)
γ ⁰	100.515(2)	90	86.989(9)
<i>V</i> /Å ³	1026.70(9)	2224.8(14)	1164.0(8)
<i>Z</i>	2	4	2
<i>D</i> _{calc} /g cm ⁻³	1.295	1.401	1.536
<i>m</i> /mm ⁻¹	0.079	0.317	0.535
<i>F</i> (000)	420	299	548
<i>Ab. Correct.</i>	multi-scan	multi-scan	multi-scan
<i>T</i> _{min} / <i>T</i> _{max}	0.9906/0.9721	0.9250/0.8785	0.9789/0.8516
2 θ _{max}	50	50	50
Total reflns.	14837	15605	7995
uniquereflns.	3597	3907	3727
<i>h, k, l</i> (min, max)	(-11, 11), (-12, 11), (-12, 12)	(-17, 17), (-8, 8), (-24, 22)	(-5, 5), (-12, 9), (-27, 27)
<i>R</i> _{int}	0.0429	0.0597	0.0374
No. of para	281	299	367
<i>R</i> 1 [<i>I</i> > 2 σ (<i>I</i>)]	0.0420	0.0392	0.0782
<i>wR</i> 2 [<i>I</i> > 2 σ (<i>I</i>)]	0.1125	0.0992	0.1245
<i>R</i> 1 [all data]	0.0461	0.0550	0.1028
<i>wR</i> 2 [all data]	0.1169	0.1112	0.1328
goodness-of-fit	1.047	1.015	1.155
$\Delta\rho$ _{max} , $\Delta\rho$ _{min} (eÅ ⁻³)	+0.254, -0.247	+0.206, -0.242	+0.406, -0.390
CCDC no.	1454945	1454946	1454949

Crystal Data	4b	4c	4d
Formula	C ₂₈ H ₁₉ Cl ₃ N ₂ O	C ₂₈ H ₁₇ Cl ₃ F ₂ N ₂ O	C ₃₂ H ₂₀ Cl ₅ N ₂ O. 3(CHCl ₃)
M _r	505.80	541.79	932.79
Crystal Size, mm	0.32 x 0.25 x 0.09	0.31 x 0.12 x 0.07	0.25 x 0.16 x 0.07
Temp. (K)	100(2)	150(2)	150(2)
Crystal Syst.	Triclinic	Triclinic	Triclinic
Space Group	<i>P</i> -1	<i>P</i> -1	<i>P</i> -1
<i>a</i> /Å	10.0909(2)	10.2779(6)	11.7728(3)
<i>b</i> /Å	11.4151(2)	11.2636(7)	13.0601(4)
<i>c</i> /Å	11.8920(2)	12.4001(8)	14.0799(4)
α°	65.4230(10)	104.883(4)	113.9700(10)
β°	67.1890(10)	113.436(4)	97.3810(10)
γ°	78.7450(10)	101.427(4)	100.8700(10)
<i>V</i> /Å ³	1147.35(4)	1197.70(13)	1891.24(9)
<i>Z</i>	2	2	2
<i>D</i> _{calc} /g cm ⁻³	1.464	1.502	1.638
<i>m</i> /mm ⁻¹	0.425	0.424	1.050
<i>F</i> (000)	520	552	932
<i>Ab. Correct.</i>	multi-scan	multi-scan	multi-scan
<i>T</i> _{min} / <i>T</i> _{max}	0.9627/0.8759	0.9709/0.8797	0.9301/0.7792
2 θ _{max}	50	50	50
Total reflns.	90904	15686	27766
uniquereflns.	4039	4203	6640
<i>h, k, l</i> (min, max)	(-11, 11), (-13, 13), (-14, 14)	(-12, 12), (-13, 13), (-14, 14)	(-14, 14), (-15, 15), (-16, 16)
R _{int}	0.0407	0.0830	0.0409
No. of para	308	329	485
<i>R</i> 1 [<i>I</i> > 2 σ (<i>I</i>)]	0.0296	0.0736	0.0889
<i>wR</i> 2 [<i>I</i> > 2 σ (<i>I</i>)]	0.0772	0.1194	0.1571
<i>R</i> 1 [all data]	0.0304	0.1178	0.1093
<i>wR</i> 2 [all data]	0.0779	0.1330	0.1651
goodness-of-fit	1.057	1.123	1.198
$\Delta\rho_{\max}$, $\Delta\rho_{\min}$ (eÅ ⁻³)	+0.852, -0.295	+0.343, -0.411	+ 0.913, -0.655
CCDC no.	1454947	1454948	1454950

References:

1. F. I. Khan and S. A. Abbasi, *J. Loss Prevent. Proc.*, 1999, **12**, 361-378.
2. (a) M. E. Germain and M. J. Knapp, *Chem. Soc. Rev.*, 2009, **38**, 2543-2555; (b) C. McDonagh, C. S. Burke and B. D. MacCraith, *Chem. Rev.*, 2008, **108**, 400-422.
3. (a) X. Deng and L. S. Liebeskind, *JACS*, 2001, **123**, 7703-7704; (b) X. Chen, T. Pradhan, F. Wang, J. S. Kim and J. Yoon, *Chemi. Rev.*, 2012, **112**, 1910-1956; (c) J. Ern, A. T. Bens, H.-D. Martin, K. Kuldova, H. P. Trommsdorff and C. Kryschi, *J. Phys. Chem. A.*, 2002, **106**, 1654-1660; (d) Y. Liu, Y. Sun, J. Du, X. Lv, Y. Zhao, M. Chen, P. Wang and W. Guo, *Org. Biomol. Chem.*, 2011, **9**, 432-437.; (e) X. Chen, X. Wang, S. Wang, W. Shi, K. Wang and H. Ma, *Chem. Eur. J.*, 2008, **14**, 4719-4724.
4. (a) G. Sivaraman, B. Vidya and D. Chellappa, *RSC Adv.*, 2014, **4**, 30828-30831; (b) H. N. Kim, M. H. Lee, H. J. Kim, J. S. Kim and J. Yoon, *Chem. Soc. Rev.*, 2008, **37**, 1465-1472; (c) M. Tian, X. Peng, J. Fan, J. Wang and S. Sun, *Dyes and Pigments*, 2012, **95**, 112-115; (d) Z. Li, S. Wu, J. Han and S. Han, *Analyst*, 2011, **136**, 3698-3706; (e) M. Bradley, L. Alexander, K. Duncan, M. Chennaoui, A. C. Jones and R. M. Sanchez-Martin, *Bioorg. Med. Chem. Lett.*, 2008, **18**, 313-317; (f) H. Sun, A. M. Scharff-Poulsen, H. Gu and K. Almdal, *Chem. Mater.*, 2006, **18**, 3381-3384.
5. Z.-Q. Hu, M. Li, M.-D. Liu, W.-M. Zhuang and G.-K. Li, *Dyes and Pigments*, 2013, **96**, 71-75.
6. S. Kang, S. Kim, Y.-K. Yang, S. Bae and J. Tae, *Tetrahedron Lett.*, 2009, **50**, 2010-2012.
7. K. Tateno, R. Ogawa, R. Sakamoto, M. Tsuchiya, T. Otani and T. Saito, *Org. Lett.*, 2014, **16**, 3212-3215.
8. (a) R. M. Suarez, P. Bosch, D. Sucunza, A. M. Cuadro, A. Domingo, F. Mendicuti and J. J. Vaquero, *Org. Biomol. Chem.*, 2015, **13**, 527-538; (b) D. Sucunza, A. M. Cuadro, J. Alvarez-Builla and J. J. Vaquero, *J. Org. Chem.*, 2015, **19**, 4214-4223.
9. (a) A. Albert, R. Goldacre and J. Phillips, *J. Chem. Soc.*, 1948, 2240-2249; (b) A. Albert, D. J. Brown and H. C. S. Wood, *J. Chem. Soc.*, 1956, 2066-

- 2075;(c) A. Albert, W. Armarego and E. Spinner, *J. Chem. Soc.*, 1961, 2689; (d) C. K. Bradsher, R. W. L. Kimber and S. D. Mills, *J. Org. Chem.*, 1965, 30, 1539-1541.
10. N. P. Peet, S. Sunder, R. J. Barbuch, M. R. Whalon, E. W. Huber and J. C. Huffman, *J. Heterocycl. Chem.*, 1989, **26**, 1611-1617.
11. Bernstein, R. E. Davis, L. Shimoni and N. L. Chang, *Angew. Chem., Int. Ed.*, 1995, **34**, 1555-1573.
12. (a) A. D. Becke, *J. Chem. Phys.*, 1993, **98**, 5648–5652;(b) P. J. Stephens; F. J. Devlin, C. F. Chabalowski and M. J. Frisch, *J. Phys. Chem.*, 1994, **98**, 11623–11627; (c) W. J. Hehre, R. Ditchfeld and J. A. Pople, *J. Chem. Phys.* 1972, **56**, 2257.
13. Frisch, M. J.; Trucks, G. W.; Schlegel, H. B.; Scuseria, G. E.; Robb, M. A.; Cheeseman, J. R.; Scalmani, G.; Barone, V.; Mennucci, B.; Petersson, G. A.; Nakatsuji, H.; Caricato, M.; Li, X.; Hratchian, H. P.; Izmaylov, A. F.; Bloino, J.; Zheng, G.; Sonnenberg, J. L.; Hada, M.; Ehara, M.; Toyota, K.; Fukuda, R.; Hasegawa, J.; Ishida, M.; Nakajima, T.; Honda, Y.; Kitao, O.; Nakai, H.; Vreven, T.; Montgomery, J. A.; Peralta, J. E.; Ogliaro, F.; Bearpark, M.; Heyd, J. J.; Brothers, E.; Kudin, K. N.; Staroverov, V. N.; Kobayashi, R.; Normand, J.; Raghavachari, K.; Rendell, A.; Burant, J. C.; Iyengar, S. S.; Tomasi, J.; Cossi, M.; Rega, N.; Millam, J. M.; Klene, M.; Knox, J. E.; Cross, J. B.; Bakken, V.; Adamo, C.; Jaramillo, J.; Gomperts, R.; Stratmann, R. E.; Yazyev, O.; Austin, A. J.; Cammi, R.; Pomelli, C.; Ochterski, J. W.; Martin, R. L.; Morokuma, K.; Zakrzewski, V. G.; Voth, G. A.; Salvador, P.; Dannenberg, J. J.; Dapprich, S.; Daniels, A. D.; Farkas; Foresman, J. B.; Ortiz, J. V.; Cioslowski, J.; Fox, D. J. Gaussian 09, Revision B.01; Gaussian, Inc.: Wallingford, CT, 2009.
14. S. A. Jenekhe, L. Lu and M. M. Alam, *Macromolecules*, 2001, **34**, 7315-7324.
15. B.-K. An, S.-K. Kwon, S.-D. Jung and S. Y. Park, *JACS*, 2002, **124**, 14410-14415.
16. M. Segado, I. Gomez and M. Reguero, *Phys. Chem. Chem. Phys.*, 2016, **18**, 6861-6874.
- 17 P. Metrangolo, G. Resnati, T. Pilati and S. Biella, *Halogen Bonding in Crystal Engineering*, Springer Berlin Heidelberg, 2007, 105-136.

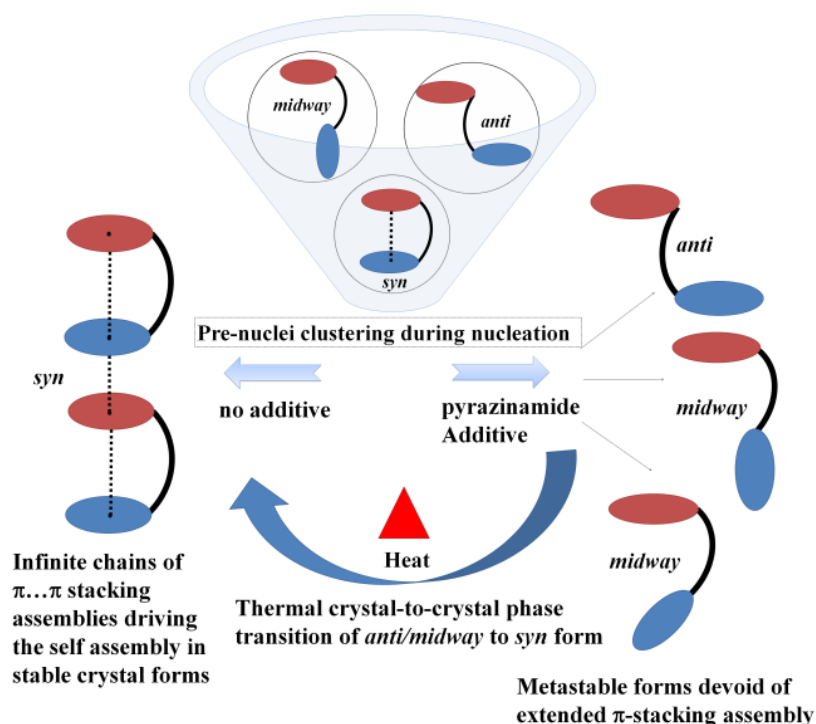
18. W.-S. Zou, S. Lin, J.-Y. Li, H.-Q. Wei, X.-Q. Zhang, D.-X. Shen, J.-Q. Qiao, H.-Z. Lian, D.-Q. Xie and X. Ge, *New J. Chem.*, 2015, **39**, 262-272.
19. K. Eskandari and M. Lesani, *Chem. Eur. J.*, 2015, **21**, 4739-4746.

Chapter 3

Study of Conformational Polymorphism of Flexible Sulfonamides and Sulfoesters having Alternating Electron Rich and Electron Deficient Aromatics

Most of the results presented in this chapter are published in the following paper:

R. L. Gawade, D. K. Chakravarty, A. Kotmale, E. Sangtani, P. V. Joshi, A. Ahmed, M. V. Mane, S. Das, K. Vanka, P. R. Rajamohanam, V. G. Puranik and R. G. Gonnade "Additive Mediated *Syn-Anti* Conformational Tuning at Nucleation to Capture Elusive Polymorphs: Remarkable Role of Extended π -Stacking Interactions in Driving the Self-Assembly", *Cryst. Growth Des.*, **2016**, *16*, 2416–2428



Conformationally flexible sulfonamide/sulfoester derivatives constituting electron-rich and electron-deficient aromatic rings were synthesized to study the interplay between π -stacking and hydrogen bonding synthons. The structure directing role played by the extended chain of π -stacking assemblies even in the presence of strong hydrogen bonding in tuning the *syn-anti* conformational switching during nucleation has been investigated by capturing their thermodynamically stable and additive mediated elusive metastable polymorphs.

Introduction:

Nucleation is the most crucial event during the crystallization process that has wide applications in various disciplines of science and technology.¹⁻⁸ Many experimental reports highlighted the formation of prenuclei clusters (PNC) at the supersaturation stage by self-assembly of molecules through well recognized supramolecular synthons.⁹⁻¹² Study of various polymorphic forms of the compounds provide structural insight of PNC which subsequently helps in the understanding of nucleation phenomena.^{13,14} Generally, strong intermolecular forces dominate the molecular aggregation event during the nucleation. However, sometimes the cumulative effect of weak interactions plays structure directing role and perturb the favorable assembly even in the presence of strong interactions. Hitherto, classical hydrogen bonds, halogen bonds are well studied by the crystal engineering approach.¹⁵⁻¹⁷ However, the role of stacking interactions for the molecular aggregation during the crystallization is unexplored.^{18,19} π -stacking assemblies between the aromatic moieties play a fundamental role in supramolecular assembly,²⁰ crystal engineering²¹ and molecular recognition^{22,23} processes. Their strength can be modulated by external influence that forms the basis of various biological as well as chemical processes such as proof-reading ability of DNA polymerases,²⁴ DNA intercalation,²⁵ drug receptor binding²⁶ and chemical sensing.²⁷ The molecular basis of π -stacking interaction is still debated²⁸⁻³². The electron rich and electron-deficient aromatic units are used in conjunction as a building blocks for designing functional materials.^{33,34} To gain insight into the nucleation dynamics and to investigate the interplay of π -stacking and hydrogen bonding synthons during nucleation, we synthesized aromatic sulfonamides **1**, **2** and sulfoesters **3**, **4** (**Figure 3.1**) possessing electron-deficient and electron-rich aromatic rings. Aromatic sulfonamides and sulfoesters were chosen for our study mainly due to their inherent polymorphic nature.³⁵⁻³⁷ and medicinal importance.³⁸ Our polymorphic trials with aromatic sulphonamide **1** (**Figure 3.1**) yielded thermodynamic stable crystal of form **II**. Surprisingly, we came across disappearing polymorph of **1** (form **III**) during its purification by chromatography which could not be reproduced later by traditional polymorph screening approaches and thus termed as disappeared polymorph.³⁹ Additive mediated polymorphism is routinely researched because of its implication in promotion, inhibition of crystal nucleation and growth, and assist in selective

nucleation of particular polymorphs.⁴⁰⁻⁴³ In a hunt for obtaining disappearing polymorph of **1**, we had screened many carboxamide group containing additives (as amides are known to form cocrystals with sulfonamides) that could alter nucleation event to generate new polymorphs. Finally, in the presence of pyrazinamide additive, we obtained elusive conformational and packing polymorphs of sulfonamide **1** (forms **1II**, **1III** and **1IV**). We further investigated the additive effect of pyrazinamide during crystallization of other sulfonamide i.e. **2** and sulfoester **3** and **4**. In this chapter, we report the additive mediated polymorphic behavior of compounds **1**, **2**, **3** and **4**. Co-crystallization trials of **1**, **2**, **3** and **4** with pyrazinamide additive in methanol/chloroform solution gave three new metastable polymorphs for **1** (forms **1II**, **1III** and **1IV**) and one new polymorph (form **II**) for each **2**, **3** and **4**. DSC, HSM, X-ray crystallographic studies substantiated thermal crystal-to-crystal transformation of all metastable polymorphs of **1** to its form **II** crystals suggesting the structure directing role of extended $\pi \cdots \pi$ stacking interaction in driving the self-assembly in crystals. The comparative analysis of the polymorphism, crystal-to-crystal phase transition, solution state ^1H NMR, HSM, ESEM study, melt crystallization, lattice matching analysis (Grace) and CSD survey helped us to unravel the mystery behind preferential stabilization of *syn* PNC during nucleation by extended chain of π -stacking assemblies in the crystal.

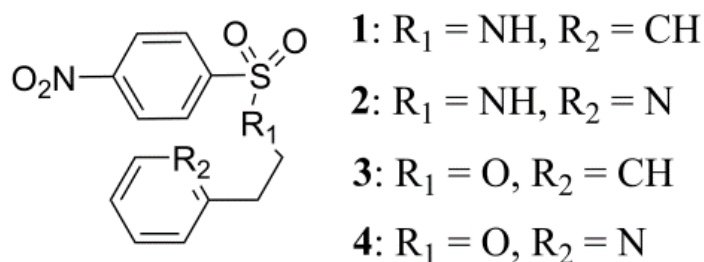


Figure 3.1. Structures of aromatic sulfonamides (**1**, **2**) and sulfoesters (**3**, **4**).

Results and Discussion:

Polymorphs of 1: Crystallization of sulfonamide **1** from common organic solvents yielded thick plate-like crystals which belong to monoclinic $P2_1/c$ space group (form **1I**). The crystallization from column fraction (10/90; ethyl acetate/petroleum ether) of **1** once gave polymorph of **1** (form **1III**) under the influence of unknown impurity. The form **1III** also crystallized in monoclinic $P2_1/c$ space group. However, the form **1III** crystals could not be reproduced again even after changing the crystallization conditions. The curious case of disappearing polymorph (form **1III** crystal) was used as the clue and screened many carboxamide containing additives like acetamide, formamide, benzamide, pyrazinamide etc. to capture metastable form **1III**. The carboxamides are used as additives because they are known to form cocrystals with sulfonamides through $N-H \cdots O=C$ hydrogen bonding synthons. Fortunately, we could capture disappeared polymorph form **1III** crystals in the presence of pyrazinamide additive. The use of pyrazinamide as an additive in various proportions during crystallization of **1** produced three metastable conformational polymorphs i.e. forms **1II**, **1III** and **1IV** crystals. Cocrystallization of **1** with pyrazinamide from a methanol/chloroform mixture (3/1, v/v) and in 1:3 stoichiometric ratio yielded the disappeared polymorph i.e form **1III** crystals along with form **1II** crystals (triclinic, $P-1$) concomitantly. These two forms could be differentiated by measuring their unit cell parameters. The crystallization of **1** and pyrazinamide in 1/1 ratio yielded the form **1II** crystals whereas crystallization of **1** with excess of pyrazinamide (ratio 1:10) produced thin plates, i.e. form **1IV** crystals (monoclinic $P2_1/c$) crystals. However, further attempts to obtain the form **1IV** crystals yielded the mixture of form **1II** and form **1III** crystals. Concentration of additives, the ratio and nature of solvents seemed to play a significant role in capturing the metastable polymorphs of **1** that is systematically investigated by crystallization trials.

Crystal structure details of all the polymorphs of **1** are summarized in **Table 3.5 (Experimental methods)**. Asymmetric unit of Forms **1I** and **1IV** crystals contained one molecule ($Z' = 1$) whereas Forms **1II** and **1III** crystals accommodated two molecules ($Z' = 2$). Both the symmetry independent molecules in form **1II** and form **1III** crystals are labeled as primed and unprimed. Crystal structures revealed significant conformational differences in the orientation of the phenyl rings due to the

flexible ethyl chain. The similarity in the unit-cell parameters of the polymorphs grossly resulted in isostructural molecular arrangement in crystals of form **1II** and form **1III** (**Table 3.5**). All the polymorphs of **1** reveal conformational polymorphism which display differences in the relative orientation of C1-S1-N2-C7 (τ_1), S1-N2-C7-C8 (τ_2) and N2-C7-C8-C9 (τ_3) torsions (**Table 3.6, Experimental methods**). Due to torsional variations, molecules in the polymorphs of **1** adopt either *synclinal*, *anticlinal* or *antiperiplanar* conformations at torsions τ_1 , τ_2 and τ_3 (**Figure 3.2**). Based on the relative orientation of phenylethane group with respect to the nitrobenzene sulfonyl group, form **1I** is found to be *syn* form, forms **1II** is *anti*, **1III** and takes *midway* conformation in form **1IV** crystals (**Figure 3.3**). The intra-molecular parallel displaced $\pi \cdots \pi$ stacking interaction between the electron deficient nitrobenzene ring and electron-rich benzene ring ($Cg \cdots Cg = 3.9178(11)$ Å, Cg-centroid of the benzene ring, **Figure 3.4a**) promote *syn* conformation of molecule in form **1I** crystals. Molecules in crystal structures of all the polymorphs of **1** are linked by N-H \cdots O=S hydrogen bonding that can be categorized into three types, type A and B (catemeric) which depends on the H-bonding with either *anti* (type A) or *syn* (type B) O acceptor atom and type C (dimeric supramolecular motifs, **Figure 3.5**). Additionally, weak interactions such as $\pi \cdots \pi$ also played a dominant role in the stabilization of the solid structures.

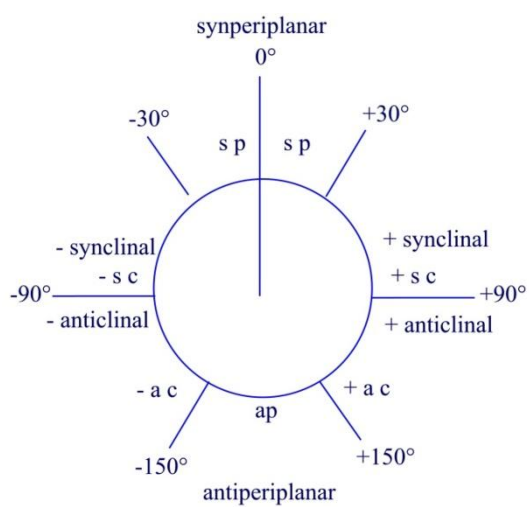


Figure 3.2. Description of conformations about a single bond.

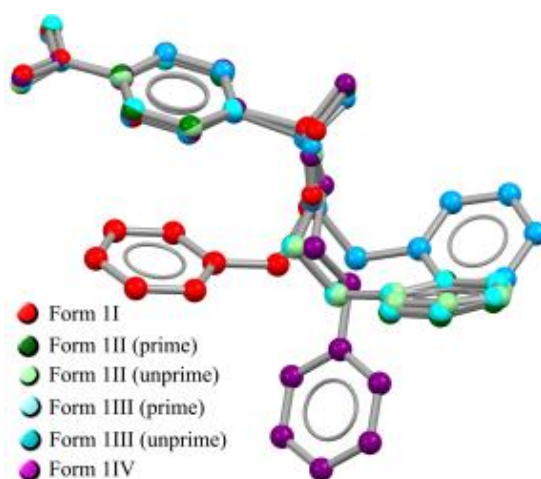


Figure 3.3. Structural overlay of polymorphs of **1**

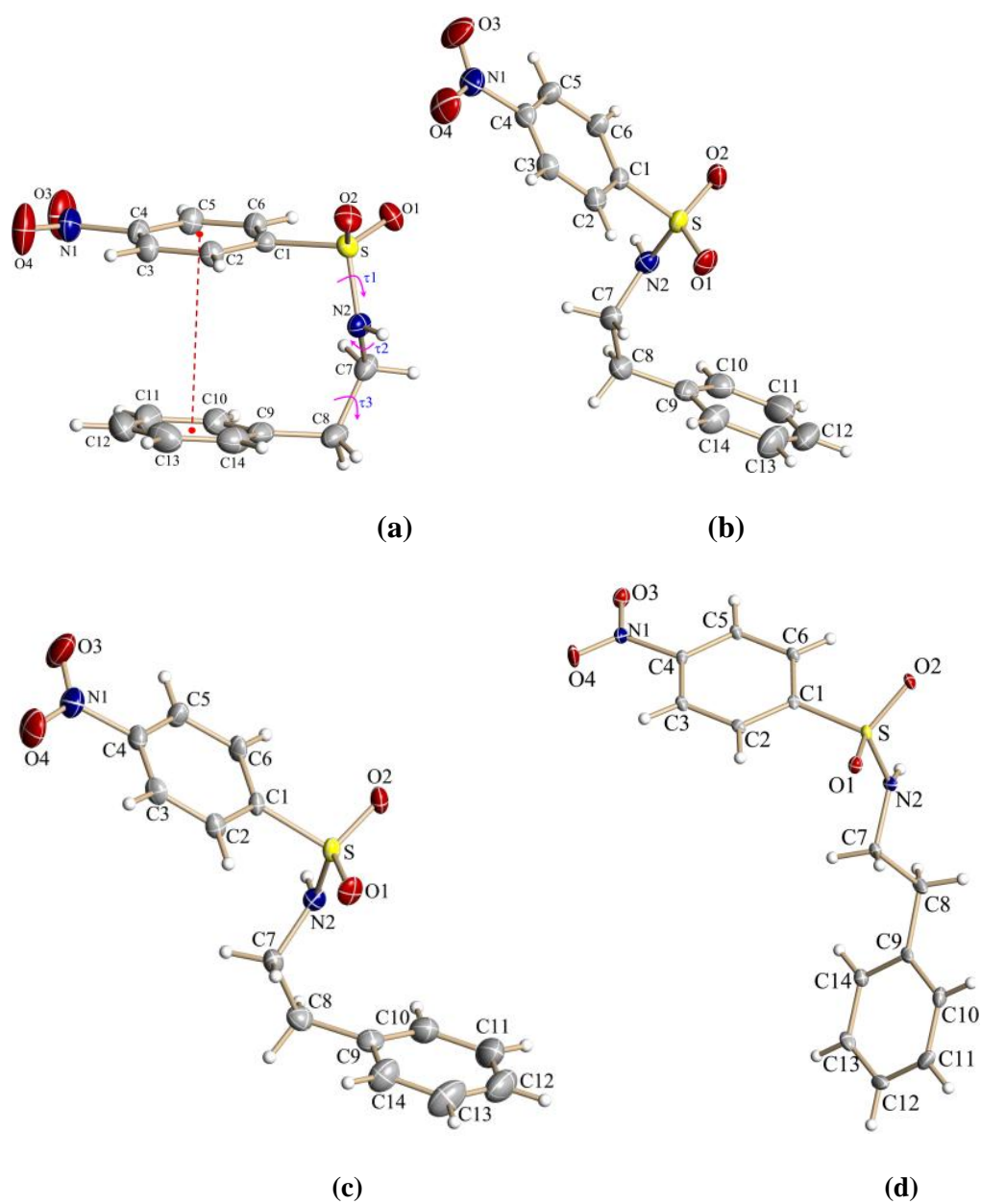


Figure 3.4 ORTEP of form (a) **1I**, (b) **1II**, (c) **1III** and (d) **1IV** crystals of **1** showing the atom numbering scheme. The displacement ellipsoids are drawn at the 50% probability level and H-atoms are shown as small spheres with arbitrary radii.

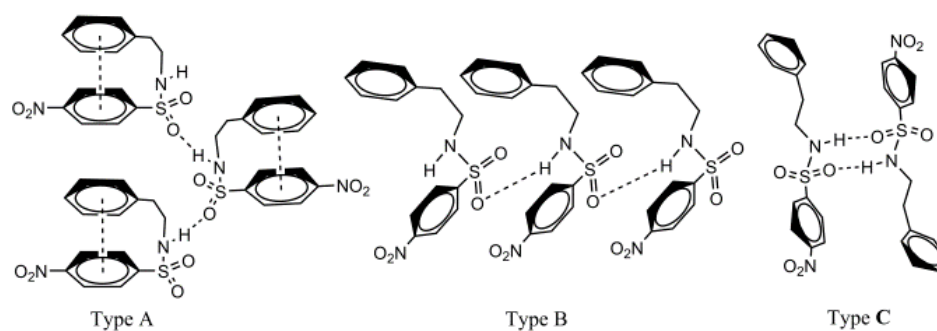


Figure 3.5. Different hydrogen bonding motifs observed in polymorphs of sulphonamide 1.

Neighboring molecules in form **II** crystals are associated to generate the type A motif that comprises of helical assembly across the crystallographic two-fold screw axis *via* conventional N2-H2N...O1 (entry 1, **Table 3.7, Experimental methods**) hydrogen bonds [Graph set⁴⁵: C(4)] involving amide H-atom and *anti* O acceptor atom of sulfonyl group (**Figure 3.6a**). The helical architecture is also supplemented by short C-H...O contacts (entry 2, **Table 3.7**). The helical association of molecules also brings the intra-molecularly stacked phenyl rings (entry 6, **Table 3.7**) in intermolecular stacking mode (entry 5, **Table 3.7**) to generate an extended chain of π -stacking assemblies ($Cg \cdots Cg = 3.8124(11) \text{ \AA}$). The neighboring helical assemblies are interconnected *via* centrosymmetric C-H...O interactions (entry 3, **Table 3.7**) along *a*-axis to produce 2D arrangement (**Figure 3.7a**). The formation of form **II** crystals exclusively in all the crystallization experiments signifies the importance of N-H...O and aromatic $\pi \cdots \pi$ stacking interactions in molecular aggregation. Molecular packing viewed down the helical axis reveals that $\pi \cdots \pi$ stacking assembly of molecules connected via C-H...O (entry 4, **Table 3.7**) contacts along the *c*-axis (**Figure 3.8**).

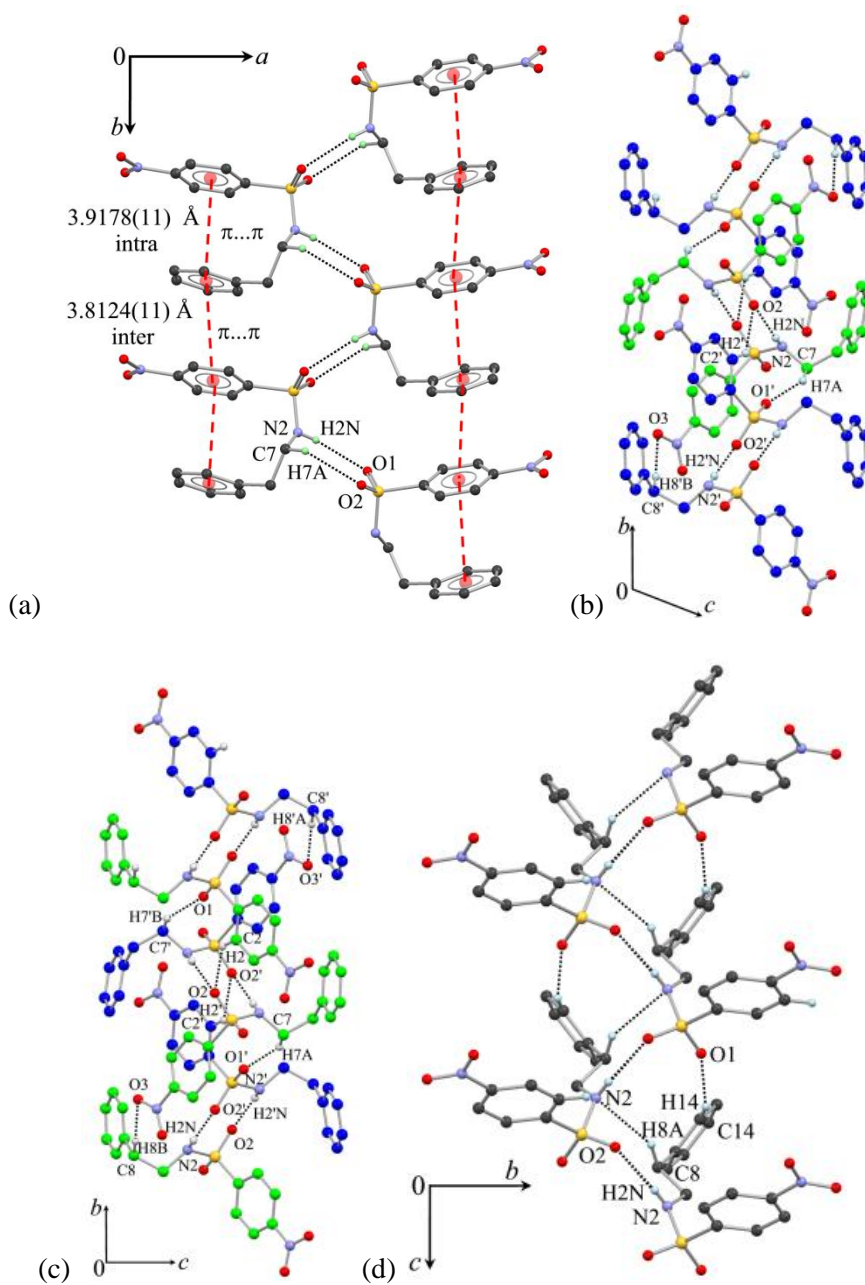


Figure 3.6. (a) and (d) helical association of molecules in form II and form IV crystals, (b) and (c) columnar arrangement of molecules in form III and form IIII crystals.

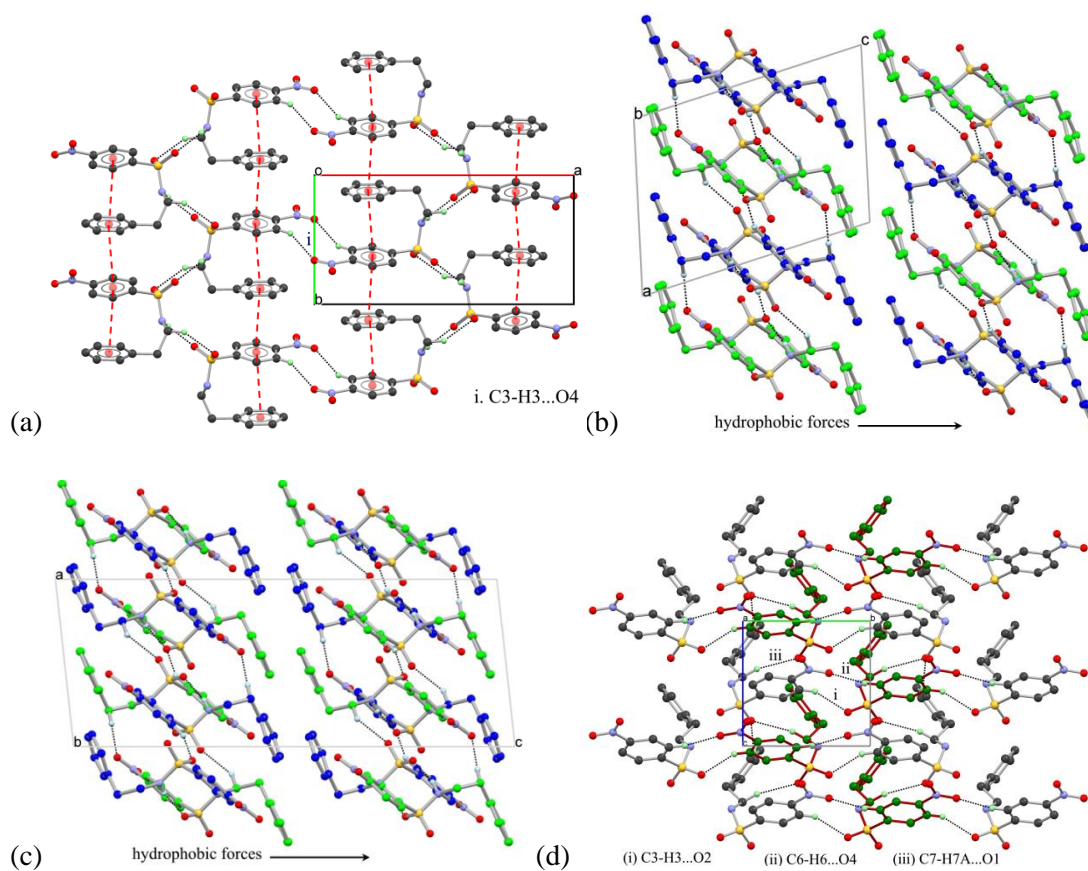


Figure 3.7. View of molecular packing in polymorphs of **1**, (a) form **1I**, (b) form **1II**, (c) form **1III** and (d) form **1IV** crystals.

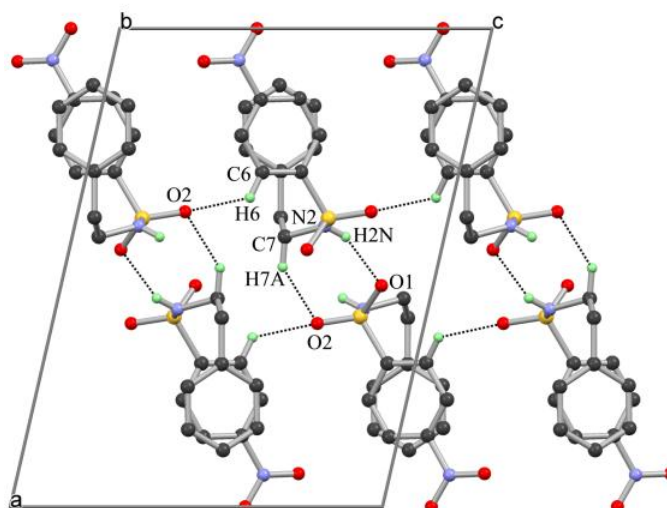


Figure 3.8. View of molecular packing down the helical axis (*b*-axis) in form **1I** crystals of **1**.

Crystal structure of forms **III** and **IIII** crystals of **1** reveals three dimensional isostructurality. In form **III** crystals both the symmetry independent molecules form their respective dimeric units *via* centrosymmetric N-H \cdots O hydrogen bonding [Graph set: R₂²(8)] involving *syn* O acceptor atom and N-H group (entries, 7-8, **Table 3.7**, **Figure 3.6b**). On the other hand, symmetry independent molecules in form **IIII** crystals together make a composite dimeric motifs (**Figure 3.6c**) through N-H \cdots O hydrogen bond [Graph set: R₂²(8)] involving *syn* O acceptor atom of primed molecule and N-H group of unprimed molecule and *vice versa* (entries 17, 18, **Table 3.7**). The dimeric units in both forms are linked through C-H \cdots O interactions to generate an extended columnar structure [**Figures 4.6b and 4.6c**, entries 9-11, 19-24, **Table 3.7**]. The adjoining columns in both forms are associated weakly along the *c*-axis *via* hydrophobic interactions (**Figures 4.7b and 4.7c**). No π -stacking extended assemblies were observed in these two crystal forms. The significant difference in the molecular organization in crystals of form **III** and form **IIII** crystals was seen along the third dimension (*b*-axis). The dimeric units are centrosymmetrically connected *via* C-H \cdots O interactions in form **III** (entries 9-13, **Table 3.7**, **Figure 3.9a**) whereas in form **IIII** crystals they are related by two fold screw axis (entries 19-25, **Table 3.7**, **Figure 3.9b**) to generate the extended chain structure. In Form **IIIV**, the *c*-glide related neighboring molecules formed catemeric type B assembly (**Figure 3.5**) *via* conventional N₂-H₂ \cdots O₂ hydrogen bond in C(4) motif involving amide H-atom and *syn* O acceptor atom supplemented by C-H \cdots O and C-H \cdots N contacts (**Figure 3.6d**, entries 27-29, **Table 3.7**). Although, π -stacking extended assembly observed in form **IIIV** crystals, but it is involved in combining the N-H \cdots O linked catemeric assemblies along with C-H \cdots O and C-H \cdots π contacts (entries, 30-35, **Table 3.7**, **Figure 3.6d**; **4.10**). Molecular packing viewed down the helical assembly revealed joining of neighboring helical chains *via* C-H \cdots O interactions (entry 33, **Table 3.7**) along the two-fold screw axis to generate discrete packing (**Figure 3.7d**, **3.10**). An interesting feature observed in all the polymorphs of **1** is the significant variation of their intramolecular geometries and their thermodynamic relationship. Based on the relative orientation of both the aromatic rings, form **II** crystal adopts *syn* geometry, however, molecules in forms **III** and **IIII** crystals acquired *anti* geometry whereas in form **IIIV** crystals, it achieved *midway* conformation (**Figure 3.3**; **Table 3.6**).

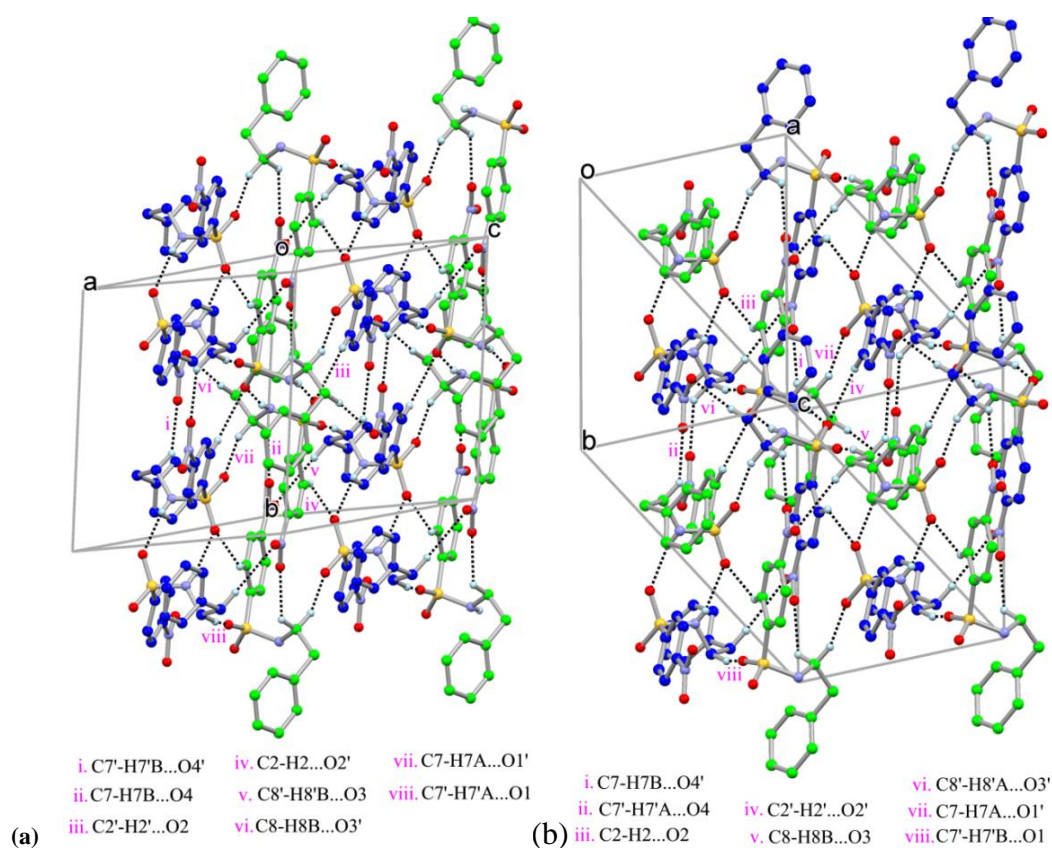


Figure 3.9. Molecular packing viewed along the *b*-axis revealing joining of the chains in (a) form 1II and (b) form 1III crystals of **1**.

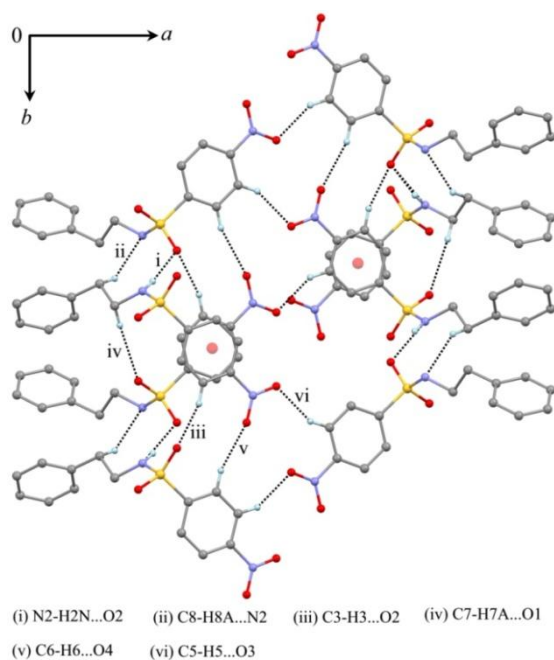


Figure 3.10. Molecular packing viewed along the *b*-axis revealing sparse packing in form 1IV crystals of **1**.

The *XPac* calculations⁴⁶ (see experimental methods for details) revealed high degree of similarity in three dimensional supramolecular construct of forms **1II** and **1III** with value of dissimilarity index $x = 2.8$. The *XPac* plot of δa against δp (mean differences in corresponding intermolecular angles and planes) for forms **1II** and **1III** revealed all $(\delta a, \delta p)$ points near to the origin of the coordinate system suggesting close similarity between the two structures (**Figure 3.11**).

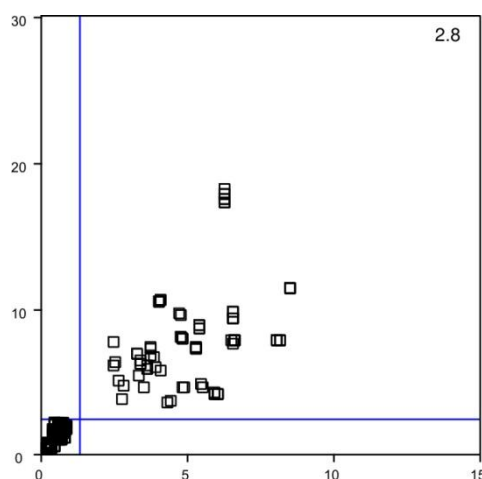


Figure 3.11. Plot of interplanar angular deviation (δp , x-axis) vs angular deviation (δa , y-axis) in *XPac* with dissimilarity index of 2.8 for form **1II** and form **1III** crystals of **1**

Differential scanning calorimeter (DSC) analysis (**Figure 3.12a**) of form **1II** and form **1III** crystals revealed a single melting endotherm centered at 94.8 °C and 78.2 °C respectively. DSC thermogram of form **1II** and form **1IV** showed small endothermic peaks centered around 78.0 °C and 72.0 °C respectively before their respective melting endotherms observed at 93.0 °C and 91.2 °C, indicating possibility of structural phase transition. Interestingly, the melting endotherm temperature of form **1III** crystals matched with the phase transition temperature of form **1II** crystals. This suggests that at 78.0 °C, crystal lattice in form **1II** crystals could sustain the structural rearrangement and precluded the collapse of lattice. However, the molecular movements involved in form **1III** crystals might be too large at 78.0 °C, resulting into crumbling of the lattice and eventually melting of the crystals. Interestingly, the DSC profile of crushed sample of form **1III** crystals was found to be similar to that of form **1II**, indicating the existence of phase transformation of form **1III** crystals to form **1II** crystals on gentle grinding.

The *in situ* variable temperature PXRD studies revealed that the form **1II** crystals undergo phase transition to form **1I** crystals after the transition temperature (**Figure 3.12b**). Overlay of the experimental PXRD of form **1III** crystal completely matched with experimental PXRD pattern of grinded sample of form **1III** crystals validating the phase transition of form **1III** to form **1II** crystals on grinding (**Figure 3.12c**). Experimental PXRD measurement of form **1IV** crystals could not be carried out due to its non-reproducibility. Interestingly, HSM studies of form **1II** (**Figure 3.12d-top**) and form **1IV** (**Figure 3.12d-bottom**) crystals have showed some alterations on the crystal surface at temperature 77 °C and 71 °C respectively. During HSM study, in both the crystal forms, rapid movement of transition front from one end to the other was observed, that resulted in the generation of multiple crystals. The determination of the unit cell parameters of a single crystalline fragment of both the crystal forms revealed them to be the crystals of form **1I**, suggesting irreversible phase transition. Interestingly we also observed that crystals and grinded sample (marked in circle) of form **1III** crystals behaved differently during HSM experiment. Crystals of **1III** melted at 78°C while the grinded sample of the same, melted at around 90°C (**Figure 3.12d-middle**).

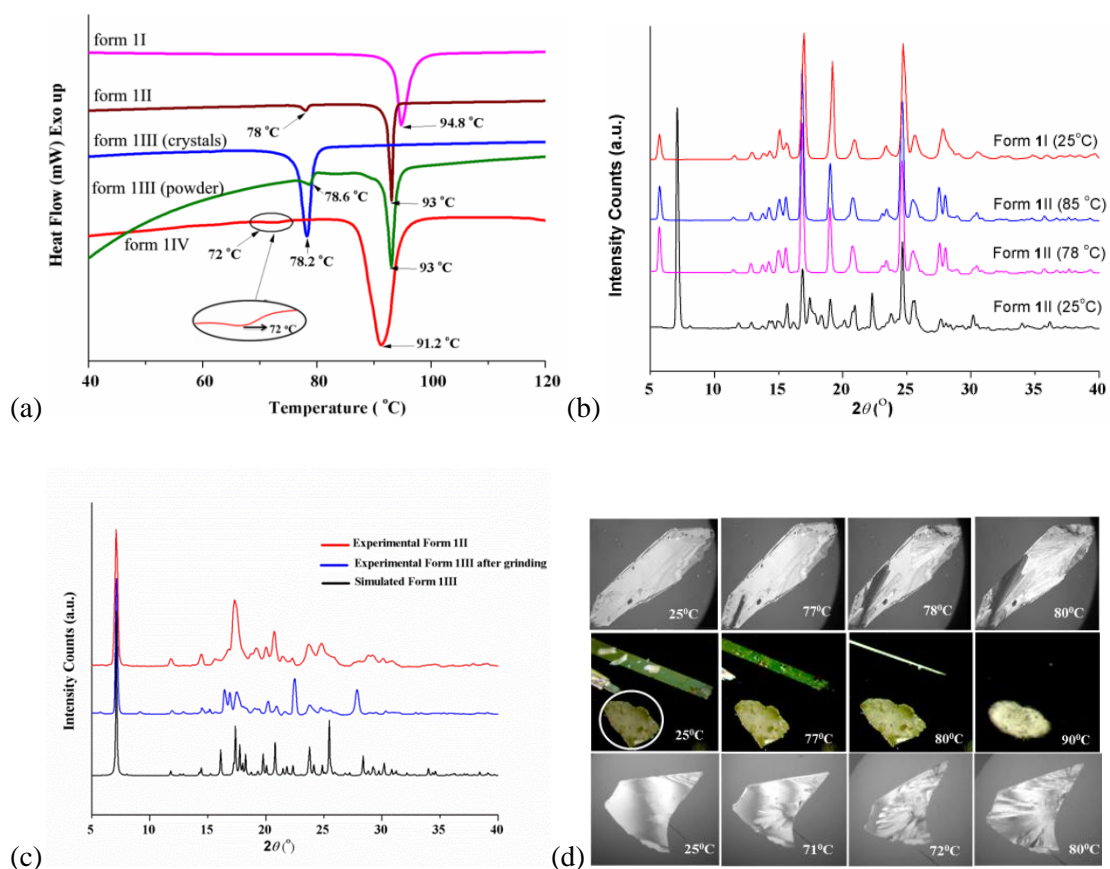


Figure 3.12 (a) Overlay of DSC profiles of polymorphs of **1**, form **II** (magenta), form **III** (brown), form **III** (crystals, blue), form **III** (powder, green) and form **IIV** (red). (b) Variable temperature *in-situ* PXRD experiment showing overlay of diffractograms of form **II** and form **III** crystals of **1**. (c) Overlay of PXRD patterns of form **III** (experimental) and form **III** (simulated and experimental) crystals of **1** showing phase transition of form **III** crystals to form **III** crystals through grinding. (d) Photomicrographs of the crystals during HSM studies (top) form **III** crystals, (middle) form **III** crystals and its grinded powder (circled), (bottom) form **IIV** crystals.

The evaluation of lattice energies using CLP package⁴⁷ gave a value of -137.8 kJ/mol, -157.4 kJ/mol, -159.0 kJ/mol and -159.2 kJ/mol for forms **II**, **III**, **III** and **IIV** respectively, indicating that form **III**, **III** and **IIV** have comparable stability while form **II** crystals are least stable. The estimation of crystal densities 1.415 g cm⁻³ (form **II**), 1.395 g cm⁻³ (form **III**), 1.406 g cm⁻³ (form **III**) and 1.442 g cm⁻³ (form **IIV**) indicates that form **IIV** is the most stable form, however it is not consistent with the calculated lattice energies pertaining to other polymorphs. Additionally, using CLP

package, intermolecular interaction energies for N-H \cdots O interaction was also calculated, that was observed to be present in all the polymorphs of **1**. The observed value of intermolecular interaction energies for N-H \cdots O interactions was found to be similar (-47 to -50 kJ/mole) in all the polymorphs of **1**, demonstrating its comparable strength and equal contribution to the overall crystal lattice stabilization. However, the preferential growth of form **1I** crystals and conversion of all the captured elusive polymorphs of **1** to form **1I** crystals, suggests indispensable contribution of other interactions. In form **1I** crystals, other than N-H \cdots O interactions, the contributions of aromatic $\pi\cdots\pi$ contacts is dominant which generates an extended helical chain structure. The evaluation of the intermolecular potential⁴⁸⁻⁴⁹ gave the first rank to the extended chain of $\pi\cdots\pi$ interactions (-35.0 kJ/mol) even in the presence of stronger N-H \cdots O interactions which gets third rank (-25.9 kJ/mol) which is lower than C-H \cdots O interactions (-30.8 kJ/mol, **Figure 3.13, Table 3.1**). In form **1II** and form **1III**, where molecules do not associate via extended chain of $\pi\cdots\pi$ interactions, only N-H \cdots O interactions significantly dominates the intermolecular potential values (**Figures 3.14-3.15, Table 3.1**). However, in form **1IV** crystals, the $\pi\cdots\pi$ contacts dominates over stronger N-H \cdots O interactions which is ranked second (**Figure 3.16, Table 3.1**). It implies that although $\pi\cdots\pi$ stacking interactions are usually considered to be weak compared to the conventional N-H \cdots O hydrogen bonding interactions, the extended series of such association assists in the maximum overlap between the molecules and also dictated the molecular packing as observed in form **1I** crystals. This can be a major reason behind preferential formation of form **1I** crystals during all the crystallization events (thermodynamically stable form) as well as the thermal transformation of all the metastable polymorphs to form **1I** crystals.

Table 3.1. Intermolecular interactions and potentials values for polymorphs of **1**.

Interactions	Intermolecular potentials
form 1I Crystals	
Extended chain of $\pi \cdots \pi$ interactions	-35.0 kJ/mol
Linking of molecules <i>via</i> weak C-H \cdots O interactions namely C13-H13 \cdots O3 and C8-H8 \cdots O2	-30.8 kJ/mol
Intermolecular potential associated with N2-H2N \cdots O1 and C7-H7A \cdots O2 interactions	-25.9 kJ/mol
form 1II	
Dimeric association through N-H \cdots O [$R_2^2(8)$] hydrogen bonds N2-H2N \cdots O2 N2'-H2'N \cdots O2'	-58.9 kJ/mol -57.9 kJ/mol
Linking of asymmetric unit molecules through C2'-H2' \cdots O2, C7-H7A \cdots O1' and C8'-H8'B \cdots O3 and C2-H2 \cdots O2' and C7-H7 \cdots O1' along the columnar assembly	-46.8 kJ/mol and -46.3 kJ/mol
form 1III	
Dimeric association involving both the asymmetric unit molecules through N-H \cdots O [$R_2^2(8)$] interactions N2-H2N \cdots O2' N2'-H2'N \cdots O2	-59.7 kJ/mol -59.7 kJ/mol
Linking of these dimeric units along the columnar assembly through C7-H7A \cdots O1' and C7'-H7'B \cdots O1 interactions	-46.8 kJ/mol and -46.5 kJ/mol
form 1IV	
Molecules associated via C7-H7A \cdots O1, C13-H13 \cdots π and $\pi \cdots \pi$ interactions	-67.9 kJ/mol
Catameric association through N2-H2N \cdots O2 and C8-H8A \cdots N2 interactions	-42.5 kJ/mol

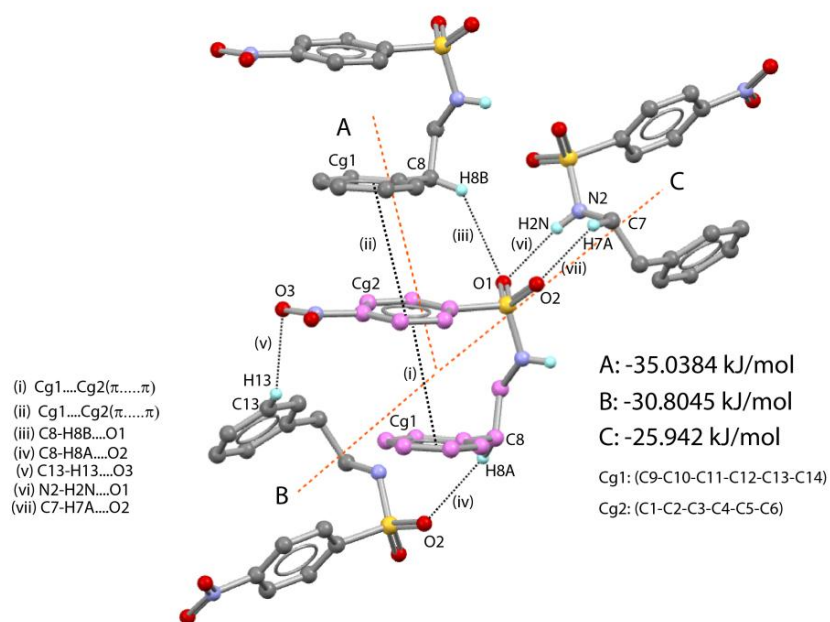


Figure 3.13. Intermolecular potentials values for form II crystals of **1**.

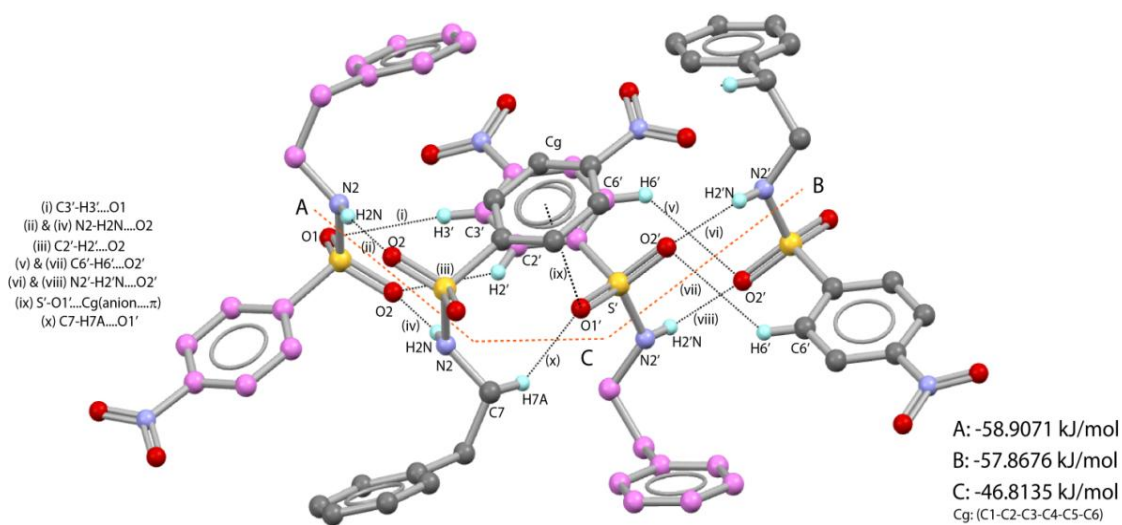


Figure 3.14. Intermolecular potentials values for form III crystals of **1**.

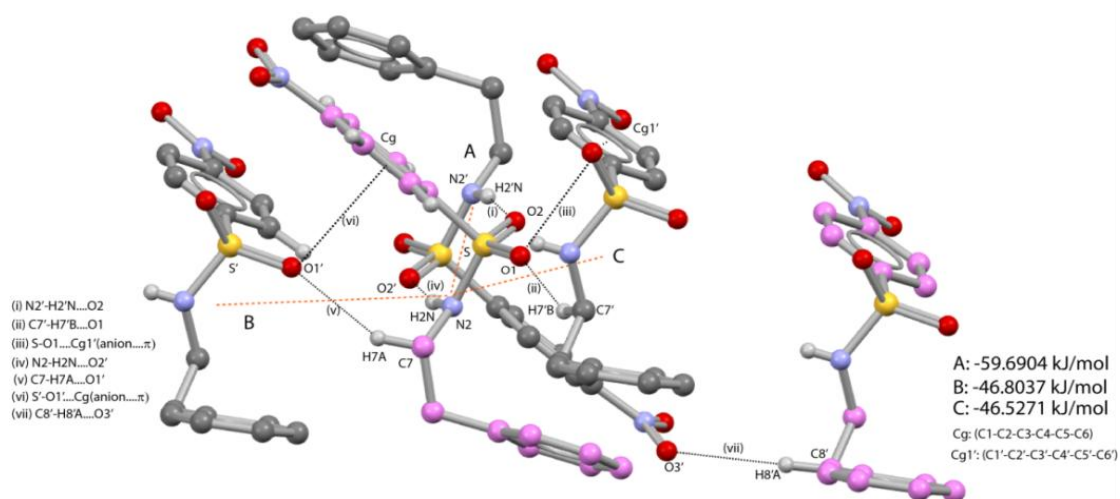


Figure 3.15. Intermolecular potentials values for form III crystals of **1**.

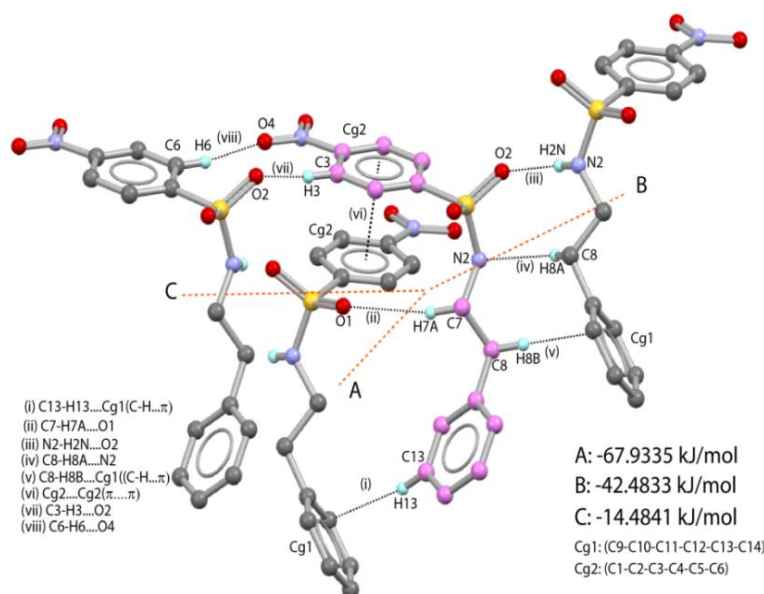


Figure 3.16. Intermolecular potentials values for form IIV crystals.

The thermal conversion of all metastable polymorphs of **1** to their most stable form **II** crystals, as evidenced by DSC, HSM, and X-ray crystallographic studies, could be attributed to the molecular zeal to attain the most preferred *syn* geometry supplemented by the infinite chain of $\pi\cdots\pi$ stacking assemblies. Although it is difficult to recognize the exact mechanistic pathways concerning the molecular movements for the conversion of forms **III**, **III** and **IIV** crystals to form **II** crystal, the comparison of the molecular packing in all the four crystal forms can somewhat ascertain the mechanism of transition. Probable mechanism involving the molecular

movement during phase transition of the metastable forms of **1III** and **1IV** crystals to form **1I** crystals is hypothesized (**Figure 3.17**). For the conversion of form **1III** and form **1IV** crystals to form **1I** crystals, the molecules possessing *anti* (form **1III**) and *midway* (form **1IV**) conformations, and are assembled *via* dimeric (form **1III**), and catemeric (form **1IV**) N-H...O hydrogen bonding interactions have to exhibit significant conformational change to establish the *syn* conformation observed in form **1I** crystals at the transition temperature. The conformational flexibility will thus facilitate intra-molecular orientation to achieve *syn* conformer and generate the catemeric chain linked by N-H...O hydrogen bonding interactions leading to the formation of an extended chain of π -stacking interactions contained in form **1I** crystals.

The Form **1III** to Form **1I** transition can be visualized along the *a*-axis wherein N-H...O linked neighboring dimeric motifs places the symmetry independent molecules in proximity thus creating the extended chain of molecules connected by C7-H7A...O1' and C7'-H7'A...O1 interactions (**Figure 3.17**). This would involve the breaking of N-H...O linked dimeric association of the neighboring asymmetric unit molecules accompanied by conformational change to achieve the most favored *syn* geometry and the subsequent generation of catemeric assembly through N-H...O interactions involving *anti* O atom and chain of intra as well as intermolecular π ... π stacking interactions. Thus it appears that during the phase transition molecules sacrifice strong dimeric N-H...O interactions in Form **1III** crystal to attain an N-H...O linked catemeric assembly dictated by π ... π stacking interactions in thermodynamically stable Form **1I** crystals.

The crystal-to-crystal transformation of Form **1IV** crystals to Form **1I** crystals should also involve the considerable conformational change to achieve the conformation of molecules comprising intramolecular π ... π stacking geometry observed in Form **1I** crystals. Molecules in Form **1IV** crystals are associated more strongly through N-H...O hydrogen bonding interactions engaging N-H and *syn* O atom to generate catemeric assembly having *c*-glide relationship between the molecules while in Form **1I** crystals molecules formed similar assembly through 2_1 screw axis related molecules supported by extended chain of π ... π stacking interactions. The transformation of Form **1IV** to Form **1I** crystals should involve molecular arrangement to bring about these changes, irrespective of the mechanistic

pathways followed. The transition can be envisaged along the *c*-axis wherein N-H···O linked molecules formed the catemeric assembly through *c*-glide symmetry. The transition would involve the breaking of N-H···O hydrogen bonding interaction between the N-H and *syn* O atom followed by conformational change to achieve the most preferred *syn* geometry facilitated by intramolecular $\pi\cdots\pi$ stacking pull with subsequent generation of catemeric assembly through N-H···O interactions involving anti O atom and chain of intra as well as intermolecular $\pi\cdots\pi$ stacking interactions (**Figure 3.17**).

The shear-induced conversion of form **1III** to form **1II** crystals on mechanical grinding is noteworthy. The transition can be simply achieved by small sliding of dimeric synthons along *b*-axis in form **1III** crystals (**Figure 3.18A**). The transition mechanism was also hypothesized using the understanding of morphotropism (**Figure 3.18B**).⁵⁰ In both crystal forms, molecules displayed roughly three-dimensional isostructurality confirmed by *XPac* calculations. The dimeric motifs formed through N-H···O hydrogen bonding interactions generate the extended columnar assembly. The only difference is that inversion center relates dimeric motifs in form **1II** crystals whereas molecules in form **1III** crystals have two-fold screw relationship. The transition of form **1III** crystals to form **1II** crystals by gentle grinding indicates conversion could be achieved by simple sliding of the layers along the *b*-axis. The conversion of form **1III** crystals to form **1II** crystals has also been sought from the knowledge of morphotropism. Careful examination of the packing patterns of molecules revealed that they are closely related and differ by only one or two rotation of common motifs i.e. ‘dimers’ (morphotrops) thus making it an interesting case of morphotropism. The topological pattern of molecular organization during phase transition that involves non-crystallographic rotation and translation is hypothesized. Each dimeric unit is represented by gray and blue ovals with suitable connectors. Dashed and solid lines represents molecule is down and up the plane respectively. The conversion of form **1III** ($P2_1/c$) to form **1II** ($P-1$) crystal involves non crystallographic 90° rotation (clockwise) of every dimeric units related by screw-axis perpendicular to their plane. The non-crystallographic 90° rotation (clockwise) of every dimeric units related by inversion center to generate a two-fold axis between them and finally the non-crystallographic 180° rotation (anticlockwise) of alternate dimeric units

perpendicular to their plane keeping other alternate dimeric units motionless to generate $P-1$ structure.

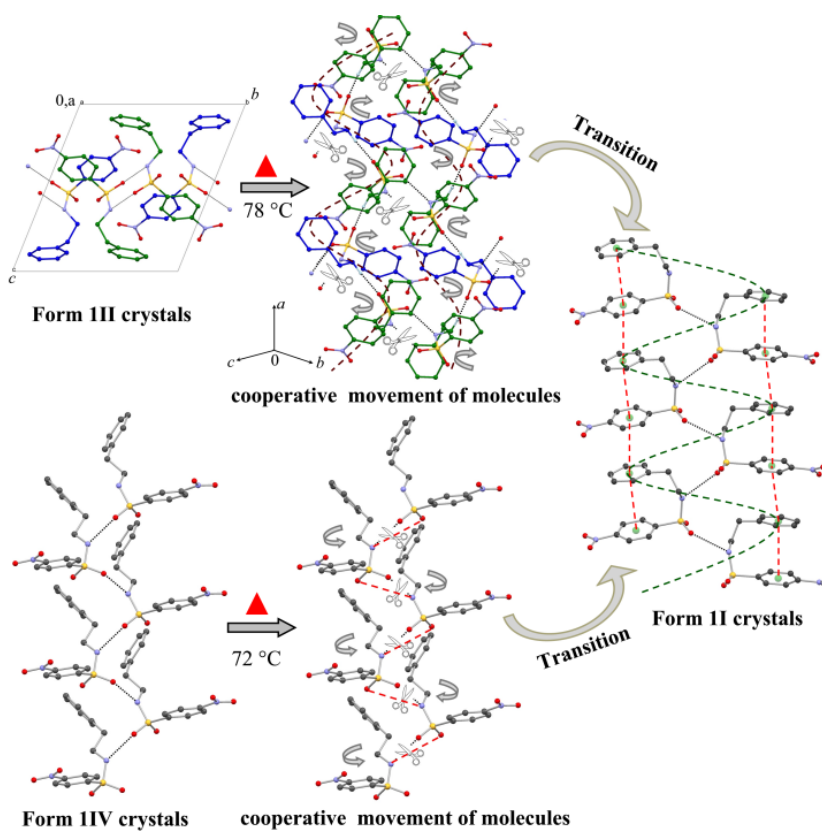


Figure 3.17. Possible mechanism of structural changes during the phase transition form III (top) and form IIV (bottom) crystals to form II crystals.

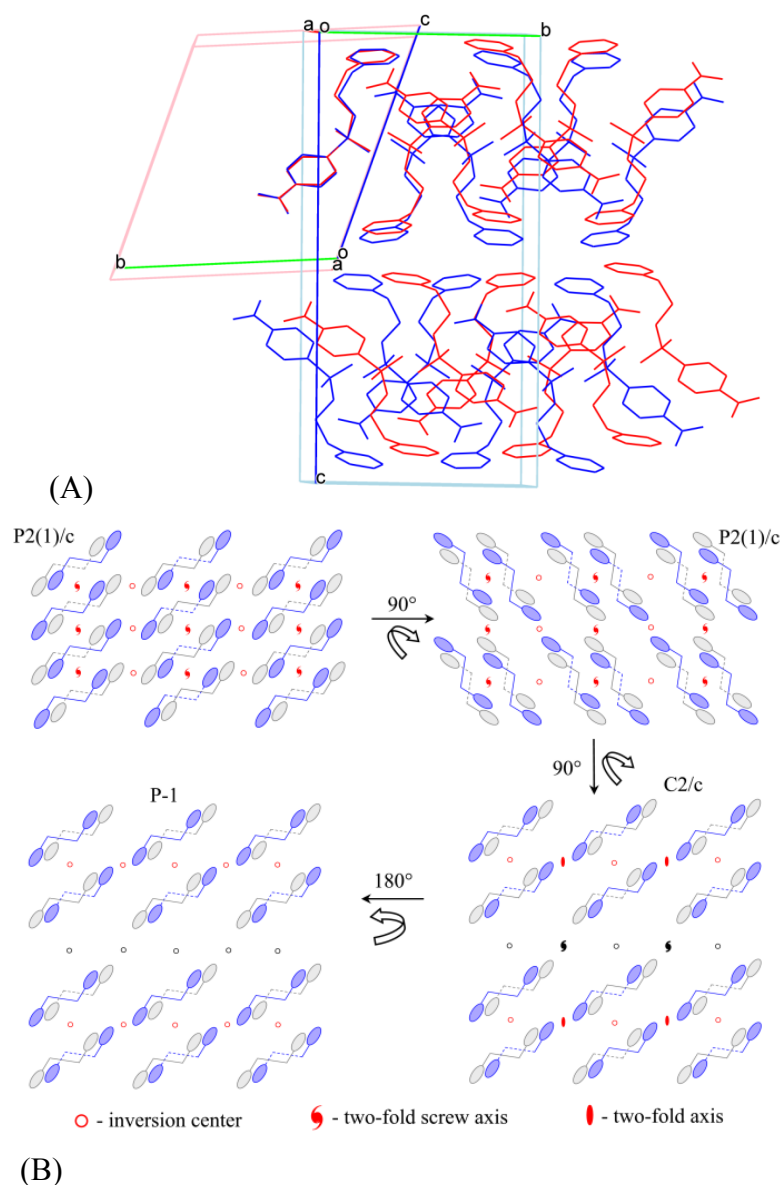


Figure 3.18.(A) Overlay of packing of molecules in form 1II (red) and form 1III (blue) crystals showing slight mismatch between the structures which can be overcome by simple sliding of the layers along the *b*-axis. (B) Topological patterns of the molecular organization during phase transition, (a) columnar arrangement of dimers as depicted in **figures 3.6c-3.7c**, (b) molecular arrangement after non-crystallographic 90° rotation (clockwise) of every dimeric units related by screw axis perpendicular to their plane, (c) the non-crystallographic 90° rotation (clockwise) of every dimeric units related by inversion center to generate a two-fold axis between them and (d) the non-crystallographic 180° rotation (anticlockwise) of alternate dimeric units perpendicular to their plane keeping other alternate dimeric units motionless to generate *P*-1 structure depicted in **figures 3.6b-3.7b**.

The conformational and interaction study in the solution state was carried out using 2D NOESY NMR in two different solvents, nonpolar CDCl_3 and polar CD_3OD . The characteristic nOes observed in nonpolar solvents suggested the close association between protons of 4-nitro benzene sulfonamide with protons of the phenyl ring in **1** indicating intramolecular π -stacking interaction between aromatic rings yielding *syn* geometry (similar to form **II** crystals) thus confirming that the *syn* conformation, which is the most preferred conformation in nonpolar solution (**Figure 3.19**). In contrast, the absence of corresponding nOes in polar solvent methanol (CD_3OD) indicates the solute-solvent interaction is inhibiting the achievement of *syn* conformation (**Figure 3.20**).

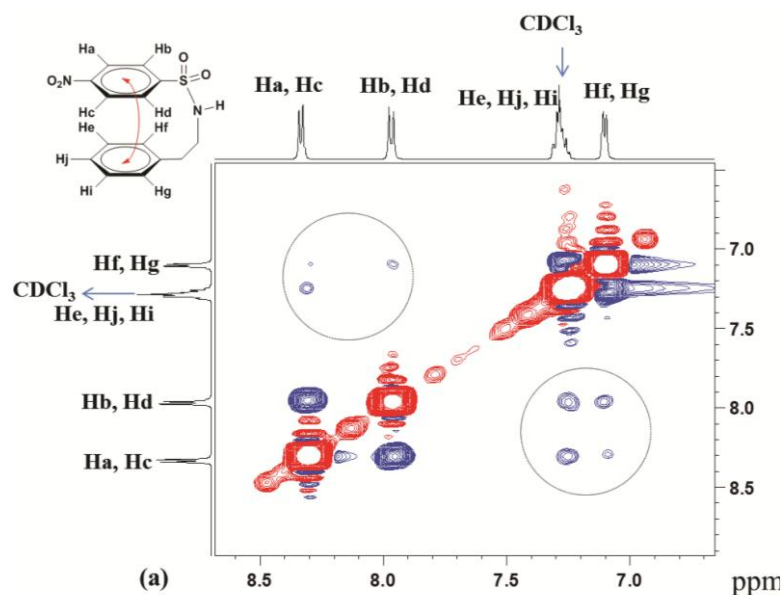


Figure 3.19. Solution state 2D NOESY study for compound **1** in CDCl_3 confirming solution state *syn* conformation.

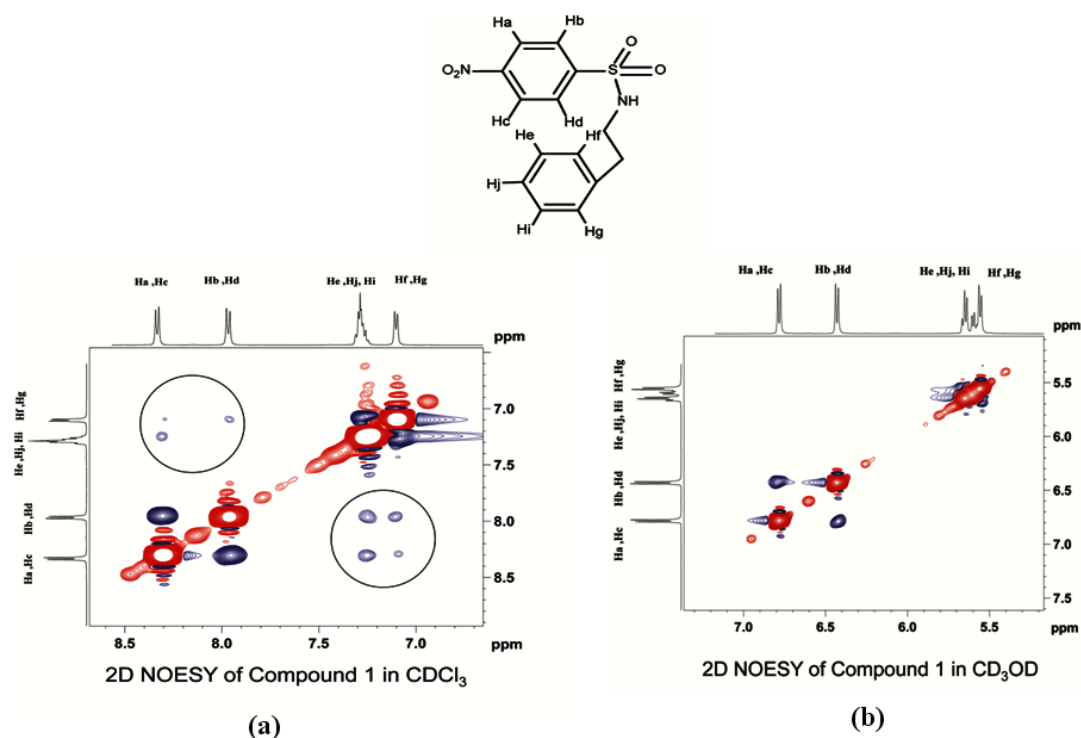


Figure 3.20. (a) 2D NOESY of compound **1** in CDCl_3 (characteristic nOe observed is highlighted with black circle) and (b) 2D NOESY of compound **1** in CD_3OD revealing absence of characteristic nOe.

To evaluate the conformational stability of **1** in the gaseous phase, the density functional theory (DFT) calculations were carried out with M06-2X functional⁵¹ and the 6-31+g* basis set using the Gaussian 09 suite of programs⁵² (See experimental methods for details). Atomic coordinates of form **1I** (*syn* conformer), form **1III** (*anti* conformer) and form **1IV** (*midway* conformer) crystals were investigated for the geometry optimization. The calculation shows that energy values of *anti* and *midway* conformers are higher by 4.98 kcal/mol and 3.89 kcal/mol respectively than *syn* conformer. The energy difference (ΔE) and structure overlays of crystal structures along with optimized geometries of the same (**Figure 3.21**) suggested that *syn* conformation is the most stable conformation whereas *anti* conformations is the least stable of them all.

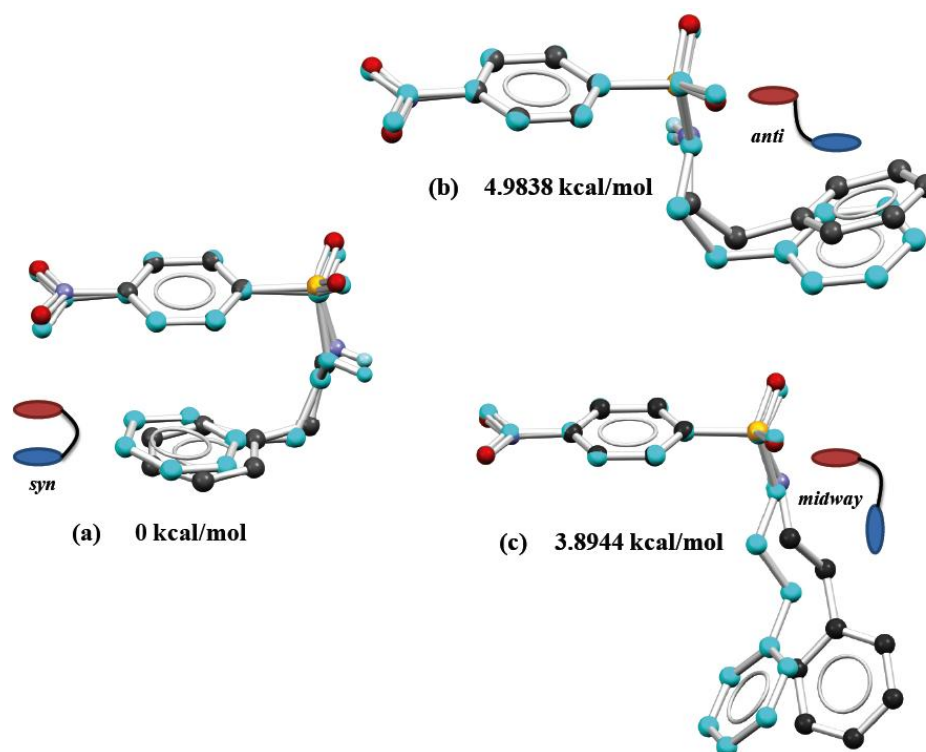


Figure 3.21. Structure overlay of crystal and DFT optimized (M062X/6-31+g*) conformers (cyan) of (a) *syn*, (b) *anti* and (c) *midway* forms of compound **1**, all values are in kcal/mol.

From the above discussion, it is evident that the *syn* orientation of **1** is the most stable conformation in solid (form **1I**), solution as well as in gaseous state. This indicates that molecules attempt to achieve the *syn* conformation in all the crystallization trials (without additive) and on heating the metastable forms. The obvious question is what makes crystals of form **1I** the most stable and what prevented it to crystallize into other polymorphs. The calculation of lattice energies was also inconclusive to provide possible explanation for the preferential formation of form **1I** crystals over the other metastable crystal forms. The extended π -stacking assembly seemed to play the crucial role in forcing the self-assembly of molecules and subsequently stabilizing the crystal lattice in association with hydrogen bonding interactions.

Polymorphs of **2**, **3** and **4**

To validate our observations, we extended our research to the other derivatives of **1** i.e. compounds **2**, **3** and **4** (Figure 3.1). Screening of polymorphs of

2, **3** and **4** (without additive) from methanol-benzene and other solvents/solvent mixtures gave only thermodynamically stable crystals form **2I**, form **3I** and form **4I** crystals respectively. Both form **3I** and form **4I** crystals belongs to monoclinic, $P2_1/c$ space group wherein the molecules have *syn* geometry. In both the crystal forms the nitro-substituted benzene ring and other benzene/pyridine rings are involved in parallel displaced π -stacking interaction with Cg...Cg distances of 3.9031(18) Å (form **3I**) and 3.9031(18) Å (form **4I**). Crystals of form **2I** crystallized in orthorhombic $Pbcn$ space group with molecule having *midway* conformation that evidently rules out the possibility of π -stacking assembly. However, the dimeric association of form **2I** molecules via classical N-H...N hydrogen bonding interactions places the pyridine moieties that are related by two-fold, in stacking mode to generate intermolecular π -stacking interaction with Cg...Cg distance of 3.6625(12) Å.

Cocrystallization attempts of compounds **2**, **3** and **4** in the presence of pyrazinamide in stoichiometric ratio of 1:3 to 1:5 from methanol/chloroform mixture (3/1, v/v) yielded polymorph for each **2**, **3** and **4** i.e. form **2II**, form **3II** and form **4II** crystals respectively. The reproducibility of polymorphs forms **3II** and **4II** were possible only in few attempts as in most of the trials we failed to obtain these polymorphs.

Crystallographic details of polymorphs of compounds **2**, **3** and **4** are summarized in **Table 3.5**. Form **2I** crystallizes in orthorhombic $Pbcn$ space group, whereas forms **2II** and **4II** belong to triclinic $P-1$ and forms **3I**, **3II** and **4I** crystallizes in monoclinic $P2_1/c$ space groups respectively, with $Z' = 1$. The unit cell parameters of form **2I** and form **2II** have minor dissimilarity (**Table 3.5**). The *a*-axis nearly same in both forms whereas *b* and *c* axes lengths in form **2I** crystals is almost double to these axes in form **2II** crystals. This similarity in the unit-cell dimensions of forms **2I** and **2II** crystals resulted in their isostructurality of molecular arrangement. The dimorphs of compounds **2** and **4** are found to be conformational polymorphs whereas dimorphs of **3** exists in packing polymorphs. In case of conformational polymorphs of **2** and **4**, the torsions τ_1 , τ_2 and τ_3 show major difference, as observed in polymorphs of **1** (**Table 3.6**). Molecules in forms **3I**, **3II**, **4I** attain *syn* geometry (similar to form **1I** crystals), whereas molecules in form **2II** crystals adopted *anti* conformation (similar to form **1II** and form **1III** crystals) and molecules in forms **2I** and **4II** crystals took a

midway orientation (Figure 3.22, 3.23). Similar to form 1I crystals, the *syn* orientation in forms 3I, 3II and 4I crystals facilitates the arrangement of parallel displaced intramolecular $\pi\cdots\pi$ stacking contact between the electron deficient nitrobenzene ring and opposite aromatic ring having ring centroid distance as $Cg\cdots Cg = 3.9031(18) \text{ \AA}$, $3.8109(11) \text{ \AA}$ and $4.004(2) \text{ \AA}$ for forms 3I, 3II and 4I respectively (Figures 3.23c, 3.23d and 3.23e).

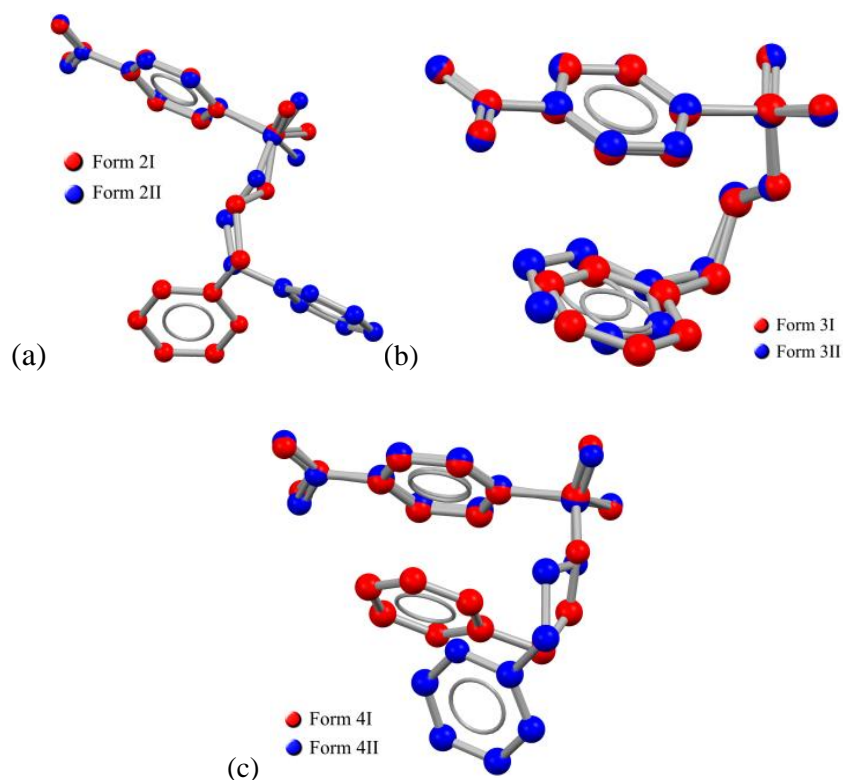


Figure 3.22. Structural overlay of the polymorphs of 2(a), 3(b) and 4(c) respectively

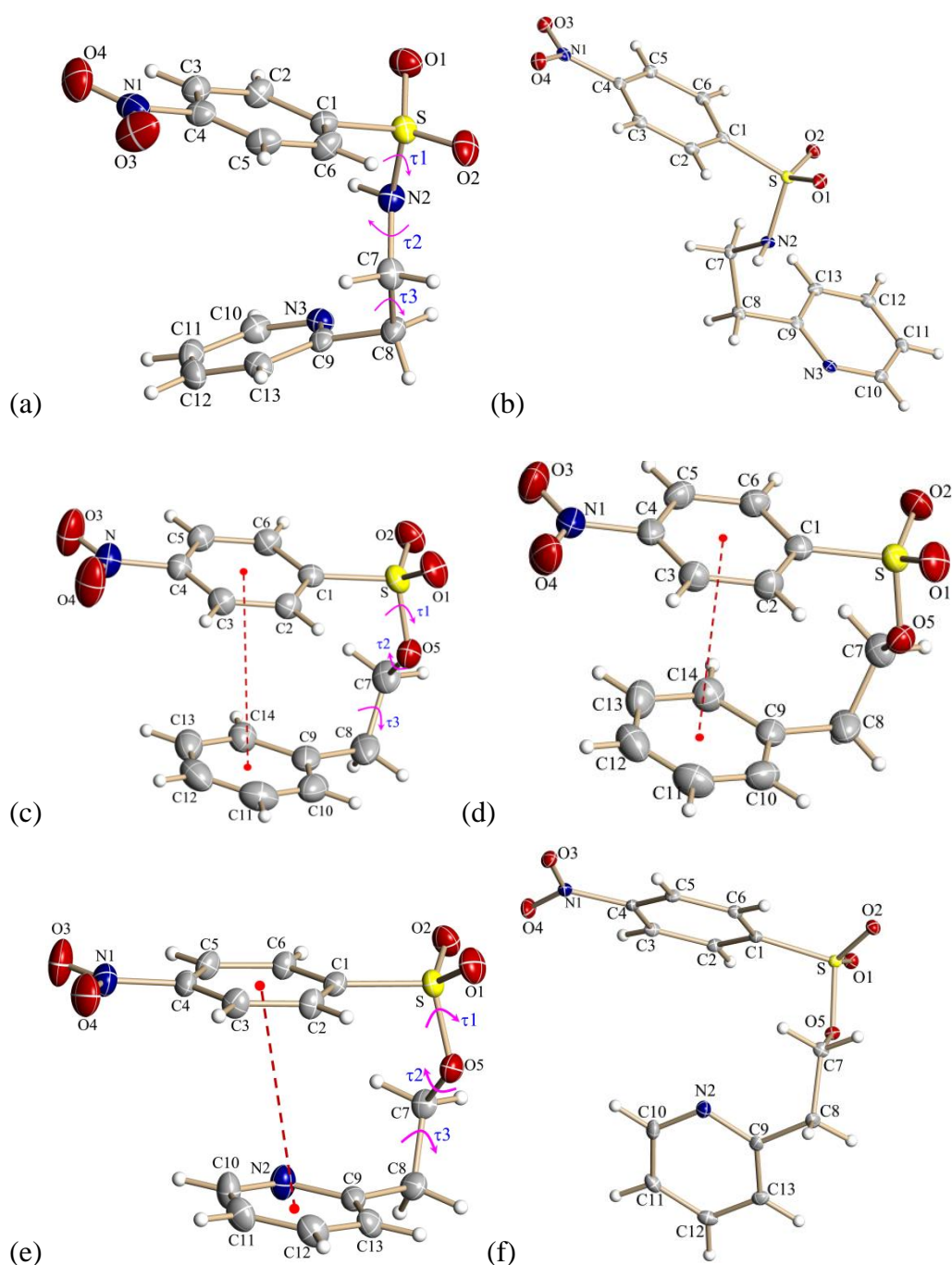
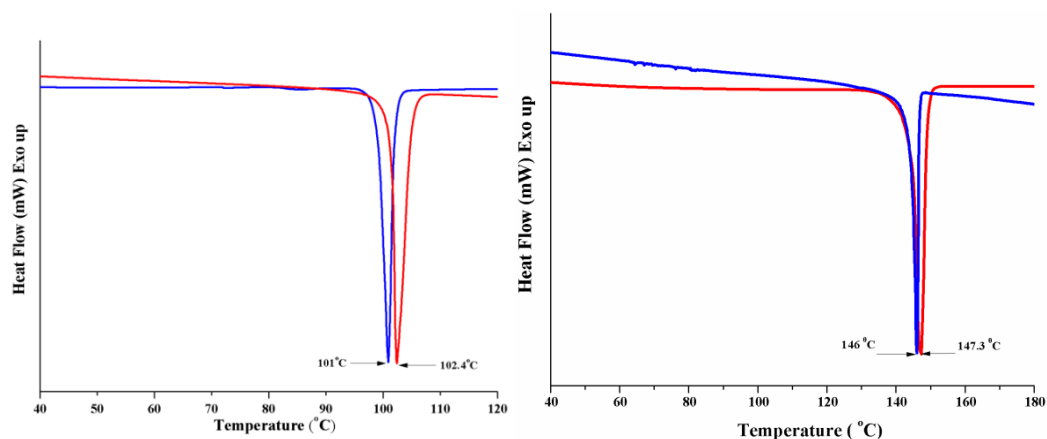


Figure 3.23. ORTEPs of polymorphs of compounds **2**, **3** and **4**, (a) form **2I**, (b) form **2II**, (c) form **3I**, (d) form **3II**, (e) form **4I** and (f) form **4II** crystals. Ellipsoids are drawn with 30 % probability for (a), (c), (d) and (e) whereas for (b) and (f) with 25 % probability.

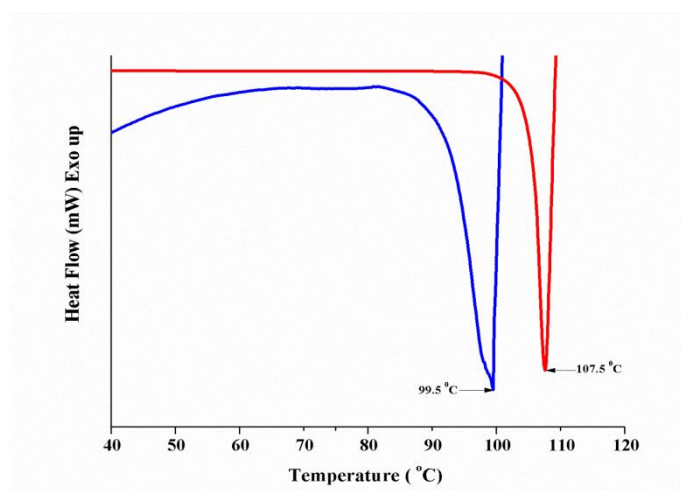
DSC study of polymorphic forms of **2**, **3** and **4** did not show any phase transition before melting unlike polymorphs of **1** (**Figure 3.24**). Evidently, overlay of the experimental

PXRD patterns of form **2I** and form **2II** crystals along with experimental PXRD patterns of form **3I** and **4I** with the respective simulated patterns of form **3II** and **4II** showed clear structural differences thus confirming the polymorphic nature of the compounds (**Figures 3.66, 3.67, 3.68, experimental methods**). The HSM studies were not performed on dimorphs of **2**, **3** and **4** due to the absence of phase transition endotherm during DSC measurements of these respective compounds.



(a)

(b)



(c)

Figure 3.24. Overlay of DSC profiles of polymorphs of **2**, **3** and **4**, (a) form **2I** crystals (red) and form **2II** crystals (blue), (b) form **3I** crystals (red) and form **3II** crystals (blue), (c) form **4I** crystals (red) and form **4II** crystals (blue).

In forms **2I** and **2II** crystals, molecules generate a two-fold (**Figure 3.25a**) and centrosymmetric (**Figure 3.25b**) dimeric assemblage respectively via N-H...N hydrogen bonding interactions [**Graph set: $R_2^2(12)$, entries 36, 45, Table 3.7**]. The two-fold linked dimeric association in form **2I** crystals makes way for the formation of extended chain of π -stacking assembly relating pyridine rings via by C-H...O contact (**Figure 3.25a, entries 43, 37, Table 3.7**). In contrast, centrosymmetrically linked dimeric synthon in form **2II** arranges both the pyridine rings in *anti*-orientations that averts their association via π ... π contacts, however it generates the extended chain structure via C-H... π interactions involving ethyl C-H and pyridine ring (**Figure 3.25b**). The adjacent chains in both the forms are associated centrosymmetrically along the *c*-axis to produce a 2D packing by means of C-H...O interaction (**entry 38, Table 3.7**) in form **2I** crystals and through C-H...O, π ... π (**entries 46, 52, Table 3.7**) and H...H (2.283 Å) interactions in form **2II** crystals. In **Figure 3.25**, it is roughly evident that two-dimensional isostructurality exists in both forms only if the relative orientation of the pyridine ring is overlooked. Molecular packing down the third direction shows the variation between the dimorphs of **2** which explains the doubling of the *b*-axis in form **2I** crystals as compared to form **2II** crystals. The doubling of the *b*-axis in form **2I** could be attributed to the glide symmetry association between the dimeric units connected via C-H...O interactions (**Figure 3.26a, entries 38-41, Table 3.7**). On the other hand, dimeric units in form **2II** are unit-translated (along *b*-axis) that are further linked centrosymmetrically along *c*-axis by C-H...O contact (**entries 47-48, Table 3.7**) and H...H contacts (**Figure 3.26b**). The *XPac* calculations showed 1D resemblance in supramolecular construct of forms **2I** and **2II** with dissimilarity index of $x = 10.8$. The *XPac* plot of δp vs δa is given in **figure 3.27**.

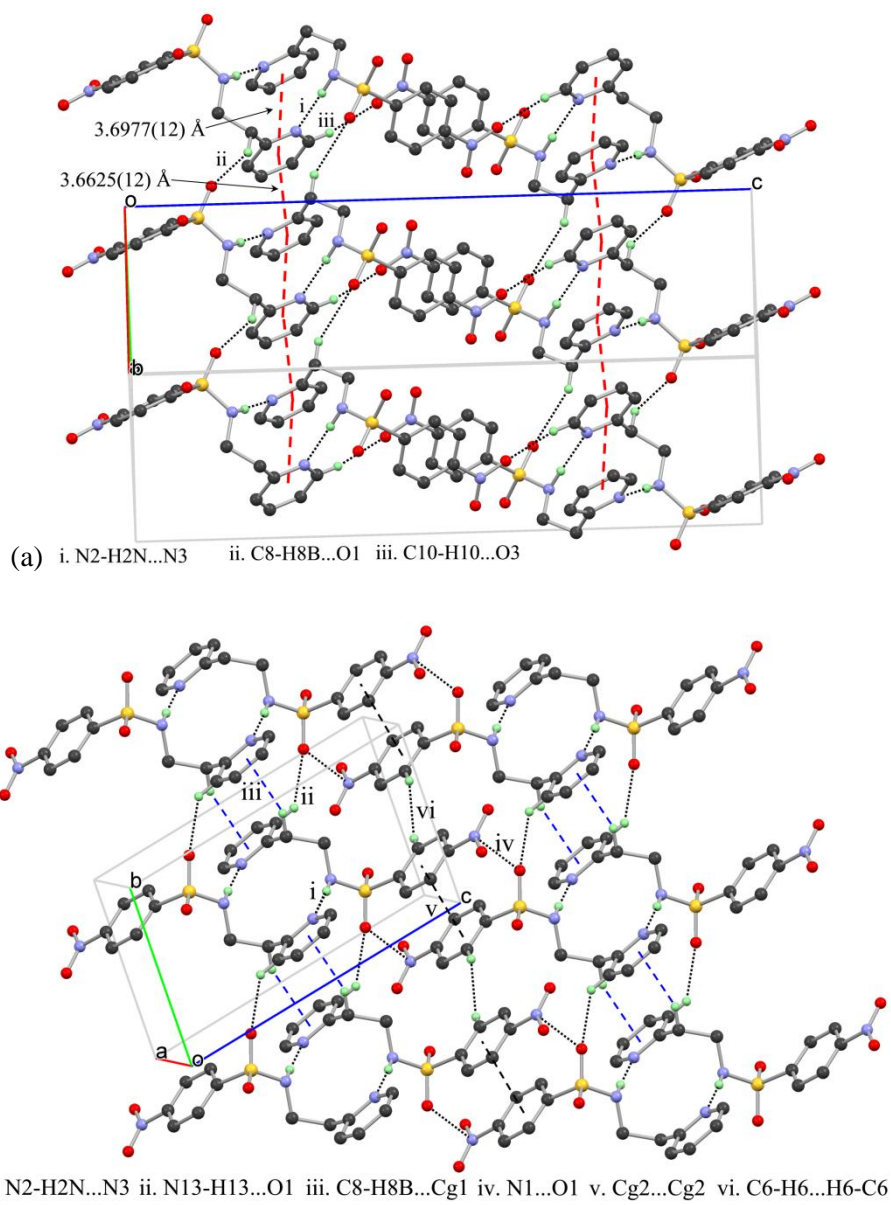


Figure 3.25. Differences in joining of N-H...N linked dimeric motifs in (a) form **2I** (two-fold related dimeric motif) and (b) form **2II** crystals (centrosymmetrically related dimeric motif).

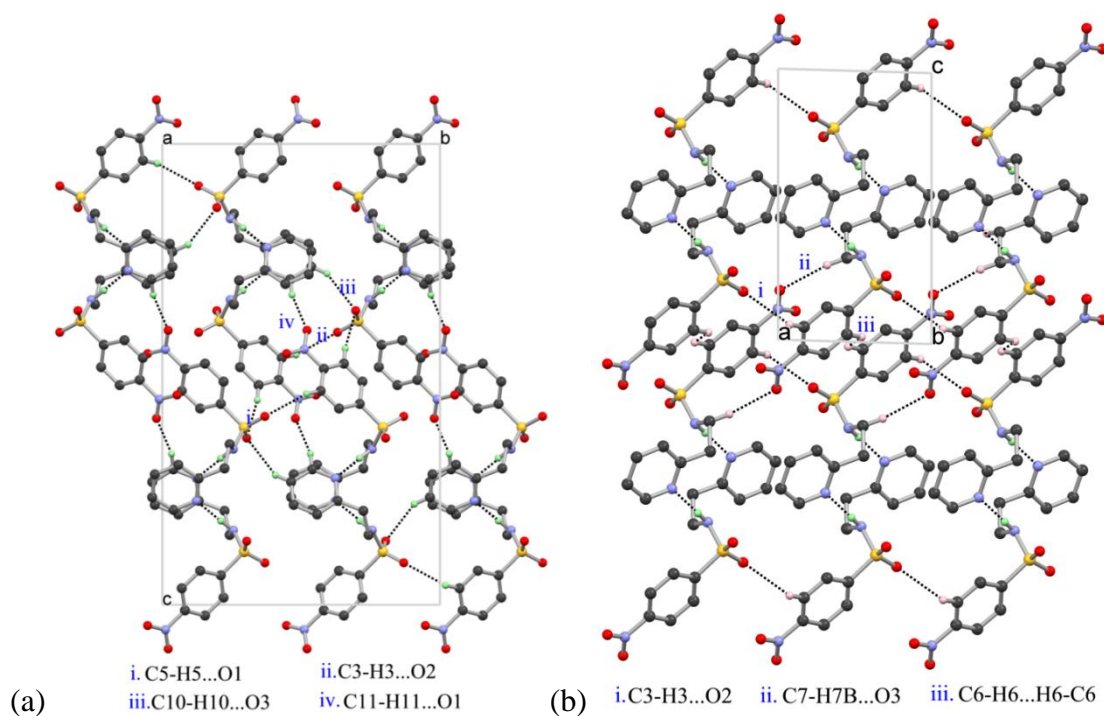


Figure 3.26. Molecular packing viewed down a -axis and b -axis in (a) form **2I** and (b) form **2II** crystals.

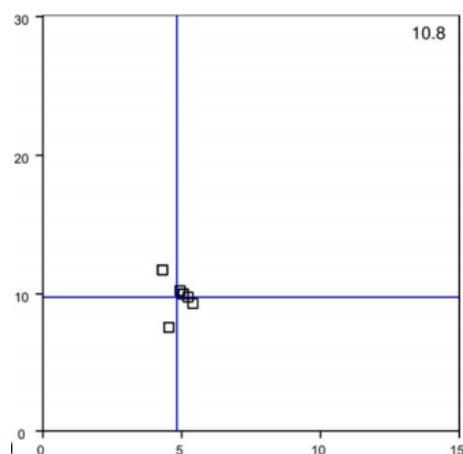


Figure 3.27. Plot of interplanar angular deviation (δ_p , x -axis) vs angular deviation (δ_a , y -axis) in *XPac* with dissimilarity index 10.8 for form **2I** and **2II** crystals of **2**.

Although the conformation of molecules in both polymorphs of **3** is similar, but their arrangement differs significantly, making it an interesting case of packing polymorphism. The unit cell parameters of form **3I** are similar to that of form **1I**, suggesting comparable molecular packing arrangement. The close association of molecules in form **3I** crystals produce a type A (**Figure 3.5**) helical assembly along

the crystallographic two-fold screw axis which is similar to form **1I** by rather a weak C-H \cdots O (entry **56**, Table 3.7) contact (Figure 3.28a). The helical relationship arranges the phenyl rings of unit translated molecules down the *b*-axis in parallel fashion to produce the extended series of π -stacking assemblies that are facilitated via intra as well as intermolecular $\pi\cdots\pi$ interactions (entries **57**, **58**, Table 3.7). The adjacent helical assemblies down the *a*-axis are associated *via* centrosymmetric C-H \cdots O interactions (Figure 3.28a, entry **54**, Table 3.7). On the contrary, molecules in form **3II** crystals forms linear assemblage along the *a*-axis, wherein each unit-translated molecules are connected solely *via* intra as well as intermolecular π -stacking contacts that leads to the generation of an extended chain (Figure 3.28b, entries **63**, **64**, Table 3.7). The adjoining linear chains are loosely connected via two C-H \cdots O interactions (entries **60**, **62**, Table 3.7, Figure 3.28b) on the *ac* plane. Molecular packing when viewed along the π -stacking assembly, in both forms, are found to have similar association via C-H \cdots O interactions that generate similar molecular packing (entries **54-56**, **59-60**, Table 3.7, Figure 3.29).

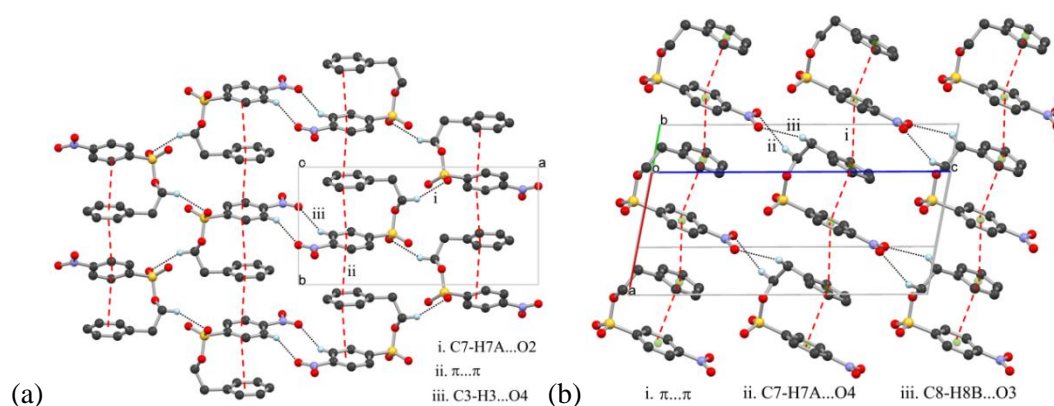


Figure 3.28. Molecular packing in forms **3I** and **3II** crystals showing, (a) helical arrangement of molecules along the *b*-axis and (b) linear assembly of molecules along the *a*-axis respectively exclusively driven by extended chain of aromatic π -stacking interactions with support from C-H \cdots O interactions.

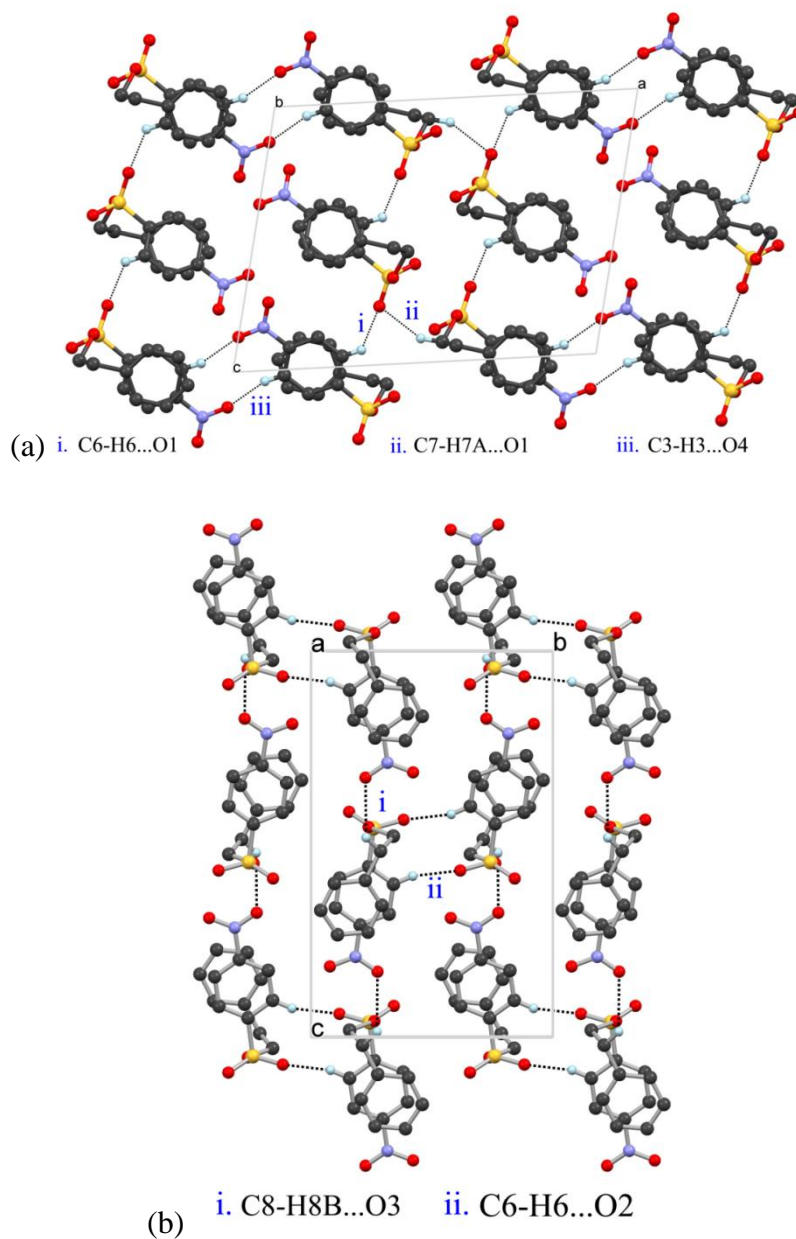


Figure 3.29. View of molecular packing down the π -stacking assembly in (a) form **3I** and (b) form **3II** crystals.

Like other stable polymorphs of compounds **1**, **2** and **3**, the *syn* conformer of form **4I** crystals also aggregates *via* intermolecular parallel displayed extended $\pi \cdots \pi$ stacking interactions (entries **69**, **70**, Table 3.7) along the direction of *a*-axis to form an extended linear chain (Figure 3.30a). The packing of molecules in form **4I** crystal reveals similarity to form **3II** crystals. The neighboring chains along the *c*-axis are unit translated *via* rather a long C-H \cdots O (entry **67**, Table 3.7) interactions. Such a

extended assembly of π -stacking interactions is not possible in form 4II crystals because of its *midway* conformation. The *P*-1 lattice of molecules in form 4II crystals assist the centrosymmetric arrangement of molecules to form chain structure directed by two different aromatic $\pi\cdots\pi$ interactions; one involving both benzene rings and other engaging pyridine rings (**entries 74-75, Table 3.7**) along the *bc*-diagonal. These neighboring chains are linked centrosymmetrically *via* C-H \cdots O (**entry 73, Table 3.7**) contacts (**Figure 3.30b**). The packing of molecules viewed down the π -stacked assembly in form 4I crystal reveals the formation of linear chain through the linking of *c*-glide related molecules *via* C-H \cdots O contacts (**entry 67, Table 3.7**). The adjacent chains are connected *via* C-H \cdots O and C-H \cdots N interactions (**entries 65-66, 68 Table 3.7, Figure 3.31a**). In form 4II crystals, the molecular arrangement viewed down the *c*-axis reveals dense packing of molecules through C-H \cdots O contacts (**entries 71-72, Table 3.7, Figure 3.31b**) to create 2D arrangement.

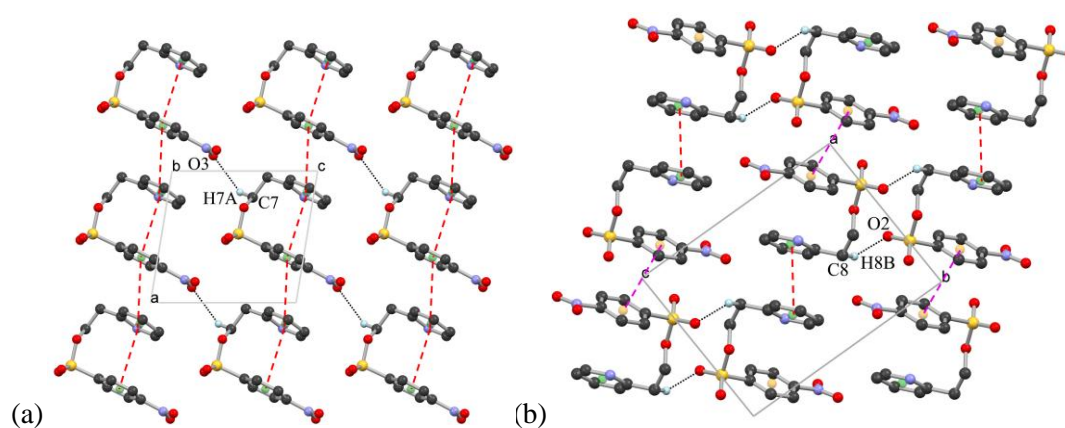


Figure 3.30. Molecular packing in (a) forms 4I crystals showing linear arrangement of molecules along the *a*-axis exclusively driven by an extended chain of aromatic π -stacking interactions and (b) centrosymmetric assemblies of molecules along the *a*-axis, well connected *via* two different aromatic $\pi\cdots\pi$ stacking interactions in form 4II crystals.

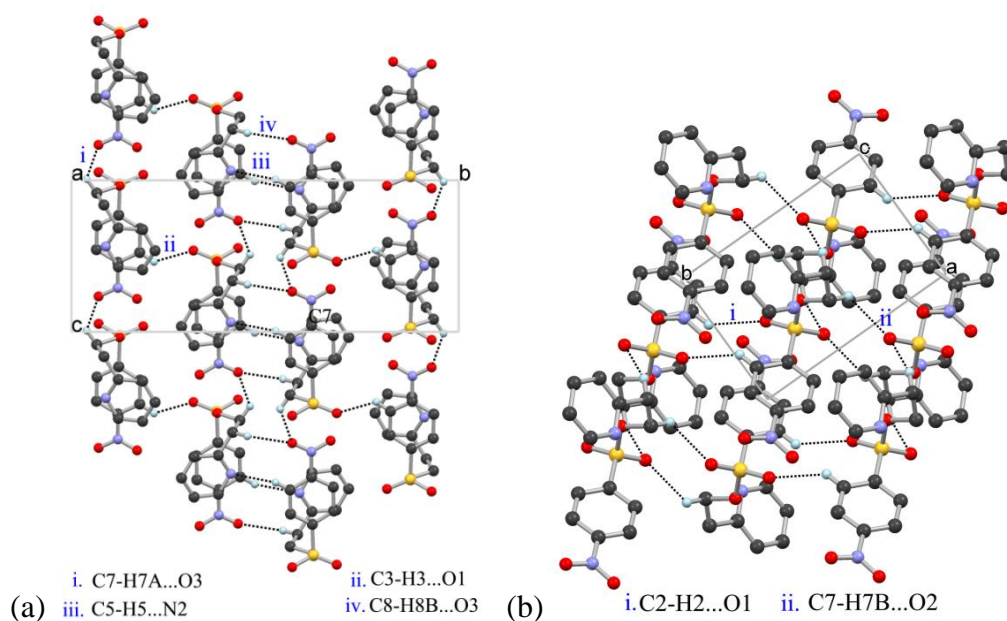


Figure 3.31. Molecular packing viewed down the π -stack assemblies in (a) form **4I** and (b) form **4II** crystals.

The lattice energy using CLP package were estimated that revealed the values of -178.7 kJ/mol for form **2I**, -181.2 kJ/mol for form **2II**, -133.5 kJ/mol for form **3I**, -134.8 kJ/mol for form **3II**, -147.6 kJ/mol for form **4I** and -163.6 kJ/mol for form **4II** crystals which suggests that form II crystals of compounds **2**, **3** and **4** are more stable than their form I crystals. The values of the crystal densities 1.489 g cm⁻³ (form **2I**), 1.519 g cm⁻³ (form **2II**), 1.425 g cm⁻³ (form **3I**), 1.450 g cm⁻³ (form **3II**), 1.491 g cm⁻³ (form **4I**) and 1.554 g cm⁻³ (form **4II**) are consistent with the lattice energies. Therefore, preferential formation of form I crystals during all the crystallization trials (without additive) could not be explained on the basis of lattice energy and crystal density as discussed in case study of **1**. As observed in polymorphs of **1**, the preferential formation of form I crystals in polymorphic forms of compounds **2** and **4**, could also be attributed to the aggregations of molecules through extended chain of π -stacking assembly which have high intermolecular potential values (**Figure 3.32-3.33, 3.34-3.35, Table 3.2-4.3**) compared to form II crystals which devoid of such assemblies. The high intermolecular potential values for comprehensive π -stacking assemblies seemed to play pivotal role in driving the self-assembly and subsequently the formation of PNC. Intermolecular potential values for form **3I** and form **3II** crystals are similar (-35.4 kJ/mol for form **3I** and -37.0 kJ/mol for form **3II** crystals,

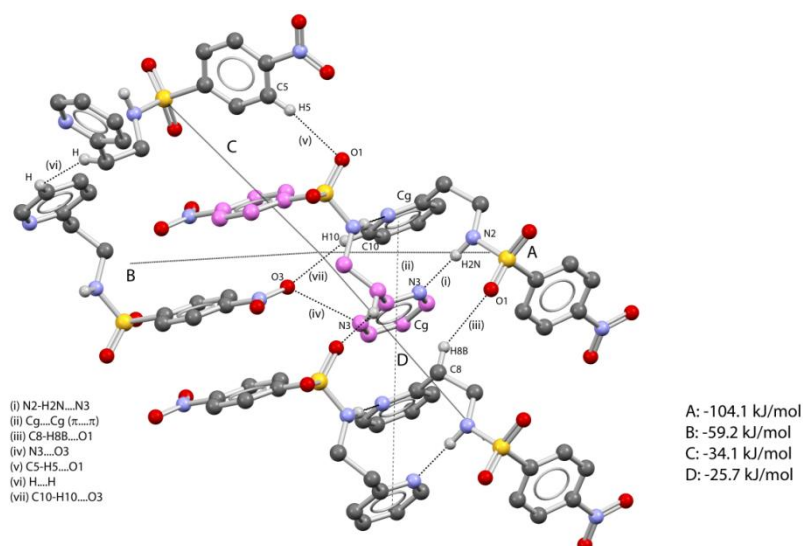
Figures 3.36-3.37, Table 3.4) and was inconclusive as both polymorphs form extended chain of π -stacking assemblies. The intermolecular potentials for interlinking the adjacent π -stacking assemblies *via* C-H \cdots O interactions across the inversion center showed a slight difference, -23.7 kJ/mol (form **3I**) and -15.0 kJ/mol (form **3II**), suggesting slightly stronger association of molecules in form **3I** crystals in comparison to form **3II** crystals thus may explain the preferential formation of form **3I** crystals during crystallization.

Table 3.2. Intermolecular interactions and intermolecular potentials in polymorphs of 2.

Interaction	Intermolecular potentials
form 2I	
Dimeric association <i>via</i> N2-H2N...N3 and $\pi \cdots \pi$ interactions	-104.1 kJ/mol
Extended π stacking assembly supported by weak C8-H8B...O1 interactions.	-25.7 kJ/mol
Bridging of these monolayers along the <i>c</i> -axis <i>via</i> C10-H10...O3 and C5-H5...O1 interactions.	-59.2 and -34.1 kJ/mol
form 2II	
Dimeric association <i>via</i> N2-H2N...N3 interactions	-78.2 kJ/mol
Extension of N-H...N dimers along <i>b</i> -axis <i>via</i> C-H... π interactions	-23.9 kJ/mol
Joining of adjacent monolayers by short N...O, C-H...O, H...H and $\pi \cdots \pi$ contacts	-44.1 and -23.9 kJ/mol

Table 3.3. Intermolecular interactions and intermolecular potentials values for polymorphs of **4**.

Interactions	Intermolecular Potentials
form 4I	
Stacking of molecules through infinite chain of $\pi \cdots \pi$ interactions	-36.3 kJ/mol
Linking of stacked layers <i>via</i> C5-H5 \cdots N2 and C8-H8B \cdots O3 interactions	-35.4 kJ/mol and -30.7 kJ/mol
form 4II	
Linking of molecules <i>via</i> $\pi \cdots \pi$ and weak C8-H8A \cdots π interaction along the <i>ac</i> diagonal	-47.6 kJ/mol and -26.7 kJ/mol
Linking of monolayers <i>via</i> bifurcated C8-H8B \cdots O1 and C8-H8B \cdots O2 interactions as well as C6-H6 \cdots O5 and other van der Waals contacts	-34.2 kJ/mol and -51.5 kJ/mol

**Figure 3.32.** Intermolecular potentials values for form **2I** crystals.

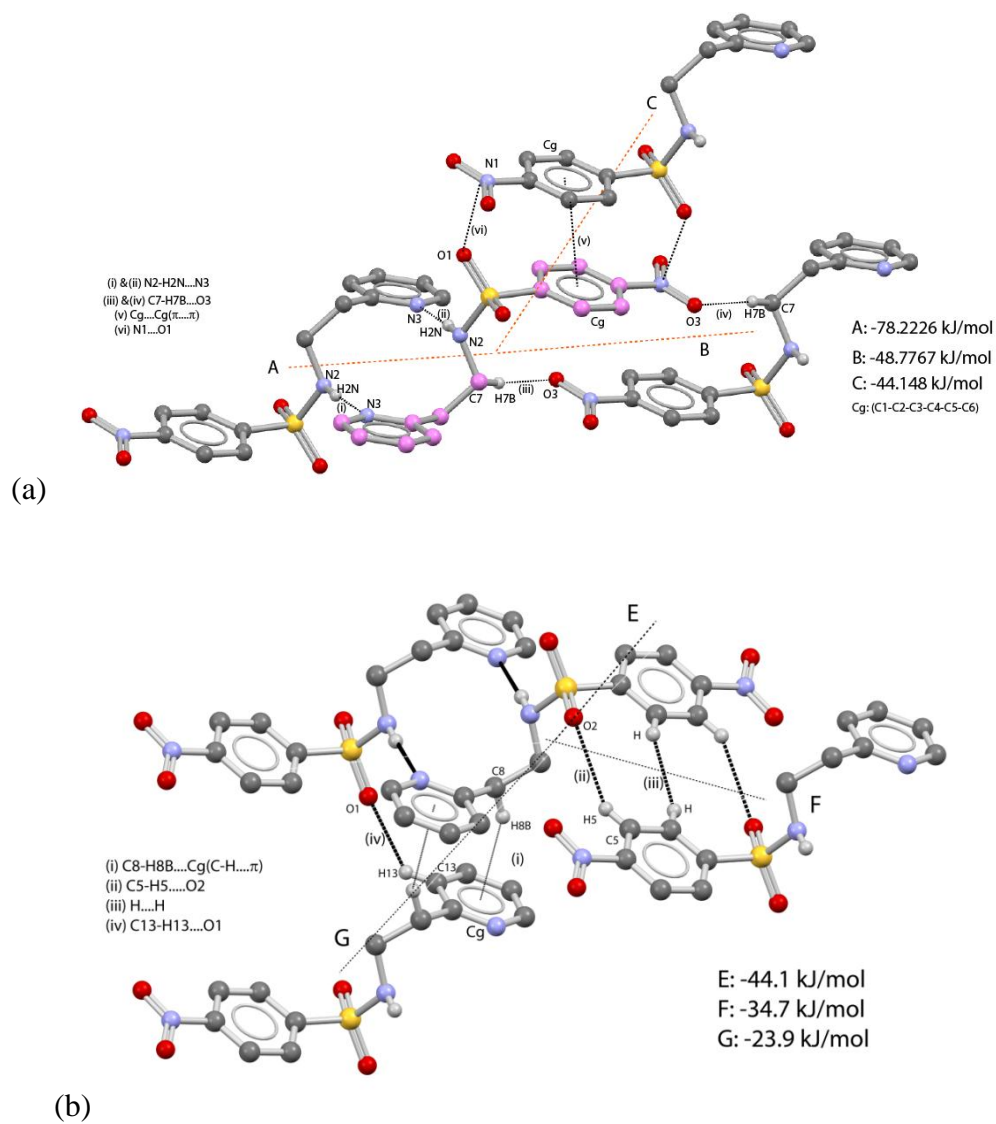


Figure 3.33. (a) and (b) shows the intermolecular potentials values for form 2II crystals.

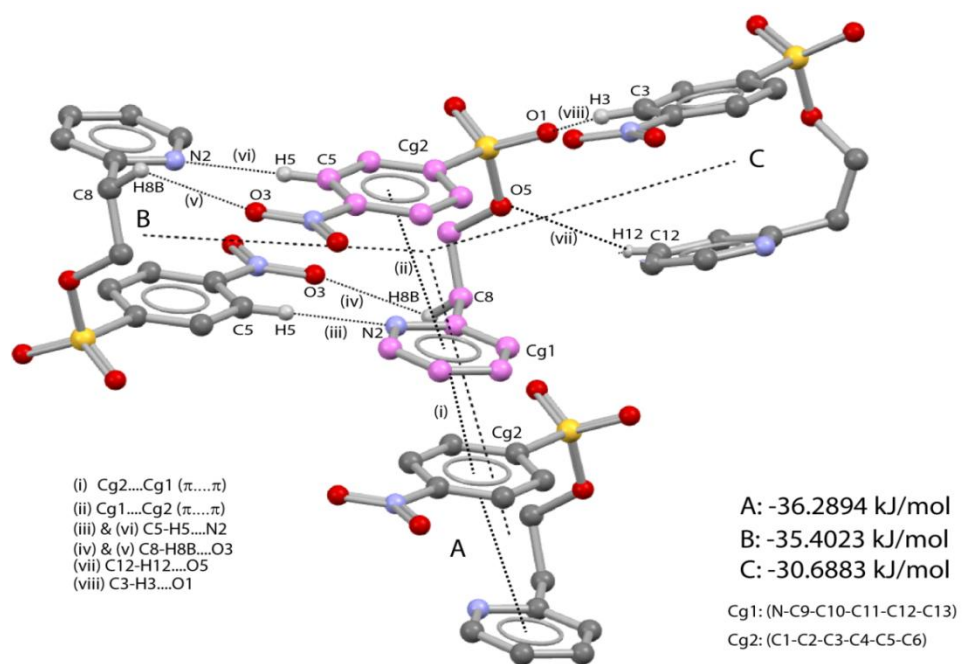


Figure 3.34. Intermolecular potentials values for form 4I crystals.

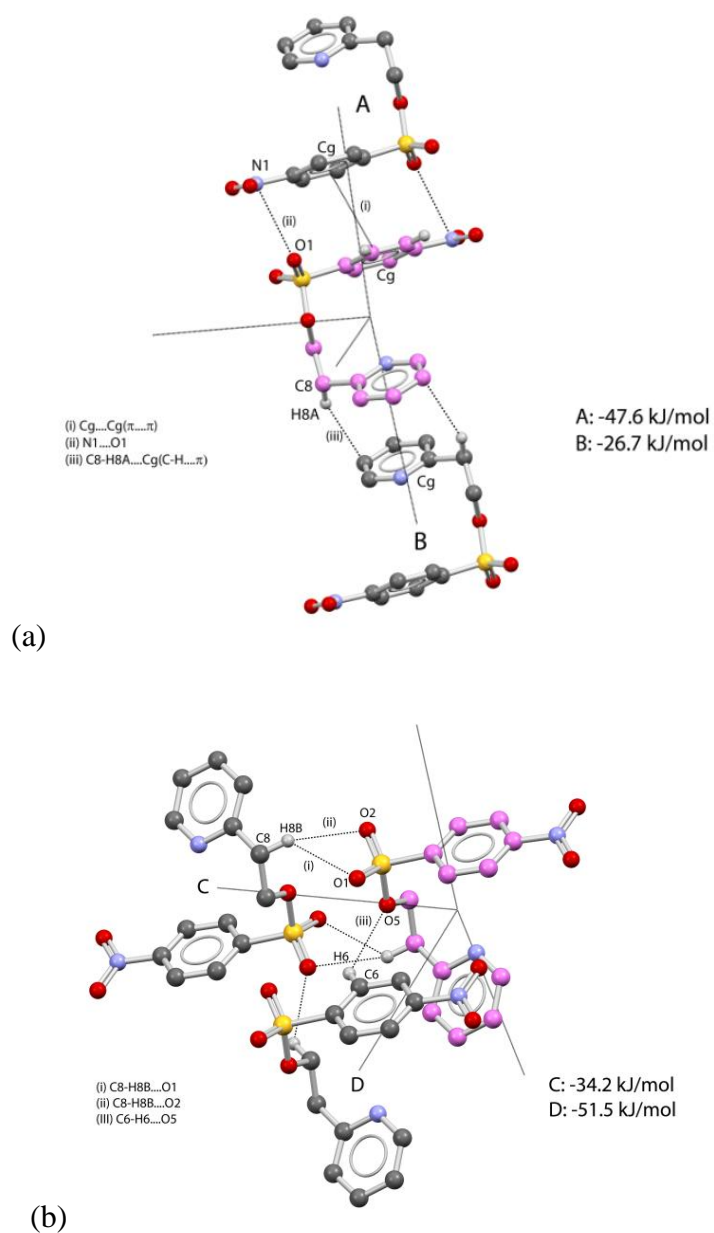
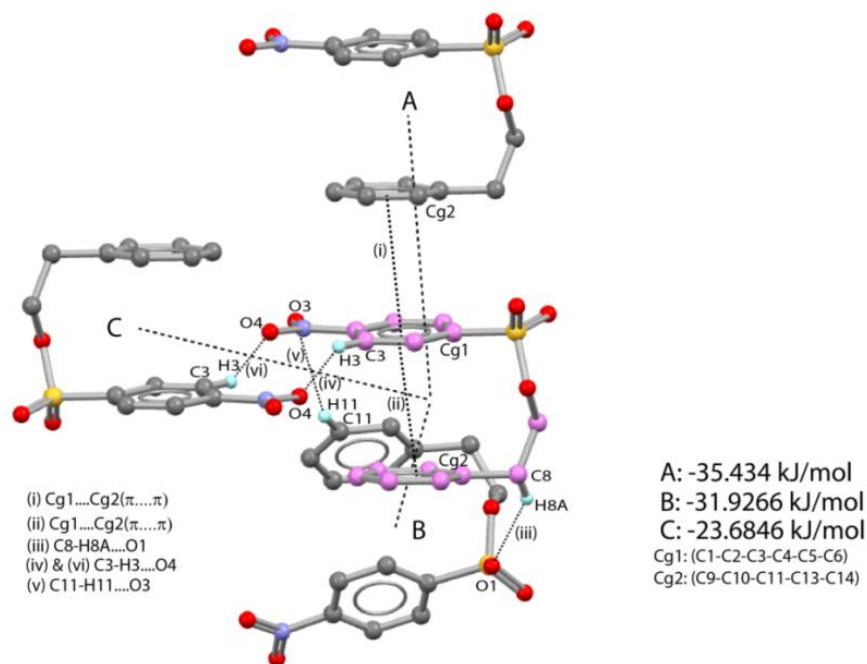


Figure 3.35. (a) and (b) shows the intermolecular potentials values for form 4II crystals.

Table 3.4. Intermolecular interaction and intermolecular potentials values for polymorphs of **3**.

Interactions	Intermolecular Potentials
form 3I	
Infinite chain of $\pi \cdots \pi$ stacking interactions	-35 kJ/mol
Association of molecules across the inversion center through C3-H3 \cdots O4 interactions	-23.7 kJ/mol
form 3II	
Infinite chain of $\pi \cdots \pi$ stacking interactions	-37 kJ/mol
Association of the molecules across the inversion via C6-H6 \cdots O2 interactions	-15.0 kJ/mol

**Figure 3.36.** Intermolecular potentials values for form **3I** crystals.

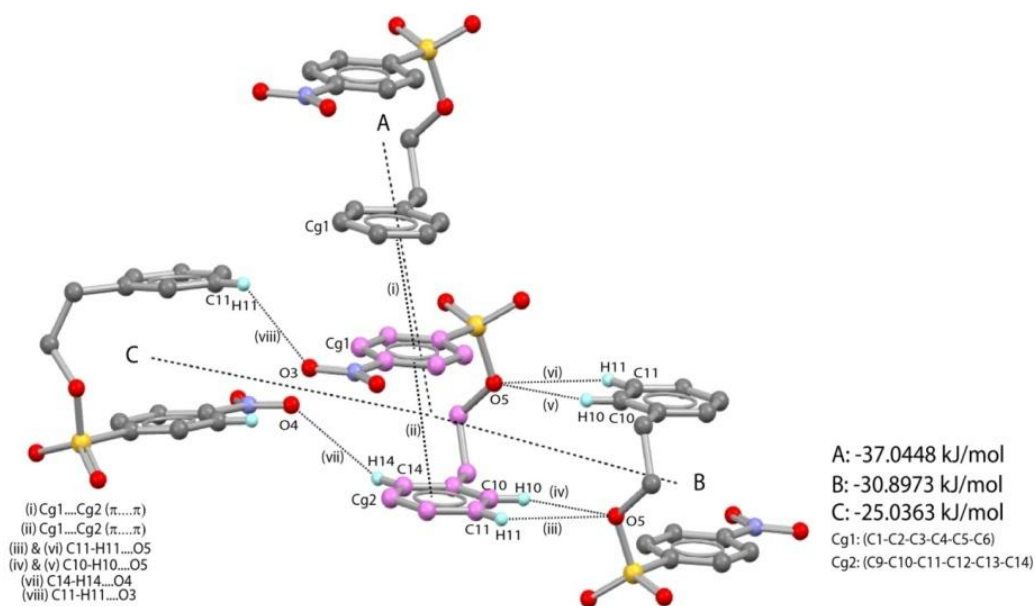


Figure 3.37. Intermolecular potentials values for form 3II crystals.

The gas phase conformational energy calculation was conducted using DFT calculations that also revealed higher stability for *syn* conformation than *anti* and *midway* conformations for polymorphs of **2** and **4** (**Figures 3.38-3.39**). The structure overlay of geometries of compounds obtained from single crystal structure analysis and optimization (DFT, the color of the elements is cyan) was shown. The DFT optimization revealed the optimized geometry of Form **2II** is 2.0167 Kcal/mol higher in energy than the optimized geometry of Form **2I** (**Figure 3.38**). Interestingly, starting midway conformation of Form **4II**, achieves *syn* geometry during optimization which is most stable and matched energetically with Form **4I** (*syn*, **Figure 3.39**).

Atomic coordinates from crystal structures of *midway* and *anti*-conformers of form **2I** and form **2II** crystals were used as input geometries which were further optimized using DFT calculations (**Figure 3.38**). Calculations suggested subtle differences between the crystal structure conformation and optimized conformations. Optimization of the single molecule geometry of *midway* and *anti*-conformations gave *syn* and *midway* geometries respectively. Energy difference reveals *syn* geometry (achieved *via* optimization) is more stable than *midway* geometry. DFT calculation for compound **4** also revealed the expected results. Fine tuning of the *syn* conformation (form **4I**) was observation after geometry optimization whereas geometry

optimization of *midway* conformer (form **4II**) produced most the stable *syn* conformer. Structure overlay of optimized *syn* geometries for forms **4I** and **4II** crystals showed intramolecular stacking of phenyl and pyridine rings, although orientations of pyridine ring is opposite with respect to the benzene ring (**Figure 3.39**).

This shows that *syn* conformer is the most stable conformation in gas phase compared to *anti* and *midway* conformers

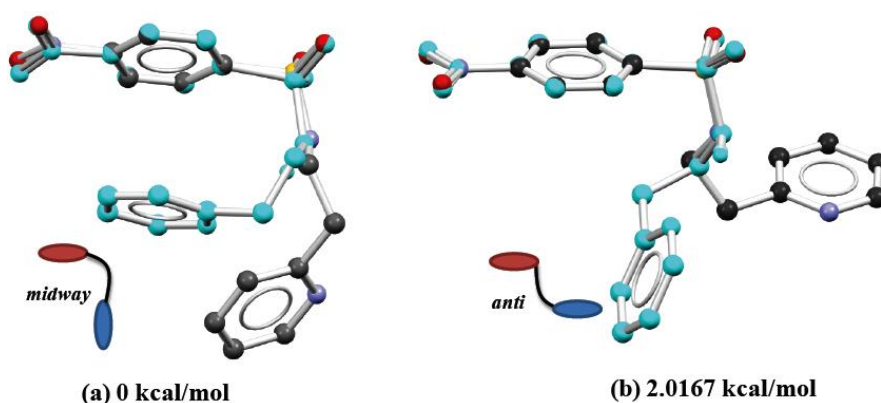


Figure 3.38. Structure overlay of crystal (black) and DFT optimized (M062X/6-31+g*) conformers (cyan) of *midway* and *anti*-forms of compound **2**, all values are in kcal/mol.

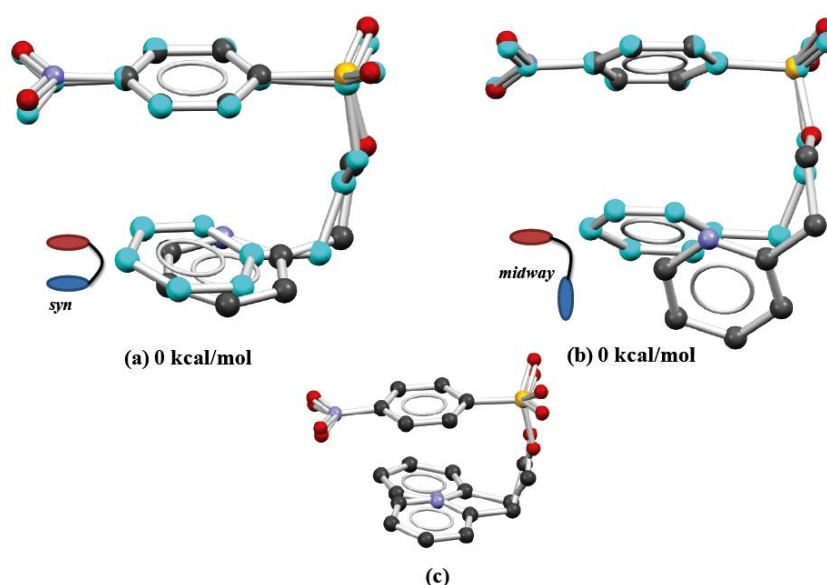


Figure 3.39. Structure overlay of crystal and DFT optimized (M062X/6-31+g*) conformers (cyan) of *syn* and *midway* forms of compound **4**, all values are in kcal/mol.

The solution state 2D NOESY investigations (CDCl_3 500 MHz) confirmed the *syn* conformation of molecules of **3** and **4** as observed in their most preferred form I crystals therefore suggesting the presence of π -stacking assemblies even in solution (Figure 3.40). The similar investigation for **2** displayed the absence of characteristic nOes suggesting the absence of π stacking assemblies (Figure 3.41).

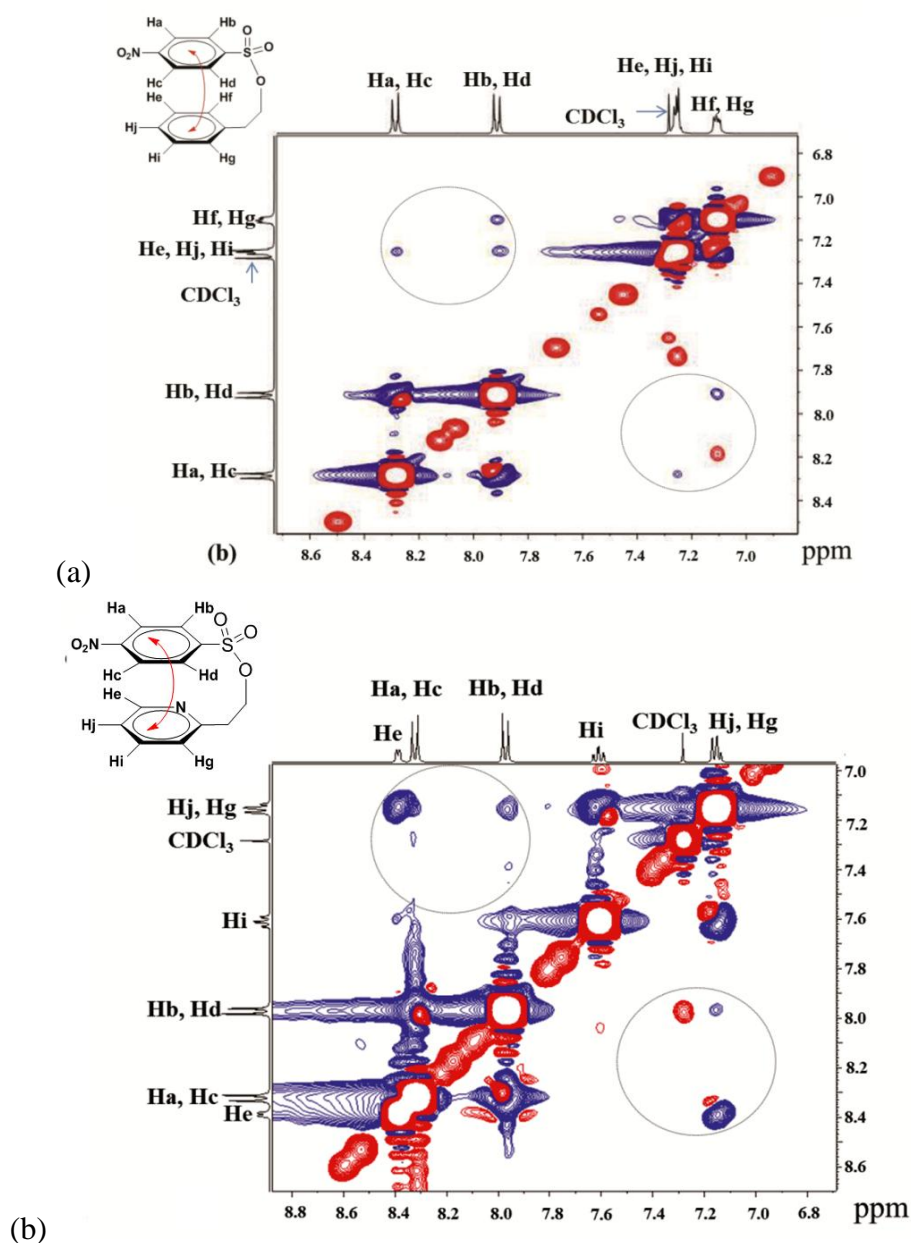


Figure 3.40. Solution state 2D NOESY study for compounds (a) **3** and (b) **4** in CDCl_3 confirming their solution state *syn* conformation.

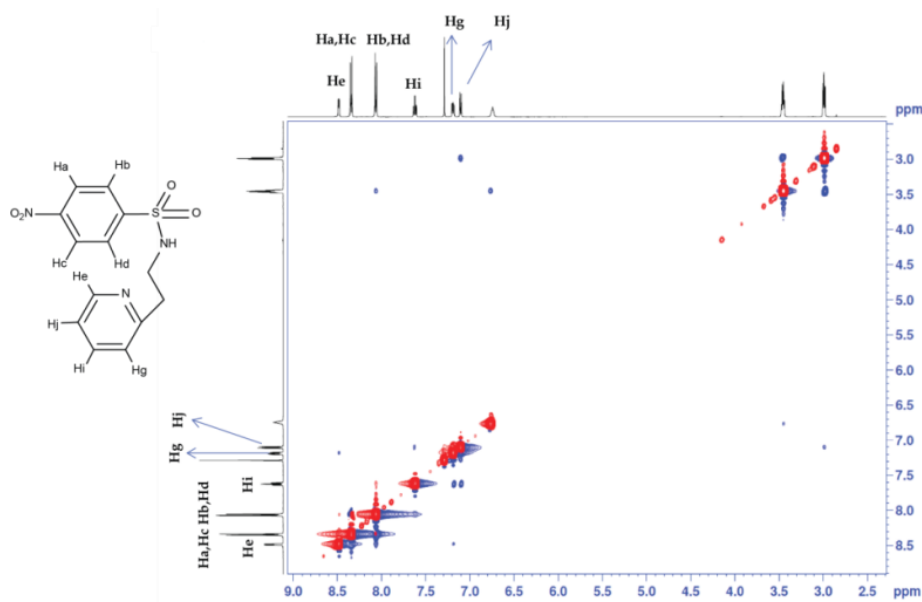
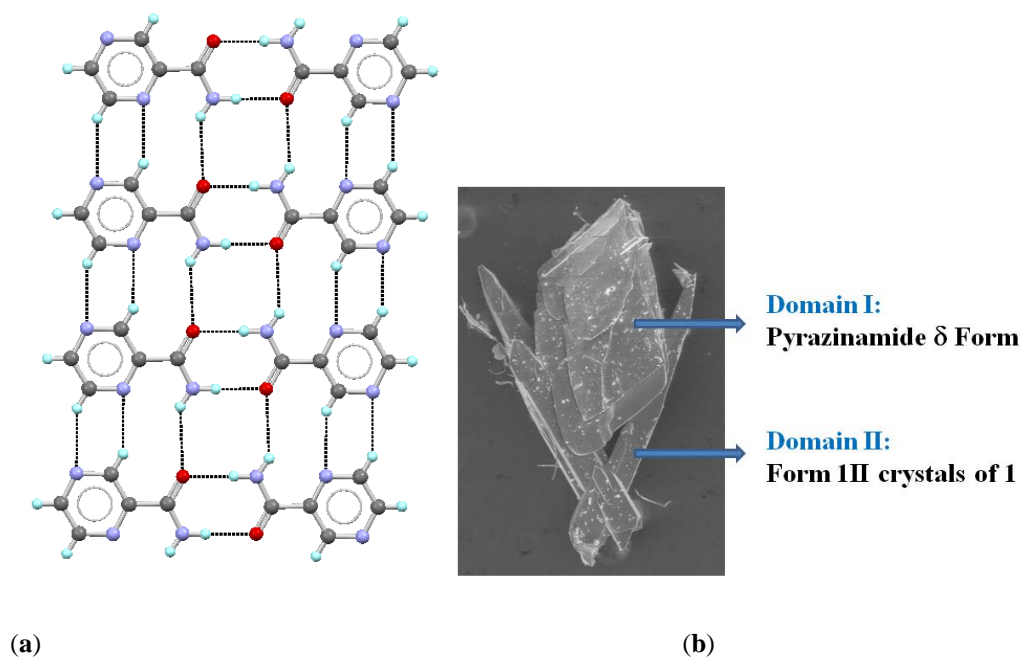


Figure 3.41. Solution state 2D NOESY study for compound **2** in CDCl_3 .

Role of pyrazinamide in capturing elusive polymorphs: The presence of pyrazinamide at the nucleation event modifies the nucleation pathway during crystallization which resulted in the generation of three new polymorphs for **1** and one new polymorph for each **2**, **3** and **4**. During cocrystallization trials of compound **1** with pyrazinamide in the stoichiometric ratio 1:3, concomitant formation of crystals of different morphologies were obtained. E-SEM image (**Figure 3.42**) of the crystals clearly indicates the close contact of petal shaped crystals of form **1III** (domain II) to the 001 face of the δ -polymorph⁵³ (**Figure 3.43**) of pyrazinamide (domain I, the face indexing of pyrazinamide crystal was carried out using single crystal X-ray diffractometer, **Figure 3.69**). On the basis of observations like, pyrazinamide was always used in excess to obtain the elusive polymorphs, and relative solubility of pyrazinamide is less (solvent condition: methanol/chloroform mixture, 3/1, v/v) as compared to the compound **1**, it is possible that δ -polymorph of pyrazinamide would have been nucleated first. The (001) face of pyrazinamide may have served as template which supports the preferential formation of the elusive polymorphs by epitaxial crystal growth at the supersaturation stage.⁵⁴⁻⁵⁵



Crystallographic parameters of pyrazinamide δ form

Crystal System	$a/\text{\AA}$	$b/\text{\AA}$	$c/\text{\AA}$	α°	β°	γ°	$V/\text{\AA}^3$
Triclinic	5.1186(10)	5.7053(11)	9.857(2)	97.46(3)	98.17(3)	106.47(3)	268.82(9)

(c)

Figure 3.42. (a)E-SEM image of epitaxial growth of form III crystals of **1** on the surface of δ -polymorph of pyrazinamide (confirmed by its unit cell measurement on X-ray diffractometer), (b) 1D molecular arrangement observed in δ -polymorph of pyrazinamide and (c) unit cell parameters of pyrazinamide δ form.

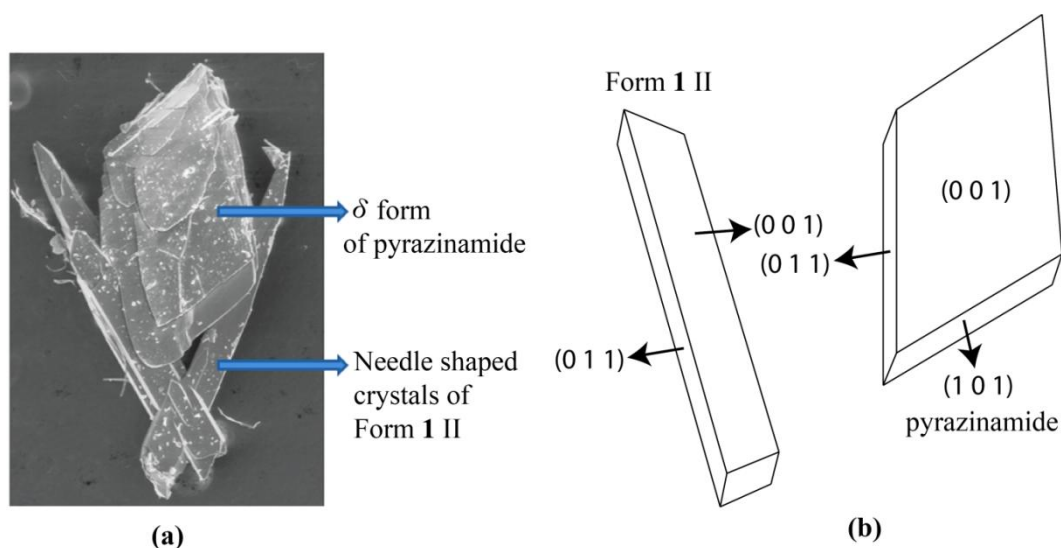


Figure 3.43. Face indexing revealing different faces of form 1II crystals of **1** and δ -pyrazinamide crystals.

Seed crystallization using isostructural additives is used as common strategy for the generation of metastable or disappeared polymorphs⁵⁶⁻⁵⁷ wherein the speculated hydrogen bonding interactions between the additive and the solute molecules play significant role for the enrichment of metastable form. However in the present cases both the solute and the pyrazinamide additive are structurally different, hence it is difficult to predict how pyrazinamide molecules acted as seed or provided nucleation sites for the generation of metastable polymorphs. In order to gain more insight and to obtain direct evidence of pyrazinamide as additive, we designed MCHS experiment (melt crystallization on heterogeneous surface). In this experiment we used compound **1** as candidate owing to its two important properties such as melting point of **1** is remarkably less than the pyrazinamide, and many polymorphic forms of **1** (*syn-midway-anti*) were obtained in the presence of pyrazinamide. E-SEM image of concomitantly grown crystals (form 1II and pyrazinamide) showed multiple interfacial contacts between the form 1II (*anti* form) and δ -pyrazinamide crystals. This observation served as important clue for setting MCHS experiment between **1** and pyrazinamide. We divided experimental strategy in two parts, control and test. In control experiment, form 1II crystals of **1** was kept on glass surface and heated till it completely melts (94 °C). The melt was allowed to cool to room temperature. In the test experiment (001) surface of pyrazinamide was used as heterogeneous surface onto which crystal of form 1II was kept. The assembly is heated till 95-96 °C (melting

temperature of form **II** crystals) however, δ form of pyrazinamide remained undisturbed. The care was taken to prevent further increase of temperature as δ -pyrazinamide show phase transition at 110 °C. Melted compound is allowed to crystallize exclusively over pyrazinamide surface as shown in the **figures 3.44-3.45**. The outcome from both the experiments was characterized by DSC and PXRD analysis.

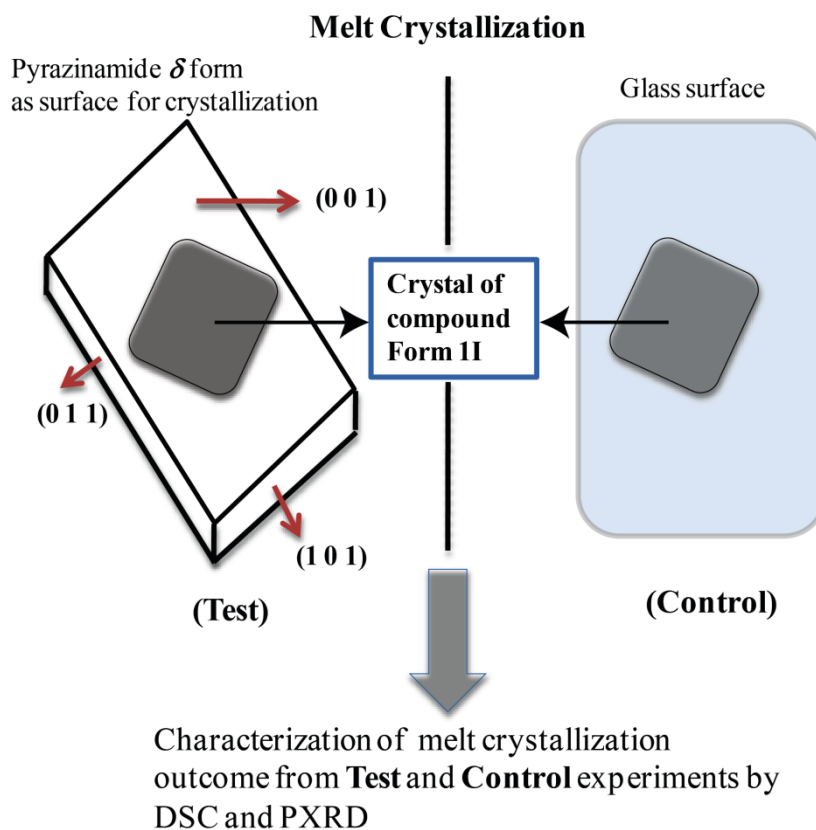


Figure 3.44. Schematic representation of melt crystallization on heterogeneous surface.

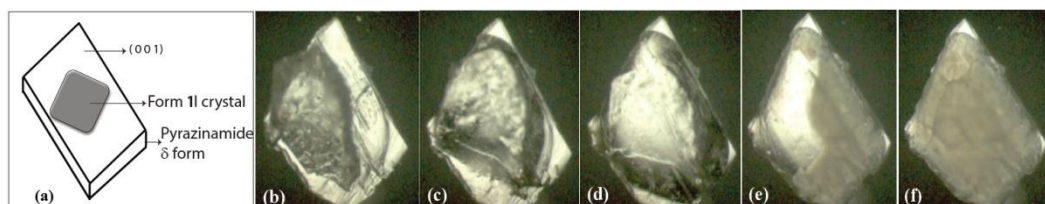


Figure 3.45. Figure showing melt crystallization of form **II** crystals of **1** on 001 face of δ -pyrazinamide, (a) the 2D depiction of MCHS experimental assembly, (b) the photomicrograph of assembly at 30 °C, (c) the photomicrograph of assembly at 90 °C when the melting of Form **II** crystals initiated, (d) the photomicrograph of assembly at 95 °C when the crystals of form **II** completely melt over pyrazinamide, the (0 0 1) face, (e) and (f) the melt crystallization of **1** over pyrazinamide surface.

DSC thermograms and PXRD patterns of control and test revealed subtle differences. DSC profile of the crystal crystallized on the glass surface showed sharp melting endotherm centered at 93.7 °C that matched with form **II** crystals (**Figure 3.46, red**). Further, the PXRD patterns of these crystals matched with the PXRD patterns of form **II** (**Figure 3.47**). This shows that crystallization of form **II** crystals on glass surface yielded only form **II** crystals. DSC profile of crystals obtained from 001 face of δ -pyrazinamide revealed two endotherms, a small hump at 63°C and melting endotherm at 73.6 °C which matched with the melting endotherm of form **III** crystals (**Figure 3.46, black**). PXRD pattern also revealed the presence of diffractions peaks of forms **III** and **III** crystals (**Figure 3.48**).

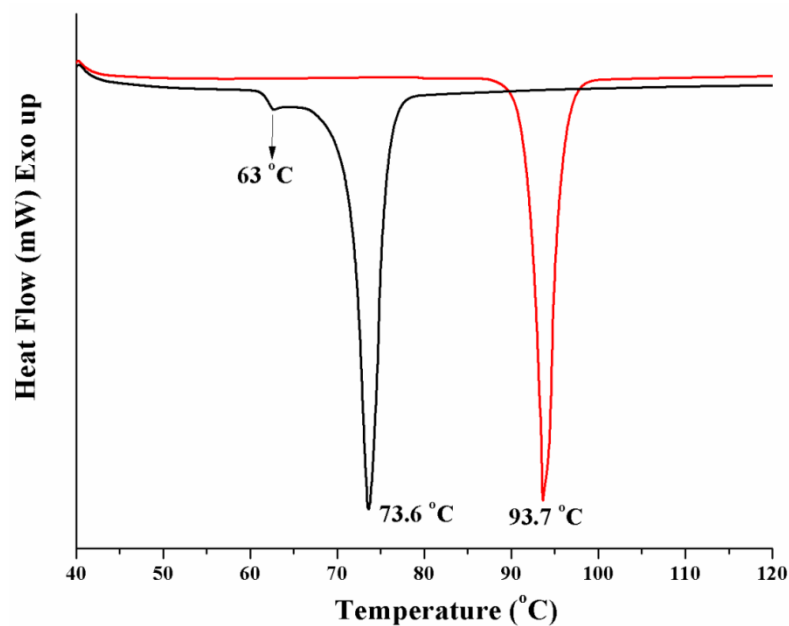


Figure 3.46. DSC profiles of crystals obtained from melt crystallization, on the surface of glass (red) and on 001 face of δ -pyrazinamide (black).

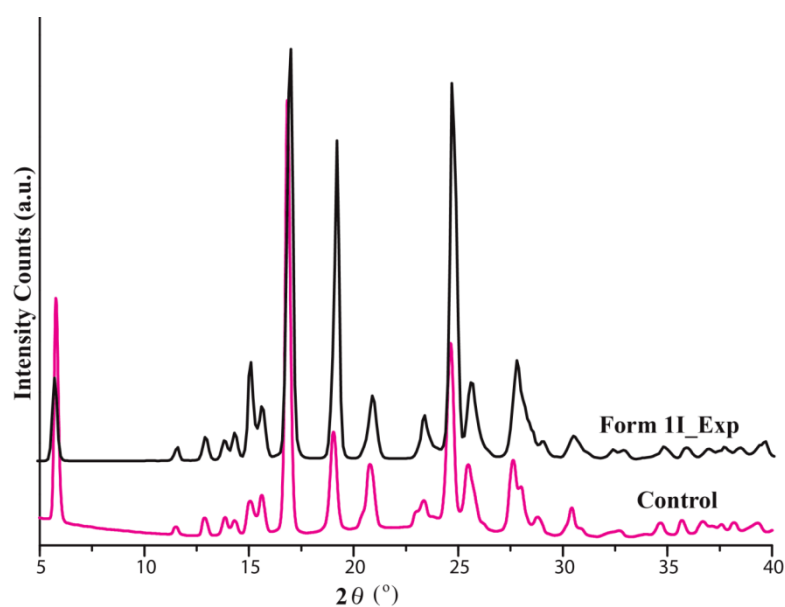


Figure 3.47. Overlay of PXRD patterns of form **II** crystals with crystals obtained from the melt crystallization of form **II** crystals from the glass surface.

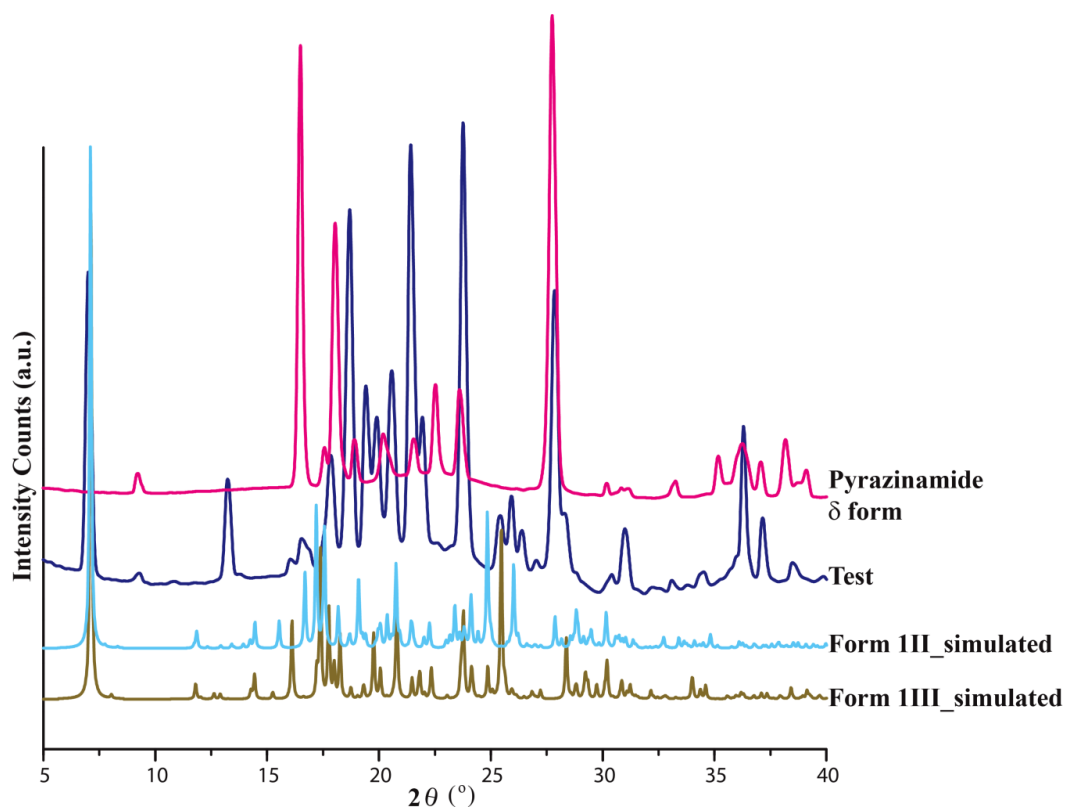


Figure 3.48. Overlay of PXRD patterns of form **1**III (green), **1**III (cyan) crystals, crystals obtained from the melt crystallization of form **1**I crystal form 001 face of δ -pyrazinamide (blue) and δ polymorph of pyrazinamide (pink).

This indicates that there is epitaxial interaction between nucleation promoting surface of pyrazinamide (001) face of δ polymorph) and prenucleation aggregate of form **1**I crystals which selectively inhibits its nucleation and promotes the growth of metastable polymorphs (form **1**III or form **1**III). This confirmed the efficacy of δ polymorph of pyrazinamide as substrates for controlling nucleation of compounds **1**, **2**, **3** and **4**.

The lattice matching program GRACE (Global Real-Space Analysis of Crystal Epitaxy)⁵⁸ was employed to calculate the epitaxy score (E) for δ -pyrazinamide (substrate) and polymorphs of **1** (*syn-anti*) (overlayer) over specified range of θ value to investigate the selective nucleation of metastable *anti* forms of **1** on the (001) face of δ -pyrazinamide. The substrate parameters for (001) face of δ -pyrazinamide were utilized for lattice matching with the crystal parameters of forms **1**I, **1**III and **1**III crystals. Other search parameters were kept default while total 145 planes (hkl ranging from -3 to 3) were used for searching the epitaxial match. Search strategy

with normalization was utilized to calculate E value. The results revealed, the highest E -value (8.75%) for (010) plane of form III amongst all the polymorphs suggesting its best epitaxial match and high affinity toward 001 face of δ -pyrazinamide (**Figure 3.50**).

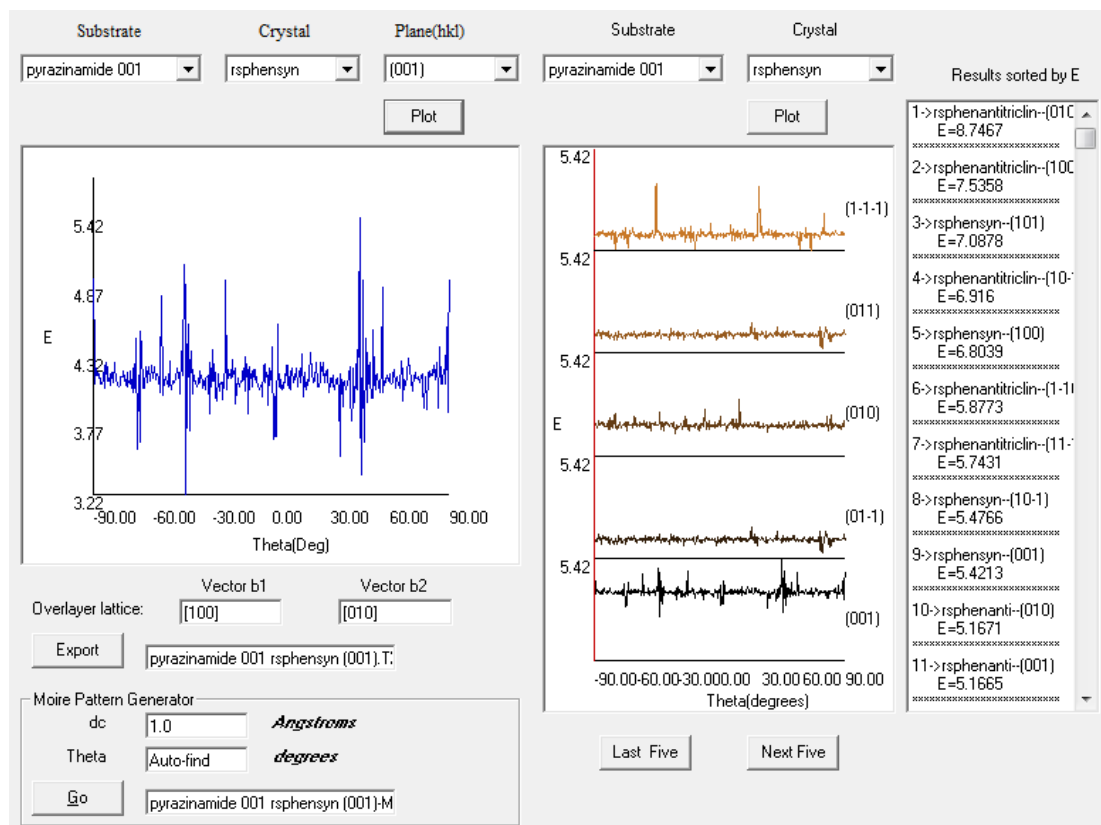


Figure 3.50. E vs θ output for the (001) δ -pyrazinamide / (101) form III crystal interface calculated with GRACE for different search areas.

MCHS experiment and Grace analysis proved that the epitaxial relation exists between the pyrazinamide (carboxamide) and **1** (sulfonamide), however, to envisage the molecular level interaction, we carried out binding studies between pyrazinamide and compounds **1**, **2** at under-saturated condition in non-polar solvent. As discussed earlier, 2D NOESY NMR studies revealed that compound **1** adopts *syn* conformation in chloroform whereas compound **2** exists in *midway* conformation. To investigate the effect of increasing concentrations of pyrazinamide on molecular conformation of compounds **1** and **2**, the titration studies were undertaken in CDCl_3 (**Figure 3.51a and 3.51b**). The ^1H NMR and 2D NOESY analysis of **1** and **2** in the absence of pyrazinamide revealed *syn* conformation of **1** with corresponding δ value for amide

proton 4.6 ppm and *midway* conformation of **2** with δ value for amide Hr proton 6.75 ppm. The higher downfield chemical shift of amide proton (δ -NH) = 2.15 ppm) in **2** as compared to **1** could be due to the dimeric strong hydrogen bonding interactions with pyridine N atom (**Figure 3.51d**). The gradual deshielding effect was observed for the chemical shift of sulfonamide proton Hr with the increasing amount of pyrazinamide and the δ value attains a plateau at 5.1 ppm for **1** and 6.84 for **2** at ~ 2 equivalent of pyrazinamide (**Figure 3.52-4.53**). The significant downfield chemical shift [$\Delta\delta$ -NH) = 0.54 ppm for **1**] and less chemical shift [$\Delta\delta$ -NH) = 0.09 ppm for **2**] of Hr proton could be due to the involvement of Hr proton of **2** in H-bonding interaction with either pyridine N-atom of **2** (dimeric homo-synthon) or N-atom of pyrazinamide or dynamic equilibrium between them as these bonds are more vibrant in solution i.e. constantly forming and breaking due to Brownian motion. The bifurcated H-bond shown is actually the average picture of the same (**figure 3.51d**). The chemical shift of amide Hp (δ =7.5-7.8) proton of pyrazinamide in **1** and **2** remained unchanged that may be due to engagement in the formation of intramolecular H-bonding interaction with pyridyl N-atom. The chemical shift (0.22-0.23 ppm) of amide Hq proton of pyrazinamide with or without sulfonamide (**Figure 3.54**) was observed suggesting extended one dimensional (1D) chain association of pyrazinamide dimers in solution *via* hydrogen bonding interactions which engages amide Hq proton and carbonyl oxygen of pyrazinamide (**Figures 3.51c and 3.51d, blue chain**). Chemical shift of aromatic or aliphatic protons of sulfonamide **1** and **2** also remained unchanged after addition of pyrazinamide suggests retention of their solution state conformation. Based on the CSD survey (conducted to know the preferential mode of association of pyrazinamide molecules in its crystals/cocrystals, version 5.35)⁵⁹, ¹H NMR titration data and evidences of close association of δ -form of pyrazinamide and *anti*-forms of **1**, we speculated solution state interaction between compounds **1**, **2** and pyrazinamide. Proposed model (cartoon representation of pyrazinamide with **1** and **2**) suggests that 1D organization of molecules of pyrazinamide (observed in its δ -polymorph, **Figures 3.51c and 3.51d**, blue chain) forms hydrogen bonding interactions with N-H proton of monomer (**1**) and dimer (**2**) in CDCl₃ (**Figure 3.51c and 3.51d**). Although speculative but based on important clues such self-assemblies of pyrazinamide in its δ -polymorph could be serving as template for enrichment of metastable forms of **1**, **2**, **3** and **4**.

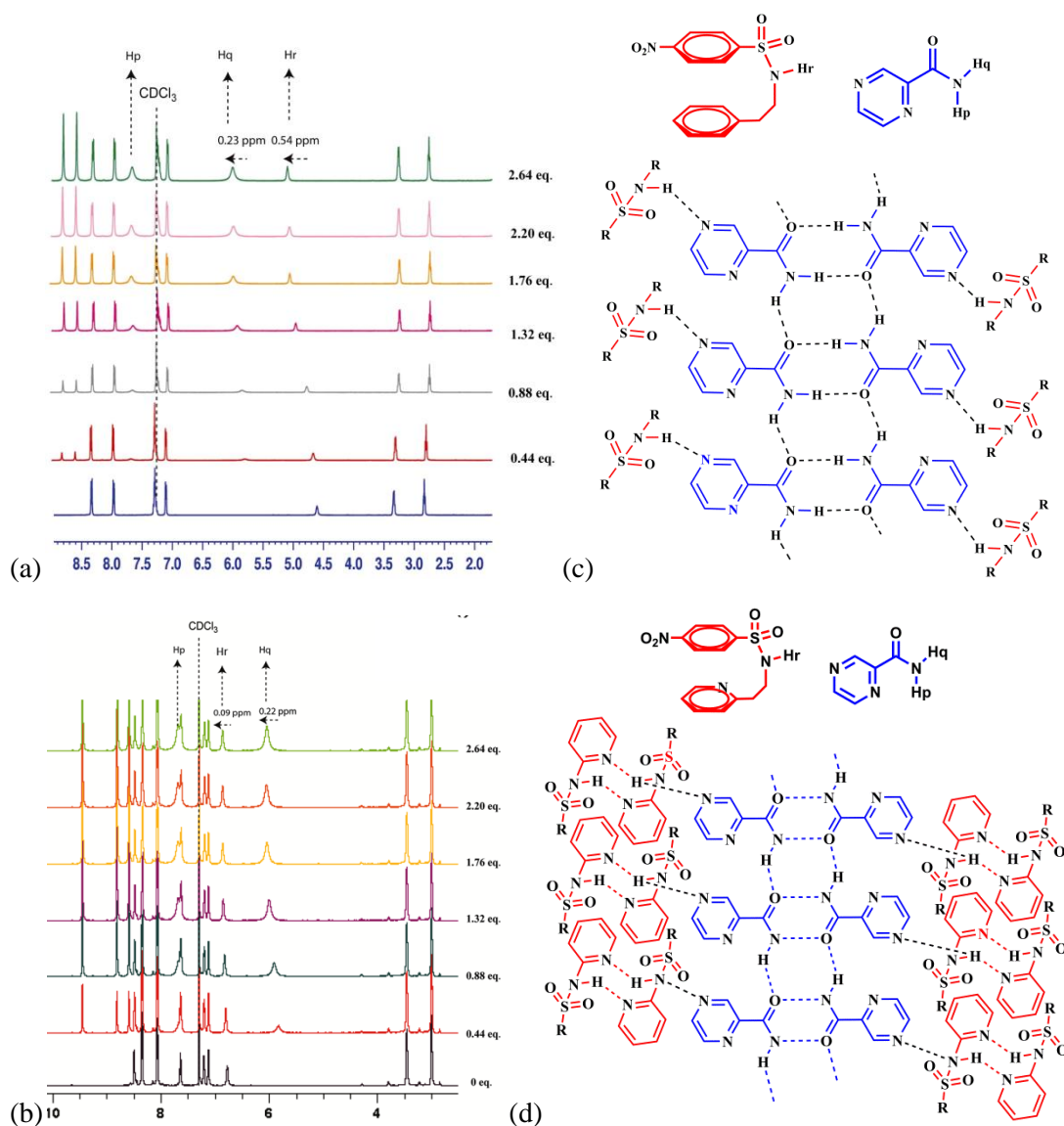


Figure 3.51. Overlay of ^1H NMR spectra of titration study carried out upon serial addition of 0, 0.44, 0.88, 1.32, 1.76, 2.20 and 2.64 equivalent of pyrazinamide to compounds (a) **1** and (b) **2** in CDCl_3 , associated chemical shifts of proton H_q and H_r are shown with arrows. Cartoon representation of predicted solution state association of (c) **1** and (d) **2** with pyrazinamide self-assembly.

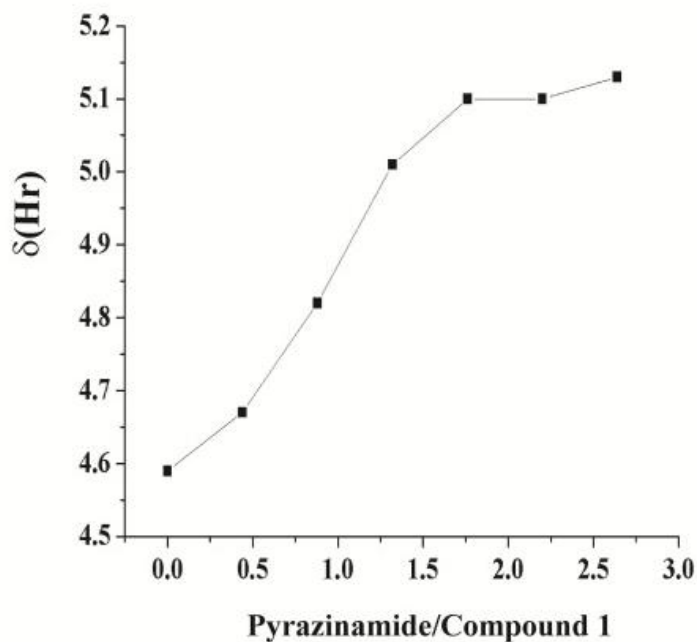


Figure 3.52. Graphical representation of chemical shift of Hr proton; along x -axis is the ratio of pyrazinamide to compound 1 and along y -axis the chemical shifts (δ) of protons H in ppm.

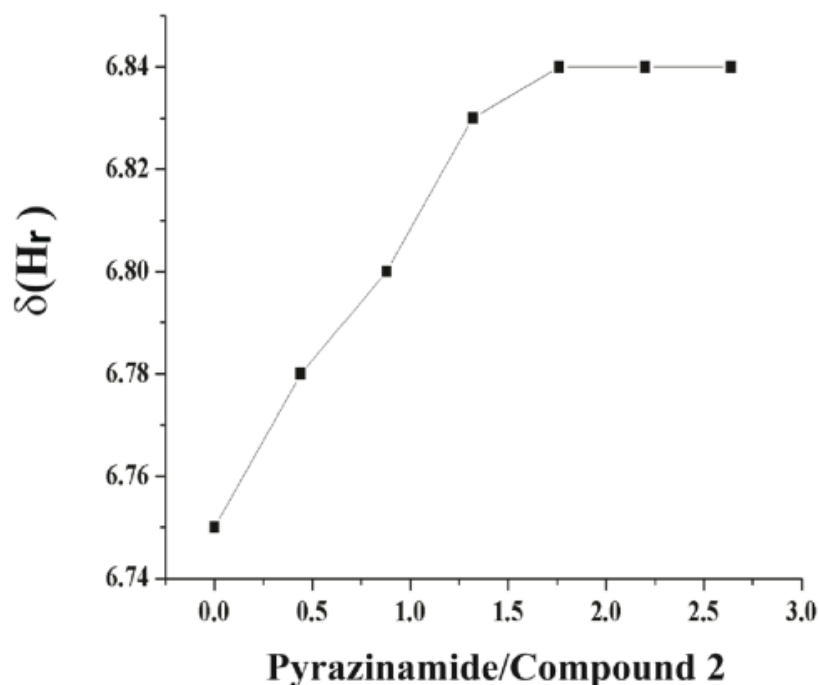


Figure 3.53. Graphical representation of chemical shift of Hr proton; along x -axis is the ratio of pyrazinamide to compound 2 and along y -axis its chemical shifts (δ) of protons H in ppm.

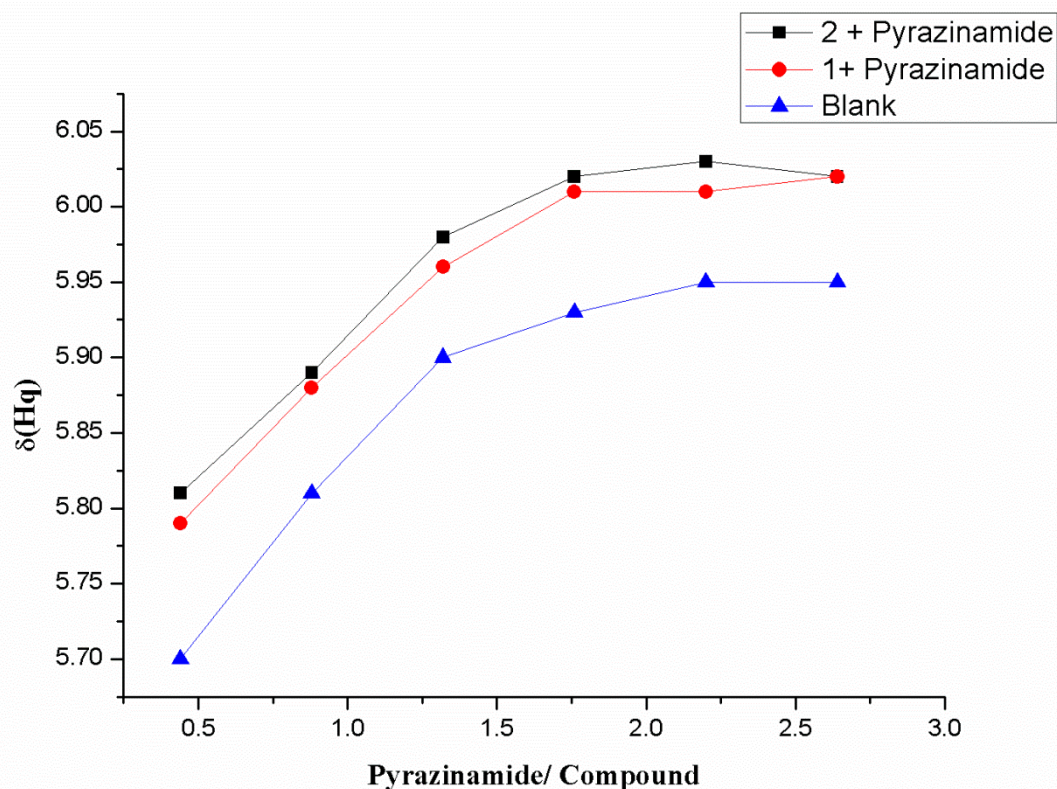


Figure 3.54. Chemical shift in ppm of Hq proton during ^1H NMR titration study with compounds **1** and **2** and blank titration.

Lattice matching analysis and solution state binding studied were further used to hypothesize the interactions between molecular arrangement on (001) face of δ polymorph of pyrazinamide and association of molecules of form **1III** crystal on its (010) face (**Figures 3.55-3.56**). The large surface of pyrazinamide crystals (001 face) formed *via* weak interactions of the parallel 2D sheets (created by joining of $\text{N-H}\cdots\text{O}=\text{C}$ homo dimers by $\text{C-H}\cdots\text{N}$ contacts, **Figure 3.55a**) could be acting as the nucleation site for the generation of forms **1II** or **1III** crystals.

We proposed two step models for selective enrichment of metastable nuclei of *anti*-form of compound **1**. Initially (step 1), molecules of **1** would be interacting with homodimers ($\text{N-H}\cdots\text{O}=\text{C}$ linked) of pyrazinamide at the interface (001 face), followed by propagation step (step 2) wherein subsequent assembling of $\text{N-H}\cdots\text{O}=\text{S}$ linked dimeric motifs of molecules of **1** *via* weak interactions could have occurred similar to the arrangements on 010 face of form **1III** crystals (**Figure 3.56**).

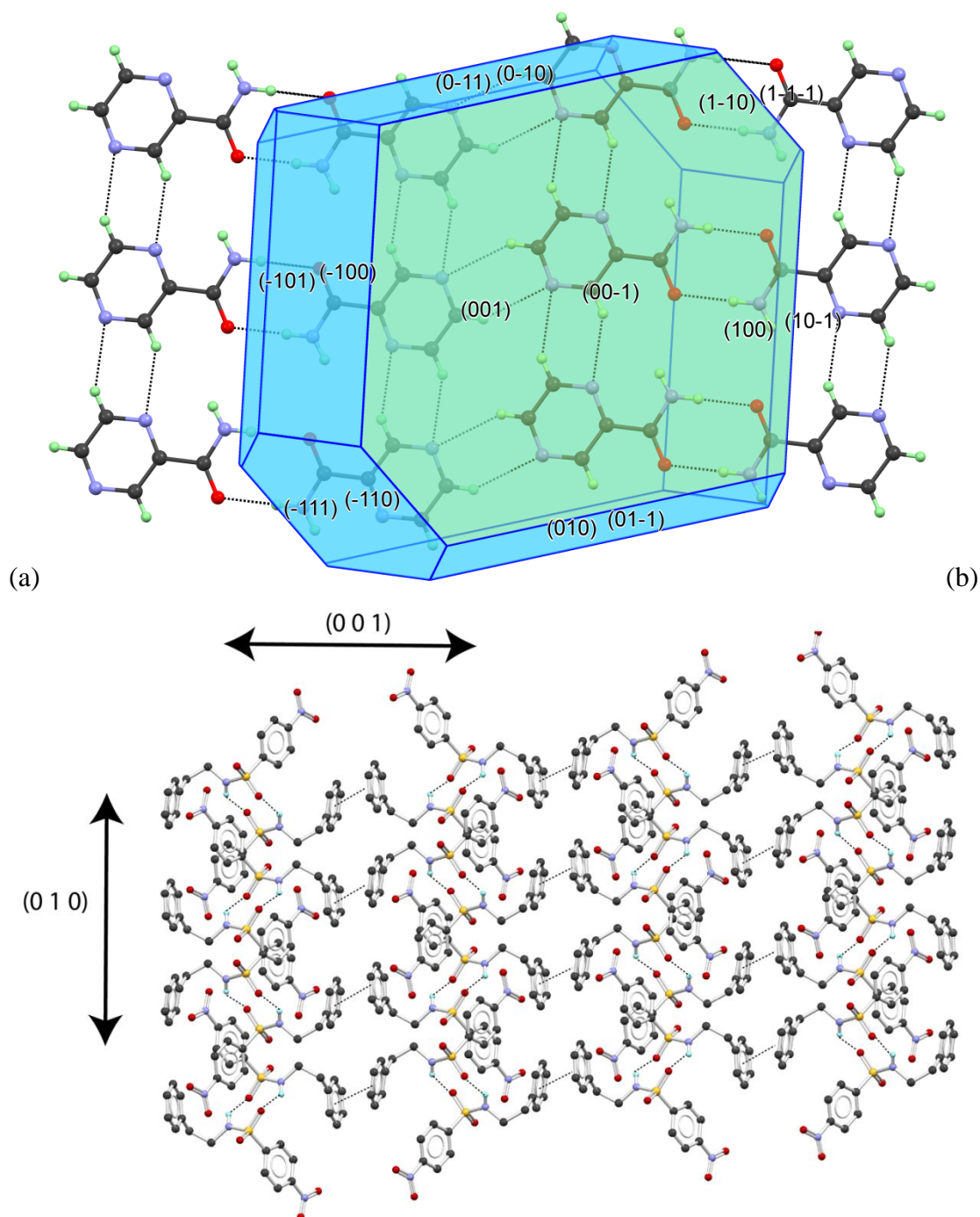


Figure 3.55. (a) Packing of molecules of δ -pyrazinamide on 001 face through N-H...O and C-H...N interactions and (b) association of molecules of forms **1II** or **1III** along the 010 face of the crystals revealing linking of the N-H...O=S dimers.

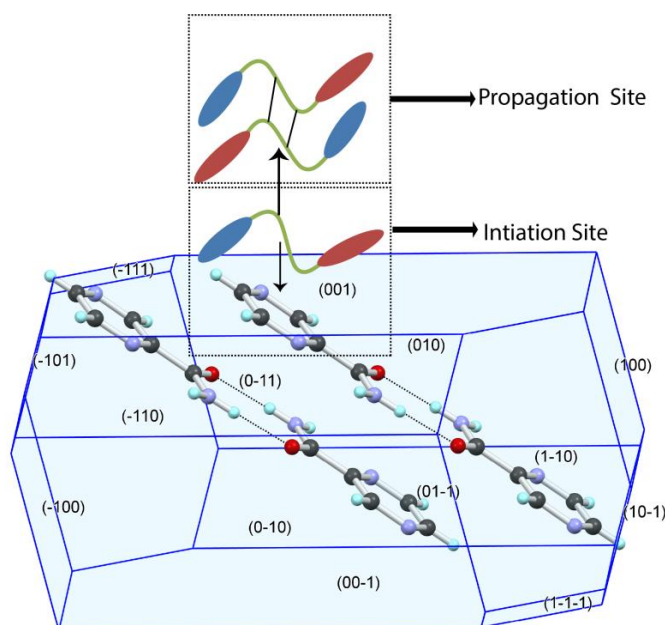


Figure 3.56. Cartoon representation of the proposed nucleation of forms **III** or **IIII** crystals of **1** on 001 face of δ -pyrazinamide crystals.

A comprehensive compilation of the study revealed the pivotal role played by $\pi \cdots \pi$ stacking interactions in locking the conformation of flexible sulfonamides **1**, **2** and sulfoesters **3**, **4** thereby driving the self-assembly to generate the stable crystal lattice albeit having higher lattice energy. It also blocks the manifestation of polymorphism that is an inherent property of these compounds. The 2D solution state NMR studies of compounds **1**, **3** and **4** also indicate the *syn* geometry of molecules in non-polar solvent (CDCl_3). However, the same study revealed the absence of *syn* conformation of molecules of **1** in methanol indicating the strong interaction between the solute and the solvent molecules by that inhibiting the existence of its typical *syn* conformation. It suggest that the prenuclei clusters (PNC) possessing either *syn*, *anti* or midway conformation may be present in chloroform-methanol mixture at the supersaturation stage, but the prevalence of the *syn* confirmation during nucleation dominates the crystallization event due to the extended chain of $\pi \cdots \pi$ stacking supramolecular assembly. However, the use of pyrazinamide in excess as an additive during crystallization prevents the formation of prenuclei cluster of *syn* and midway conformers of **1** and **2** respectively due to their affinity towards pyrazinamide self-assembly (confirmed by solution state ^1H NMR analysis and crystallization

experiment on 001 face of δ -pyrazinamide). It perturbed the stable stacking arrangement of substrate molecules thereby enabling the enrichment of metastable prenuclei (*anti* or *midway* conformer) whose successive aggregation lead to the generation of metastable polymorphs. The crystal-to-crystal thermal phase transition of forms **1II**, **1III** and **1IV** to form **1I** crystals of **1** is studied by DSC, HSM and crystallographic studies. The conversion of form **1III** crystals to form **1II** crystals just by gentle grinding is very interesting could be achieved by just sliding the layers. The mechanism of transition was also sought from the knowledge of morphotropism.

Conclusion:

In conclusion, the results highlighted the pivotal role played by extended $\pi\cdots\pi$ stacking supramolecular assembly along with N-H \cdots O/N-H \cdots N/C-H \cdots O hydrogen bonding in dictating the self-assembly thereby provide stability to *syn* PNC during nucleation process. The intervention of a stable stacking assembly by introduction of an additive generates new metastable polymorphs. The pyrazinamide additive played a pivotal role for providing an alternate nucleation path (crystallographic gene!) which aid in capturing the elusive polymorphs by epitaxial method. This technique is commonly used to control the polymorphism where the surface of the impurity/additive is utilized to promote the growth of the preferred phase of the crystal. With this insight, it is possible to predict and generate selective polymorphic form using tailor made auxiliaries, although, it is critical for designing such additives in more general way to control its inhibition or promotion. Our study put forth the need for development of high throughput screening technology to study the effect of additives on crystallization process.

Experimental Methods:

Preparation of 4-nitro-N-phenethylbenzenesulfonamide (1): To a solution of 2-phenylethanamine (1.71 mL, 13.536 mmol, 1.5 eq.) in dry DCM (20 mL), dry triethylamine (1.9 mL, 13.536 mmol, 1.5 eq.) was added dropwise followed by slow addition of 4-nitrobenzenesulfonyl chloride (2g, 9.024 mmol) in dry DCM at 0 °C. The reaction mixture was allowed to reach room temperature and was further stirred for 8 h. The reaction mixture was then sequentially washed twice with saturated solution of NaHCO₃ and once with brine. The organic layer was dried over anhydrous Na₂SO₄ and evaporated under vacuum to get crude product which on purification by column chromatography (eluent: pet ether/ethyl acetate: 90:10) yielded (1). ¹H NMR (500 MHz, CDCl₃), δ = 8.32 (d, *J* = 8.5 Hz, 2 H), 7.95 (d, *J* = 8.5 Hz, 2 H), 7.34 - 7.20 (m, 4 H), 7.08 (d, *J* = 7.0 Hz, 2 H), 4.59 (br. s., 1 H), 3.32 (q, *J* = 6.1 Hz, 2 H), 2.81 (t, *J* = 6.7 Hz, 2 H), ¹³C NMR (125 MHz, CDCl₃), δ 149.8, 145.6, 137.2, 128.7, 128.6, 128.1, 126.8, 124.3, 44.3, 35.7 ppm.

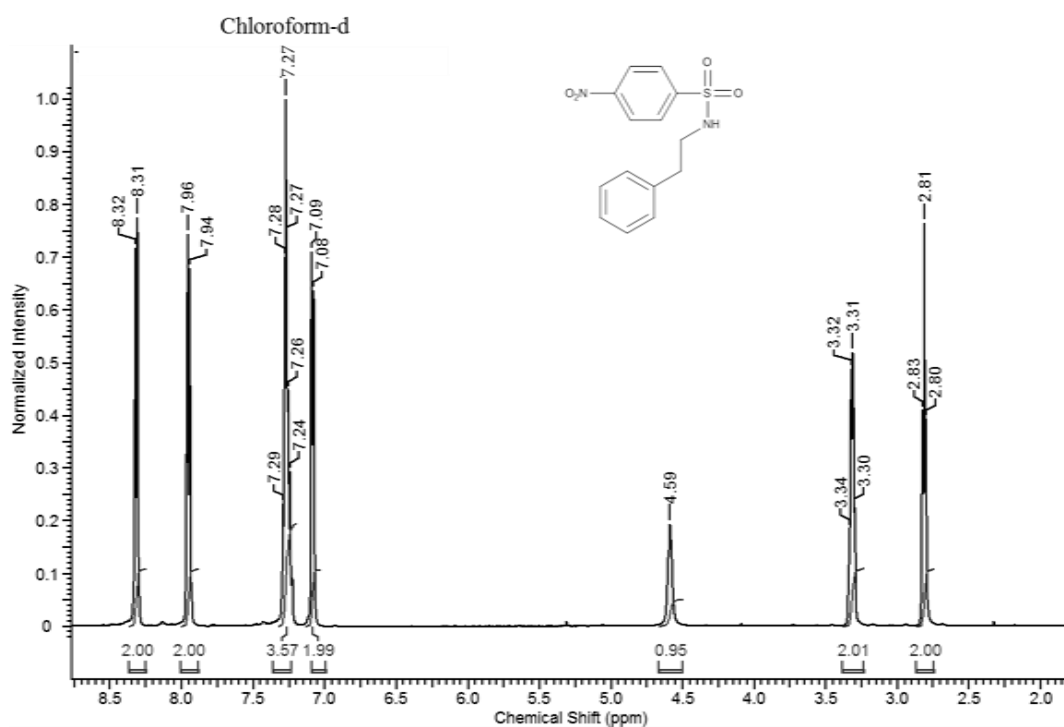


Figure 3.57. ¹H NMR spectrum of 1 in CDCl₃

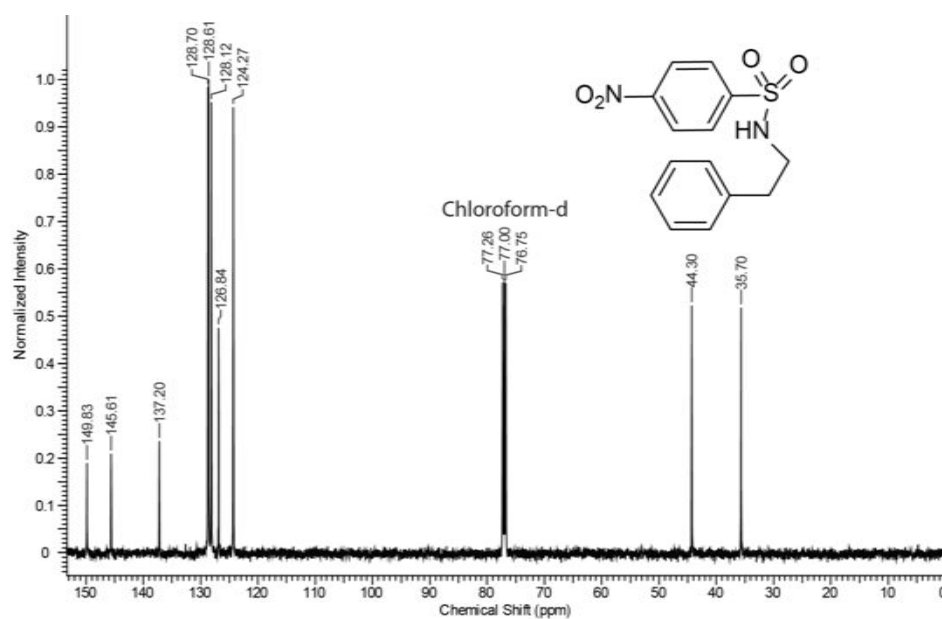


Figure 3.58. ^{13}C NMR spectrum of **1** in CDCl_3

Preparation of 4-nitro-N-(2-(pyridin-2-yl)ethyl)benzenesulfonamide(2): The aromatic sulfonamide **2** was prepared as above using 2-(2-Pyridyl)ethylamine (1.62 mL, 13.536 mmol, 1.5 eq.) instead of 2-phenylethanamine; yield 1.52 g (55%). mp. 408-409 K, $^1\text{H NMR}$ (500 MHz, CDCl_3), δ 8.47 (d, $J = 4.6$ Hz, 1 H), 8.37 - 8.29 (m, 2 H), 8.08 - 8.00 (m, 2 H), 7.60 (m, 1 H), 7.17 (dd, $J = 5.0, 7.2$ Hz, 1 H), 7.09 (d, $J = 7.9$ Hz, 1 H), 6.73 (br. s., 1 H), 3.44 (q, $J = 5.8$ Hz, 2 H), 3.00 - 2.93 ppm (m, 2 H); $^{13}\text{C NMR}$ (125 MHz, CDCl_3), δ 158.8, 149.9, 149, 146.3, 137, 128.2, 124.3, 123.5, 122, 42.3, 35.6 ppm.

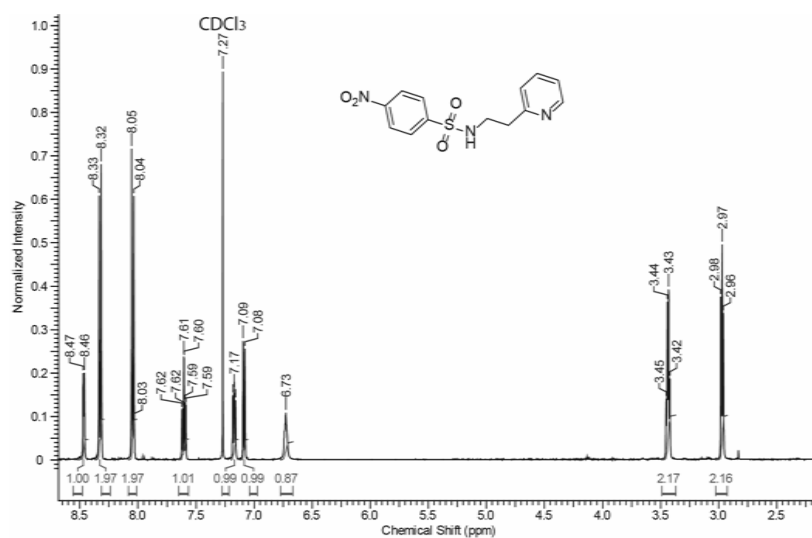


Figure 3.59. $^1\text{H NMR}$ spectrum of **2** in CDCl_3

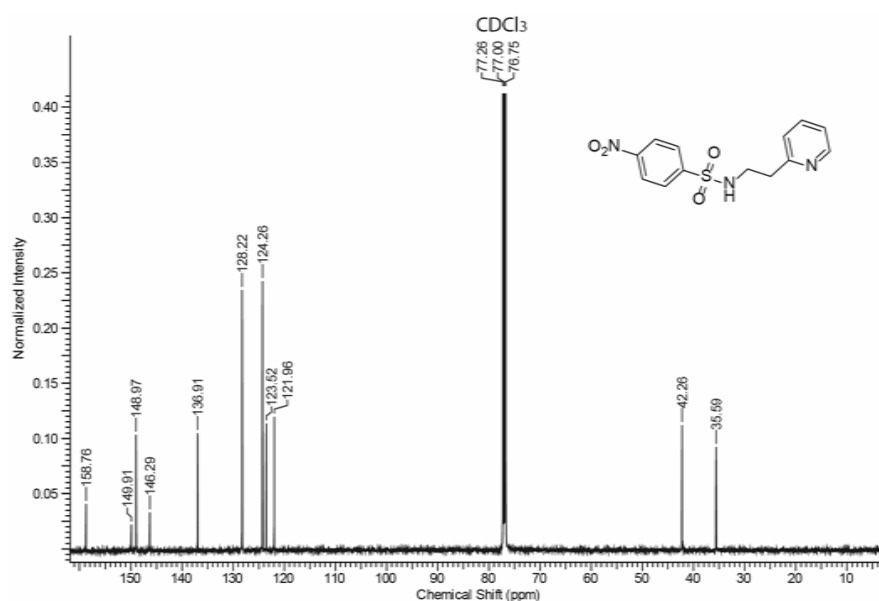


Figure 3.60. $^{13}\text{C NMR}$ spectrum of **2** in CDCl_3

Preparation of phenethyl 4-nitrobenzenesulfonate (3): The aromatic sulphoester **3** was prepared as above using 2-phenylethanol (1.62 mL, 13.536 mmol, 1.5 eq.) instead of 2-phenylethanamine; yield 1.4 g (50%). mp. 370-371 K. $^1\text{H NMR}$ (500 MHz, CDCl_3), δ 8.30 - 8.23 (m, 2 H), 7.93 - 7.87 (m, 2 H), 7.26 - 7.22 (m, 3 H), 7.09 (m, 2 H), 4.34 (t, $J = 6.7$ Hz, 2 H), 3.00 ppm (t, $J = 6.7$ Hz, 2 H); $^{13}\text{C NMR}$ (125 MHz, CDCl_3): δ 150.5, 141.6, 135.8, 129, 128.9, 128.7, 127.1, 124.3, 72, 35.3 ppm.

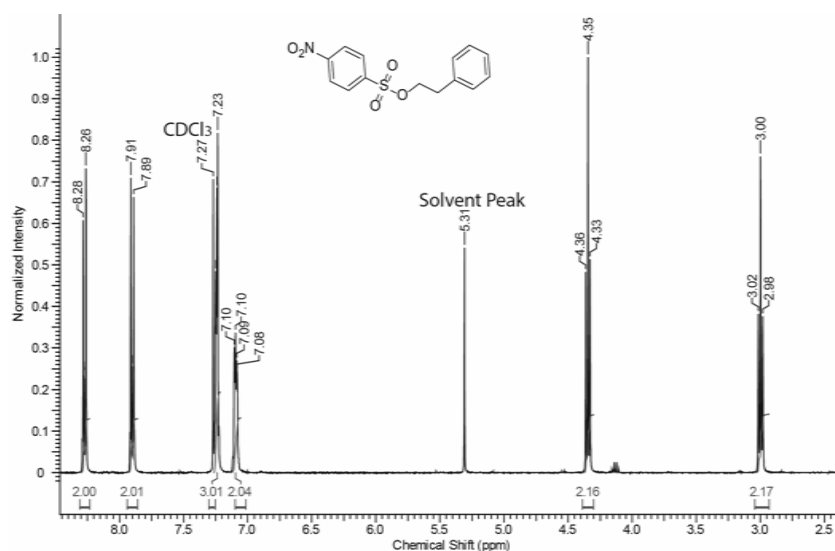


Figure 3.61. $^1\text{H NMR}$ spectrum of **3** in CDCl_3

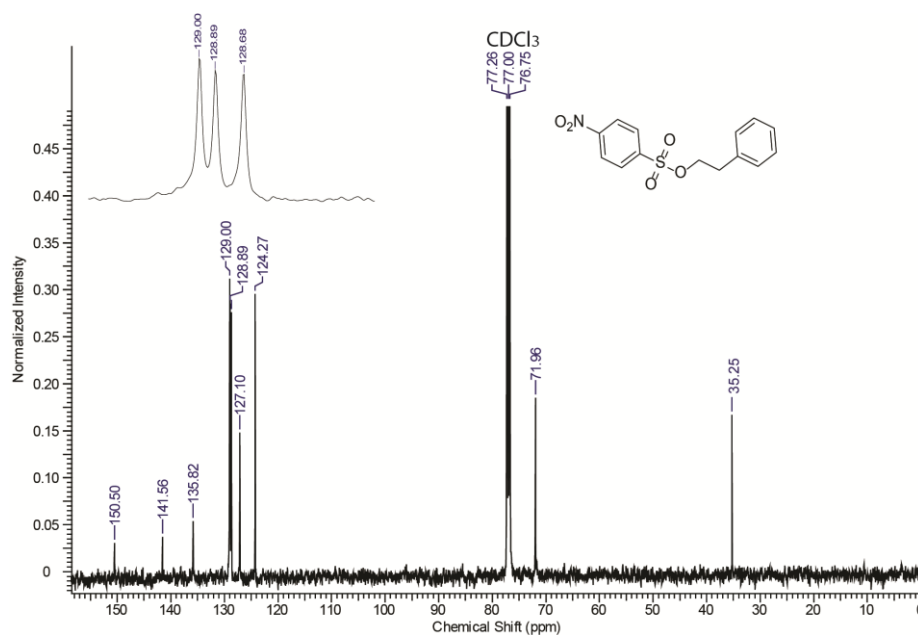


Figure 3.62. $^{13}\text{C NMR}$ spectrum of **3** in CDCl_3

Preparation of 2-(pyridin-2-yl)ethyl 4-nitrobenzenesulfonate(4): The aromatic sulphoester **4** was prepared as above using 2-pyridine-ethanol (1.53 mL, 13.536 mmol, 1.5 eq.) instead of 2-phenylethanamine, yield 1.4 g (50%). mp. 374-375 K. ^1H NMR (400 MHz, CDCl_3), δ 8.37 (d, $J = 4.6$ Hz, 1 H), 8.34 - 8.28 (m, 2 H), 7.99 - 7.93 (m, 2 H), 7.63 - 7.56 (m, 1 H), 7.17 - 7.11 (m, 2 H), 4.58 (t, $J = 6.4$ Hz, 2 H), 3.16 ppm (t, $J = 6.4$ Hz, 2 H); ^{13}C NMR (100MHz, CDCl_3): δ 156, 150.6, 149.4, 141.7, 136.6, 129.1, 124.2, 123.9, 122, 70.6, 37.1 ppm.

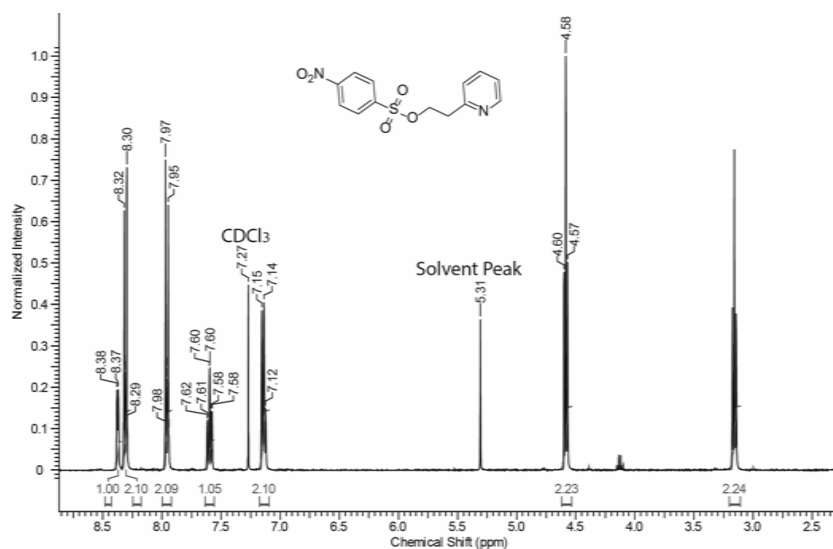


Figure 3.63. ^1H NMR spectrum of **4** in CDCl_3

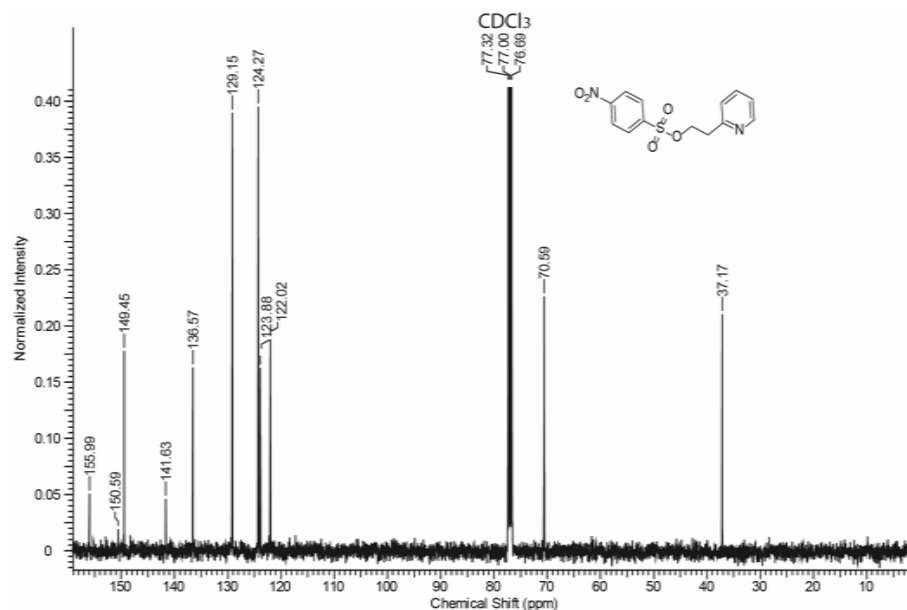


Figure 3.64. ^{13}C NMR spectrum of **4** in CDCl_3

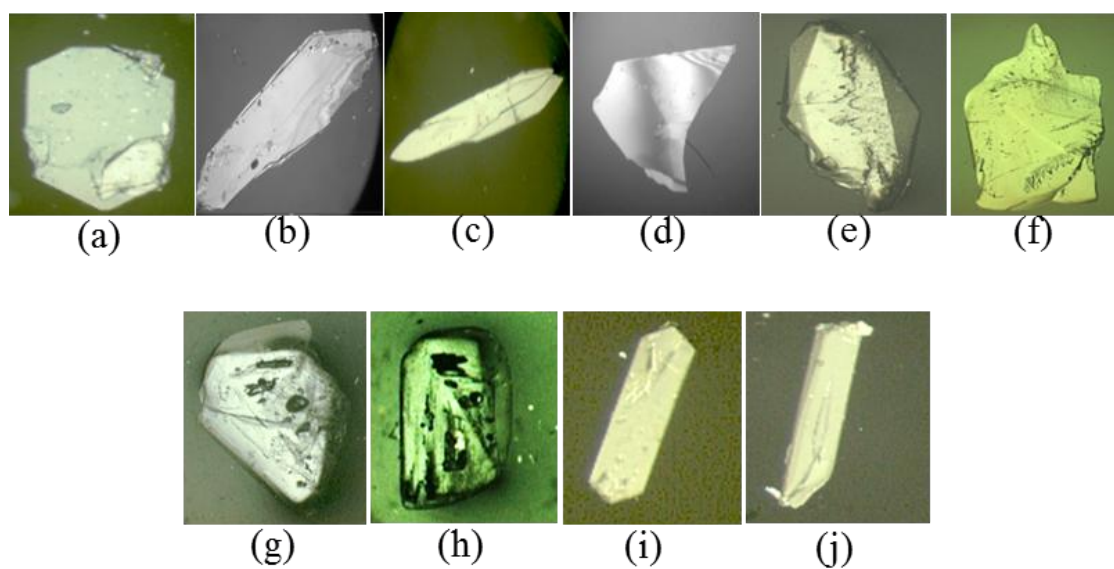


Figure 3.65. Photomicrographs of polymorphs of compounds **1**, **2**, **3** and **4**; (a) form **1I**, (b) form **1II**, (c) form **1III**, (d) form **1IV**, (e) form **2I**, (f) form **2II**, (g) form **3I**, (h) form **3II**, (i) form **4I** and (j) form **4II** crystals.

Table 3.5. Crystallographic data table for polymorphs of **1**, **2**, **3** and **4**

Crystal Data	form II	form III	form IIII	form IIIV	form 2I
Formula	C ₁₄ H ₁₄ N ₂ O ₄ S	C ₁₄ H ₁₄ N ₂ O ₄ S	C ₁₄ H ₁₄ N ₂ O ₄ S	C ₁₄ H ₁₄ N ₂ O ₄ S	C ₁₃ H ₁₃ N ₃ O ₄ S
M _r	306.33	306.33	306.33	306.33	307.32
Crystal Size, mm	0.52×0.43×0.15	0.48×0.25×0.11	0.45×0.26×0.09	0.35×0.25×0.05	0.45×0.35×0.15
Temp. (K)	296 (2)	296 (2)	296 (2)	100 (2)	296 (2)
Crystal Syst.	monoclinic	triclinic	monoclinic	monoclinic	orthorhombic
Space Group	<i>P</i> 2 ₁ / <i>c</i>	<i>P</i> -1	<i>P</i> 2 ₁ / <i>c</i>	<i>P</i> 2 ₁ / <i>c</i>	<i>Pbcn</i>
<i>a</i> /Å	15.8926(4)	9.5434(6)	9.516(5)	25.618(3)	7.375(7)
<i>b</i> /Å	7.7145(2)	12.2943(7)	12.261(7)	7.4924(9)	14.966(10)
<i>c</i> /Å	12.0336(3)	13.8259(8)	24.949(14)	7.3829(8)	24.834(17)
α^0	90	111.324(3)	90	90	90
β^0	102.8840(10)	104.125(3)	96.236(10)	95.368(9)	90
γ^0	90	90.018(3)	90	90	90
<i>V</i> /Å ³	1438.22(6)	1458.30(15)	2894(3)	1410.9(3)	2741(4)
<i>Z</i>	4	4	8	4	4
<i>D</i> _{calc} /g cm ⁻³	1.415	1.395	1.406	1.442	1.489
<i>m</i> /mm ⁻¹	0.242	0.239	0.241	0.247	0.256
<i>F</i> (000)	640	640	1280	640	1280
<i>Ab. Correct.</i>	multi-scan	multi-scan	multi-scan	multi-scan	multi-scan
<i>T</i> _{min} / <i>T</i> _{max}	0.884/0.965	0.894/0.975	0.899/0.980	0.919/0.988	0.893/0.963
2 θ _{max}	50	50	50	50	50
Total reflns.	23254	21524	19618	9975	6206
uniquereflns.	2520	5134	5094	2484	2182
Obs. reflns.	2174	3898	3404	2013	1448
<i>h, k, l</i> (min, max)	(-17, 18), (-9, 9), (-14, 14)	(-11, 11), (-14, 14), (-16, 16)	(-11, 11), (-14, 10), (-29, 29)	(-30, 28), (-8, 8), (-8, 8)	(-4, 8), (-17, 14), (-28, 28)
<i>R</i> _{int}	0.0309	0.0394	0.0655	0.0571	0.0379
No. of para	194	388	387	194	194
<i>RI</i> [<i>I</i> > 2 σ (<i>I</i>)]	0.0323	0.0476	0.0794	0.0539	0.0604
<i>wR2</i> [<i>I</i> > 2 σ (<i>I</i>)]	0.0815	0.1227	0.2117	0.1122	0.1804
<i>RI</i> [all data]	0.0393	0.0653	0.1128	0.0698	0.1073
<i>wR2</i> [all data]	0.0868	0.1379	0.2396	0.1179	0.2795
goodness-of-fit	1.089	1.029	1.111	1.119	1.148
$\Delta\rho_{\max}, \Delta\rho_{\min}$ (eÅ ⁻³)	+0.23, -0.28	+0.61, -0.30	+0.64, -0.54	+0.27, -0.42	+0.69, -0.87
CCDC no.	1007411	1007413	1007414	1007412	1035742

Crystal Data	form 3I	form 3II	form 4I	form 4II	form 2II
Formula	C ₁₄ H ₁₃ NO ₅ S	C ₁₄ H ₁₃ NO ₅ S	C ₁₃ H ₁₂ N ₂ O ₅ S	C ₁₃ H ₁₂ N ₂ O ₅ S	C ₁₃ H ₁₃ N ₃ O ₄ S
M _r	307.31	307.31	308.31	308.31	307.32
Crystal Size, mm	0.45×0.41×0.11	0.45×0.15×0.10	0.35×0.15×0.08	0.40×0.21×0.07	0.49×0.45×0.15
Temp. (K)	296(2)	296(2)	296(2)	100(2)	100 (2)
Crystal Syst.	monoclinic	monoclinic	monoclinic	triclinic	triclinic
Space Group	<i>P</i> 2 ₁ / <i>c</i>	<i>P</i> 2 ₁ / <i>c</i>	<i>P</i> 2 ₁ / <i>c</i>	<i>P</i> -1	<i>P</i> -1
<i>a</i> /Å	16.0646(7)	7.5823(3)	7.7486(10)	6.1631(7)	7.5651(7)
<i>b</i> /Å	7.6950(3)	10.7711(5)	21.296(3)	9.1150(10)	7.7551(7)
<i>c</i> /Å	11.8416(5)	17.5885(8)	8.4358(10)	11.8406(13)	12.8433(12)
α^0	90	90	90	93.420(5)	74.294(6)
β^0	101.916(3)	101.458(2)	99.266(8)	93.038(5)	82.687(6)
γ^0	90	90	90	90.628(5)	67.939(6)
<i>V</i> /Å ³	1432.28(10)	1407.82(11)	1373.9(3)	662.98(13)	671.97(11)
<i>Z</i>	4	4	4	2	2
<i>D</i> _{calc} /g cm ⁻³	1.425	1.450	1.491	1.544	1.519
<i>m</i> /mm ⁻¹	0.247	0.251	0.259	0.269	0.261
<i>F</i> (000)	640	640	640	320	320
<i>Ab. Correct.</i>	multi-scan	multi-scan	'multi-scan'	'multi-scan'	multi-scan
<i>T</i> _{min} / <i>T</i> _{max}	0.897/0.973	0.895/0.975	0.915/0.981	0.900/0.981	0.883/0.962
2 θ _{max}	50	50	50	50	50
Total reflns.	12431	28257	9693	9477	10483
uniquereflns.	2514	2474	2364	2318	2361
Obs. reflns.	2046	2214	2087	2227	1979
<i>h, k, l</i> (min, max)	(-18, 19), (-9, 9), (-13, 14)	(-9, 9), (-12, 12), (-20, 20)	(-9, 9), (-25, 25), (-10, 9)	(-7, 7), (-10, 10), (-14, 13)	(-8, 8), (-9, 9), (-15, 15)
<i>R</i> _{int}	0.0637	0.0575	0.0210	0.0217	0.0516
No. of para	191	191	191	191	195
<i>RI</i> [<i>I</i> > 2 σ (<i>I</i>)]	0.0533	0.0343	0.0495	0.0289	0.0381
<i>wR2</i> [<i>I</i> > 2 σ (<i>I</i>)]	0.1119	0.0886	0.0852	0.0731	0.0954
<i>RI</i> [all data]	0.0680	0.0387	0.0580	0.0302	0.0479
<i>wR2</i> [all data]	0.1195	0.0933	0.0884	0.0739	0.0989
goodness-of-fit	1.088	1.068	1.095	1.079	1.187
$\Delta\rho_{\max}, \Delta\rho_{\min}$ (eÅ ⁻³)	+0.29, -0.26	+0.15, -0.30	+0.31, -0.31	+0.36, -0.36	+0.39, -0.41
CCDC no.	1035744	1007415	1035745	1035746	1035743

Table 3.6. Torsion angles ($^{\circ}$) for polymorphs of **1**, **2**, **3** and **4**

		form 1I	form 1II		form 1III		form 1IV
			Mol 1	Mol 2	Mol 1	Mol 2	
τ_1	C1-S-N2-C7/ C1'-S'-N2'-C7'	68.94(16)	-75.5(2)	-73.4(2)	-74.0(5)	74.2(5)	-90.3(3)
τ_2	S-N2-C7-C8/ S'-N2'-C7'-C8'	-144.49(16)	-143.2(2)	-143.3(2)	-143.4(5)	144.3(5)	-163.9(2)
τ_3	N2-C7-C8-C9/ N2'-C7'-C8'-C9'	63.7(2)	64.2(3)	65.2(3)	64.4(7)	-64.2(7)	-177.3(3)
		form 2I			form 2II		
τ_1	C1-S-N2-C7	69.63(17)			61.34(17)		
τ_2	S-N2-C7-C8	168.16(13)			154.59(16)		
τ_3	N2-C7-C8-C9	75.7(2)			-69.1(2)		
		form 3I			form 3II		
τ_1	C1-S-O5-C7	76.1(2)			79.53(12)		
τ_2	S-O5-C7-C8	-147.3(2)			-145.90(11)		
τ_3	O5-C7-C8-C9	63.4(3)			66.92(19)		
		form 4I			form 4II		
τ_1	C1-S-O5-C7	71.01(19)			-70.37(11)		
τ_2	S-O5-C7-C8	-151.30(19)			172.85(10)		
τ_3	O5-C7-C8-C9	63.9(3)			-62.34(17)		

Table 3.7. Geometrical parameters of intermolecular interactions in polymorphs of the 1,2, 3 and 4

Compound	entry	D-H...A	D-H (Å)	H...A (Å)	D...A/ Cg...Cg (Å)	D-H...A / α (°)	Symmetry codes
form II	1.	N2-H2N...O1	0.82(2)	2.30(2)	3.0649(19)	155.3(19)	1-x,- 1/2+y,1/2-z
	2.	C7-H7A...O2	0.99	2.52	3.309(2)	137	1-x,- 1/2+y,1/2-z
	3.	C3-H3...O4	0.95	2.57	3.435(3)	151	-x,1-y,-z
	4.	C6-H6...O2	0.95	2.54	3.238(2)	130	x,3/2-y,- 1/2+z
	5.	Cg1...Cg2			3.8124(11)	7.00(9)	x,1+y,z
	6.	Cg1...Cg2 (intra)			3.9178(11)	7.00(9)	x,y,z
form III	7.	N2-H2N...O2	0.76(3)	2.25(3)	2.995(3)	168(3)	1-x,1-y,1-z
	8.	N2'-H2'N...O2'	0.78(3)	2.22(3)	2.991(3)	168(3)	-x,-y,1-z
	9.	C7-H7A...O1'	0.99	2.49	3.382(3)	150	1-x,1-y,1-z
	10.	C2'-H2'...O2	0.95	2.61	3.371(3)	137	x,y,z
	11.	C8'-H8'B...O3	0.99	2.72	3.704(4)	176	-1+x,- 1+y,z
	12.	C7-H7B...O4	0.99	2.53	3.275(3)	132	1-x,2-y,1-z

	13.	C7'-H7'B...O4'	0.99	2.50	3.247(3)	132	-x,1-y,1-z
	14.	C2-H2...O2'	0.95	2.63	3.394(3)	138	x,1+y,z
	15.	C8-H8B...O3'	0.99	2.70	3.683(4)	174	1+x,y,z
	16.	C7'-H7'A...O1	0.99	2.48	3.379(3)	151	-x,1-y,1-z
form 1III	17.	N2-H2N...O2'	0.85(6)	2.15(6)	2.968(6)	163(6)	1-x,- 1/2+y,1/2 -z
	18.	N2'-H2'N...O2	0.73(6)	2.27(6)	2.982(7)	165(6)	1- x,1/2+y,1 /2-z
	19.	C7-H7A...O1'	0.99	2.46	3.355(7)	150	-1+x,- 1+y,z
	20.	C2'-H2'...O2'	0.95	2.60	3.354(6)	137	2- x,1/2+y,1 /2-z
	21.	C8-H8B...O3	0.99	2.70	3.685(9)	175	- x,1/2+y,1 /2-z
	22.	C7'-H7'B...O1	0.99	2.49	3.385(7)	150	x,1+y,z
	23.	C2-H2...O2	0.95	2.62	3.383(6)	138	1-x,- 1/2+y,1/2 -z
	24.	C8'-H8'A...O3'	0.99	2.68	3.670(9)	174	1-x,- 1/2+y,1/2 -z
	25.	C7'-H7'A...O4	0.99	2.53	3.262(8)	131	1- x,3/2+y,1 /2-z
	26.	C7-H7B...O4'	0.99	2.48	3.227(8)	132	1-x,- 3/2+y,1/2 -z
	27.	N2-H2N...O2	0.80(3)	2.19(3)	2.985(4)	173(3)	x,3/2-y,-

form 1IV							$1/2+z$
	28.	C14-H14...O1	0.95	2.53	3.421(4)	156	$x,y,-1+z$
	29.	C8-H8A...N2	0.99	2.68	3.562(4)	149	$x,3/2-y,-$ $1/2+z$
	30.	C3-H3...O2	0.95	2.44	3.313(4)	153	$x,-1+y,z$
	31.	C6-H6...O4	0.95	2.43	3.343(4)	162	$x,1+y,z$
	32.	C7-H7A...O1	0.99	2.62	3.591(4)	165	$x,1/2-y,-$ $1/2+z$
	33.	C5-H5...O3	0.95	2.48	3.352(4)	153	- $x,1/2+y,3$ $/2-z$
	34.	Cg1...Cg1			3.6948(18)	0	$x,1/2-y,-$ $1/2+z$
	35.	C13-H13...Cg2			3.653(4)	165	$x,1/2-y,-$ $1/2+z$
form 2I	36.	N2-H2N...N3	0.86(2)	2.07(2)	2.921(2)	177(2)	2- $x,y,3/2-z$
	37.	C8-H8B...O1	0.97	2.66	3.533(3)	150	$-1+x,y,z$
	38.	C10-H10...O3	0.93	2.65	3.540(3)	161	$x,1-$ $y,1/2+z$
	39.	C3-H3...O2	0.93	2.71	3.594(3)	160	$5/2-$ $x,1/2+y,z$
	40.	C11-H11...O1	0.93	2.52	3.365(3)	152	- $1/2+x,1/2$ $+y,3/2-z$
	41.	C5-H5...O1	0.93	2.58	3.497(3)	169	- $1/2+x,1/2$ $-y,1-z$
	42.	Cg3...Cg3			3.6625(12)	6	1- $x,y,3/2-z$
	43.	Cg3...Cg3			3.6977(12)	6	2- $x,y,3/2-z$
	44.	C6-H6...Cg1			3.668(2)	151	- $1/2+x,1/2$ $-y,1-z$

form 2II	45.	N2-H2N...N3	0.83(3)	2.08(3)	2.909(2)	176(2)	1-x,1- y,1-z
	46.	C13-H13...O1	0.93	2.50	3.220(2)	135	x,1+y,z
	47.	C3-H3...O2	0.93	2.61	3.277(2)	129	-1+x,y,z
	48.	C7-H7B...O3	0.97	2.47	3.431(3)	172	-x,1-y,2- z
	49.	C11-H11...N2	0.93	2.84	3.693(3)	153	2-x,1- y,1-z
	50.	C3-H3...O4	0.93	2.63	2.295(2)	129	-x,-y,2-z
	51.	Cg3...Cg3			3.8250(12)	0	2-x,1- y,1-z
	52.	Cg1...Cg1			3.7444(13)	0	1-x,-y,2- z
	53.	C8-H8B...Cg3			3.633(2)	154	1-x,2- y,1-z
form 3I	54.	C3-H3...O4	0.93	2.59	3.436(4)	151	-x,1-y,-z
	55.	C6-H6...O1	0.93	2.53	3.219(3)	131	x,3/2-y,- 1/2+z
	56.	C7-H7A...O1	0.97	2.61	3.446(4)	144	1-x,- 1/2+y,1/2 -z
	57.	Cg1...Cg2(intra)			3.9031(18)	5.80(15)	x,y,z
	58.	Cg1...Cg2			3.8022(18)	7.87	x,1+y,z
form 3II	59.	C6-H6...O2	0.95	2.48	3.300(2)	144	1-x,1- y,1-z
	60.	C8-H8B...O3	0.99	2.67	3.385(3)	130	-1+x,1/2- y,-1/2+z
	61.	C3-H3...O1	0.95	2.72	3.234(2)	114	1-x,-y,1- z
	62.	C7-H7A...O4	0.99	2.71	3.582(2)	148	-1+x,1/2- y,-1/2+z
	63.	Cg1...Cg2 (intra)			3.8109(11)	1.86(9)	x,y,z
	64.	Cg1...Cg2			3.9395(11)	1.86(9)	1+x,y,z
	65.	C3-H3...O1	0.93	2.58	3.207(4)	125	x,1/2-

form 4I							y,1/2+z
	66.	C5-H5...N2	0.93	2.52	3.414(4)	161	1-x,1- y,2-z
	67.	C7-H7A...O3	0.97	2.71	3.332(4)	122	-1+x,y,- 1+z
	68.	C8-H8B...O3	0.97	2.67	3.354(4)	128	1-x,1- y,2-z
	69.	Cg3...Cg1 (intra)			4.004(2)	4.27(16)	x,y,z
	70.	Cg3...Cg1			3.930(2)	4.27(16)	-1+x,y,z
form 4II	71.	C2-H2...O1	0.95	2.44	3.221(2)	140	1-x,-y,-z
	72.	C7-H7B...O2	0.99	2.57	3.248(2)	126	-x,1-y,-z
	73.	C8-H8B...O2	0.99	2.65	3.559(2)	153	1-x,1-y,- z
	74.	Cg3...Cg3			3.9734(11)	0	1-x,1- y,1-z
	75.	Cg1...Cg1			3.8310(10)	0	-x,-y,-z
Cg is the centroid of the phenyl ring; Cg1=C1-C6 , Cg2=C9-C14, Cg3=C9-N3-C10-C11-C12-C13, α = Dihedral angle between phenyl/pyridine rings,							

XPac Dissimilarity Analysis

Program *XPac* has been utilized for the structural comparison of form **1II** and form **1III** crystals and the calculation of the dissimilarity index (x). The value of x between 0 and 3 indicates 3D structural similarity between the polymorphs. Full molecule (total 21 non hydrogen atoms) is used to define COSP (Corresponding Ordered Sets of Points) for calculations. The filter parameters, which are used to set the limit for (a) angular deviation, (p) interplanar angular deviation and corresponding molecular centroid distance deviation (d), were kept at default values (i.e. $a=10^\circ$, $p=14^\circ$ and $d=1.5\text{\AA}$).

^1H NMR study in polar (CD_3OD) and non-polar (CDCl_3) solvents

We observed a distinct difference in the chemical shifts in the ^1H NMR plots of compound **1** in CDCl_3 and CD_3OD . For e.g. of compound **1** exists in the *syn* conformation in CDCl_3 and the chemical shift of aromatic protons of 4-nitro benzene ring (Ha-Hd) lie in the range of 7.9 to 8.4 ppm whereas in CD_3OD it exists in the *midway* or *anti* conformation (absence of NOE's) and the chemical shift of aromatic protons of 4-nitro benzene ring (Ha-Hd) lie in the range of 6.4 to 6.9 ppm.

DFT optimization:

The geometries of the ground state structures were optimized using density functional theory (DFT) (with the M062x functional¹ and the 6-31+g* basis set and employing the Gaussian 09 suite of programs²). This level of theory was demonstrated to be adequate for stacking interactions. Atomic coordinates from crystals structures of *Syn-anti-midway* conformational polymorphs of compound **1**, **2** and **4** were used as starting conformers and further, subjected to geometry optimization. For compound **1**, atomic coordinates of *syn* conformer were extracted from form **1II** crystals whereas for structures having *anti* and *midway* conformations, atomic coordinates were obtained from form **1III** and form **1IV** crystals respectively.

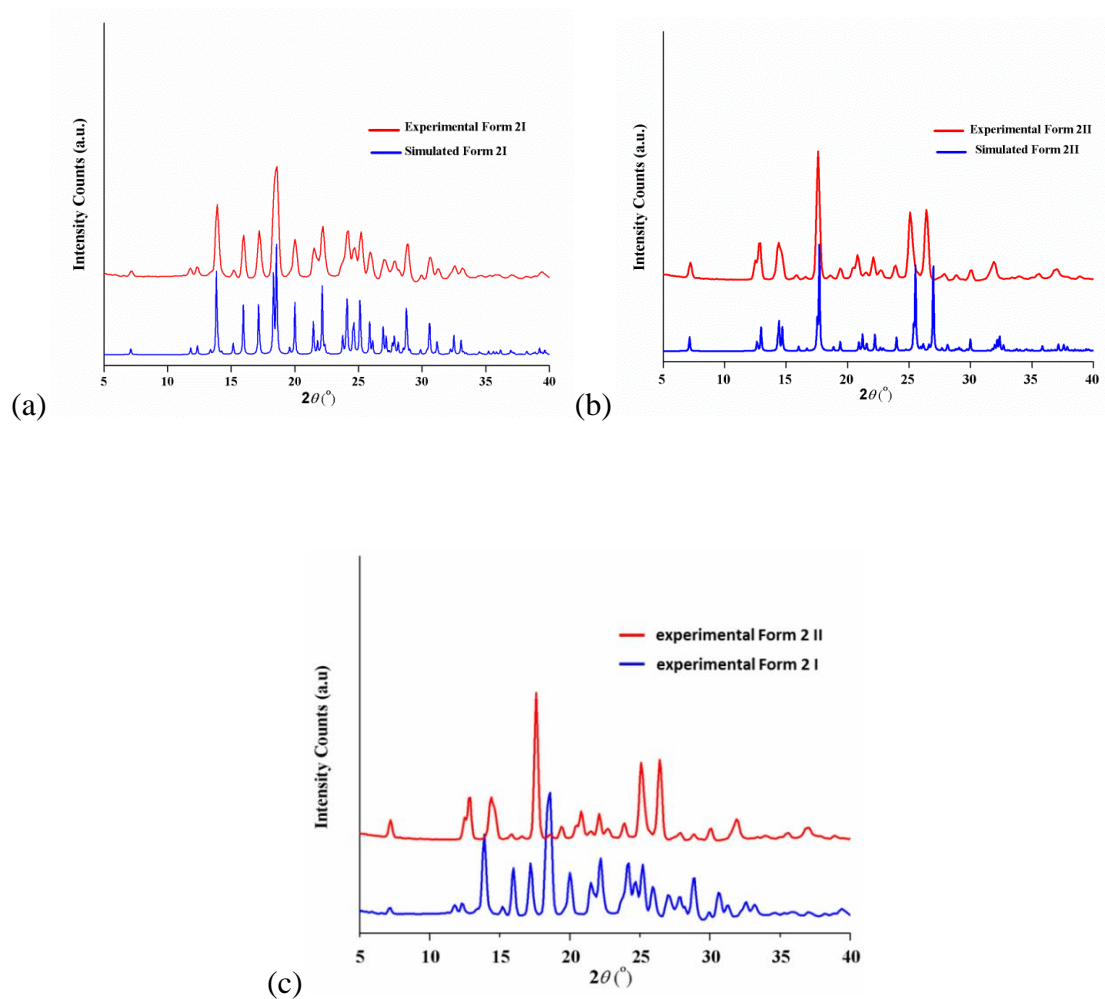


Figure 3.66. Overlay of experimental and simulated PXRD patterns of polymorphs of compound **2**, (a) form **2I** crystals, (b) form **2II** crystals and (c) experimental diffractograms of form **2I** and form **2II** crystals.

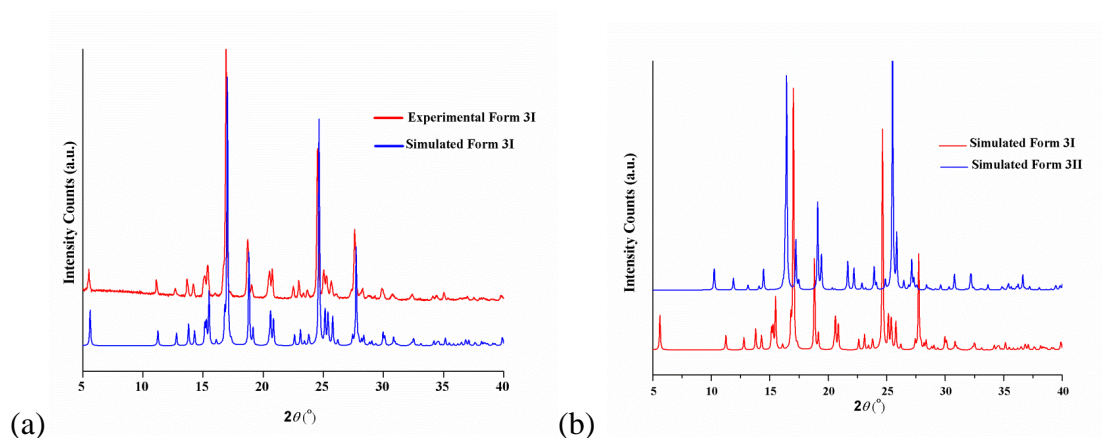


Figure 3.67. Overlay of experimental and simulated PXRD patterns of polymorphs of compound **3**, (a) form **3I** crystals and (b) form **3II** crystals.

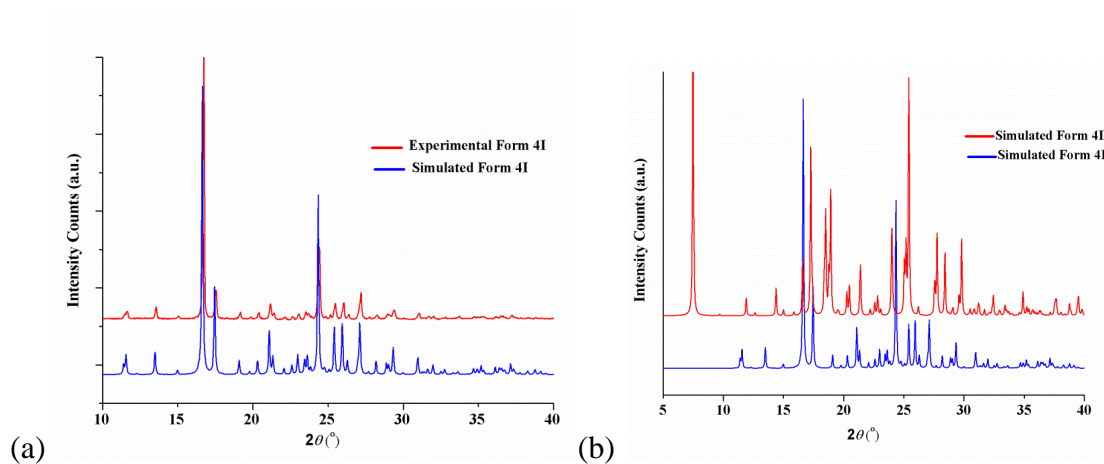


Figure 3.68. Overlay of experimental and simulated PXRD patterns of polymorphs of compound **4**, (a) form **4I** crystals and (b) form **4II** crystals.

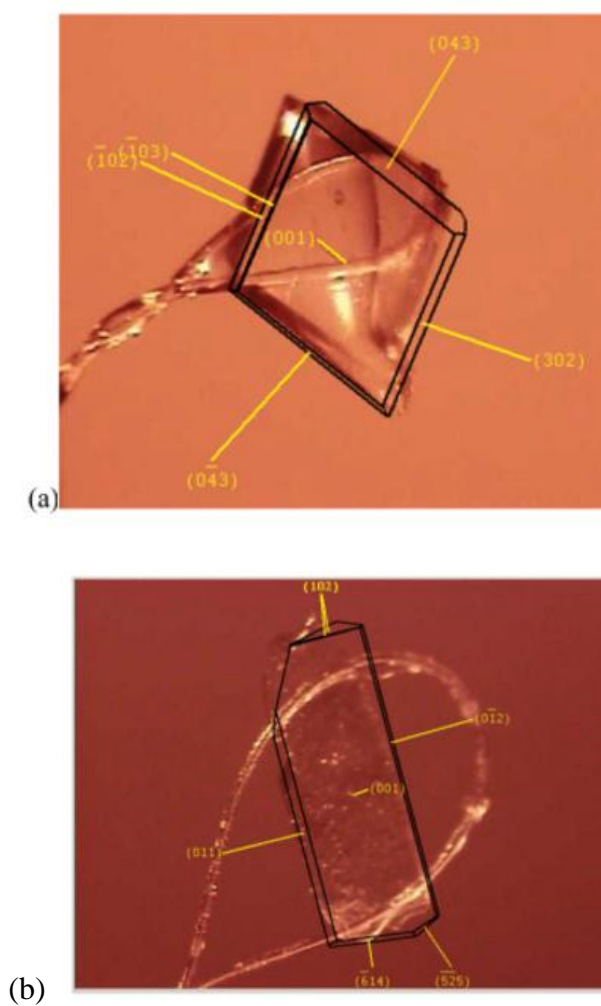


Figure 3.69. Face indexing of (a) δ -polymorph of pyrazinamide crystals and (b) form III crystals of **1**.

References:

1. F. Gaidies, D. R. M. Pattison and C. De Capitani, *Contrib. Mineral. Petrol.*, 2011, **162**, 975-993.
2. A. Veis and J. R. Dorvee, *Calcif. Tissue Int.*, 2013, **93**, 307-315.
3. Dubrovskii, V. G. *Nucleation theory and growth of nanostructures*; Berlin Heidelberg: Springer, 2014.
4. Garcia-Ruiz, J. M. *J. Struct. Biol.*, 2003, **142**, 22-31.
5. Myerson, A. *Handbook of industrial crystallization*; Butterworth-Heinemann, 2002.
6. Mehta, C. M.; Batstone, D. J. *Water Res.*, 2013, **47**, 2890-2900.
7. Kim, K. J.; Kim, K. M. *Powder Technol.*, 2001, **119**, 109-116.
8. Taden, A.; Landfester, K.; Antonietti, M. *Langmuir* ,2004, **20**, 957-961.
9. Desiraju, G. R. *Angew. Chem., Int. Ed. Engl.* ,1995, **34**, 2311-2327.
10. Erdemir, D.; Lee, A. Y.; Myerson, A. S. *Acc. Chem. Res.* ,2009, **42**, 621-629.
11. Gebauer, D.; Kellermeier, M.; Gale, J. D.; Bergström, L.; Cölfen, H. *Chem. Soc.Rev.*,2014,**43**, 2348-2371.
12. Fermani, S.; Vettraino, C.; Bonacini, I.; Marcaccio, M.; Falini, G.; Gavira, J. A.; Garcia Ruiz, J. M. *Cryst. Growth Des.* ,2013, **13**, 3110-3115.
13. Davey, R. J.; Dent, G.; Mughal, R. K.; Parveen, S. *Cryst. Growth Des.*, 2006, **6**, 1788-1796.
14. Erdemir, D.; Lee, A. Y.; Myerson, A. S. *Curr. Opin. Drug Discovery Dev.* ,2007, **10**, 746- 755.
15. Khavasi, H. R.; Tehrani, A. A. *CrystEngComm.* ,2013, **15**, 5813-5820.
16. Aakeröy, C. B.; Schultheiss, N. C.; Rajbanshi, A.; Desper, J.; Moore, C. *Cryst.GrowthDes.*,2009, **9**, 432-441.

17. Guru Row, T. N. *Coordin. Chem. Rev.* ,1999, **183**, 81-100.
18. Chang, Y. C.; Chen, Y. D.; Chen, C. H.; Wen, Y. S.; Lin, J. T.; Chen, H. Y.; Kuo, M. -Y.; Chao, I. *J. Org. Chem.* ,2008, **73**, 4608-4614.
19. Chakraborty, S.; Rajput, L.; Desiraju, G. R. *Cryst. Growth Des.* ,2014, **14**, 2571-2577.
20. Diskin-Posner, Y.; Kumar, R. K.; Goldberg, I. *New J. Chem.*, 1999, **23**, 885-890.
21. Tiekink, E. R. T.; Zukerman-Schpector, J. *The Importance of Pi-Interactions in Crystal Engineering – Frontiers in Crystal Engineering III*; John Wiley & Sons, 2012.
22. Muehldorf, A. V.; Van Engen, D.; Warner, J. C.; Hamilton, A. D. *J. Am. Chem. Soc.*,1988,**110**, 6561-6562.
23. Salonen, L. M.; Ellermann, M.; Diederich, F. *Angew. Chem., Int. Ed.* ,2011, **50**, 4808-4842.
24. Kool, E. T. *Annu. Rev. Biophys. Biomol. Struct.*, 2001, **30**, 1-22.
25. Li, S.; Cooper, V. R.; Thonhauser, T.; Lundqvist, B. I.; Langreth, D. C. *J. Phys. Chem. B*, ,2009, **113**, 11166-11172.
26. Stornaiuolo, M.; De Kloe, G. E.; Rucktooa, P.; Fish, A.; van Elk, R.; Edink, E. S.; Bertrand, D.; Smit, A. B.; de Esch, I. J. P.; Sixma, T. K. *Nat. Commun.* ,2013, **4**, 1875.
27. Giancane, G.; Borovkov, V.; Inoue, Y.; Conoci, S.; Valli, L. *Soft Matter* ,2013, **9**, 2302- 2307.
28. Hunter, C. A.; Sanders, J. K. M. *J. Am. Chem. Soc.* ,1990, **112**, 5525-5534.
29. Cockroft, S. L.; Hunter, C. A.; Lawson, K. R.; Perkins, J.; Urch, C. J. *J. Am. Chem. Soc.*,2005, **127**, 8594-8595.
30. Rashkin, M. J.; Waters, M. L. *J. Am. Chem. Soc.* ,2002, **124**, 1860-1861.
31. Wheeler, S. E.; Houk, K. N. *J. Am. Chem. Soc.* ,2008, **130**, 10854-10855.

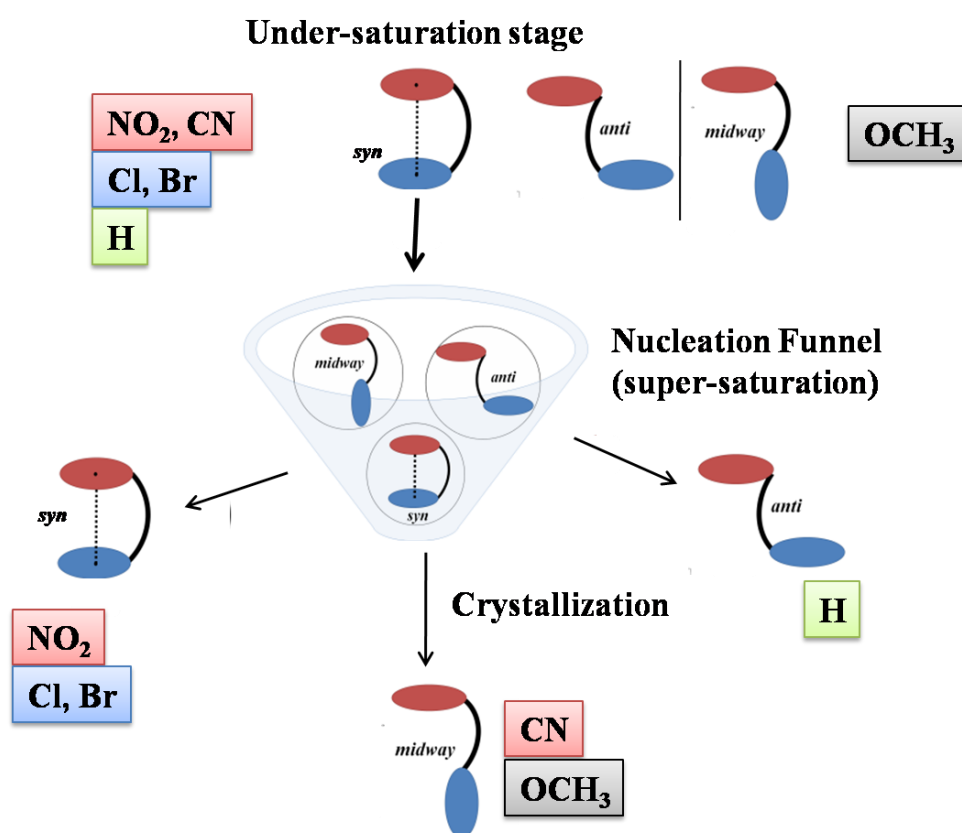
-
32. Grimme, S. *Angew. Chem., Int. Ed.* ,2008, **47**, 3430-3434.
 33. Gabriel, G. J.; Sorey, S.; Iverson, B. L. *J. Am. Chem. Soc.* ,2005, **127**, 2637-2640.
 34. Nakano, T. *Polym. J.*, 2010, **42**, 103-123.
 35. Sanphui, P.; Sarma, B.; Nangia, A. *Cryst. Growth Des.* ,2010, **10**, 4550-4564.
 36. Yang, S. S.; Guillory, J. K. *J. Pharm. Sci.* ,1972, **61**, 26-40.
 37. Terada, S.; Katagiri, K.; Masu, H.; Danjo, H.; Sei, Y.; Kawahata, M.; Tominaga, M.; Yamaguchi, K.; Azumaya, I. *Cryst. Growth Des.* ,2012, **12**, 2908-2916.
 38. Shoaib Ahmad Shah, S.; Rivera, G.; Ashfaq, M. *Mini Rev. Med. Chem.* ,2013, **13**, 70-86.
 39. Dunitz, J. D.; Bernstein, J. *Acc. Chem. Res.* ,1995, **28**, 193-200.
 40. Davey, R. J.; Blagden, N.; Potts, G. D.; Docherty, R. *J. Am. Chem. Soc.* ,1997, **119**, 1767- 1772.
 41. Weissbuch, I.; Lahav, M.; Leiserowitz, L. *Cryst. Growth Des.*, 2003, **3**, 125-150.
 42. Anwar, J.; Boateng, P. K.; Tamaki, R.; Odedra, S. *Angew. Chem., Int. Ed.* ,2009, **48**, 1596- 1600.
 43. Bhattacharya, S.; Saha, B. *Cryst. Growth Des.* ,2011, **11**, 2194–2204.
 44. Ramunno, A.; Cosconati, S.; Sartini, S.; Maglio, V.; Angiuoli, S.; Pietra, V. L.; Maro, S. D.; Giustiniano, M.; Motta, C. L.; Settimo, F. D.; Marinelli, L.; Novellino, E. *Eur. J. Med. Chem.*, 2012, **51**, 216-226.
 45. Bernstein, J.; Davis, R. E.; Shimoni, L.; Chang, N. L. *Angew. Chem., Int. Ed.* 1995, **34**, 1555-1573.
 46. Gelbrich T.; Hursthouse M. B. ,*CrystEngComm* 2006, **8**, 448-460.

47. Gavezzotti, A. *New J. Chem.*, 2011, **35**, 1360-1368.
48. Gavezzotti, A. *Acc. Chem. Res.*, 1994, **27**, 309-314.
49. Gavezzotti, A.; Filippini, G. *J. Phys. Chem.*, 1994, **98**, 4831-4837.
50. Kalman, A.; Fabian, L. *Acta Cryst.*, 2007, **B63**, 411-417.
51. Zhao, Y.; Truhlar, D. G. *Theor. Chem. Acc.*, 2008, **120**, 215-241.
52. Frisch, M. J.; Trucks, G. W.; Schlegel, H. B.; Scuseria, G. E.; Robb, M. A.; Cheeseman, J. R.; Scalmani, G.; Barone, V.; Mennucci, B.; Petersson, G. A.; Nakatsuji, H.; Caricato, M.; Li, X.; Hratchian, H. P.; Izmaylov, A. F.; Bloino, J.; Zheng, G.; Sonnenberg, J. L.; Hada, M.; Ehara, M.; Toyota, K.; Fukuda, R.; Hasegawa, J.; Ishida, M.; Nakajima, T.; Honda, Y.; Kitao, O.; Nakai, H.; Vreven, T.; Montgomery, J. A.; Peralta, J. E.; Ogliaro, F.; Bearpark, M.; Heyd, J. J.; Brothers, E.; Kudin, K. N.; Staroverov, V. N.; Kobayashi, R.; Normand, J.; Raghavachari, K.; Rendell, A.; Burant, J. C.; Iyengar, S. S.; Tomasi, J.; Cossi, M.; Rega, N.; Millam, J. M.; Klene, M.; Knox, J. E.; Cross, J. B.; Bakken, V.; Adamo, C.; Jaramillo, J.; Gomperts, R.; Stratmann, R. E.; Yazyev, O.; Austin, A. J.; Cammi, R.; Pomelli, C.; Ochterski, J. W.; Martin, R. L.; Morokuma, K.; Zakrzewski, V. G.; Voth, G. A.; Salvador, P.; Dannenberg, J. J.; Dapprich, S.; Daniels, A. D.; Farkas, J. B.; Foresman, J. B.; Ortiz, J. V.; Cioslowski, J.; Fox, D. J. In *Gaussian 09, Revision B.01*, Gaussian, Inc., Wallingford CT Wallingford CT, 2009.
53. Cherukuvada, S.; Thakuria, R.; Nangia, A. *Cryst. Growth Des.*, 2010, **10**, 3931-3941.
54. Staab, E.; Addadi, L.; Leiserowitz, L.; Lahav, M. *Adv. Mater.*, 1990, **2**, 40-43.
55. Tidey, J. P.; O'Connor, A. E.; Markevich, A.; Bichoutskaia, E.; Cavan, J. J.; Lawrance, G. A.; Wong, H. L.; McMaster, J.; Schröder, M.; Blake, A. J. *Cryst. Growth Des.*, 2015, **15**, 115-123.
56. Weissbuch, I.; Lahav, M.; Leiserowitz, L. *Adv. Mater.*, 1994, **6**, 952-956.

57. Davey, R. J.; Blagden, N.; Potts, G. D.; Docherty, R. *J. Am. Chem. Soc.* ,1997, **119**, 1767- 1772.
58. Mitchell, C. A; Yu, L; Ward, M. D.*J. Am. Chem. Soc.* ,2001, **123**,10830-10839.
59. Allen, F. H. *ActaCryst.* ,2002, **B58**, 380-388.

Chapter 4

Design and Synthesis of Conformationally Flexible *p*-substituted Sulphoester Trimers: Investigating Substituent Effect on π -stacking Interaction in Solution and Solid State



The nucleation funnel of *p*-substituted aromatic trimers

Introduction:

Aromatic interactions are non-covalent association that exists between molecules containing π -electrons. Depending on the nature of donor and acceptors, these interactions are classified as cation $\cdots\pi$, anion $\cdots\pi$, and $\pi\cdots\pi$ interactions. Among these, $\pi\cdots\pi$ interactions are the most important and commonly observed. In this, two arene moieties are associated with weak non-covalent interaction. Generally, $\pi\cdots\pi$ interactions are divided into two types: $\pi\cdots\pi$ stacking interactions and C-H $\cdots\pi$ (or ‘T’ shaped or edge-to-face) interactions. $\pi\cdots\pi$ stacking interactions can be further divided depending on the position of arene units with respect to each other; type 1) face-to-face stacking (sandwich conformation) and type 2) parallel displaced stacking. In face-to-face π -stacking, atoms in the two aromatic rings are perfectly eclipsed onto each other when viewed from the top. Both the aromatic units remain perfectly coplanar with dihedral angle of 0° . In the parallel displaced configuration, one of the arene unit is shifted in the horizontal molecular plane so that the atoms are no longer eclipsed (**Figure 4.1**).

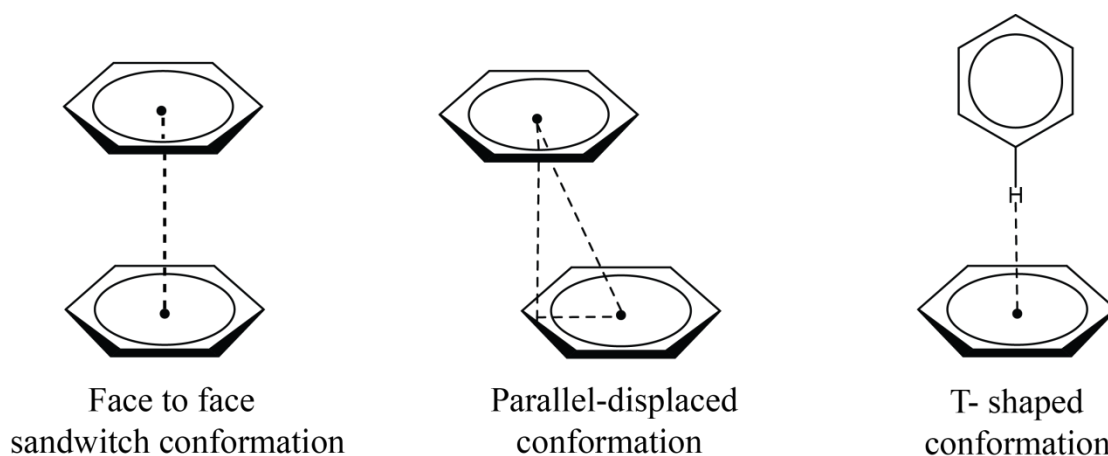


Figure 4.1 Types of aromatic interactions

Stacking interaction has numerous applications in various fields like structural biology,¹ medicinal chemistry,² organic chemistry³ and materials science.⁴ Although, the stacking association is relatively weaker than other non-covalent interactions such as hydrogen bonding, their cumulative effect shown to have structure directing role for self assembly of small molecules and large biomolecules.⁵ Moreover, nucleobases of DNA and side-chains of aromatic aminoacids in proteins form stacking interaction with small molecules that forms the basis of drug-DNA,⁶ drug-protein⁷ and enzyme-

substrate association.⁸ The stacking interaction provides structure fitting of hydrophobic moieties of small molecules inside the major/minor groove or regulatory pocket of the protein. Thus, the stacking interactions assist in molecular recognition between the host and guest.⁹ The detailed investigation of their interactions offers a good platform for drug designing programs.¹⁰ The conformational flexibility plays important role for achieving the stacking association. In the absence of conformational flexibility, the stacking interaction can't be established. The best example is the structure of DNA, in which the flexible phosphodiester linkage provides the flexibility for achieving the extended stacking amongst nucleobases and generates helical arrangement. The dynamic nature and topological variation (required for gene regulation) of DNA such as B-Z transition, B-A transition and protein-DNA binding involves the alteration of handedness and helix pattern without altering Watson-Crick base pairing.¹¹⁻¹²

The interactions between two monomers are achieved *via* effective collision (maximum association). However, the transition from dimeric to multimeric organization requires intra and intermolecular extended interactions to generate three dimensional assemblies. The molecular arrangement (packing) decides the physico-chemical properties of the assembly. The chemical nature of building blocks (monomers) can be modulated to tune the properties of materials and improve their applications. For the design and synthesis of functional materials chemical crystallographer while using crystal engineering approach employ the stacking interaction as synthons to generate supramolecular architecture.¹³ It is observed that the stacking interaction serve as elastic ladders which show variable slippage depending on the interaction strength between the two arene units, nature of substituent and the surrounding hydrogen poor or rich environment. The interaction strength between the arene units can be modulated by manipulating the nature of substituent. Therefore, it is crucial to study the effect of substituent on the stacking interactions to understand this phenomenon. In synthetic chemistry, the stacking interactions are known to play pivotal role for the stereo-selectivity of reactive intermediate, thereby greatly modify the yield of reaction product (isomer).¹⁴

In material science, the stacking interactions have shown to play important role in self-assembly of the polymers, nano-sized materials and porous compounds.¹⁵ The literature survey yields many evidences where stacked structures

have been used as building blocks to generate multimeric architecture. Moreover, the modulation of stacking efficiency has affected the electrical, photo-physical and sensing properties that provide cost-effective platform for the field of material engineering. Hence, it's important to understand the exact nature of stacking interaction to tune the properties of the materials.

Although, the nature of stacking interaction is important for structural point of view, it is not clearly understood yet. Many theories have been put forth which are based on electrostatic (dipole-dipole), dispersion and charge transfer phenomenon. In 1990, the Hunter and Sanders,¹⁶ published milestone article on nature of $\pi\cdots\pi$ interactions. They proposed the electrostatic model also regarded as polar/pi model to explain the energetics and stacking geometries of complexes. According to this model, the electron density of the arene units is polarized to create quadrupole moment. The partial negative charge (π -electron density) of quadrupole resides over aromatic face whereas the partial positive charge (σ electron density) is sandwiched between partial negative charges and located at the periphery. Furthermore, substituent plays important role by polarizing the electron density. The presence of electron withdrawing groups (EWG) on the aromatic ring decreases the π -electron density over the aromatic ring that favours $\pi\cdots\sigma$ interaction between the two arene units thereby promoting face-to-face or parallel off-set stacking interactions. In contrast, the electron donating group (EDG) increase the π -electron density and disfavor the stacking interaction due to $\pi\cdots\pi$ repulsion. According to this model, two un-substituted arene units favour the edge-to-face interaction due to $\pi\cdots\sigma$ attraction.¹⁷⁻

19

Some clues were sought from the polarization theory for explaining the charge transfer association between alternately arranged electron rich and electron deficient aromatics. The donor-acceptor relation shared between the opposite arene units are attributed to the mixing of their π -orbitals for excited state charge transfer. The π -orbital of electron rich aromatic unit serve as HOMO (Highest Occupied Molecular Orbital) and π -orbital of electron deficient aromatic is served as LUMO (Lowest Unoccupied Molecular Orbital). The charge transfer complex formation is evidenced by the absorption peak in the visible region. These special cases of stacking interactions are observed between interacting aromatic units that significantly differ in

their electrostatic potential and separated by the distance shorter than their sum of van der Waals radii. However, the charge transfer theory does not explain the stacking interaction between the aromatic units that does not share donor-acceptor relation in the excited state. Therefore for more generalized explanation, dipole-dipole interaction and dispersion (polarizability) terms were taken into account.

The concept of the synchronicity of electrostatic and dispersion interaction was primarily used for explaining the stacking interaction between the mono and multi-substituted arene units. The attractive interaction between multi-substituted aromatic units over un-substituted ones is better elucidated by considering dipole/dipole charge separation and increasing polarizability. Each EWG substituent polarizes the π -electron density and induces charge separation over the aromatic rings. Moreover, charge separation is further enhanced by multiple EWG groups that establish strongest dipole/dipole and dispersive attraction. The face-to-face stacking geometry between hexafluorobenzene and dimethyl aniline can be explained by these theory.²⁰⁻²¹

However, this presumption of Hunter and Sanders was challenged by many research groups who carried out the theoretical calculations using advanced computational methods. Their calculation clearly suggested that the π -stacking interactions are not governed by electrostatic interaction between the aromatic units. The direct interaction model of Wheeler and Houk stated that both EWG and EDG groups enhances the stacking geometry of aromatic moieties due to their through space interaction with the opposite aromatic unit, however, π electron density over aromatic units does not contribute for the stabilization of stacking interactions.²²⁻²⁶ Thus, the direct through space interaction contradicted the polar/ π model and consideration of polarization of π electron density (**Figure 4.2**).

Hunter and co-workers used hydrogen bonded zipper complexes abbreviated as double mutant cycle for their study.¹⁸ The mutation is denoted for changing the substituent of aromatic units; change in one substituent is abbreviated as single mutation whereas change in the two substituents is considered as double mutation. The effect of mutation is quantified in terms of change in the hydrogen bonding strength that is quantified by NMR studies. This study reveals that EWG (electron withdrawing groups) substituents favor stacking whereas EDG (electron donating

group) disfavors the stacking assembly.¹⁷ The observed trend obeyed the principles of polar/pi model. The compelling evidence of polarization theory was provided by experimental investigations of Siegel *et al.* They reported a series of substituted *syn*- and *anti*-1,8-di-o-tolynaphthalenes. The substituted arene units are stacked one above the other which creates torsional constraints for the epimerization. Higher the face-to-face stacking, higher would be the torsional barrier. On the contrary, disfavoring association between the aromatic units would promote the epimerization. Based on the data, EWG substituents revealed higher torsional constraints by favoring the stacking association.

Direct interaction model was mainly supported by high end theoretical calculation conducted by different groups. Sherill and co-workers used high level theory for studying the stacking association of substituted dimers.²⁵ In their reports, they highlighted the additivity of substituents irrespective of their EWG and ED nature. They observed strong dispersion interaction between the substituents that are strong contributors of stabilizing force of stacking interaction. The sandwich conformation between the aromatic units is favored by the presence of substituents (EWG/ED) and their dispersive interactions. Later on series of review articles and reports were published by Houk and Wheeler groups substantiating the observation made by Sherril and co-workers.²⁶ For their analysis they used series of substituted benzene dimers and observed that sandwich conformation is solely supported by direct through space dispersive interaction between the substituents and opposite aromatic ring. Their data clearly denied any evidences of polarization effect of arene units caused by substituents and their role for stabilizing the stacking association.

The substituent additivity was also reported by recently published report by Shimuzu *et. al.*,²⁸ In their reports they used small molecular model system comprising pendant arm which can adopt folded or unfolded conformation depending on the additivity of substituent. The folded or unfolded conformations were estimated by NMR study. They used CH₃, OCH₃, Cl, CN, and NO₂ substituents (EWG and EDG) and found that the additivity trend obeyed the Wheeler and Houk direct interaction model. However, they have also mentioned the involvement of polarization terms which needs to be investigated further.

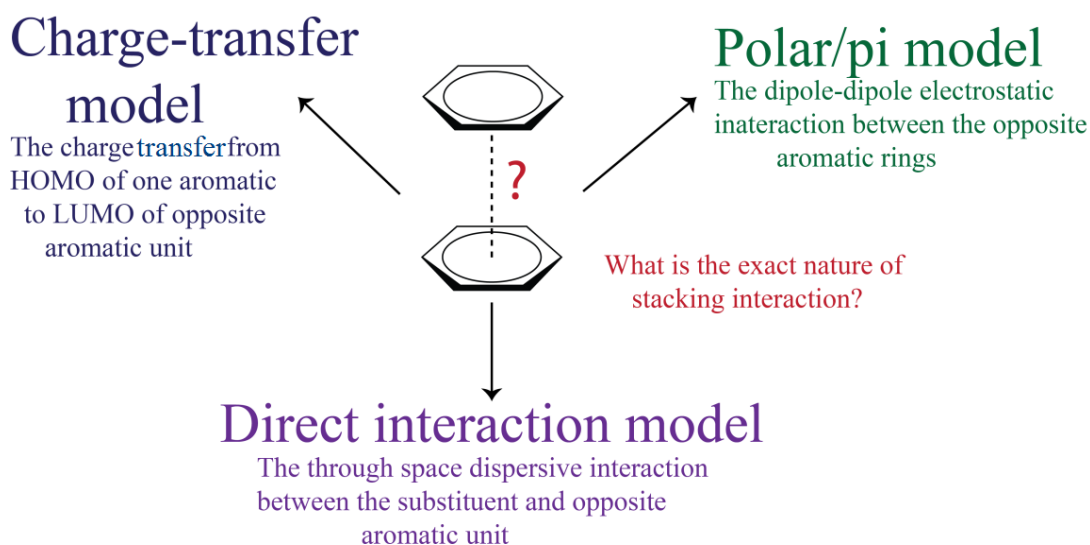


Figure 4.2. The discrepancy between the theories elucidating the nature of π -stacking interactions.

So far, studies were undertaken in gaseous, solution and solid state to investigate the nature of stacking interactions. However, no substantial evidences were reported for the behavior of same stacked structures in different states of the matter. In solution state, the molecules have intramolecular rotational motion and possess higher entropy. However, the same molecule in solid crystalline state acquires lower entropy under restricted environment. Although, the solid state geometry shares significant analogy with solution state conformation, many times due to the packing constraints, both the conformations reveal significant differences. The intramolecular geometry of conformationally flexible molecules revealed much variation in solution and solid state mainly due to the susceptibility of pre-nuclei clustering (PNC) at the nucleation for crystallization conditions such as solvent, temperature, impurity etc (Figure 4.3).

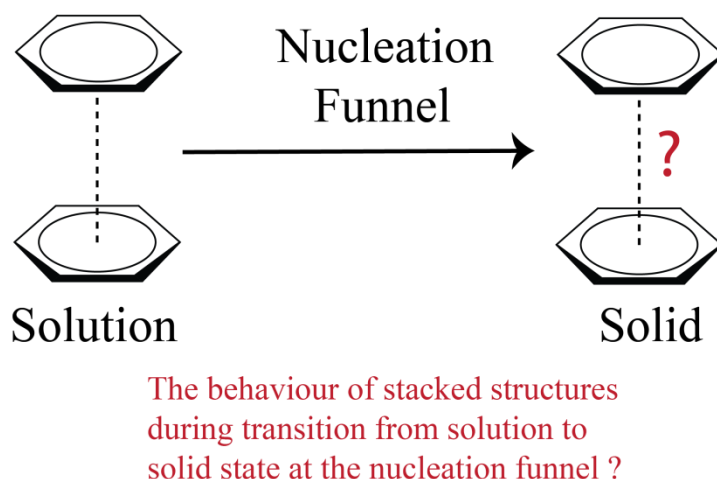


Figure 4.3. The transition of stacking interaction from solution to solid state and their role at the pre-nuclei clustering is still not understood yet.

It is difficult to envisage the solid state geometry of the alternating electron rich and electron deficient aromatic units that display stacking conformation in solution state. It is mainly due to many governing factors such as stacked structures provide highest intra-molecular constraints for packing and further due to the weak nature of interaction between the aromatic units. Therefore the enthalpy change does not compensate the entropic penalty during crystallization. Hence, in order to study the role of substituent on stacking interaction, it is crucial to design the system that takes these factors into consideration. In chapter 3, we demonstrated central dogma of the intra-molecularly stacked sulfoester and sulphonamide dimers. Nitro-substituted (aromatic unit 1) and un-substituted benzene rings (aromatic unit 2) joined together with hinge comprising of sulfoester/sulfonamide and $-\text{CH}_2-\text{CH}_2-$ flexible spacers. The compounds achieve, stable *syn* conformation in non-polar solvent at under-saturation condition. Prenuclei clustering during the nucleation process can form heterogeneous clusters of stacked (*syn*) and unstacked conformations (*midway* or *anti*). The extent of conformational variation amongst the prenuclei clusters depends on the conformational flexibility and presence of H-bond donor/acceptors groups in the molecules. The compounds under study revealed that the extended stacking interaction play pivotal role for enrichment of *syn* prenuclei irrespective of having higher packing energy than the metastable forms (*anti/midway*).

We elucidated the remarkable role of extended stacking interaction for stabilization of intra-molecular *syn* (stacking geometry) in the absence of additives.

During additive mediated crystallization trials, we observed that, the compound **1** with sulphonamide containing hinge provided highest number of conformational polymorphs namely *syn*, *midway* and *anti* (**Figure 4.4**). In each polymorph, the N-H proton displayed varying H-bonding propensities. Similarly, when the phenyl group was replaced with pyridine and sulfonamide is replaced with sulfoester (compound **4**), we obtained *syn* and *midway* conformational polymorphs in the crystallization trials (**Figure 4.5**). On the contrary, the compound with sulfoester hinge and phenyl as aromatic unit 2, i.e. compound **3** did not produce any conformational polymorphs in spite of many crystallization trials (**Figure 4.6**). The frequency or chance of obtaining the conformational polymorph was shown to have significant relation with the presence of strong H-bond forming groups.

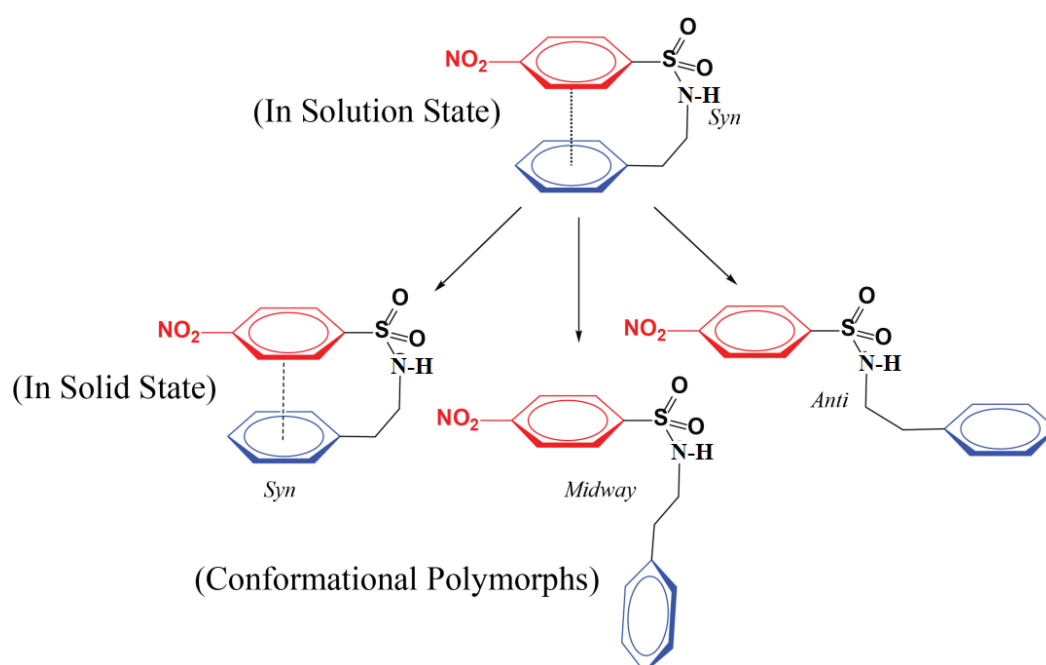


Figure 4.4. The compound **1**, existed in *syn* (stacking) conformation in solution state and yielded three conformational polymorphs having stacked (*syn*) and unstacked (*midway*, *anti*) during crystallization trial with and without additive.

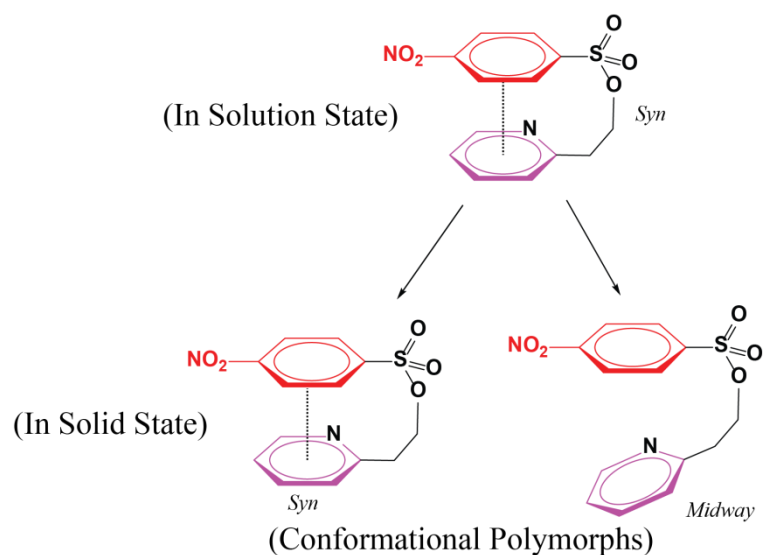


Figure 4.5. Compound **4** existed in *syn* (stacking) conformation in solution state and yielded two conformational polymorphs having stacked (*syn*) and unstacked (*midway*) geometry during crystallization trial with and without additive.

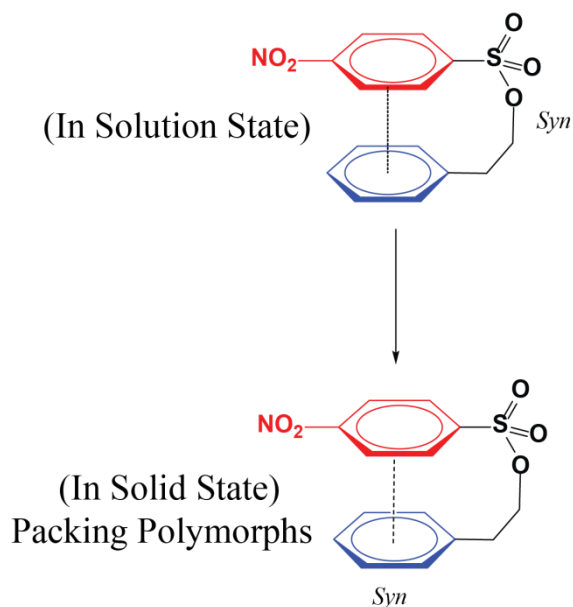


Figure 4.6. The compound **3** existed in *syn* (stacking) conformation in solution state and yielded two packing polymorphs possessing stacked (*syn*) during crystallization trial with and without additive.

In order to evaluate the role of substituent for stabilizing the stacking interactions in solution and solid state, we used trimeric system over dimers of chapter 3. The dimers in the chapter 3 comprised of *p*-nitro substituted and unsubstituted

phenyl/pyridine aromatic units joined together with sulphonamide/sulfoester hinge and $-\text{CH}_2-\text{CH}_2-$ spacer. The trimer contains two *p*-substituted aromatic units present at the extreme end of the molecules and one aromatic unit as base. The *p*-substituted aromatic units (aromatic unit 1) and aromatic base (aromatic unit 2) are joined together *via* sulfoester hinge and $-\text{CH}_2-\text{CH}_2-$ spacer with centre of symmetry lies at the centroid of the base (**Figure 4.7**). The trimers were chosen for obtaining amplified nOe in solution state 2D NMR studies for stacked structures. Further, the enthalpy change for extended stacking interaction may compensate entropic barrier of intramolecular stacked geometry. We envisaged that the trimers will have more constrain for achieving the stacking geometry than dimers in solid state that would provide better insight for the role of substituent in order to achieve the *syn* geometry. To study the role of substituent, strong electron withdrawing ($-\text{NO}_2$, $-\text{CN}$), weakly electron withdrawing ($-\text{Cl}$, $-\text{Br}$), neutral ($-\text{H}$) and electron donating ($-\text{OCH}_3$) groups were used for substitution at the para position of the aromatic unit 1 (**Figure 4.8**). For investigating stacked conformation in solution state 2D NOESY studies were undertaken. Proximity of the aromatic units within 5 Å results in the nOe signalling that suggests the stacked conformation i.e. *syn* conformation. On the similar note, if the aromatic units are away from each other i.e. distance more than 5 Å, then nOe will not be observed which is attributed to their *midway/anti* geometry (**Figure 4.9**). Solid state geometries were investigated by single crystal structure analysis. The geometries extracted from their crystal structure data were abbreviated based on the orientation of aromatic units with respect to each other. Stacked conformations were abbreviated as *syn* whereas non-stacked conformations were abbreviated as *midway* or *anti* as shown in the figure (**Figure 4.9**).

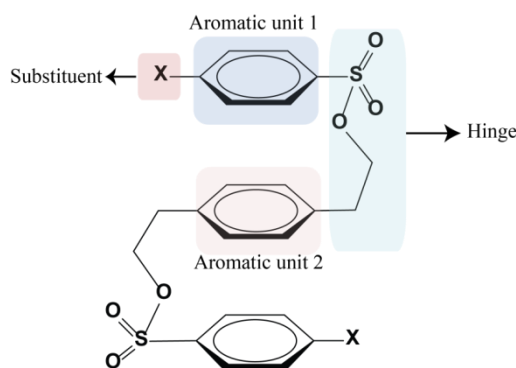


Figure 4.7. Design of trimer system for study of stacking interaction in solution state and solid state.

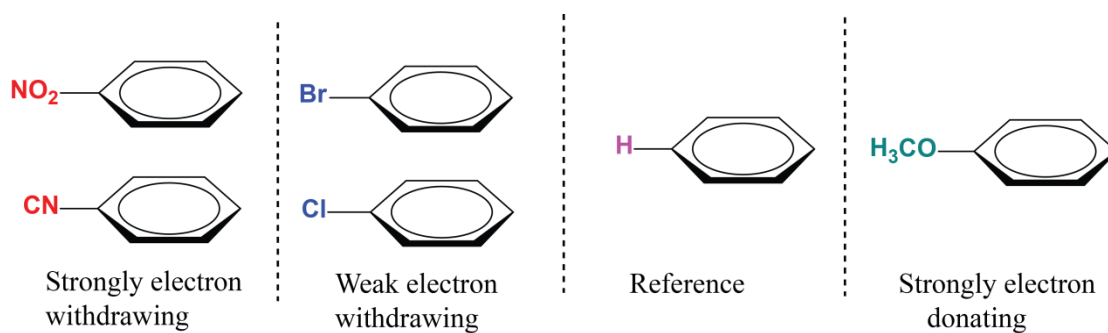


Figure 4.8. The substituent at the *para* position of aromatic unit 1 used for the investigation.

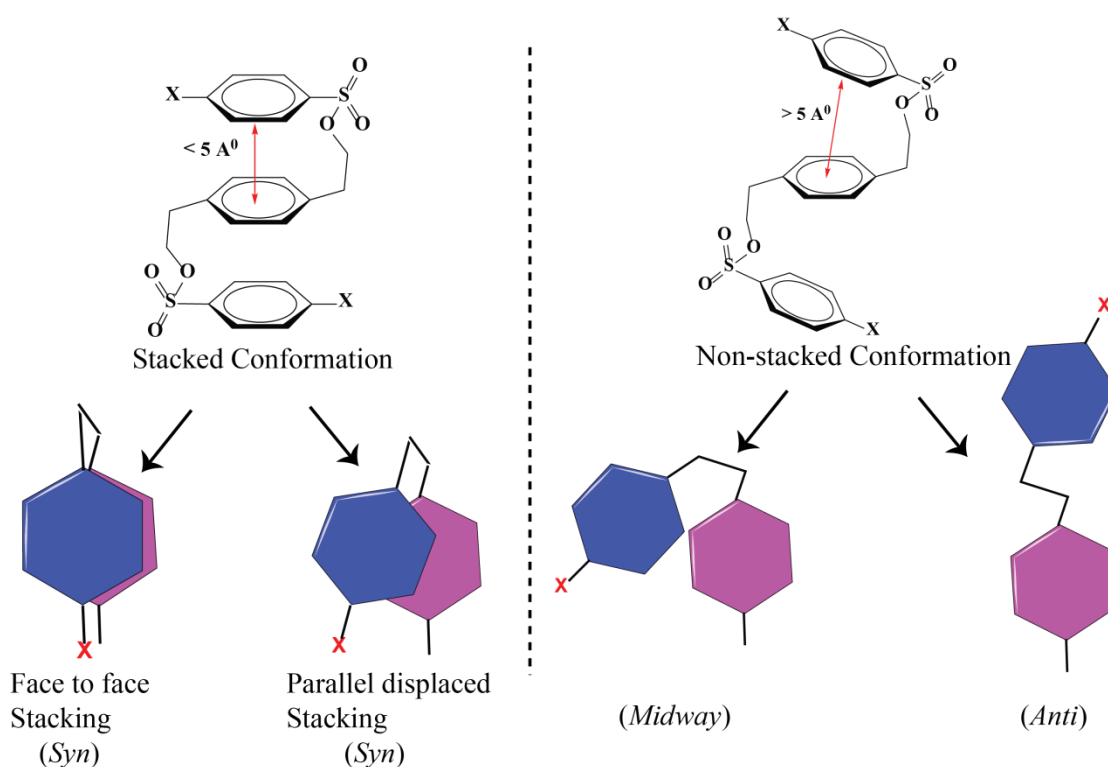


Figure 4.9. The abbreviation to the intra-molecular geometries based on the solution state NOESY study and single crystal structure analysis.

Result and discussion:

The trimers were synthesized by simple synthetic procedure. 2 eq. of *p*-substituted benzene sulfonyl chlorides were reacted with 1,4-Bis(2-hydroxyethyl)benzene under inert condition in the presence of catalytic amount of triethylamine to give corresponding *p*-substituted benzene sulfoester trimers. The trimers were named on the basis of their substituent at the para position and numbered as (1) -NO₂, (2) -CN, (3) -Cl, (4) -Br, (5) -H and (6) -OCH₃. The compounds were purified by flash column chromatography except **1** (NO₂trimer). Due to low solubility of compound **1** (-NO₂trimer), it was purified by differential solubility. The reaction product of **1** was washed with DMF to remove the impurities. All the purified compounds were further crystallized in chloroform/methanol solvent mixture except **1** which was crystallized using DMF by slow cooling. Detailed synthetic procedure and characterization data is provided in the experimental section. 2D NOESY studies were undertaken for investigating the solution state configuration of the trimers whereas the single crystal structure analysis was carried out for studying the solid state geometry. Stacking parameters, 1D extended stacking assembly and intramolecular contacts were used for comparative analysis. The thermal profiles of solid state stacked structures were analyzed.

2D NOESY study of CN trimer (2)

Inter-residual nOe between the aromatic protons of aromatic unit 1 and aromatic unit 2 were used to decide the solution state geometry. Solution state 2D NOESY data on CN (2), Cl (3), Br (4) and H (5) trimers exist in the *syn* conformations in solution state as shown in the **figures 4.10-4.13**. In case of the OCH₃ trimer (6), the inter residual nOe excerpts were not observed between the aromatic protons of the opposite aromatic rings that suggested its unfolded conformation in the solution state and abbreviated as *midway/anti*. The solution state NMR study could not be carried out for NO₂ trimer (**1**) due to its low solubility.

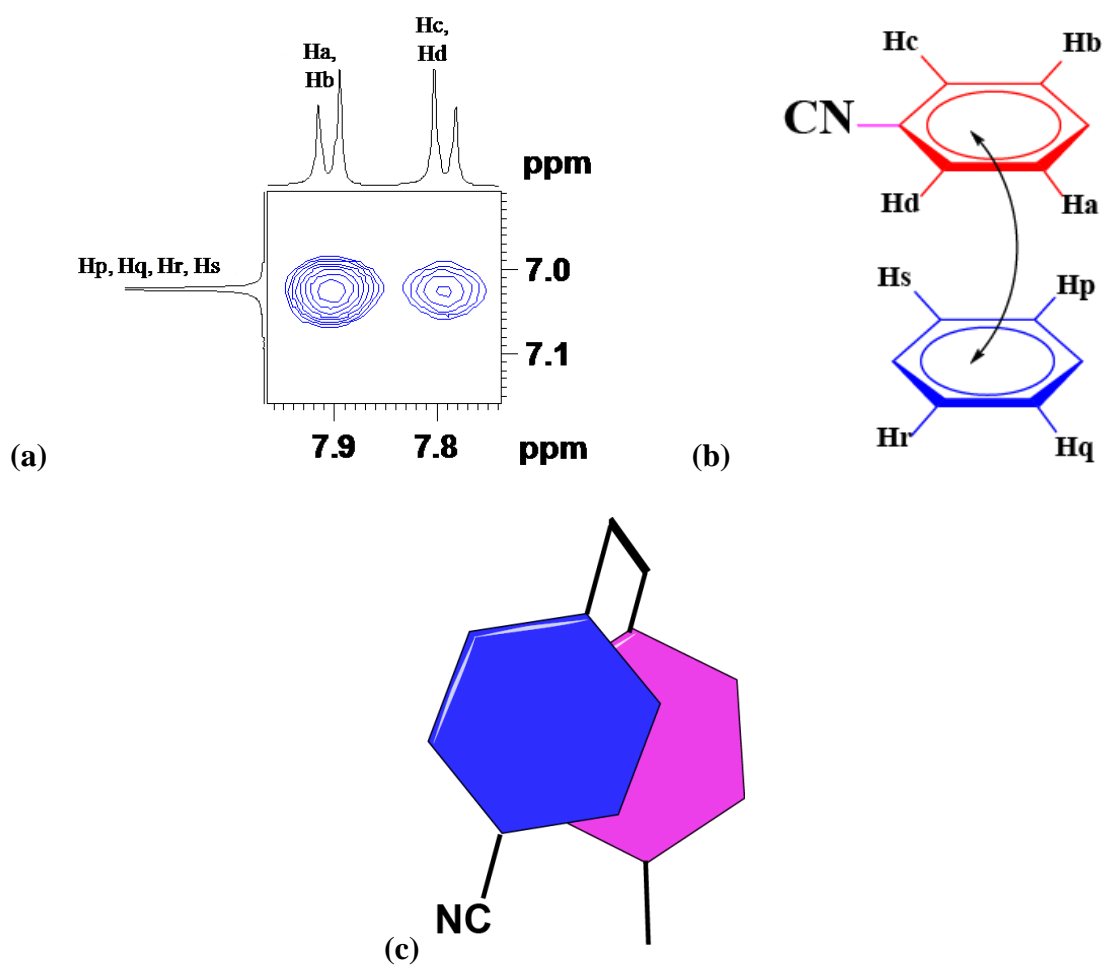


Figure 4.10. (a) Selected nOe excerpts of **2** (CN trimer), (b) the predicted arrangement of CN-substituted and un-substituted arene units based on nOe extract and (c) cartoon depiction of *syn* arrangement of aromatic units when viewed from the top.

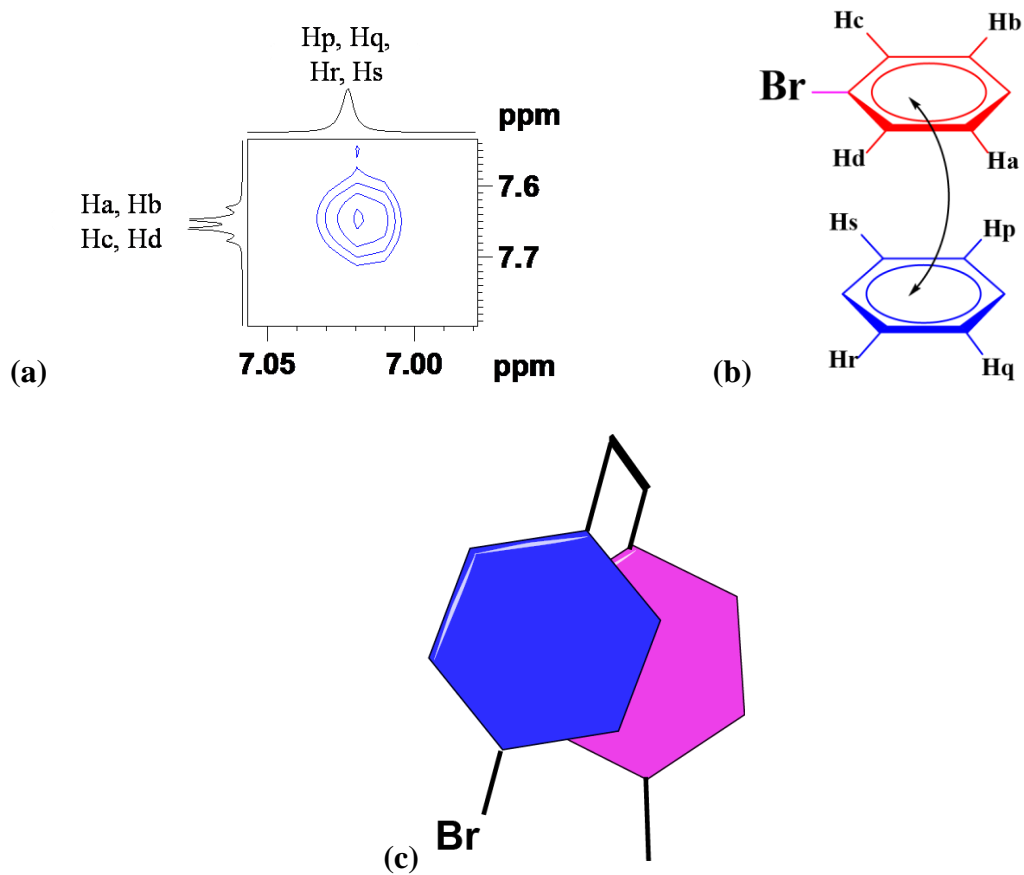


Figure 4.11. (a) Selected nOe excerpts of **4** (Br trimer), (b) the predicted arrangement of Br-substituted and un-substituted arene units based on nOe extract and (c) cartoon representation of *syn* arrangement of aromatic units when viewed from the top.

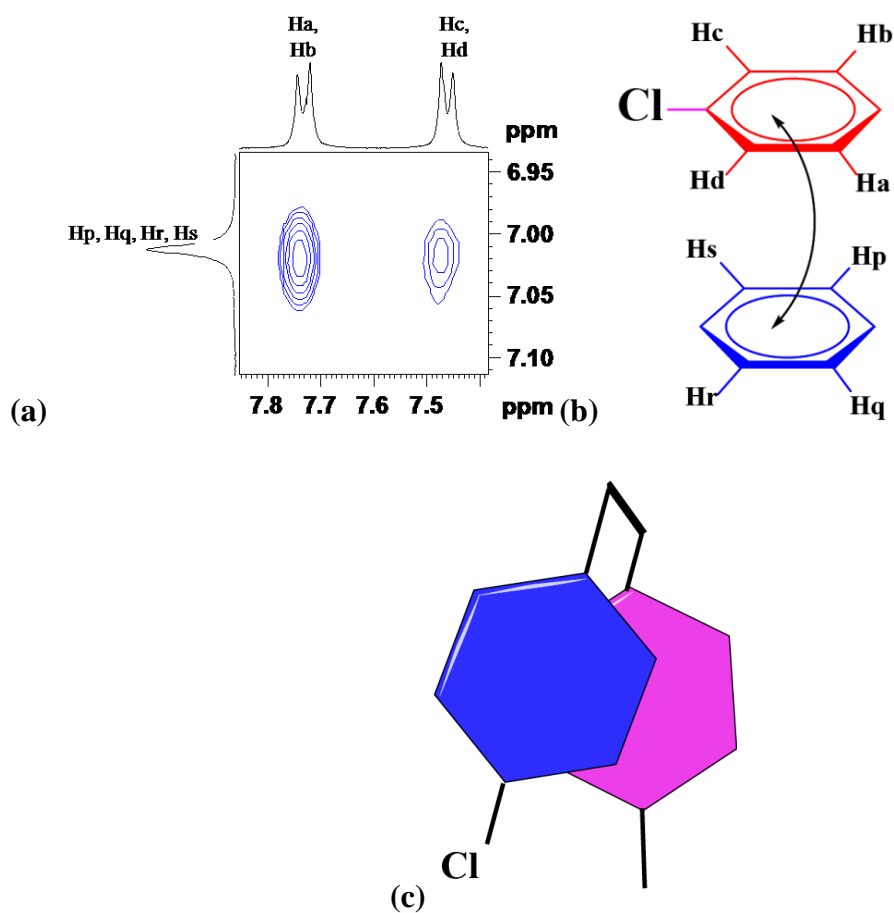


Figure 4.12.(a) Selected nOe excerpts of **3** (Cl trimer), (b) the predicted arrangement of Cl-substituted and un-substituted arene units based on nOe extract and (c) cartoon depiction of *syn* arrangement of aromatic units when viewed from the top.

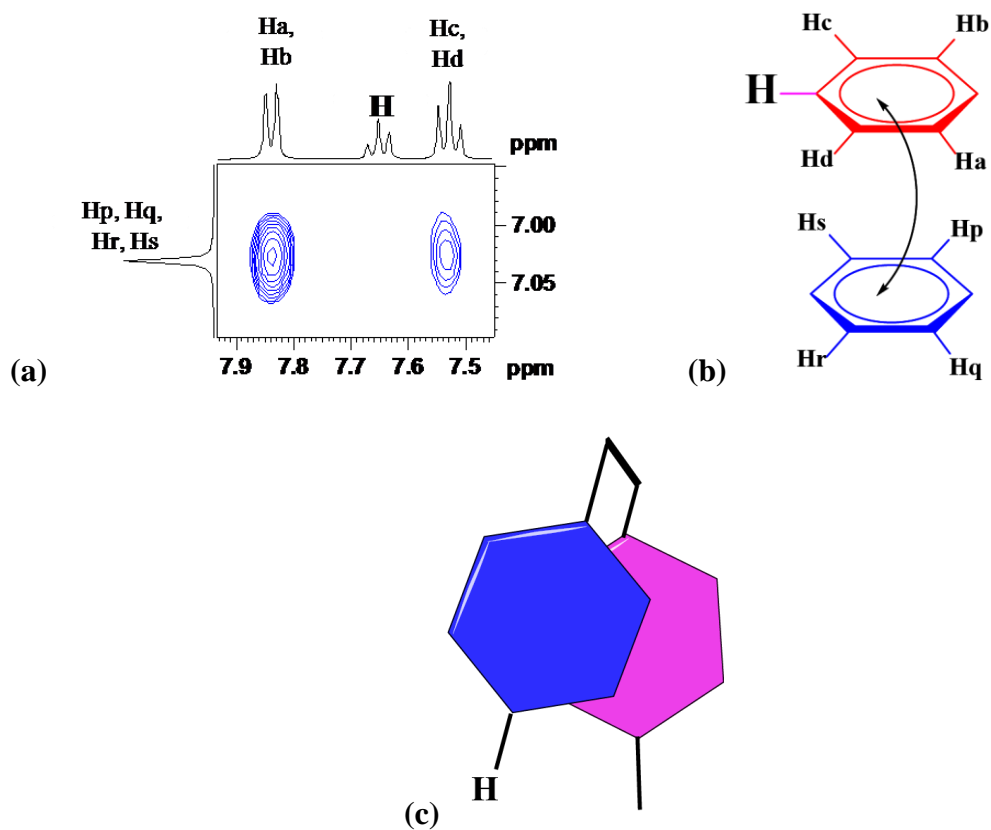


Figure 4.13. (a) Selected nOe excerpts of **5** (H trimer), (b) the predicted arrangement of H-substituted and un-substituted arene units based on nOe extract and (c) cartoon display of *syn* arrangement of aromatic units when viewed from the top.

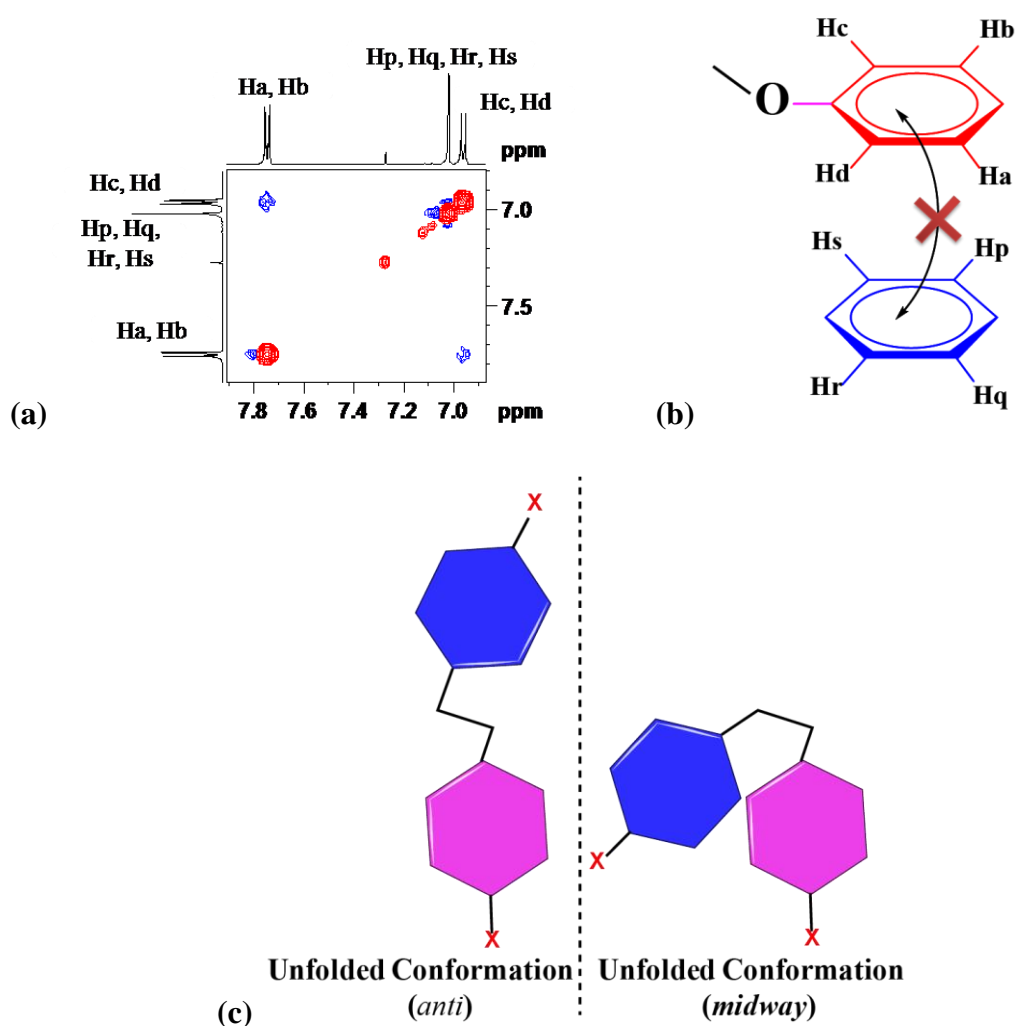


Figure 4.14.(a) Selected nOe excerpts of **6** (OCH₃ trimer), (b) the predicted arrangement of OCH₃-substituted and un-substituted arene units based on nOe extract and (c) cartoon depiction *anti/midway* arrangement of aromatic units when viewed from the top.

The single crystal structures of most of these derivatives were analyzed. More attention was given to their intra-molecular geometries and the influence of the EWG and EDG on these geometries. The stacking parameters such as centroid to centroid distance between the two phenyl rings and dihedral angle between the two aromatic units were used to evaluate the stacking efficiency along with other parameters. If the compound contains more than half molecule in the asymmetric unit then best stacked pose was chosen for the comparison. The crystal structure (ball and stick style), the position of aromatic unit 1 and aromatic unit 2 with respect to each other is shown in

the **figure 4.15** and **4.16**. The ORTEPs of all the compounds are provided in the **figure 4.17**. From the intramolecular geometries it is evident that the compounds **2** and **6** have adopted *midway* conformation, compound **5** (H) displayed an *anti* orientation whereas compounds **1**, **3** and **4** showed *syn* geometry in their crystals. Both the arene units in **1** showed eclipsed structure when viewed from the top and abbreviated as sandwiched *syn* structure whereas **3** and **4** trimers displayed parallel displaced *syn* configuration. The stacking parameters of the solid state stacked structures of compounds **1**, **3** and **4** (**Figure 4.18**) were evaluated to study the stacking efficiency and other intramolecular contacts which is tabulated in **table 4.1**. Based on the geometric data, on stacking behaviour, compound **1** showed sandwich type stacking with dihedral angle value 4.34° and the centroid to centroid distance between the opposite aromatic rings was found to be 3.694 Å. Comparison of the similar parameters in compounds **3** and **4**, showed better stacking behaviour in compound **3** than in compound **4** (**Table 4.1**).

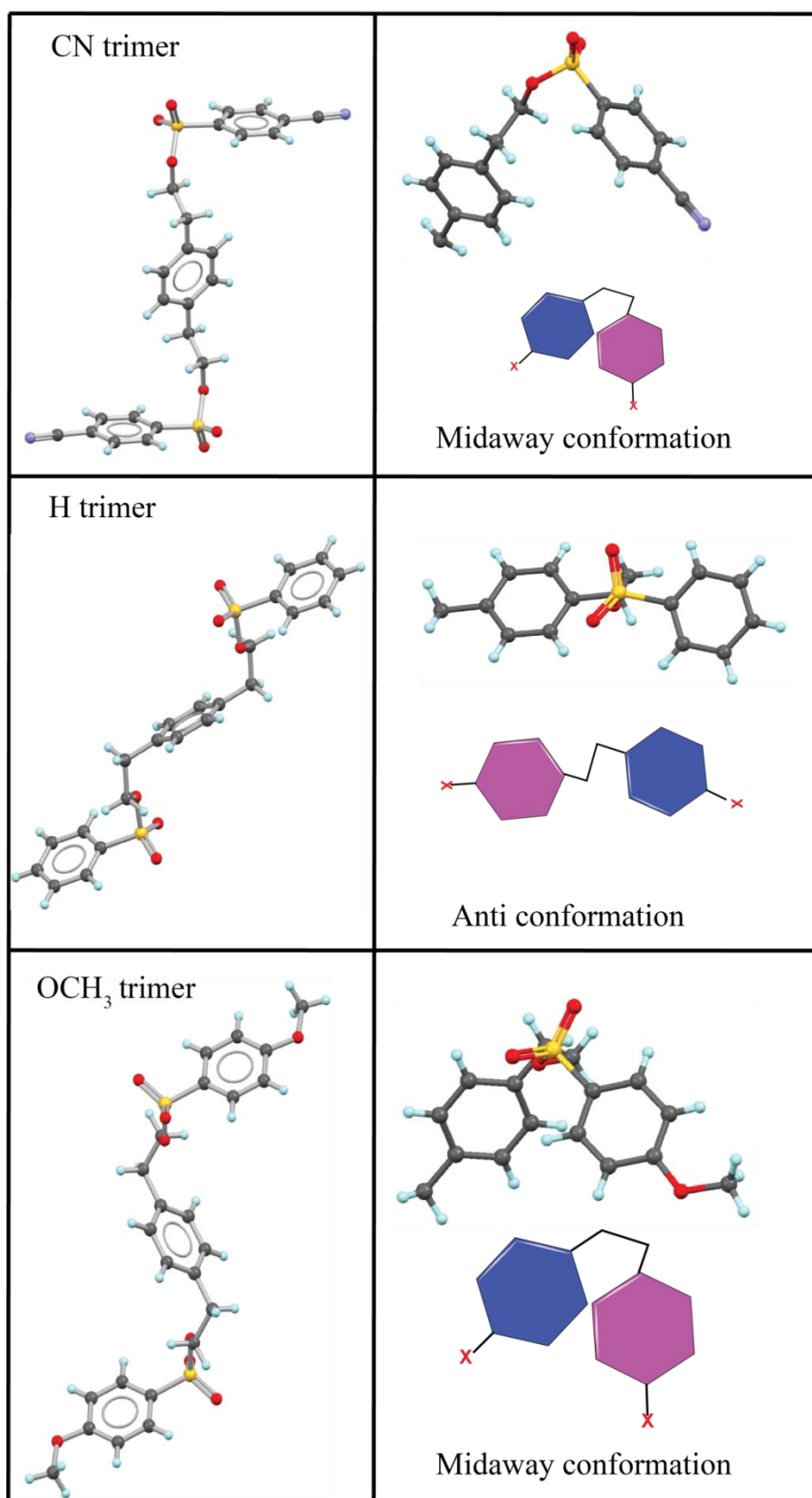


Figure 4.15. Ball and stick view of compounds **2** (CN), **5** (H) and **6** (OCH₃) showing *midway*, *anti* and *midway* configuration respectively. The top-to-bottom view of the same is displayed in (b).

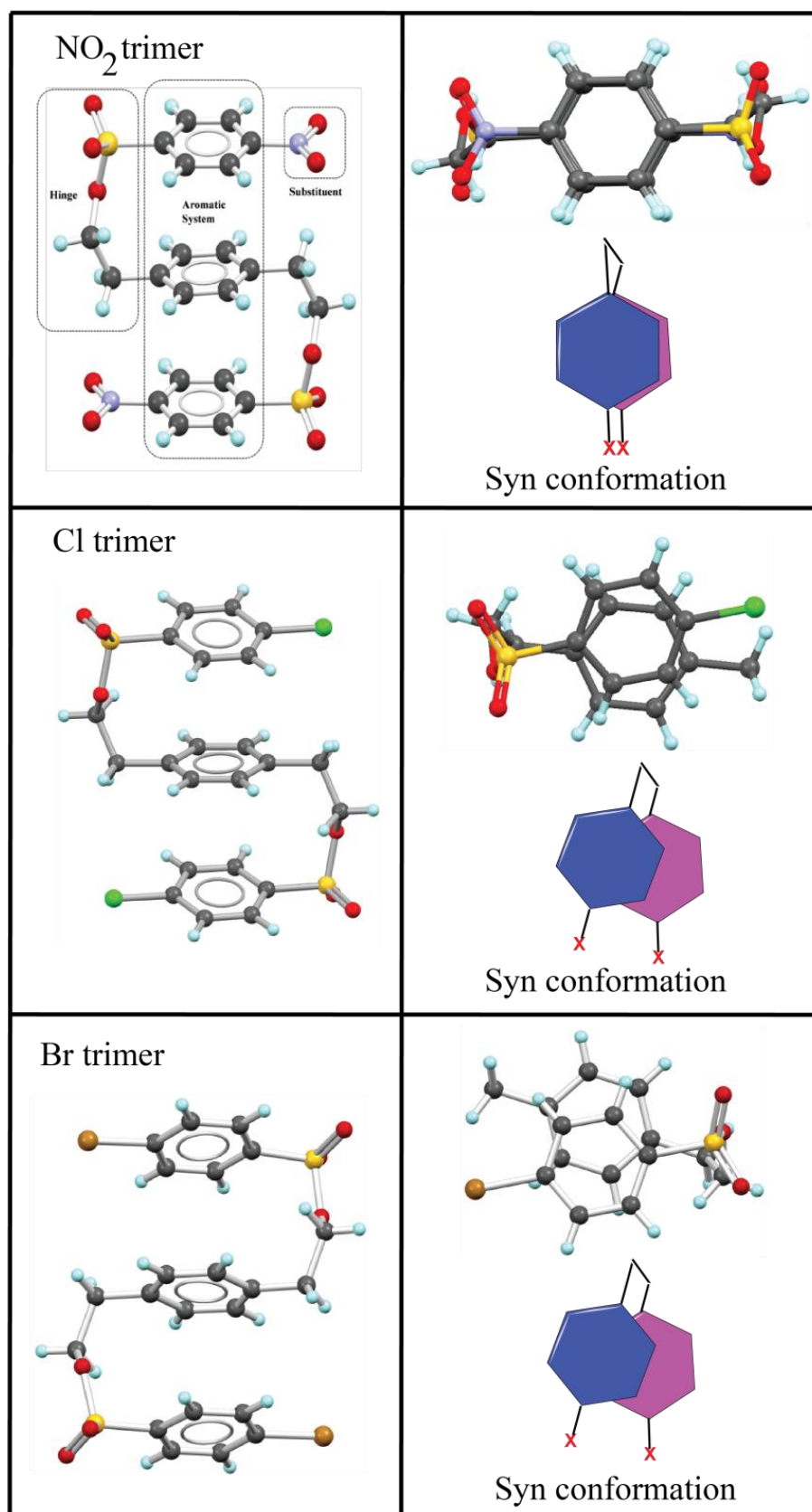
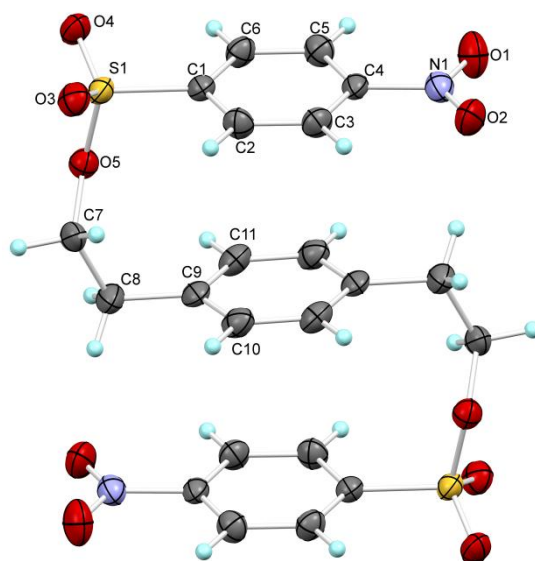
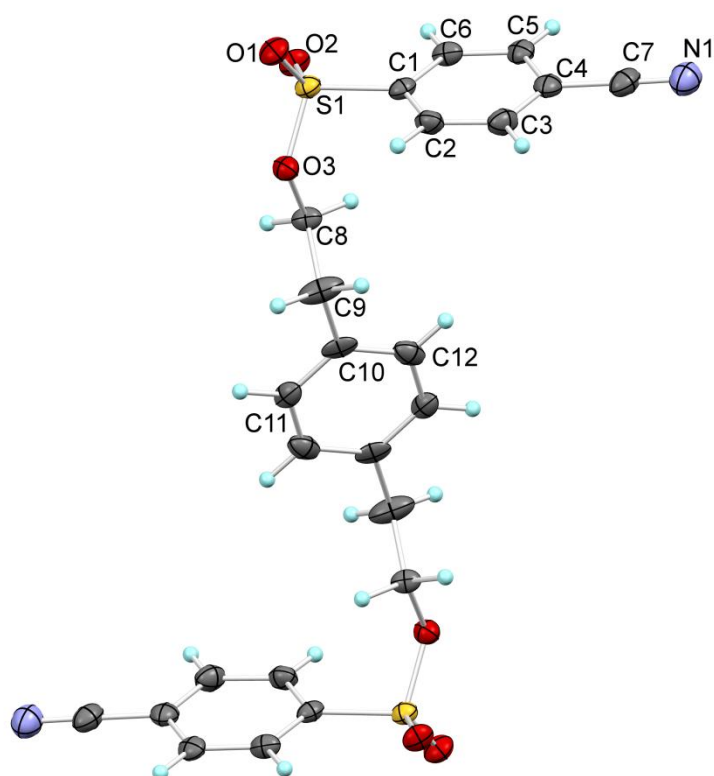


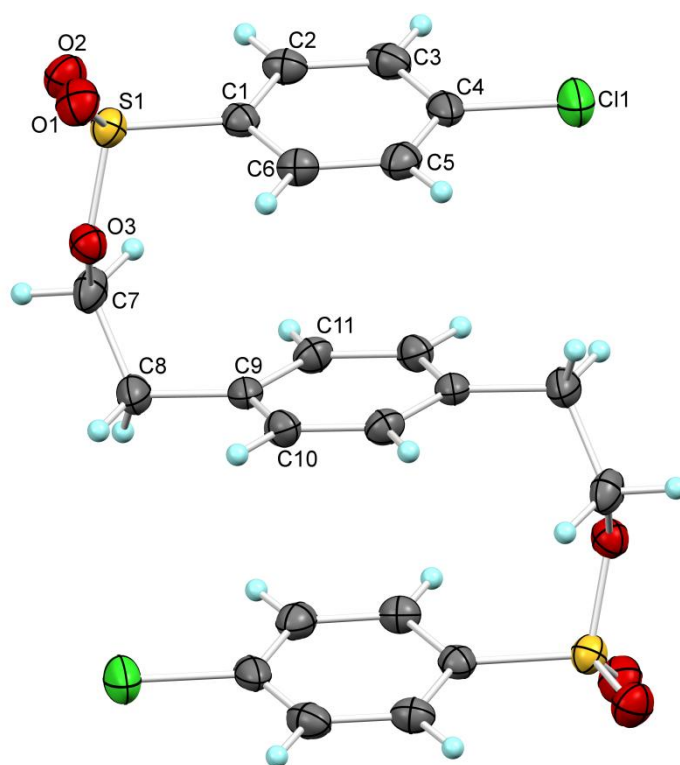
Figure 4.16. Ball and stick view of compounds **1** (NO₂), **3** (Cl) and **4** (Br) showing *syn* configuration respectively. The top-to-bottom view of the same is displayed in (b).



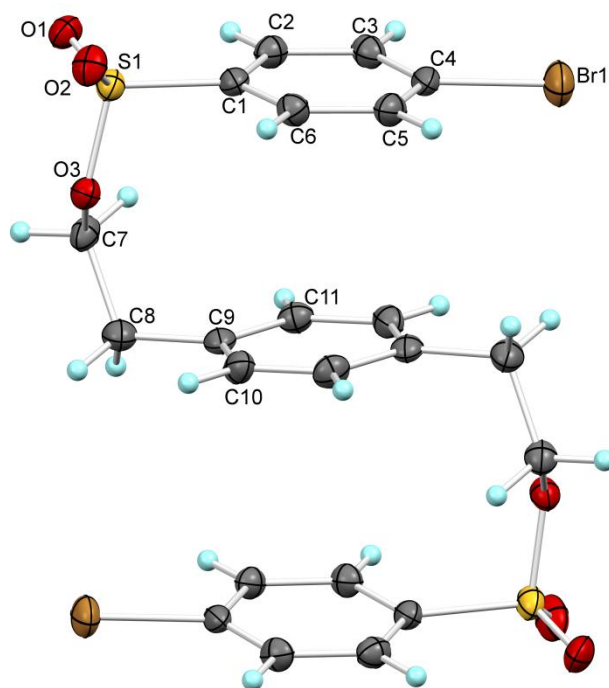
(a)



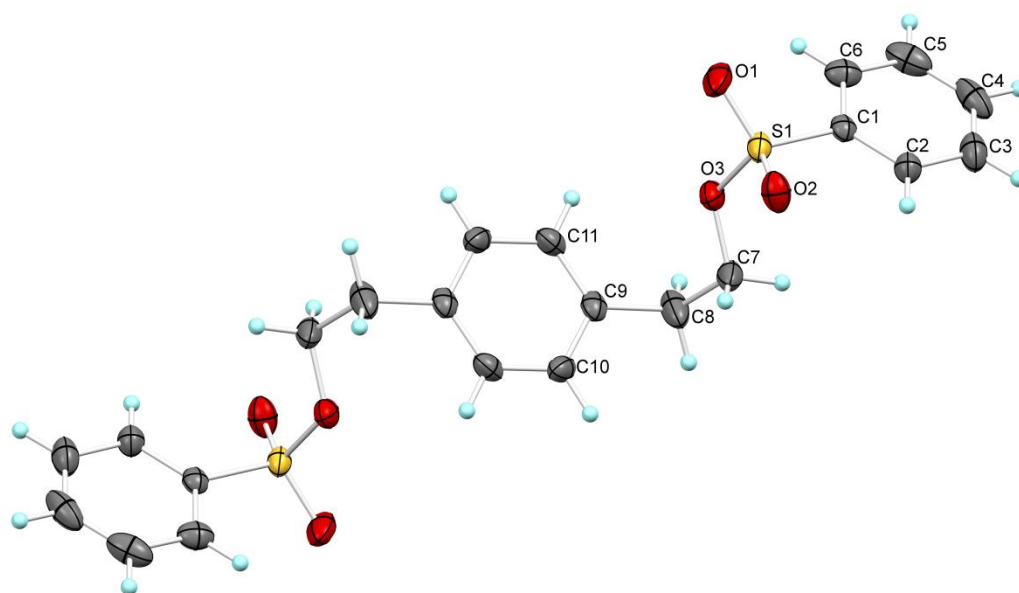
(b)



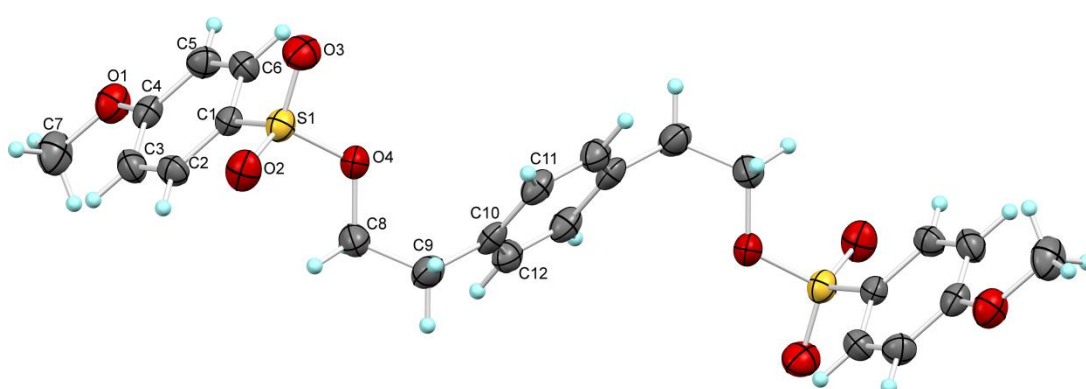
(c)



(d)



(e)



(f)

Figure 4.17. The ORTEPs of compounds (a) **1**, (b) **2**, (c) **3**, (d) **4**, (e) **5** and (f) **6** with 50% probability level. The numbering is given for the molecule in the asymmetric unit.

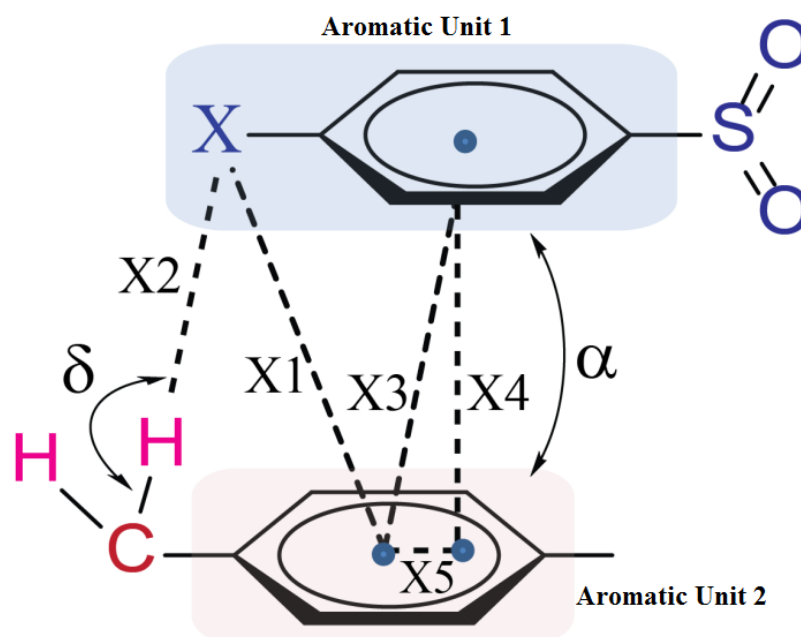


Figure 4.18. Schematic representation of stacking parameters, **X1**: the distance between the substituent atom attached to the aromatic unit 1 to the centroid of the opposite aromatic unit 2; **X2**: the distance between the C-H proton to the aromatic unit 2 and substituent atom of the aromatic unit 1; **X3**: the centroid-to-centroid distance between the aromatic units 1 and 2; **X4**: the distance of the perpendicular drawn from centroid of aromatic unit 1 to the plane of the aromatic unit 2; **X5**: the slippage distance between the aromatic unit 1 and aromatic unit 2; δ the angle C-H...X and α is the dihedral angle between the aromatic units 1 and 2.

Table 4.1. Geometrical parametrical of stacking interactions.

Trimer	X1	X2	X3	X4	X5	δ	α
	(Å)	(Å)	(Å)	(Å)	(Å)	(°)	(°)
1 (NO₂)	4.709	2.908	3.694	3.609	0.788	123.28	4.34
4 (Br)	5.082	3.449	3.731	3.538	1.49	131.96	6.79
3 (Cl)	4.990	3.483	3.757	3.492	1.39	127.20	6.61

Detailed structural analysis of stacked structures of **1** (NO₂), **3** (Cl) and **4**(Br) trimers revealed formation of 1D stacking. The trimer **1** is crystallized in triclinic *P*-1 space group with half molecule in the asymmetric unit and other half is generated by inversion operation. In trimer **1**, 1D chains are associated *via* weak C-H...O interactions between the sulfoester group and C-H proton of the flexible -CH₂-CH₂-spacer (**Figure 4.19**). The stacking parameters are tabulated in **table 4.1**. Both the aromatic units i.e. aromatic unit 1 and aromatic 2 are perfectly co-planar with dihedral angle of 4.34°. The Cg...Cg (centroid-to-centroid) distance is 3.694 Å and slippage parameter is 0.788 Å reveals significant overlapping between the opposite aromatic units with minimum slippage value. The aromatic units are stacked one above the other to form sand-witched type conformation (**Figure 4.16**). We calculated intermolecular potentials of NO₂ trimer to gain more insight into its packing behaviour. The total packing energy of NO₂ (**1**) crystal is -257.9 kJ/mol. The highest ranked intermolecular association (-67.5kJ/mol) is observed perpendicular to *bc* plane between the centrosymmetrically associated trimer molecules *via* C-H...O=S hydrogen bonding interactions. The extended stacking interaction is ranked second with intermolecular potential value being -50 kJ/mol. The trimers are perfectly aligned with each other to generate extended stacking assembly perpendicular to (1 0 1) plane. The third ranked intermolecular association is observed perpendicular to *ac* plane with IP value -34.5 kJ/mol in which the centrosymmetrically associated trimers establish conventional C-H...O=S contacts (**Figure 4.20**). The effect of the substituents attached to the aromatic unit 1 for intra and intermolecular interaction was investigated by Hiershfield surface analysis²⁷ and contacts were extracted from the crystal structures for comparison. Based on the fingerprint filtering of elements, the dipolar interaction between the N and O atom revealed highest association that contributes almost 65.1 % (**Figure 4.21**) to the overall crystal stability. This observation is further substantiated by the crystal structure analysis in which, short contact between the N atom of *p*-substituent and O atom of sulfo group (3.112Å) was observed. This proves that the substituent atom not only participate in intramolecular stacking mode but also establishes the intermolecular pulling effect to achieve intermolecular stacking (**Figure 4.22**).

Crystal structures of compounds **3** (Cl) and **4** (Br) belongs to triclinic *P*-1 space group. Compound **3** contains one molecule in the asymmetric unit whereas **4**

contain one and half molecule in the asymmetric unit. The asymmetric unit of Cl and Br trimers contain more than one *syn* conformers having different stacking parameters, however, for comparison the conformations with less slippage and higher co-planarity between the arene units were taken into consideration. The stacking parameters of best stacking mode in **3** revealed the dihedral angle of 6.61° between the aromatic units 1 and 2. The Cg...Cg (centroid-to-centroid distance) 3.757 Å and slippage parameters (1.39 Å) are well within the range to substantiate the stacking interaction. In **4**, the dihedral angle between the aromatic units (6.79°) is slightly non-planar in comparison to **3**. However, the cg...cg distance (3.731 Å) and slippage parameters (1.49 Å) revealed the displaced stacking mode. These stacking parameters indicate that both compounds show higher slippage value in comparison with **1** and display parallel- displaced stacking interaction in their crystals. Both the structures also revealed two dimensional isostructurality in their molecular packing. One-dimensional stacking chain perpendicular to (110) plane in **3** and (100) plane in **4**, are associated *via* C-H...O hydrogen bonding and C-H...X halogen bonding (X: Cl, Br) (**Figures 4.23-4.24**) contacts. The additivity of the substituent in solid state was investigated by Hiershfield analysis. The Cl atom of **3** displayed highest Hiershfield association with H atom (53.3 %) which is also substantiated by presence of Cl...H hydrogen bonding in its crystal structure (**Figure 4.25-4.26**). The second highest Hiershfield association is observed between the Cl and O (20.9%) atoms; which is attributed to intermolecular Cl...O halogen bonding contacts observed between the Cl atom of aromatic unit 1 and with O atom of sulfoester group (**Figure 4.25-4.26**). We calculated intermolecular potential to investigate the role of extended stacking interaction for stabilizing the 3D assembly. The packing energy of trimer **3** is -216.1 kJ/mol. The intermolecular potential along extended stacking is ranked second (cluster 1: -36.1 kJ/mol) and third (cluster 2: -35.5 kJ/mol) in **3** (Cl trimer) (**Figure 4.27**). Similarly, **4** (Br trimer) revealed Br...H hydrogen contacts and Br...O=S halogen bonding interactions contributing for first and second ranked association with H and O atom respectively in Hiershfield analysis (**Figure 4.28-4.29**). Furthermore, the extended stacking assembly is ranked third (-41.7 kJ/mol) (**Figure 4.30**) which participate in stabilizing 3D assembly with packing energy of -232.7 kJ/mol for trimer **4**.

Interestingly, the compound **2** (CN trimer) existed in the non-stacking conformation in solid state irrespective of electron withdrawing nature of CN substituent. Similarly, although trimer **5** (H trimer) existed in the stacking mode in solution state, it did not achieve stacked organization in solid state. However, the compound **6** (OCH₃ trimer) revealed the midway in solid state similar to its solution state organization (**Figure 4.16-4.17**). Based on the orientation of aromatic units 1 and 2, the configuration is assigned as *midway*, *anti* and *midway* for trimer of **2**, **5** and **6** respectively. Due to their unstacked conformations in solid state they were not used for the comparative analysis. Their crystal structure parameters are provided in the experimental methods.

The DSC profiles of stacked structure were compared with packing energy and intermolecular potential values of extended stacking assembly. The DSC profile of **1** revealed melting endotherm centered at 189 °C. The DSC thermograms of **4** and **3** trimer revealed melting endotherms centered at 160 °C and 143 °C respectively. The thermal analysis displayed significant correlation with the intermolecular potential values and crystal packing energies. The trend observed in their intermolecular potential along 1D stacked assembly and packing energy was found be strongest for **1** trimer and least for **3**. Similarly the melting endotherm was observed to be highest for the **1** and least for **3**. The melting endotherm for **4** was observed to be intermediate (**Figure 4.31**).

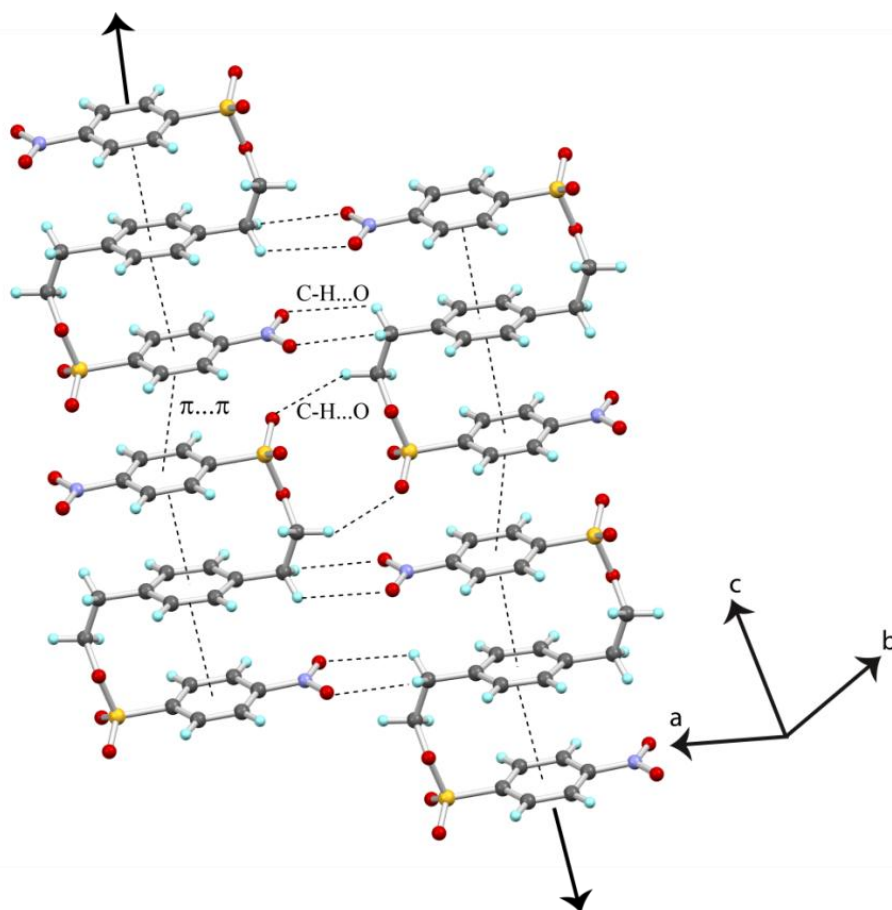


Figure 4.19. 2D depiction of crystal structure of trimer **1**, revealing formation of 1D chain of extended stacking interaction and their association *via* C-H...O interactions.

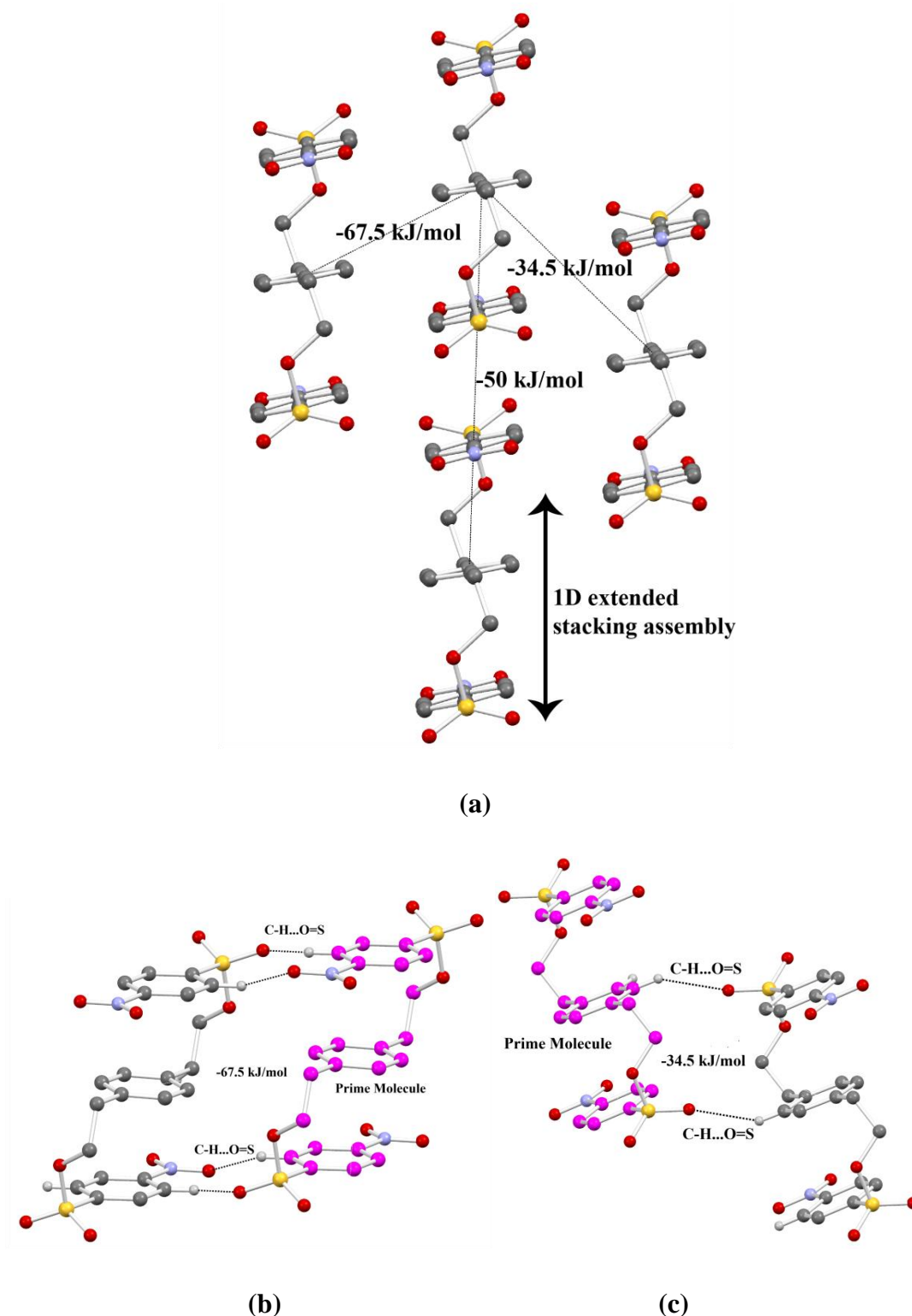


Figure 4.20. (a) Intermolecular potentials values across different layers of trimer **1** (NO_2) with the participating fragments, (b) detailed depiction of molecular interactions along ranked 1 intermolecular potential (-67.5 kJ/mol) and (c) detailed depiction of molecular interaction along ranked 3 intermolecular potential values (-34.5 kJ/mol).

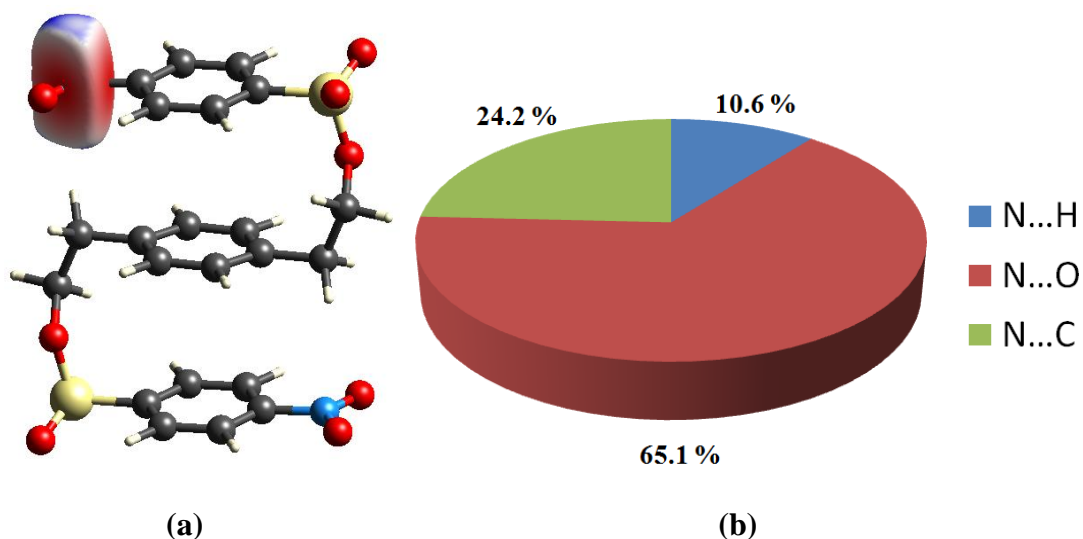


Figure 4.21. (a) The Hirschfeld surface over N atom of NO₂ group attached to para position of aromatic unit 1 and (b) pie chart of closed association extracted from fingerprint filtering of N with H, O and C atoms.

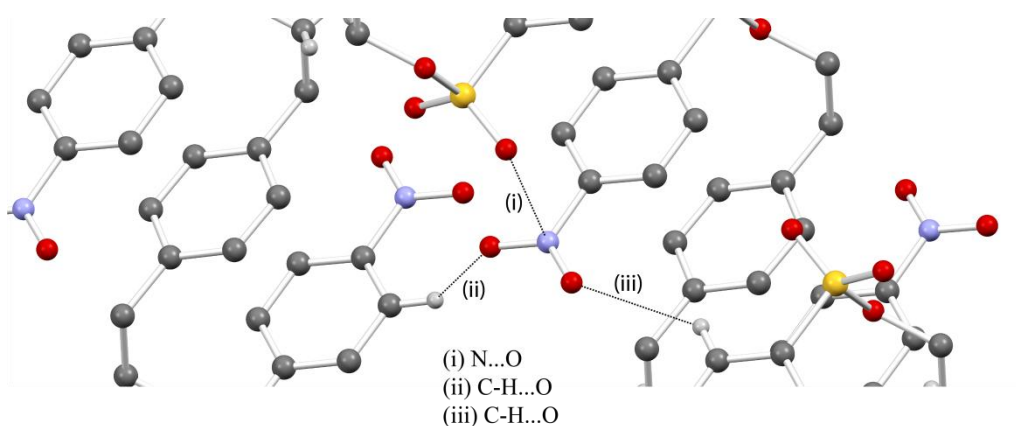


Figure 4.22. Zoomed view of intra and intermolecular short contacts displayed by *p*-substituent i.e. NO₂ group attached to the aromatic unit 1 in trimer **1**.

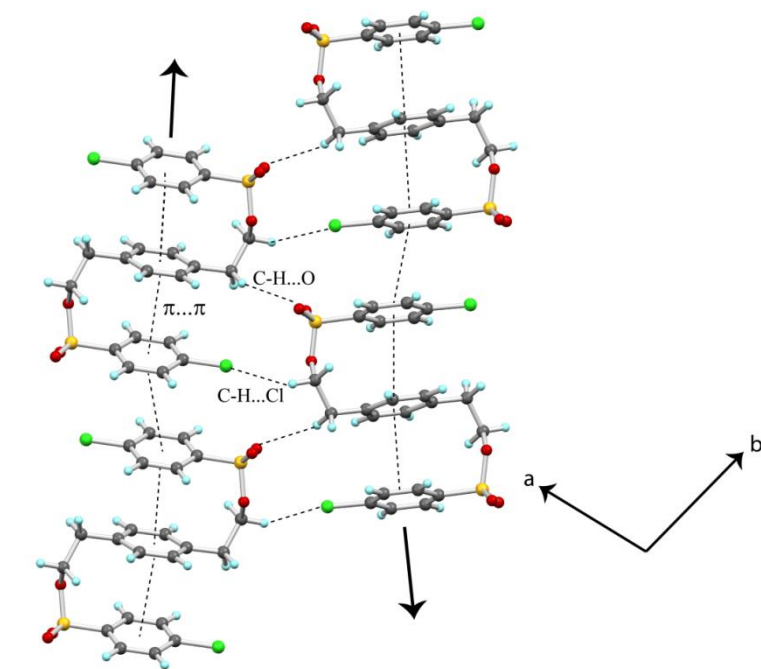


Figure 4.23. 2D depiction of crystal structure of **3**, revealing formation of 1D chain of extended stacking interaction and their association *via* C-H...O and C-H...Cl interactions.

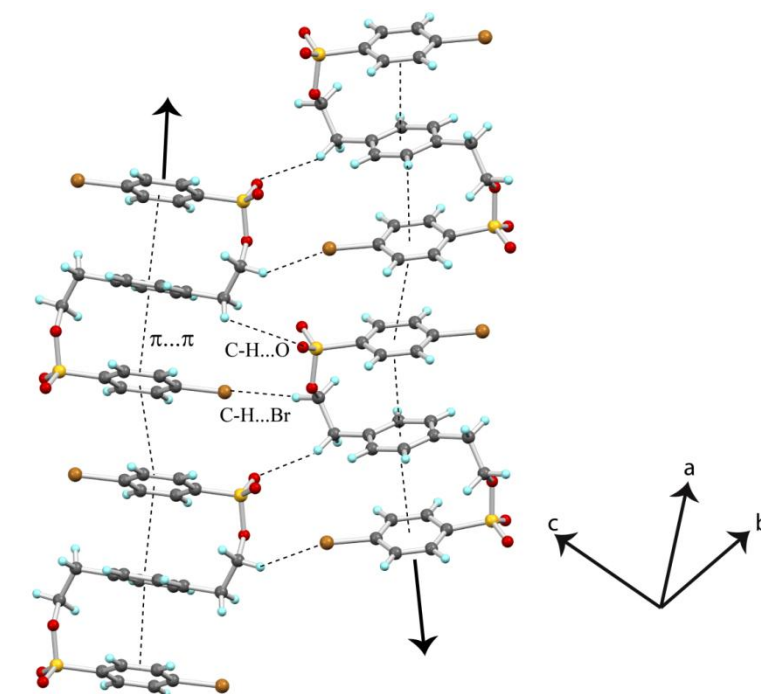


Figure 4.24. 2D depiction of crystal structure of **4**, revealing formation of 1D chain of extended stacking interaction and their association *via* C-H...O and C-H...Br interactions.

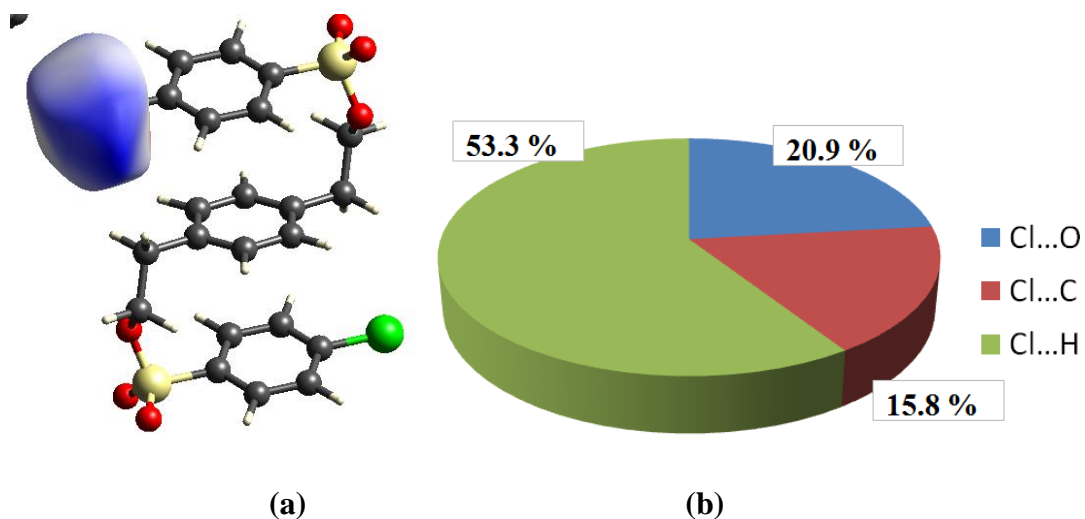


Figure 4.25. (a) The Hirschfeld surface over Cl atom attached to aromatic unit 1 and (b) pie chart of closed association extracted from fingerprint filtering of Cl with O, C and H atoms.

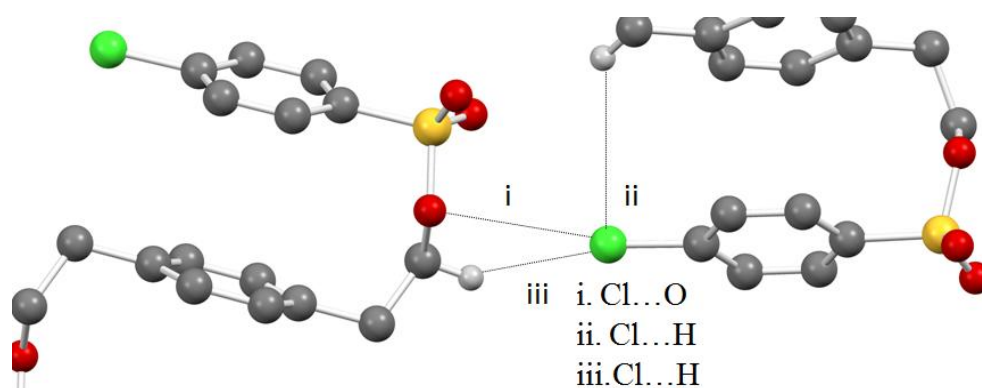


Figure 4.26. Zoomed view of intra and intermolecular short contacts displayed by *p*-substituent i.e. Cl atom attached to the aromatic unit 1.

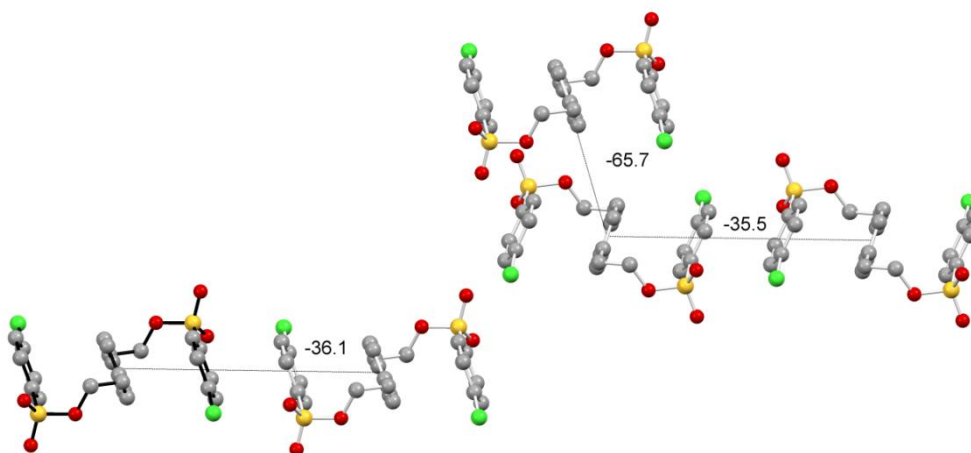


Figure 4.27. Intermolecular potentials values across different layers of trimer 3 (Cl) with the participating fragments.

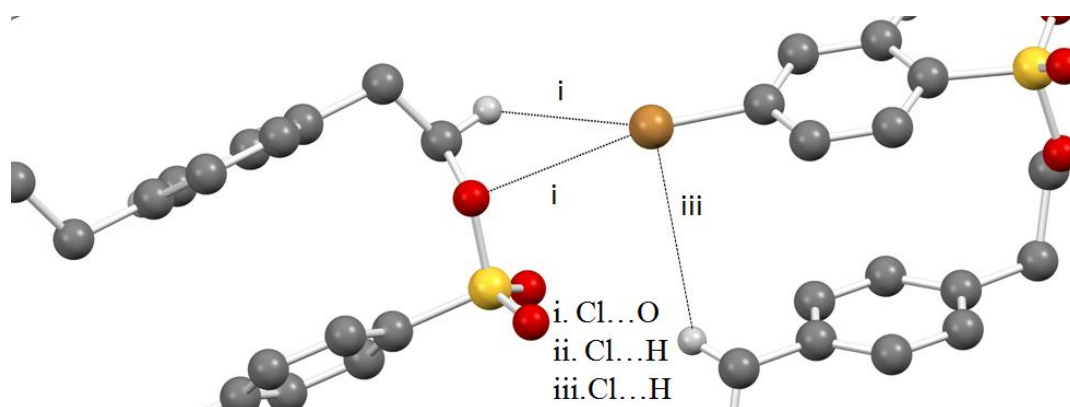


Figure 4.28. Zoomed view of intra and intermolecular short contacts displayed by *p*-substituent i.e. Br atom attached to the aromatic unit 1 in trimer **4**.

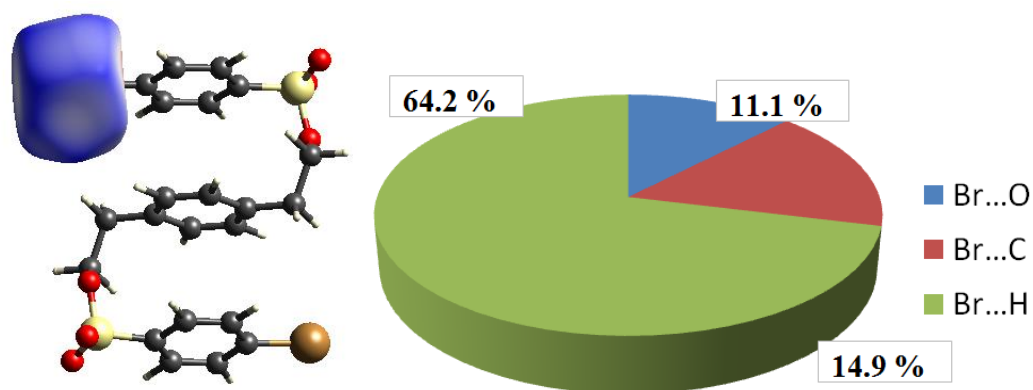


Figure 4.29. (a) The Hirschfeld surface over Br atom attached to aromatic unit 1 and (b) pie chart of closed association extracted from fingerprint filtering of Br with O, C and H atoms in trimer **4**.

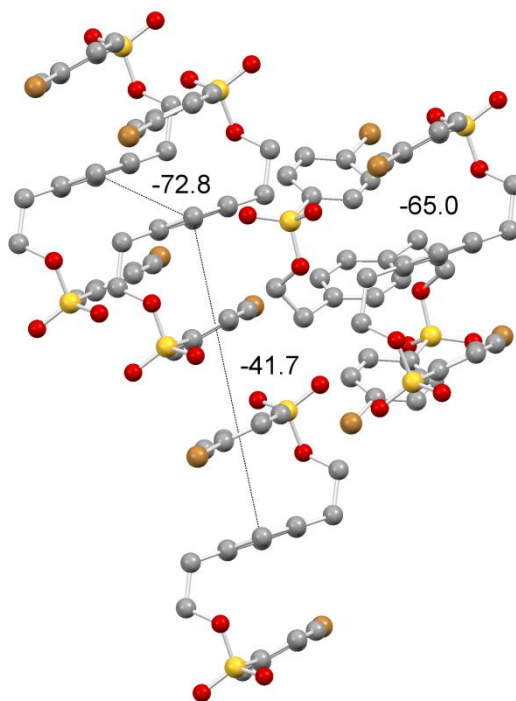


Figure 4.30. Intermolecular potentials values across different layers of trimer **4** (Br) with the participating fragments.

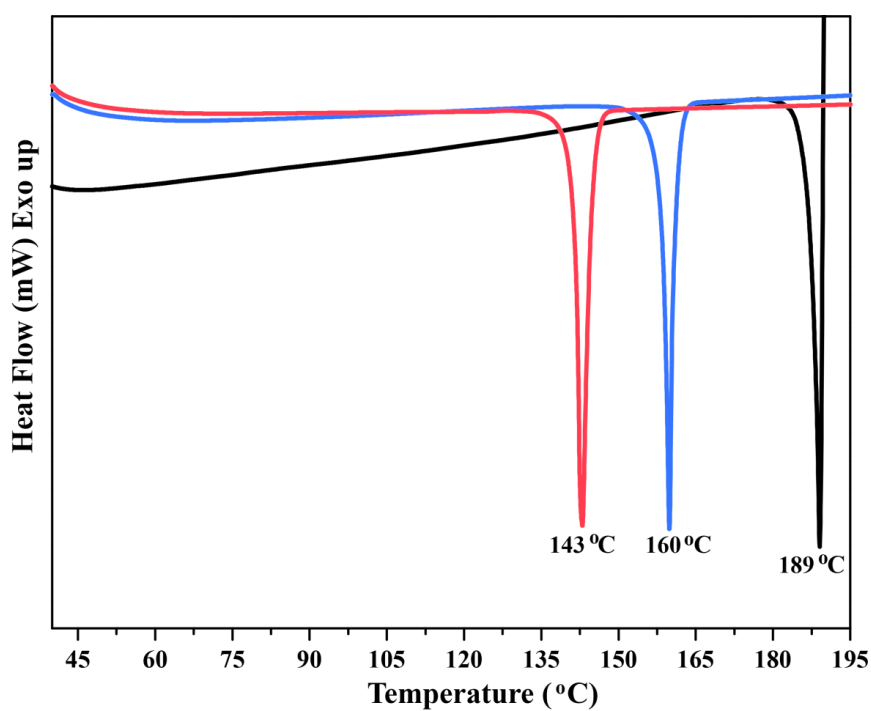


Figure 4.31. DSC thermograms of **1** (black), **4** (blue) and **3** (red).

Conclusion:

After analyzing the stacking parameters obtained from crystal structures and 2D NOESY studies, we speculated the transition mechanism between solution state stacking to solid state stacking assembly through nucleation funnel **figure 4.32**. Based on the 2D NOESY studies, trimer **2** (CN), **3** (Cl), **4** (Br) and **5** (H) exist in *syn* conformation in under-saturated solution state. Trimer **6** (OCH₃) reveals *anti* conformation under similar conditions. During the nucleation stage, the PNC of these trimers may achieve either of *syn*, *midway* or *anti* conformation that depends on the balance between the entropy cost of stacking and non-stacking conformation in multimeric association. Constrained intra-molecular stacking geometry may possess lowest entropy than the *midway* or *anti* conformation, however, intra and intermolecular extended stacking interactions may compensate overall entropy barrier. Here, the crucial role is played by the intramolecular stacking pull which is corroborated by intramolecular non-covalent interactions other than stacking interactions. Out of four *syn* trimers in solution state, trimer **3** (-Cl) and **4** (-Br) achieves *syn* conformation in the solid state, whereas, trimers **2** (-CN) and **5** (-H) exist in the non-stacked conformation i.e. *midway* and *anti* conformation respectively. The trimer **1** (-NO₂trimer) existed in the *syn* conformation with faceto-face stacking geometry. However, we could not carry out solution state investigation for **1** due to its poor solubility. Moreover, we envisioned that if the molecule has achieved *syn* geometry in more constrained solid state, it is more likely that it could be existing in *syn* geometry in solution too. Therefore, we predicted that trimer **1** may also be exist in the *syn* conformation in solution state. As expected the trimer **6** (-OCH₃trimer) form unstacked *midway* structure in solid state.

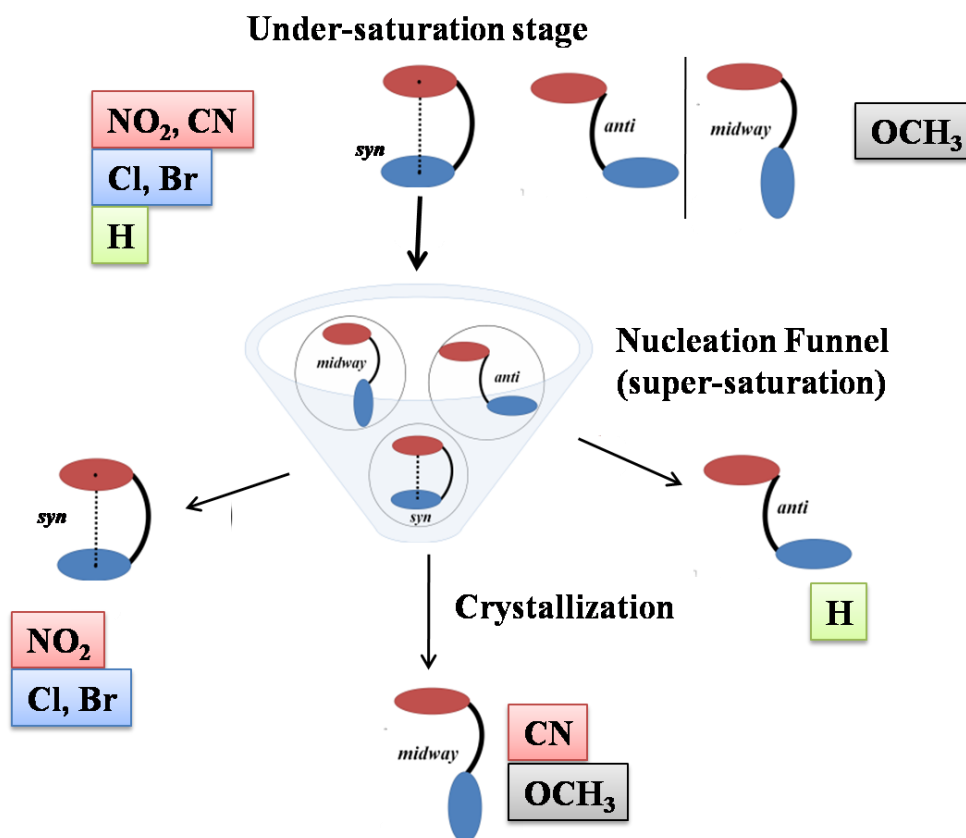


Figure 4.32. The nucleation funnel and solution to solid state transition of NO_2 , CN, Cl, Br and H trimers.

To rationalize the reason behind the difference between the stacking geometries of trimer **2** (-CN) and trimer **5** (-H) in solution and solid state, we investigated the role of substituent in the crystal structure of all the trimers. We observed that, the trimers that form stacked structures in both solution and solid state reveal short contacts between the atom of substituent attached to the aromatic unit 1 and C-H proton of the opposite aromatic ring (aromatic unit 2). The trimers which precludes the *syn* geometry in solid state are devoid of such interaction i.e. compounds **2** and **5** that may not form intramolecular association with C-H proton of the opposite aromatic ring.

In compilation we put forth different models for explaining the role of substituent interaction in solution and solid state. For elucidating the solution state stacking interaction we gave combined model which takes into account, contribution from electrostatic and dispersive terms. According to our model, stacking interactions in solution is determined by E_{stacking} which is the sum of $E_{\text{X-cg}}$, $E_{\text{S-cg}}$, E_{prep} and E_{att} .

P_{rep}: Polarized repulsion between aromatic rings

P_{att}: Polarized attraction between aromatic rings

For solid state stacking interactions, we put forth substituent-substituent interaction model. Polarization of electron density is by far the most striking feature of the any supra-molecular interactions. Anisotropic distribution of electron density causes partitioning of electrostatic potential forming δ^+ and δ^- regions. Last few decades this was mystery for supramolecular chemist, but evolution of solid state and NMR instrumentation has made possible to probe non-covalent interactions between two atoms. Charge density and high end theoretical calculations have proved that non-covalent interaction are the result of attractive interaction between positive regions of one atom with negative region of other atom (σ hole bonding). Polarization of electron density is observed in many atoms such as oxygen and halogens, it increases with the lighter to heavier atom which is experiential validated. According to our model, interactions between substituents of opposite aromatic rings majorly contributes as one of the driving force for stabilizing $\pi \cdots \pi$ stacking interactions in crystalline state. The stacking geometry of **1**(NO₂), **3**(Cl) and **4**(Br) trimers in solid state is attributed to C-H \cdots N, C-H \cdots Br, and C-H \cdots Cl interactions respectively (**Figure 4.33**). However, the similar interaction C-H \cdots H and C-H \cdots C of **5** (H trimer) and **2**(CN trimer) respectively, could not serve as pulling effect against the entropic barrier.

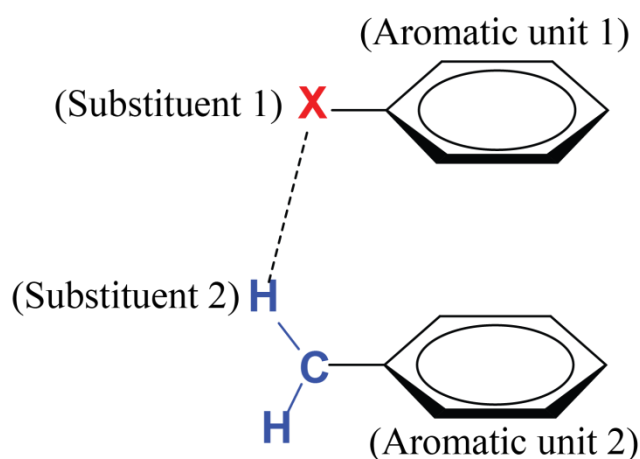


Figure 4.33. The substituent-substituent interaction model for explaining the solid state stacking

In summary, we hypothesized solution state stacking interaction of any two aromatic units is governed by the 1) the intra-molecular pull (attractive interaction between the aromatic units and 2) the conformational flexibility to achieve the desired conformation (stacking mode). The transition of solution state interaction to solid state stacking *via* nucleation funnel requires the intermolecular structural fitting (association). The substituent plays pivotal role by acting as bridge between the intra- and intermolecular stacked association to generate multimeric assembly with extended association.

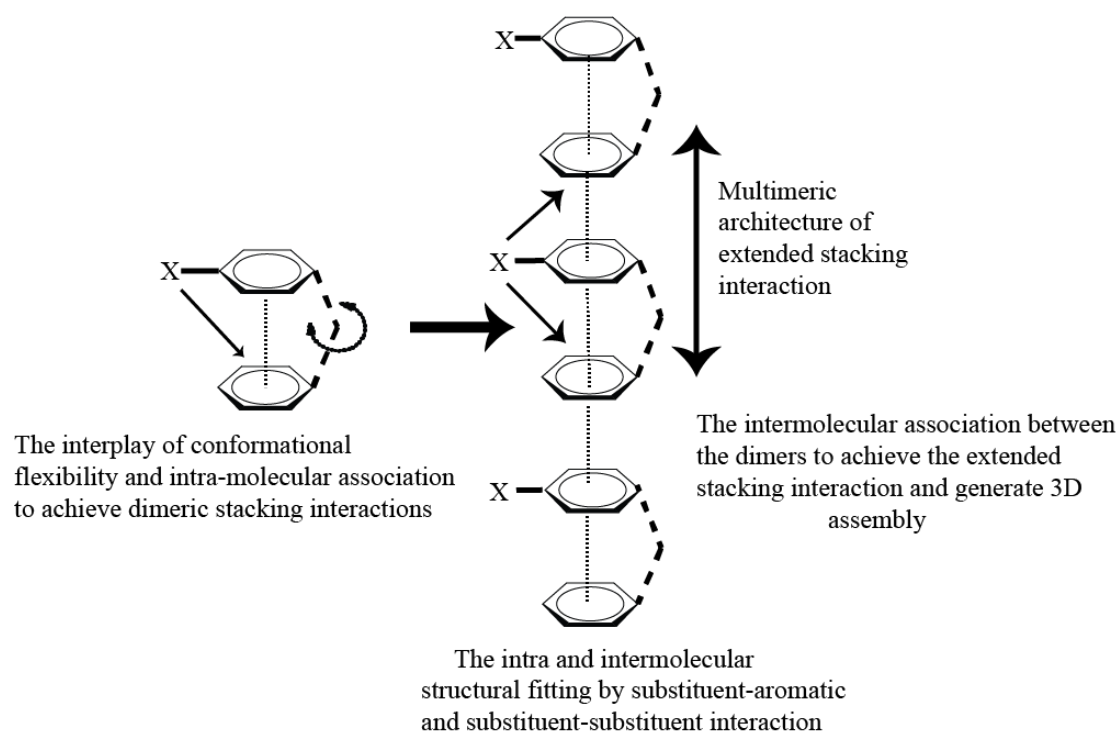


Figure 4.34. Depiction of the role of conformational flexibility and additivity of substituent in achieving solution state stacking association and its transition to solid state extended interaction via nucleation funnel.

Experimental Methods:

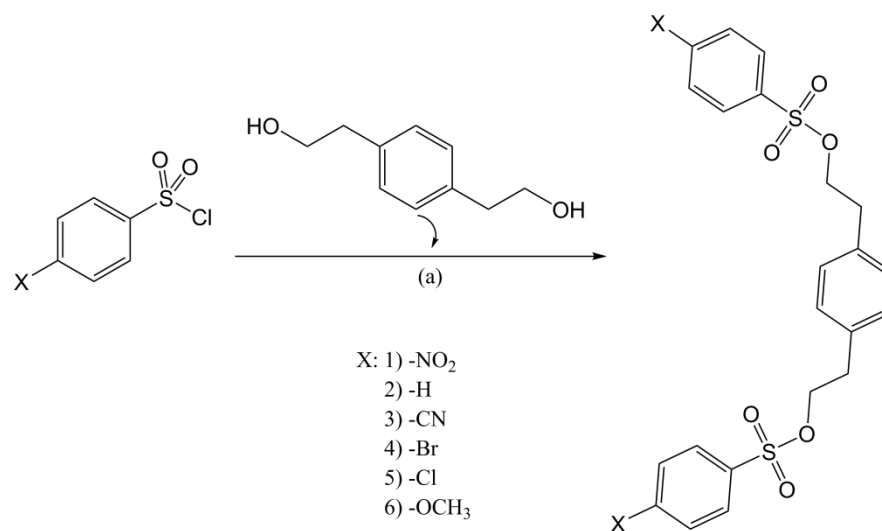


Figure 4.35. General scheme of synthesis of trimers; (a) DCM, TEA, rt.

2 eq. of *p*-substituted benzene sulfonyl chloride is reacted with one eq. 1,4-Bis(2-hydroxyethyl)benzene, under inter atmosphere in the presence of 2.1 eq. of triethylamine to yield corresponding trimeric sulfoesters. The crude reaction mixture is then purified by flash column chromatography in ethyl acetate/ light petroleum ether system except for trimer **1** (NO₂trimer). The trimer **1** was purified by differential solubility of impurity and product. The purified products other than **1** were crystallized from chloroform/methanol solvent mixture by slow evaporation. The trimer **1** was crystallized in DMF solvent by slow cooling.

Synthesis of trimer 1 (NO₂ trimer) (1,4-phenylenebis(ethane-2,1-diyl) bis(4-nitrobenzenesulfonate): To the cooled (0 °C) solution of 1,4-Bis(2-hydroxyethyl)benzene (1 g, 6.02 mmol, 1 eq.) and triethylamine (1.76 mL, 12.6 mmol, 2.1 eq.) in DCM, 4-nitrobenzenesulfonyl chloride (2.67 g, 12.04 mmol, 2 eq.) in DCM was added sequentially under inert atmosphere. The solution was warmed to room temperature and stirred for 8 h. The solvent was evaporated under vacuum and serially washed with water, cold methanol, chloroform and cold DMF to remove the impurities. The compound was further purified by re-crystallization from DMF(heating and slow cooling) to yield NO₂ trimer (**1**); ¹H NMR (400 MHz, DMSO-d₆) δ = 8.25 - 8.16 (m, 4 H), 7.84 (d, *J* = 8.7 Hz, 4 H), 7.25 (s, 4 H), 4.49 (t, *J* = 6.9 Hz, 4 H), 2.99 (t, *J* = 6.9 Hz, 4 H); ¹³C NMR (100 MHz, DMSO-d₆) δ = 134.9, 129.1, 126.9, 123.3, 76.3, 34.8 chemical shift in ppm.

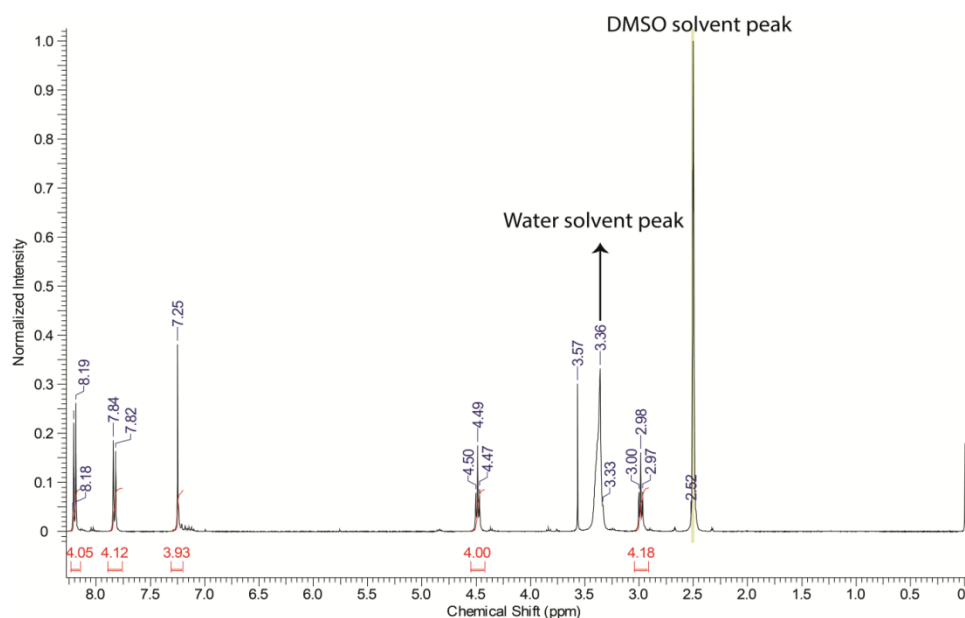


Figure 4.46. ¹H NMR of 1,4-phenylenebis(ethane-2,1-diyl) bis(4-nitrobenzenesulfonate).

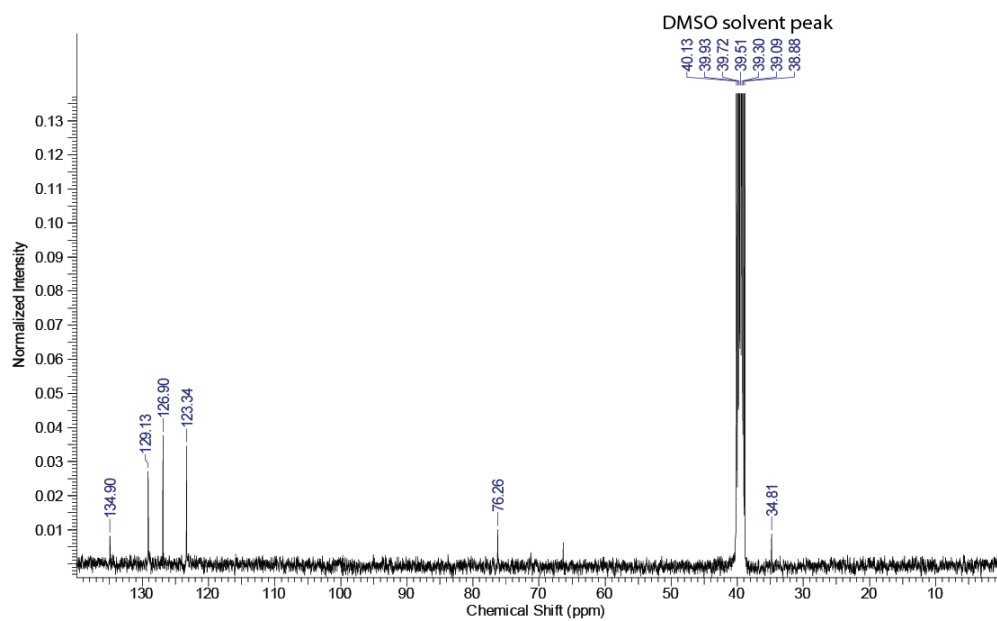


Figure 4.47. ^{13}C NMR of 1,4-phenylenebis(ethane-2,1-diyl) bis(4-nitrobenzenesulfonate).

Synthesis of trimer 2 (CN trimer) (1,4-phenylenebis(ethane-2,1-diyl) bis(4-cyanobenzenesulfonate)): To the cooled (0 °C) solution of 1,4-Bis(2-hydroxyethyl)benzene (1 g, 6.02 mmol, 1 eq.) and triethylamine (1.76 mL, 12.6 mmol, 2.1 eq.) in DCM, 4-cyanobenzenesulfonyl chloride (2.43 g, 12.04 mmol, 2 eq.) in DCM was added sequentially under inert atmosphere. The solution was warmed to room temperature and stirred for 8 h. The solvent was evaporated under vacuum and crude reaction mixture was suspended in ethyl acetate which is then serially washed with saturated sodium bicarbonate and brine. The traces of aqueous layer were removed by suspending the organic layer in sodium sulphate. The crude product was then filtered and purified by flash column chromatography (ethyl acetate : light petroleum ether solvent system) to yield CN trimer (**2**), ^1H NMR (400 MHz, DMSO- d_6) δ = 7.90 (d, J = 8.3 Hz, 2 H), 7.79 (d, J = 8.6 Hz, 4 H), 7.02 (s, 4 H), 4.30 (t, J = 6.7 Hz, 4 H), 2.97 (t, J = 6.6 Hz, 4 H); ^{13}C NMR (100 MHz, CDCl_3) δ = 140, 134.8, 132.9, 129.2, 128.4, 71.5, 34.8 chemical shift in ppm.

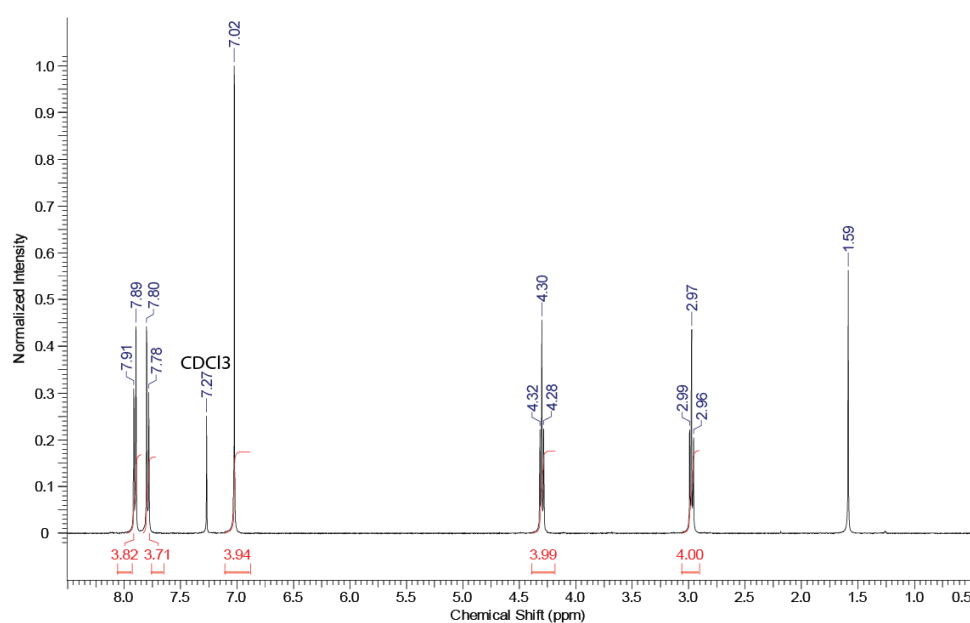


Figure 4.42. ^1H NMR of 1,4-phenylenebis(ethane-2,1-diyl) bis(4-cyanobenzenesulfonate).

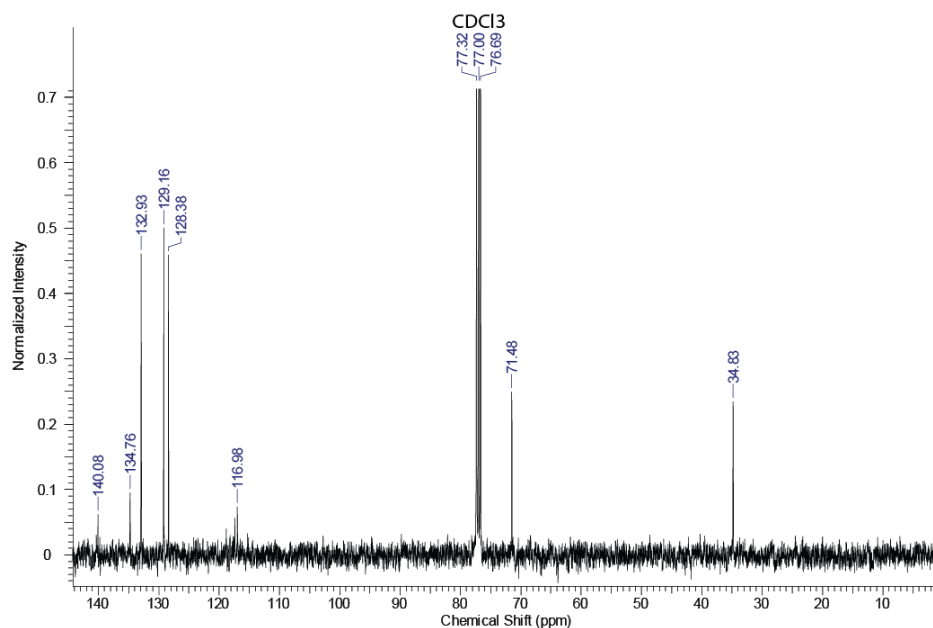


Figure 4.43. ^{13}C NMR of 1,4-phenylenebis(ethane-2,1-diyl) bis(4-cyanobenzenesulfonate).

Synthesis of trimer 3 (Cl) (1,4-phenylenebis (ethane-2,1-diyl) bis (4-chlorobenzenesulfonate): To the cooled ($0\text{ }^{\circ}\text{C}$) solution of 1,4-Bis(2-hydroxyethyl)benzene (1g, 6.02mmol, 1eq.) and triethylamine (1.76 mL, 12.6 mmol, 2.1 eq.) in DCM, 4-chlorobenzenesulfonyl chloride (2.54g, 12.04mmol, 2eq.) in DCM was added sequentially under inert atmosphere. The solution was warmed to the room temperature and stirred for 8 h. The solvent was then evaporated under vacuum and crude reaction mixture was suspended in the ethyl acetate which is then serially washed with saturated sodium bicarbonate and brine. The traces of aqueous layer were removed by suspending the organic layer in sodium sulphate. The crude product was then filtered and purified by flash column chromatography (ethyl acetate: light petroleum ether solvent system) to yield Cl trimer (**3**). ^1H NMR (400 MHz, CDCl_3) δ = 7.73 (d, J = 8.6 Hz, 4 H), 7.46 (d, J = 8.3 Hz, 4 H), 7.01 (s, 4 H), 4.24 (t, J = 6.7 Hz, 4 H), 2.95 (t, J = 6.7 Hz, 4 H); ^{13}C NMR (100 MHz, CDCl_3) δ = 140.4, 134.8, 129.5, 129.2, 70.9, 34.8, chemical shift in ppm.

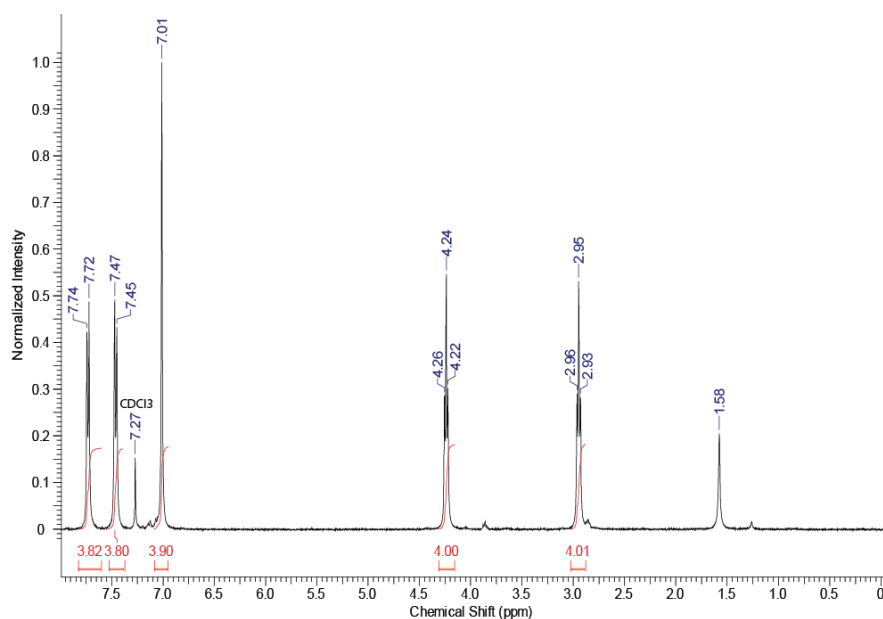


Figure 4.36. ^1H NMR of 1,4-phenylenebis(ethane-2,1-diyl) bis(4-chlorobenzenesulfonate).

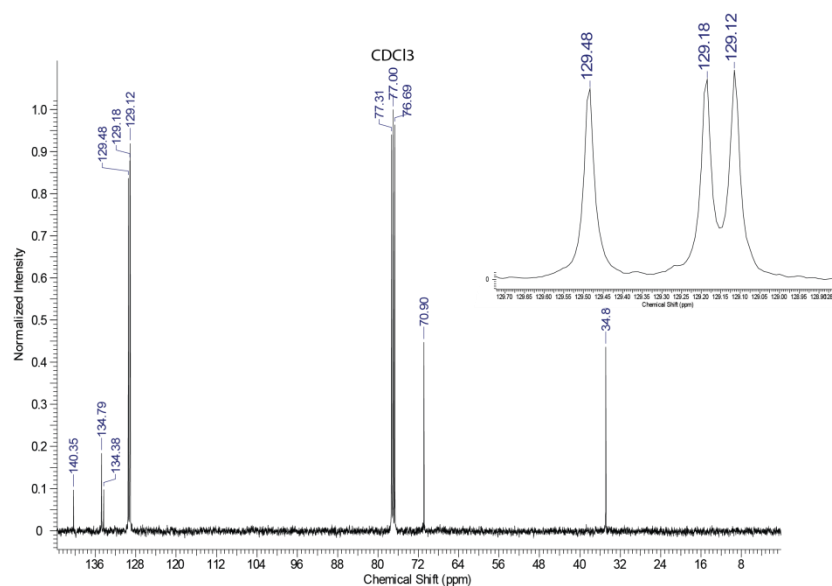


Figure 4.37. ^{13}C NMR of 1,4-phenylenebis(ethane-2,1-diyl) bis(4-chlorobenzenesulfonate).

Synthesis of trimer 4 (Br) (1,4-phenylenebis(ethane-2,1-diyl) bis(4-bromobenzenesulfonate): To the cooled ($0\text{ }^{\circ}\text{C}$) solution of 1,4-Bis(2-hydroxyethyl)benzene (1 g, 6.02 mmol, 1eq.) and triethylamine (1.76 mL, 12.6 mmol, 2.1 eq.) in DCM, 4-bromobenzenesulfonyl chloride (3.06 g, 12.04 mmol, 2eq.) in DCM was added sequentially under inert atmosphere. The solution was then warmed to the room temperature and stirred for 8 h. The solvent was evaporated under

vacuum and crude reaction mixture was suspended in the ethyl acetate which is then serially washed with saturated sodium bicarbonate and brine. The traces of aqueous layer were removed by suspending the organic layer in sodium sulphate. The crude product was then filtered and purified by flash column chromatography (ethyl acetate: light petroleum ethersolvent system) to yield Br trimer (**4**). ^1H NMR (400 MHz, CDCl_3) $\delta = 7.70 - 7.58$ (m, 8 H), 7.01 (s, 4 H), 4.24 (t, $J = 6.9$ Hz, 4 H), 2.95 (t, $J = 6.9$ Hz, 4 H); ^{13}C NMR (100 MHz, CDCl_3) $\delta = 134.9, 134.8, 132.5, 129.2, 128.9, 70.9, 34.9$ chemical shift in ppm.

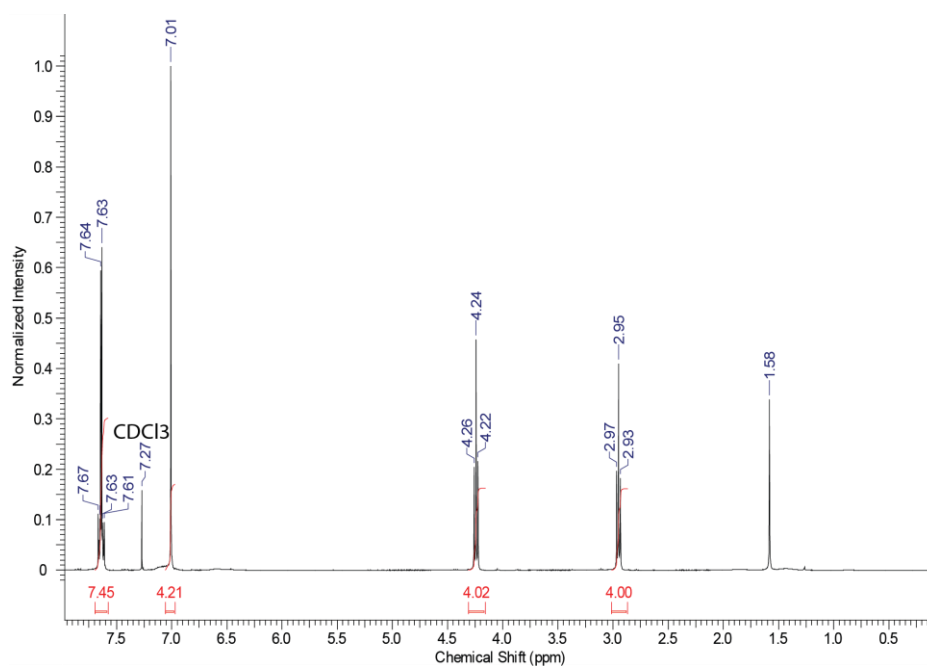


Figure 4.38. ^1H NMR of 1,4-phenylenebis(ethane-2,1-diyl) bis(4-bromobenzenesulfonate).

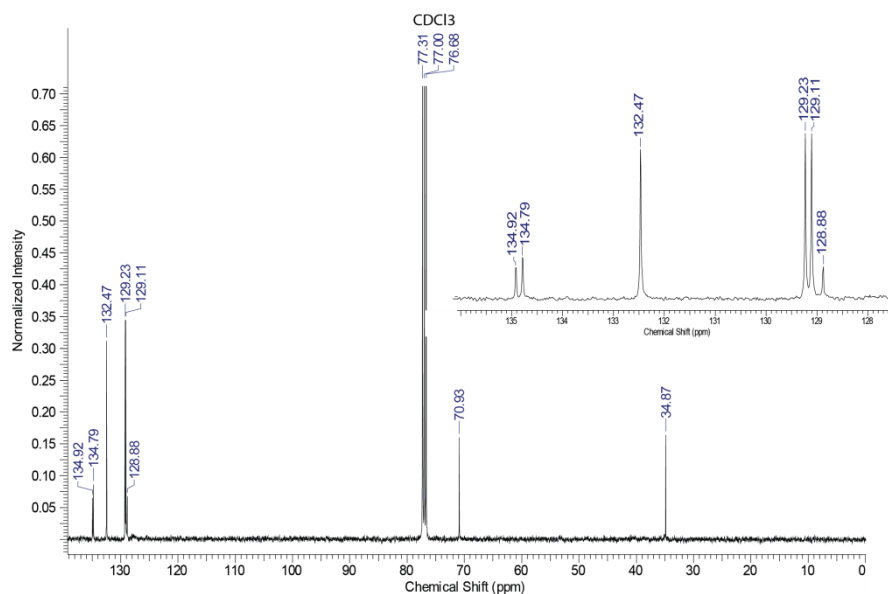


Figure 4.39. ^{13}C NMR of 1,4-phenylenebis(ethane-2,1-diyl) bis(4-bromobenzenesulfonate).

Synthesis of trimer 5 (H-trimer) (1,4-phenylenebis(ethane-2,1-diyl) dibenzenesulfonate): To the cooled ($0\text{ }^{\circ}\text{C}$) solution of 1,4-Bis(2-hydroxyethyl)benzene (1 g, 6.02 mmol, 1eq.) and triethylamine (1.76 mL, 12.6 mmol, 2.1 eq.) in DCM, benzenesulfonyl chloride (2.13 g, 12.04 mmol, 2 eq.) in DCM was added sequentially under inert atmosphere. The solution was warmed to room temperature and stirred for 8 h. The solvent was evaporated under vacuum and crude reaction mixture was suspended in the ethyl acetate which is then serially washed with saturated sodium bicarbonate and brine. The traces of aqueous layer were removed by suspending the organic layer in sodium sulphate. The crude product was then filtered and purified by flash column chromatography (ethyl acetate: light petroleum ethersolvent system) to yield H trimer (**5**). ^1H NMR (400 MHz, CDCl_3) δ = 7.88 - 7.78 (m, 4 H), 7.69 - 7.59 (m, 2 H), 7.57 - 7.46 (m, 4 H), 7.02 (s, 4 H), 4.22 (t, J = 7.0 Hz, 4 H), 2.93 (t, J = 7.0 Hz, 4 H); ^{13}C NMR (100 MHz, CDCl_3) δ = 135.9, 134.8, 133.7, 129.2, 127.8, 70.6, 34.9 chemical shift in ppm.

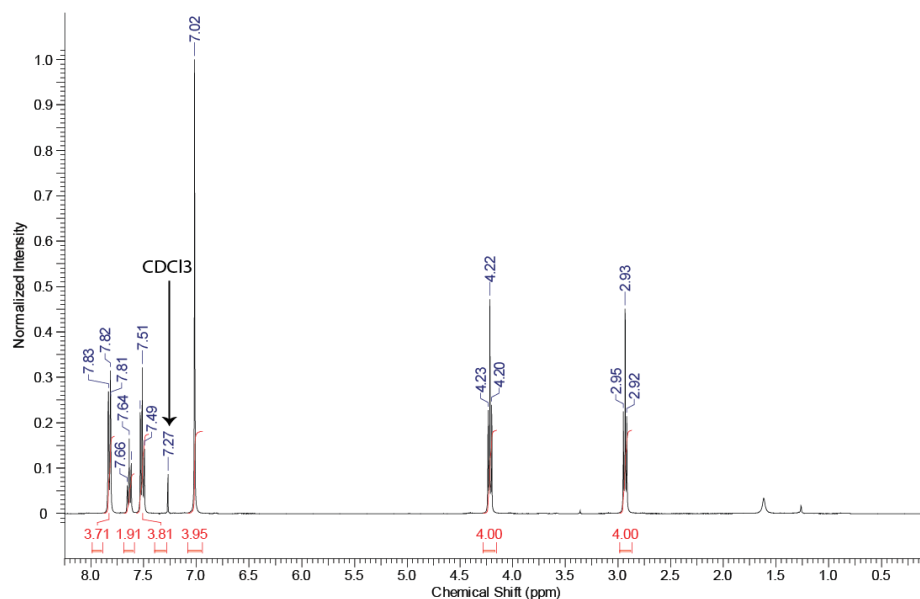


Figure 4.40. ^1H NMR of 1,4-phenylenebis(ethane-2,1-diyl) dibenzenesulfonate.

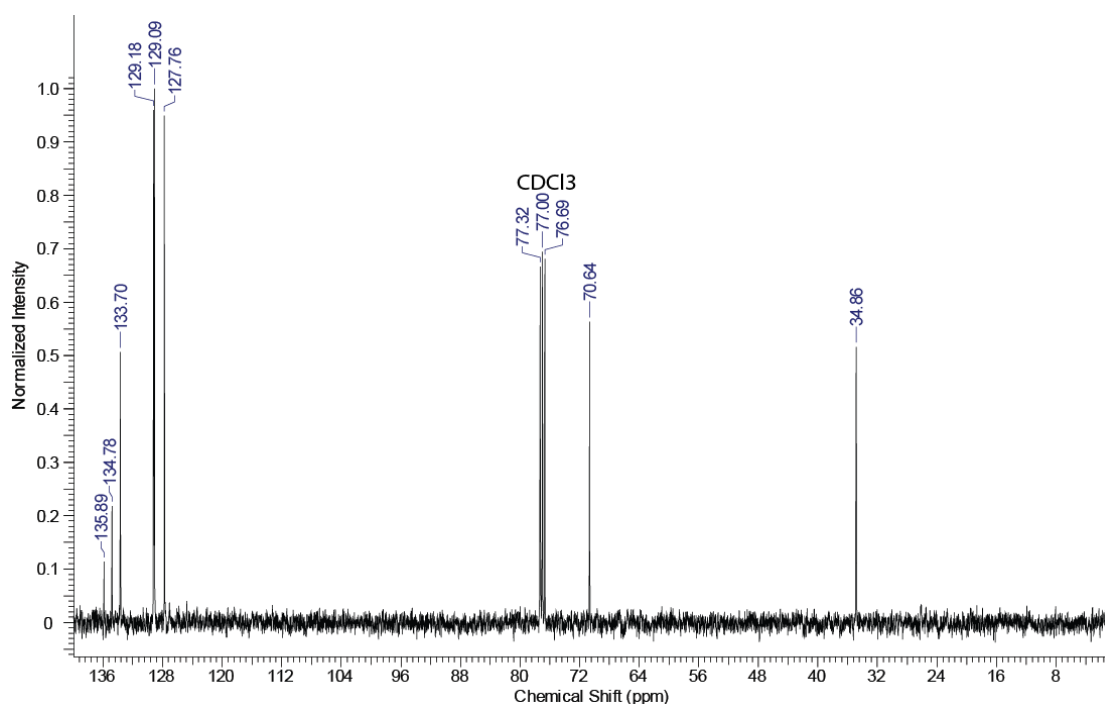


Figure 4.41. ^{13}C NMR of 1,4-phenylenebis(ethane-2,1-diyl) dibenzenesulfonate.

Synthesis of trimer 6 (OCH₃ trimer) (1,4-phenylenebis(ethane-2,1-diyl) bis(4-methoxybenzenesulfonate): To the cooled (0 °C) solution of 1,4-Bis(2-hydroxyethyl)benzene (1 g, 6.02 mmol, 1 eq.) and triethylamine (1.76 mL, 12.6 mmol, 2.1 eq.) in DCM, 4-methoxybenzenesulfonyl chloride (2.49 g, 12.04 mmol, 2 eq.) in DCM was added sequentially under inert atmosphere. The solution was warmed to room temperature and stirred for 8 h. The solvent was evaporated under

vacuum and crude reaction mixture was suspended in the ethyl acetate which is then serially washed with saturated sodium bicarbonate and brine. The traces of aqueous layer were removed by suspending the organic layer in sodium sulphate. The crude product was then filtered and purified by flash column chromatography (ethyl acetate:light petroleum ether solvent system) to yield OCH₃ trimer (**6**); ¹H NMR (400 MHz, CDCl₃) δ = 7.80 - 7.70 (m, 4 H), 7.02 (s, 4 H), 6.99 - 6.93 (m, 4 H), 4.17 (t, *J* = 7.0 Hz, 4 H), 2.92 (t, *J* = 7.1 Hz, 4 H); ¹³C NMR (100 MHz, CDCl₃) δ = 163.7, 134.9, 129.9, 129.0, 114.4, 70.2, 55, 7, 34.9 chemical shift in ppm.

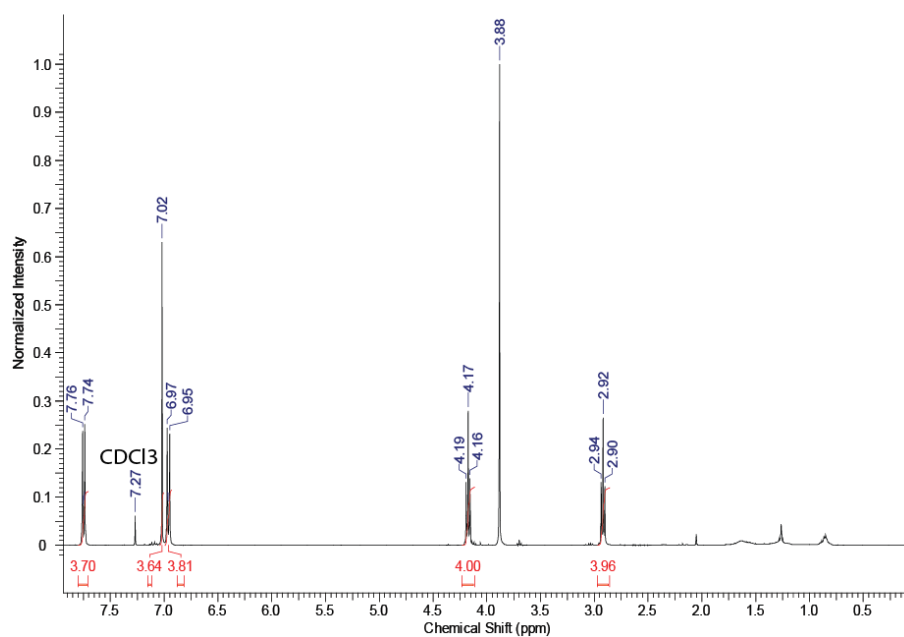


Figure 4.44. ¹H NMR of 1,4-phenylenebis(ethane-2,1-diyl) bis(4-methoxybenzenesulfonate).

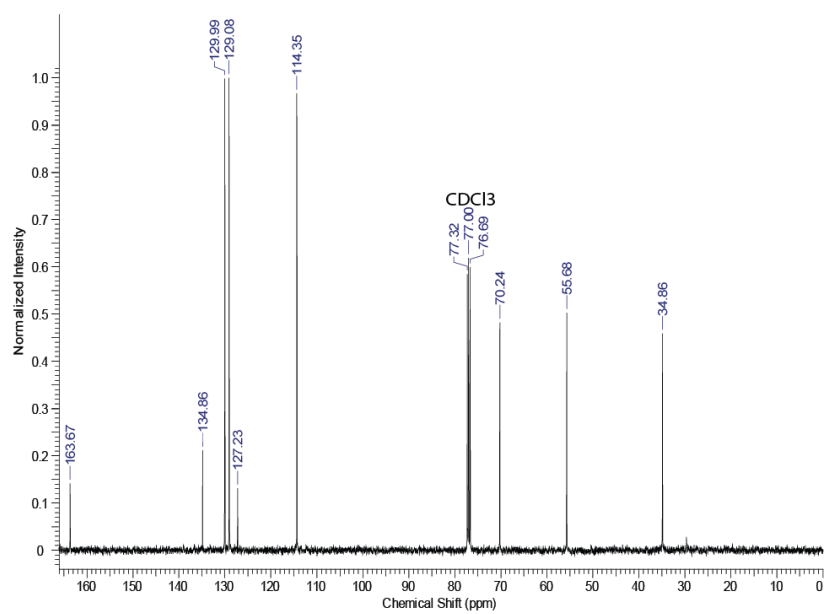


Figure 4.45. ^{13}C NMR of 1,4-phenylenebis(ethane-2,1-diyl) bis(4-methoxybenzenesulfonate).

X-ray Crystallography: Single crystal structure of all compounds were determined by measuring X-ray intensity data on a Bruker SMART APEX II single crystal X-ray CCD diffractometer having graphite-monochromatised Mo-K α ($\lambda = 0.71073$ Å) radiation. The X-ray generator was operated at 50 kV and 30 mA. A preliminary set of cell constants and an orientation matrix were calculated from total 36 frames. The optimized strategy used for data collection consisted different sets of φ and ω scans with 0.5° steps in φ/ω . Data were collected keeping the sample-to-detector distance fixed at 5.00 cm. The X-ray data acquisition was monitored by APEX2 program suit. All the data were corrected for Lorentz-polarization and absorption effects (Multi-scan) using SAINT and SADABS programs integrated in APEX2 package. The structures were solved by direct methods and refined by full matrix least squares, based on F^2 , using SHELX-97. Molecular diagrams were generated using ORTEP-3 and Mercury programs. Geometrical calculations were performed using SHELXTL and PLATON. The H-atoms for the compounds **1**, **2**, **3**, **4**, **5**, **6** were placed in idealized positions however with different C-H distances (C-H = 0.95 Å for the phenyl H atoms, C-H = 0.99 Å for the methyl H-atoms) and constrained to ride on their parent atoms [$U_{\text{iso}}(\text{H}) = 1.2 U_{\text{eq}}(\text{C})$].

Table 4.2. Crystallographic data table

Crystal Data	1 (NO ₂)	6 (OCH ₃)	2 (CN)
Formula	C ₂₂ H ₂₀ N ₂ O ₁₀ S ₂	C ₂₄ H ₂₆ O ₈ S ₂	C ₂₄ H ₂₀ N ₂ O ₆ S ₂
M _r	536.52	506.57	496.54
Crystal Size, mm	0.190 x 0.130 x 0.060	0.210 x 0.100 x 0.060	0.160 x 0.090 x 0.050
Temp. (K)	150(2)	150(2)	150(2)
Crystal Syst.	Triclinic	Monoclinic	Monoclinic
Space Group	<i>P</i> -1	<i>P</i> 2 ₁ /c	<i>P</i> 2 ₁ /c
<i>a</i> /Å	6.8905(6)	13.5900(9)	17.8710(11)
<i>b</i> /Å	9.2502(8)	5.7869(4)	8.0377(4)
<i>c</i> /Å	10.3112(9)	16.2304(12)	8.1470(5)
α°	111.037(5)	90	90
β°	106.466(5)	114.045(4)	99.262(4)
γ°	98.777(5)	90	90
<i>V</i> /Å ³	564.01(9)	1165.66(14)	1154.99(12)
<i>Z</i>	1	2	2
<i>D</i> _{calc} /g cm ⁻³	1.580	1.443	1.428
<i>m</i> /mm ⁻¹	0.300	0.277	0.275
<i>F</i> (000)	278	532	516
<i>Ab. Correct.</i>	multi-scan	multi-scan	multi-scan
<i>T</i> _{min} / <i>T</i> _{max}	0.982/0.954	0.984/0.967	0.986/0.971
2 θ _{max}	50	50	50
Total reflns.	8268	12413	7061
uniquereflns.	1948	2044	2039
<i>h, k, l</i> (min, max)	(-8, 8), (-10, 10), (-11, 12)	(-16, 15), (-6, 6), (-19, 18)	(-21, 17), (-9, 9), (-9, 9)
<i>R</i> _{int}	0.0363	0.0499	0.0751
No. of para	163	155	154
<i>R</i> 1 [<i>I</i> > 2 σ (<i>I</i>)]	0.0367	0.0484	0.0666
<i>wR</i> 2 [<i>I</i> > 2 σ (<i>I</i>)]	0.1018	0.1064	0.1086
<i>R</i> 1 [all data]	0.1074	0.0550	0.1035
<i>wR</i> 2 [all data]	= 0.1101	0.1096	0.1194
goodness-of-fit	1.101	1.148	1.127
$\Delta\rho_{\max}, \Delta\rho_{\min}$ (eÅ ⁻³)	+0.435, -0.511	+0.208, -0.356	+0.253, -0.413

Crystal Data	5(H)	3 (Cl)	4(Br)
Formula	C ₂₂ H ₂₂ O ₆ S ₂	C ₂₂ H ₂₀ Cl ₂ O ₆ S ₂	C ₂₂ H ₂₀ Br ₂ O ₆ S ₂
M _r	446.52	515.40	604.32
Crystal Size, mm	0.35 x 0.23 x 0.10	0.18 x 0.09 x 0.05	0.32 x 0.11 x 0.08
Temp. (K)	150(2)	150(2)	150(2)
Crystal Syst.	Monoclinic	Triclinic	Triclinic
Space Group	C2/c	P-1	P-1
a/Å	20.8735(14)	9.3972(5)	11.3983(5)
b/Å	8.8065(6)	11.1752(6)	11.7170(6)
c/Å	15.1007(12)	12.3656(6)	14.3146(6)
α^0	90	106.723(2)	82.300(2)
β^0	131.181(2)	90.281(2)	74.677(2)
γ^0	90	114.375(2)	67.317(2)
V/Å ³	2089.2(3)	1121.36(10)	1700.09(13)
Z	4	2	3
D _{calc} /g cm ⁻³	1.420	1.526	1.771
m/mm ⁻¹	0.292	0.514	3.798
F(000)	936	532	906
Ab. Correct.	multi-scan	multi-scan	multi-scan
T _{min} /T _{max}	0.9714/0.9047	0.9748/0.9132	0.7509/0.3762
2 θ _{max}	50	50	50
Total reflns.	5680	11481	17122
uniquereflns.	1838	3942	5972
h, k, l (min, max)	(-24, 24), (-10, 10), (-17, 17)	(-11, 10), (-13, 13), (-14, 14)	(-13, 13), (-13, 12), (-16, 17)
R _{int}	0.0169	0.0173	0.0325
No. of para	136	289	433
RI [I > 2 σ (I)]	0.0311	0.0303	0.0286
wR2 [I > 2 σ (I)]	0.0808	0.0756	0.0600
RI [all data]	0.0343	0.0336	0.0363
wR2 [all data]	0.0834	0.0778	0.0610
goodness-of-fit	1.053	1.060	1.495
$\Delta\rho_{\max}, \Delta\rho_{\min}$ (eÅ ⁻³)	+0.258, -0.369	+0.391, -0.409	+0.480, -0.406

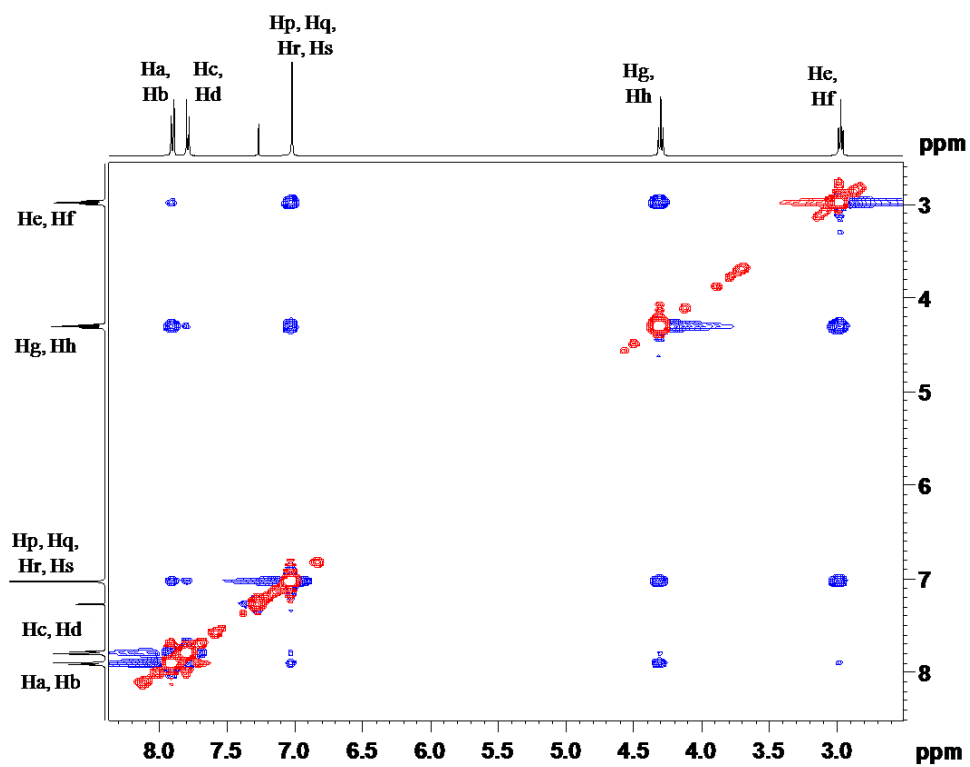


Figure 4.48. 2D NOESY spectra of trimer 2.

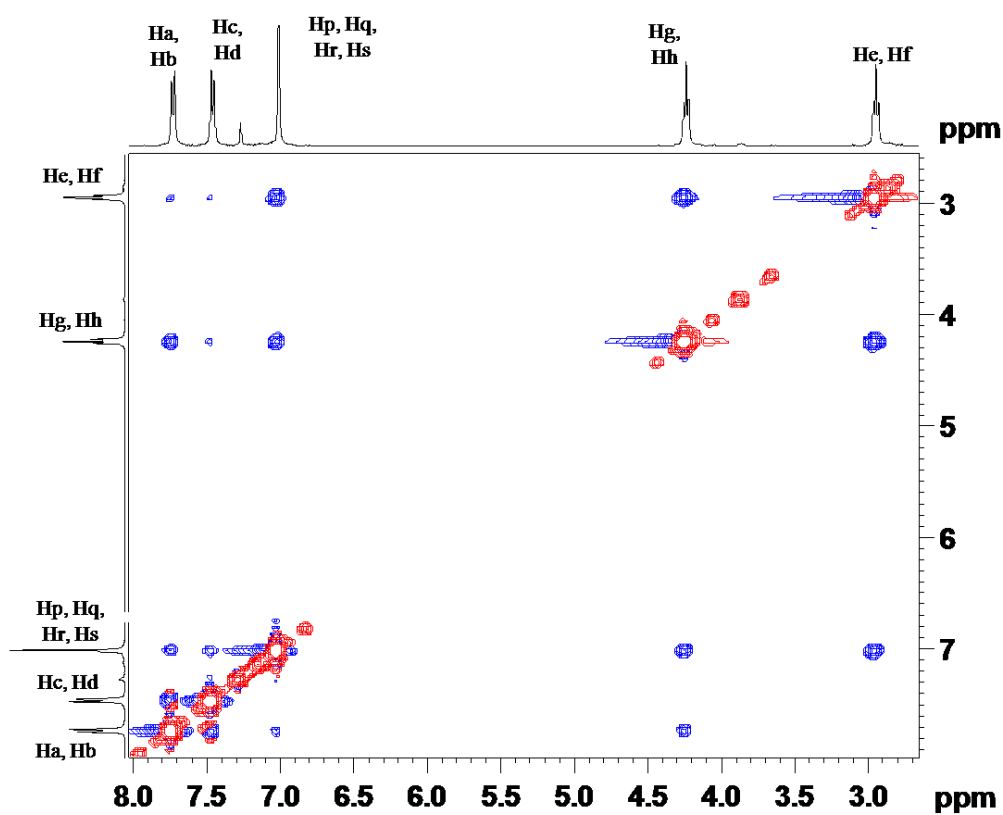


Figure 4.49. 2D NOESY spectra of trimer 3.

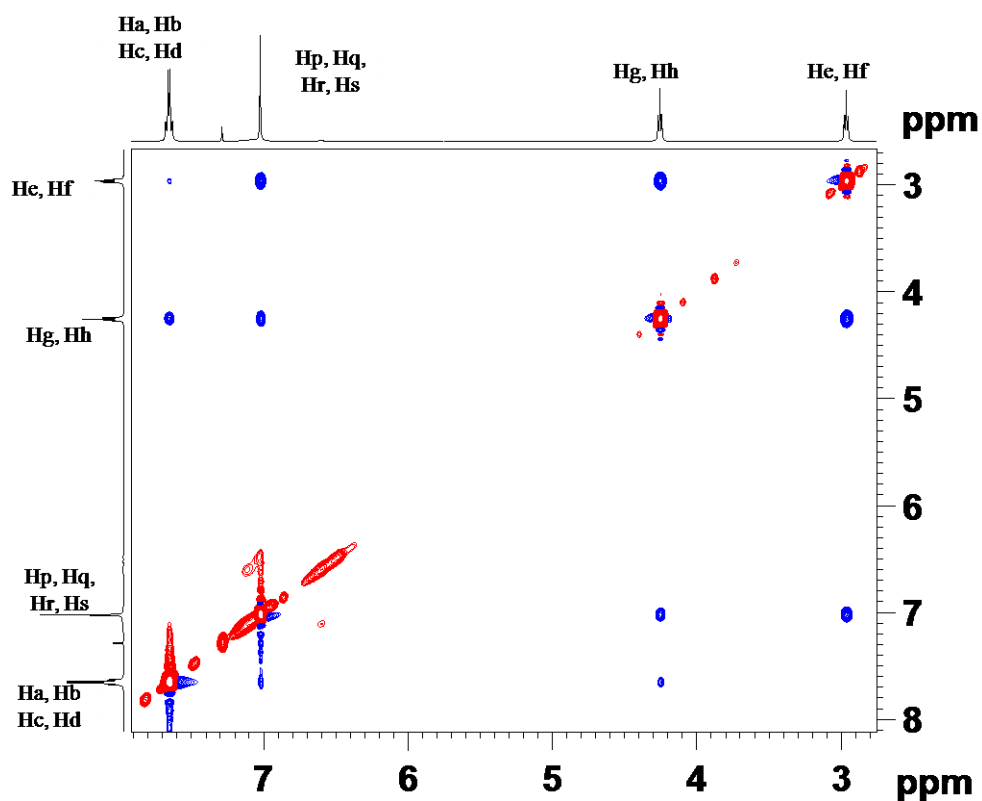


Figure 4.50. 2D NOESY spectra of trimer 4.

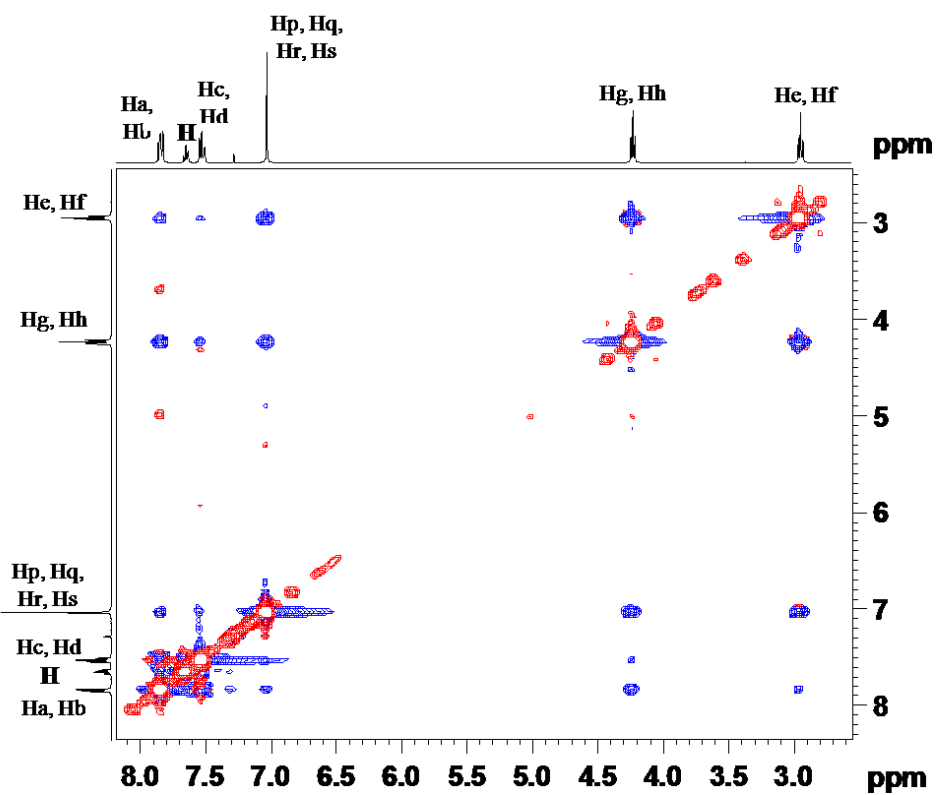


Figure 4.51. 2D NOESY spectra of trimer 5.

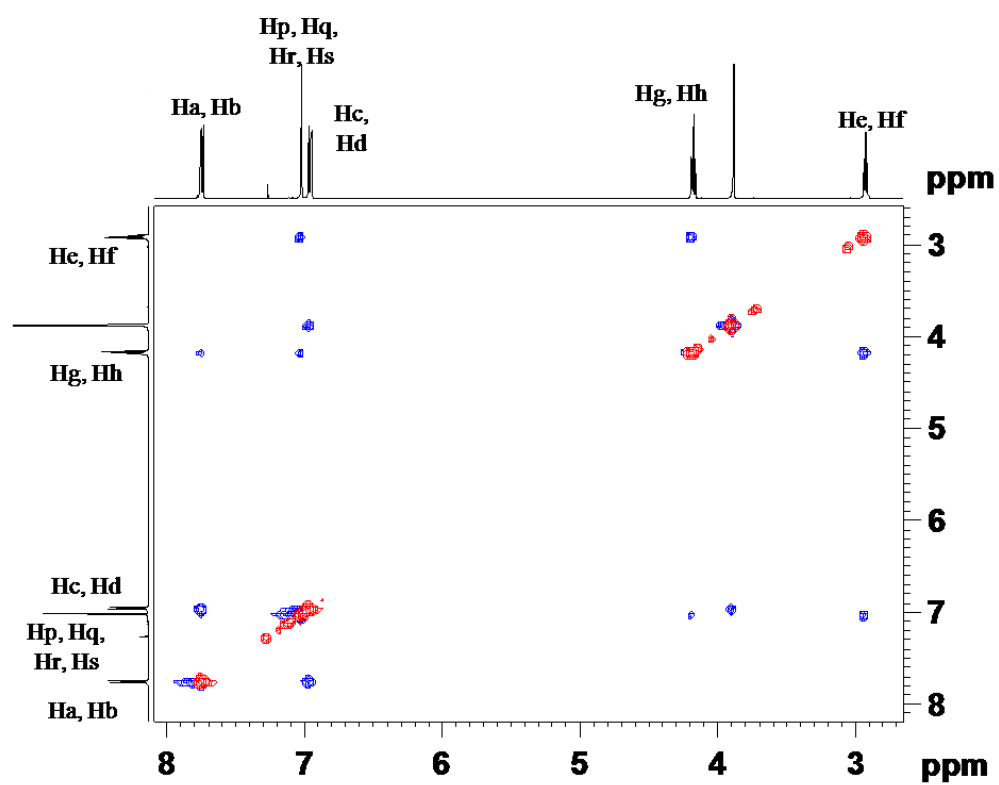


Figure 4.52. 2D NOESY spectra of trimer 6.

References:

1. G. B. McGaughey, M. Gagné and A. K. Rappé, *J. Bio. Chem.*, 1998, **273**, 15458-15463.
2. H.-J. Huang, K.-J. Lee, H. W. Yu, C.-Y. Chen, C.-H. Hsu, H.-Y. Chen, F.-J. Tsai and C. Y.-C. Chen, *J. Biomol. Struct. Dyn.*, 2010, **28**, 23-37.
3. T. Caronna, R. Liantonio, T. A. Logothetis, P. Metrangolo, T. Pilati and G. Resnati, *J. Am. Chem. Soc.*, 2004, **126**, 4500-4501.
4. A. Le Goff, F. Moggia, N. Debou, P. Jegou, V. Artero, M. Fontecave, B. Jousselme and S. Palacin, *J. of Electroanalytic. Chem.*, 2010, **641**, 57-63.
5. S. Burley and G. Petsko, *Science*, 1985, **229**, 23-28.
6. C. A. Frederick, L. D. Williams, G. Ughetto, G. A. Van der Marel, J. H. Van Boom, A. Rich and A. H. Wang, *Biochemistry*, 1990, **29**, 2538-2549.
7. T. Klabunde and G. Hessler, *Chembiochem*, 2002, **3**, 928-944.
8. R. L. Haining, J. P. Jones, K. R. Henne, M. B. Fisher, D. R. Koop, W. F. Trager and A. E. Rettie, *Biochemistry*, 1999, **38**, 3285-3292.
9. J. Rebek Jr, B. Askew, P. Ballester, C. Buhr, S. Jones, D. Nemeth and K. Williams, *JACS*, 1987, **109**, 5033-5035.
10. E. De Clercq, *Nature Rev. Drug Discov.*, 2002, **1**, 13-25.
11. S. M. Kerwin, *Curr. Pharm. Des.*, 2000, **6**, 441-471.
12. Sponer, H. Gabb, J. Leszczynski and P. Hobza, *Biophys. J.*, 1997, **73**, 76-87.
13. G. S. Papaefstathiou, A. Tsohos, C. P. Raptopoulou, A. Terzis, V. Psycharis, D. Gatteschi and S. P. Perlepes, *Cryst. Growth. Des.*, 2001, **1**, 191-194.
14. J. L. Garcia Ruano, J. Alemán, I. Alonso, A. Parra, V. Marcos and J. Aguirre, *Chem.–Eur. J.*, 2007, **13**, 6179-6195.
15. F. Tournus, S. Latil, M. Heggie and J.-C. Charlier, *Phys. Rev. B*, 2005, **72**, 075431.
16. C. A. Hunter and J. K. Sanders, *JACS*, 1990, **112**, 5525-5534.
17. F. Cozzi, M. Cinquini, R. Annuziata and J. S. Siegel, *J. Am. Chem. Soc.*, 1993, **115**, 5330-5331.
18. S. L. Cockroft, C. A. Hunter, K. R. Lawson, J. Perkins and C. J. Urch, *J. Am. Chem. Soc.*, 2005, **127**, 8594-8595.
19. C. A. Hunter, *Angew. Chemie Int. Ed.*, 1993, **32**, 1584-1586.

20. S. L. Cockroft, J. Perkins, C. Zonta, H. Adams, S. E. Spey, C. M. Low, J. G. Vinter, K. R. Lawson, C. J. Urch and C. A. Hunter, *Org. Biomol. Chem.*, 2007, **5**, 1062-1080.
21. C. R. Martinez and B. L. Iverson, *Chem. Sci.*, 2012, **3**, 2191-2201.
22. M. J. Rashkin and M. L. Waters, *J. Am. Chem. Soc.*, 2002, **124**, 1860-1861.
23. M. O. Sinnokrot and C. D. Sherrill, *J. Phys. Chem. A*, 2003, **107**, 8377-8379.
24. A. L. Ringer, M. O. Sinnokrot, R. P. Lively and C. D. Sherrill, *Chem. Eur. J.*, 2006, **12**, 3821-3828.
25. M. O. Sinnokrot and C. D. Sherrill, *J. Phys. Chem. A*, 2006, **110**, 10656–10668.
26. S. E. Wheeler and K. N. Houk, *J. Am. Chem. Soc.*, 2008, **130**, 10854–10855.
27. M. A. Spackman and P. G. Byrom, *Chem. Phys. Lett.*, 1997, **267**, 215-220.
28. J. Hwang, P. Li, W. R. Carroll, M. D. Smith, P. J. Pellechia, and K. D. Shimizu, *J. Am. Chem. Soc.*, 2014, **136**, 14060-14067.

Summary

In summary, we constructed conformationally flexible molecular architecture comprising rigid moieties interconnected by 1) amides (carboxamide/sulfonamide) or esters (carboester/sulfoester) and 2) flexible short chain spacers (-CH₂-CH₂-or C-NH-C-). We studied their bioactive (DNA hypomethylation, **Chapter 1**), sensing (anion sensing, acid sensing, **Chapters 2A** and **2B** respectively) and polymorphic properties (stacking vs. unstacked polymorphs, **Chapters 3**). The derivatives of lead compound were systematically designed in order to investigate the mechanistic basis of their properties. In chapter **1**, the lead compound was chosen as procainamide drug whose conformationally flexible side chain derivatives were used for structure property relation. The binding affinity of these derivatives towards guest i.e. CpG rich DNA was used to evaluate their differential DNA hypomethylating effect. In chapter **2A**, conformationally flexible Cu(II) coordination complex displaying metamorphic property in three dimensional packing architecture was constructed as host. The guest (anions and solvent) exchange ability of the complex was investigated in solid state to elucidate the mechanism and exploring its sensing applications. In chapter **2B**, the shift in the absorption and emission properties of designed benzophenones-quinoline conjugates (host) were used for studying their application for solid state detection of acids vapors and chemical warfare agent. Differential reactivity and turn-on response of the derivatives were used to investigate the putative mechanism of their action and lead improvement. In chapter **3**, alternating electron rich (phenyl/pyridine) and electron poor (*p*-nitro benzene) aromatic units joined together with sulfonamide/sulfoester containing flexible hinge (host) were designed for studying their conformational polymorphism (stacking vs. non-stacking) in solid state in the presence of additive. The study unravels the nucleation funnel of sulfonamide/sulfoester containing compounds possessing varying H-bonding propensities and the role of additive effect at prenucleation clustering. We further extended our research by synthesizing the aromatic stacking trimers (**chapter 4**) to unravel the mystery behind the 1) effect of substituent on stacking geometry in different medium (solution and solid state) and 2) the behavioral pattern and role of substituent during the prenuclei clustering at nucleation process. Finally we put forth new

theories for explaining the role of substituent for stabilizing the $\pi\cdots\pi$ stacking interaction in the solution and the solid state. The stacking interactions in solution are explained by combining the electrostatic polarization and dispersion terms whereas the stacking interaction in solid state is described by substituent-substituent interaction model. The atomic coordinates, anisotropic thermal parameters, bond length, bond angle and torsion angle of all the compounds are depicted in the form of tables along with the cif files that are provided in the CD.

Future Scope

In this research work we employed the conformational flexibility as effective tool to design the compounds for studying their structure-property relationship. Moreover, the studies revealed the putative mechanism as well as the strategy for lead improvement. The outcome and roadmap of the research work can be used to address and investigate the unanswered queries. The sulphonamide derivatives of the procainamide studied in chapter 1, can be further synthesized for studying the effect of enhanced conformational flexibility of sulphonamide group over carboxamide moiety for the DNA binding and DNA hypomethylating effect. In chapter 2A, the 2D head-to-tail arrangement of side-chains in the crystal structure of ligand provides suitable geometry for studying the (2 + 2) cycloaddition reaction in the solid state. 1D polymerization may further improve the stability of the sensing material. In chapter 2B, the quinolone-benzophenone conjugates used in our study can be derivatised further to enhance the turn-on response and LOD (limit of detection). In chapter 3, the effect of pyrazinamide as an additive can be further investigated on other sulfonamide and sulfoester containing compounds to prepare the library. The polymeric surface functionalized with interacting fragment of pyrazinamide can be constructed to explore the elusive polymorphs of medicinally important sulfonamides and sulfoesters. The sulphonamide analogs of the sulfoester trimers studied in chapter 4 can be synthesized to investigate the effect of sulphonamide group during the nucleation funnel of stacking trimers. The trimers can be further extended to penta, hepta and deodecamer to generate the stacking assemblies of variable lengths. These stacking aedemers have immense applications in photovoltaics and sensing.

List of papers and patents published (related to thesis)

1. **Rupesh L. Gawade**, D. K. Chakravarty, A. Kotmale, E. Sangtani, P. V. Joshi, A. Ahmed, M. V. Mane, S. Das, K. Vanka, P. R. Rajamohanan, V. G. Puranik, and R. G. Gonnade, "Additive Mediated *Syn-Anti* Conformational Tuning at Nucleation to Capture Elusive Polymorphs: Remarkable Role of Extended π -Stacking Interactions in Driving the Self-Assembly," *Cryst. Growth Des.*, 2016, **16**, 2416–2428.
2. **Rupesh L. Gawade**, D. K. Chakravarty, J. Debgupta, E. Sangtani, S. Narwade, R. G. Gonnade, V. G. Puranik, and D. D. Deobagkar, "Comparative study of dG affinity vs. DNA methylation modulating properties of side chain derivatives of procainamide: insight into its DNA hypomethylating effect," *RSC Adv.*, 2016, **6**, 5350–5358.
3. **Rupesh L. Gawade**, R. G. Gonnade and V. G. Puranik, "Metal coordination complex for detection of vapors and anions and process for the preparation thereof " 2016, WO2016056027 A1

List of conferences attended

1. Delivered oral presentation at mini symposium "The Wonderland of Molecular Structures through the Looking Glass of X-Ray Crystallography" held at the CSIR-National Chemical Laboratory, Pune 2013.
2. Presented paper "B-Z transition inhibitors and DNA hypomethylating agent " held at C-DAC Pune, 2013.
3. Presented paper at ICSIC (International conference of structural and inorganic chemistry) "Additive mediated *syn-anti* conformational tuning at nucleation " held at IISER Pune, 2014.

List of papers not related to thesis (crystal structure analysis)

1. Vijayadas, Kuruppanthara N., Hilda C. Davis, Amol S. Kotmale, **Rupesh L. Gawade**, Vedavati G. Puranik, Pattuparambil R. Rajamohanam, and Gangadhar J. Sanjayan, *Chem. Comm.*, 2012, **48**, 9747-9749.
2. Ramesh, Veera VE, Sangram S. Kale, Amol S. Kotmale, **Rupesh L. Gawade**, Vedavati G. Puranik, P. R. Rajamohanam, and Gangadhar J. Sanjayan, *Org. Lett.*, 2013, **15**, 1504-1507.
3. Bhosale, Shrikar M., **Rupesh L. Gawade**, Vedavati G. Puranik, and Radhika S. Kusrkar, *Tet. Lett.*, 2012, **53**, 2894-2896.
4. Priya, Gowri, Amol S. Kotmale, **Rupesh L. Gawade**, Deepti Mishra, Sourav Pal, Vedavati G. Puranik, Pattuparambil R. Rajamohanam, and Gangadhar J. Sanjayan, *Chem. Comm.*, 2012, **48**, 8922-8924.
5. Thorat, Vijaykumar H., Tukaram S. Ingole, Kuruppanthara N. Vijayadas, Roshna V. Nair, Sangram S. Kale, Veera VE Ramesh, Hilda C. Davis, **Rupesh L. Gawade** and Gangadhar J. Sanjayan, *Eur. J. Org. Chem.*, 2013, **17**, 3529-3542.
6. Kanhe, Nilesh S., Ashok B. Nawale, **Rupesh L. Gawade**, Vedavati G. Puranik, Sudha V. Bhoraskar, Asoka K. Das, and Vikas L. Mathe, *J. Cryst. Growth*, 2012, **339**, 36-45.
7. Chavan, Subhash P., Kishor R. Harale, Vedavati G. Puranik, and **Rupesh L. Gawade**, *Tet. Lett.*, 2012, **53**, 2647-2650.
8. Bhosale, Shrikar M., Aadil A. Momin, **Rupesh L. Gawade**, Vedavati G. Puranik, and Radhika S. Kusrkar, *Tet. Lett.*, 2012, **53**, 5327-5330.
9. Vijayadas, Kuruppanthara N., Roshna V. Nair, **Rupesh L. Gawade**, Amol S. Kotmale, Panchami Prabhakaran, Rajesh G. Gonnade, Vedavati G. Puranik, Pattuparambil R. Rajamohanam, and Gangadhar J. Sanjayan, *Org. Biomol. Chem.* 2013, **11**, 8348-8356.
10. Kale, Sangram S., Shrikant M. Kunjir, **Rupesh L. Gawade**, Vedavati G. Puranik, P. R. Rajamohanam, and Gangadhar J. Sanjayan, *Chem. Comm.*, 2014, **50**, 2886-2888.

-
11. Nair, Roshna V., Amol S. Kotmale, Snehal A. Dhokale, **Rupesh L. Gawade**, Vedavadi G. Puranik, Pattuparambil R. Rajamohanan, and Gangadhar J. Sanjayan, *Org. Biomol. Chem.*, 2014, **12**, 774-782.
 12. Vangala, Madhuri, Snehal A. Dhokale, **Rupesh L. Gawade**, Rajamohanan R. Pattuparambil, Vedavati G. Puranik, and Dilip D. Dhavale, *Org. Biomol. Chem.*, 2013, **11**, 6874-6878.
 13. Sangtani, Ekta, Sanjay K. Sahu, Shridhar H. Thorat, **Rupesh L. Gawade**, Kunal K. Jha, Parthapratim Munshi, and Rajesh G. Gonnade, *Cryst. Growth Des.*, 2015, **15**, 5858-5872.
 14. Kale, Sangram S., Gowri Priya, Amol S. Kotmale, **Rupesh L. Gawade**, Vedavati G. Puranik, P. R. Rajamohanan, and Gangadhar J. Sanjayan, *Chem. Comm.*, 2013, **49**, 2222-2224.
 15. Baravkar, Sachin B., Arup Roy, **Rupesh L. Gawade**, Vedavati G. Puranik, and Gangadhar J. Sanjayan, *Syn. Comm.*, 2014, **44**, 2955-2960.
 16. D Dindulkar, S, Ira Bhatnagar, **Rupesh L. Gawade**, Vedavati G. Puranik, Se-Kwon Kim, Dong Hyun Anh, Paramasivam Parthiban, and Yeon Tae Jeong, *J. Chem. Sci.*, 2014, **126**, 861-873.
 17. Roy, A., Kotmale, A. S., **Rupesh L. Gawade**, Puranik, V. G., Rajamohanan, P. R. and Gangadhar J. Sanjayan. *RSC Adv.*, 2014, **4**, 13018-13025.
 18. Ingole, Tukaram S., Kuruppanthara N. Vijayadas, K. N. Chaitanya, Amol S. Kotmale, **Rupesh L. Gawade**, R. G. Gonnade, P. R. Rajamohanan, and Gangadhar J. Sanjayan, *Eur. J. Org. Chem.*, 2016, **7**, 1380-1388.